

# **EXPERIMENTAL INVESTIGATIONS, MODELING, AND ANALYSES OF HIGH-TEMPERATURE DEVICES FOR SPACE APPLICATIONS**

## **Part 2 of 2**

**Jean-Michel Tournier  
Mohamed S. El-Genk  
Lianmin Huang**

**Institute for Space and Nuclear Power Studies  
Department of Chemical and Nuclear Engineering  
University of New Mexico  
Farris Engineering Center, Room 239  
Albuquerque, NM 87131**

**January 1999**

**Final Report**

**19990817 075**

**APPROVED FOR PUBLIC RELEASE; DISTRIBUTION IS UNLIMITED.**



**AIR FORCE RESEARCH LABORATORY  
Space Vehicles Directorate  
3550 Aberdeen Ave SE  
AIR FORCE MATERIEL COMMAND  
KIRTLAND AIR FORCE BASE, NM 87117-5776**


Using Government drawings, specifications, or other data included in this document for any purpose other than Government procurement does not in any way obligate the U.S. Government. The fact that the Government formulated or supplied the drawings, specifications, or other data, does not license the holder or any other person or corporation; or convey any rights or permission to manufacture, use, or sell any patented invention that may relate to them.

This report has been reviewed by the Public Affairs Office and is releasable to the National Technical Information Service (NTIS). At NTIS, it will be available to the general public, including foreign nationals.


If you change your address, wish to be removed from this mailing list, or your organization no longer employs the addressee, please notify AFRL/VSDV, 3550 Aberdeen Ave SE, Kirtland AFB, NM 87117-5776.

Do not return copies of this report unless contractual obligations or notice on a specific document requires its return.

This report has been approved for publication.

  
Clay S. Mayberry  
Project Manager

FOR THE COMMANDER

  
CHRISTOPHER N. BURNS, Lt Col, USAF  
Chief, Vehicles Technologies Branch

  
CHRISTINE M. ANDERSON, SES  
Director, Space Vehicles

# REPORT DOCUMENTATION PAGE

Form Approved  
OMB No. 074-0188

Public reporting burden for this collection of information is estimated to average 1 hour per response, including the time for reviewing instructions, searching existing data sources, gathering and maintaining the data needed, and completing and reviewing this collection of information. Send comments regarding this burden estimate or any other aspect of this collection of information, including suggestions for reducing this burden to Washington Headquarters Services, Directorate for Information Operations and Reports, 1215 Jefferson Davis Highway, Suite 1204, Arlington, VA 22202-4302, and to the Office of Management and Budget, Paperwork Reduction Project (0704-0188), Washington, DC 20503

1. AGENCY USE ONLY (Leave blank)		2. REPORT DATE January 1999	3. REPORT TYPE AND DATES COVERED Final; June 1996 - December 1998	
4. TITLE AND SUBTITLE Experimental Investigations, Modeling, and Analyses of High-Temperature Devices for Space Applications Part 2 of 2			5. FUNDING NUMBERS C: F29601-97-K-0123 PE: 63401F PR: 682J TA: TG WU: 18	
6. AUTHOR(S) Jean-Michel Tournier Mohamed S. El-Genk Lianmin Huang				
7. PERFORMING ORGANIZATION NAME(S) AND ADDRESS(ES) University of New Mexico Institute for Space and Nuclear Power Studies Department of Chemical and Nuclear Engineering Farris Engineering Center Rm 239 Albuquerque, New Mexico 87131			8. PERFORMING ORGANIZATION REPORT NUMBER	
9. SPONSORING / MONITORING AGENCY NAME(S) AND ADDRESS(ES) Air Force Research Laboratory 3550 Aberdeen Ave. SE Kirtland AFB, NM 87117-5776			10. SPONSORING / MONITORING AGENCY REPORT NUMBER AFRL-VS-PS-TR-1998-1108, Part 2 of 2	
11. SUPPLEMENTARY NOTES				
12a. DISTRIBUTION / AVAILABILITY STATEMENT Approved for public release; distribution is unlimited				12b. DISTRIBUTION CODE
13. ABSTRACT (Maximum 200 Words) The Institute of Space and Nuclear Power Studies at the University of New Mexico has developed a computer simulation of cylindrical geometry alkali metal thermal-to-electric converter cells using a standard Fortran 77 computer code. The objective and use of this code was to compare the experimental measurements with computer simulations, upgrade the model as appropriate, and conduct investigations of various methods to improve the design and performance of the devices for improved efficiency, durability, and longer operational life-time. The Institute of Space and Nuclear Power Studies participated in vacuum testing of PX series alkali metal thermal-to-electric converter cells and developed the alkali metal thermal-to-electric converter Performance Evaluation and Analysis Model. This computer model consisted of a sodium pressure loss model, a cell electrochemical and electric model, and a radiation/conduction heat transfer model. The code closely predicted the operation and performance of a wide variety of PX series cells which led to suggestions for improvements to both lifetime and performance. The code provides valuable insight into the operation of the cell, predicts parameters of components within the cell, and is a useful tool for predicting both the transient and steady state performance of systems of cells.				
14. SUBJECT TERMS AMTEC, Solar Thermal AMTEC, APEAM, AMTEC System, computer modeling, Spacecraft Power, Advanced Solar, Radioisotope Power Source				15. NUMBER OF PAGES 270
				16. PRICE CODE
17. SECURITY CLASSIFICATION OF REPORT Unclassified	18. SECURITY CLASSIFICATION OF THIS PAGE Unclassified	19. SECURITY CLASSIFICATION OF ABSTRACT Unclassified	20. LIMITATION OF ABSTRACT UL	

NSN 7540-01-280-5500

Standard Form 298 (Rev. 2-89)  
Prescribed by ANSI Std. Z39-18  
298-102

## 10. EVALUATION OF HEAT LOSSES IN PX-SERIES CELL TESTS

The conversion efficiency of an AMTEC cell is an important performance parameter. In the AFRL single-cell vacuum tests, electric power to the heater and electric power output of the cell are measured. However, to evaluate the cell's conversion efficiency using experimental data, the thermal power input to the cell's hot side must be known. This chapter describes a number of calibration experiments designed in an attempt to evaluate the heat losses in the heater block of the cell and the surrounding insulation, identify critical loss paths, and improve the experimental setup at AFRL.

One method of obtaining the temperature of the Boro-electric heater on the cell's hot side was to measure the electric voltage and current of the heater and deduce its electric resistance. The electric resistivity of the wire is a function of temperature, therefore the average heater temperature can be deduced from the value of the heater resistance. For this purpose, a resistivity calibration experiment was designed to measure the electrical resistance of the Boro-electric heater as a function of temperature (Section 10.1).

An indirect-heat-loss measurement technique was devised to evaluate the conduction heat losses in the single-cell test from the measured temperature profiles along the insulation surface and the cell wall. A two-dimensional, transient heat conduction model was developed (Section 10.2), and benchmarked (Section 10.3), using a number of sample thermal problems with known analytical solution. This 2-D heat conduction model was then used in conjunction with temperature measurements to predict the heat losses in the alumina powder insulation of the PX-1 series of cells (Section 10.3).

Knowledge of the heat losses and heat flux profiles at the different boundaries of the insulation, and examination of test and model results led to some improvements in the insulation of single-cell setups. Also, based on the results of these experiments, the radiation/conduction heat flow model in APEAM was modified to more accurately mimic and predict the cell wall losses through the insulation package surrounding the cell.

A heater calorimeter experiment was also designed to calibrate the heat losses from the heater's Boron Nitride block (Section 10.5). The heater block was instrumented with 15 K-type shielded thermocouples, and boundary temperature profiles were extrapolated and used in the two-dimensional heat conduction model to calculate the heat losses at the faces of the block. To simulate the actual single-cell test setup, the Boro-electric heater was sandwiched between the BN cylindrical block and the top of the air calorimeter. The heat from the bottom of the cell heater was removed and measured by the calorimeter, which had the shape and dimensions of a typical, 1.25-inch diameter PX-series cell. The heat input to the calorimeter was removed by an impinging air jet inside the confinement.

These calibration experiments and their results are described in details in the following subsections.



## 10.1 BORO-ELECTRIC HEATER RESISTIVITY CALIBRATION EXPERIMENT

One method of obtaining the temperature of the Boro-electric heater on the cell's hot side is to measure the electric voltage and current of the heater and deduce its electric resistance. The electric resistivity of the wire is a function of temperature, therefore the average heater temperature can be deduced from the value of the heater resistance. To this purpose, a resistivity calibration experiment was designed to measure the electrical resistance of the Boro-electric heater as a function of temperature. The heater resistance was easily determined from the measured electrical current and voltage. The surface temperature of the heater was measured in vacuum using both a K-type thermocouple and a fiber optics probe (lightpipe). Results of the calibration experiment are collected in Table 10.1. The difference between the temperatures measured using the thermocouple and fiber optics probe was as large as 100 K for temperatures below 1050 K, with the K-type thermocouple consistently giving a lower reading than the lightpipe. Above 1050 K, the difference between the two methods of measurements decreased with increasing temperature (Table 10.1).

The measured heater resistance was then fitted as a function of temperature (Figures 10.1a, 10.1b and 10.1c) using the following 3 choices of temperatures: measured by the lightpipe; measured by the K-type thermocouple; and the average of these two temperature measurements.

Using the electric resistivity of the heater provided by the manufacturer (Figure 10.2), the geometric factor of the heater (wire length,  $L$  divided by cross-sectional area,  $A$ ) was determined by dividing the heater resistance fit by the fit of the heater resistivity. Results are shown in Figure 10.3. All 3 choices of temperatures gave a fairly consistent value of:

$$L / A = 3.55 \pm 0.17 \mu\text{m}^{-1} (\pm 4.8\%)$$

Unfortunately, measurements of the heater resistance could not lead to accurate evaluation of the heater temperature, because of the relatively small slope of the curve in the temperature range of interest  $> 1000$  K (Figure 10.1c); the uncertainty in the calculated heater temperature was quite large, about  $\pm 40$  K (see Appendix E).

In the following sections, the two-dimensional heat conduction model developed to evaluate the conduction heat losses in the single-cell test insulation package is described. This model was used in conjunction with temperature measurements in the alumina powder insulation of the PX-1 series of cells to predict the heat losses in the test setup.

Table 10.1. Experimental Data Collected in Heater Calibration Experiment.

Voltage (V)	Current (A)	Resistance ( $\Omega$ )	Measured Temperatures ( $^{\circ}\text{C}$ )		
			Lightpipe	K-type TC	Average
22.0	2.16	10.185	598	532	565
23.8	2.40	9.917	646	575	611
28.1	2.98	9.430	750	671	710
29.1	3.10	9.387	773	689	731
30.3	3.28	9.238	798	714	756
31.0	3.38	9.172	811	726	769
32.0	3.51	9.117	828	753	790
32.7	3.60	9.083	834	774	804
33.7	3.75	8.987	843	805	824
34.7	3.88	8.943	854	821	838
35.7	4.00	8.925	864	837	851
41.5	4.78	8.682	918	909	913

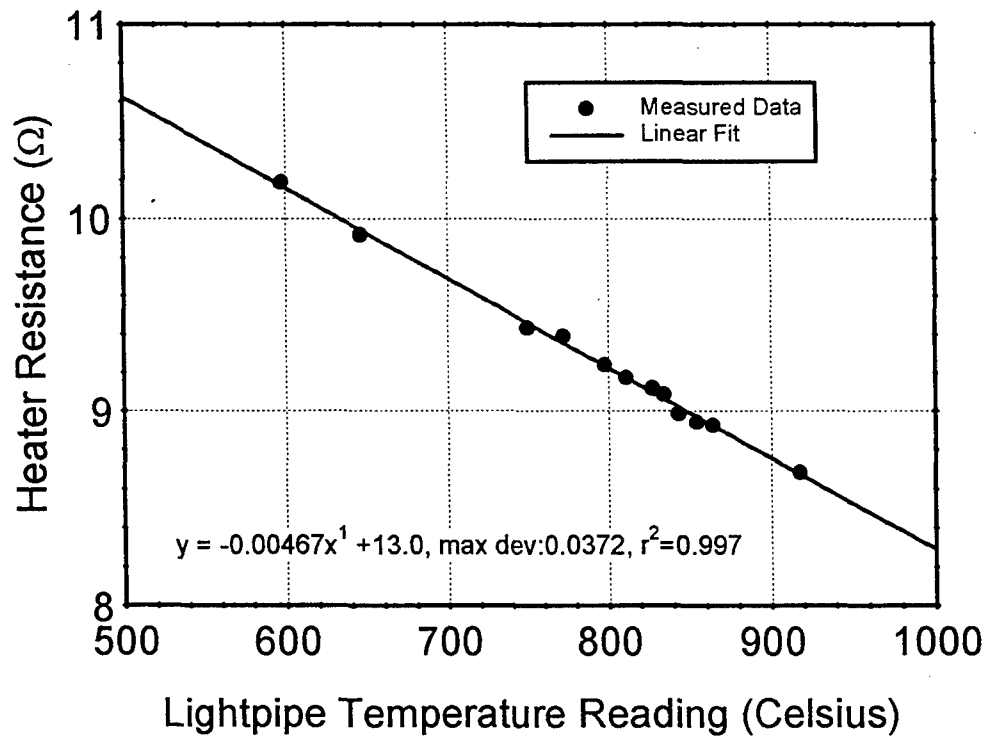


Figure 10.1a. Heater Resistance versus Lightpipe Temperature Reading.

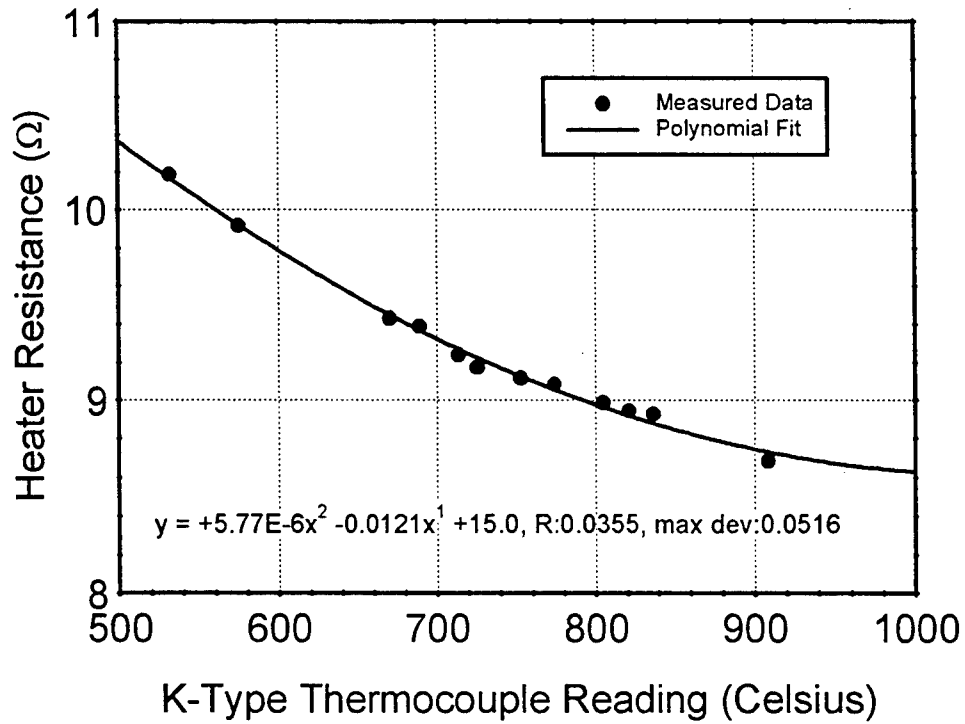


Figure 10.1b. Heater Resistance versus K-Type Thermocouple Reading.

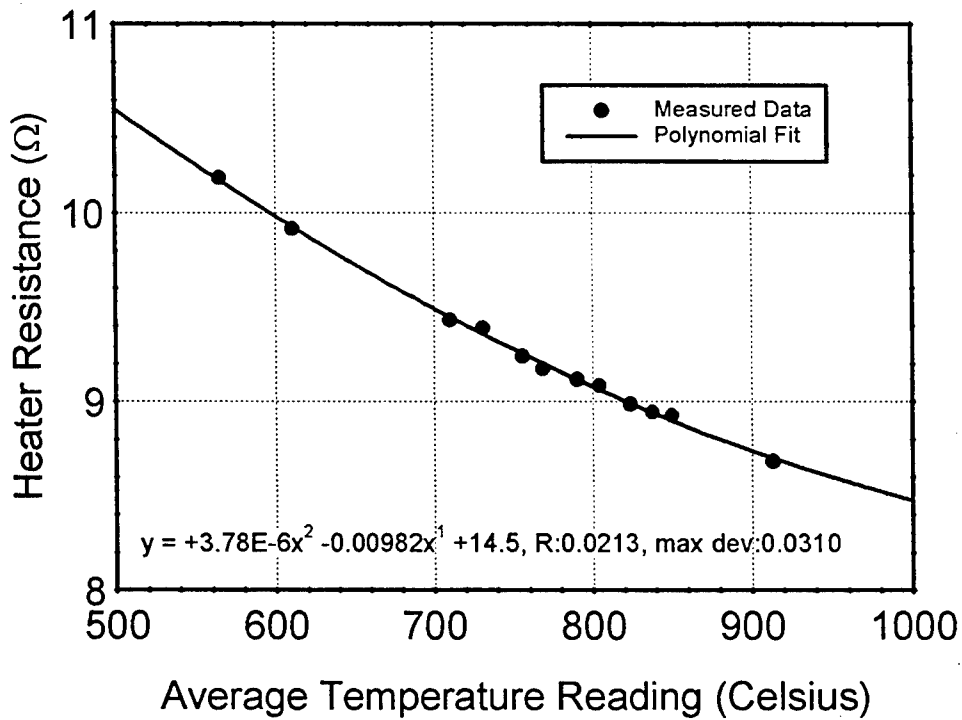


Figure 10.1c. Heater Resistance versus Average Temperature Reading.

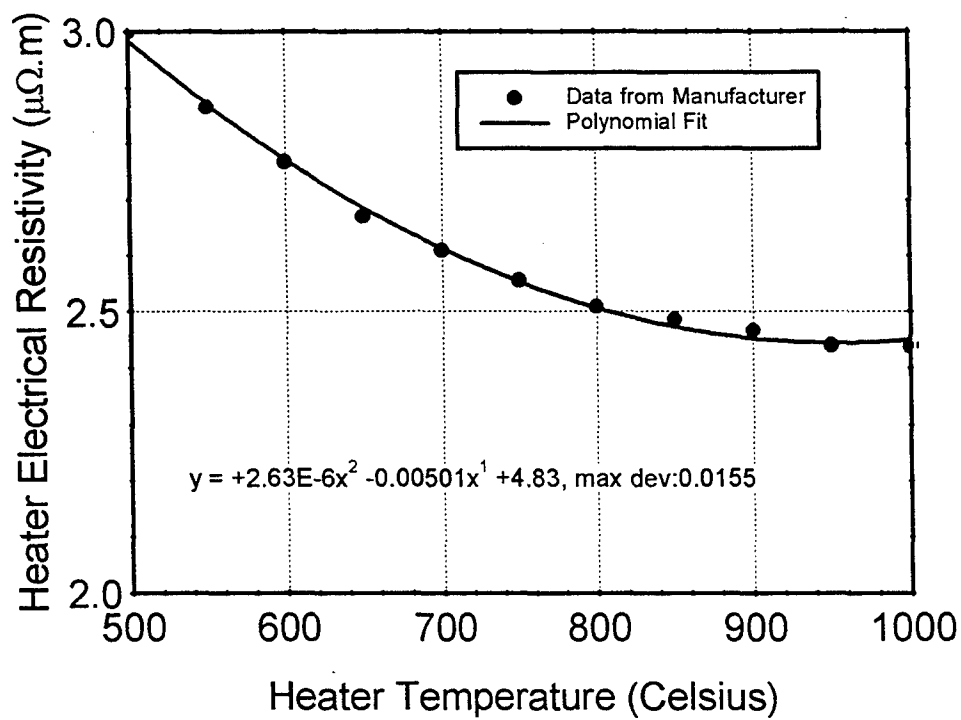


Figure 10.2. Heater Electrical Resistivity.

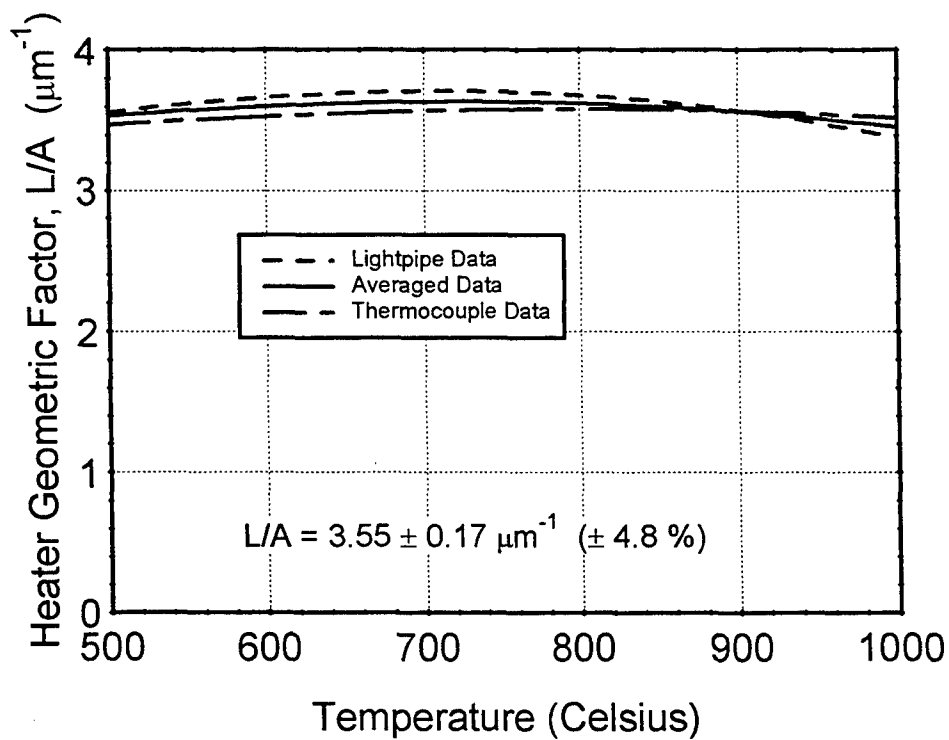


Figure 10.3. Heater Geometric Factor.

## 10.2 HEAT CONDUCTION MODEL FOR PREDICTING INSULATION LOSSES

Thermal insulation of the AMTEC cell during operation is essential to maximize the thermal-to-electric conversion efficiency of the device. The cell efficiency,  $\eta$ , is defined as:

$$\eta = \frac{P_e}{Q_{in}} = \frac{P_e}{Q_h - Q_{loss}} \quad (10.1)$$

In the AFRL vacuum tests, the cell's electric power output,  $P_e$ , and the heater power,  $Q_h$ , were directly measured. However, the fraction of heater power lost through the insulation,  $Q_{loss}$ , cannot be directly measured. The performance of the AMTEC cell will also depend on the heat losses through the cell wall to the insulation package, and these losses are difficult to evaluate accurately.

In this section, an indirect-heat-loss measurement technique is devised to evaluate the conduction heat losses in the single-cell test from the measured temperature profiles along the insulation surface and the cell wall. A two-dimensional, transient heat conduction model was developed, which handles a number of boundary conditions at the insulation surface, such as given temperature or heat flux profiles, and radiative and convective heat losses. The model was benchmarked using a number of sample thermal problems with existing analytical solution. The user's manual of this model is provided in a separate document. The model has the capability to handle temperature-dependent thermophysical properties.

This 2-D heat conduction model was then used in conjunction with temperature measurements to predict the heat losses in the alumina powder insulation of the PX-1B cell. A specially-designed thermocouple arrangement was designed to provide temperature distributions along the boundaries of the insulation package (Figure 10.4). These measurements provided the necessary boundary conditions to the 2-D conduction model, to predict the heat losses through the insulation. The measured temperatures along the cell and insulation boundaries are fitted using a polynomial fit subroutine developed in this work, and the resulting temperature profiles are input as boundary conditions to the cylindrical conduction model. The thermocouple arrangement also provided some measurements in the bulk of the insulation to verify the 2-D thermal conduction model developed in this work. Details on the design and setup of the experimental test can be found in Chapter 8.

The physical model of the insulation package surrounding the cell is illustrated in Figure 10.5. Using the temperature profiles measured by distributed thermocouples along the insulation surface and cell wall, the 2-D conduction model can predict the temperatures in the bulk of the insulation and evaluate the heat flux distribution and total heat flow along each insulation boundary,  $Q_i$  ( $i = 1$  to 5). At steady-state condition, the thermal heat balance in the insulation can be written:

$$Q_{loss} = Q_1 + Q_2 = Q_3 + Q_4 + Q_5 \quad (10.2)$$

Knowledge of the heat losses and heat flux profile at the different boundaries of the insulation is useful to analyze the insulation performance and propose ways to improve it.

### 10.2.1 NOMENCLATURE

#### English

A	cross sectional area ( $\text{m}^2$ )
[A]	coefficient matrix of linear equations
$C_p$	specific heat ( $\text{J/kg.K}$ )
D	flow diffusivity coefficient ( $\text{m}^2/\text{s}$ )
e	massic internal energy ( $\text{J/kg}$ )
g	gravity acceleration, $g=9.81 \text{ m/s}^2$
h	enthalpy per unit mass, $h=e+P/\rho$ ( $\text{J/kg}$ )
$h^{cv}$	convective heat transfer coefficient ( $\text{W/m}^2.\text{K}$ )
k	thermal conductivity ( $\text{W/m.K}$ )
Nr	number of radial numerical cells
Nz	number of axial numerical cells
P	pressure (Pa)
$P_e$	cell electric power output ( $W_e$ )
q	heat flux ( $\text{W/m}^2$ )
$\bar{q}$	heat flux on the boundary ( $\text{W/m}^2$ )
$Q_{cond}$	heat rejected at the cell condenser (W)
$Q_h$	heat output from the electric heater (W)
$Q_{in}$	heat input into the cell's hot end (W)
$Q_{loss}$	heat loss through insulation
r	radial coordinate
R	radius (m)
T	temperature (K)
$T_{sp}$	space environment temperature (K)
$T_\beta$	BASE tube temperature (K)
$T^*$	best estimate of temperature available at the time of computation (K)
$\tilde{T}$	temperature on the boundary (K)
Vol	numerical cell volume ( $\text{m}^3$ )
z	axial coordinate

#### Greek

$\alpha$	thermal diffusivity, $\alpha = k/(\rho C_p)$ ( $\text{m}^2/\text{s}$ )
$\Delta t$	discretization time step (s)
$\Delta R$	radial size of numerical cell (m)
$\Delta Z$	axial size of numerical cell (m)
$\epsilon$	radiative emissivity
$\eta$	cell conversion efficiency

$\mu$  dynamic viscosity (kg/m.s)  
 $\nu$  kinematic viscosity,  $\nu = \mu/\rho$  (m<sup>2</sup>/s)  
 $\rho$  density (kg/m<sup>3</sup>)

### Subscript / Superscript

*i* radial cell number  
*j* axial cell number  
*n* temporal discretization number  
*w* wall region  
*z* axial component  
 \* best available estimate at new time  
 ' correction

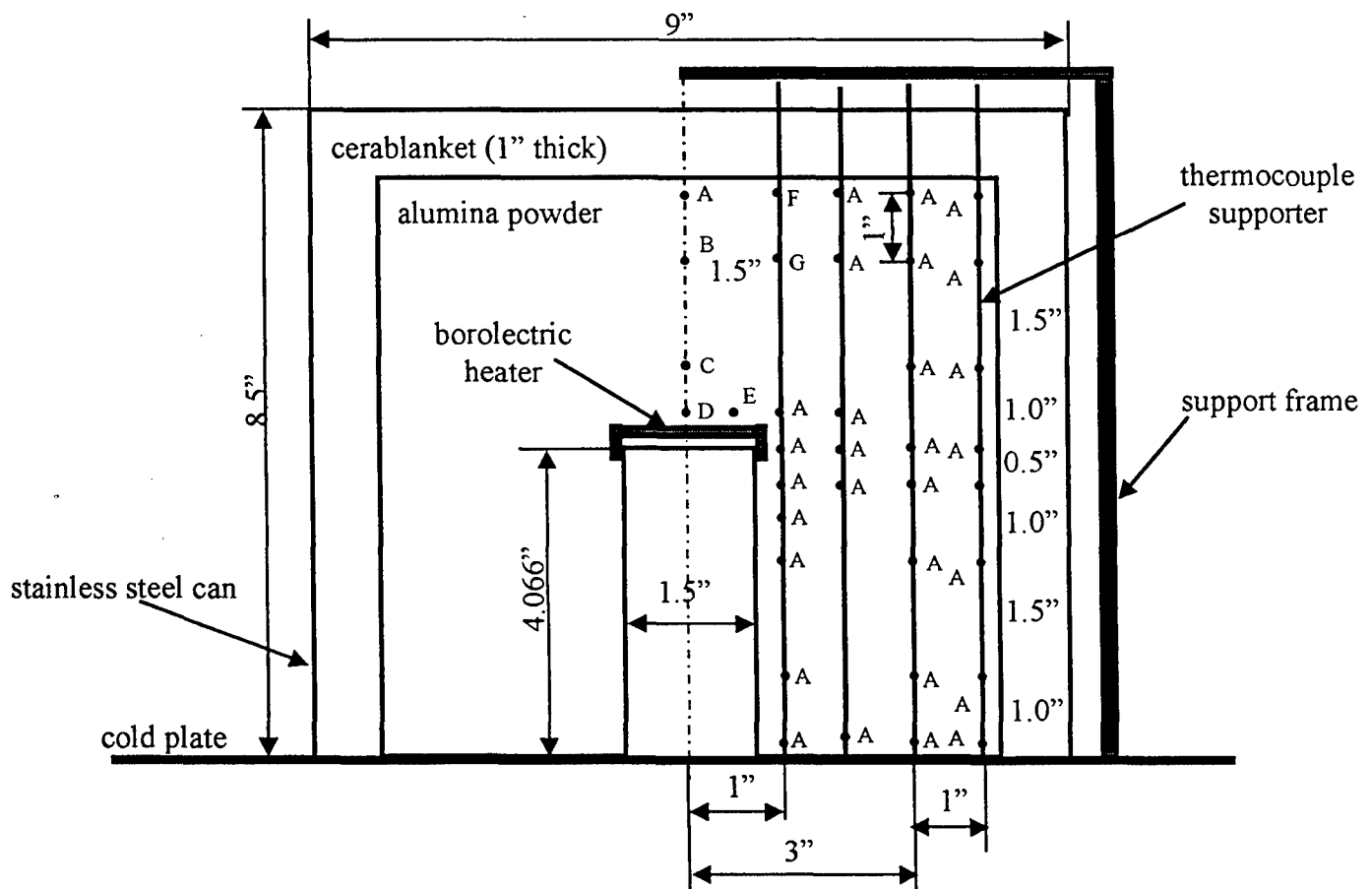


Figure 10.4. Thermocouples Arrangement in Insulation Package of PX-1B and PX-1C Cells.

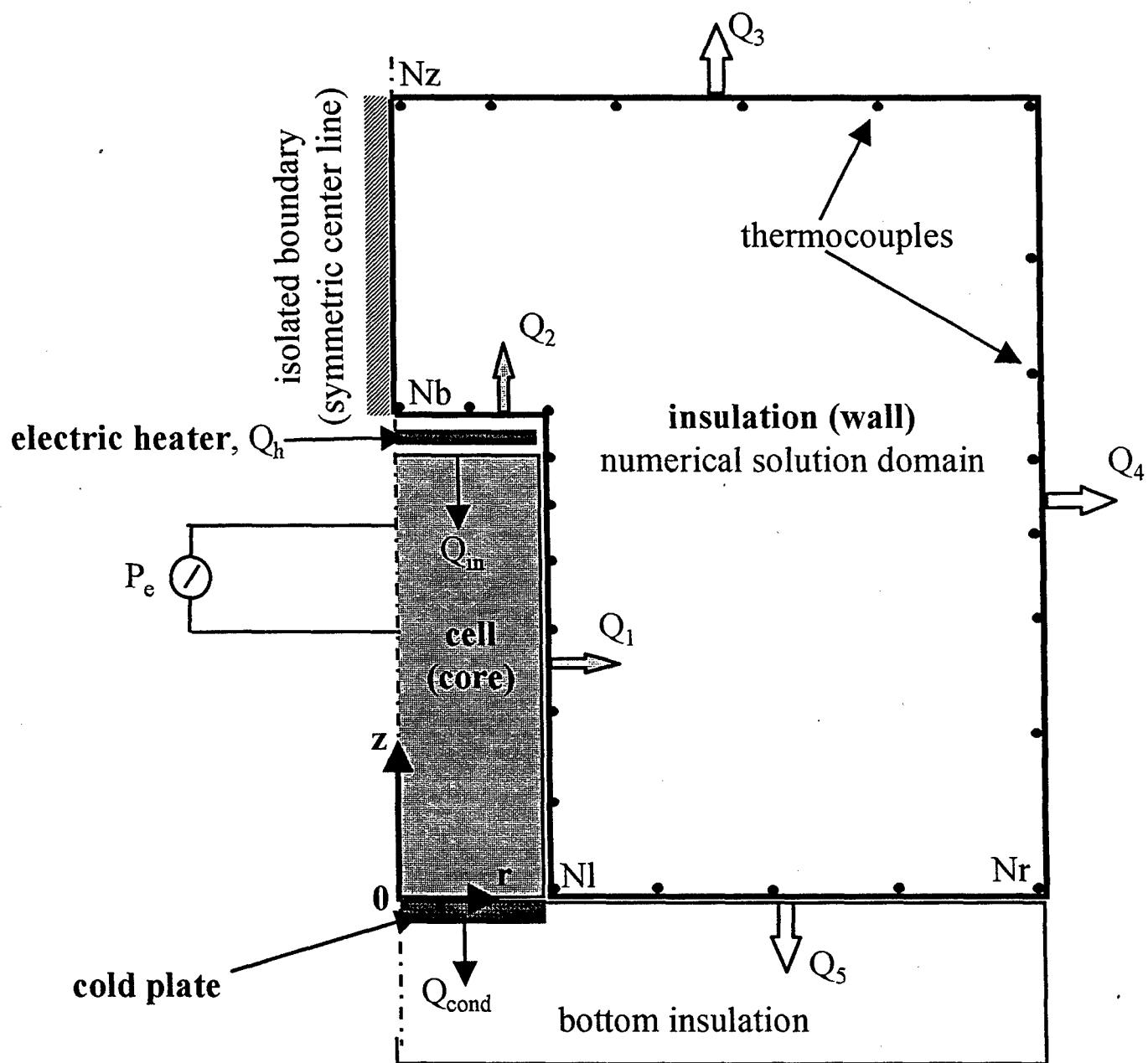


Figure 10.5. Thermal Model of Insulation Package of PX-1B and PX-1C Cells.



### 10.2.2 GOVERNING EQUATIONS AND BOUNDARY CONDITIONS

The governing equation for transient enthalpy balance without any heat source/sink is:

$$\frac{\partial}{\partial t}(\rho h) + \text{div}(\vec{q}) = 0. \quad (10.3)$$

For a solid thermal conduction system, in which the density,  $\rho$ , can be considered as a constant:

$$\frac{\partial}{\partial t}(\rho h) = \rho \frac{\partial}{\partial t}(C_p T), \quad (10.4)$$

where  $C_p$  is the specific heat at a constant pressure. The heat transfer in the cell-insulation system is two-dimensional (cylindrical) and axially-symmetric. In cylindrical coordinates, it can be modeled using Equation (10.3) as:

$$\frac{\partial}{\partial t}(\rho h) - \frac{1}{r} \frac{\partial}{\partial t} [rk_r(T) \frac{\partial T}{\partial r}] - \frac{\partial}{\partial z} [rk_z(T) \frac{\partial T}{\partial z}] = 0, \quad (10.5)$$

where  $k_r$  and  $k_z$  are the thermal conductivities in the  $r$  and  $z$  directions, respectively, and are functions of temperature. Most metallic materials are isotropic, i.e.  $k_r = k_z$ , but for some non-metal material, there may be  $k_r \neq k_z$ . The specific heat,  $C_p$ , is also a function of temperature.

The model can solve the thermal problem with five kinds of boundary conditions:

**a) Given heat flux on the boundary,  $q_o(r, z)$ :**

$$\vec{q}(r, z) = q_o(r, z). \quad (10.6)$$

**b) Given temperature on the boundary,  $T_o(r, z)$ :**

$$\vec{T}(r, z) = T_o(r, z). \quad (10.7)$$

**c) Radiative boundary:**

With known environmental temperature,  $T_{sp}$ , the emissivity and view factor on every boundary element need to be specified:

$$\vec{q}(r, z) = \sigma \epsilon F_{w \rightarrow env} (T_w^4 - T_{sp}^4). \quad (10.8)$$

**d) Convective heat transfer boundary:**

With known environmental temperature,  $T_{env}$ , the heat transfer coefficient on the boundary element is specified:

$$\tilde{q}(r, z) = h^{cv} (T_w - T_{env}). \quad (10.9)$$

**e) Fitting of measured temperature on all boundaries:**

$$\tilde{T}_i(r, z) = T_i^o(r, z), \quad i = 1, 2, \dots, n. \quad (10.10)$$

Usually the number of measured temperature profiles,  $n$ , is less than the number of boundary elements. In general, a boundary condition must be specified on each boundary of the domain. For the e) case, the model reads the measured temperature data,  $T_i^o(r, z)$  from the input data file "expdata.inp" and fits it using a polynomial function of specified degree. Then, the model calculates the temperatures at the center of each boundary element.

### 10.2.3 THERMOPHYSICAL PROPERTIES

The thermophysical properties in the above equations are temperature-dependent. The model incorporates 13 different materials which are encountered in the AMTEC cells and the test setup. These materials are tungsten, niobium, zirconium, stainless steel 304/316, carbon, copper, glass, boron nitride (grade HP), boron nitride (grade AX05), kaowool, alumina powder (1 $\mu$ m), alumina powder (0.01 $\mu$ m), and molded Min-K. Additional materials are easily incorporated, as they only require knowledge of density, thermal conductivity and heat capacity as a function of temperature. In addition to the thermophysical properties, inverse functions and derivative functions are needed in many cases to perform the numerical solution of the problem. For these reasons, all of the property information is in the form of functional evaluations. Most of these functions were derived by using least squares regression on table values from the literature (except for the thermal conductivity of the last three materials mentioned above, see Chapter 7). In most cases, good agreement was found between the various references, and a consistent set of data was selected that would cover the widest range of temperature. It is important to specify the temperature range of validity, since all too often a function obtained by least squares regression gives nonphysical results (such as very large or negative values) outside the temperature interval of interpolation.

The single-cell test setup at AFRL uses alumina powder (particle sizes of 1 and 0.01  $\mu$ m) and molded Min-K as the insulation materials. However, thermal conductivity data could not be found in the open literature for these materials. Therefore, experimental measurements of the thermal conductivity of these three insulation materials were conducted at AFRL (see Chapter 7).

The results showed that these thermal conductivities could be well described by the following second-order polynomials in temperature (temperature expressed in Kelvin;  $k$  is in W/m.K):

**a) Alumina powder with 1  $\mu\text{m}$  particle size:**

$$k = 0.09893 - 5.283 \times 10^{-4}T + 9.148 \times 10^{-7}T^2; \quad (10.11)$$

**b) Alumina powder with 0.01  $\mu\text{m}$  particle size:**

$$k = -0.01025 + 7.170 \times 10^{-5}T + 6.803 \times 10^{-8}T^2; \quad (10.12)$$

**c) Molded Min-K:**

$$k = 0.03151 - 2.051 \times 10^{-5}T + 4.176 \times 10^{-8}T^2. \quad (10.13)$$

#### 10.2.4 DISCRETIZATION OF GOVERNING EQUATIONS

Integrating the two-dimensional enthalpy conservation Equation (10.3) over a control volume  $(i, j)$ , and applying the conventional finite-difference discretization method to it on a  $N_r \times N_z$  domain (Figure 10.5), leads to the following discretized form between the times  $t^{n+1}$  and  $t^n$  (the time step is  $\Delta t = t^{n+1} - t^n$ ):

$$(A_r q_r)_{i,j}^{n+1} - (A_r q_r)_{i-1,j}^{n+1} + (A_z q_z)_{i,j}^{n+1} - (A_z q_z)_{i,j-1}^{n+1} = -\frac{\text{Vol}_{i,j} \rho}{\Delta t} [h(T^*) + C_p^* T' - h(T^n)] \quad (10.14)$$

$T^n$  and  $T^{n+1} = T^* + T'$  are the temperatures at time step  $t^n$  and  $t^{n+1}$ , respectively.  $T^*$  is the best estimate of the new-time temperature (available at the time of computation) during iterations, and  $C_p^*$  is the specific heat of the material at the temperature  $T^*$ .  $T'$  is the correction vector of  $T^*$  to the numerical solution  $T^{n+1}$ .  $q_r$  and  $q_z$  represent the conduction heat fluxes across the faces of the control volume  $(i, j)$ , and can be expressed as:

$$(A_r q_r)_{i,j}^{n+1} = D_{i,j}^r (T_{i+1,j}^{n+1} - T_{i,j}^{n+1}) \quad (10.15)$$

$$(A_z q_z)_{i,j}^{n+1} = D_{i,j}^z (T_{i,j+1}^{n+1} - T_{i,j}^{n+1})$$

where  $A_r$  and  $A_z$  are the areas of the control volume interfaces,  $k_r$  and  $k_z$  are the thermal conductivities in the  $r$  and  $z$  directions, respectively, and  $D_{i,j}^r$  and  $D_{i,j}^z$  are the thermal diffusion coefficients in  $r$  and  $z$  directions, given by:

$$D_{i,j}^r = \frac{(A_r)_{i,j}}{\frac{\Delta R_i}{2k_i} + \frac{\Delta R_{i+1}}{2k_{i+1}}} (T_{i+1,j}^{n+1} - T_{i,j}^{n+1}) \quad (10.16)$$

$$D_{i,j}^z = \frac{(A_z)_{i,j}}{\frac{\Delta Z_i}{2k_i} + \frac{\Delta Z_{i+1}}{2k_{i+1}}} (T_{i,j+1}^{n+1} - T_{i,j}^{n+1})$$

Substituting Equations (10.15) and (10.16) into Equation (10.14) gives the following linear discretized equations for the correction vector over the domain ( $i = 1$  to  $N_r$ ,  $j = 1$  to  $N_z$ ):

$$P_{ij} T'_{ij} + E_{ij} T'_{i+1,j} + W_{ij} T'_{i-1,j} + N_{ij} T'_{i,j+1} + S_{ij} T'_{i,j-1} = R_{ij}. \quad (10.17)$$

The coefficients  $P_{ij}$ ,  $E_{ij}$ ,  $W_{ij}$ ,  $N_{ij}$ , and  $S_{ij}$  contain the geometric and thermal conductive information for cell  $(i,j)$  and its four neighboring cells. Equations (10.17) form a 5-point (pentadiagonal)  $N_r \times N_z$  linear system that must be solved for the temperature correction vector (Figure 10.6). Since the matrix coefficients are also function of temperatures because of the temperature-dependence of the thermophysical properties (thermal conductivity and specific heat capacity), the transient heat conduction problem is practically non-linear. To resolve this non-linearity, the thermophysical properties are calculated using the best estimate  $T^*$  available at the time of computation, before solving Equations (10.17) for the temperature correction vector. The solution is iterated until the convergence of temperatures (the correction vector goes to zero). The solution procedure is described in the next section.

Some particular treatments must be performed in the control volumes along the boundaries of the axially-symmetric insulation. First of all, the centerline of the domain ( $r = 0$ ) can be considered thermally insulated, so that:

$$(\tilde{q}_r)_0^{n+1} = 0. \quad (10.18)$$

The boundary condition on the insulation surface can be either isoflux, isothermal, radiative or convective. The thermal energy flux leaving the radial and axial insulation surfaces by conduction can be expressed in terms of the surface temperature  $T^s$ , as:

$$(\tilde{q}_r)_{i,j}^{n+1} = k_{i,j} \frac{\tilde{T}_{i,j}^{n+1} - \tilde{T}_{i,j}^s}{\Delta R_i / 2}, \quad (10.19)$$

$$(\tilde{q}_z)_{i,j}^{n+1} = k_{i,j} \frac{\tilde{T}_{i,j}^{n+1} - \tilde{T}_{i,j}^s}{\Delta Z_i / 2}. \quad (10.20)$$

#### a) Isoflux thermal boundary condition

In the case of a given radial thermal energy flux,  $(\tilde{q}_r)_0^{n+1}$  or  $(\tilde{q}_z)_0^{n+1}$  are simply equated to their specified value.

#### b) Isothermal boundary condition

In the case of a given outer wall temperature  $T^s$ , Equation (10.19) is used as it is to express the radial thermal energy flux.

#### c) Radiative boundary condition

In the case of a radiative boundary condition, we have formally:

$$(\tilde{q}_r)_{i,j}^{n+1} = k_{i,j} \frac{\tilde{T}_{i,j}^{n+1} - \tilde{T}_{i,j}^s}{\Delta R_i / 2} = (\sigma \epsilon F)_{\text{rad}} [(\tilde{T}_{i,j}^s)^4 - T_{\text{sp}}^4]. \quad (10.21)$$

In order to eliminate  $T^s$  in the radial energy flux, we must linearize the right hand side of Equation (10.21). Since the temperature drop across the discretized boundary element is relatively small, it can be written:

$$\delta \tilde{T} = \tilde{T}_{i,j} - \tilde{T}_j^s \ll \tilde{T}_{i,j}. \quad (10.22)$$

To a first approximation, then, the following linearization applies:

$$(\tilde{T}_j^s)^4 = (\tilde{T}_{i,j} - \delta \tilde{T})^4 = (\tilde{T}_{i,j})^4 \left(1 - \frac{\delta \tilde{T}}{\tilde{T}_{i,j}}\right)^4 \cong (\tilde{T}_{i,j})^4 \left(1 - 4 \frac{\delta \tilde{T}}{\tilde{T}_{i,j}}\right). \quad (10.23)$$

Using this approximation (Equation 10.23) to eliminate the fourth power of the wall temperature in Equation (10.21), we find that:

$$\left[ \frac{k_{i,j}}{\Delta R_i / 2} + 4\tilde{T}_{i,j}^3 (\sigma \epsilon F)_{\text{rad}} \right] \delta \tilde{T} = (\sigma \epsilon F)_{\text{rad}} [(\tilde{T}_{i,j})^4 - T_{\text{sp}}^4]. \quad (10.24)$$

so that the radial energy flux at the insulation surface can be expressed as:

$$(q_r)_{i,j}^{n+1} = \left[ \frac{1}{(\sigma \epsilon F)_{\text{rad}}} + 4 \frac{\Delta R_i / 2}{k_{i,j}} \tilde{T}_{i,j}^3 \right]^{-1} [(\tilde{T}_{i,j})^4 - T_{\text{sp}}^4]. \quad (10.25)$$

Finally, Equation (10.25) is linearized in terms of the temperature correction using the best estimate of new-time temperature available at the time of computation:

$$(\tilde{T}^4)^{n+1} = \tilde{T}^{*4} + 4\tilde{T}^{*3} \theta T'. \quad (10.26)$$

### 10.2.5 SOLUTION PROCEDURE

To solve the five point linear equations resulting from the discretization of energy balance Equations (10.17), a direct solution routine using Gaussian elimination (Golub and van Loan 1984) was developed and tested, which included partial pivoting and row normalization options. While this method is very efficient for solving relatively small linear systems, it is very cumbersome for large matrices. To solve a set of discretized conservation equations on a rectangular domain of  $N = N_r \times N_z$  cells, the computational time increases with the number of equations raised to the third power, that is as  $(N_r \times N_z)^3$ .

In this case, it is useful to consider the banded version of the solver. A banded linear equation solver is organized around a data structure that takes advantage of the many zeros in the pentadiagonal matrix of the linear system. By construction, this matrix has lower and upper bandwidths  $N_r$  and can be represented in a  $(2N_r+1) \times N$  band array (Figure 10.6). The bandwidth of the matrix is preserved as long as no pivoting is performed. If pivoting is necessary, the matrix can still be represented in a  $(3N_r+1) \times N_z$  band array. Fortunately, such permutation of line was never necessary in solving the present heat transfer problem. A quick estimate of the number of flops in the banded Gauss elimination algorithm shows that the computational time increases as  $N_r^3 \times N_z$  only.

Therefore, the use of the band structure considerably reduces the amount of memory storage and computational time required. More precisely, if we make use of the "corner zeros" in the band storage matrix, the computational time is proportional to  $N_r^{8/3} \times N_z$ , which is confirmed by

The following linear system is considered:

$$aP_{i,j}(T)_{i,j} + aE_{i,j}(T)_{i+1,j} + aW_{i,j}(T)_{i-1,j} + aN_{i,j}(T)_{i,j+1} + aS_{i,j}(T)_{i,j-1} = S_{i,j}$$

for  $i=1$  to  $N_r$ , and  $j=1$  to  $N_z$ .

If each cell  $[i,j]$  is given the cell number  $k=i+(j-1) \times N_r$ , the matrix  $[a]$  has lower and upper bandwidths  $N_r$  ( $N_r < N_z$  for max. efficiency).

Example for  $N_r=4$ ,  $N_z=5$  :

$[a]$  is a  $20 \times 20$  matrix.

The banded matrix  $[b]$  has  $2N_r+1$  diagonals, that is :  
 $[b]$  is a  $20 \times 9$  matrix.

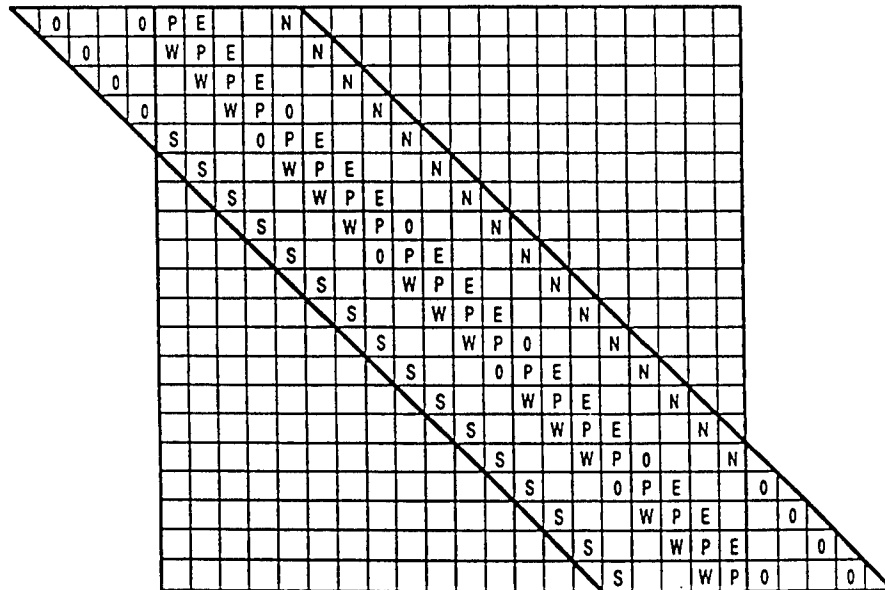
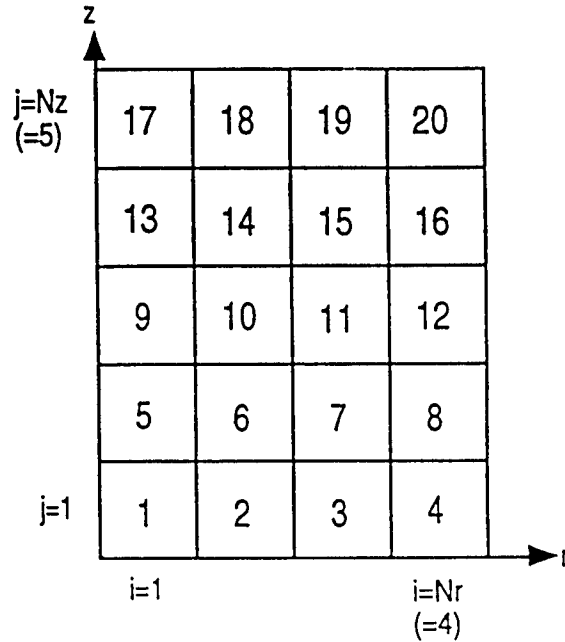


Figure 10.6. Illustration of Band Storage of a Linear system Matrix which Results from the Discretization of Conservation Equations on a Two-Dimensional Domain.

numerical experiments on a DEC VAX 6320 (Tournier 1996). Several 5 point iterative solvers have been examined and tested which combine strongly implicit procedures with successive overrelaxation, additive block (row and column) corrections and conjugate gradient.

The Strongly Implicit Solver of Lee (1989) is found to be the most efficient in solving the energy discretized equations of the present problem. The SIS procedure of Lee has the advantage of not requiring a partial cancellation parameter, as most of the implicit iterative solvers do. Also a SOR (strongly Over Relaxation) factor of unity is found to be the best choice for the convergence of the iterations. In this work, the LU decomposition of Lee, combined with the iterative method of solution devised by Stone (1968), is used.

One pass of the selected iterative solver is constituted of the following steps. Given a vector approximation, or best estimate,  $T^*$ , to the solution of the linear system  $[A]T = S$ , we use Stone's iterative method to obtain a correction  $T'$  to the vector  $T^*$ , such that:

$$[A+A'] (T^*+T') = [A+A'] T^* + S - [A]T^* , \quad (10.27)$$

or

$$[A+A']T' = S - [A]T^* . \quad (10.28)$$

It is apparent that the vector correction is null upon convergence. The alteration matrix  $[A']$  to the system matrix  $[A]$  is obtained from the SIS procedure of Lee (1989) such that:

$$[A+A'] = [L][U] , \quad (10.29)$$

where  $[L]$  is a lower triangular matrix and  $[U]$  is an upper triangular matrix. Both  $[L]$  and  $[U]$  have the same dimension  $N \times N$  as the matrix  $[A]$ . While  $[A]$  has only 5 non zero elements per line when it originates from the discretization of conservation equations on a two-dimensional domain, the triangular matrices  $[L]$  and  $[U]$  have only 3 non zero elements per line, which makes the computations particularly easy. Making use of Equation (10.29) into Equation (10.28), the linear system becomes:

$$[L][U]T' = R , \quad (10.30)$$

where  $R = S - [A]T^*$  is the residual vector. The linear system (10.30) is readily solved by making use of the properties of triangular matrices:

$$[L]V = R , \quad (10.31)$$

$$[U]T' = V . \quad (10.32)$$



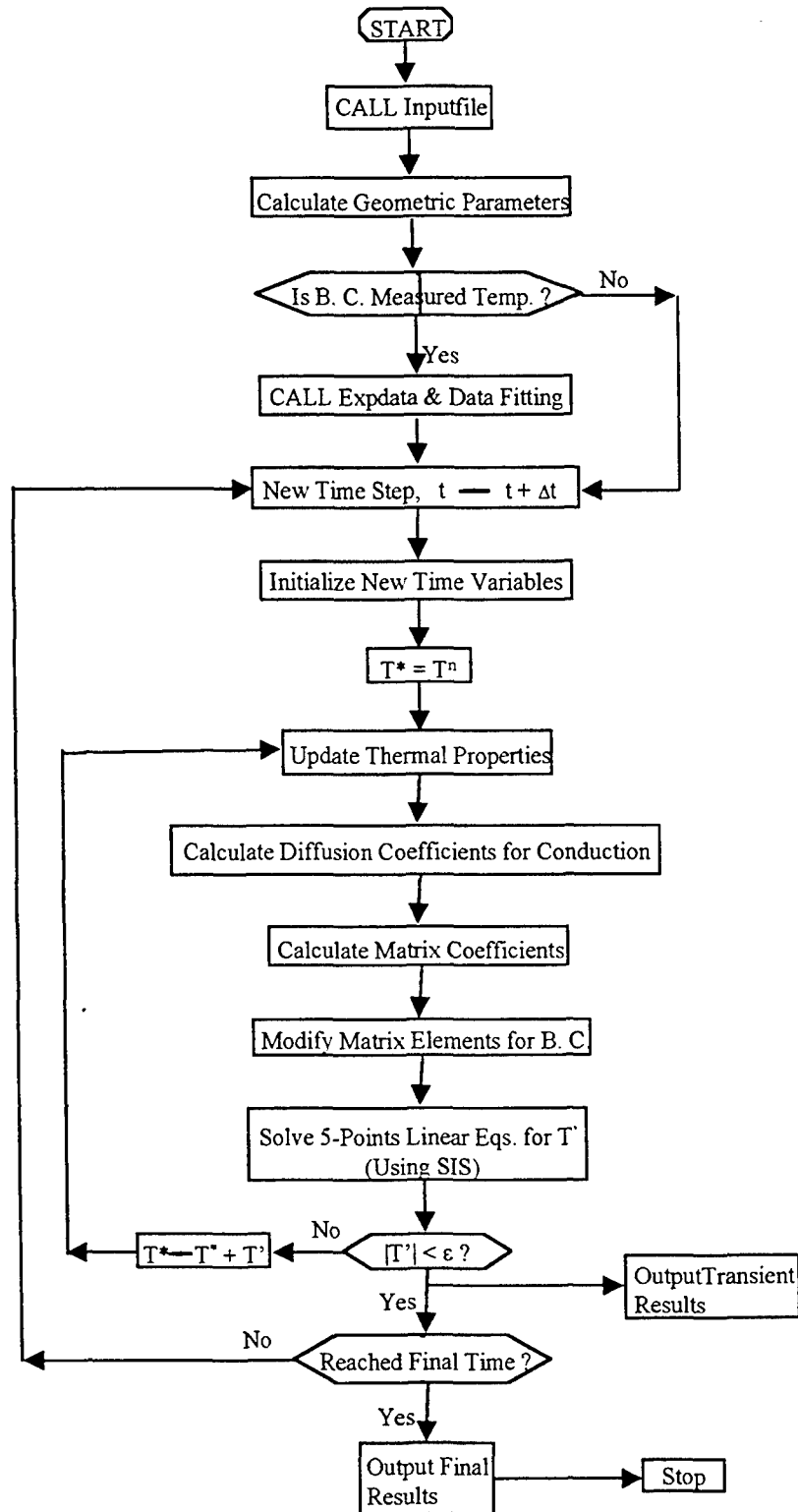


Figure 10.7. Flow Chart of Two-Dimensional Conduction Model.

Once  $T'$  is obtained, the vector  $T^*$  is corrected as  $T^* = T^* + T'$ , and the residual vector is recalculated as  $R = S - [A]T^*$ . Another iteration is performed if  $R$  does not satisfy the specified convergence criteria.

It is apparent that the iterative solution algorithm of Stone has the disadvantage of using more computational time than Lee's, since it requires calculation of the residual vector at the end of every iteration. However, knowledge of these residuals permits better control of the internal iterations of the iterative segregated algorithm, resulting in an overall saving in the CPU time.

The number of flops of the iterative solver SIS is proportional to the number of equations  $N$  and to the number of internal iterations. Because the SIS solver is iterative in nature, the computational time for this solver is a function of the number of iterations performed. On the other hand, the amount of CPU time necessary when using the direct Gauss algorithm is solely a (strong) function of the size of the discretized domain. For a given number of radial cells,  $N_r$ , (it defines the bandwidth of the matrix), there is an optimal number of internal iterations for the SIS solver such that it is competitive with the Gauss solver in terms of CPU time. It is worth noting that in practice, for a simple heat conduction problem, the amount of CPU time needed for the SIS solver is only a small fraction of that needed for the Gauss direct solver.

The solution (iteration) procedure is shown in Figure 10.7. First, the model reads the input data file which includes all information on geometry, materials, thermal boundary conditions, parameters for numerical iteration, and output selection. If the boundary conditions are measured temperature profiles, another data file which contains the measured temperatures and their locations on the insulation surface is read by the model, and temperature polynomial fits are developed along each boundary. After meshing automatically the insulation domain and applying the boundary conditions on it, the model sets the temperature  $T^*$  to an initial value, and calculates all temperature-dependent thermophysical properties using  $T^*$ . Then, the diffusion coefficients for the governing equations and the matrix coefficients are calculated (Figure 10.7). The model solves the resulting 5-point linear system using the Strongly Implicit Solver developed above to obtain the temperature corrections,  $T'$ . The best estimate vector of new-time temperatures,  $T^*$ , is updated using the correction vector, and the procedure is iterated, until the temperatures converge (the correction vector goes to zero). The time step is then incremented, and the calculation procedure is repeated, until the maximum time has been reached (as specified in the input file) or until a steady-state solution of the problem has been reached. Then, the model calculates the heat fluxes and heat flows at the domain boundaries, plots the isotherms in the insulation, and outputs all necessary information into data files that are formatted for the EasyPlot plotting software, on Personal Computer.

### 10.3 HEAT CONDUCTION MODEL BENCHMARK

The model for calculating conduction heat losses in the insulation package surrounding the AMTEC cell was verified by comparing its predictions with analytical solutions for some simple geometries, and some modifications were made in the code to extend its domain of applications. In addition to the standard cylindrical configuration of cell insulation system (the cell sitting in

bottom center of the insulation, Figure 10.5), the code can also handle simpler geometries such as that of a single solid cylinder and of a hollow cylinder. The code was tested for all of these three domains.

In the benchmark problems, the thermal conductivity of the insulation material was assumed to be either a constant,  $k = 0.1 \text{ W / m.K}$ , or a linear function of temperature:

$$k = a + bT = 0.02 + 3 \times 10^{-3} T. \quad (10.33)$$

**a) One dimensional (axial) heat conduction through a constant-cross section rod with insulated side wall, and given temperatures  $T_1$  and  $T_2$  at the end faces ( $k = \text{constant}$ ):**

The analytical temperature distribution is a linear function of position:

$$T(z) = T_1 - \frac{(T_1 - T_2)}{L} z, \quad (10.34a)$$

and the conduction heat flow is constant and given by:

$$q = \frac{Ak(T_1 - T_2)}{L} \quad (10.34b)$$

The model predictions of temperature and heat flux obtained with only five numerical cells are in perfect agreement with the analytical solution, see Figure 10.8.

**b) One dimensional (axial) heat conduction through a constant-cross section rod with insulated side wall, given temperature  $T_1$  at one face and radiative condition at the other ( $k$  is linear):**

The analytical solution for this problem is:

$$T(z) = (1/b)\{[(a + bT_1)^2 - 2bqz]^{0.5} - a\}, \quad (10.35a)$$

where

$$q = \sigma \epsilon F_{w \rightarrow env}(T_2^4 - T_{env}^4), \quad (10.35b)$$

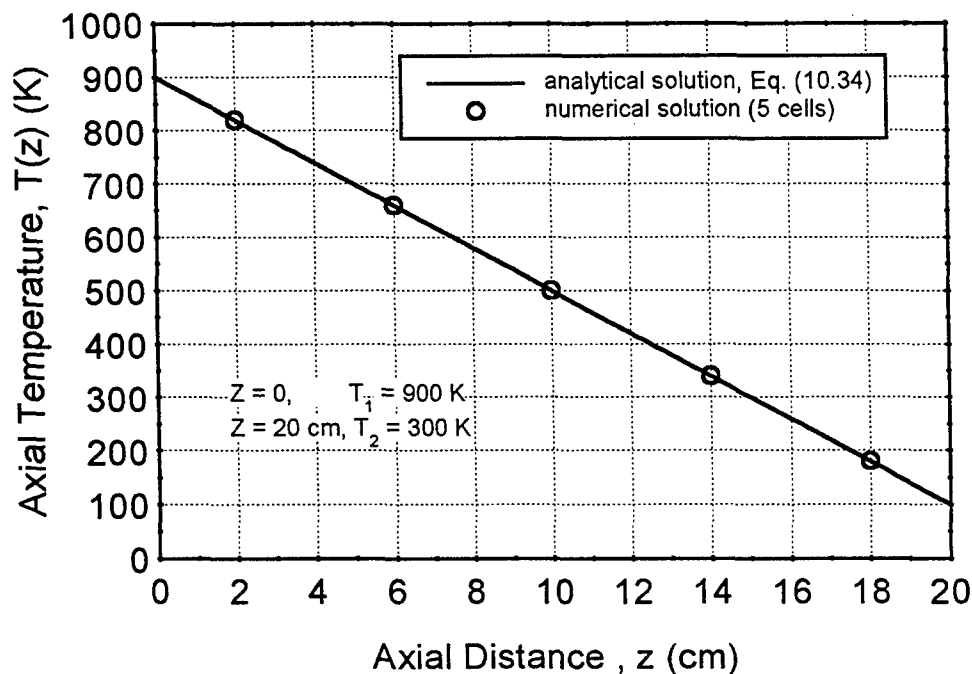


Figure 10.8. Comparison of Analytical and Predicted Axial Temperature Distributions for the Case of One-D Axial Conduction with Constant Thermal Conductivity.

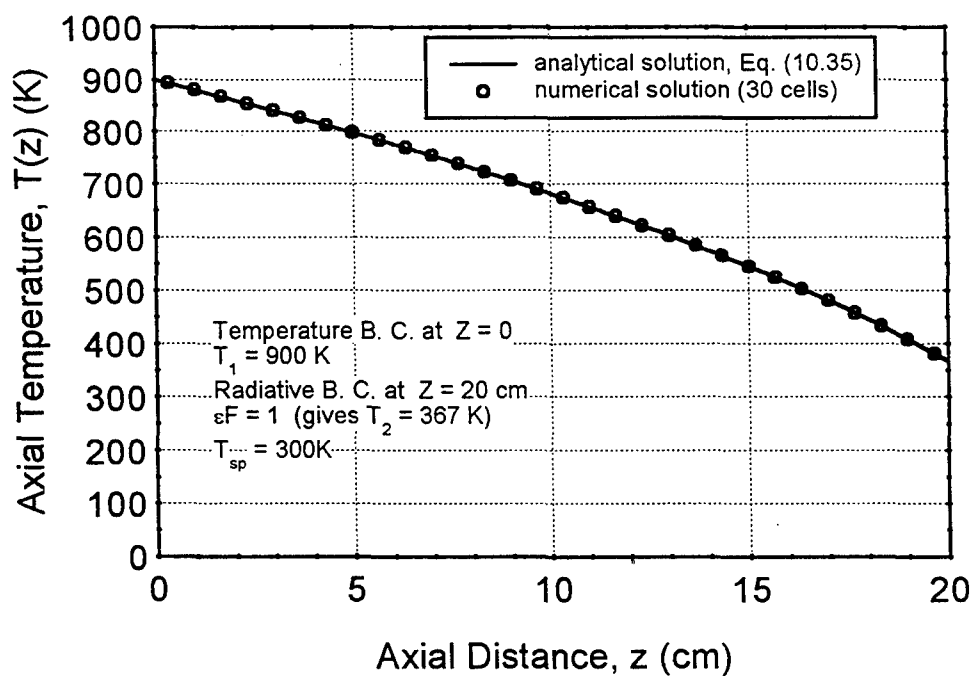


Figure 10.9. Comparison of Analytical and Predicted Axial Temperature Distributions for the Case of One-D Axial Conduction with Linear Thermal Conductivity.

and  $a$  and  $b$  are the constants in Equation (10.33).  $q$  is the (constant) heat flux through the insulation domain, and can be calculated by coupling Equation (10.35a) at the radiative face with  $T = T_2$  and the radiation heat transfer Equation (10.35b).

The axial temperature distribution along the rod was calculated by the analytical solution and the numerical model, and the two profiles are shown in Figure 10.9, for the case of unity emissivity and view factor ( $\epsilon F_{2 \rightarrow sp} = 1$ ) and an environment temperature  $T_{sp} = 300$  K. As shown in this figure, the predicted temperature profile matched the analytical solution very well. The total heat conducted through the rod is 17.586 W from the numerical solution, compared to 17.587 W from the analytical solution. The numerical results were obtained with 30 numerical cells of identical size ( $Nl = 0$ ;  $Nb = 0$ ,  $Nr = 30$ , and  $Nz = 30$ ).

**c) One dimensional (radial) heat conduction with fixed temperatures  $T_1$  and  $T_2$  at the annular faces ( $k$  is constant):**

The analytical temperature distribution across the annulus is:

$$T(r) = T_1 - \frac{\ln(\frac{r}{r_1})}{\ln(\frac{r_2}{r_1})} (T_1 - T_2). \quad (10.36)$$

As shown in Figure 10.10, the numerical solution, obtained with  $Nl = 2$ ,  $Nb = 18$ , and  $Nr = Nz = 20$  proved to agree very well with the analytical solution.

**d) One dimensional (radial) heat conduction with given temperature  $T_1$  at inner face and radiative condition at the outer face ( $k$  is linear):**

The analytical solution for this problem is:

$$T(z) = \frac{1}{b} \left\{ \left[ -\frac{bQ_r}{\pi L} \ln\left(\frac{r}{r_2}\right) + k_2^2 \right]^{0.5} - a \right\}$$

$$k_1 = a + bT_1, \quad k_2 = a + bT_2, \quad (10.37)$$

$$Q_r = \frac{\pi L(k_1 + k_2)(T_1 - T_2)}{\ln(\frac{r_2}{r_1})}$$

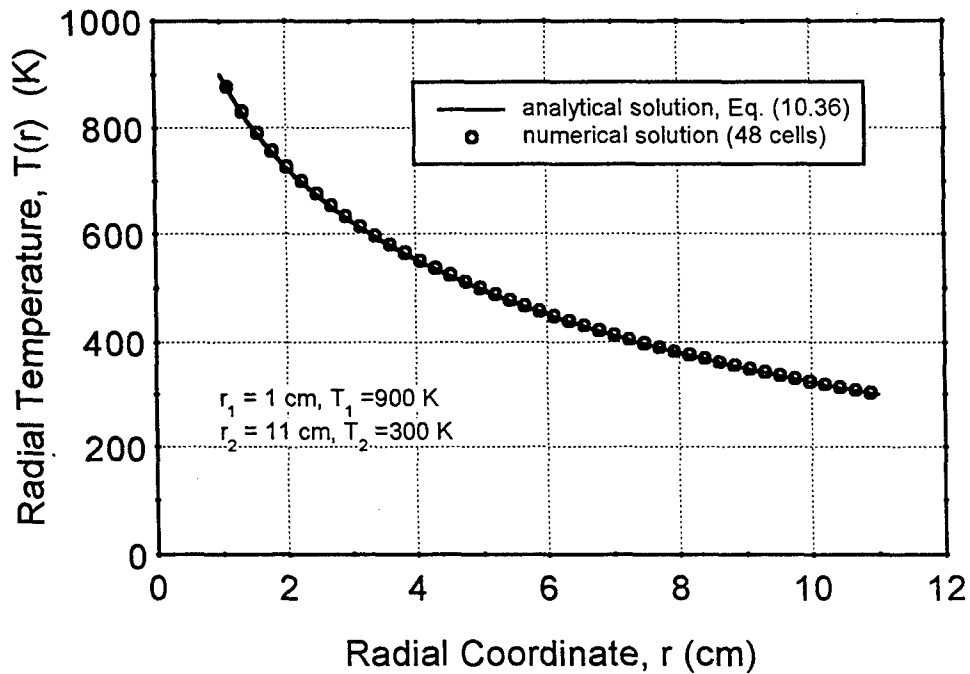


Figure 10.10. Comparison of Analytical and Predicted Radial Temperature Distributions for the Case of One-D Radial Conduction with Constant Thermal Conductivity.

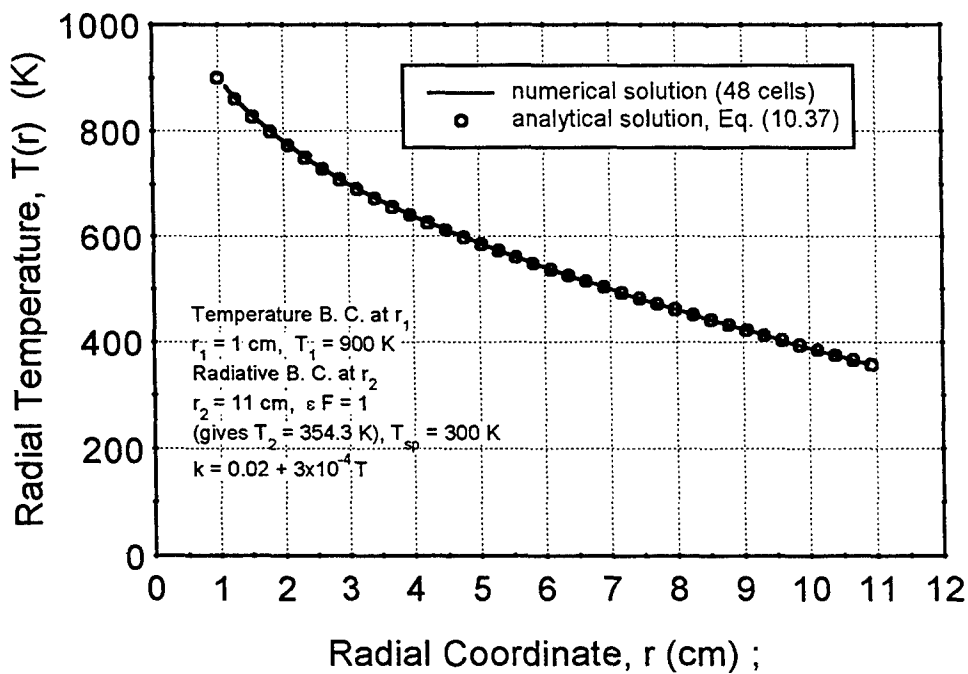


Figure 10.11. Comparison of Analytical and Predicted Radial Temperature Distributions for the Case of One-D Radial Conduction with Linear Thermal Conductivity.

The radial temperature distributions calculated by the analytical solution and numerical model are compared in Figure 10.11 for the case of unity emissivity and view factor ( $\epsilon F_{2 \rightarrow sp} = 1$ ), an environment temperature  $T_{sp} = 300$  K, and  $Nl = 2$ ,  $Nb = 18$ , and  $Nr = Nz = 20$ . The total heat conducted through the cylinder was 63.302 W from the numerical solution, compared to 62.880 W from the analytical solution.

In the next section, the two-dimensional heat conduction model is used to predict the heat conduction losses in the Alumina powder insulation surrounding the PX-1 series of cells. Heat losses through the insulation are calculated by the model using the measured temperature profiles on the insulation surfaces as boundary conditions.

## 10.4 HEAT LOSSES IN ALUMINA POWDER INSULATION OF PX-1 CELLS

The 2-D heat conduction model developed in Section 10.2 was used to predict the heat conduction losses in the Alumina powder insulation surrounding PX-1B and PX-1C cells (see Section 8.9). Heat losses through the insulation were calculated by the code, using the measured temperature profiles on the insulation surfaces as boundary conditions. A typical map of measured temperature profiles in the insulation of PX-1B is shown in Figure 10.12, for a heater temperature of 1220 K. Alumina rods supporting K-type thermocouples at different heights were inserted in the alumina powder, and measured the temperatures along the bottom, side and top surfaces of the insulation, and along the cell wall and top of heater block. The data were input to the 2-D conduction model and fitted using polynomial functions of appropriate order. The numerical fits of temperatures in Figure 10.12 and the conduction heat flux profiles predicted by the model are shown in Figures 10.13 – 10.17. The predicted isotherms in the insulation and the calculated heat losses at the boundaries are shown in Figure 10.18. In this particular experiment,  $31.1 + 6.4 = 37.5$  W were lost through the insulation (Also,  $6.6 + 25.6 + 5.3 = 37.5$  W, showing that the model conserves energy well, since no heat is created or dissipated within the insulation).

Calculated results have been consistent with experimental measurements in most cases. For example, for the PX-1B cell operating at BASE tube and condenser temperatures of 1140 K and 520 K, respectively, and an heater electric power,  $Q_h = 55.9$  W, the heat extracted by the cooling air loop at the condenser was measured as  $Q_{\text{cond}} = 17.1$  W, and the measured cell's electric power output was  $P_e = 1.2$  W. The heat losses through the insulation package calculated by the 2-D conduction model were  $Q_{\text{loss}} = 35.2$  W (Table 10.2). From the measured heat balance,  $Q_{\text{loss}}$  was 37.6 W, the difference being less than 5%. In many cases, the predicted heat losses in the insulation of PX-1 series cells matched that obtained from the overall experimental heat balance very well, within 7% (Table 10.2). This good agreement gives confidence in the soundness of the numerical approach and solution procedure used in the 2-D conduction model.

Table 10.2. Predicted Heat Losses in Insulation of PX-1 Series Cells.

Cell	Heater electric power $Q_h$ (W)	Cell electric power output $P_e$ (We)	Condenser heat rejection $Q_{\text{cond}}$ (W)	Insulation heat loss $Q_{\text{loss}}$ (W) (from conduction model)	Total output $Q_{\text{out}} = P_e + Q_{\text{cond}} + Q_{\text{loss}}$ (W)	Overall energy balance $(Q_h - Q_{\text{out}})/Q_h$
PX-1A	55.9	1.17	17.1	35.2	53.5	4.3%
PX-1B	77.9	1.45	13.5	58.9	73.8	5.3%



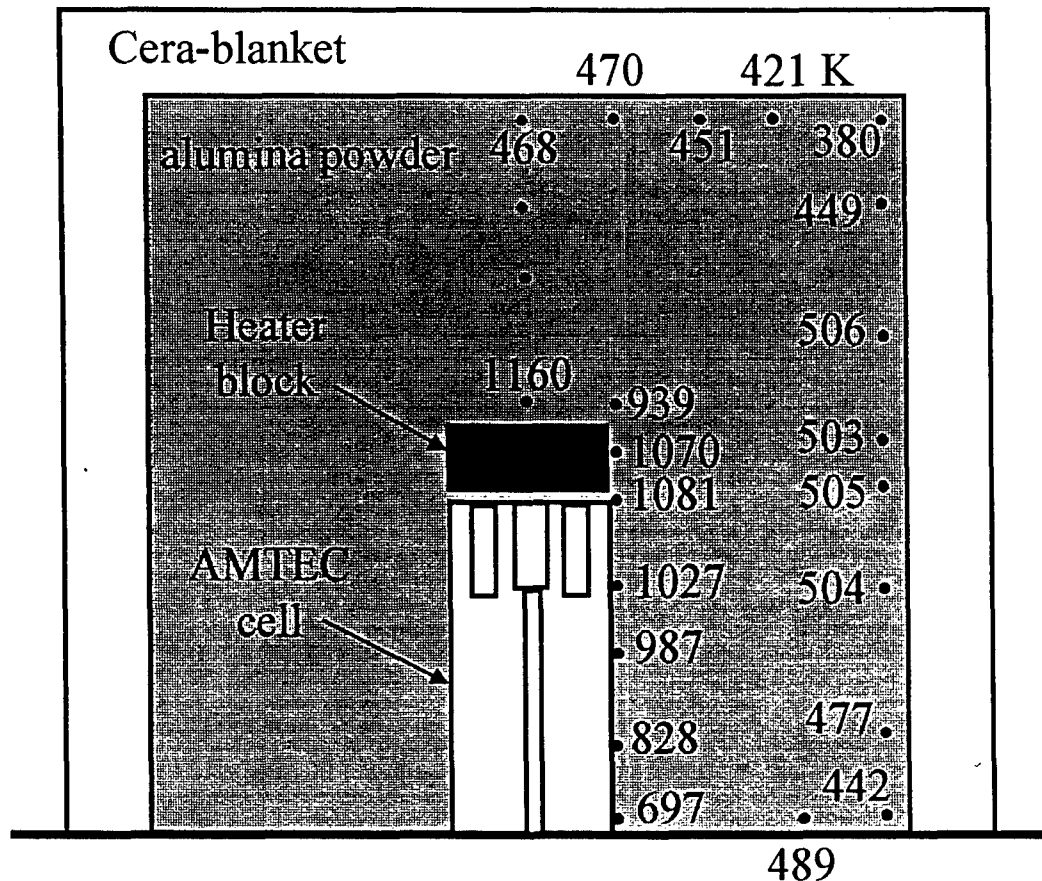


Figure 10.12. Thermocouple Temperature Measurements in the Alumina Powder Insulation of PX-1B ( $T_{\text{heater}} = 1220$  K).

The 2-D conduction model was also used to predict the heat conduction losses in the insulation package surrounding the PX-2C cell. The insulation material used in this experiment was Min-K (see Section 8.9). The thermal conductivity used in the code for this material was fitted as a second order polynomial using thermal conductivity test results reported in Chapter 7. The measured temperatures along the insulation package and the AMTEC cell wall were fitted numerically and the resulting profiles were used as boundary conditions in the code. For a heater electric power of  $Q_h = 50.84$  W, the heat extracted by the cooling air loop at the condenser was measured as  $Q_{\text{cond}} = 23.56$  W, and the measured cell's electric power output was  $P_e = 4.04$  W. The heat losses through the insulation package calculated by the conduction model were  $Q_{\text{loss}} = 14.8$  W. From the measured overall heat balance,  $Q_{\text{loss}}$  was:

$$Q_{\text{loss}}' = 50.84 - (23.56 + 4.04) = 23.24 \text{ W.}$$

The difference  $|Q_{\text{loss}} - Q_{\text{loss}}'| = 8.4$  W is large and might come from the experimental measurements. In the test setup, the heat loss through the bottom stainless steel plate was not measured. It might be that because of poor insulation, a significant fraction of the heat input was conducted between the condenser and the stainless steel plate. In the next cell setup (PX-4B), the

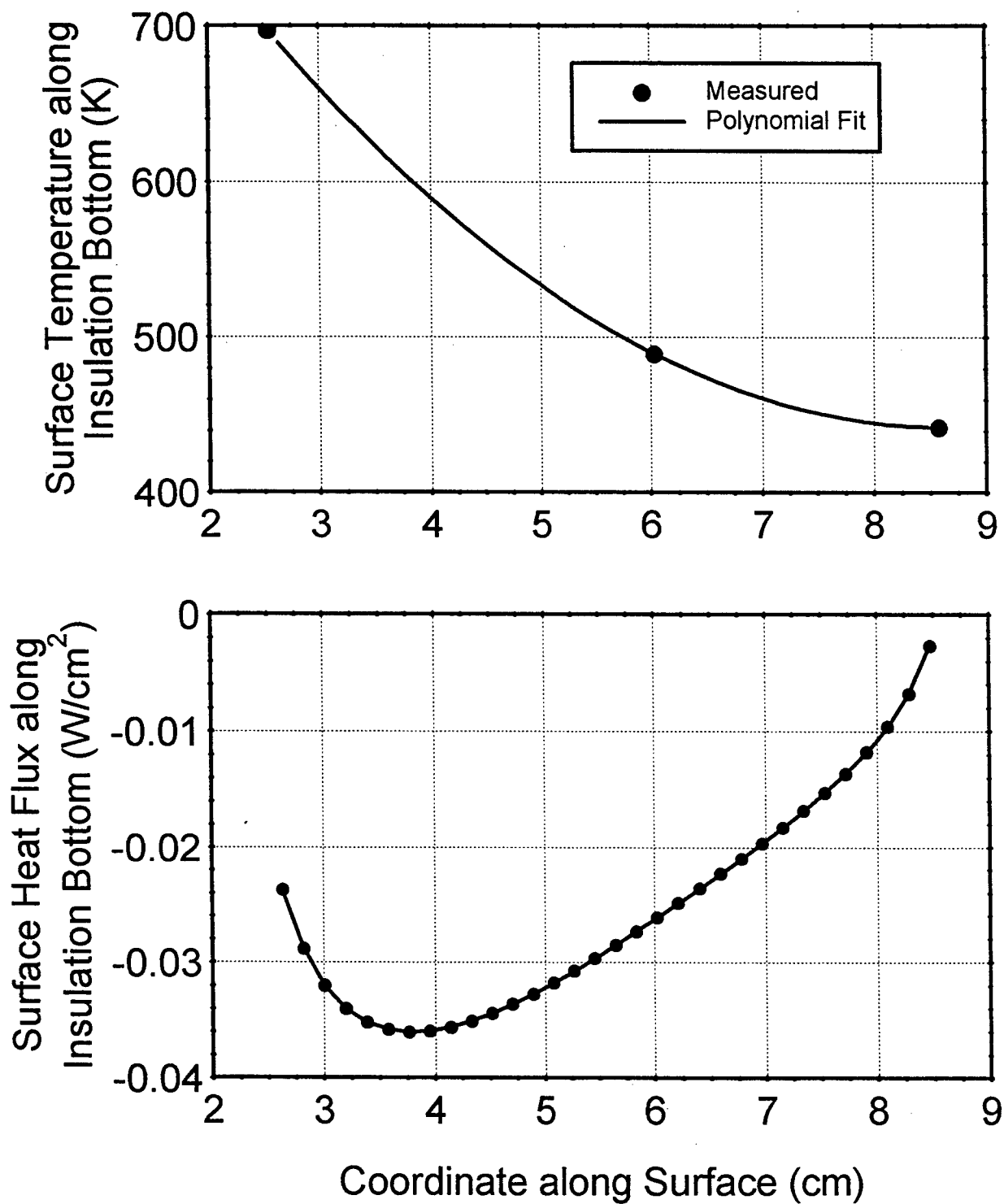


Figure 10.13. Temperature and Heat Flux Profiles along the Bottom Surface of PX-1B Insulation ( $T_{\text{heater}} = 1220 \text{ K}$ ).

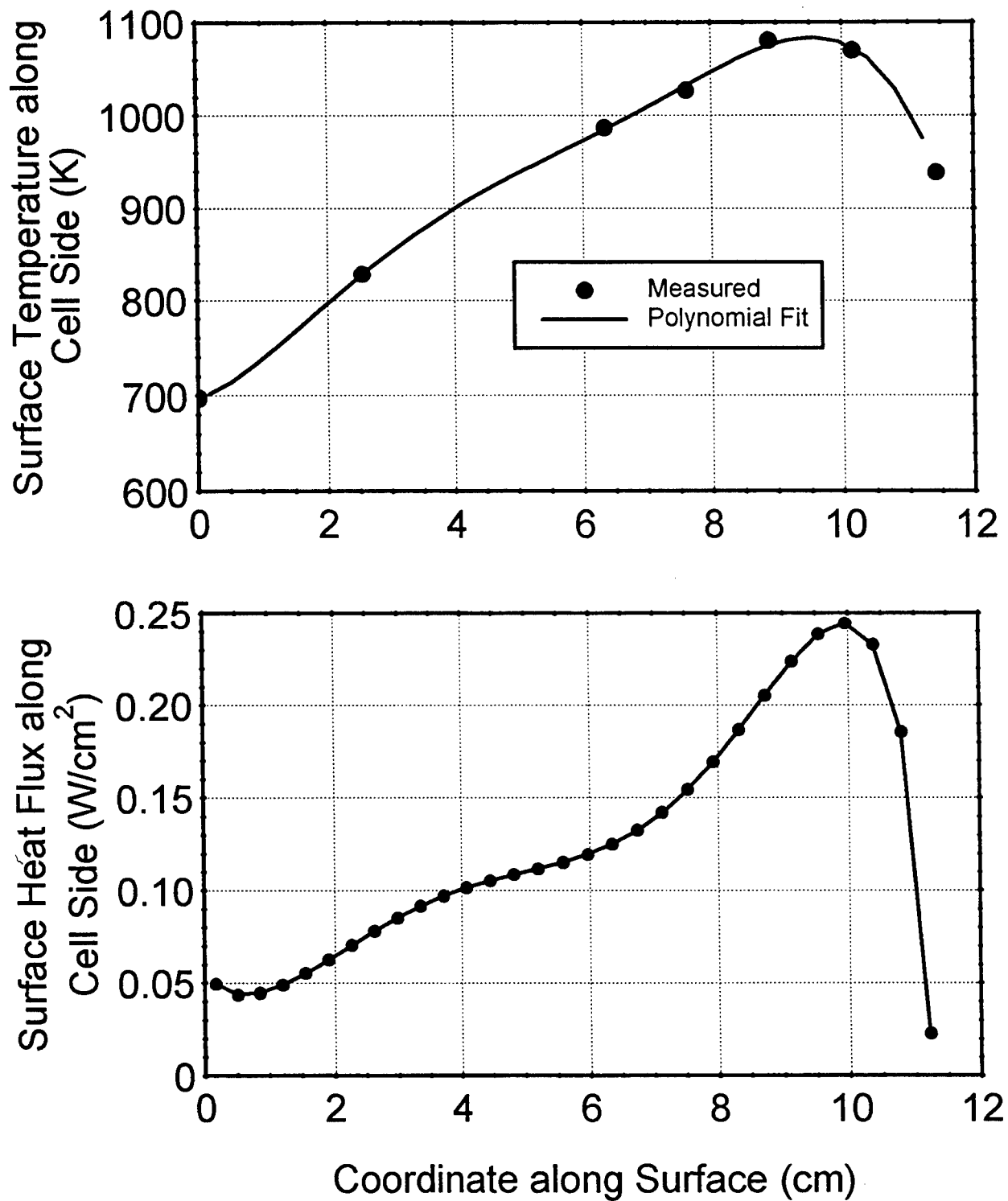


Figure 10.14. Temperature and Heat Flux Profiles along PX-1B Cell Wall ( $T_{heater} = 1220$  K).

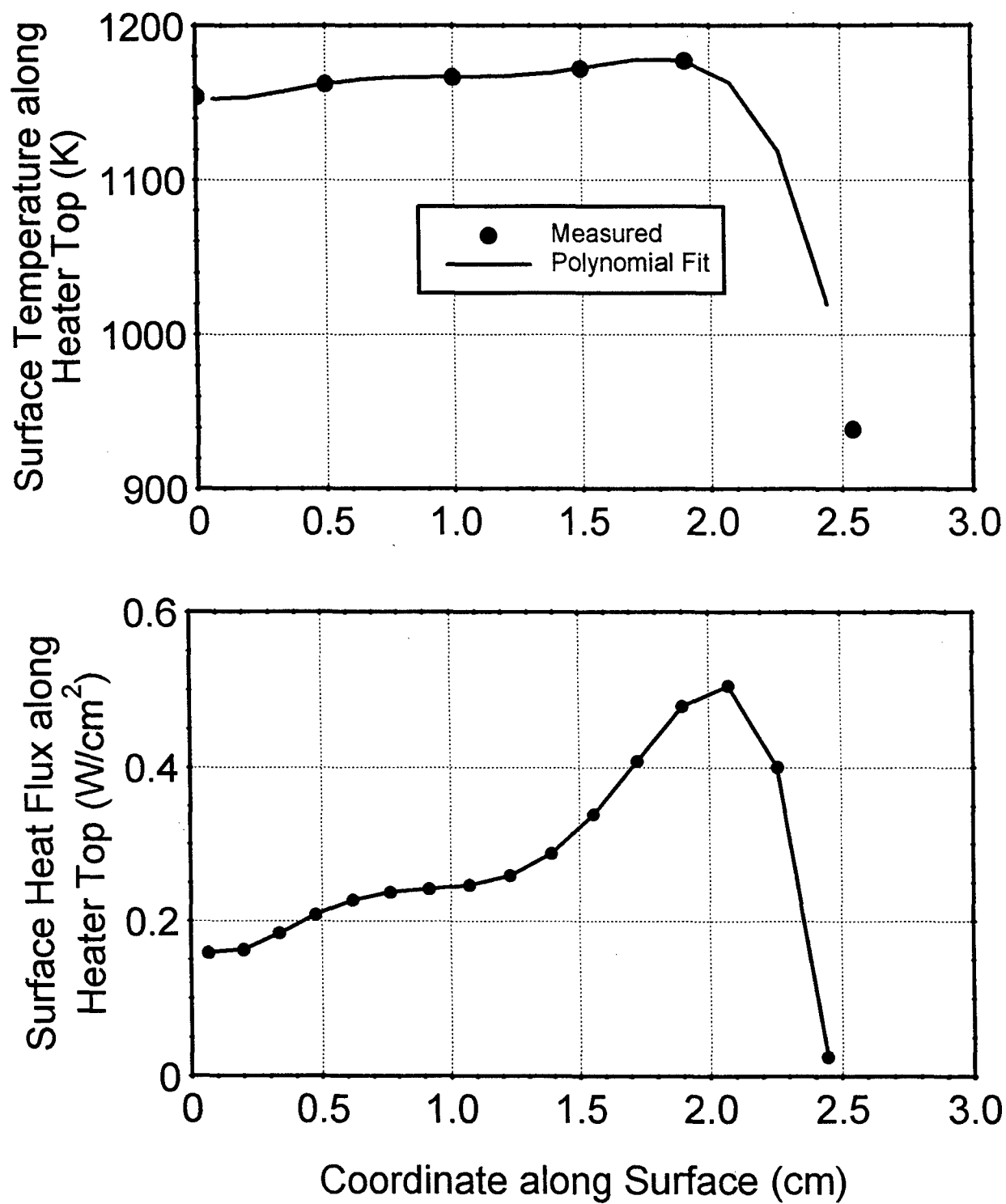


Figure 10.15. Temperature and Heat Flux Profiles along PX-1B Heater Top ( $T_{heater} = 1220$  K).

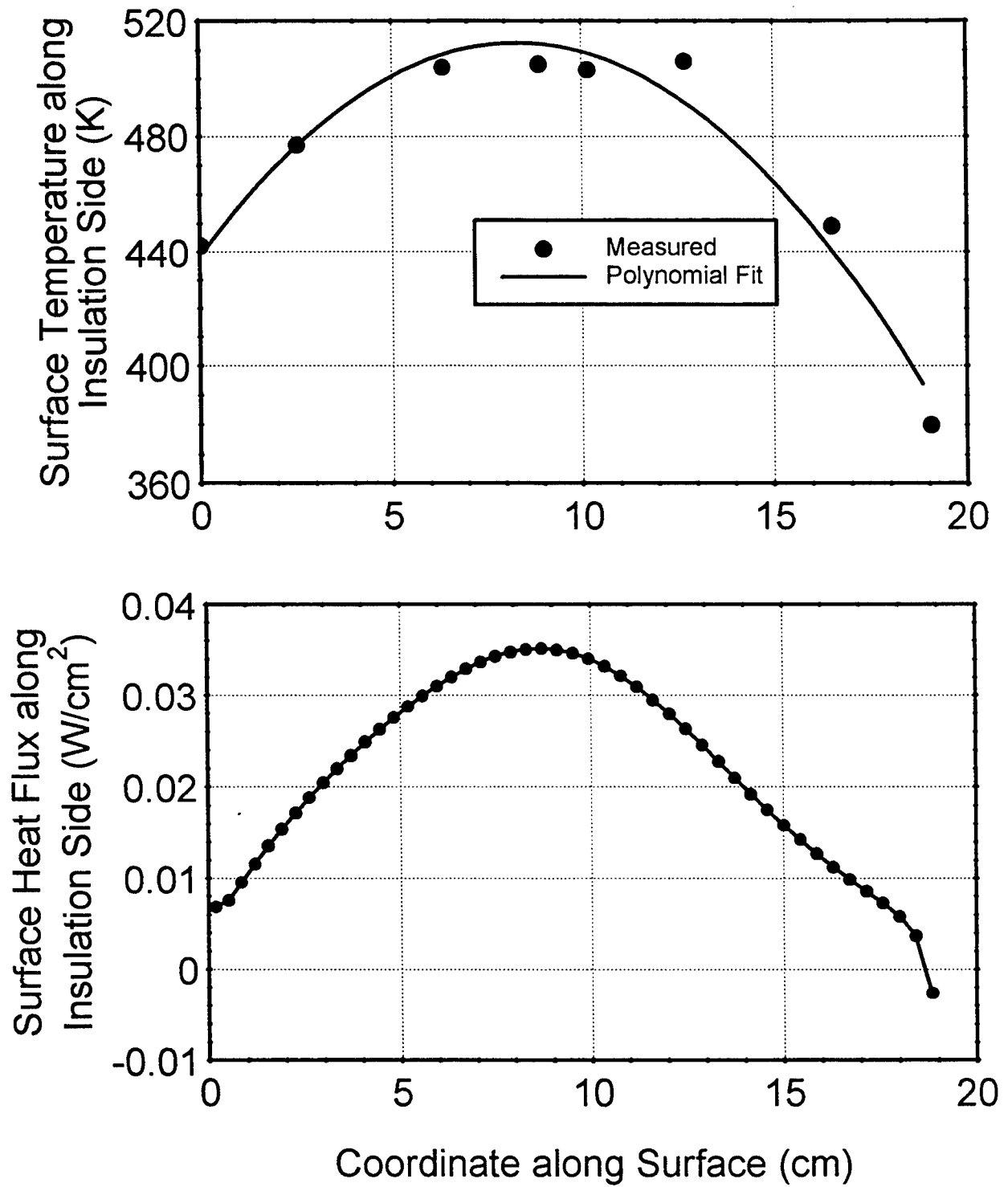


Figure 10.16. Temperature and Heat Flux Profiles along the Side Surface of PX-1B Insulation ( $T_{\text{heater}} = 1220 \text{ K}$ ).

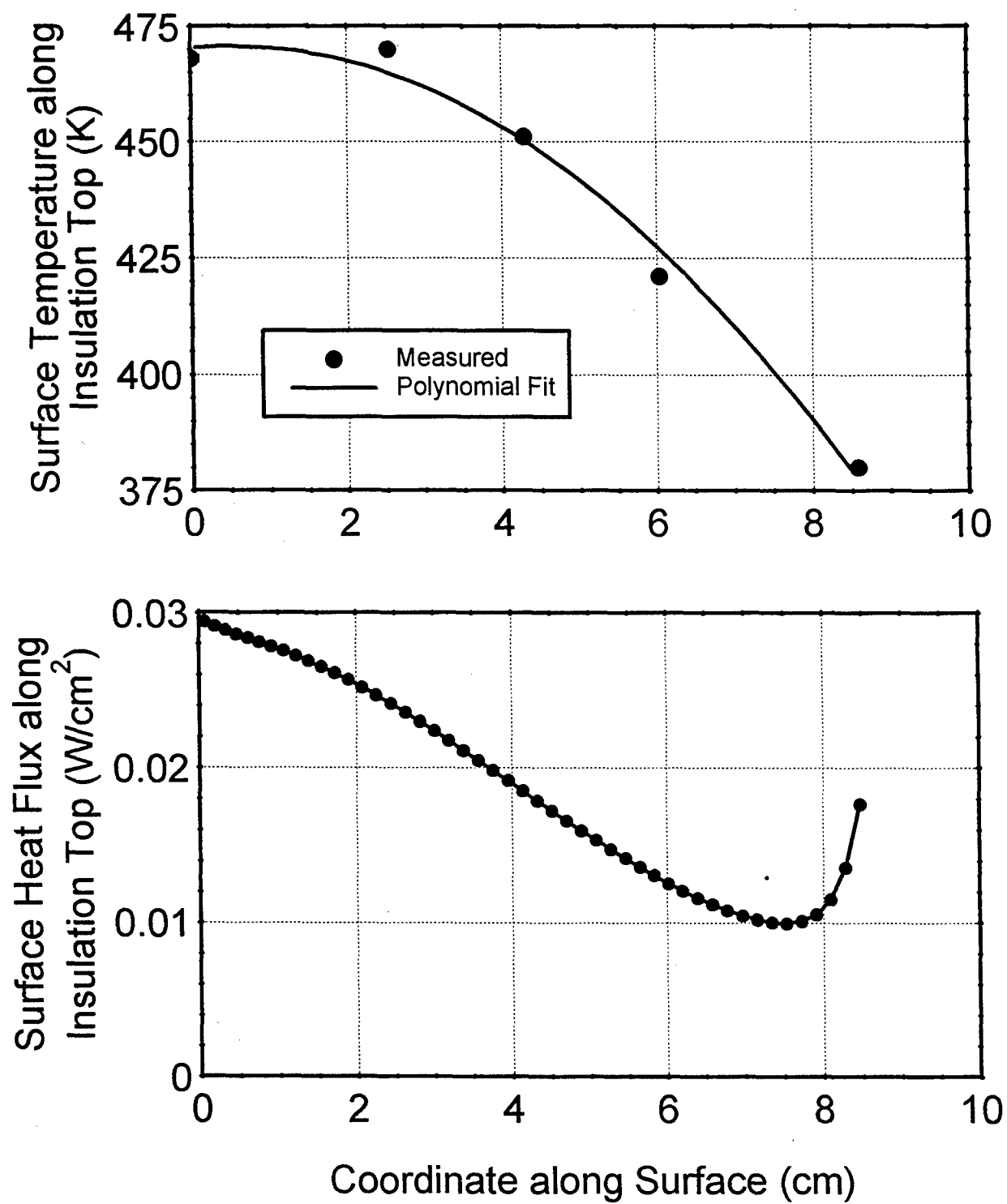


Figure 10.17. Temperature and Heat Flux Profiles along the Top Surface of PX-1B Insulation ( $T_{\text{heater}} = 1220 \text{ K}$ ).

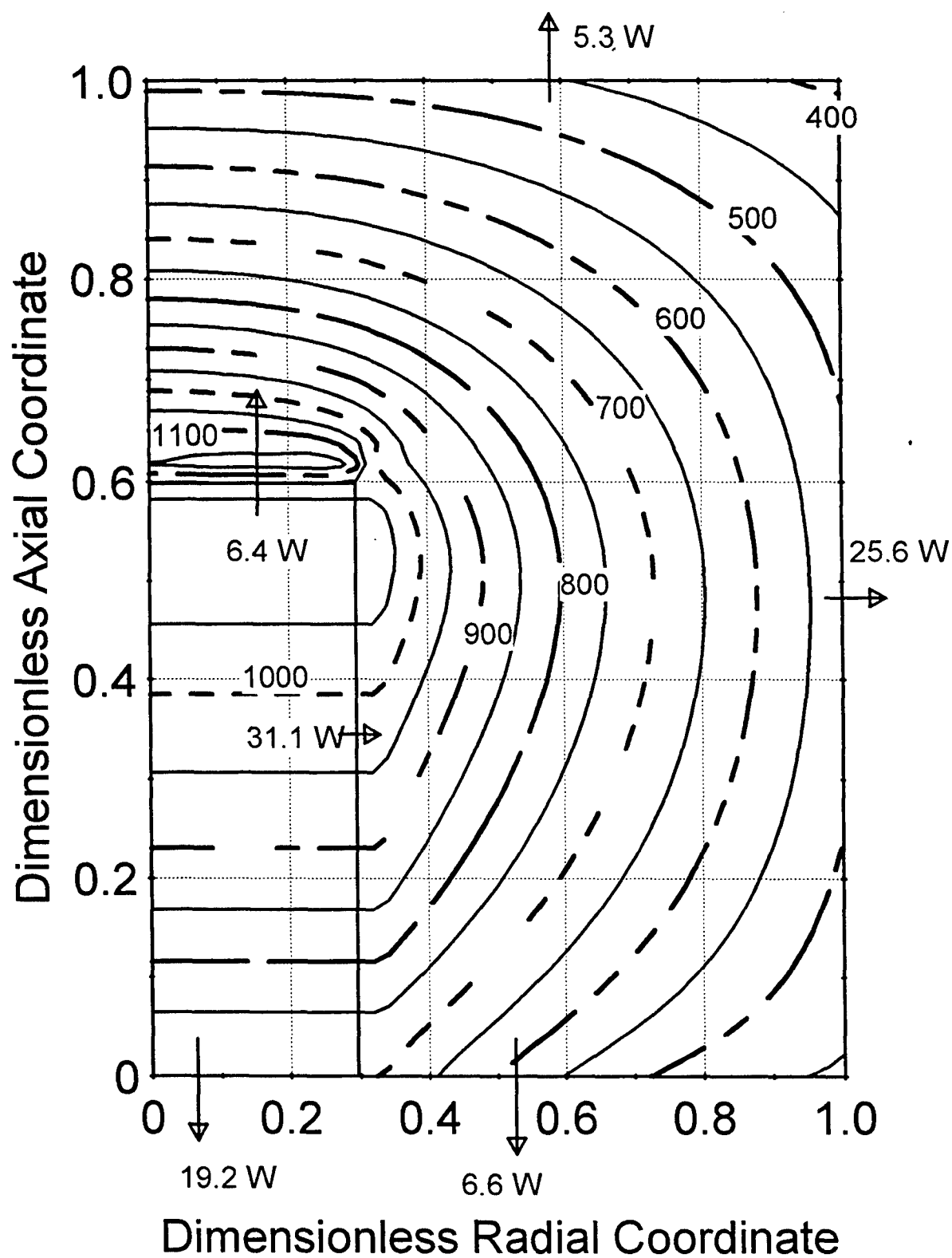


Figure 10.18. Predicted Isotherms and Heat Losses in the Insulation of PX-1B Cell ( $T_{heater} = 1220$  K).

insulation support plate was insulated with a thicker piece of Kaowool insulation material. Another improvement in the bottom insulation was made by substituting the supporting alumina rods between the stainless steel plate and the cell's cold plate with less thermally conductive stainless steel rods. Also, the inner radius of the stainless steel plate was increased. It was expected that with these improvements the difference  $|Q_{\text{loss}} - Q_{\text{loss}}'|$  for PX-4B would be significantly smaller than that for PX-2C.

Based on the results of these experiments, the radiation/conduction heat flow model in APEAM was also modified to include a variety of thermal boundary conditions and the potential to more accurately mimic and predict the cell wall losses through the insulation package surrounding the cell. The thermal boundary conditions at the cell ends were extended as follows:

- (1) The heat input, or the temperature, is specified at the hot end of the cell;
- (2) At the cold end of the cell (condenser), the user can either specify the heat removed, use convective air cooling (in this case, air flow rate and inlet temperature must be specified), or assume a radiative heat loss (then the emissivity of the cold plate and the radiative ambient temperature are specified). The latter can be used to evaluate the cell performance in space when coupled to a General Purpose Heat Source (GPHS), for example.
- (3) The user has the option of assuming an adiabatic cell side wall, or of coupling the cell heat flow model with a simplified radial insulation model. In the latter, a radiative gap is assumed between the cell wall and the insulation material, and the insulation ring can be surrounded with a metallic housing. The model accounts for both axial and radial conduction losses in the insulation/housing shell and dissipates heat by radiation at the outer surface of the housing. In an attempt to closely approximate the experimental setup at AFRL, the model was modified to include conduction losses through support rods between the copper condenser block and the insulation support plate. Also, the support plate can radiate heat. This condition is useful for investigating the performance in space of AMTEC cells coupled to GPHS units. In such case, the area of the cold end of the cell is not sufficient to dissipate the waste heat by radiation, and a large fraction of this heat is conducted along the generator metallic housing, to be radiated away.

The next section describes the air calorimeter experiment that was designed in an attempt to calibrate the cell's Boron Nitride heater block.



## 10.5 HEATER CALORIMETER EXPERIMENT TO EVALUATE HOT SIDE LOSSES

The conversion efficiency of an AMTEC cell is an important performance parameter. In the AFRL single-cell tests, electric power to the heater and electric power output of the cell are measured. However, to evaluate the cell's conversion efficiency, the thermal power into the cell's hot end,  $Q_{in}$ , must be known.

In the single-cell test setup, the heat is produced by a thin disk-like Boro-electric heater. The electric power to the heater, which can be accurately measured, goes either into the cell through its top (as net heat input into the cell) or into the insulation above the heater (as heat loss). If the heat loss can be predicted, the heat input to the cell can be simply calculated by subtracting the heat loss from the heater electric power.

A calorimeter of the cell heater was designed based on this conjuncture. The objective of this experiment was to calibrate the Boron Nitride (BN) heater block of the PX-series cells. The heater block was designed to fit over the hot side of the cell. The thermal heat input was provided by a Boro-electric heater rated at 200 W. The heater was covered by a 1-inch thick circular block of BN, instrumented with thermocouples. The inside of the calorimeter was cooled by air at atmospheric pressure. This experiment was designed to determine the actual heat input to the cell. The conduction heat losses into the BN heater block would be determined with the assistance of a two-dimensional heat conduction model.

To simulate the actual single-cell test setup, the Boro-electric heater was sandwiched between the bottom of the BN cylindrical block and the top of the air calorimeter (Figure 10.19), and a cooling confinement was used to thermally simulate the cell, as a heat sink for the heater. The heat from the bottom of the cell heater was removed and measured by the calorimeter, which had the shape and dimension of a typical, 1.25-inch diameter PX-series cell (Figure 10.19). The heat input to the calorimeter was removed by an impinging air jet inside the confinement. The heat removed by the air jet was easily calculated from the measured inlet and outlet temperatures and flow rate of the air. Then, the heat losses in the BN heater block can be estimated by subtracting the heat removed by the air jet from the Boro-electric heater electric power.

Fifteen K-type stainless-steel-shielded thermocouples were distributed in the heater block to measure temperature profiles along its boundaries (Figure 10.20). In order to determine the conduction heat losses from the Boro-Electric heater into the BN block, the two-dimensional heat conduction model developed in Section 10.2 was used. The heater block has temperature-specified boundary conditions at the top, bottom and side surfaces. Once the temperatures at these surfaces are obtained experimentally, the profiles can be fitted numerically and fed to the conduction model.

All parts were manufactured (BN heater block and supporter, cooling air confinement cell, flanges and air inlet and outlet tubings, stand and thermocouple supporters) and assembled, and the experimental setup was instrumented. The data acquisition software and the experimental package were prepared for testing in vacuum chamber. The calorimeter experiment became

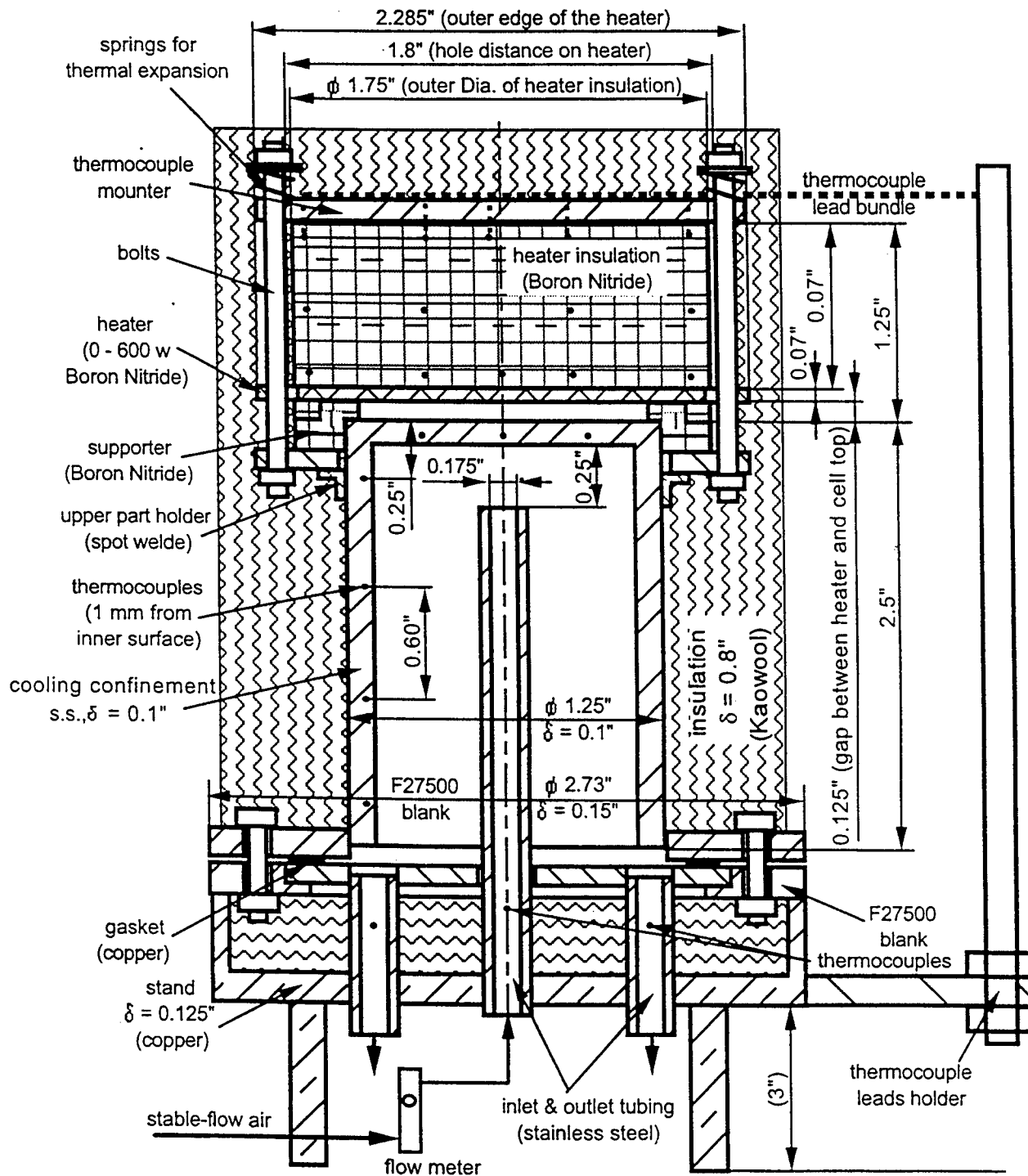


Figure 10.19a. Schematic of Calorimeter Experiment for Cell Heater Calibration.

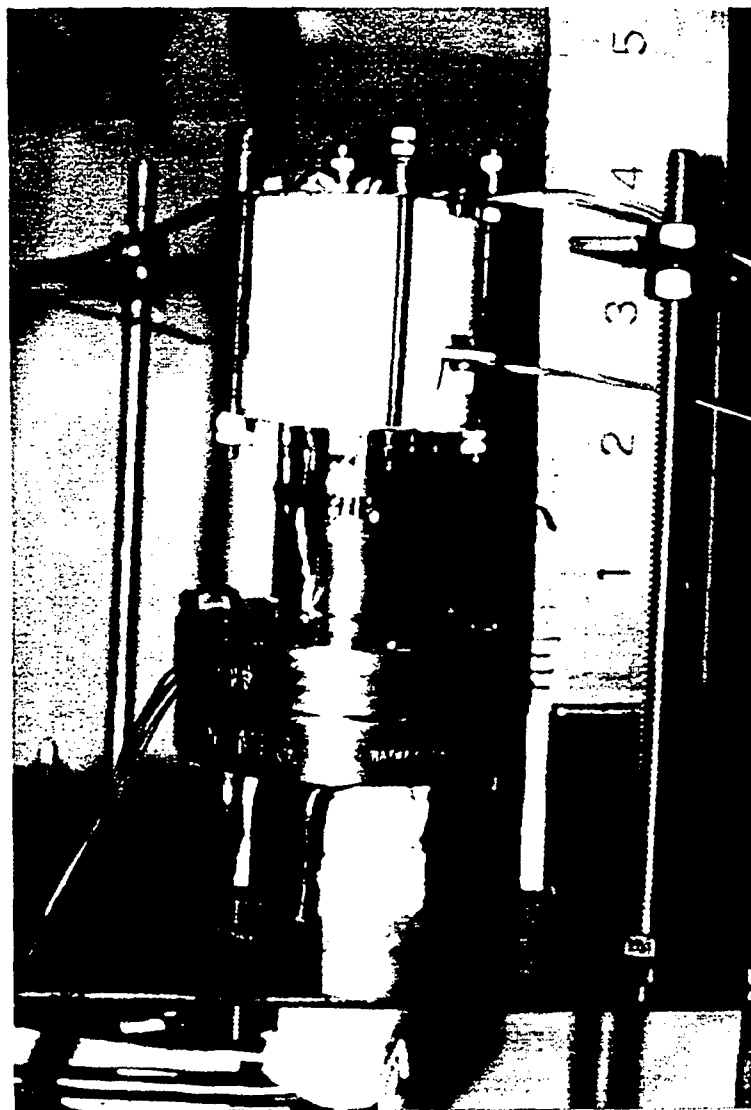


Figure 10.19b. Photograph of Calorimeter Experiment for Cell Heater Calibration.

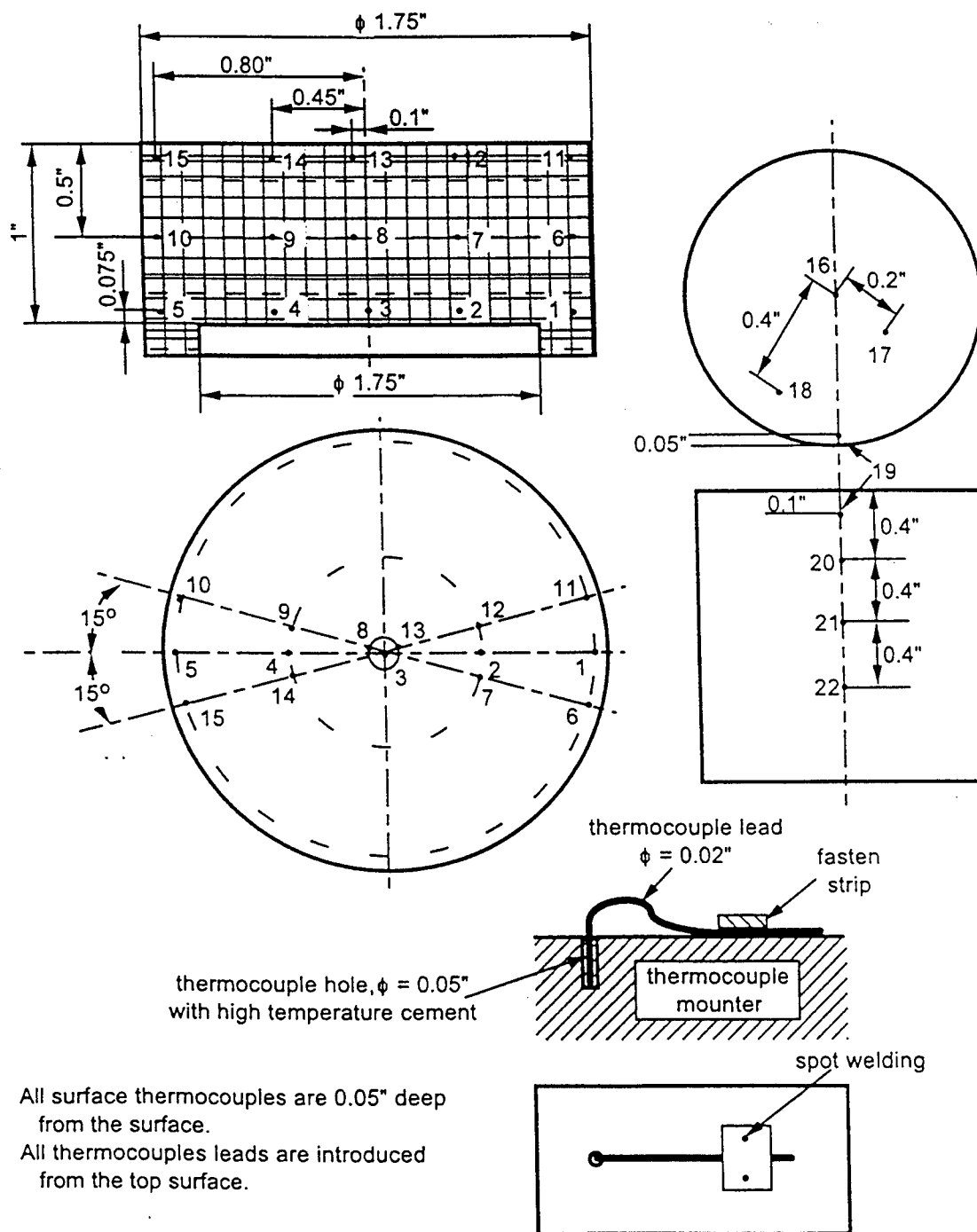


Figure 10.20a. Thermocouples Arrangement in Boron Nitride Heater Block.



Figure 10.20b. Photograph of Boron Nitride Heater Block.

operational in August 1997. Experimental results were obtained at heater electrical input powers of 30, 60 and 90 W. The Boron Nitride heater block was instrumented with 15 K-type shielded thermocouples and boundary temperature profiles were extrapolated and used in the two-dimensional heat conduction model to calculate the heat losses at the faces of the block. Unfortunately, the test was terminated early due to detection of air leakage in some of the connecting joints. The test of the calorimeter was then postponed indefinitely in order to meet the deadline for testing the PX-series cells.

The test results were not conclusive because Boron Nitride has a relatively high thermal conductivity (comparable to stainless steel), and the block was relatively small in size ( $\sim 1$  inch). The temperature gradient in the Boron Nitride block was less than 10 K at an average block temperature of  $\sim 700$  K. The uncertainty in the temperature measurements was about 4 K, causing unrealistic measured temperature profiles along the block surfaces. Consequently, the heat losses calculated based on the measured temperatures in the BN heater block were not reliable (the error in heat losses was as large as 50%).

## 10.6 SUMMARY AND CONCLUSION

The conversion efficiency of an AMTEC cell is an important performance parameter. In the AFRL single-cell tests, electric power to the heater and electric power output of the cell are measured. However, to evaluate the cell's conversion efficiency using experimental data, the thermal power into the cell's hot end,  $Q_{in}$ , must be known.

In this chapter, a number of calibration experiments were designed to attempt to evaluate the heat losses in the heater block of the cell and the surrounding insulation, identify critical loss paths, and improve the experimental setup at AFRL.

One method of obtaining the temperature of the Boro-electric heater on the cell's hot side is to measure the electric voltage and current of the heater and deduce its electric resistance. The electric resistivity of the wire is a function of temperature, therefore the average heater temperature can be deduced from the value of the heater resistance. To this purpose, a resistivity calibration experiment was designed to measure the electrical resistance of the Boro-electric heater as a function of temperature. Unfortunately, measurements of the heater resistance could not lead to accurate evaluation of the heater temperature, because of the relatively small slope of the heater resistivity in the temperature range of interest  $> 1000$  K; the uncertainty in the calculated heater temperature was quite large, about  $\pm 40$  K.

An indirect-heat-loss measurement technique was devised, to evaluate the conduction heat losses in the single-cell test from the measured temperature profiles along the insulation surface and the cell wall. A two-dimensional, transient heat conduction model was developed, and benchmarked, using a number of sample thermal problems with known analytical solution. This 2-D heat conduction model was then used in conjunction with temperature measurements to predict the

heat losses in the alumina powder insulation of the PX-1 series of cells. A specially-designed thermocouple arrangement was used to provide temperature distributions along the boundaries of the insulation package. These measurements provided the necessary boundary conditions to the 2-D conduction model, to predict the heat losses through the insulation. The measured temperatures along the cell and insulation boundaries were fitted using a polynomial fit subroutine, and the resulting temperature profiles were input as boundary conditions to the 2-D, cylindrical heat conduction model. Calculated results were consistent with experimental measurements in most cases.

Knowledge of the heat losses and heat flux profiles at the different boundaries of the insulation, and examination of test and model results led to some improvements in the insulation of single-cell setups. Results led to believe that because of poor insulation, a significant fraction of the heat input was conducted between the PX-2C cell condenser and the stainless steel, insulation support plate. In the following cells' setup, the support plate was insulated with a thicker piece of Kaowool insulation material. Another improvement in the bottom insulation was made by substituting the supporting alumina rods between the stainless steel plate and the cell's cold plate with less thermally conductive stainless steel rods. Also, the inner radius of the stainless steel plate was increased.

Based on the results of these experiments, the radiation/conduction heat flow model in APEAM was also modified to include a variety of thermal boundary conditions and the potential to more accurately mimic and predict the cell wall losses through the insulation package surrounding the cell.

Next, a heater calorimeter experiment was designed to calibrate the heat losses in the heater Boron Nitride block. The heater block was instrumented with 15 K-type shielded thermocouples, and boundary temperature profiles were extrapolated and used in the two-dimensional heat conduction model to calculate the heat losses at the faces of the block. To simulate the actual single-cell test setup, the Boro-electric heater was sandwiched between the BN cylindrical block and the top of the air calorimeter. The heat from the bottom of the cell heater was removed and measured by the calorimeter, which had the shape and dimensions of a typical, 1.25-inch diameter PX-series cell. The heat input to the calorimeter was removed by an impinging air jet inside the confinement. The heat removed by the air jet could be easily calculated from the measured inlet and outlet temperatures and flow rate of the air.

The test results were not conclusive because Boron Nitride has a relatively high thermal conductivity (comparable to stainless steel), and the block was relatively small in size (~ 1 inch). The temperature gradient in the Boron Nitride block was less than 10 K at an average block temperature of ~ 700 K. The uncertainty in the temperature measurements was about 4 K, causing unrealistic measured temperature profiles along the block surfaces. Consequently, the heat losses calculated based on the measured temperatures in the BN heater block were not reliable (the error in heat losses was as large as 50%).

The difficulties encountered in these calibration experiments reflect the challenges of evaluating the heat losses in the experimental setup. In early tests of PX-series cells, experimental data were

obtained at fixed heater electrical power and air cooling flow rate. Therefore, these data were more difficult to use to benchmark the model, since the power input to the hot end of the cell was unknown, and because of the difficulty of predicting the effective heat transfer coefficient and area in the air loop (it is believed that axial conduction and heat losses along the air lines are the principal cause of this problem). Another limitation that was encountered was that, originally, experimental measurements focused on the high-current peak power region, at external load resistances below  $2.5\ \Omega$ . In this region, the cell current is relatively high (usually above 2 A), and we found that the former thermal model of the conical evaporator wick underpredicted the evaporator temperature by as much as 70 K.

Because of these limitations, early analyses of PX-Series cells data focused on matching the cell electrical peak power output by adjusting the (unknown) input power to the cell (see PX-2C data analysis in Chapter 11). As a result, the calculated temperatures in the cell, while reasonable, were only approximate, within 40 K of the measured temperatures.

In subsequent testing of PX-4C and PX-5A cells, the external load resistance was varied to values as high as  $10\ \Omega$ , to allow analysis of the load-following characteristic of the cells. At resistances above  $3\ \Omega$ , the cell current was typically below 2 A, and the measured temperatures could be used with more confidence to benchmark the thermal model of PX-series cells. Also, the latest experiments were consistently performed at fixed (controlled) cell hot end and cold (condenser) end temperatures, removing the need of guessing the cell input power and convective heat transfer coefficient for modeling purposes. To facilitate cell data analysis and model benchmarking, the thermal model was modified to allow specification of the cell hot end temperature, and of the cold plate (condenser) temperature, independently. Also, the thermal model of the conical evaporator wick was modified after the observation that the conical evaporator performed better (i.e. provided higher evaporator temperature) at high current than a simulated flat-end evaporator. At high cell electrical currents, the improvement is essentially due to the effect of the increased effective evaporation area of the wick, which practically results in an increased effective conductance near the evaporative surface. The new evaporator model, which takes that effect into account, predicts evaporator temperatures typically about 50 K higher than the original model, which are within 20 K of the measurements.

In the next chapter, test results and performance data analysis of single cells tested at AFRL are presented, along with APEAM's predictions. The model is useful since it can provide information on the cell's electric and thermal performances that cannot be obtained experimentally.



## 11. SINGLE-CELL TEST RESULTS AND PERFORMANCE DATA ANALYSIS

In this chapter, the vacuum test data of single-cell PX-series AMTEC cells performed at the Air Force Research Laboratory (AFRL) during the past 3 years are presented. Results of the performance data analyses and model's predictions are also presented. Model predictions are also compared with experimental measurements for most of the PX-series cells tested at AFRL.

The experimental setup, data acquisition, and test procedures were described in Chapter 8. The measurement uncertainties in the vacuum tests were calculated in Chapter 9 and Appendix E.

### 11.1 NOMENCLATURE

#### English

$B$	Temperature-independent, charge-exchange current coefficient ( $A.K^{1/2}/Pa.m^2$ )
$F$	Faraday's constant, $F = 96,485$ Coulomb / mole
$G$	Dimensionless factor for pressure losses
$h_{ev}$	Height of the evaporator wick surface measured from BASE tubes' support plate (m)
$I$	Cell electrical current (A)
$J$	Electrode current density ( $A/m^2$ )
$k$	Thermal conductivity ( $W/m.K$ )
$L_E$	Electrode length (m)
$\dot{m}$	Sodium mass flow rate in cell (kg/s)
$M$	Molecular weight of sodium, $M = 23$ gm / mole
$Mo$	Molybdenum
$N_B$	Number of BASE tubes in cell (electrically connected in series)
$Ni$	Nickel
$P$	Sodium pressure (Pa)
$P_e$	Cell electrical power output ( $W_e$ )
$Q$	Heat flow (W)
$Q_{heater}$	Heater electric power (W)
$Q_{in}$	Cell heat input (W)
$R_c$	Contact radius between spherical particles in sintered wick (m)
$R_{cont}$	Contact resistance between BASE/electrode/current collector ( $\Omega.cm^2$ )
$Rh$	Rhodium (reflective coating)
$R_L$	External load resistance per cell ( $\Omega$ )
$R_{leak}$	Leakage resistance of BASE braze joint ( $\Omega$ )
$R_p$	Effective pore radius of wick (m)
$R_s$	Radius of spherical particles in sintered wick (m)
$SS$	Stainless steel
$T$	Temperature (K)
$TC$	Thermocouple

$V_L$  External load voltage (V)

## Greek

$\Delta P_{loss}$  Sodium liquid pressure losses in wick (Pa)  
 $\Delta P_{cap}$  Wick capillary pressure head (Pa)  
 $\Delta T$  Temperature margin,  $\Delta T = T_\beta - T_{ev}$  (K)  
 $\Delta T_{min}$  Temperature margin,  $\Delta T_{min} = T_\beta - T_{ev}$  (K)  
 $\Delta T_{max}$  Brazes temperature margin,  $\Delta T_{max} = T_{braz} - T_{ev}$  (K)  
 $\varepsilon$  Volume porosity of sintered wick  
 $\varepsilon'$  Prime porosity of sintered wick, Equations 11.2 and 11.4  
 $\varepsilon_{cd}$  Effective radiative emissivity of condenser surface  
 $\eta$  Cell conversion efficiency (%)  
 $\sigma$  Surface tension of liquid sodium (N / m)

## Subscript / Superscript

air Air calorimeter at condenser end  
 braze BASE tube metal-to-ceramic braze  
 cd Cell condenser  
 E Cathode metal electrode  
 eff Effective property of sintered wick  
 ev Wick evaporator  
 hot Cell's hot end  
 in Input at hot end of cell  
 L Liquid sodium  
 loss Side wall losses  
 max Maximum value  
 plen Plenum side wall  
 sat Liquid-vapor saturation line  
 stud Conduction stud  
 W Metal wick matrix (SS)  
 wall Cell's side wall  
 $\beta$  Cold end of BASE tube

## 11.2 CELLS DESIGNS, OPERATING CONDITIONS AND PERFORMANCE DATA

Table 11.1 lists the materials and dimensions of the PX-series cells tested at the AFRL. These cells, which used TiN anode and cathode electrodes, were cylindrical in shape, and weighted approximately 150 grams each.

The sodium vapor pressure on the anode side is approximately equal to its saturation pressure at the evaporator temperature,  $T_{ev}$ . Thus, at typical  $T_{ev}$  of 950 K and 1100 K, the sodium vapor pressure is 10 and 60 kPa, respectively. The sodium vapor pressure on the cathode side, however, is 2 to 3 orders of magnitude lower ( $< 50$  Pa). In the AFRL tests, the cell's hot end temperature ( $T_{hot}$ ) was varied from 1023 to 1186 K and the condenser temperature ( $T_{cd}$ ) from 550 K to 650 K. In some of the cells, the vapor temperature in the cavities of the BASE tubes ( $T_{\beta}$ ) and the evaporator were measured using inserted, metal sheathed thermocouples. Most tests were performed at constant hot side and condenser temperatures, a few of the earlier cells were tested at constant heat input,  $Q_{in}$ . The former reduces experimental uncertainties associated with determining the actual heat input to the cell from the electric heater. The electric heater was radiatively coupled to the cell's hot side. The cells were thermally insulated on the sides using alumina powder, or Min-K, a light-weight, low-conductivity material. The outer surface of the electric heater block of the cell was insulated using Min-K. Heat removal from the cell condenser was accomplished using an air calorimeter. The condenser plate was insulated using a Kaowool blanket. Parasitic heat losses in the cell wall were transported by radiation across a small gap to the surrounding insulation package, then to the vacuum chamber wall. The AFRL tests were performed in hard vacuum ( $< 10^{-7}$  torr). More details on the single-cell experimental test setup at AFRL can be found in Chapter 8. In particular, Section 8.9 focuses on the differences and improvements from one cell setup to another.

The actual interior surface temperature of the cell's condenser, needed to perform modeling calculations of the cells, was higher than that measured in the tests at the outer surface of the cold side of the cell (Table 11.2), by the temperature drop across the condenser wall and wick structure. This temperature drop, including an uncertainty in the measured condenser temperature of 0.4%, varied between 10-20 K. The uncertainty in the hot side temperature was also 0.4%, and was  $\sim 2\%$  in the electric power ( $Pe$ ) measurements (see Chapter 9 and Appendix E). Detailed analyses of PX-series cells' data were performed using the AMTEC Performance and Evaluation Analysis Model (APEAM) developed in Chapters 3 – 5.

As indicated in Table 11.1, the PX-1B and PX-1C cells each had 7 BASE tubes covered with short TiN electrodes, but no conduction stud nor evaporator standoff rings. The anode and the cathode current collectors were made of 100-mesh copper screens tied with molybdenum wires. PX-1C was identical to PX-1B, except it had a SS circumferential radiation shield. PX-1B failed prematurely because the silver in the TiCuAg cold feed-through braze was dissolved by the sodium working fluid. This problem was eliminated in the next generation cells by using a TiCuNi feed-through braze instead. The presence of a thermal radiation shield in PX-1C increased the electric power output by about 0.35  $W_e$ , over PX-1B, at BASE tube and condenser temperatures

Table 11.1. Design Parameters of PX-Series Cells Tested at AFRL.

Cell design	PX-1B	PX-1C	PX-2A	PX-2C	PX-4C	PX-5A	PX-5B	PX-3G	PX-3A	PX-3C
Cell diameter	1.5"	1.5"	1.5"	1.5"	1.5"	1.5"	1.5"	1.5"	1.25"	1.25"
Cell height	4.0"	4.0"	3.5"	3.5"	4.0"	4.0"	4.0"	4.0"	4.0"	4.0"
Evaporator shape	deep cone	deep cone	deep cone	deep cone	deep cone	deep cone	shallow cone	shallow cone	deep cone	flat
Evaporator position	0.5"	0.5"	0.15"	0.15"	0.15"	0.15"	0.15"	0.15"	0.204"	0.3"
Evaporator standoff thickness	0.71mm	0.71mm	0.71mm	1.5 mm	0.71mm	0.71mm	0.71mm	0.71mm	0.71mm	0.71mm
Evaporator standoff material	SS	SS	SS	SS	SS	SS	SS	SS	SS	Ni
Standoff rings thickness	-	-	-	-	2.5 mm	2.5 mm	1.25 mm	1.25 mm	1.1 mm	-
Standoff rings material	-	-	-	-	SS	SS	Ni	Ni	Ni	-
Conduction stud area	-	-	100 mm <sup>2</sup>	100 mm <sup>2</sup>	100 mm <sup>2</sup>	100 mm <sup>2</sup>	100 mm <sup>2</sup>	100 mm <sup>2</sup>	38 mm <sup>2</sup>	OSC
Stud material	-	-	SS	SS	SS	SS	SS	SS	SS	Ni
Number of BASE tubes	7	7	7	7	6	6	6	6	5	5
Total length of tubes	27 mm	27 mm	40 mm	40 mm	40 mm	40 mm	40 mm	40 mm	32 mm	40 mm
Electrode area per tube	3 cm <sup>2</sup>	3 cm <sup>2</sup>	6 cm <sup>2</sup>	6 cm <sup>2</sup>	6 cm <sup>2</sup>	6 cm <sup>2</sup>	6 cm <sup>2</sup>	6 cm <sup>2</sup>	6 cm <sup>2</sup>	6 cm <sup>2</sup>
BASE tube braze material	TiCuNi	TiCuNi	TiCuNi	TiCuNi	TiNi	TiNi	TiNi	TiNi	TiNi	TiNi
Current collector networks	100-mesh Cu	100-mesh Cu	100-mesh Cu	100-mesh Cu	60-mesh Mo	60-mesh Mo	60-mesh Mo	60-mesh Mo	60-mesh Mo	60-mesh Mo
Feedthrough braze material	TiCuAg	TiCuAg	TiCuNi	TiCuNi	TiCuNi	TiCuNi	TiCuNi	TiCuNi	TiCuNi	TiCuNi
Radiation shield	-	circular SS	chevrons SS	circular SS	circular SS	circular SS	circular Ta	circular SS	circular SS	(Rh coating)
Condenser type	SS mesh	SS mesh	SS mesh	SS mesh	SS mesh	SS mesh	SS mesh	SS mesh	SS mesh	SS mesh
Hot side structural material	SS	SS	SS	SS	SS	SS	SS	SS	SS	Ni
Cell wall material	alumina powder	alumina powder	Min-K / powder	Min-K / powder	Min-K / powder	Min-K / powder	Min-K / powder	Min-K / powder	Min-K (tight fit)	Min-K (tight fit)
Type of thermal insulation	alumina powder	alumina powder	Min-K / powder	Min-K / powder	Min-K / powder	Min-K / powder	Min-K / powder	Min-K / powder	Min-K (tight fit)	Min-K (tight fit)
Hours of operation	240 hrs	240 hrs	96 hrs	600 hrs	1800 hrs	672 hrs	3729 hrs	1590 hrs	9900 hrs	2040 hrs
Comments	feed-through braze failure (loss of Ag)	dissected before failure	dissected before failure. Condensation of sodium in conical chevrons	Pe slowly dropped to zero. Cu from collector clogged artery/tubes? Cu, Ni lost from brazes	stable > 500 hr maturing. Observe power hump (maybe due to $\Delta T < 0$ )	Creare reduced power hump ( $\Delta T < 0$ ). Loss of cooling caused $T_p \sim 1136$ K (tubes detached)	enhanced heat transfer to tubes (shorter/thicker insulator). Low sodium inventory when dissected	8-cell Ground-Demo system	stable > 500 hr maturing (16% degradation during maturation)	OSC design. Cell wall and artery are coated with Rhodium (no internal shield)

Table 11.2. Measured and Predicted Performance Characteristics of PX-Series Cells Tested at AFRL.

Cell tested	# of $\beta$ -tubes / electrode area per tube	$T_{hot}$ (K)	$T_p$ (K)	$T_{cd}$ (K)	$Pe^{max}$ (We)	cell current	$\eta^{exp}$ (estimate)	$\eta^*$ (APEAM)
PX-1B	7 / 3 cm <sup>2</sup>	-	975	550	0.45	-	-	-
		-	1140	520	1.17	-	5.6%	-
PX-1C	7 / 3 cm <sup>2</sup>	-	975	550	0.80	-	4.7%	-
		-	1074	575	1.45	-	7.6%	-
PX-2A	7 / 6 cm <sup>2</sup>	-	975	550	2.40	-	6.1%	-
PX-2C	7 / 6 cm <sup>2</sup>	-	975	550	4.30	~1.4 A	-	-
		1186	1010	529	4.35	1.47 A	-	11.1%
PX-4C	6 / 6 cm <sup>2</sup>	1130	981	565	3.90		10.1%	10.5%
PX-5A	6 / 6 cm <sup>2</sup>	1023	938	623	2.80	1.87 A	11.2%	9.3%
		1123	1010	623	4.25	2.62 A	10.9%	11.8%
PX-5B	6 / 6 cm <sup>2</sup>	1023	-	623	1.59	1.13 A	-	8.6%
		1123	-	623	3.52	2.16 A	-	11.2%
PX-3G*	6 / 6 cm <sup>2</sup>	1073	976*	523	2.74	1.55 A	-	11.7%
		1123	1011*	553	3.71	1.80 A	-	13.1%
PX-3A	5 / 6 cm <sup>2</sup>	1023	935	623	2.10	1.65 A	12.4%	9.7%
		1123	1014	623	3.90	2.32 A	15.0%	13.0%
		1173	1044	623	4.70	2.54 A	14.7%	14.2%
PX-3C	5 / 6 cm <sup>2</sup>	1023	933*	623	1.44	1.11 A	-	7.7%
		1073	967*	623	2.01	1.37 A	-	8.9%
		1123	1000*	598	2.76	1.78 A	-	10.2%

\* Calculated using APEAM model

# ground demonstration test of 8-cell power unit

of 975 K and 550 K, respectively (Table 11.2). PX-1C did not fail in the tests, and post-test examination showed no sodium condensing on the radiation shield nor the cell wall.

In PX-2A and PX-2C cells, the surface area of the electrodes was double that in PX-1 cells. They also had a conduction stud between the hot plate and the BASE tubes support plate and the evaporator was moved closer to the hot plate (Table 11.1). In the test setup of these cells, the alumina powder insulation that surrounded the PX-1 series cells was replaced by Min-K, to reduce heat losses along the sidewall of the cell. As a result of these changes, PX-2A produced three times as much electric power (2.4 We) as PX-1C (0.80 We). However, the performance of PX-2A became erratic after only 96 hrs. The post-test examination revealed that a large amount of sodium had condensed on the conical chevrons heat shield of the cell.

The PX-2C cell, which had circumferential heat shields, instead of conical chevrons, did not experience Na condensation on the shield. The PX-2C evaporator, however, ran much hotter than in PX-2A, because of using a thicker evaporator standoff. As a result, PX-2C produced

roughly twice as much electric power as PX-2A (Table 11.2), or 4.3 We, a very significant improvement over previous cells. PX-2C had an estimated peak efficiency of ~ 11% and operated well for about 500 hrs.

Subsequently, the electric power output of the PX-2C cell decreased slowly to nil in about 100 hrs. Post-test examination revealed that the copper in the current collectors evaporated and deposited onto the surfaces of the shield, artery, and feed-through, and possibly clogged the liquid sodium return wick and/or the BASE tubes (Alger 1997 and Svedberg et al. 1997). A Scanning Electron Microscopy analysis of the cell revealed that Cu and Ni were no longer present in the BASE tubes brazes.

In all subsequent cells, the copper current collectors were replaced with 60-mesh molybdenum screens. Copper was also eliminated from the BASE tubes brazes by using TiNi braze material. The number of BASE tubes in PX-4C, PX-5A, PX-5B and PX-3G was also reduced from 7 to 6, and metal rings were placed around the evaporator structure to enhance heat conduction from the support plate (Table 11.1).

Upon loading the PX-2C cell from nominal short circuit condition, the electrical output power initially spiked, then dropped gradually to its nominal value. This power spike was attributed to an initial large negative temperature margin due to a pressure build up at the BASE anode, following the sudden reduction in the cell electric current upon applying the external load (Merrill et al. 1998). A negative margin  $\Delta T$  (*the temperature difference between the cold end of the BASE tubes and the evaporator*) means that condensation of sodium vapor could occur inside the BASE tubes. Such condensation would be detrimental to the cell operation, since it would deplete the amount of working fluid available for circulation in the cell and cause an electrical shortage among the BASE tubes in the cell. Therefore, the evaporator structure must be designed carefully to insure that it runs sufficiently cooler than the BASE tubes.

As shown in Table 11.2, PX-4C performed almost as well as PX-2C, which had one extra BASE tube. The operation of PX-4C was stable for about 1300 hrs, following a period of electrodes maturation of ~500 hrs.

The PX-5A cell was identical to PX-4C, except for using a Creare condenser. As shown in Table 11.2, the use of a Creare condenser, combined with an increased condenser temperature (from 565 K to 623 K), reduced the parasitic heat losses in PX-5A. The higher evaporator and BASE tubes temperatures increased the cell electrical power output to 4.25 We.

The predicted efficiency of PX-5A (11.8%) was higher than that of PX-4C (10.5%) (Table 11.2). Unfortunately, PX-5A failed shortly after an accidental loss of the condenser cooling that caused the BASE tubes temperature to reach ~1136 K, and the tubes brazes to overheat and eventually fail.

PX-5B was similar to PX-5A, except that it had a shallow cone evaporator, a tantalum sidewall shield, 1.255 mm-thick nickel rings along the evaporator standoff, and improved BASE brazes

conductance, using a shorter and thicker  $\alpha$ -alumina insulator (Table 11.1). PX-5B, however, did not perform satisfactory, due to too low initial sodium inventory.

PX-3A had smaller dimensions than PX-4C and PX-5A, and only 5 shorter BASE tubes. It used a Creare condenser, a deep conical evaporator, a SS sidewall shield, a thinner conduction stud, and five 1.1 mm-thick nickel rings around the evaporator standoff (Table 11.2). The evaporator of PX-3A was moved away from the tubes support plate, to eliminate the potential for sodium condensation inside the BASE tubes. Such condensation would be detrimental, since it would deplete the amount of working fluid available for circulation in the cell, and could cause an electrical shortage among the BASE tubes.

Table 11.2 shows the effect of increasing the hot side temperature of PX-3A. A 100 K increase from 1023 K to 1123 K increased the peak efficiency from 9.7% to 13.0%, and the cell electric power output from 2.1 to 3.9  $W_e$ . Since increasing the hot side temperature also increased radiation and conduction parasitic losses, the percent increase in the cell efficiency was lower than that in  $Pe$ .

The predicted peak efficiency of PX-3A was 1.2 points higher than that of PX-5A, at identical hot and cold side temperatures (Table 11.2). PX-3A was the most efficient cell tested at AFRL. The power density of the electrodes in PX-3A was 130  $mW/cm^2$  versus 118  $mW/cm^2$  in PX-5A, a 10% increase, at hot and cold side temperatures of 1123 K and 623 K, respectively.

The best performance was that of PX-3A, at a hot side temperature of 1173 K (Table 11.2). This cell reached a peak electric power of 4.7  $W_e$  (or power density of 157  $mW/cm^2$ ) and a predicted peak efficiency of 14.2 %. Since about 6.1 Watts of thermal energy were lost through the cell wall, an adiabatic side wall, a condition that is approximately met in a PX multi-cell generator, would have produced a peak power of 5.1  $W_e$  and a peak efficiency > 17 %. At a hot side temperature of 1173 K, the evaporator temperature in PX-3A was  $\sim 1050$  K, and the BASE tube brazes operated at  $\sim 1150$  K.

The PX cells tested at AFRL to date were intended for long-term (7-15 years) space missions. However, acceleration tests and corrosion studies have shown that SS structural material might not be suitable for use in such missions (Alger 1997, Svedberg et al. 1997). There is a concern the iron dissolved from SS by liquid sodium in the condenser mesh pad will rapidly saturate liquid sodium in the return wick. Eventually, Fe will precipitate at the intake of the return wick, gradually decreasing its permeability. Also, Mn and Fe from the SS could contaminate the TiN electrode surfaces, degrading their performance.

In order to alleviate these concerns, other structural materials were used in PX-3C. This cell was similar to PX-3A, except for the use of nickel for the hot plate, conduction stud, BASE tubes support plate, and evaporator standoff. The sidewall was made of Haynes-25, an alloy with 25% lower thermal conductivity than SS-316. Instead of an internal heat shield, PX-3C had a highly-reflective rhodium (Rh) coating on the inside surface of the wall and on the outer surface of the artery SS guide tube, and the evaporator surface was flat. PX-3C did not perform as well as PX-

3A, however, because the evaporator of the former ran about 50 K cooler. It is also possible that the rhodium coatings had evaporated after only a few 100 hrs of operation at high temperature.

The following sections present in details vacuum test results and data analysis and model predictions of a number of PX-series cells tested at AFRL: PX-1A, PX-2C, PX-4C, PX-5A, PX-3A and PX-3C.

### 11.3 PX-1A CELL DATA ANALYSIS

Heating, insulation, and instrumentation packages were designed for testing the multi-tube PX-1A AMTEC cell. Because the Boro-electric heaters used for the PL-9 Series cells were too small for the PX-1 cell, a heater using conventional Tungsten bulb wires was manufactured at the lab (see Chapter 8). The heater was covered with another self-made Boron Nitride block, which was instrumented with K-type thermocouples. Because of the high thermal conductivity of the block material (Boron Nitride), the uncertainty in the temperature measurements, and the non-symmetric heating wire arrangement, the analysis of the heat conducted through the heater block was inconclusive (see Section 10.5). Testing of cell PX-1A was terminated because of the failure of the cell (sodium leak).

A preliminary study of the measured performance and of the heat and mass flows in the PX-1A cell suggested that the liquid-return artery was probably capillary limited and cannot provide the optimum 9 gram/hr of sodium to the evaporator in its current design (7.5 cm long, 7 mm<sup>2</sup> in cross section area, and 0.20 volume porosity). Also, it is doubtful that the conductive and radiative modes of heat transfer in the cell are sufficient to provide enough heat to the evaporator end of the artery.

#### 11.3.1 Liquid-Return Artery Capillary Limit

The liquid-return artery cannot provide the optimum 9 gram/hr of sodium to the evaporator in its current design (7.5 cm long, 7 mm<sup>2</sup> in cross section area, and 0.20 volume porosity). An analysis of the pressure losses in the artery and of the capillary limit shows that an artery with identical length and cross section needs a porosity greater than 0.23 if the capillary action occurs at the cold condenser end, and greater than 0.26 when the capillary action occurs at the hot evaporator end of the artery. A chart has been constructed which shows the relationship between volume porosity,  $\epsilon$  and average pore radius,  $R_p$  of the metal powder to insure that the capillary limit is not reached (see Chapter 6, Section 6.4). The temperatures of the condenser and the evaporator were taken as 600 K and 975 K respectively, and the sodium flow rate was assumed to be 10 gram/hr in this analysis. As shown in Figure 11.1, the maximum value of the pore size is limited by the fact that the wick must at least provide a pressure head equal to the vapor pressure on the anode side,  $P_{ev}$  (at large  $R_p$ , the pressure losses in the wick are small compared to  $P_{ev}$ ). The minimum value of  $R_p$  is limited by the pressure losses in the wick, since the wick permeability varies as the



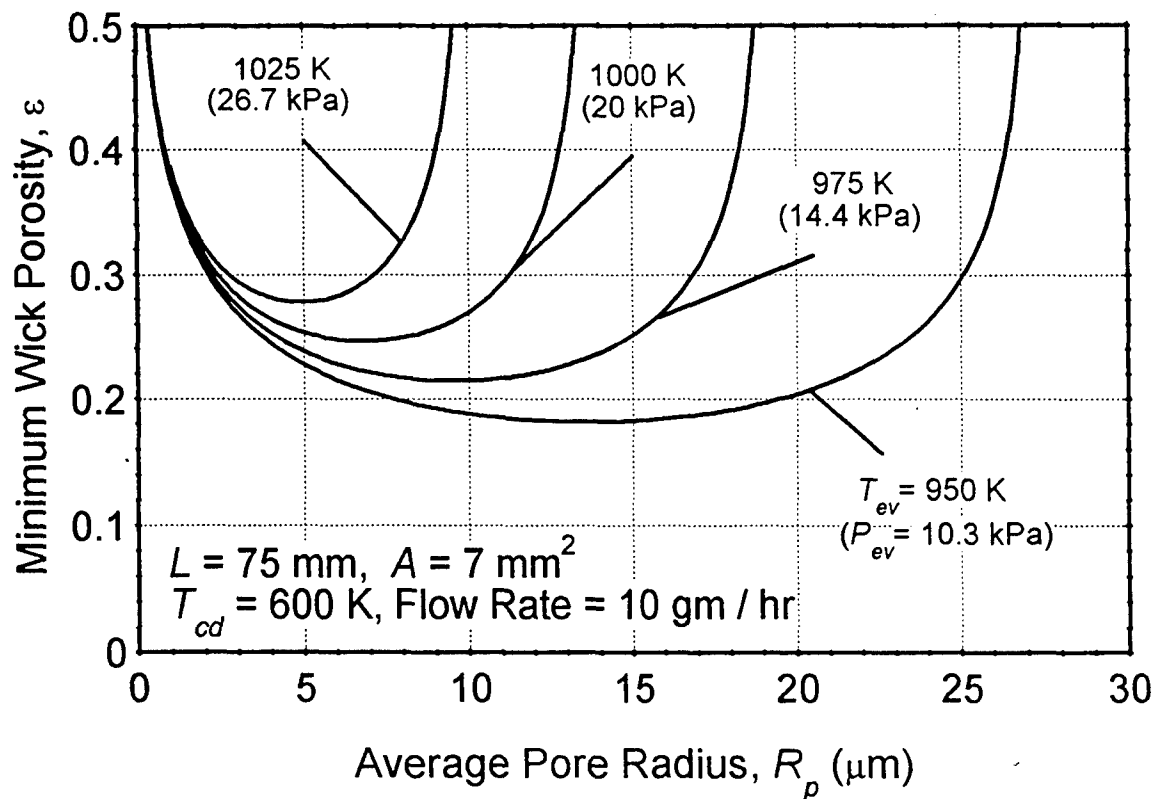


Figure 11.1. Minimum Wick Porosity at a Sodium Flow Rate of 10 gm/hr.

square of  $R_p$ . Since the capillary pressure head is inversely proportional to the pore radius, the pressure losses eventually overcome the capillary pressure head at low  $R_p$ .

The analysis shows that the current design of the PX-1A wick (with 0.2 volume porosity) is only capable of delivering 4 gm/hr (at  $T_{ev} = 1025$  K, see Section 6.4), well below the expected nominal value of 10 gm/hr. Based on the analysis in Section 6.4, the following specifications of the wick are recommended for achieving the nominal sodium flow rate: a porosity  $> 0.30$ , and an evaporator wick pore size between 3 and 7  $\mu$ m. Chris Borkowski has stated that AMPS has the capability of controlling both the volume porosity and the pore size of the metallic powder during the sintering process. In that case, the chart in Figure 11.1 can be used in conjunction with the manufacturing chart to insure that the artery will provide enough capillary action.

### 11.3.2 Effective Thermal Conductivity of Sintered Metal Wick and Conduction Losses along the Artery

Increasing the volume porosity of the artery as recommended in Section 11.3.1 above would increase the effective thermal conductivity of the wick and therefore the conduction losses along the artery to the condenser. Maxwell has derived an expression for the effective thermal conductivity of a continuous liquid phase containing randomly dispersed and randomly-sized solid spheres (Chi 1976):

$$\frac{k_{\text{eff}}}{k_L} = \frac{(k_W + 2k_L) + 2(1 - \varepsilon)(k_W - k_L)}{(k_W + 2k_L) - (1 - \varepsilon)(k_W - k_L)} = \frac{\phi + 2(1 - \varepsilon)}{\phi - (1 - \varepsilon)}, \quad (11.1a)$$

where

$$\phi = \frac{k_W + 2k_L}{k_W - k_L} \quad (11.1b)$$

Because Maxwell did not take into account the interaction between the spherical inclusions, his solution is admissible only when the conductivity ratio  $k_W/k_L$  is much less than 1, or for porous media with large volume porosity. In order that the action of the spheres may not produce effects depending on their interference, their radii must be small compared to their distance, therefore the wick porosity must be large.

As the volume porosity of the wick decreases, the radius of contact between adjacent particles increases, and the accuracy of Equation (11.1) decreases. For a sintered metal wick with a large contact radius, the effective wick conductivity should be calculated as (Chi 1976):

$$\frac{k_{\text{eff}}}{k_W} = \frac{\pi \left( \frac{R_c}{R_s} \right)^2}{8} + \left[ 1 - \frac{\pi \left( \frac{R_c}{R_s} \right)^2}{8} \right] \times \left[ \frac{k_L}{\varepsilon' k_W + (1 - \varepsilon') k_L} \right], \quad (11.2a)$$

where

$$\varepsilon' = \frac{\varepsilon}{1 - \frac{\pi \left( \frac{R_c}{R_s} \right)^2}{8}} \quad (11.2b)$$

This Equation was derived by considering two parallel heat flow paths for sintered porous wicks. One of the path involves homogeneous wick material, and the other involves both liquid and wick material in series. In addition, in the absence of data for the contact radius,  $R_c$  can be estimated by means of a material balance for the idealized geometry (cubic array of truncated spheres). The result is the following equation (Chi 1976):

$$\varepsilon = \frac{\pi}{6 \left[ 1 - \left( \frac{R_c}{R_s} \right)^2 \right]^{2/3}} \left\{ 1 - \left( \frac{R_c}{R_s} \right)^2 \left[ 2 - \sqrt{1 - \left( \frac{R_c}{R_s} \right)^2} \right] \right\} \quad (11.3)$$

As shown in Figure 11.2, the wick porosity given by Equation (11.3) reaches a maximum value  $\varepsilon = \varepsilon' = \pi/6$  at a contact radius,  $R_c = 0$  (this is the case of a cubic array of spheres of liquid, of radius  $R_s$ , that are touching). For Equation (11.2a) to be of practical use,  $\varepsilon'$  must be expressed as a function of wick porosity,  $\varepsilon$ . This was accomplished by plotting  $\varepsilon'$  as a function of  $\varepsilon$ , by combining Equations (11.2b) and (11.3), and fitting the resulting curve (Figure 11.3). The

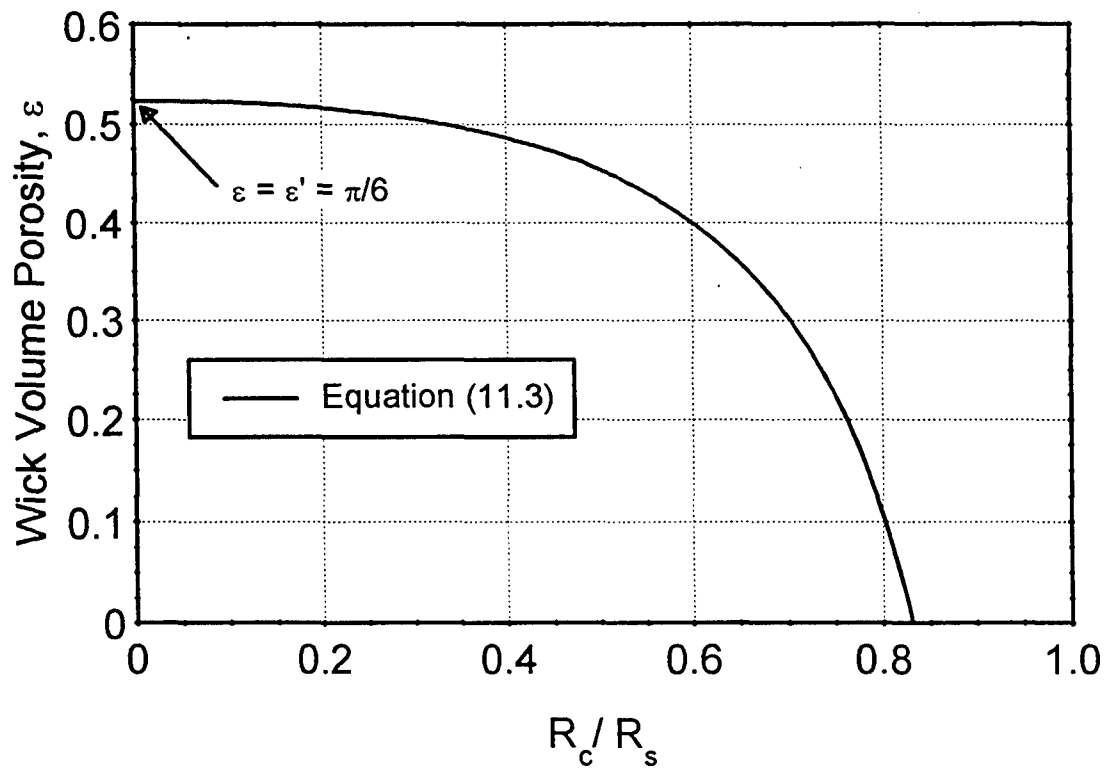


Figure 11.2. Volume Porosity of Sintered Porous Wick as a Function of  $R_c/R_s$ .

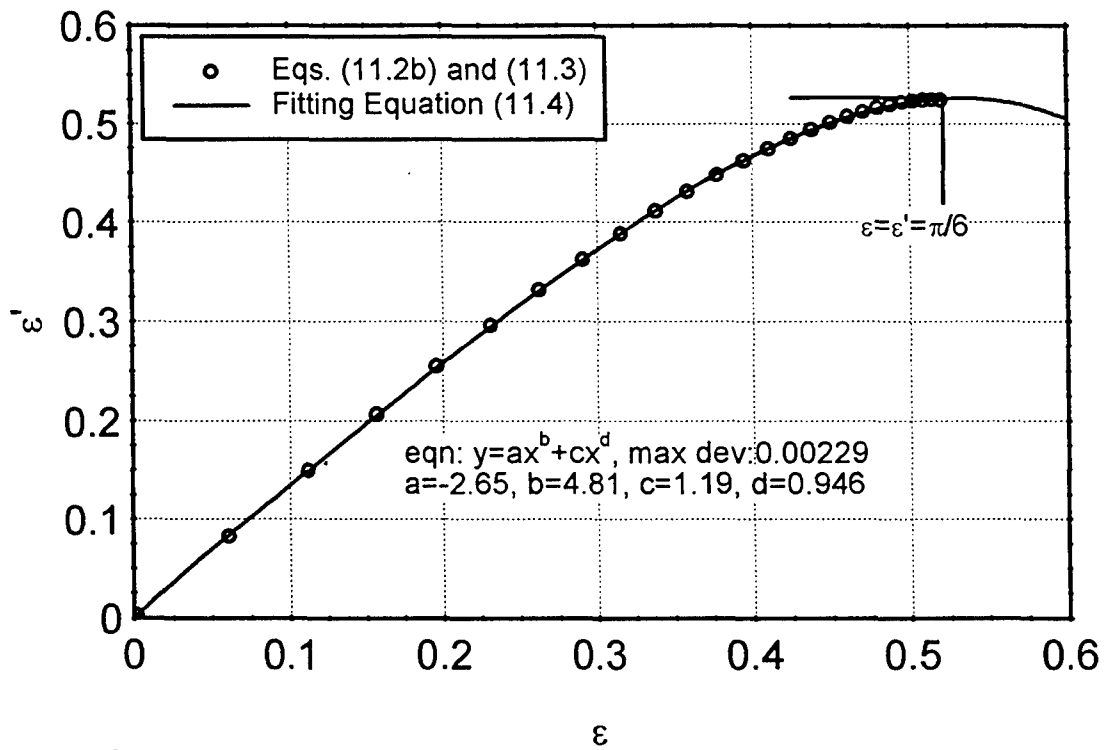


Figure 11.3. Prime Porosity of Sintered Porous Wick as a Function of Volume Porosity.

relationship between  $\epsilon'$  and  $\epsilon$  could be represented with good accuracy (a maximum deviation of 1.0%) over the whole range of practical values,  $0 < \epsilon < \pi/6$ , by the following function (Figure 11.3):

$$\epsilon' = 1.19 \times \epsilon^{0.946} - 2.65 \times \epsilon^{4.81} \quad (11.4)$$

The thermal conductivities of liquid sodium and stainless steel (304 / 316) were calculated as:

$$\begin{aligned} k_L &= 103.86 - 4.8523 \times 10^{-2} \times T, \\ k_W &= 11.624 + 1.338 \times 10^{-2} \times T, \end{aligned} \quad (11.5)$$

where  $T$  is expressed in Kelvin and  $k$  is in [W/m.K]. These correlations match well thermal conductivity data in the range  $400 \text{ K} < T < 1200 \text{ K}$ .

The effect of volume porosity on the effective thermal conductivity of a stainless steel sintered wick saturated with liquid sodium, predicted by Equations (11.1) and (11.2), is shown in Figure 11.4 for a temperature,  $T = 775 \text{ K}$ . Figure 11.5 shows the calculated effective wick conductivity as a function of temperature for a volume porosity of 0.20. The model developed by Maxwell for a bed of randomly-packed solid spheres gives a more conservative value (higher) than the model for sintered spheres with a large contact area. At an average temperature of 775 K, the thermal conductivities of liquid sodium and stainless steel are 66.3 W/m.K and 22.0 W/m.K, respectively. Maxwell's model gives an effective thermal conductivity of 29.0 W/m.K, which gives a conduction loss of 0.95 W. At a volume porosity of 0.28, the effective conductivity becomes 32.3 W/m.K, and the resulting conduction loss is 1.06 W, an increase of only 12 %, which should not concern us. Of course, the actual problem is a radiation-conduction combined one, however one does not expect the loss by conduction to the condenser to be much different than about 1 W.

### 11.3.3 Heat Balance in the PX-1A Cell

In order for the cell to operate at its optimum current, it is necessary that the latent heat of vaporization be delivered to liquid sodium at the evaporator end of the artery, and that the heat input at the hot plate be also delivered to the cell. To verify that it is the case, it is necessary to perform a heat balance of the cell.

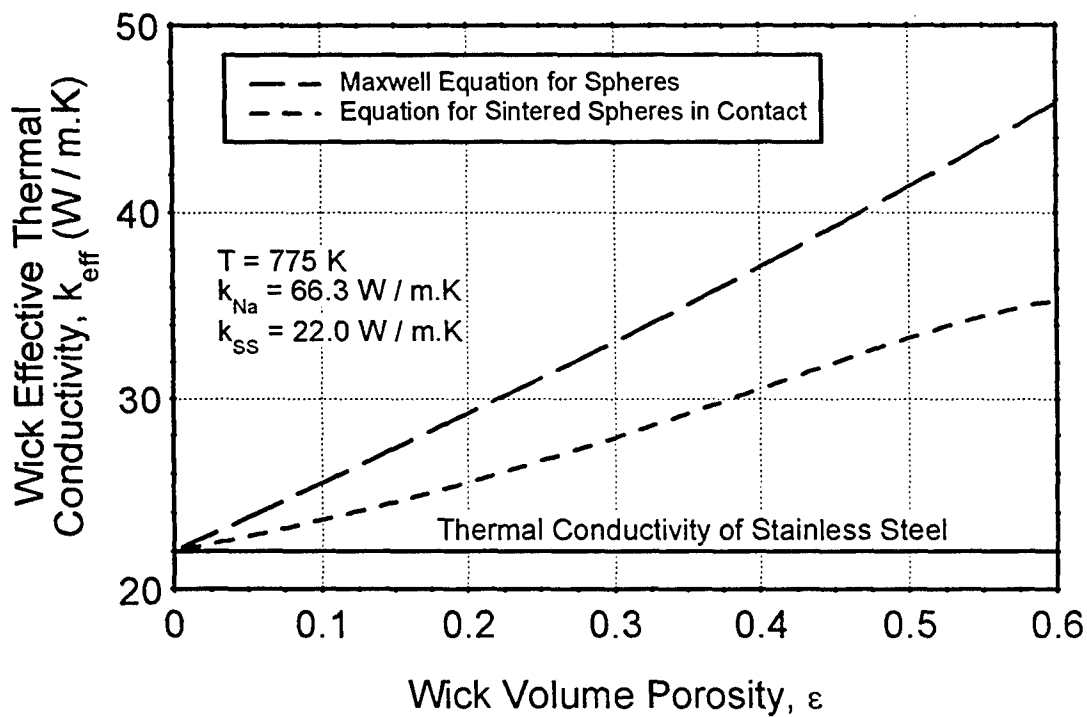


Figure 11.4. Effective Thermal Conductivity of SS Wick Saturated with Liquid Sodium as a Function of Wick Volume Porosity.

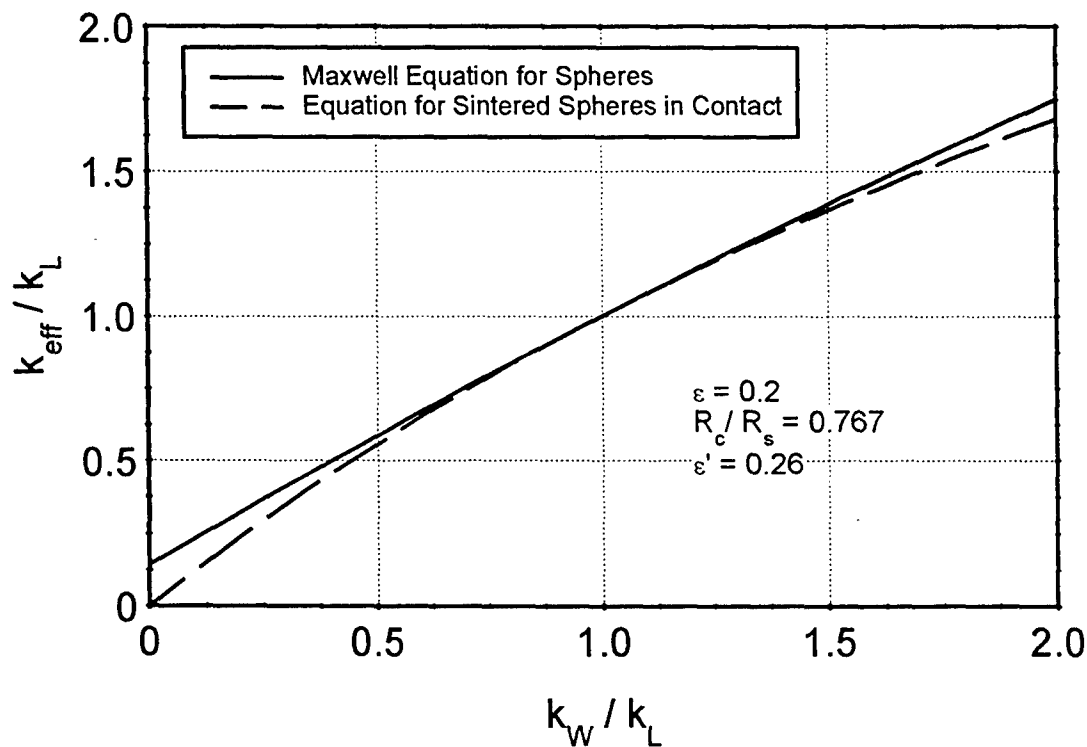


Figure 11.5a. Effective Thermal Conductivity of Fully-Saturated Porous Wick with a 20% Volume Porosity.

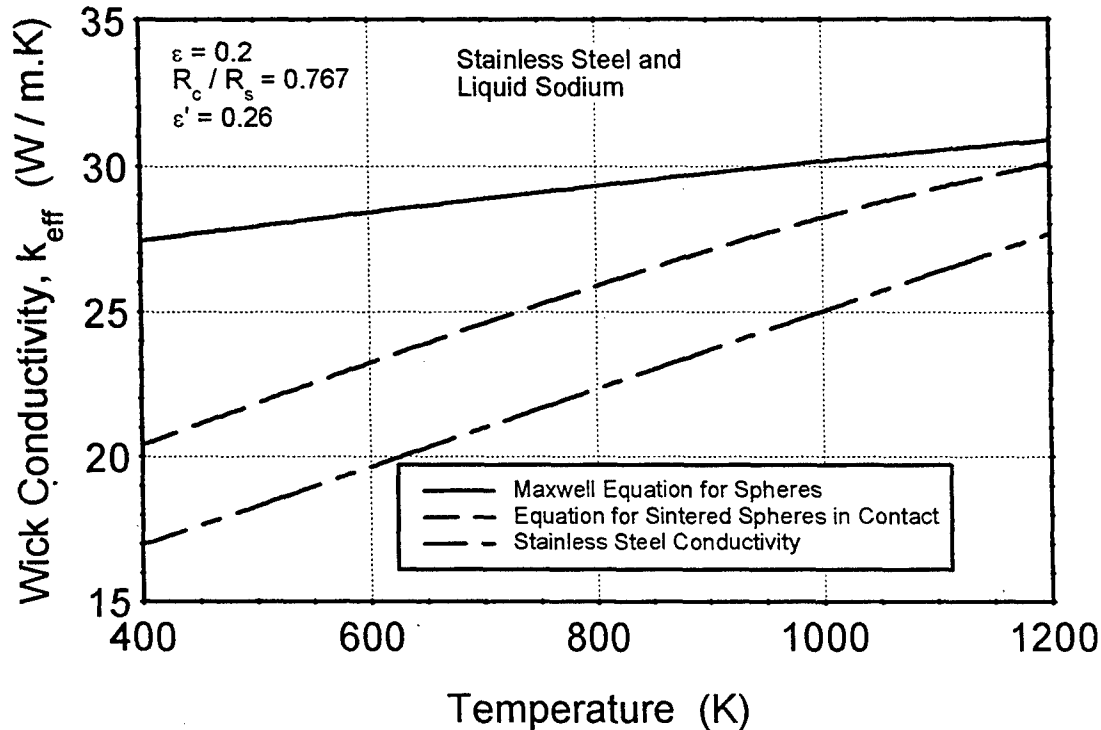


Figure 11.5b. Effective Thermal Conductivity of Stainless Steel Sintered Wick Saturated with Liquid Sodium, with a 20% Volume Porosity.

The design and operating parameters of the reference cell are as follows:

Number of BASE tubes = 7

Outer diameter of BASE tube = 6.35 mm

Thickness of BASE Tube = 0.5 mm

Electrode length = 17.54 mm

Total electrode area = 24.5 cm<sup>2</sup>

Voltage output of 0.5 V per tube, so that  $V = 7 \times 0.5 = 3.5$  V

Current output  $I = 1.5$  A, so that  $P_e = 3.5 \times 1.5 = 5.25$  We

Thermal input power per cell  $Q_{in} = 30$  Wt

overall efficiency  $\eta = 5.25 / 30 = 17.5\%$

Total sodium mass rate:  $7 \times I \times M / F = 9$  gram / hr

Note that the electrical performance of the reference cell is consistent with calculations using AMPS TK-Solver model and APEAM model.

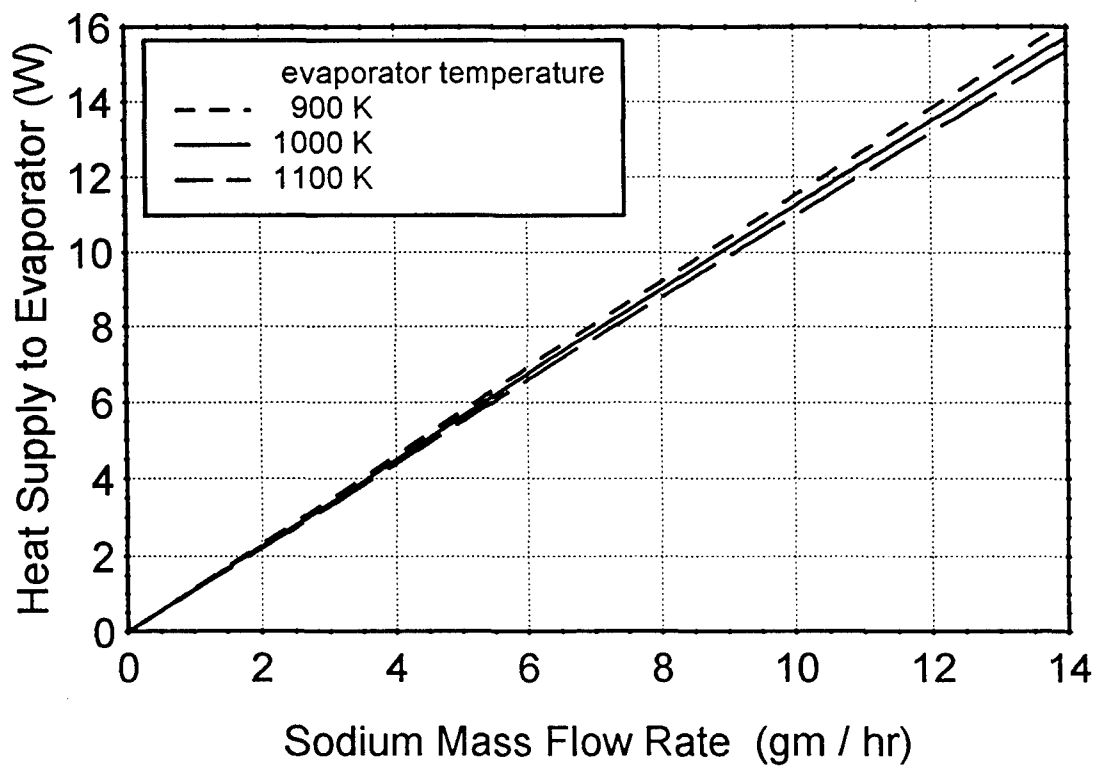


Figure 11.6. Heat Supply to Cell Evaporator as a Function of Sodium Mass Flow Rate.

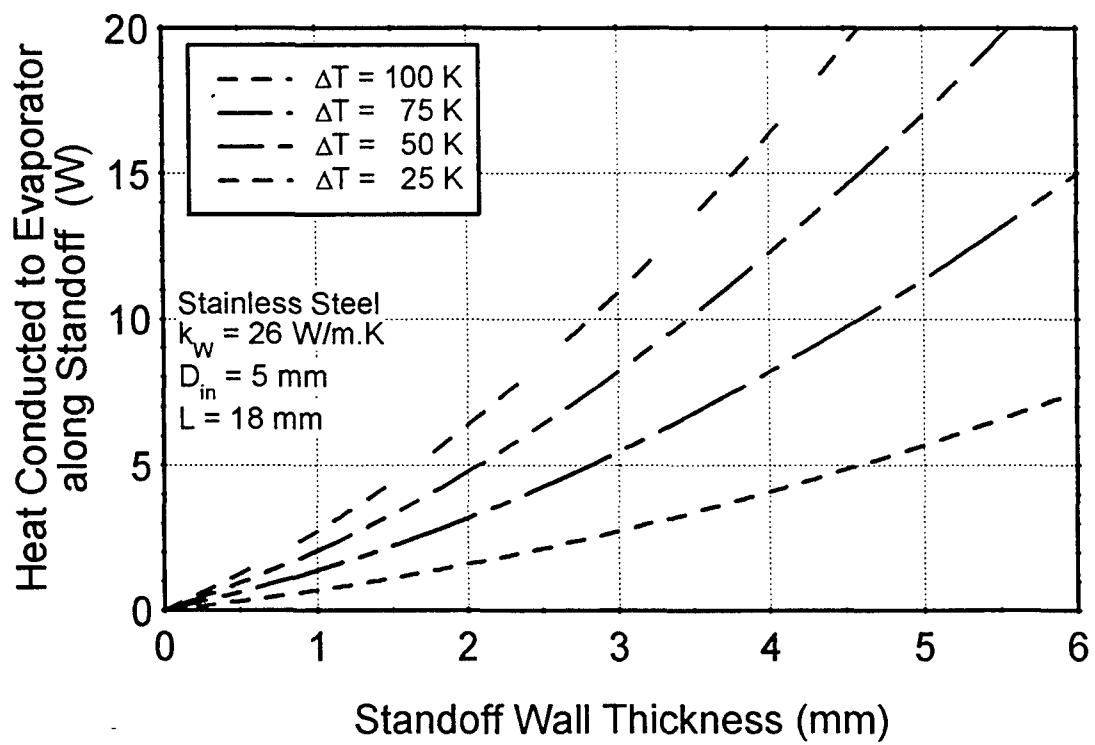


Figure 11.7. Heat Conducted to Evaporator as a Function of Standoff Wall Thickness.

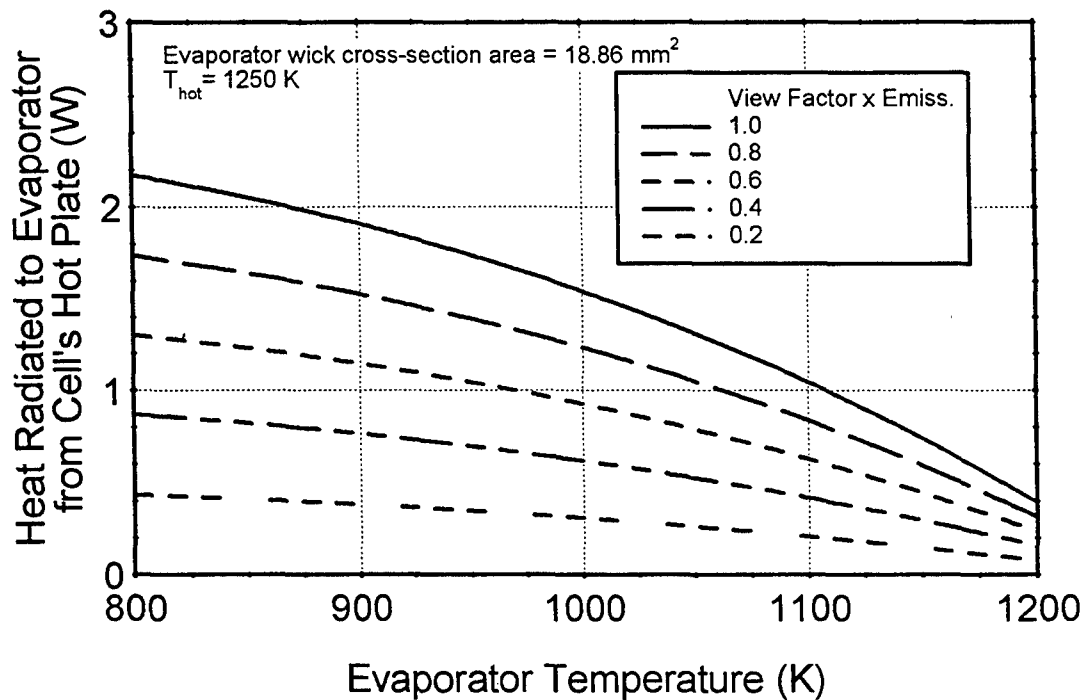


Figure 11.8. Estimate of Heat Radiated to Evaporator from Cell's Hot Plate in PX-1A.

The heat balance in the cell can be computed as follows. Since the side wall of the cell is assumed to be thermally insulated (8 cells are packaged in alumina powder or Min-K next to each other), we have:

$$Q_{in} = \text{sodium sensible heat} + \text{sodium vaporization heat} + \text{losses to the condenser} + P_e$$

$$\begin{aligned} \text{sodium sensible heat} &= 9 \text{ [gram/hr]} / 3600 \text{ [s/hr]} \times 1.286 \text{ [J/gram.K]} \times (950 - 600) \text{ [K]} \\ &= \mathbf{1.13 \text{ W}} \end{aligned}$$

$$\begin{aligned} \text{sodium vaporization heat} &= 9 \text{ [gram/hr]} / 3600 \text{ [s/hr]} \times 4090 \text{ [J/gram]} \\ &= \mathbf{10.22 \text{ W}} \end{aligned}$$

So that the total losses to the condenser are:

$$\text{losses to the condenser} = 30 \text{ Wt} - 1.13 \text{ W} - 10.22 \text{ W} - 5.25 \text{ We} = \mathbf{13.40 \text{ W}}$$

The losses to the condenser can be broken down into the following terms:



$$\begin{aligned} \text{losses to the condenser} = & \text{sodium condensation heat} \\ & + \text{artery conduction loss} \\ & + \text{side wall conduction loss} \\ & + \text{radiation loss} \end{aligned}$$

$$\begin{aligned} \text{sodium condensation heat} &= 9 \text{ [gram/hr]} / 3600 \text{ [s/hr]} \times 4400. \text{ [J/gram]} \\ &= \mathbf{11.00 \text{ W}} \end{aligned}$$

$$\text{artery conduction loss} = \mathbf{0.95 \text{ W}} \quad (\text{in the current design}).$$

Assuming a cell outer diameter of 31.75 mm and a uniform side wall thickness of 0.125 mm, the axial conduction area of the side wall is  $A = 12.42 \text{ mm}^2$ . Using the same length ( $L=7.5 \text{ cm}$ ) and temperature drop ( $950 - 600 = 350 \text{ K}$ ) as for the artery:

$$\begin{aligned} \text{side wall conduction loss} &< A k \Delta T / L = 12.42 \times 10^{-6} \times 22.0 \text{ [W/m.K]} \times 350 / 0.075 \\ &< \mathbf{1.27 \text{ W}} \end{aligned}$$

Of course this is an upper limit. In the actual design, different and smaller wall thicknesses are used along the cell to significantly reduce these conduction losses. In summary, the heat balance in the cell for the base case operating parameters is satisfied if:

$$\text{side wall conduction loss} + \text{radiation loss to condenser} = \mathbf{1.45 \text{ W}},$$

which means that the radiation losses to the condenser should be less than  $\mathbf{1.45 \text{ W}}$ .

#### 11.3.4 Heat Flow to the Evaporator End of the Artery

In order for the cell to operate at its optimum electric current, it is necessary that the latent heat of vaporization be delivered to liquid sodium at the evaporator end of the artery. The heat supply to the evaporator is the product of sodium mass flow rate and latent heat of vaporization, which is a function of evaporator temperature (Figure 11.6). At a sodium flow rate of 9 gm/hr, a vaporization heat of 10.22 W must be supplied to the evaporator of PX-1A. This energy can be supplied to the evaporator by conduction up the evaporator standoff (Figure 11.7), and by radiation from the hot plate (Figure 11.8). Again the actual problem is one of combined conduction and radiation, but an estimate of every term separately gives an upper bound of the total energy supplied. Examination of Figure 11.8 shows that an upper bound to the heat supplied by radiation to the evaporator wick surface is 2 W. Thus, in all practical cases of interest, most of the heat of vaporization must be supplied by conduction up the evaporator standoff. In PX-1A, the stainless steel, annular evaporator standoff has an outer diameter of 6.5 mm, a wall thickness of 0.8 mm and a length of about 18 mm, so that the axial conduction area is  $A = 14.3 \text{ mm}^2$ .

As shown in Figure 11.7, the thermal conductance of the evaporator standoff in PX-1A is too small, and cannot supply the 10 W of thermal energy to the evaporator required for a sodium mass flow rate of 9 gm/hr. To reach this goal, the evaporator standoff wall thickness has to increase from 0.8 mm to  $> 4$  mm (or slightly less if the evaporator standoff is also increased). This explains the very low performance of PX-1 series cells in the AFRL vacuum tests. This design flaw was corrected in subsequent series of cells by adding metal conduction rings around the evaporator standoff; also, a thick metal conduction stud was added between the cell's hot end and the BASE tubes support plate in latter cells, to increase the thermal conductance between cell's hot end and BASE tubes and evaporator.

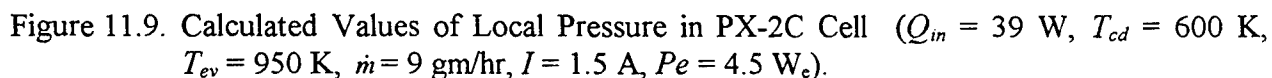
#### 11.4 PX-2C CELL DATA ANALYSIS

The PX-2C cell designed by AMPS and tested at AFRL had 7 BASE tubes brazed to a stainless steel support plate and a central felt-metal wick for returning the sodium working fluid to the cell evaporator (Table 11.1). The low-pressure side (cathode) and high-pressure side (anode) of the solid electrolyte were covered with TiN porous electrodes and copper-mesh current collectors. The 7 BASE tubes were electrically connected in series. The heat input to the cell hot plate is removed by conduction and radiation to the BASE tubes and the evaporator. The PX-2C cell had a SS circumferential radiation shield above the BASE tubes to reduce parasitic heat losses, and a solid conduction stud between the hot plate and the tubes' support plate (Table 11.1).

APEAM was used to simulate the experimental setup of the PX-2C cell at AFRL. The cell wall insulation was made of molded Min-K. A boron nitride block, which held a small electrical heater, was fitted to the cell's hot plate (Chapter 8). The heater was radiatively coupled to the cell's hot plate. Heat was removed at the condenser by an air calorimeter. The air inlet and outlet temperatures and flow rate were measured in the test. The PX-cell tests were performed in vacuum at  $5 \times 10^{-6}$  torr, or 0.7 mPa.

APEAM accounts for axial and radial conductions in the insulation surrounding the cell. Also, heat dissipation at the insulation surface by radiation to the vacuum chamber, and heat rejection at the condenser by forced convection of air were incorporated in APEAM. However, the insulation above the cell top was not modeled in APEAM. Instead, the insulation surface aligned with the top of the cell was assumed adiabatic, and the input thermal power to the cell was specified as an input to the model.

The test data used to verify APEAM were obtained at a fixed heater electrical power of 51.3 W, and fixed air mass flow rate ( $1.31 \times 10^{-4}$  kg/s) and inlet temperature (296 K). The temperature of the vacuum chamber housing was 319.4 K. The AMTEC cell used TiN electrodes, and the temperature-independent exchange current and the contact resistance between electrodes and BASE were taken equal to  $120 \text{ A.K}^{1/2}/\text{Pa.m}^2$  and  $0.08 \text{ } \Omega.\text{cm}^2$ , respectively. In the experiment, the external load resistance was varied in steps, and the cell was allowed to reach equilibrium between steps.



The momentum balance equates the pressure losses in the cell to the capillary pressure head in the evaporator wick (Figure 11.9). The pressure losses are those due to (see Chapter 3): (a) Na liquid flow in the return line and evaporator wick; (b) evaporation of Na; (c) Na vapor flow from evaporator to BASE/anode surface; (d) isothermal expansion of Na vapor through the BASE; (e) Na vapor flow from BASE/cathode interface to condenser; and (f) condensation of Na vapor. Calculated values of the local sodium pressure in the PX-2C cell are shown in Figure 11.9.

$$\Delta P_{cap} = \frac{2\sigma}{R_p} \geq P_{sat}(T_{ev}) - P_{sat}(T_{cd}) + \Delta P_{loss} . \quad (11.6)$$

The condenser saturation pressure is negligible, typically 3 to 4 orders of magnitude smaller than the evaporator saturation pressure. Figure 11.9 shows a line diagram of the local sodium pressure in the PX-2C cell. The liquid in the condenser wick is at saturation, about 5 Pa at a condenser temperature of 600 K. The pressure losses in the wick, which are much larger than the condenser saturation pressure, cause the local liquid pressure to go negative, placing the liquid sodium in the wick under tension (Figure 11.9). A local tension in liquid sodium as low as -2,400 Pa has been observed in a wick-fed, vapor-anode AMTEC cell (Anderson 1992, and Anderson et al. 1993).

An increase in pressure occurs at the liquid-vapor interface of the evaporator ( $2\sigma/R_c$ ). At an evaporator temperature of 950 K, the sodium saturation pressure is about 10 kPa (Figure 11.9). Evaporation of liquid sodium occurs at the evaporator wick surface, causing a pressure drop in the PX-2C cell of about 60 Pa, for a conical evaporator surface of 60 mm<sup>2</sup> (3 times the cross section area of the evaporator standoff), at a typical cell current  $I = 1.5$  A (a sodium mass flow rate of 9 gm/hr). The sodium vapor flows through the conduction stud, to the interior of the BASE tubes, reaching the anode side of the BASE, with negligible pressure losses ( $< 50$  Pa). The thermodynamic potential across the BASE causes ionization of the sodium atoms. The free electrons circulate through the external load, producing electric work. The sodium ions diffuse isothermally through the BASE membrane (Figure 11.9), and recombine with the returning electrons, at the interface between the BASE and the cathode electrode. The neutral sodium atoms, which emerge at a very low pressure of 20 Pa, traverse the low-pressure cavity to the cell cold end, where they condense.

In the vacuum tests at AFRL, the cell condenser was located below the evaporator, and the liquid sodium in the wick was flowing against the gravity force. The pressure loss due to gravity, however, was small compared to the evaporator saturation pressure, and can be neglected ( $< 600$  Pa).

#### 11.4.2 PX-2C Cell Electrical Power

Figure 11.10 compares the calculated and measured cell electrical powers as a function of electric current. In the experiment, the heat input to the cell varied with the cell current, as shown in Figure 11.11. The fraction of the heater power transmitted to the hot plate of the cell is equal to that transported within the cell by radiation and conduction. Increasing the cell current increases the evaporation rate of Na (about 11 W at a current of 1.5 A or a sodium flow rate of 9 gm/hr), thus lowering the evaporator temperature. This decrease in the evaporator temperature stimulates more heat flow from the hot plate, particularly by conduction in the solid stud, to the evaporator, hence increasing the fraction of the heater power absorbed by the cell hot plate. Such a dependence of the thermal power input to the cell on the cell current was determined from experimental measurements, in connection with model predictions, for the same cell electric power and heat rejection (Figure 11.11). Figure 11.11 shows that the heat input to the PX-2C cell increased with increasing cell current. For example,  $Q_{in}$  increased from 36.5 W (71% of heater power) to 41.5 W (81% of heater power) as the cell current increased from 1.47 A to 2.65 A, respectively. It is worth noting that the relationship delineated in Figure 11.11 is characteristic of the experimental setup of the PX-2C cell at AFRL.

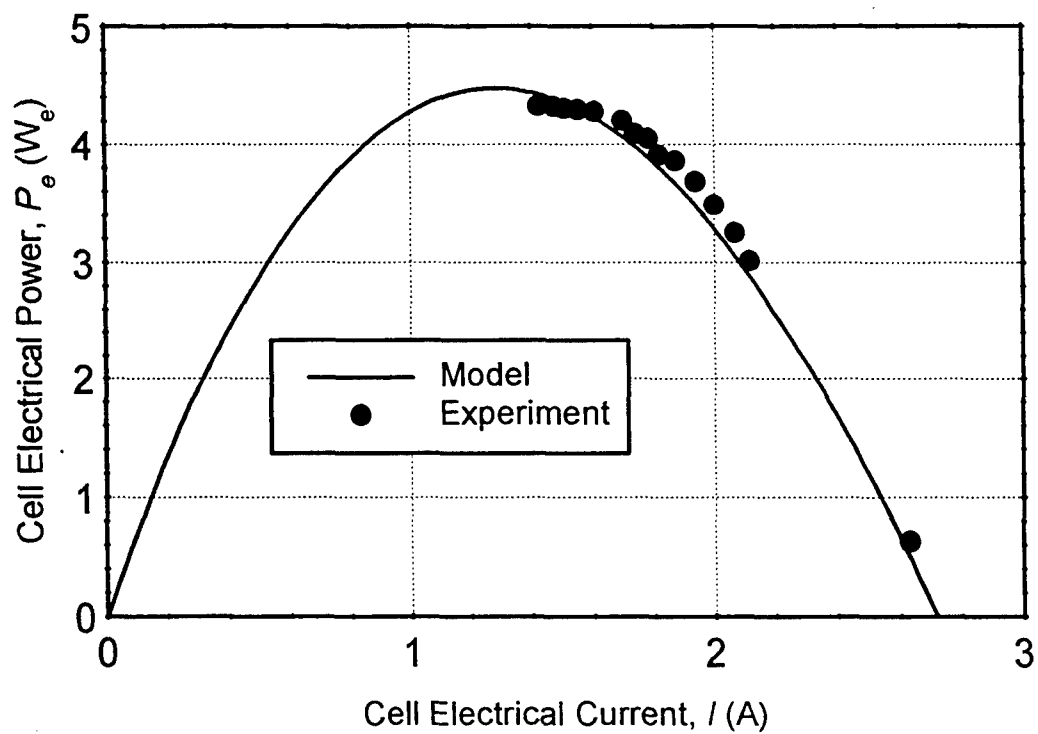


Figure 11.10. PX-2C Cell Electrical Power as a Function of Current.

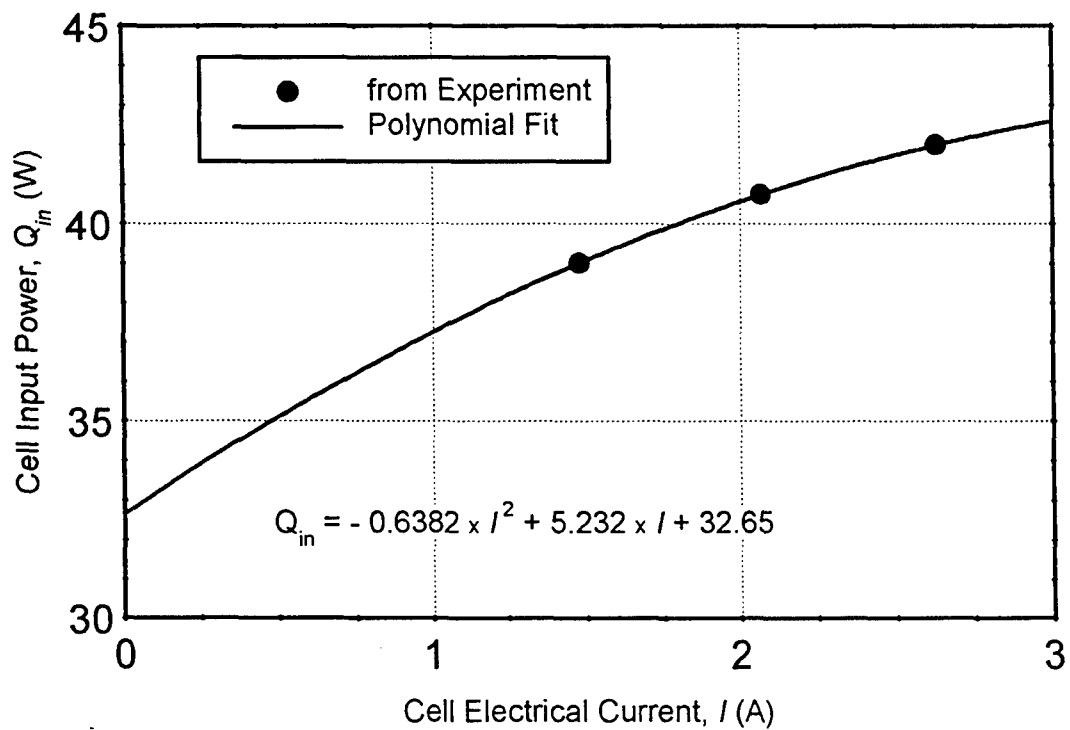


Figure 11.11. Estimate of PX-2C Cell Input Power Versus Electrical Current.

As delineated in Figure 11.10, there is a good agreement between calculated and measured cell electrical power values for the PX-2C AMTEC cell. This figure also indicates that the predicted peak electrical power output of the cell was identical to that obtained in the test (4.4 W<sub>e</sub>).

#### 11.4.3 PX-2C Cell I-V Characteristic

The cell I-V characteristic is shown in Figure 11.12. The calculated cell (load) voltage compared well with the measurements. The calculated open-circuit voltage, the concentration / polarization overpotential, and the electromotive force of the cell (the difference between open-circuit voltage and overpotential) are also shown in Figure 4. As expected, the open-circuit voltage increased with increasing BASE tube temperature, or decreasing load current. The overpotential increased rapidly with increasing current, at low values, according to the Butler-Volmer logarithmic equation. At higher electric currents, the overpotential decreased slightly, since it is proportional to the BASE tube temperature.

#### 11.4.4 Load-Following Characteristic of PX-2C Cell

When designing a generator for a spacecraft, it is important to know how the converter will respond to changes in the external load demand. Figure 11.13 shows the calculated and measured load-following characteristics of the PX-2C AMTEC cell. The cell power initially increased rapidly with decreasing load demand (or increasing external load resistance,  $R_L$ ), reaching a peak of 4.4 W<sub>e</sub> at about 2.5 Ω. At higher load resistance (or lower load demand), the cell electrical power decreased slowly with decreasing load demand. In Figure 11.13, the portion of the load-following characteristic, to the right of the peak power, is where the power system should be designed to operate. In this portion of the curve, the AMTEC cell is load-following, since increasing the load demand (or lowering  $R_L$ ) increases the electric power output of the cell. Conversely, the left side of the characteristic in Figure 11.13, should be avoided, since the cell is not load-following.

#### 11.4.5 Effects of Internal Radiation Shields

APEAM was used to study the effect of internal radiation shield on the PX-2C cell performance. Calculations were performed at a load resistance of 2 Ω, a condenser air flow rate of  $1.31 \times 10^{-4}$  kg/s, and a fixed cell input thermal power,  $Q_{in} = 39$  W. Three different designs were considered. The one labeled "No shield", was that of a PX-2C AMTEC without internal radiation shield. The second, labeled "SS shield", was the tested PX-2C cell with a circumferential stainless steel radiation shield, having an emissivity between 0.25 and 0.30. In the last design, labeled "Mo shield", the circumferential shield was made of molybdenum, having an emissivity of only 0.08.

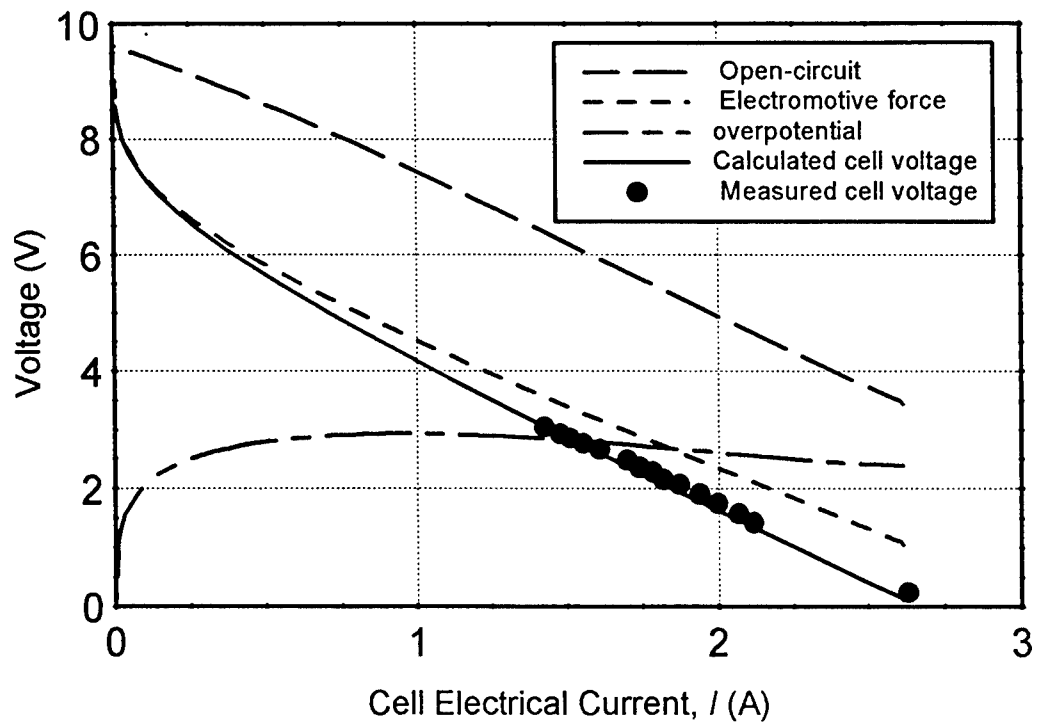


Figure 11.12. PX-2C Cell Voltages as a Function of Electrical Current.

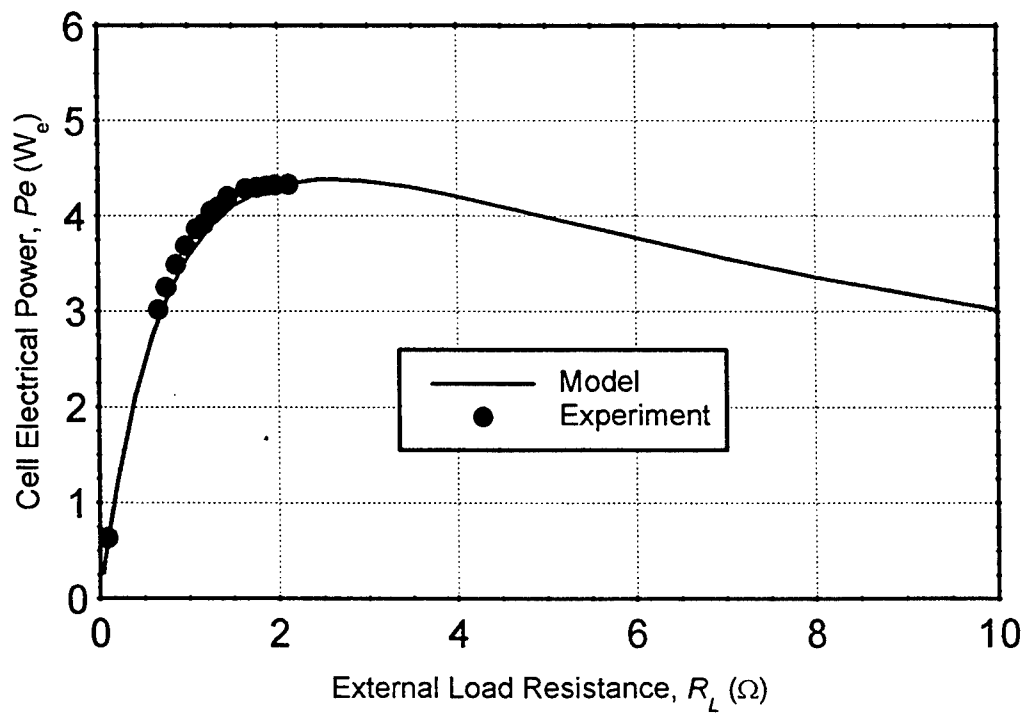


Figure 11.13. PX-2C Cell Electrical Power as a Function of External Load Resistance.

Table 11.3. Effect of Internal Radiation Shields on PX-2C Cell Performance ( $R_L = 2 \Omega$ ).

Parameters	Model Results			Exp. Data
	No shield	SS shield	Mo shield	
External load resistance ( $\Omega$ )	2.0	2.0	2.0	2.0
Cell current (A)	1.385	1.473	1.548	1.479
Cell electric power ( $W_e$ )	3.84	4.34	4.79	4.35
Cell conversion efficiency	9.85%	11.13%	12.3%	—
Open-Circuit voltage (V)	5.91	6.31	6.63	—
Polarization losses (V)	2.66	2.85	2.99	—
Cell internal resistance ( $\Omega$ )	0.349	0.349	0.350	—
Anode Na pressure (kPa)	6.97	8.62	10.32	—
Cathode Na pressure (Pa)	15.9	16.7	17.7	—
<b>Radiative Emissivities:</b>				
Condenser surface	0.12	0.12	0.12	—
Min-K (insulation)	0.25	0.25	0.25	—
Stainless steel surfaces		(0.25 to 0.30)		—
Radiation shield	—	0.28	0.08	—
BASE tubes		(0.81 to 0.92)		—
<b>Temperatures (K):</b>				
Cell hot end	1169	1186	1201	1150
Cold end of tubes	1031	1053	1072	1010
Cold end of electrodes	1031	1053	1072	—
Hot end of electrodes	1067	1087	1105	—
Brazes (maximum)	1136	1154	1169	—
Internal radiation shield	—	916-1013	930-1028	—
Evaporator wick	956	975	993	993
Evaporator end	924	939	951	—
Condenser	534	529	525	526
Insulation outer surface	358	358	358	357
Cell input power (W)	39.00	39.00	39.00	—
Cell wall heat losses (W)	7.00	7.07	7.10	—
Condenser heat reject. (W)	27.77	27.15	26.63	26.4
Liquid Na sensible heat (W)	1.16	1.30	1.42	—
Heat of Evaporation (W)	9.51	10.08	10.57	—
Heat of Condensation (W)	10.28	10.94	11.51	—
<b>Heat Conduction (W):</b>				
Hot plenum side wall	23.94	23.85	23.79	—
Studs	12.51	12.51	12.51	—
$\beta$ -tubes' brazes	10.04	9.79	9.57	—
Loss through side wall	11.68	9.34	7.38	—
Loss through artery	3.75	4.26	4.68	—
<b>Radiation (W):</b>				
from hot plate of cell	2.54	2.63	2.70	—
to inside of $\beta$ -tubes	2.65	2.72	2.77	—
from outside of $\beta$ -tubes	8.85	8.17	7.55	—
from wall facing $\beta$ -tubes	6.19	5.43	4.52	—
to inner shield/wall surface	9.72	6.58	3.71	—
to condenser	2.07	2.61	3.06	—
to outside of artery	2.54	3.21	3.79	—



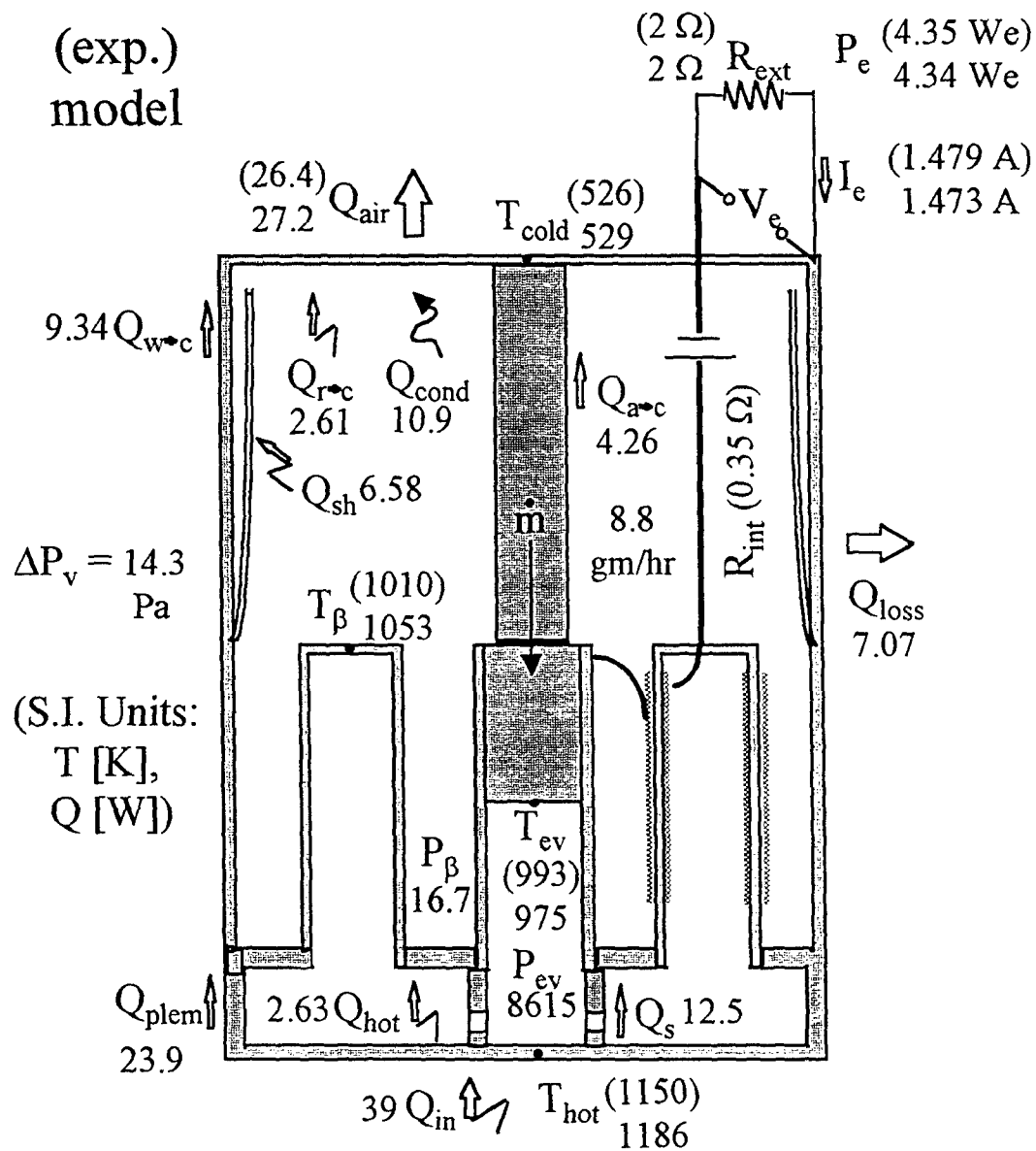


Figure 11.14. Predicted Heat Transfer and Temperatures in PX-2C, Near the Peak Power.

Results are presented in Table 11.3 and Figure 11.14. The cell without a radiation shields produced  $3.84 W_e$ , with a conversion efficiency of 9.85%. The introduction of the SS shield increased the cell electric power output by  $0.50 W_e$ , and the cell efficiency to 11.13%. Best performance was obtained with the low-emissivity molybdenum shield: a cell electrical power output of  $4.79 W_e$  and 12.3% efficiency. These results are in agreement with experimental observations.

The majority of the internal radiation losses occurred at the side wall, near the condenser. In the cell without radiation shield, the BASE tubes lost 8.85 W by radiation and the wall received 9.72 W by radiation, all of which was lost by conduction to the condenser. By contrast, in the cell with the Mo shield, the BASE tubes lost only 7.55 W by radiation, the inner shield surface received only 3.71 W by radiation, and the conduction loss through the side wall was only 7.38 W, 4.3 W less than in the cell without shield. The solid conduction stud at the hot plate in PX-2C conducted 12.5 W to the BASE tubes / standoff support plate (Figure 11.14), a very significant fraction of the cell input thermal power (32%). The heat conducted by the stud provided most of the latent heat required to vaporize the liquid sodium in the evaporator, at a rate commensurate with the cell electric current. This very efficient conduction path in the PX-2 series cells was critical for achieving a good cell performance. The calculated electrical and thermal characteristics, along with the experimental data obtained for PX-2C, are presented in Table 11.3 and Figure 11.14. As shown in this table, the calculated cell parameters with a SS internal shield compared reasonably well with the experimental data, except that the calculated temperatures ran slightly higher than measurements. The calculated cell electrical power, current, and BASE tube, evaporator wick and condenser temperatures compared also well with the measurements. These comparisons confirm the soundness of the present model.

#### 11.4.6 Vapor Pressure Losses in PX-2C Cell

Figure 11.15 shows the calculated vapor pressure distribution on the cathode (low-pressure) side of the PX-2C cell. The pressure profile along the BASE tubes is typically parabolic, due to the effect of continuous mass addition at the BASE outer surface. As expected, the vapor pressure drop increases with increasing cell current, or vapor mass flow rate. At a cell current of about 2 A, the vapor pressure at the BASE/cathode electrode interface varied between 17 Pa and 23 Pa.

The calculated vapor Knudsen number on the cathode side is shown in Figure 11.16. A Knudsen number below 0.01 indicates a continuum flow regime, while the free-molecular regime typically occurs at a Knudsen number above 1. The vapor flow in the PX-2C cell is clearly in the transition regime (with Knudsen numbers ranging between 0.08 and 0.3). Increasing the electrical current increases the vapor pressure losses, and therefore the vapor pressure on the cathode side, resulting in a lower Knudsen number.

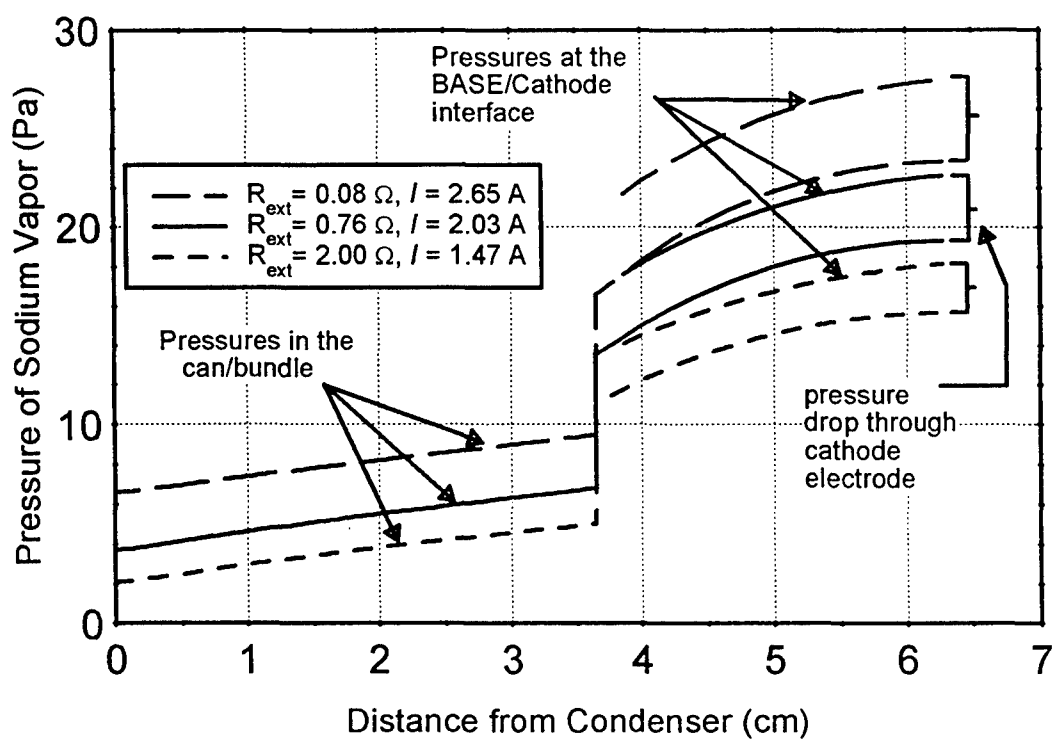


Figure 11.15. Calculated Vapor Pressure in PX-2C on Low-Pressure Side.

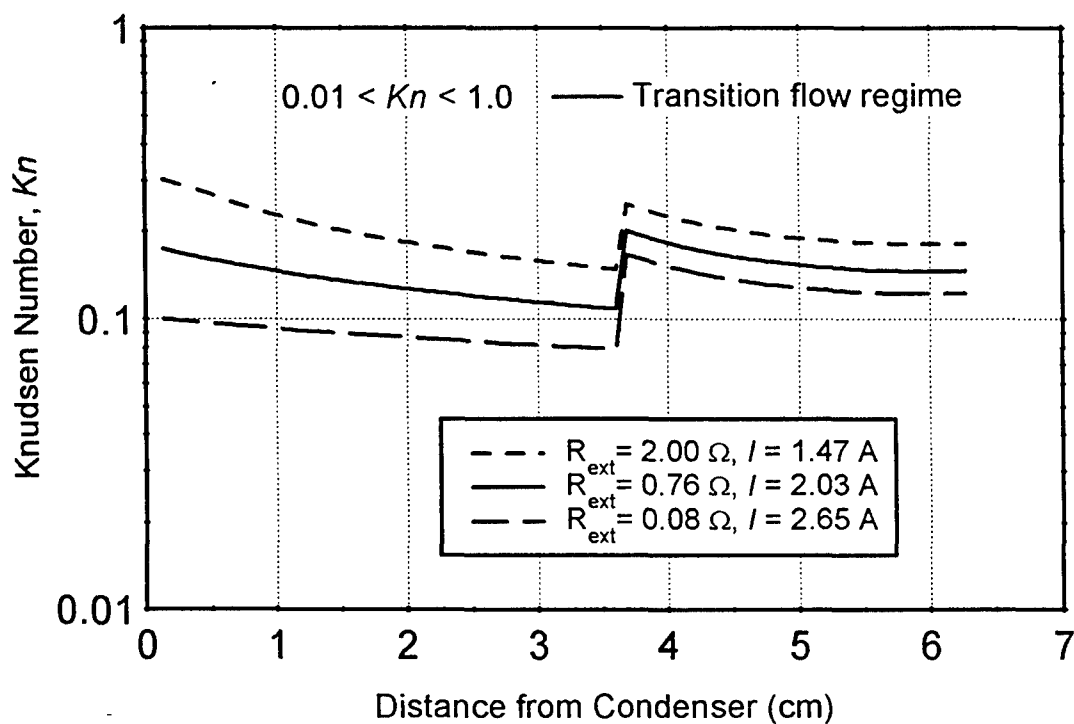


Figure 11.16. Calculated Vapor Knudsen Number on Cathode Side of PX-2C.

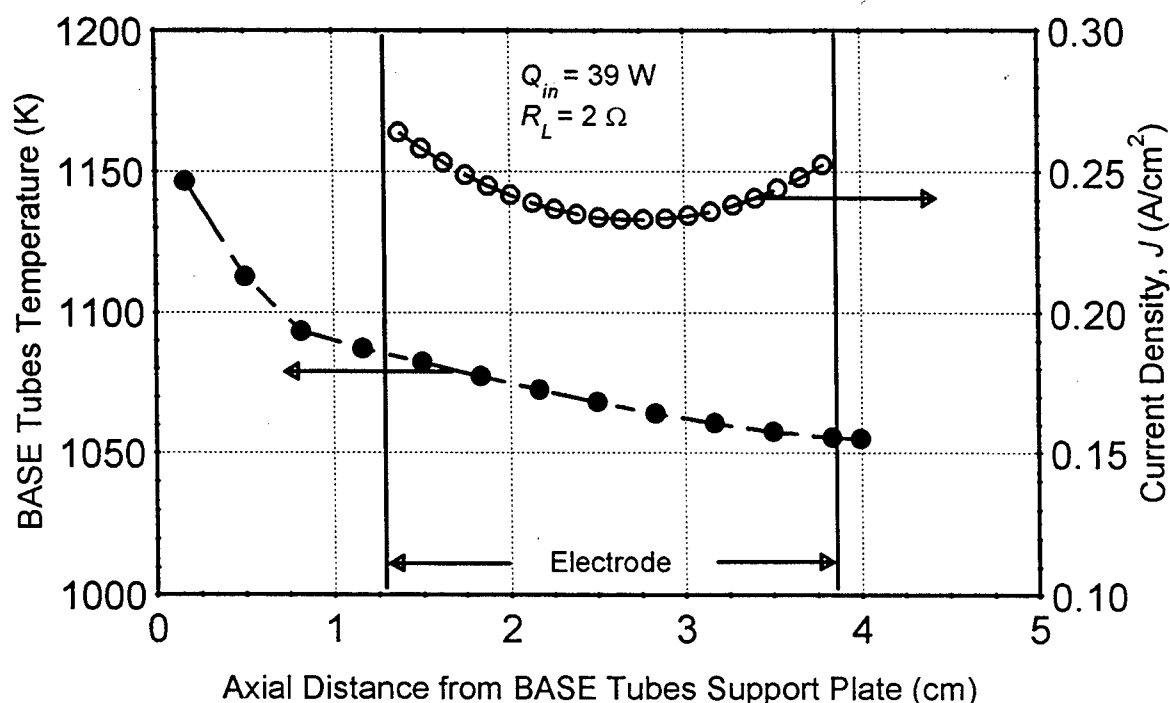


Figure 11.17. BASE Tubes Temperature and Current Density in PX-2C.

#### 11.4.7 Electrode Current Density in PX-2C

The calculated current density in PX-2C with an external load resistance of  $2\ \Omega$  ( $I = 1.47\ \text{A}$ ) is shown in Figure 11.17, along with the calculated temperature distribution along the BASE tubes. The current density only changes by a maximum of 12%, and has a minimum of  $0.23\ \text{A/cm}^2$  near the mid-plane of the electrode. This axial distribution of  $J$  results from the combined effects of vapor pressures distributions on the cathode and anode sides and the BASE axial temperature distributions. The temperature of the electrode varied linearly between 1053 K and 1087 K.

#### 11.4.8 BASE Tubes Temperature in PX-2C

Most of the heat input to the BASE tubes of the PX-2C cell was provided by conduction (9.8 W). The BASE tubes received only 2.7 W by radiation at their inside surface (Table 11.3). The copper current collectors on the inside and outside surfaces of the BASE tubes increased the effective axial conductance of the solid electrolyte membrane by 2 orders of magnitude, which limited the temperature drop along the electrode portion of the BASE tubes to only 35 K. Figure 11.17, however, indicates a larger temperature drop of about 60 K along the brazes of the BASE tubes, not covered by the current collectors. The calculated maximum temperature of the brazes in PX-2C was 1150 K (Figure 11.17).

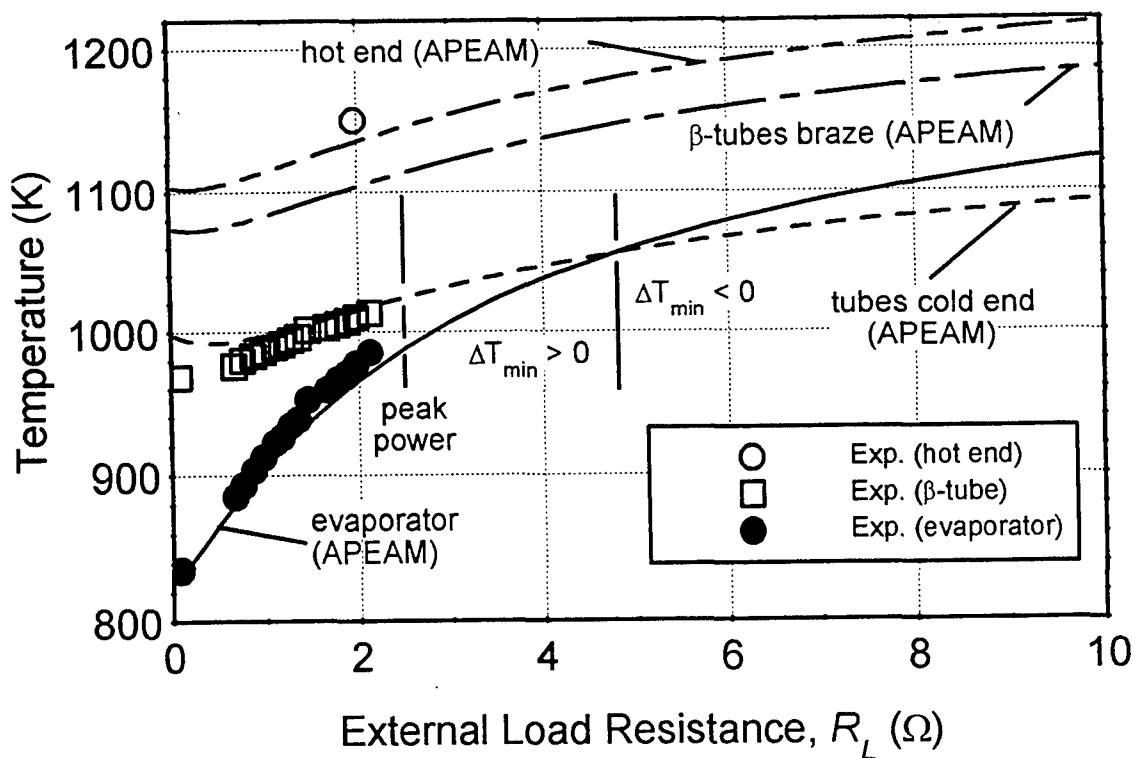


Figure 11.18. Measured and Predicted Temperatures in PX-2C, as Function of Load Resistance.

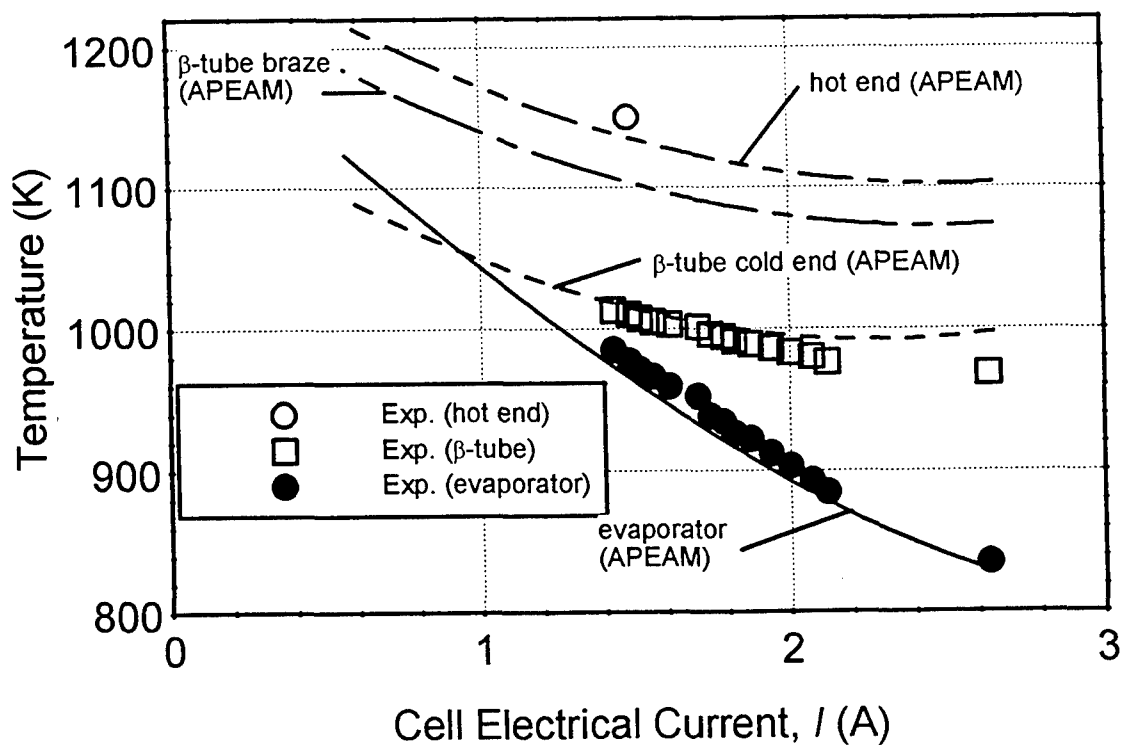


Figure 11.19. Measured and Predicted Temperatures in PX-2C, as Function of Cell Current.

#### 11.4.9 Evaporator Temperature and Temperature Margin in PX-2C

Since experimental data for PX-2C were taken at low external load resistance only (less than  $2.5\ \Omega$ ), near the peak power region, at moderate to high cell current values, the thickness of the evaporator standoff used in the model was increased to allow the model to predict the evaporator temperature well in this region. Figures 11.18 and 11.19 showed that the model predicted the temperatures of cell hot end, evaporator,  $\beta$ -tubes cold end and condenser within 10 K of the measured values, and the electrical power output within 5% (the peak power was  $4.35\ \text{W}_e$  at hot end, evaporator and condenser temperatures of 1150 K, 970 K and 526 K, respectively; the cell input power was 39 W). Typical TiN electrode parameters were used in the analysis (a BASE/electrode contact resistance,  $R_{cont} = 0.08\ \Omega\cdot\text{cm}^2$  and a temperature-independent charge-exchange current,  $B = 120\ \text{SI}$ ), and the effective emissivity of the mesh condenser surface was taken as 0.12.

Evaporator and BASE tube temperatures,  $T_{ev}$  and  $T_\beta$ , are two of three important temperatures (the third is the cell's condenser temperature) to determine electric output of a given cell. Both  $T_{ev}$  and  $T_\beta$  increase with increasing  $R_L$  (Figure 11.18) and/or decrease with increasing cell current (Figure 11.19). Figure 11.18 shows that  $T_{ev}$  increases faster than  $T_\beta$  as  $R_L$  increases. To prevent condensation of sodium inside the BASE tubes, a positive temperature margin,  $\Delta T = T_\beta - T_{ev}$ , is needed. But, the experimental data shows that the cells can work with either a (measured) positive (PX-2C) or a negative (PX-4B and PX-4C) temperature margin, as long as the BAS braze temperature is above the evaporator temperature ( $\Delta T_{max} > 0$ ). Figure 11.20 shows that the positive temperature margin in PX-2C decreased as  $R_L$  increased. However, PX-4B had a negative  $\Delta T$  for all  $R_L$  except at short circuit ( $\Delta T$  became positive after April 2, 1997, and had a value between 11 K and 17 K as load changed from short circuit to  $11\ \Omega$ ). Thermodynamically, a negative  $\Delta T$  means that condensation occurs inside the BASE tubes, near the cooler ends.

Figure 11.20 shows that a negative temperature margin ( $\Delta T_{min} = T_{\beta-min} - T_{ev} < 0$ ) would have occurred at an external load resistance  $R_L$  above  $5\ \Omega$ , meaning that some condensation of vapor would occur inside the BASE tubes, near the cold end. Since all predicted temperatures and cooling heat rejection compared well with experimental data, the calculated cell heat input and conversion efficiency are reliable. It was found that typically about 75% of the heater power was absorbed into the cell. Such a large fraction suggests that the radiative coupling of the heater and the insulation package surrounding the hot end of the cell were well designed. Based on the model calculations, PX-2C reached a conversion efficiency of 11.5%.

#### 11.4.10 PX-2C: Summary and Conclusion

APEAM's predictions of the PX-2C cell, tested at AFRL, were in good agreement with the measured electrical power output and experimental I-V characteristics. Results of the parametric analysis of PX-2C cell showed that the inclusion of a stainless steel circumferential shield increased the cell electrical power by 13%. The use of molybdenum thermal shield, however,

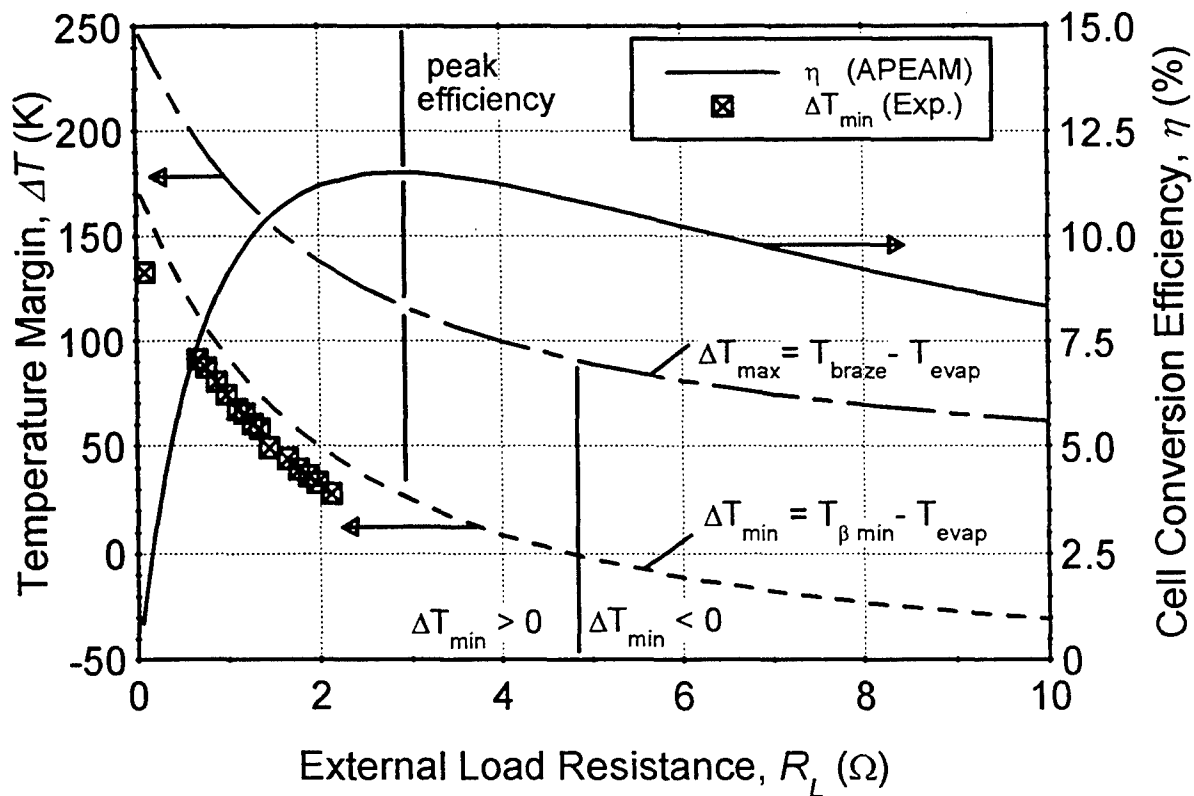


Figure 11.20. Temperature Margins and Conversion Efficiency in PX-2C.

which has a lower emissivity, would have increased the cell electric power and conversion efficiency by as much as 23%.

The analysis also showed that the good performance of the PX-2C cell (4.4  $W_e$  at 11.4% efficiency) was in part due to the presence of a conduction stud between the hot plate of the cell and the BASE tubes support plate. The metal stud in PX-2C provided a critical conduction path to the cell evaporator, instrumental in providing the necessary latent heat to vaporize the liquid sodium in the evaporator wick (as much as 20 W at a current  $I = 3$  A).

APEAM was used to predict PX-2C's load-following characteristic. The peak electric power of 4.4  $W_e$  occurred at an external load resistance of about 2.5  $\Omega$ . At higher load resistance (or lower load demand), the PX-2C cell was load-following. The operation domain of the cell when the external resistance is less than 2.5  $\Omega$  should be avoided because the cell is non load-following. It is worth noting, however, that on the load-following portion of the characteristic, the output electric power decreases slowly with increasing load resistance. The PX-2C cell could provide 3  $W_e$  at an external load of 10  $\Omega$ . Results also showed that the vapor flow on the low-pressure side of PX-2C was in the transition regime, with Knudsen numbers of about 0.2. It is worth noting that the design of the liquid-return artery and evaporator wick in PX-2C could provide the sodium flow rate (15 gm/hr for a cell current of 2.5 A) necessary to operate the cell at an evaporator temperature of about 950 K. The model predicted well the BASE tube and

evaporator temperature measurements in PX-2C. According to the model's results, the PX-2C operated with a positive temperature margin, since  $R_L < 5 \Omega$  in the experiment ( $I > 1$  A).

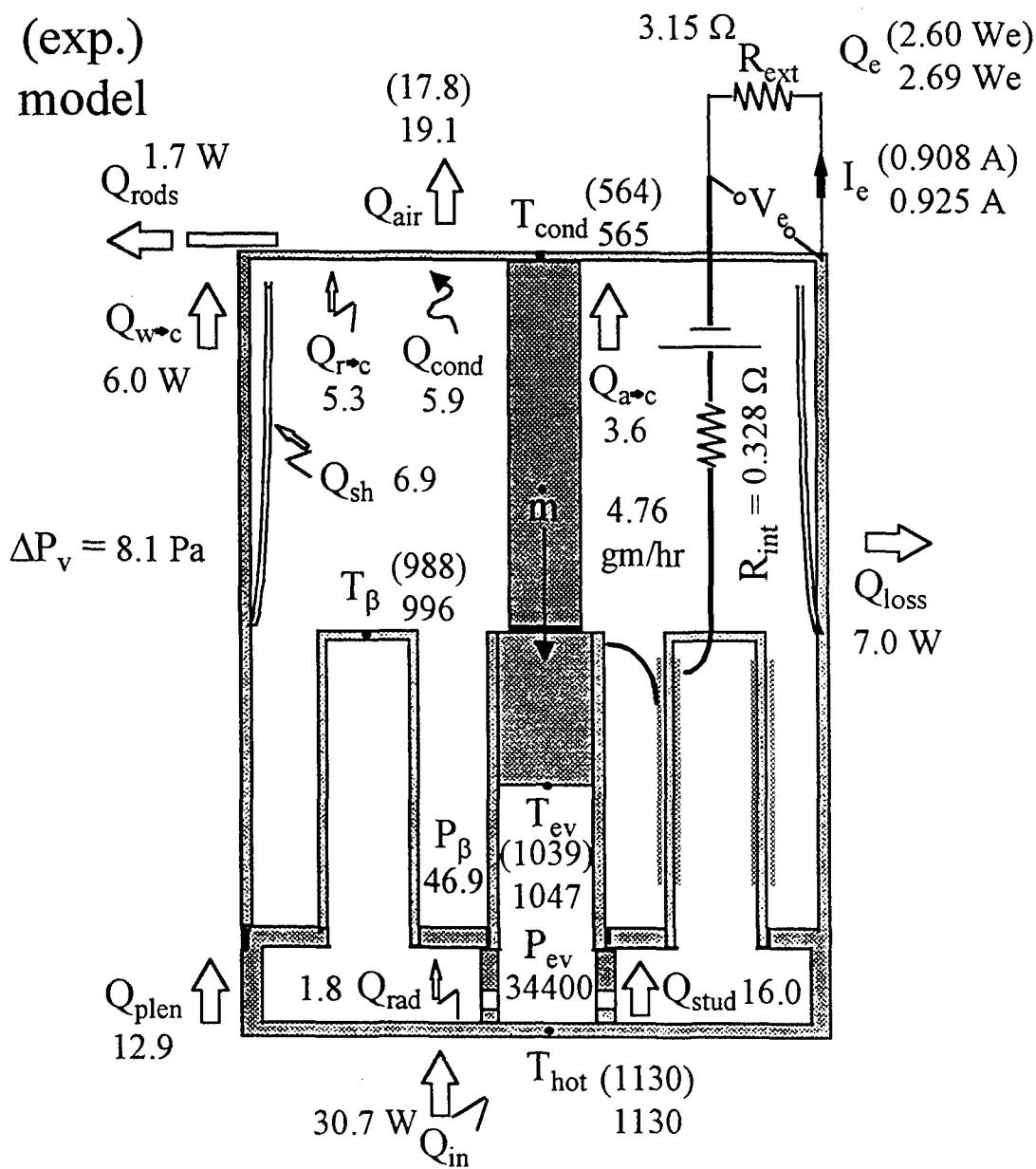
This analysis proved the very important result that, if the thermal model of conical evaporator wick can predict well the evaporator temperature in the cell, then the model is capable of accurately predicting all temperatures in the cell, as well as the peak output power. This result has also been confirmed with experimental data of other PX-Series cells.

## 11.5 PX-4C CELL DATA ANALYSIS

Test data of PX-4C were obtained at fixed hot end and condenser temperatures of 1130 K and 565 K, respectively, and at load resistance values as high as  $8.5 \Omega$ . Exact dimensions of the cell evaporator standoff were used in the modified thermal model, and the effective emissivity of the mesh condenser was taken as 0.12. Figures 11.21 to 11.25 show that predicted evaporator and BASE tube's cold end temperatures compared very well (within 10 K) with measured values for  $R_L > 1 \Omega$  ( $I < 2.2$  A). The condenser heat rejection was predicted within 6% (about 1 W error out of  $\sim 20$  W), see Figure 11.21. Because of the addition of thick conduction rings around the evaporator standoff, the evaporator temperature in PX-4C and PX-5A was much higher (above 1025 K at  $R_L > 2 \Omega$ ) than in PX-2C (Figures 11.22 and 11.23). As a result, the temperature margin  $\Delta T_{\min}$  in PX-4C became negative at  $R_L = 0.5 \Omega$ , approximately near the peak power (Figures 11.24 and 11.25). This means that some condensation occurred inside the BASE tubes over the complete practical range of operation of PX-4C. Calculated braze temperatures, however, were still above the evaporator temperature, even at high load resistance or low current ( $\Delta T_{\max} = T_{\text{braze}} - T_{\text{ev}} = 30 \text{ K} > 0$  at  $R_L = 10 \Omega$ ). It is believed that, the facts that the anode current collector mesh can retain any condensing sodium by capillary action, and that the  $\beta$ -tube brazes are operating at higher temperature than the evaporator (Figures 11.24 and 11.25), prevent the formation of a liquid bridge over the braze area (such a bridge could cause an electrical short in the cell). The fact that PX-4C and PX-5A cells have operated well and normally for hundreds of hours suggests that negative temperature margins ( $\Delta T_{\min} < 0$ ) are allowable in PX-series cells, as long as ( $\Delta T_{\max} > 0$ ). Condensation would occur inside the  $\beta$ -tubes along their colder section, while their hotter section (including the braze region) would prevent the formation of a liquid bridge by re-evaporating any liquid there.

Because of a chemical reaction between the Boron Nitride block covering the cell top and the stainless steel sheath of the thermocouples, the leads of hot end, BASE tube, and condenser end thermocouples were broken at the PX-4C cell top. The remaining portions in the TC wells were manually drilled out. The test setup for PX-4C was re-assembled and put back into the vacuum chamber. During initial testing, sodium leaking from the thermocouple well was detected, because of drilling.





S.I. Units:  $T$  [K],  $Q$  [W],  $P$  [Pa]

Figure 11.21. Predicted Heat Transfer and Temperatures in PX-4C, at  $R_L = 3.15 \Omega$ .

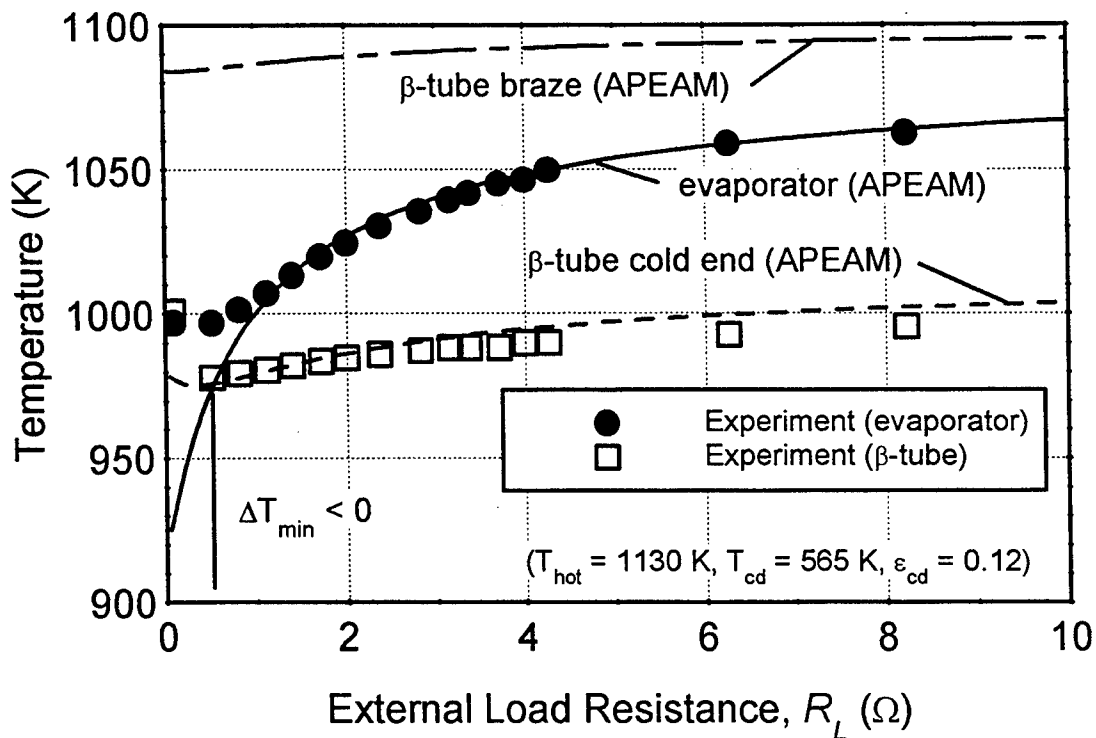


Figure 11.22. Measured and Predicted Temperatures in PX-4C, as Function of Load Resistance.

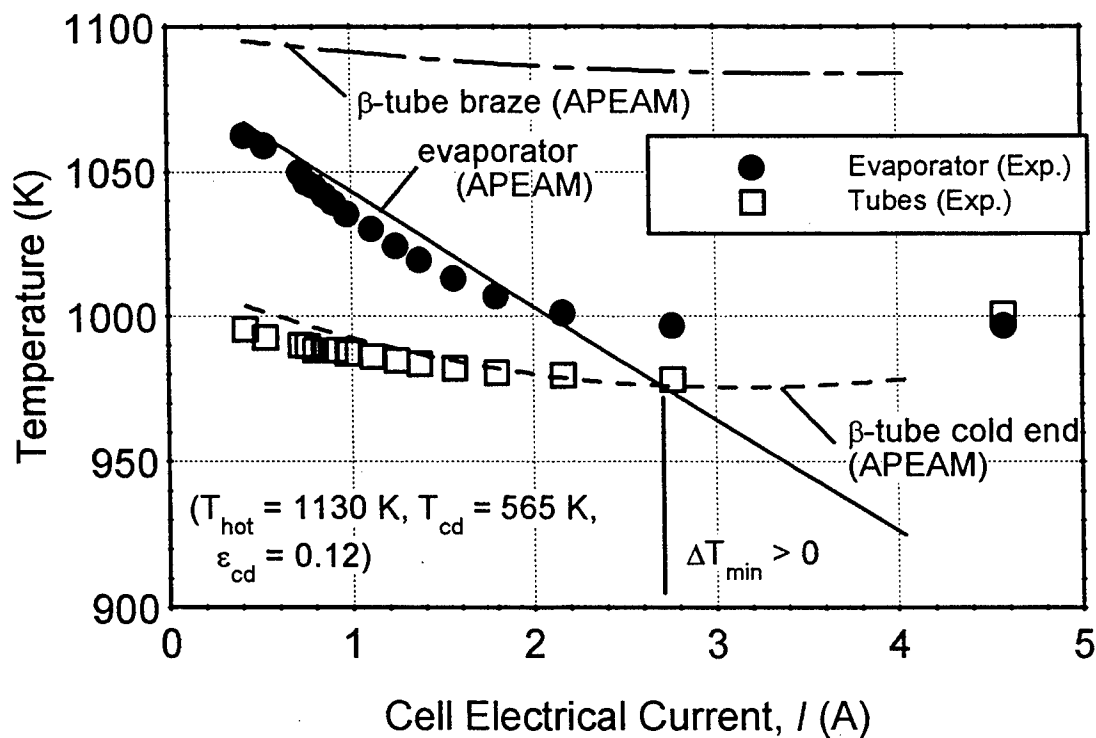


Figure 11.23. Measured and Predicted Temperatures in PX-4C, as Function of Cell Current.

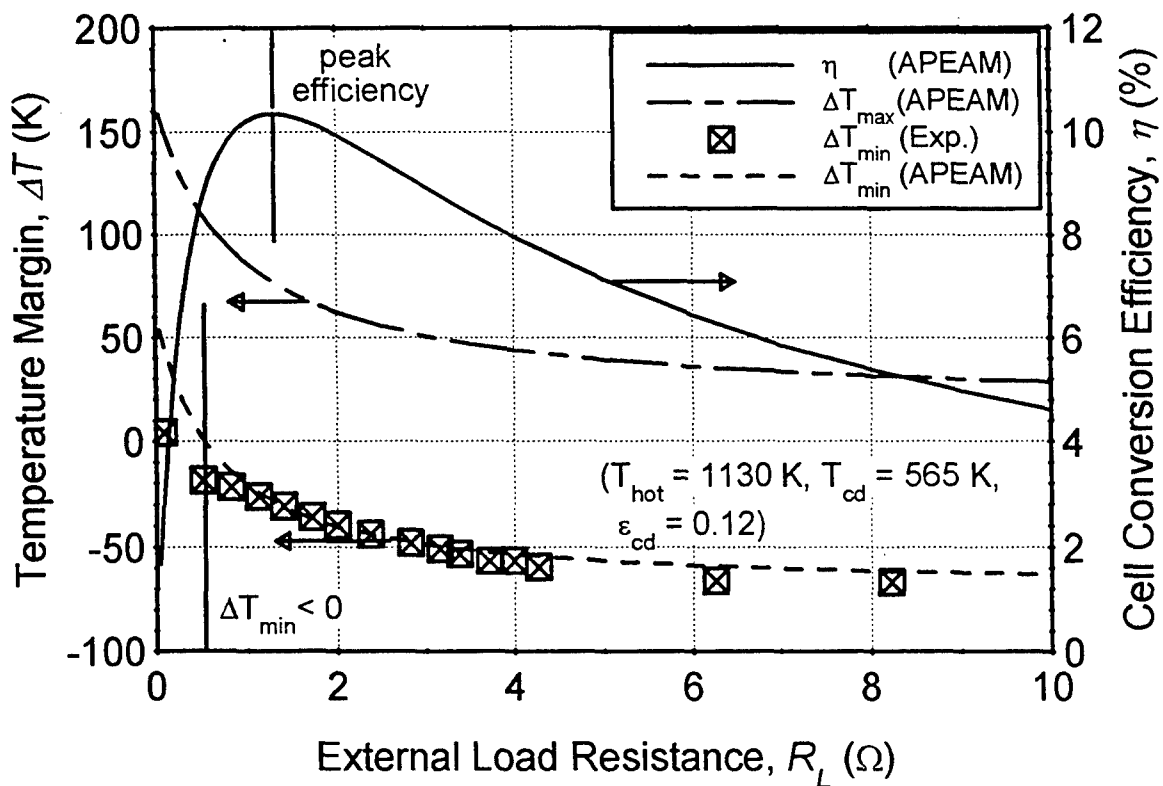


Figure 11.24. Temperature Margins and Conversion Efficiency in PX-4C.

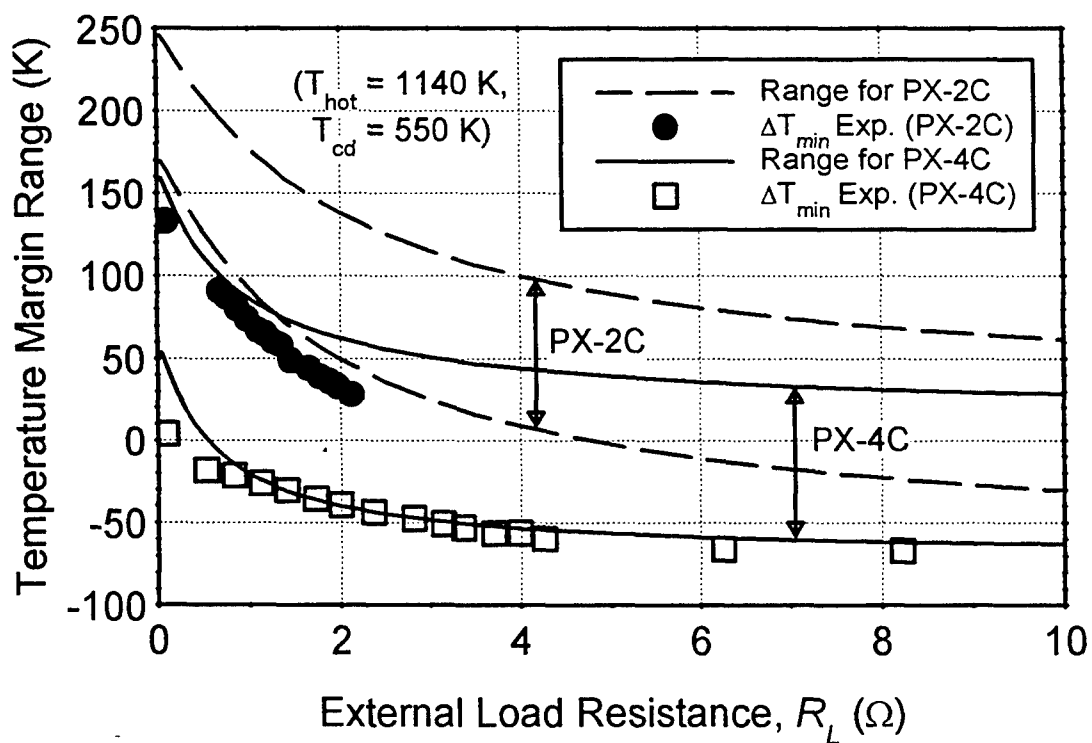


Figure 11.25. Temperature Margins in PX-2C and PX-4C Cells.

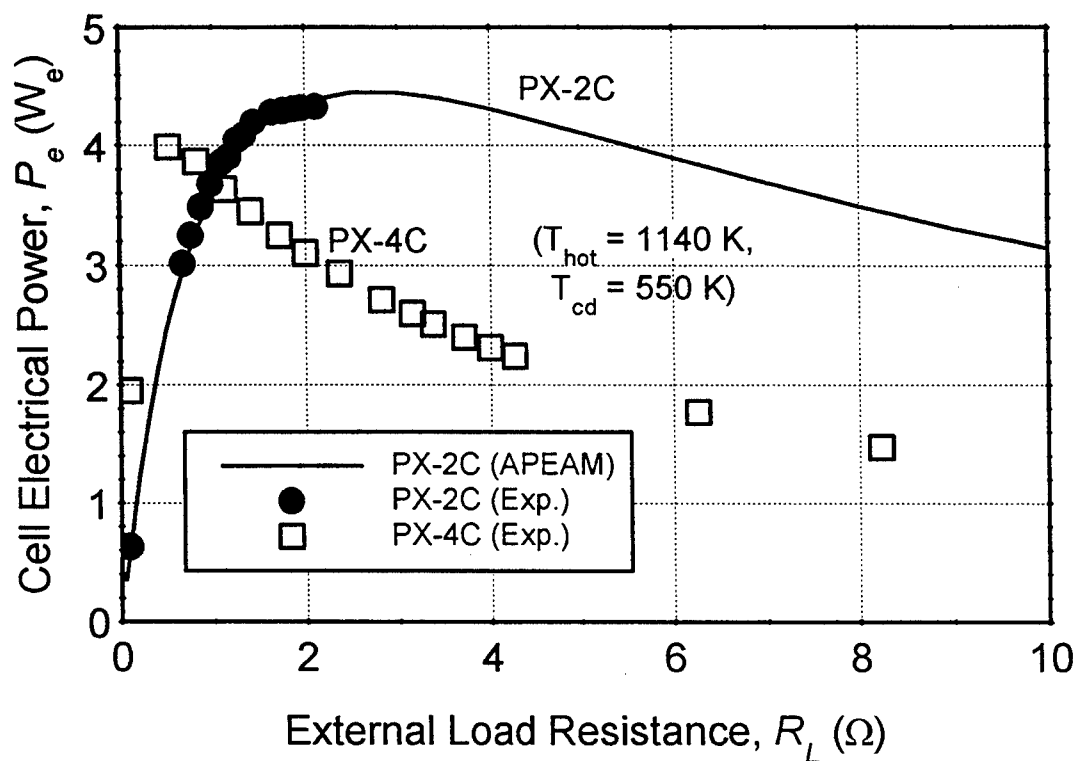


Figure 11.26. Comparison of PX-2C and PX-4C Electric Power Outputs.

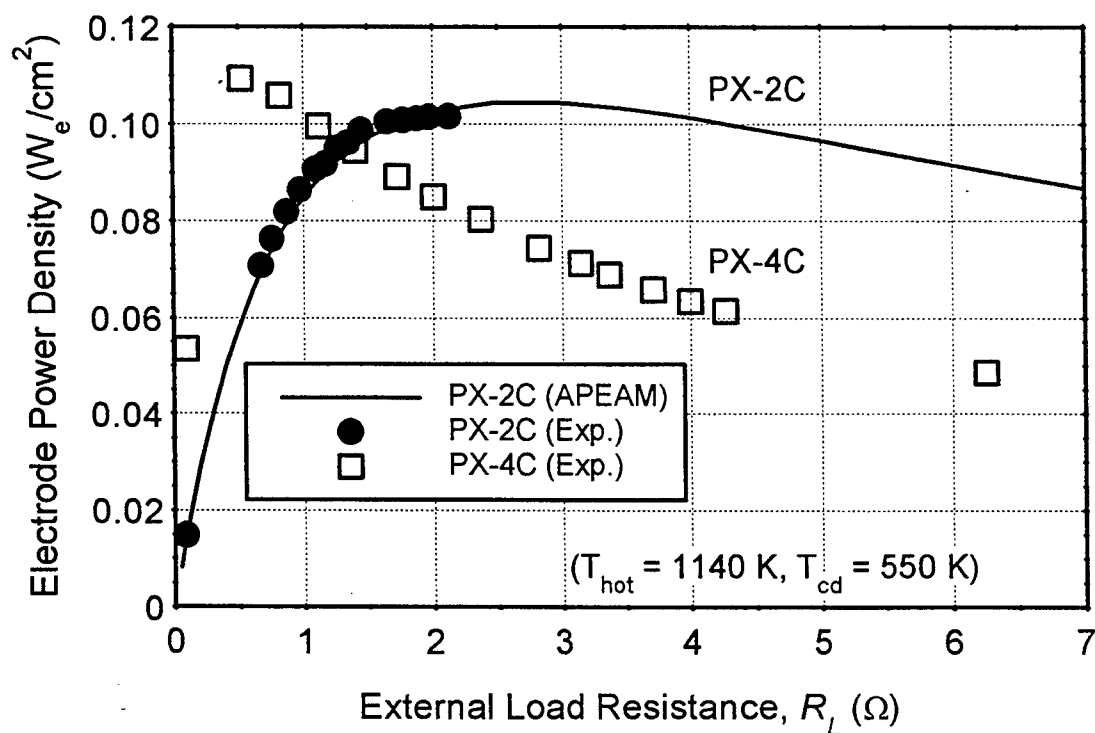


Figure 11.27. Comparison of PX-2C and PX-4C Electrode Power Densities.

As shown in Figure 11.26, PX-4C delivered less power than PX-2C at  $R_L > 1 \Omega$ . This is because PX-4C had only 6 BASE tubes compared to 7 in PX-2C. At large current ( $R_L < 1 \Omega$ ), however, PX-4C delivered more power than PX-2C, because of its much higher evaporator temperature, a consequence of the addition of thick conduction rings around its evaporator standoff (Table 11.1). Also, the height of PX-4C was larger (4 inch versus 3.5 inch for PX-2C), which reduced parasitic radiation and conduction losses in the cell, increasing the BASE tubes temperature. As a result, PX-4C operated at a maximum electrodes power density of  $0.11 \text{ W/cm}^2$ , a value 10% higher than in PX-2C (Figure 11.27). Unfortunately, while it predicted well the BASE and evaporator temperatures in the cell, the model overpredicted the cell's electrical power output. More discussion on this result follows in the next sections.

## 11.6 PX-5A CELL DATA ANALYSIS

Similar analyses were performed of PX-5A experimental data obtained at a fixed condenser temperature of 623 K and fixed hot end temperatures of 1023 K and 1123 K. The effective emissivity of the Creare condenser was taken equal to that of a sodium liquid film (0.05) in the analysis. Again, temperatures in the cell were within 15 K of the measured values (except that the evaporator temperature was underpredicted at  $R_L < 1.5 \Omega$  because of the limitation of the evaporator model at very large currents,  $I > 2.5 \text{ A}$ ), and the condenser heat rejection was within 8%. The cell electrical power output was overpredicted at high load resistance values.

## 11.7 PX-4C AND PX-5A CELLS: THE VALUE OF BASE AND EVAPORATOR TEMPERATURE MEASUREMENTS

While the predicted temperatures and condenser heat rejection compared well with measured values, the model consistently overpredicted the electrical output power of PX-4C and PX-5A by about  $0.75 \text{ W}_e$  (the measured peak power was about  $4 \text{ W}_e$ , at a cell current of  $\sim 2.7 \text{ A}$ ). Several analyses were performed to understand and/or explain this large difference. The effects of electrode characteristics, increased pressure losses on the cathode side, and of electronic leakage between the electrodes and the BASE tubes support plate, on the cell performance, and the meaning of the thermocouple temperature measurements in the cell were investigated.

### 11.7.1 Effect of Electrode Characteristics

The typical TiN electrode parameters chosen for PX-2C were used again in this analysis ( $R_{\text{cont}} = 0.08 \Omega \cdot \text{cm}^2$  and  $B = 120 \text{ SI}$ ).  $R_{\text{cont}}$  and  $B$  values were modified to see if the difference in measured and calculated cell output power could be explained by an increase in internal electrical losses in the cell. The contact resistance was doubled, and/or the exchange current  $B$  was reduced to 80 SI. While these changes reduced the predicted peak power significantly (by about

0.70  $W_e$ ), they did not affect the predicted output power at high load resistance (above 5  $\Omega$ ). This is because both ohmic internal losses and concentration and charge-exchange polarization losses increase with current and are small at low current. At  $R_L > 5 \Omega$ , the current was low enough ( $I < 0.6$  A) that these losses were small.

Therefore, reasonable increases in internal ohmic losses, concentration and charge-exchange polarization losses cannot account for the difference in predicted and measured cell output powers at low currents (high load resistances) in PX-4C and PX-5A.

### 11.7.2 Effect of Increased Pressure Losses on the Cathode Side

Another possibility investigated was that the sodium pressure model had underpredicted the pressure losses on the cathode side. The model predicted sodium pressures at the BASE/cathode interface ( $P_c$ ) in PX-4C of 11 Pa and 17 Pa, at cell currents of 0.6 A and 2.7 A, respectively. Again, the pressure drop decreases with decreasing current, or increasing load resistance.

In order to evaluate the effect of pressure losses on the cell electrical output, an additional pressure drop ( $\Delta P_c$ ) was included in the vapor pressure loss model, and an analysis was performed to find the magnitude of this pressure drop which would allow the cell output power calculated by the model to match the measured values. It was found that a constant value  $\Delta P_c = 36$  Pa (at  $T_{hot} = 1130$  K) allowed the model to predict the measured cell output power in PX-4C reasonably well. Analyses of other experimental data of PX-4C and PX-5A confirmed this result. From another series of measurements for PX-4C at a hot end temperature of 1145 K, we deduced  $\Delta P_c = 40$  Pa in order to match the measured cell output power above  $R_L > 1 \Omega$ . The PX-5A cell electrical power output was also overpredicted at high load resistance values. At hot end temperatures of 1023 K and 1123 K, we deduced  $\Delta P_c = 18$  Pa and  $\Delta P_c = 36$  Pa, respectively, in order to approximately match the measured cell output powers above  $R_L > 1.5 \Omega$ . These values were consistent with that obtained for PX-4C.

Unfortunately, these pressure drop values are about 3 times the predicted pressure drop in the model, and cannot be explained by inaccuracies in the pressure loss model alone. Even if the pressure model was off by a factor as much as 2, the model still would overpredict the cell output power by about 0.5  $W_e$  at low currents. Beside, the fact that the peak power was well predicted in PX-2C (at high current) gives some level of confidence that the vapor pressure drop model works reasonably well.

The morphology of the porous TiN electrode would greatly affect the pressure drop across it. Assuming a very thin (less than 5  $\mu\text{m}$ ) TiN electrode with a 90% volume porosity (an effective dimensionless factor,  $G = 11$ ), the pressure drop through the cathode electrode would be only 1 Pa at a current  $I = 1$  A. A drastic change in cathode electrode porosity, for example a reduction from 90% to 9% (for a  $G = 100$ ), would only increase the pressure drop through the electrode by 9 Pa, a quantity still too small to explain the large difference between predicted and measured cell output power. Note that a decrease in electrode porosity could drastically decrease the contact

resistance between electrode and BASE (as in the case of Mo electrodes), resulting actually in a net increase in cell electrical power output.

### **11.7.3 Electronic Leakage Between Electrodes and BASE Tubes Support Plate**

It was suggested at the 1997 IECEC conference that electronic leakage between electrodes and the BASE tubes support plate (or possibly through the braze joint) could be an internal loss process in multi-tube AMTEC cell, which could significantly affect the cell performance. In order to investigate this possibility, the AMTEC electrical circuit model was modified to include a leakage electrical resistance between the bottom ends of the cathode and anode electrodes (see Section 4.2). Model results showed that in order to match the cell electrical power output predicted by the model with the measured values, it was necessary to use a leakage electrical resistance smaller than  $2\ \Omega$ , resulting in leakage currents as high as 15% of the cell current. These values were not considered to be realistic, according to AMPS and JPL, at the time.

Since none of the losses mentioned above (electrode characteristics, increased pressure losses on the cathode side, and electronic leakage) could explain why the model consistently overpredicted the electrical output power of PX-4C and PX-5A, the accuracy of the evaporator and BASE tube temperature measurements was questioned. This was a natural step, because of the sensitivity of the cell electrical power output to these temperatures. In fact, a 25 K to 50 K decrease in evaporator temperature would result in about 1 W<sub>e</sub> decrease in cell electrical power output. Therefore, an effort was started to investigate the accuracy of the evaporator /BASE tube wells thermocouple readings.

### **11.7.4 Heat Transfer in Evaporator and BASE Tube Thermocouple Wells**

A radiation/conduction model was developed to calculate the heat transfer and temperature distribution along the thermocouple (TC) wells inside the AMTEC cell (see Chapter 9). Note that the TC wells pierce through the AMTEC cell's hot plate, so that some heat is conducted along the well between the hot plate and the thermocouple, affecting the temperature distribution along the well. Because of conduction and radiation heat transfers along the well, the temperature of the thermocouple end is typically higher than the temperature of the surrounding cavity. The objectives of this analysis was to calculate the actual evaporator and BASE tube temperatures using the thermocouple readings from experiments (Chapter 9).

The TC well model uses the temperature distributions in the evaporator and BASE tube cavities, predicted by the fully-integrated APEAM model, as boundary conditions. The "FIN" model accounts for conduction along the TC sheath and well, for radiation between the outside surface of the TC well and the surrounding cavity, and convective heat transfer between the well and the sodium vapor. Results showed that the latter mode of heat transfer was quite significant, and could not be overlooked. This TC-well thermal model was used to benchmark the fully-integrated APEAM model. The predicted temperatures at the end of the TC wells by "FIN"

matched the experimental TC readings, giving confidence in the temperatures predicted by APEAM in the evaporator / BASE tube cavities (see Sections 9.4 – 9.6).

The heat transfer “FIN” model was used to analyze the effect of TC well length on the temperature readings in the cell, and evaluate the temperature difference between TC readings and actual evaporator and BASE tube’s cold-end temperature predicted by APEAM. Results for PX-4C and PX-5A cells showed that the TCs measured a temperature close to that of the local sodium vapor. The actual temperature of the cold-end of the BASE tube could be as much as 20 K lower than the BASE tube TC reading, while the actual temperature of the evaporator could be as much as 60 K lower than the evaporator TC reading. Therefore, caution must be exercised when using the TC readings to characterize the AMTEC cells’ performance. In particular, the temperature margin in the cell, inferred from the TC readings in the experiment, could be in error by as much as 40 K.

## 11.8 REVISED ANALYSIS OF PX-4C CELL DATA

The PX-4C cell was 38 mm in diameter, and made entirely of SS. It had six 40 mm-long BASE tubes electrically connected in series, a deep conical evaporator, a circumferential shield above the BASE tubes, a conduction stud, that was 100 mm<sup>2</sup> in cross section area, and four 2.5 mm-thick SS rings around the evaporator standoff. Experimental data were obtained at fixed hot and cold end temperatures of 1130 K and 565 K, respectively. This was made possible by controlling the heater electric power and air mass flow rate in the experiment. The effective radiative emissivity of the stainless steel screen wick covering the condenser surface was taken equal to 0.15 in the model.

Figures 11.28a – 11.28f show the measured and predicted performance of the PX-4C cell as a function of external load resistance,  $R_L$ . Because the model assumed a flat evaporator surface, calculations were performed for three different locations of the evaporator surface ( $h_{ev}$  is the height of the evaporator wick surface measured from the BASE tubes’ support plate). Figure 11.28a shows that the flat evaporator approximation in the model typically overpredicted the cell electrical power output,  $Pe$ , at high load resistance (low cell current), and underpredicted  $Pe$  at low load resistance (or high cell current). As expected for a flat evaporator, the shorter the evaporator standoff, the higher the evaporator temperature (Figure 11.28e), and the higher the cell electrical power output (Figure 11.28a). Also, the higher the cell electrical current, the lower the evaporator temperature (Figure 11.28e). This is because the latent heat of vaporization, which is proportional to the sodium mass flow rate (or cell current), is conducted up the evaporator standoff, and the temperature drop between the BASE tubes’ support plate and the evaporator surface increases with both cell current and standoff length.

Based on the predicted cell electric performance (Figures 11.28a and 11.28b), the actual conical evaporator temperature was lower than that predicted by the flat evaporator model at high load resistance, and higher than that predicted at low load resistance (Figure 11.28e). Examination of cell data suggested that the conical evaporator provided a sodium vapor pressure that was



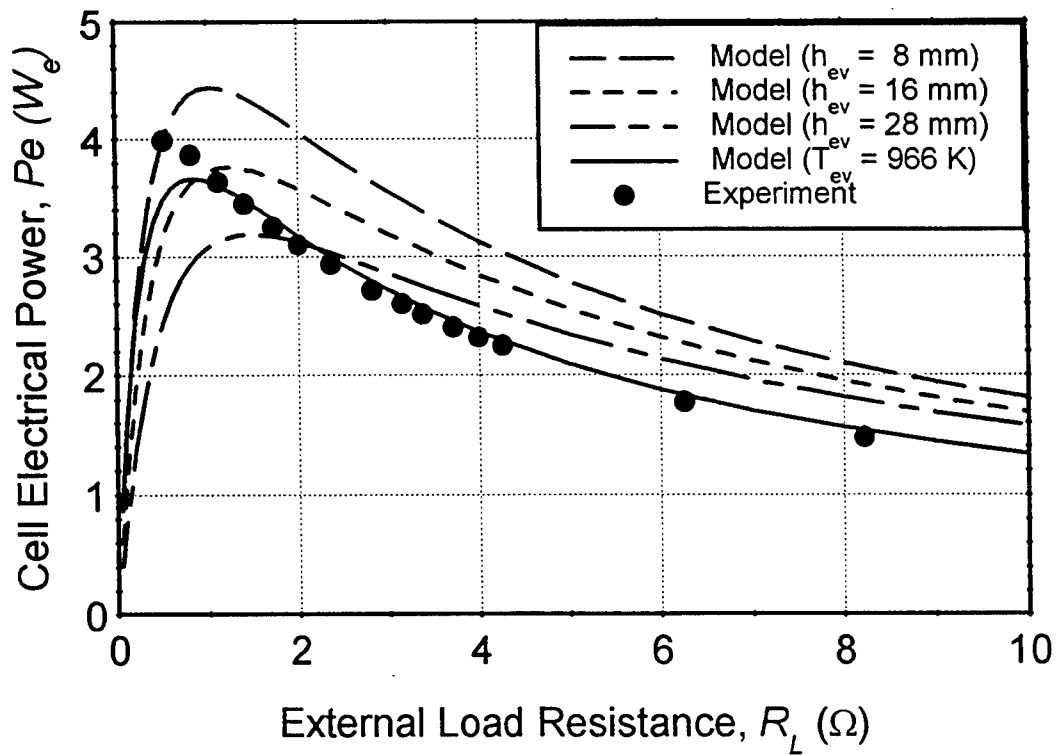


Figure 11.28a. Electric Power Output of PX-4C Cell ( $T_{hot} = 1130$  K,  $T_{cd} = 565$  K).

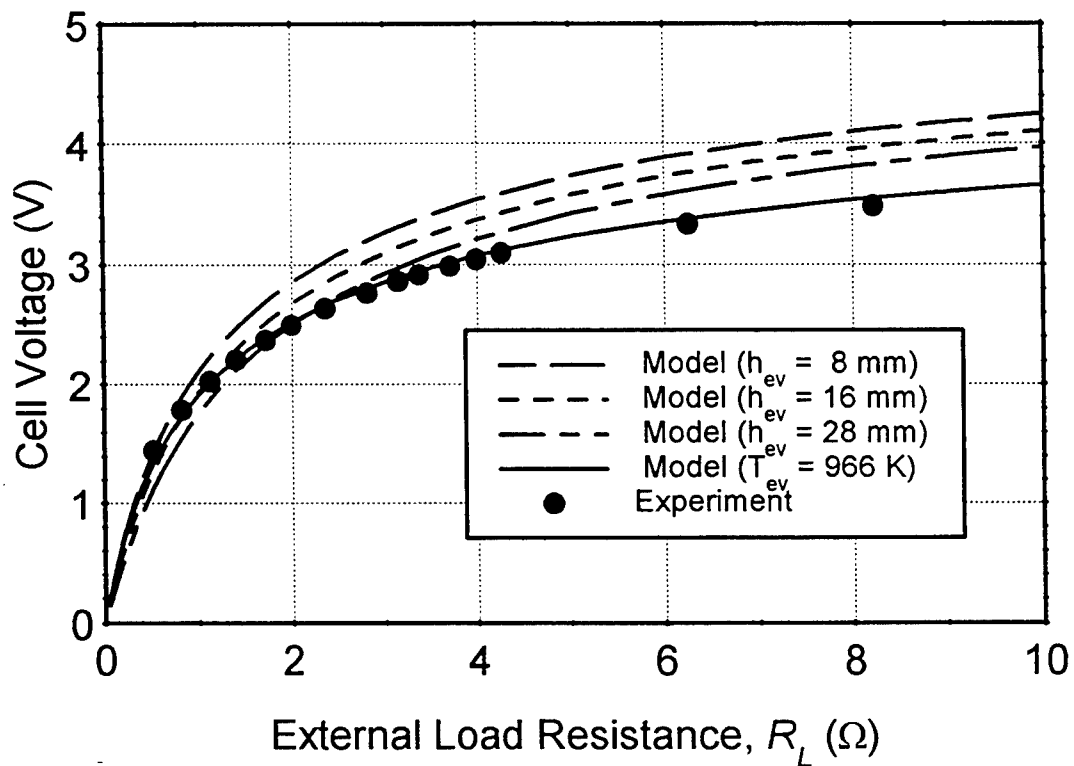


Figure 11.28b. Electric Voltage Output of PX-4C Cell ( $T_{hot} = 1130$  K,  $T_{cd} = 565$  K).

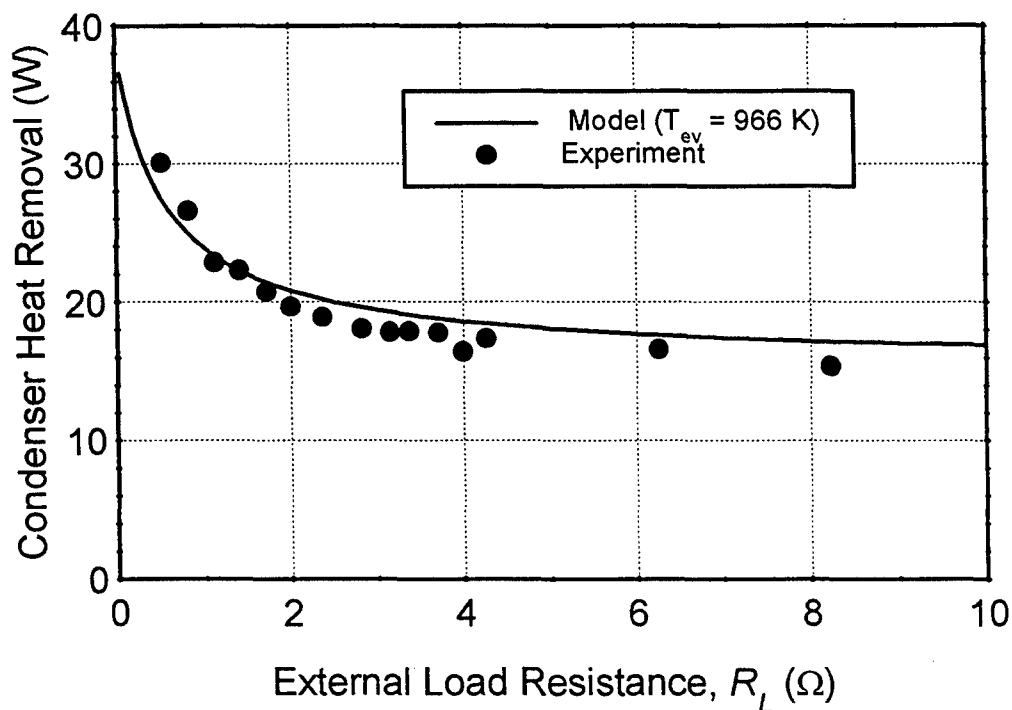


Figure 11.28c. Heat Removed at Condenser of PX-4C Cell ( $T_{hot} = 1130$  K,  $T_{cd} = 565$  K).

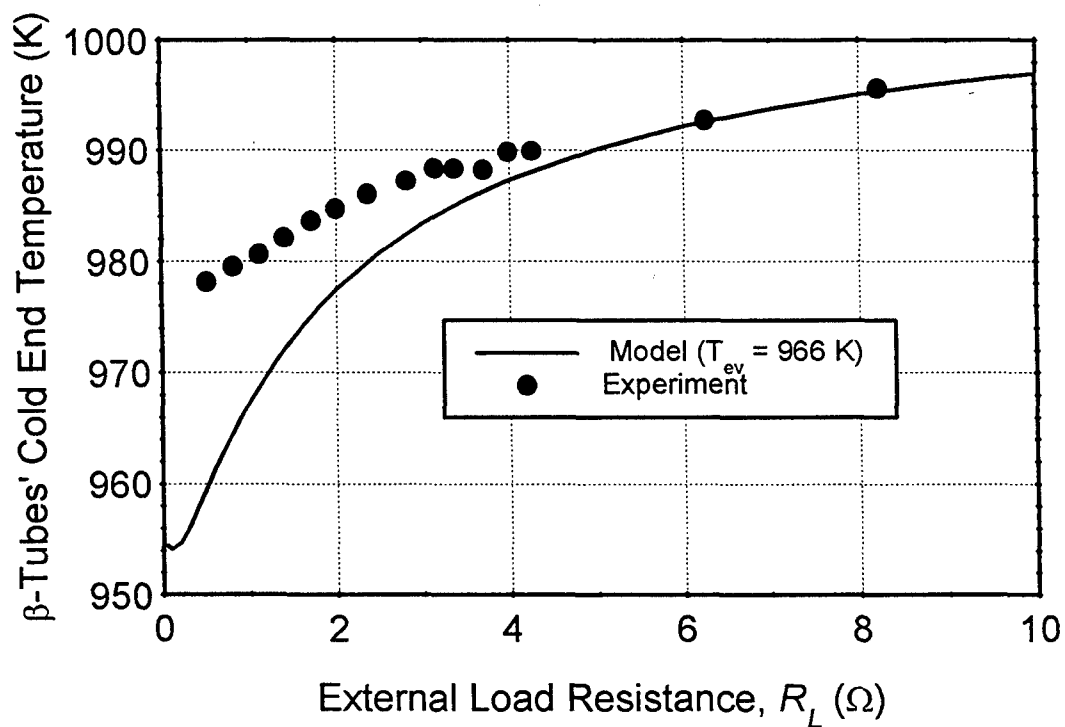


Figure 11.28d. BASE Tube's Cold End Temperature in PX-4C Cell ( $T_{hot} = 1130$  K,  $T_{cd} = 565$  K).

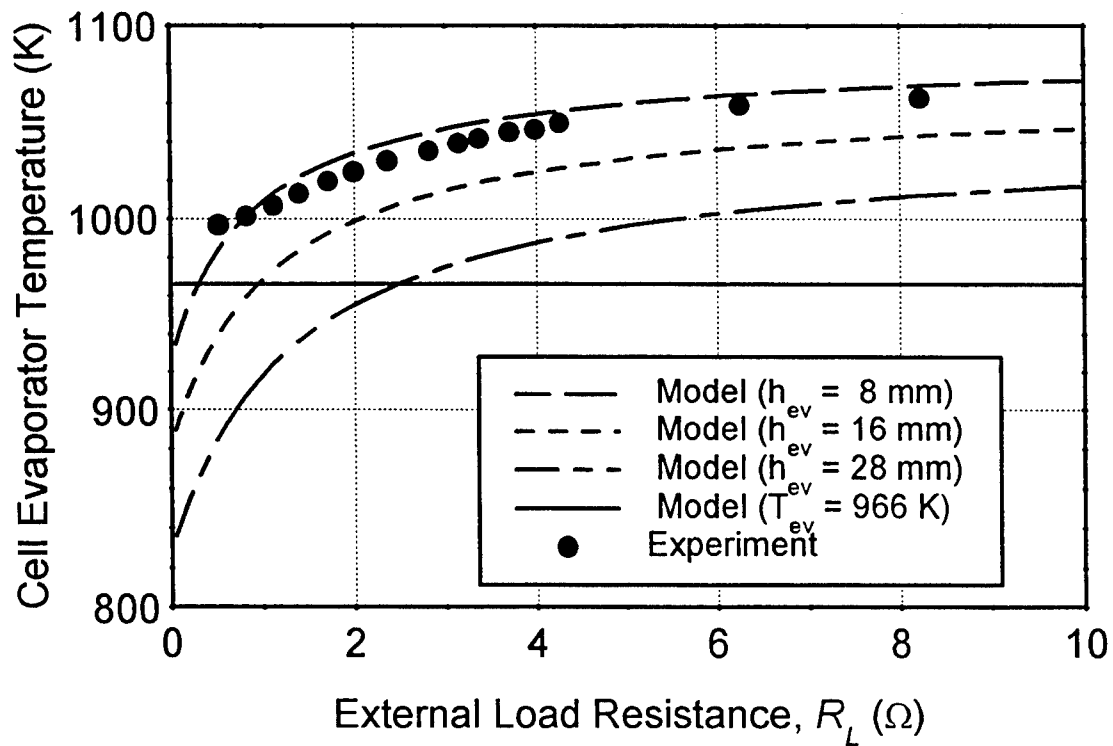


Figure 11.28e. Evaporator Temperature in PX-4C Cell ( $T_{hot} = 1130$  K,  $T_{cd} = 565$  K).

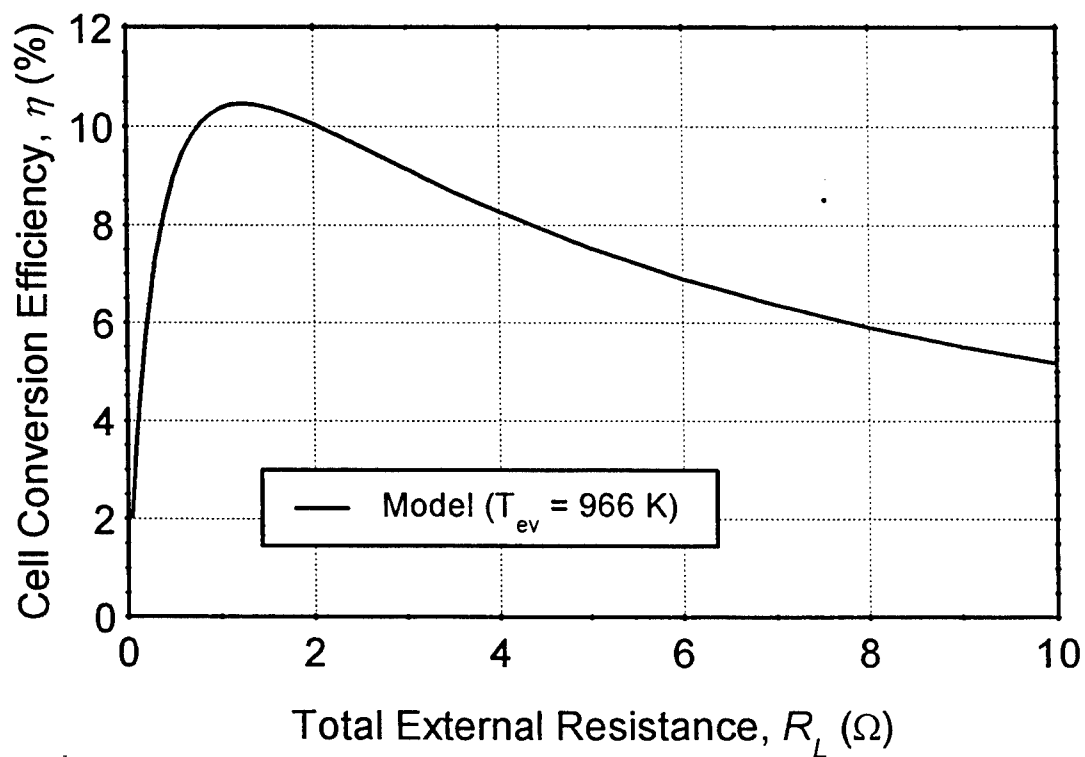


Figure 11.28f. Predicted Conversion Efficiency of PX-4C Cell ( $T_{hot} = 1130$  K,  $T_{cd} = 565$  K).

essentially independent of the cell electrical current,  $I$ , when  $I < 2.5$  A. Thus, calculations were performed at a fixed sodium anode pressure of 12.8 kPa, which corresponded to a saturation temperature of 966 K. As shown in Figures 11.28a and 11.28b, the cell electrical power output and voltage obtained at fixed evaporator temperature (or anode sodium pressure) compared well with measured values, suggesting that the electric current had negligible effect on the evaporator pressure, when operating the cell at fixed hot end temperature (except at very high cell current, when  $R_L < 0.5 \Omega$ ).

Figure 11.28c shows the predicted heat removed from the cold end of the cell. Model results compared well with measured values, with a maximum difference between 2 and 3 W. The predicted BASE tubes' cold end temperature is shown in Figure 11.28d. Heat was supplied to the BASE tubes mostly by conduction, and they lost heat by radiation to the structure in the low-pressure cavity of the AMTEC cell. The fraction of heat input to the BASE tubes that was converted into electrical power decreased with increasing  $R_L$  to the right of the peak power (Figure 11.28a), causing the BASE tubes temperature to increase (Figure 11.28d). The predicted BASE tubes' cold end temperature was 2 to 20 K lower than the reading from the thermocouple placed within the BASE tube cavity. This temperature difference increased with increasing cell electrical current. This is consistent with the thermal analysis of the thermocouple fin in the cell (see Sections 9.4 – 9.7). The thermocouple (TC) guide tube was welded to the hot end of the cell, and the thermocouple head did not touch the BASE tube. The heat conducted from the hot end up the TC well was dissipated by radiation to the inside of the BASE tube and by convection to the sodium vapor, causing the TC head temperature to be higher than the actual BASE tube temperature.

Predicted and measured evaporator temperatures in PX-4C are shown in Figure 11.28e. The predicted fixed evaporator temperature of 966 K was 30 to 90 K lower than the thermocouple reading, with the difference decreasing with cell electrical current. The fact that evaporator temperatures predicted by the flat evaporator model at  $h_{ev} = 8$  mm matched well with TC readings is misleading. This is because the effect of heat transfer along the evaporator TC well was much more dramatic than that along the  $\beta$ -tube thermocouple well (Sections 9.4 – 9.7). The higher the sodium mass flow rate, the lower the temperature of the BASE tubes and the larger the convective cooling of the TC fin by the vapor, and the lower the TC head temperature. The difference between TC reading and anode saturation temperature, predicted by the TC well heat transfer model, was as large as 45 K at a load resistance of  $2 \Omega$  and current  $I = 1.25$  A (Sections 9.4 – 9.7).

The model predicted well the conductive and radiative heat transfers in the AMTEC cell, since heat removal at the condenser, and temperatures of hot end, evaporator,  $\beta$ -tube's cold end, and condenser matched well with experimental data. Also, the heat balance at the hot end of the cell was satisfied, confirming that the predicted heat input to the cell,  $Q_{in}$ , was accurate. Note that even if the model would predict the cell electrical power output within 1 W, only, the predicted heat input to the cell would still be 4% accurate. Since the predicted cell electrical power output at constant evaporator temperature compared well with experimental data, the overall cell conversion efficiency predicted for this case is also reliable. Figure 11.28f shows that PX-4C reached a peak conversion efficiency of 10.5% at the conditions of the experiment. About 6.9 W

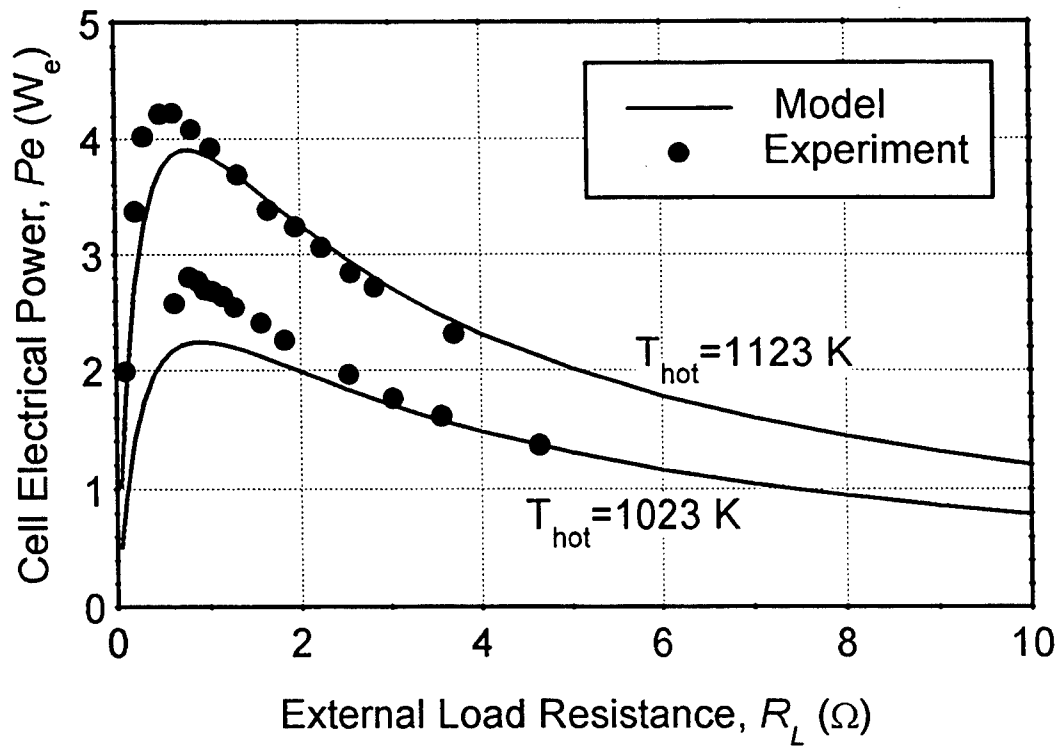


Figure 11.29a. Electric Power Output of PX-5A Cell ( $T_{cd} = 623$  K).

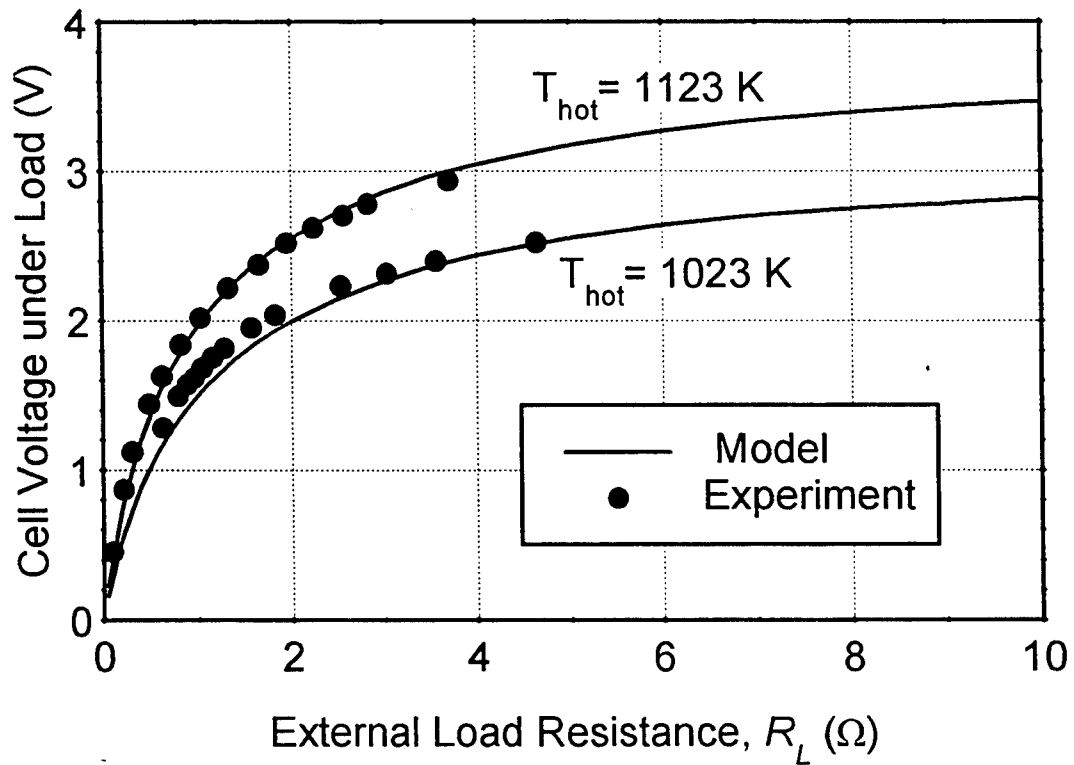


Figure 11.29b. Electric Voltage Output of PX-5A Cell ( $T_{cd} = 623$  K).

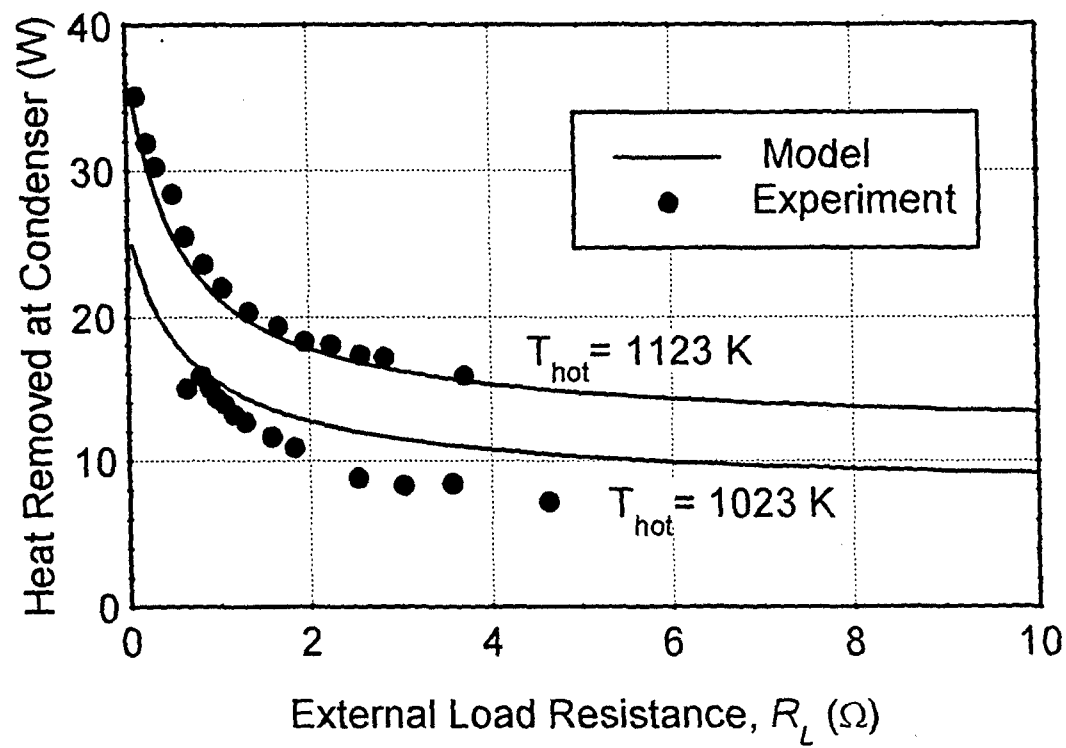


Figure 11.29c. Heat Removed at Condenser of PX-5A Cell ( $T_{cd} = 623$  K).

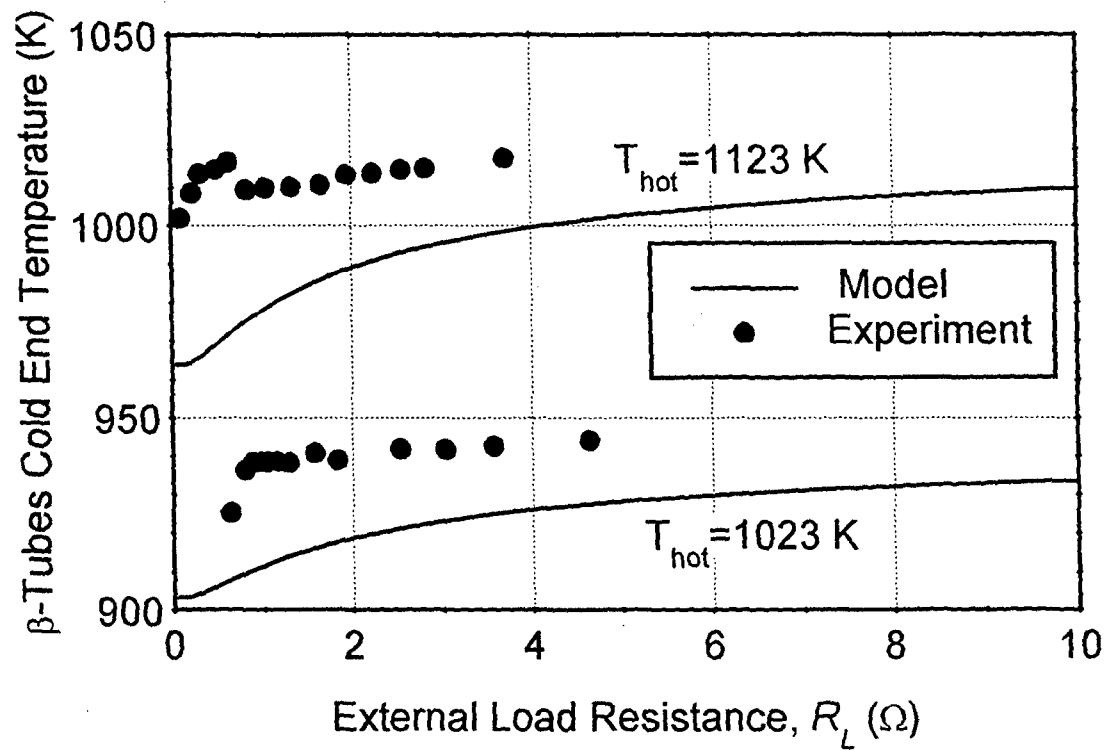


Figure 11.29d. BASE Tube's Cold End Temperature in PX-5A Cell ( $T_{cd} = 623$  K).

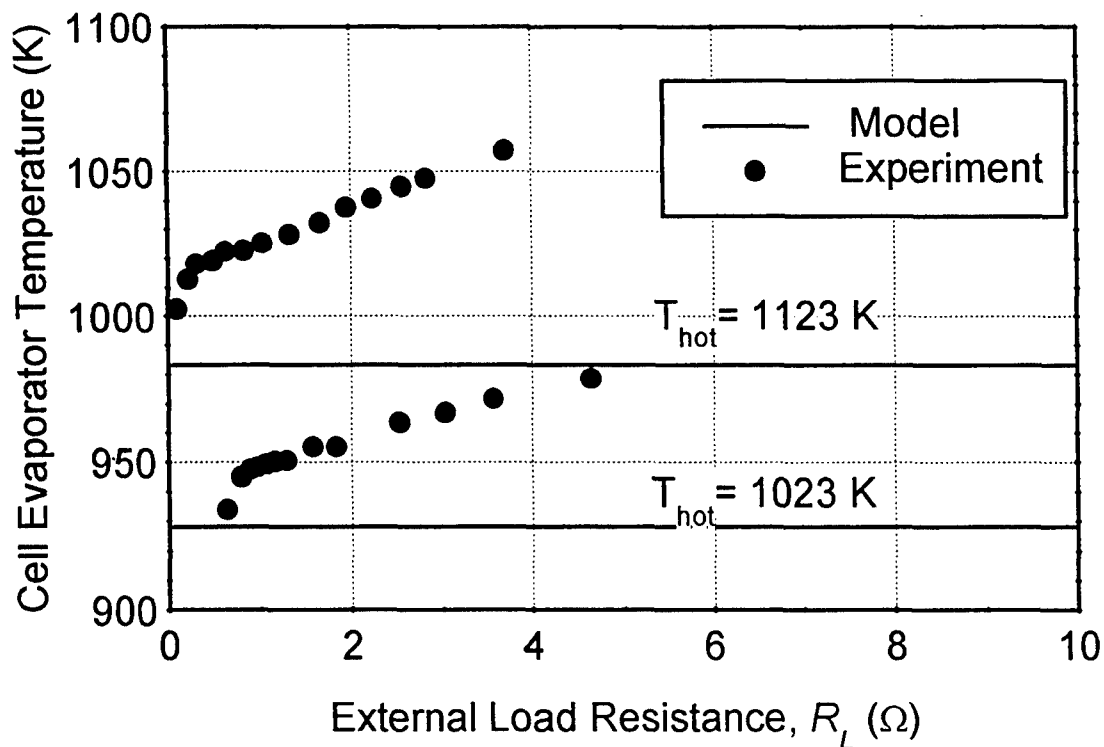


Figure 11.29e. Evaporator Temperature in PX-5A Cell ( $T_{cd} = 623$  K).

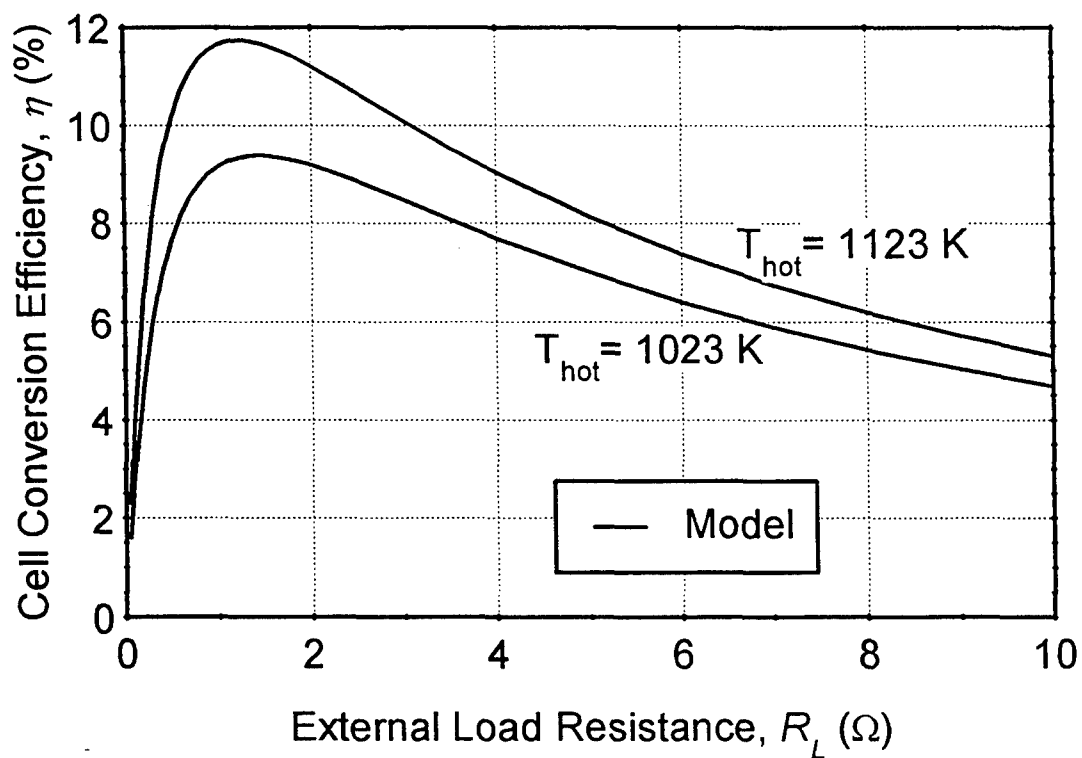


Figure 11.29f. Predicted Conversion Efficiency of PX-5A Cell ( $T_{cd} = 623$  K).

were lost at the cell wall through the Min-K insulation, and these losses increased very slowly with increasing  $R_L$ . Therefore, PX-4C could have reached an efficiency of 13.0% with an adiabatic wall condition.

Similar results were obtained when APEAM's predictions were compared with test data of PX-5A and PX-3A cells, and these results are shown in the following sections.

## 11.9 REVISED ANALYSIS OF PX-5A CELL DATA

The PX-5A cell was identical to PX-4C, except that the mesh pad condenser was replaced with a Creare condenser (Table 11.1). This condenser ensured the formation of a continuous film of liquid sodium on its surface, thus reducing the radiative heat losses to the condenser. The effective emissivity of the Creare condenser surface was taken equal to 0.05 in the model. Results are presented in Figures 11.29a – 11.29f, for a fixed cold end temperature of 623 K, and fixed hot end temperatures of 1023 K and 1123 K. Calculations were performed at fixed sodium anode pressures of 7.6 kPa and 16.0 kPa, which corresponded to saturation temperatures of 928 K and 983 K, respectively.

As shown in Figures 11.29a and 11.29b, the cell electrical power output and load voltage compared well with measured values, except at large currents. The cell peak electrical power was underpredicted by 0.4 W<sub>e</sub>, for the case of a 1023 K hot side temperature. Nevertheless, the BASE tubes cold end temperature and heat removal at the condenser were predicted reasonably well (Figures 11.29c and 11.29d). The predicted BASE tubes' cold end temperatures were 15 to 40 K lower than the TC readings recorded in the experiment, a result that is consistent with the thermal analysis of the TC measurements (see Chapter 9). Predicted anode saturation temperatures in PX-5A were also 5 to 70 K lower than the TC readings.

Based on the predicted heat input, PX-5A reached a peak efficiency of 11.8% (Figure 11.29f), which is 1.3 points higher than PX-4C. This increase in efficiency was attributed to the much reduced parasitic radiation and conduction heat losses in the PX-5A cell, since it was operated at higher condenser temperature, and used a more reflective Creare condenser. Predicted heat losses through the side wall of the PX-5A cell were 6.2 W and 7.1 W, at hot end temperatures of 1023 K and 1123 K, respectively.

## 11.10 PX-3A CELL DATA ANALYSIS

The PX-3A cell was smaller in size (29 mm in diameter) than PX-4C and PX-5A and had only five, shorter (32 mm-long) BASE tubes. It used a Creare condenser, a conical evaporator, a stainless steel circumferential shield, a conduction stud (38 mm<sup>2</sup> in cross section area), and five nickel rings (1.1 mm-thick) around the evaporator standoff (Table 11.1). Results are presented in Figures 11.30a–11.30f, for a fixed cold end temperature of 623 K, and fixed hot end temperatures of 1023 K, 1123 K, and 1173 K. Calculations were performed at fixed sodium anode pressures of 7.8 kPa, 25.2 kPa and 35.7 kPa, which corresponded to sodium saturation temperatures of 930 K,



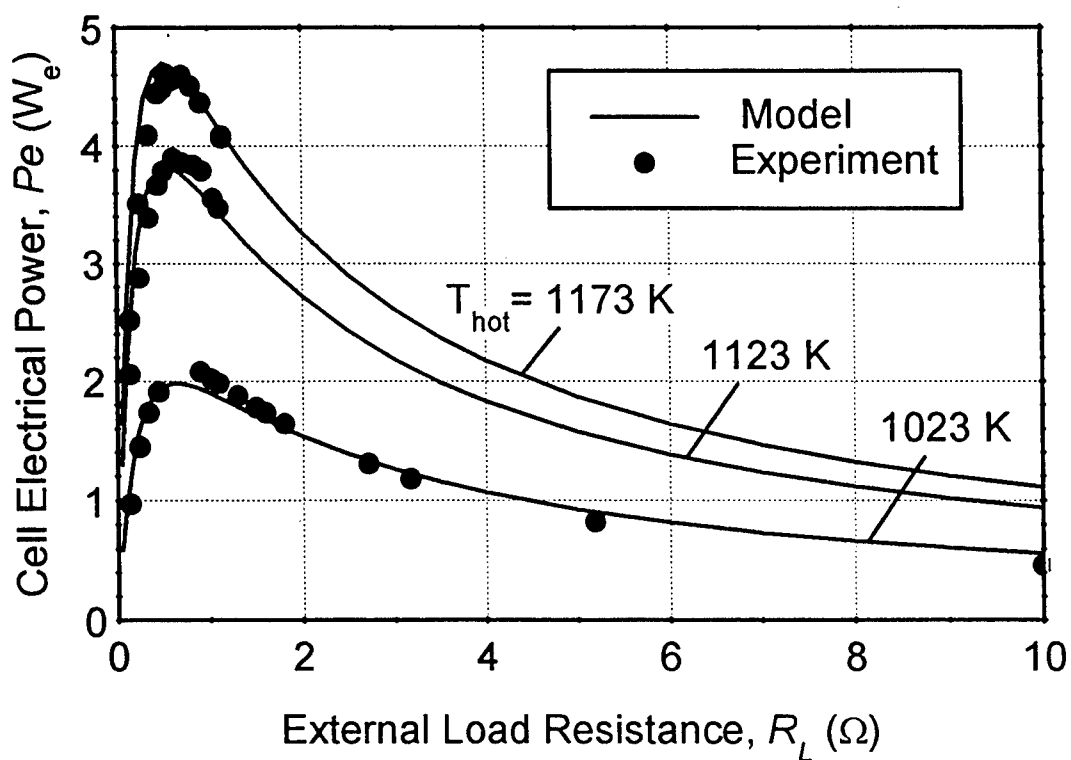


Figure 11.30a. Electric Power Output of PX-3A Cell ( $T_{cd} = 623$  K).

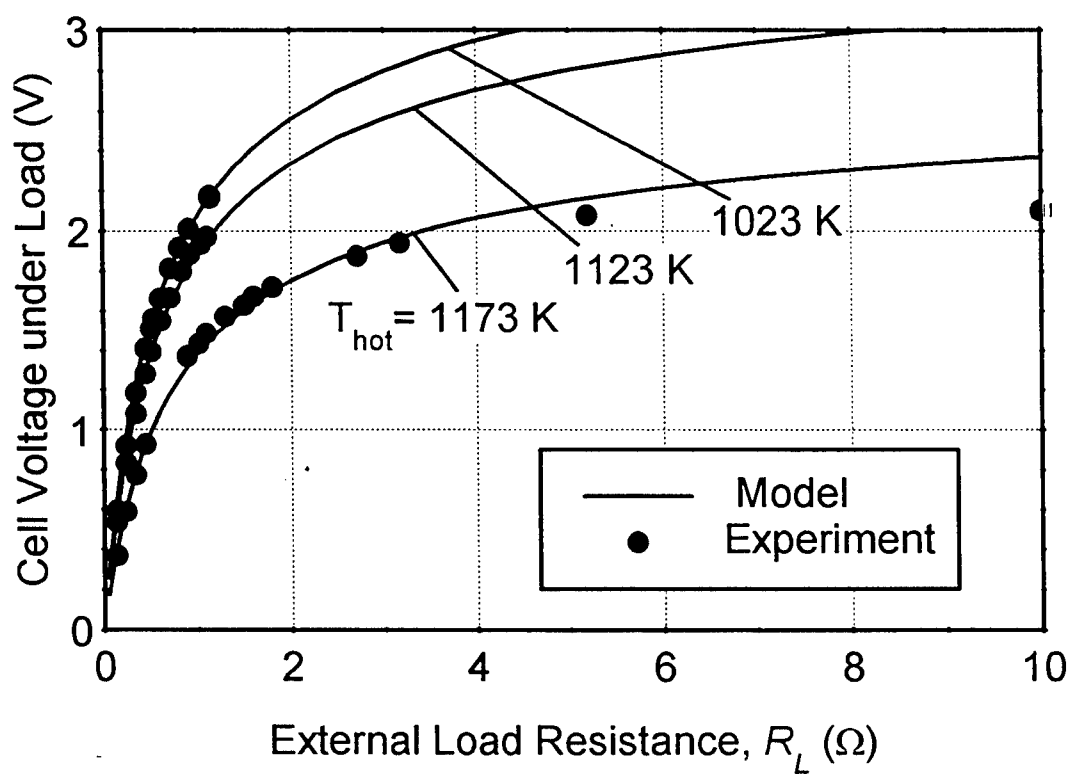


Figure 11.30b. Electric Voltage Output of PX-3A Cell ( $T_{cd} = 623$  K).

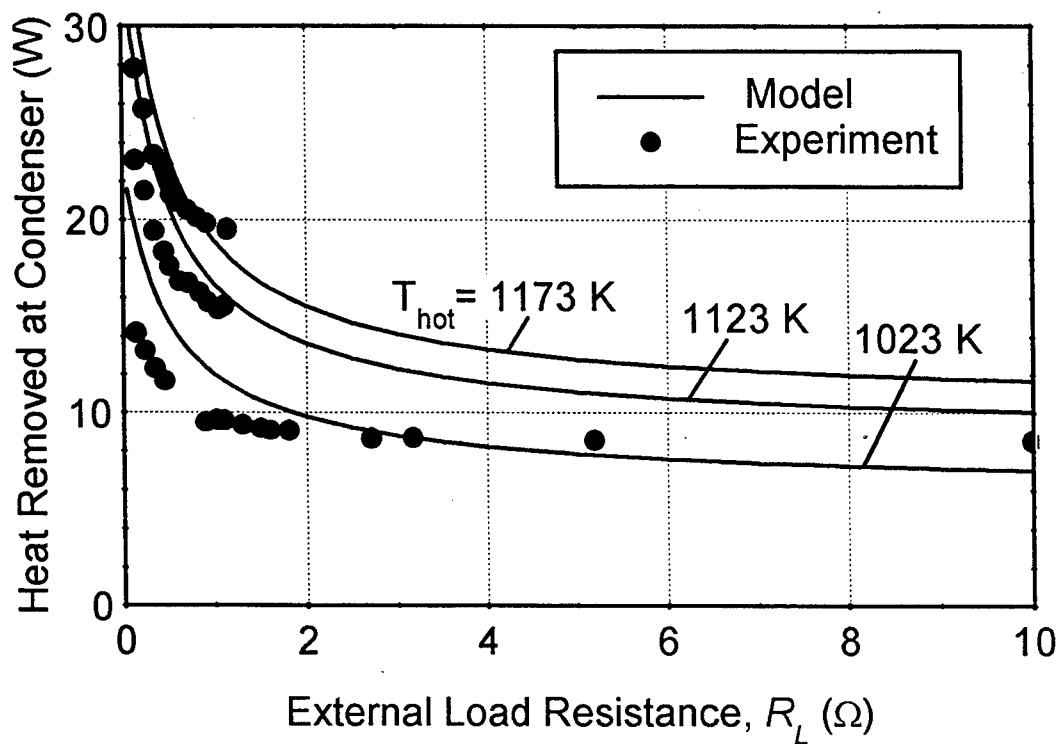


Figure 11.30c. Heat Removed at Condenser of PX-3A Cell ( $T_{cd} = 623$  K).

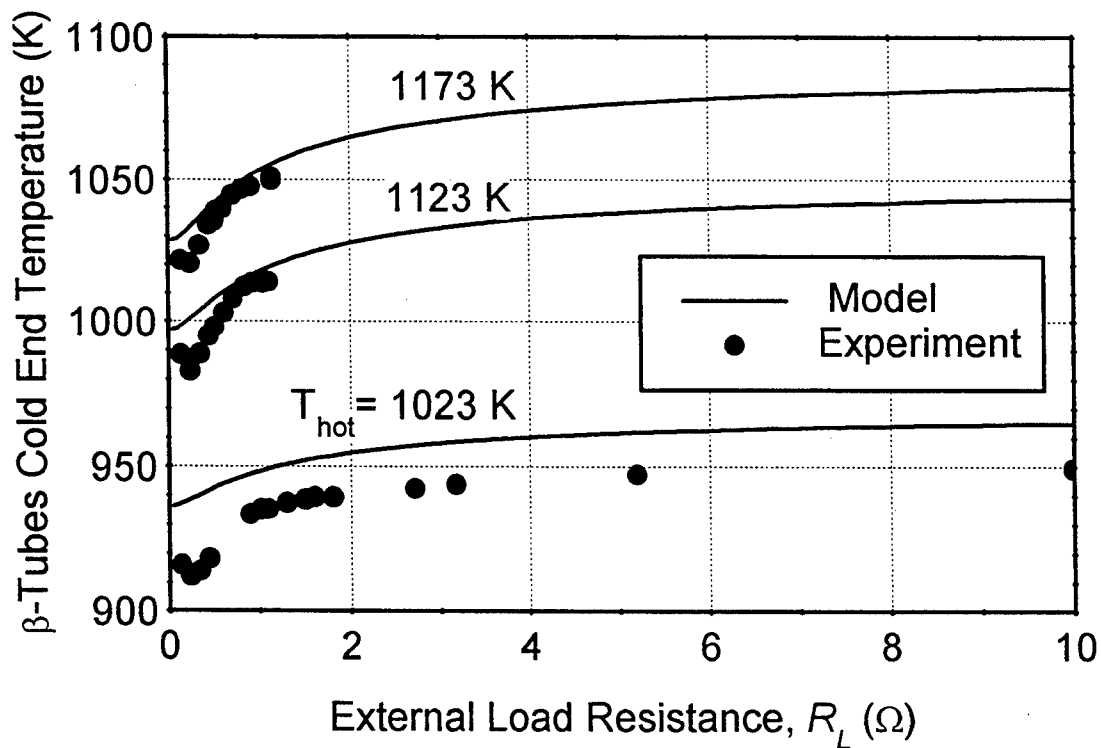


Figure 11.30d. BASE Tube's Cold End Temperature in PX-3A Cell ( $T_{cd} = 623$  K).

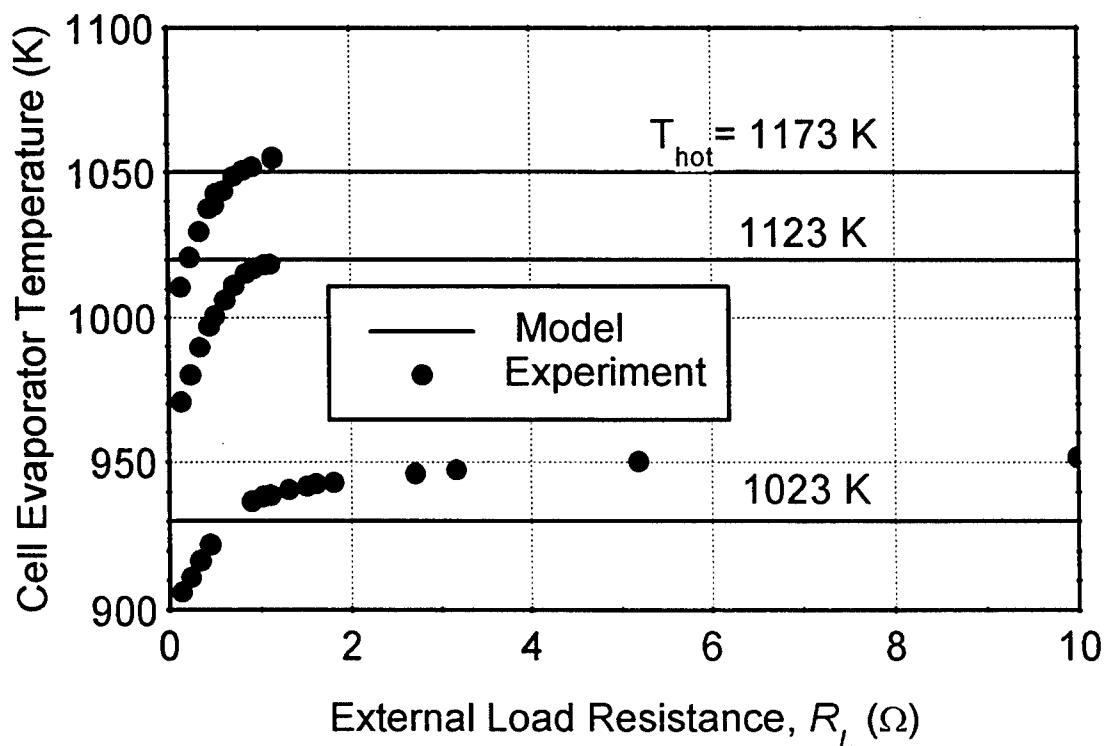


Figure 11.30e. Evaporator Temperature in PX-3A Cell ( $T_{cd} = 623$  K).

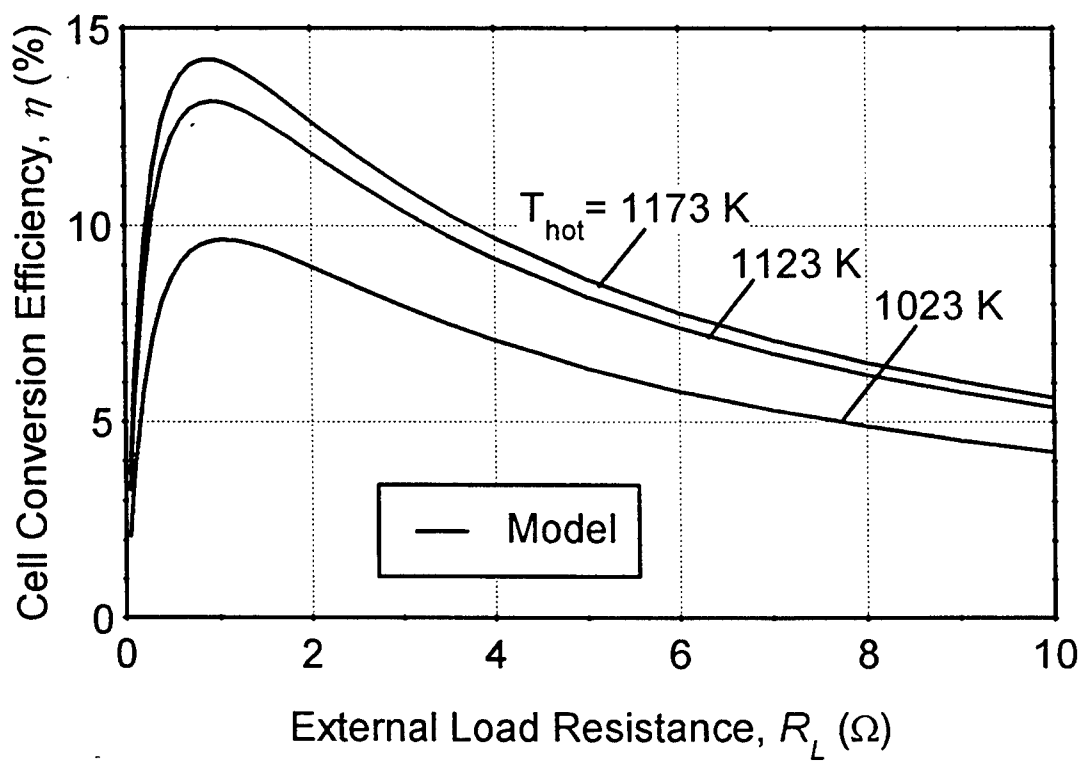


Figure 11.30f. Predicted Conversion Efficiency of PX-3A Cell ( $T_{cd} = 623$  K).

1020 K and 1050 K, respectively. As shown in Figures 11.30a and 11.30b, the cell electrical power output and voltage compared well with measured values for  $R_L > 0.6 \Omega$ . Heat removal at the condenser was predicted reasonably well, to within 2 to 3 W, except at lower hot side temperatures (Figure 11.30c). The predicted BASE tubes cold end temperatures were 5 to 20 K higher than the recorded TC readings in the experiments (Figure 11.30d).

The predicted evaporator temperatures in PX-3A were 5 to 50 K lower than the TC readings, at  $R_L < 1 \Omega$  (large cell currents). However, the predicted anode saturation temperature at the lowest hot side temperature was 5 to 20 K below the TC readings recorded in the experiments at  $R_L > 1 \Omega$  (Figure 11.30e). Better comparison could have been obtained at lower values of  $R_L$ , if the assumed sodium anode vapor pressure had been allowed to decrease with increasing electric current (Figures 11.30a and 11.30e).

Figure 11.30f shows the effect of increasing the hot end temperature of the cell, on the conversion efficiency. A 100 K increase in the hot side temperature, from 1023 K to 1123 K, caused a 3.3 points increase in the peak efficiency (from 9.7% to 13.0%). This increase in cell efficiency was caused by the doubling of the cell electrical power output, due to the increase in the expansion work through the BASE with increasing BASE tubes temperature and sodium vapor pressure on the anode side. However, a higher hot side temperature increased the radiation and conduction parasitic losses in the cell, as well as the heat losses through the side wall. As a result, the cell efficiency increased from 9.7% to 13.0%, a 34% increase only. As shown in Figures 11.30a and 11.30f, increasing the hot side temperature by another 50 K resulted in a much smaller gain, only a 20% increase in cell electric power output, and 1.2 points increase in cell efficiency (from 13.0% to 14.2%). This is because the parasitic radiation losses in the cell increased much faster (with the fourth power of temperature) with increasing  $T_{hot}$  than the isothermal work of expansion. Predicted heat losses at the side wall were 5.0 W, 5.7 W and 6.1 W, at hot end temperatures of 1023 K, 1123 K and 1173 K, respectively.

The fact that the model predicted reasonably well the performance parameters of the PX-4C, PX-5A and PX-3A cells, at different hot side temperatures, confirmed the soundness of the solution procedure developed in this work, and provided confidence in the accuracy of the different physical models (sodium vapor pressure loss model, electrochemical and electrical circuit model, and radiation/conduction heat transfer model) used in APEAM.

### 11.11 EFFECT OF DESIGN CHANGES ON PERFORMANCE OF PX-4C, PX-5A, AND PX-3A CELLS

Predicted performance parameters and measured peak powers of the PX-4C, PX-5A, and PX-3A cells, are listed in Table 11.4. This table illustrates the effects of different design changes, and of the hot and cold end temperatures on the performance parameters of these cells. The use of a Creare condenser in PX-5A, in lieu of the mesh pad condenser of PX-4C, combined with an increased condenser temperature (from 565 K to 623 K), reduced the parasitic heat losses in this cell. This increased the sodium vapor pressure on the anode side (from 12.8 kPa to 16.0 kPa), the

Table 11.4. Predicted Performance of Some PX-Series Cells Tested at AFRL.

AMTEC Cell	Predicted performance parameters	Cell's hot end temperature		
		$T_{hot} = 1023 \text{ K}$	$T_{hot} = 1123 \text{ K}$	$T_{hot} = 1173 \text{ K}$
PX-4C ( $T_{cd} = 565 \text{ K}$ )	$T_{ev} \text{ (K)}$	-	966	-
	$Pe^{max} \text{ (exp) (W}_e\text{)}$	-	3.6 (3.9)	-
	$\eta^{max}$	-	10.5 %	-
PX-5A ( $T_{cd} = 623 \text{ K}$ )	$T_{ev} \text{ (K)}$	928	983	-
	$Pe^{max} \text{ (exp) (W}_e\text{)}$	2.3 (2.7)	3.9 (4.2)	-
	$\eta^{max}$	9.3 %	11.8 %	-
PX-3A ( $T_{cd} = 623 \text{ K}$ )	$T_{ev} \text{ (K)}$	930	1020	1050
	$Pe^{max} \text{ (exp) (W}_e\text{)}$	2.0 (2.1)	3.8 (3.9)	4.6 (4.7)
	$\eta^{max}$	9.7 %	13.0 %	14.2 %

BASE tubes temperature (from 967 K to 980 K at the cold end), and finally the cell electrical power output (from 3.6  $W_e$  to 3.9  $W_e$ ) and the overall predicted cell efficiency (from 10.5% to 11.8%). The higher vapor pressure on the cathode side of PX-5A (23 Pa, compared to 16 Pa for PX-4C, at  $R_L = 1 \Omega$ ), due to the higher condenser pressure, caused the electrical power output to decrease by 2%.

As shown in Table 11.4, PX-3A reached a predicted peak efficiency of 13.0% at the conditions of the experiment, at a hot side temperature of 1123 K. This cell efficiency was 1.2 points higher than that of PX-5A, at identical hot and cold side temperatures. In fact, PX-3A only provided 3.9  $W_e$  (PX-5A reached a peak power of 4.2  $W_e$ ), because it had only 5 BASE tubes, while PX-5A had 6. However, the reduced cell diameter, and the shorter BASE tubes in PX-3A, significantly decreased the parasitic radiation and conduction heat losses in the cell, as well as the heat losses through the side wall. Such a decrease in heat losses increased the sodium vapor pressure on the anode side (from 16.0 kPa to 25.2 kPa) and the BASE tubes temperature (from 980 K to 1015 K at the cold end), increasing the conversion efficiency, from 11.8% to 13.0%.

Best performance was that of PX-3A, at the highest hot side temperature of 1173 K (Table 11.4). This cell produced a peak power of 4.6  $W_e$  and a predicted peak efficiency of 14.2 %, at the conditions of the experiment. Since about 6.1 W were lost through the cell wall, a PX-3A cell with an adiabatic side wall could have reached an efficiency above 17.0%, a situation closer to the case of a multi-cell generator. At a hot side temperature of 1173 K, the evaporator temperature was 1050 K, and the BASE tube brazes operated at 1150 K. Such high evaporator temperature could cause the liquid sodium flow in the evaporator wick to be capillary limited, at high cell

currents (see Chapter 6). Also, the high brazes temperature in PX-3A could cause the brazes to fail, if the cell were operated for an extended length of time (months or years). These issues must be addressed when concerned about lifetime operation and cell reliability.

## 11.12 PX-3C CELL DATA ANALYSIS

Structural materials other than stainless steel were used in PX-3C (Table 11.1). This cell design was similar in principle to that of PX-3A, except for the use of nickel for the hot plate, conduction stud, BASE tubes support plate, and evaporator standoff. The sidewall was made of Haynes-25, an alloy with 25% lower thermal conductivity than SS-316. Instead of an internal heat shield, PX-3C had a highly-reflective rhodium (Rh) coating on the inside surface of the cell's sidewall and on the outer surface of the artery SS guide tube, and the evaporator surface was flat. The evaporator standoff of PX-3C was designed to insure a large positive temperature margin,  $\Delta T \sim 50$  K. As a result, this cell did not perform as well as PX-3A, since the cell evaporator ran about 50 K cooler. It is also possible that the rhodium coatings had evaporated after only a few 100 hrs of operation at high temperature, increasing parasitic heat losses through the cell's sidewall.

An extensive test matrix was developed and carried out to qualitatively study the effects of  $T_{hot}$ ,  $T_{cd}$ , and  $R_L$  on the electrical performance of the PX-3C cell. The tests were temporally interrupted since the cryo-pump of the setup was needed for the 4-cell, ground-demo system tests. Up to now, thirteen groups of tests have been performed, with external load resistance in the range  $R_L \sim 0.65 - 4 \Omega$ , hot end temperature,  $T_{hot} \sim 973 - 1123$  K (by 50 K increment), and cold end temperatures,  $T_{cd} \sim 573 - 648$  K (25 K increment).

Some of the processed and analyzed experimental data are shown in Figures 11.31 and 11.32. Preliminary model results were obtained with  $B = 80$  SI,  $R_{cont} = 0.06 \Omega \cdot \text{cm}^2$  and  $R_{leak} = 2.8 \Omega$  for the TiN electrodes and BASE brazes in the cell. The cell wall above the BASE tubes and the liquid return artery were covered with a reflective coating of rhodium, and the effective emissivity of these surfaces was taken as 0.06 in the model. Also, the effective emissivity of the SS mesh condenser was taken as 0.15. APEAM's results in Figures 11.31 – 11.35 were obtained at a fixed condenser temperature,  $T_{cd} = 623$  K. As shown in Figures 11.31 and 11.32, the model predicted well the effect of hot side temperature and electric current on the electrical performance of the PX-3C cell. The effect of  $T_{cd}$  on the cell's electric performance, observed in the experiments (see Figures 11.31 and 11.32), however, could not be predicted by the cell model. Based on current physical understanding and the model results, one does not expect such large variation in the range of  $T_{cd}$  investigated.

Examination of initial test data suggested strong degradation of the cell performance. However, when the test matrix was run again, but in a different sequence, performance levels higher than previously were obtained, showing that the cell did not experience irreversible degradation. These results suggest that the variation in measured cell's electrical power output and voltage was not due to the change in the condenser temperature in the experiment, but to some other changes occurring in the cell, as the experiments were conducted in a certain sequence.

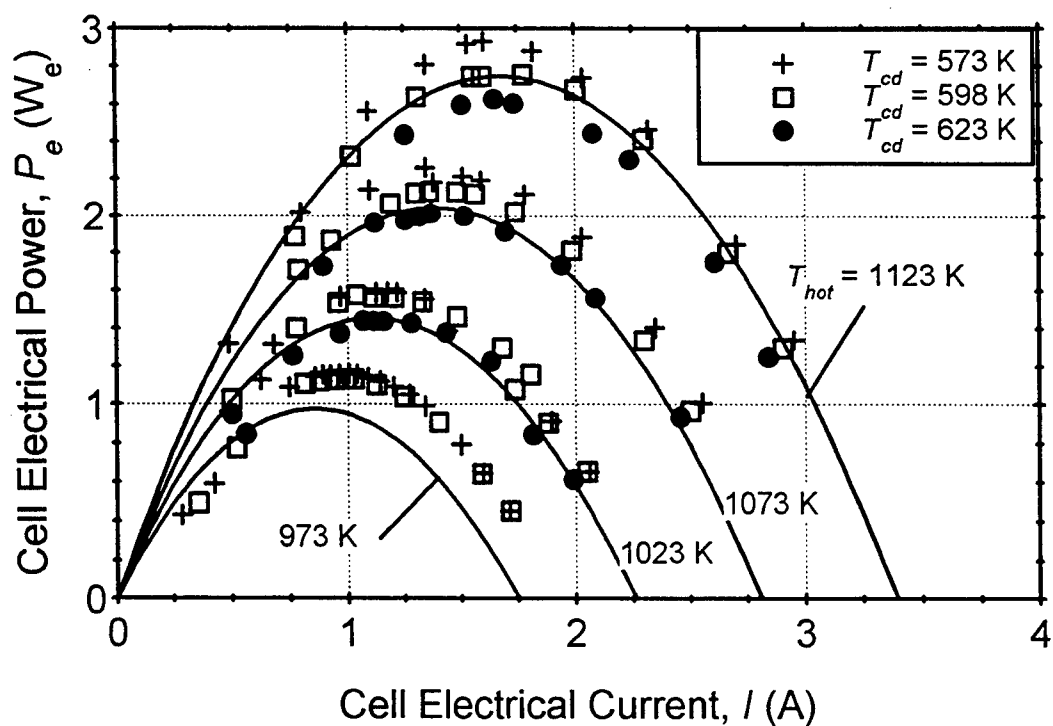


Figure 11.31. Electric Power Output of PX-3C Cell and Comparison with APEAM's Results.

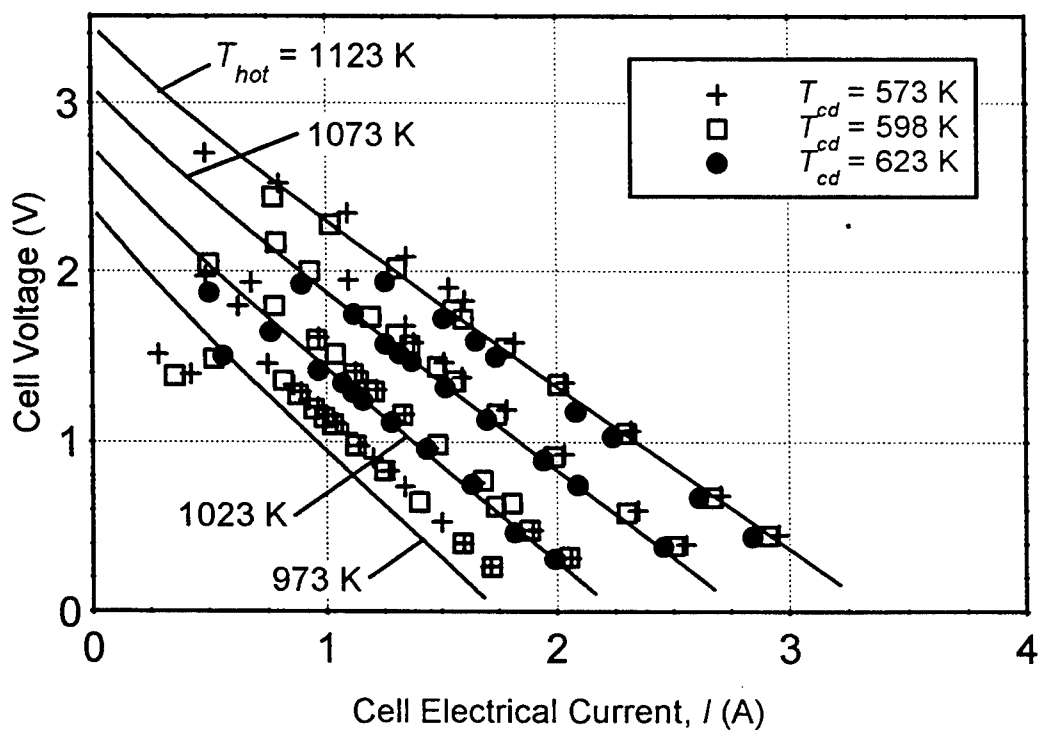


Figure 11.32. Electric Voltage Output of PX-3C Cell and Comparison with APEAM's Results.

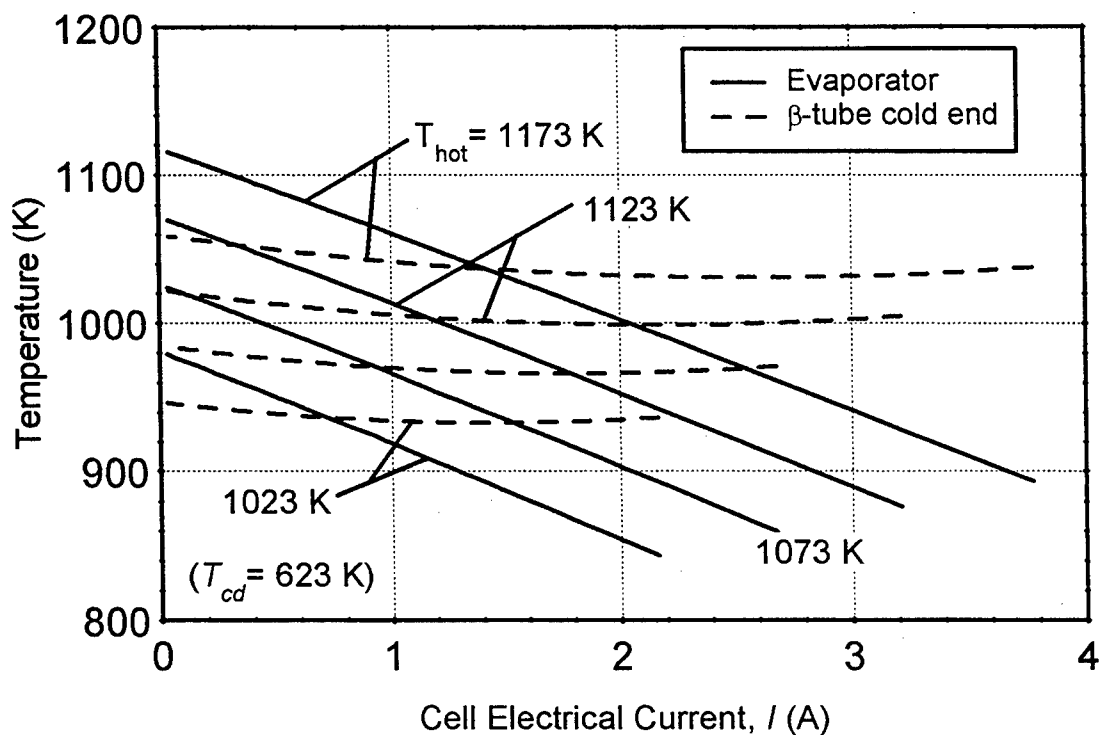


Figure 11.33. Effect of Cell Current on Evaporator and BASE Tube Temperatures in PX-3C.

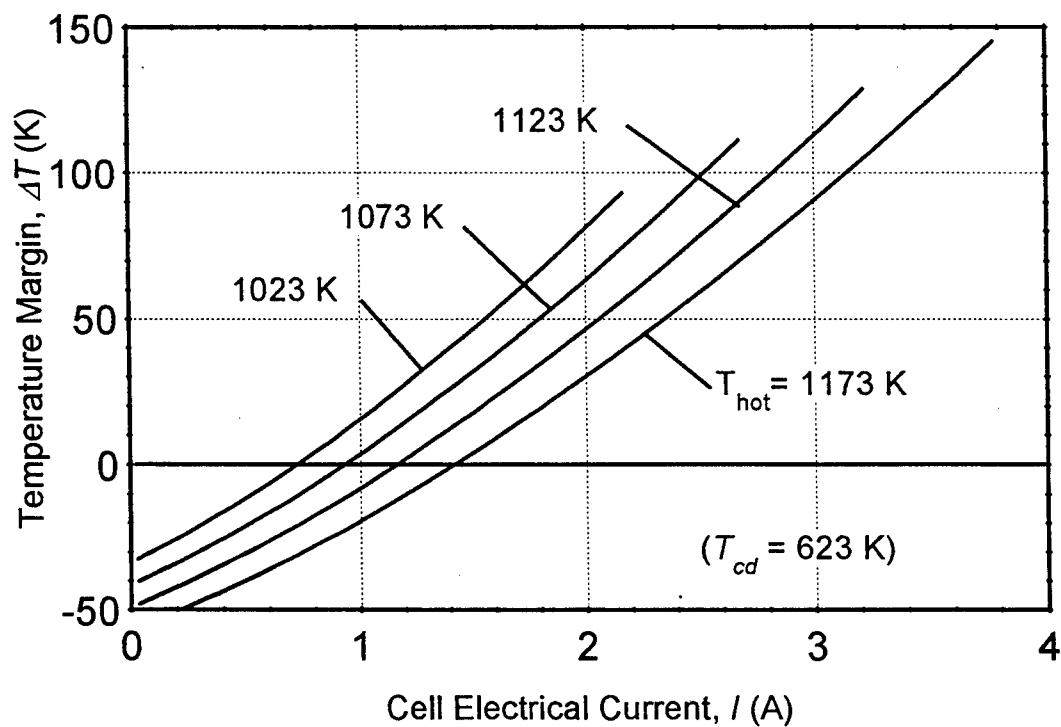


Figure 11.34. Effect of Cell Current on Temperature Margin in PX-3C.



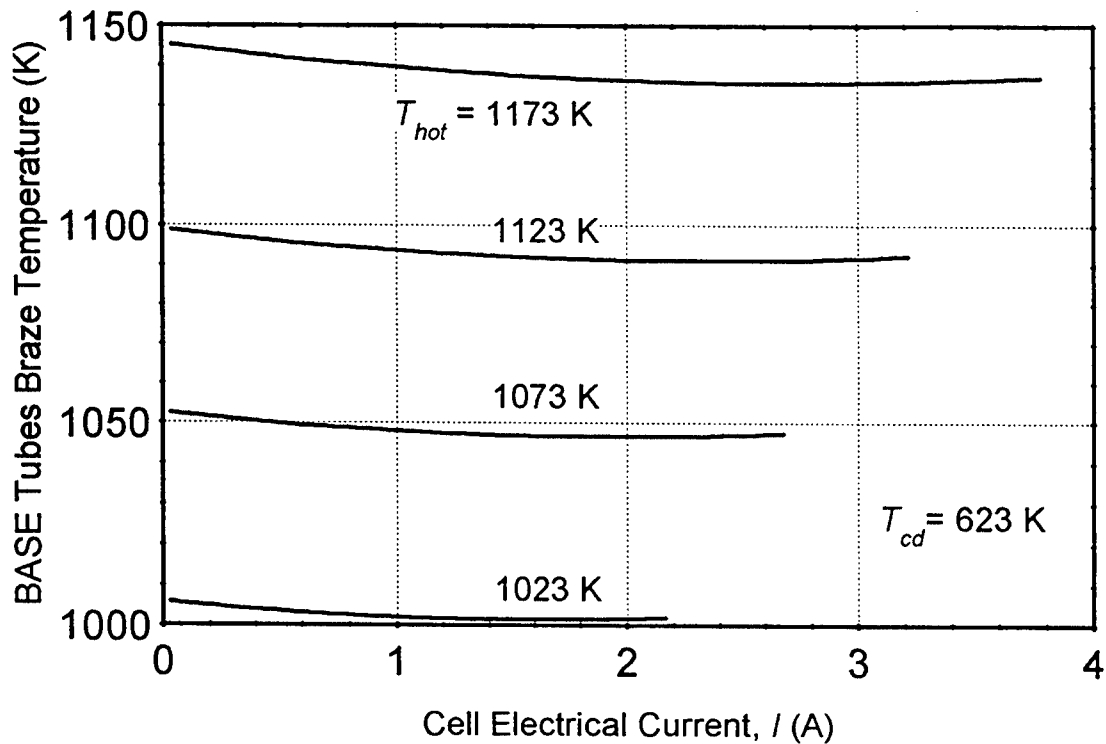


Figure 11.35. Predicted BASE Brazes Temperature in PX-3C Cell.

The cell could not be operated under low current condition for a very long period of time, since the electric output was unstable, a sign of a negative temperature margin in the cell; therefore, the data recorded at high load resistance were not at equilibrium. Deviations of experimental data at low cell current, from expected trend, as evidenced in Figures 11.31 and 11.32, occur in the range of negative temperature margin, as predicted by APEAM (see Figure 11.33 and 11.34).

Predicted BASE brazes temperature in PX-3C are shown in Figure 11.35. The brazes temperature is typically 20 K below that of the cell's hot side, because of the high thermal conductance of the hot nickel structure of the cell.

### 11.13 SUMMARY AND CONCLUSIONS

In this work, a comprehensive steady-state and transient AMTEC Performance and Evaluation Analysis Model (APEAM) was developed to simulate the operation and quantify the performance of next-generation, PX-Series. Vapor anode multi-tube cells. APEAM incorporated the following coupled submodels: (a) a *vapor pressure loss model*, which predicted free-molecule, transition, and continuum flow regimes on the low-pressure side of the cell; (b) a *cell electrical model*, which allowed the current density to vary axially along the BASE tubes; and (c) a detailed *radiation/conduction heat flow model*, which incorporated the effects of a circumferential heat shield above the BASE tubes, and of a conduction stud between the cell's hot plate and BASE

tubes support plate. An efficient iterative solution procedure was developed to couple the three submodels above.

APEAM's predictions of the performance parameters of PX-2C, PX-4C, PX-5A and PX-3A cells tested in vacuum at AFRL, at different hot side temperatures, were in good agreement with experimental data. These parameters were the load electrical power output, the cell I-V characteristic, the hot and cold end temperatures, the BASE tubes' cold end temperature, and the condenser heat rejection. Such good agreement confirmed the soundness of the modeling approach and the solution procedure used. Results showed that the conical evaporators of the cells provided an anode sodium vapor pressure that was almost independent of current, when the cells were operated at fixed hot and cold end temperatures. The anode sodium vapor pressure increased with cell hot end temperature. Also, cell designs with reduced internal parasitic heat losses provided a higher anode sodium vapor pressure.

Results showed that the use of a Creare condenser in PX-5A, in lieu of the mesh pad condenser of PX-4C, combined with an increased condenser temperature, reduced the parasitic heat losses in the cell, and increased the cell electrical power output and predicted conversion efficiency (from 10.5% to 11.8%). Predicted peak efficiency of PX-3A was 13.0%, at a hot side temperature of 1123 K. This cell efficiency was 1.2 points higher than that predicted for PX-5A at identical hot and cold side temperatures. In fact, PX-3A only provided 3.9  $W_e$  (PX-5A reached a peak power of 4.2  $W_e$ ), because it had only 5 BASE tubes, while PX-5A had 6. However, the reduced diameter of PX-3A, and the shorter BASE tubes in PX-3A, significantly decreased the radiation and conduction parasitic heat losses in the cell, as well as the heat losses through the side wall, increasing the cell conversion efficiency (from 11.8% to 13.0%). Best performance was obtained for PX-3A at a hot side temperature of 1173 K. It reached a peak power of 4.6  $W_e$  and predicted peak efficiency of 14.2 %. About 6.1 W were lost at the cell wall through the Min-K insulation.

In the next chapter, results of recent tests of the PX-3G, multi-cell Pluto/Express electric power generator ground demo are analyzed. The performance parameters of the individual cells are compared to assess potential differences in the components performance and the electrodes properties, as well as quantify potential current leakage through the BASE ceramic-metal brazes.

## 12. ANALYSIS OF TEST RESULTS OF 8-CELL PX-GENERATOR GROUND

In this chapter, the recent vacuum test results of a Pluto/Express electric power generator ground demo are analyzed. The performance parameters of each of the 8 ground demo's vapor anode, multi-tube Alkali-Metal Thermal-to-Electric Conversion (AMTEC) cells, designated PX-3G, are analyzed and compared. The ground demo cells produced a total peak electric power of 27 W<sub>e</sub> at a load voltage of 16 V, when tested at hot and cold side temperatures of 1123 K and 553 K, respectively. The electric power output and terminal voltage of the individual cells, however, differed by as much as 25%, from 2.94 to 3.76 W<sub>e</sub>, and from 1.73 to 2.21 V, respectively. These variations were attributed to differences among the cells in the values of: (a) the contact resistance of the BASE/electrode and of the electrode/current collector; (b) the leakage current between the anode and cathode electrodes through the metal-ceramic braze joint between the BASE tubes and the metal support plate; and (c) the charge-exchange polarization losses. Analysis results suggested the existence of large electrical leakage currents in some of the PX-3G cells. The performance of the PX-3G cells was below that needed for meeting the Pluto/Express mission's electric power requirement.

The experimental setups and data acquisition and test procedures were described in Chapter 8. The measurement uncertainties in the vacuum tests were calculated in Chapter 9 and Appendix E.

### 12.1 NOMENCLATURE

#### English

$B$	Temperature-independent, charge-exchange current coefficient ( $A.K^{1/2}/Pa.m^2$ )
$G$	Dimensionless factor for pressure losses in the cathode electrode
$I$	Cell electrical current (A)
$I_{leak}$	Electrical leakage current per BASE tube (A)
$P_e$	Cell electrical power output (W <sub>e</sub> )
$Q$	Heat flow (W)
$R_{cont}$	Contact resistance between BASE/electrode/current collector ( $\Omega.cm^2$ )
$R_L$	External load resistance per cell ( $\Omega$ )
$R_{leak}$	Leakage resistance of BASE braze joint ( $\Omega$ )
$T$	Temperature (K)

#### Greek

$\Delta T$	Temperature margin (temperature difference between BASE tube's cold end and evaporator)
------------	---

#### Subscript / Superscript

braze	BASE tube metal-to-ceramic braze
-------	----------------------------------

cd	Cell condenser
ev	Wick evaporator
hot	Cell's hot end
in	Input at hot end of cell
loss	Side wall losses

## 12.2 A MULTI-CELL GENERATOR FOR THE PLUTO/EXPRESS MISSION

The vapor anode, multi-tube Alkali-Metal Thermal-to-Electric Converter (AMTEC) cells, fabricated by Advanced Modular Power Systems (AMPS), and tested in vacuum at the Air Force Research Laboratory (AFRL) are being considered for providing electric power on board the NASA's Pluto Express (PX) flyby spacecraft, scheduled for launch early next century. The power requirement for this mission is 130 W<sub>e</sub> at 28 V d.c., at the end of the mission lifetime of 15 years. One PX electric power system proposed by Orbital Sciences Corporation (OSC) consists of a stack of 2 or 3 <sup>238</sup>PuO<sub>2</sub> radioisotope General Purpose Heat Source (GPHS) modules (each provides ~220 W<sub>th</sub> at End Of Mission (EOM)) and 16 AMTEC cells, in two parallel strings (Schock et al. 1997b) (Figure 12.1). Each string consists of 8 vapor anode, multi-tube AMTEC cells connected in series, which must provide about 8.2 W<sub>e</sub> per cell at 3.5 V. The AMTEC cells would operate at approximate hot and cold temperatures of 1200 K and 573 K, respectively (Schock et al. 1997b).

To demonstrate the performance of a typical multi-cell, AMTEC generator for the PX-mission, an 8-cell ground demo, manufactured by AMPS, was recently tested in vacuum at AFRL. In this chapter, the test results of the ground demo are analyzed and the performance of the individual PX-3G cells is compared and analyzed using APEAM. Analysis results are also used to deduce internal loss parameters of the individual cells, as well as extrapolate the performance of the ground demo to a higher hot side temperature that mimics the operating conditions on board of the Pluto/Express spacecraft. Unfortunately, since the only cell temperature measurements provided in the ground demo were those of the hot and cold ends of only one cell, comparisons with model results are limited to the measured current-voltage (I-V) characteristics of the individual cells in the ground demo.

## 12.3 DESCRIPTION OF PX-3G CELLS

Each PX-3G cell has 6 BASE tubes (Figure 12.2) which are connected electrically in series. BASE is a β"-alumina solid electrolyte that has a high sodium ionic conductivity, but negligible electronic conductivity. The BASE electrodes on the anode and cathode sides are made of refractory metal particles (e.g. titanium nitride, TiN), few μm in diameter, that are applied onto the BASE tubes' outer surface by Chemical Vapor Deposition or sputtering techniques. A special

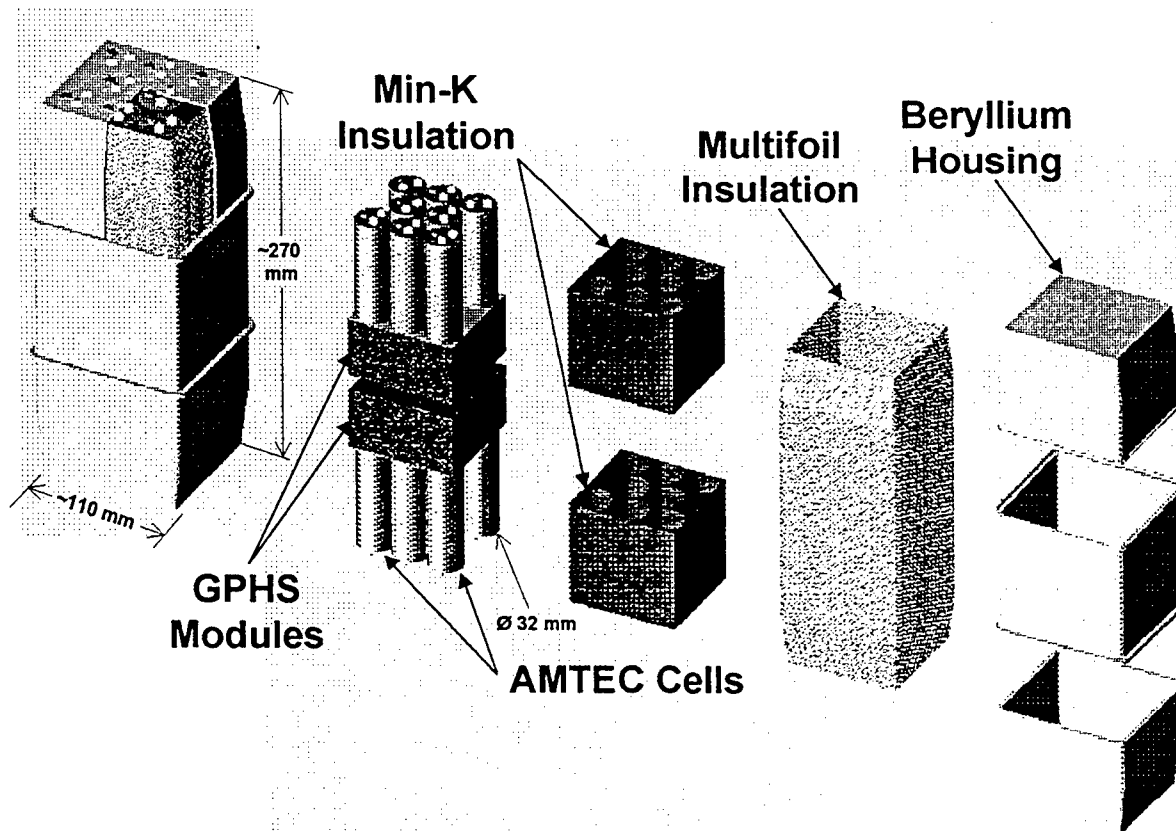
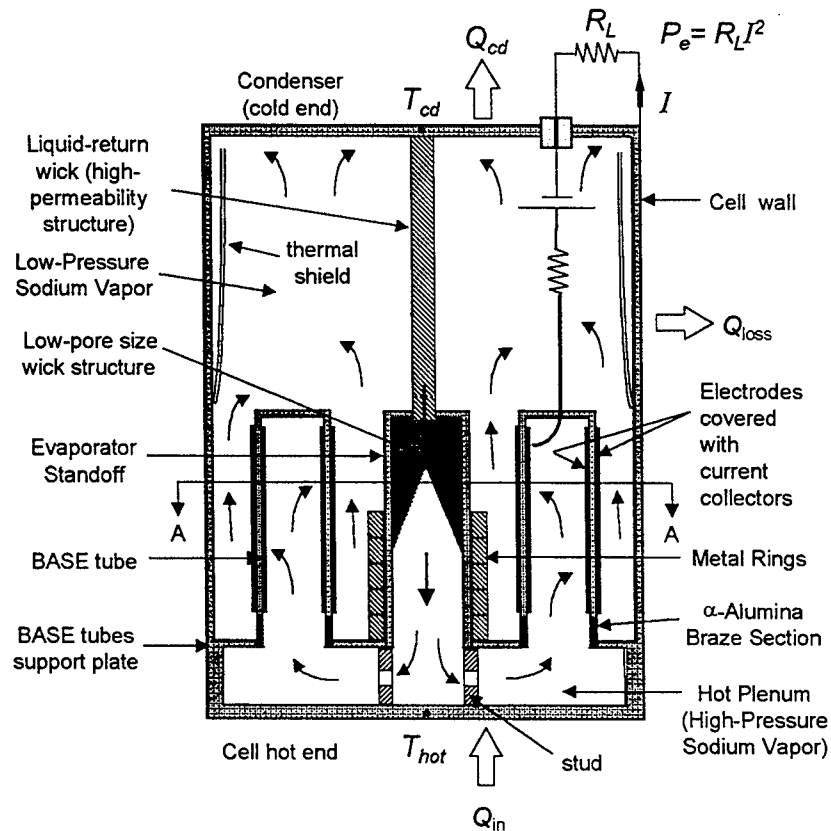


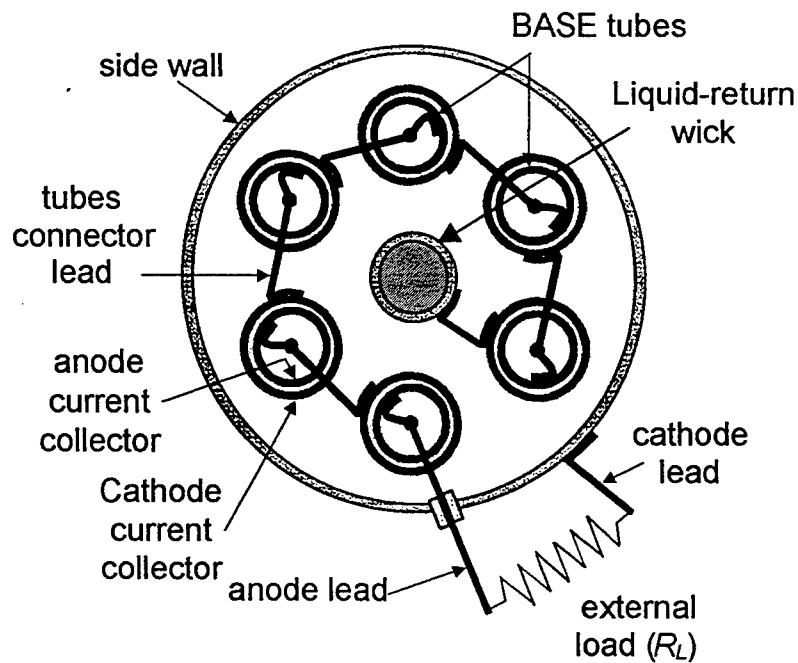
Figure 12.1. Orbital Sciences Corporation's PX-Generator Design, with 2 GPHS Modules Stack and Sixteen AMTEC Cells (Schock et al. 1997b).

(Weber) process is used to paste a (much thicker) TiN electrode on the inside surface of the BASE tube. The anode and cathode porous electrodes ( $\sim 6 \text{ cm}^2$  per BASE tube) are covered with molybdenum mesh current collectors, to minimize internal electrical losses. A high purity  $\alpha$ -alumina section, which is compatible with the sodium working fluid, is used to electrically insulate the BASE tubes from the stainless steel (SS) support plate in the cell (Figure 12.2a). Tantalum and TiNi joints, which have a thermal expansion coefficient close to that of  $\alpha$ -alumina, are used to braze the latter to the SS plate and the BASE tubes. Vacuum tests at AFRL have shown that these TiNi brazed joints performed well at temperatures as high as 1123 K.

The PX-3G cell has a  $100\text{-mm}^2$  solid stud to enhance heat conduction from the cell's hot plate to the evaporator and the BASE tubes. In addition, several nickel rings are placed around the evaporator standoff to further enhance heat conduction to the cell evaporator (Figure 12.2a and Table 12.1). The radiation shield, laid on the inside of the cell wall, above the BASE tubes, reduces parasitic heat losses from the inside of the cell to the wall. Also, the Creare condenser, which has been designed to maintain a continuous thin film of liquid sodium on its surface during operation, effectively reflects thermal radiation toward the interior of the cell, hence reducing parasitic heat losses. Liquid sodium is circulated from the condenser wick to the cell evaporator by the capillary action of the felt-metal wick in the evaporator assembly (Figure 12.2a).



(a) Elevation



(b) Plan View (Section A-A)

Figure 12.2. Cross Sections of PX-3G Cell (Not to Scale).

Table 12.1. Design Parameters of PX-5 Series Cells.

Cell design	PX-5A	PX-5B	PX-3G
Cell diameter (mm)	38.1	38.1	38.1
Cell height (mm)	101.6	101.6	101.6
Evaporator design	DC	SC	SC
Evaporator elevation (mm)	3.81	3.81	3.81
Standoff thickness (mm)	0.71	0.71	0.71
Standoff material	SS	SS	SS
Standoff rings thickness (mm)	2.5	1.25	1.25
Rings material	SS	Ni	Ni
Conduction stud material	SS	SS	SS
Stud cross section area (mm <sup>2</sup> )	100	100	100
Number of BASE tubes	6	6	6
Electrode area / tube (mm <sup>2</sup> )	600	600	600
BASE tube braze material	TiNi	TiNi	TiNi
Current collector	60-mesh Mo	60-mesh Mo	60-mesh Mo
Feedthrough braze	TiCuNi	TiCuNi	TiCuNi
Radiation shield design	Circular	Circular	Circular
Radiation shield material	SS	Ta	SS
Condenser type	Creare	Creare	Creare
Hot side material	SS	SS	SS
Cell wall material	SS	SS	SS
Initial test date	5/1/97	8/14/97	11/4/97
Operation (hrs)	672	3,729	3,000

DC = Deep Cone; SC = Shallow Cone.

Important design parameters of the PX-3G cell and its precursor PX-5 series cells (Sievers et al. 1998) are listed in Table 12.1. The first cell in the PX-5 series, PX-5A, failed shortly after an accidental loss of condenser cooling, causing the BASE tubes temperature to reach ~1136 K, and the tubes brazes to overheat and fail.

PX-5B was similar to PX-5A, except that it had a shallow cone evaporator, a tantalum sidewall shield, nickel rings instead of SS rings along the evaporator standoff, and BASE brazes with improved conductance, using a shorter and thicker  $\alpha$ -alumina insulator (Table 12.1). PX-5B, however, did not perform satisfactorily, due to a very low sodium inventory. PX-3G was essentially identical to PX-5B, except that the tantalum shield was replaced with a SS shield.

Internal electric losses in an AMTEC consist of ohmic losses due to the ionic resistance of the BASE, the contact resistance between BASE/electrodes and electrodes/current collectors, and electrical resistance of the current collectors and connecting leads, and of concentration and charge-exchange polarization losses (see Chapter 4). The latter are characterized by the charge-exchange current  $B$  (A.K<sup>1/2</sup>/Pa.m<sup>2</sup>), which affects the voltage differential developed across the BASE due to the isothermal, electrochemical expansion of Na ions through the BASE. The

polarization losses increase logarithmically with the cell current, reducing the voltage differential developed across the BASE. The concentration losses, or effect of increased sodium vapor pressure at the BASE/cathode electrode interface, increase with cell current (or sodium flow rate) and temperature of the cell's condenser. The pressure drop through the cathode electrode is characterized by a dimensionless factor  $G$ . Both  $B$  and  $G$  are characteristic of the type of electrodes used in the cell and are determined experimentally. Typical mature TiN electrodes have  $B \sim 80 \text{ A.K}^{1/2}/\text{Pa.m}^2$  and  $G \sim 50$  (Ryan et al. 1998a).

## 12.4 DESCRIPTION OF 8-CELL GROUND DEMO

In the multi-cell ground demo (GD) tested at AFRL, the PX-3G cells were connected electrically in series and insulated from each other with fibrous Min-K (Carlson et al. 1998), a lightweight insulation material recommended for operation up to 1350 K, even in load-bearing application. The cell's hot end was conductively coupled to a graphite box that contained a bora-electric heater (Carlson et al. 1998). The heat source and Min-K insulation were surrounded by multifoil insulation with zirconia-particle spacers. The length of the foils was graded to reduce the axial conduction losses in the multifoil, near the cell condenser (Schock et al. 1997b). The GD was enclosed in a black anodized, 7075 aluminum alloy housing, that radiated waste heat away, and the cells were heated electrically in vacuum inside an aluminum shroud cooled with liquid nitrogen. The hot and cold side temperatures of one of the central cells in the GD were measured in the tests. Also, the electric current and the terminal voltage of each cell and of the overall power system were measured. Vacuum tests were performed at fixed hot side and cold side temperatures of 1073 – 1123 K and 523 – 553 K, respectively. The ground demo operated continuously for about 3000 hours before it was shut down.

The interior surface temperature of the cell condenser, that was needed to perform modeling calculations, was higher than that measured in the tests, by the temperature drop across the condenser's wall and wick structure. This temperature drop, including an uncertainty in the measured condenser temperature of  $\sim \pm 0.4\%$ , varied between 10 – 20 K. The uncertainty in the reported hot side temperature was also  $\sim \pm 0.4\%$ , and in the electric power measurements was  $\sim \pm 2\%$ . Experimental results showed that the individual PX-3G cells had I-V characteristics that were similar to those of the individual PX-cells tested earlier. However, the peak electric power output and terminal voltage of the individual PX-3G cells differed by as much as 25%, from 2.94 to 3.76  $\text{W}_e$ , and 1.73 to 2.21 V, respectively.

## 12.5 RESULTS AND ANALYSES

APEAM's predictions have been benchmarked using data generated in the vacuum tests of individual PX-series cells performed at AFRL (see Chapter 11). The model's predictions of the cell electric power output and current-voltage characteristic, condenser heat rejection, as well as of the evaporator and BASE temperatures, when measured, were compared with measurements. Predicted cell electrical voltage and power output, and condenser heat rejection were in good agreement with experimental data of PX-4C, PX-5A and PX-3A cells, tested at fixed hot and cold end temperatures. For all cells, the calculated evaporator and BASE cold end temperatures were



lower than the readings of the thermocouples (TCs) in the tests, by as much as 40 K and 90 K, respectively, in some cases. These differences, which represent ~4% and 9% of measured temperatures, respectively, were due to cumulative uncertainties in the measurements, namely:

- (a) In the high-temperature cavities of the BASE tube and evaporator standoff, the TCs were not shielded, nor were they touching the BASE and the evaporator surfaces.
- (b) The TCs' guide tubes acted as a fin, conducting heat from the hot plate through the guide tube wall and the metal sheath of the TCs to the tip of the TCs, causing the recorded temperatures to be higher than that of the surrounding (Chapter 9).
- (c) In addition, owing to the small thermal inertia of the sodium vapor, a heat loss or gain by convection between TCs guide tubes and sodium vapor in the BASE tube and evaporator cavities, as small as a fraction of a watt, could result in a large swing in the vapor temperature (as much as 50 K) (Chapter 9). It is worth noting, however, that in the high temperature, sodium vapor environment in a typical multi-tube AMTEC cell, where thermal radiation exchange is significant, an uncertainty in the temperature measurements of about  $\pm 5\%$  or less should be acceptable.

APEAM was used to analyze the test data of the individual PX-3G cells. The wall of the AMTEC cell was thermally coupled to the surrounding Min-K insulation through a radiation gap. On average, each PX-3G cell in the ground demo lost  $Q_{loss} \sim 2 W_{th}$  to the surrounding Min-K. These wall losses increased slowly with increasing cell's hot side temperature,  $T_{hot}$ , or cell heat input,  $Q_{in}$ . The parameters identified to have had caused the measured variations in the individual cells' electrical power output and terminal voltage, in an order of decreasing importance, were as follows:

- (a) the average contact resistance between BASE/electrode/current collector ( $R_{cont}$ );
- (b) the leakage current between anode and cathode electrodes through the metal-ceramic braze joint between BASE tubes and SS support plate (characterized by the ohmic resistance,  $R_{leak}$ ); and
- (c) the charge-exchange polarization losses, characterized by the exchange current  $B$ .

The values of  $B$ ,  $R_{cont}$ , and  $R_{leak}$  for the individual cells, deduced from the comparison of the measured and calculated I-V characteristics, at  $T_{hot} = 1073$  K and condenser temperature,  $T_{cd} = 523$  K, are listed in Table 12.2. The deduction of the values of these parameters for each PX-3G cell was possible because of the unique way each affects the I-V characteristic. For example, since ohmic losses increase with cell current, the effect of  $R_{cont}$  is most noticeable in the low voltage region of the I-V characteristic (Figure 12.3a). Higher values of  $R_{cont}$  reduce the peak power and shift it to lower cell current (or higher cell terminal voltage), and vice versa. Conversely, the influence of  $R_{leak}$  is more noticeable in the high voltage region of the I-V characteristic (Figure 12.3b). Lower values of  $R_{leak}$  indicate higher leakage current. Such leakage current lowers the cell's electrical power output, but insignificantly affects the cell current corresponding to the peak electric power. The latter is a clear and accurate indicator of the existence of a leakage current in the cell. The exchange current coefficient,  $B$ , on the other hand, affects the entire I-V characteristic (Figure 12.3c). Higher  $B$  values shift the I-V characteristic to the upper right (i.e. toward higher current and voltage) and vice versa, where the induced shift in the characteristic manifests itself in somewhat parallel lines.

Table 12.2. Performance Parameters of PX-3G Cells Tested at  $T_{hot}=1123$  K and  $T_{cd}=553$  K.

Cell number	Cell rank	Voltage * (V)	$B^{\dagger}$ ( $A.K^{1/2}/Pa.m^2$ )	$R_{cont}^{\dagger}$ ( $\Omega.cm^2$ )	$R_{leak}^{\dagger}$ ( $\Omega$ )
1	1	2.18	75	0.06	3.0
4	2	2.20	75	0.08	6.0
2	3	2.21	75	0.06	4.0
3	4	2.08	72	0.06	2.0
8	5	1.90	68	0.08	1.7
7	6	1.81	68	0.08	1.3
5	7	1.73	64	0.11	1.6
6	8	1.74	64	0.12	1.6
Average cell		1.98	70	0.08	2.0

\* Measured at peak power ( $I = 1.7$  A);  $^{\dagger}$  Calculated with APEAM

Analysis of the GD test data indicated that the 8 PX-3G cells had different values of  $B$  (64 to 75  $A.K^{1/2}/Pa.m^2$ ),  $R_{cont}$  (0.06 to 0.12  $\Omega.cm^2$ ), and  $R_{leak}$  (1.3 to 6.0  $\Omega$ ). The spread in the values of these parameters reflects differences in the assembly and fabrication of the individual cells. The measured and predicted I-V characteristics and electric power outputs of one of the best PX-3G cell in the ground demo (cell #1) are shown in Figures 12.4 and 12.5. The demonstrated agreement of APEAM's predictions with measurements in these figures was for  $B = 75$   $A.K^{1/2}/Pa.m^2$ ,  $R_{cont} = 0.06$   $\Omega.cm^2$ , and  $R_{leak} = 3.0$   $\Omega$  (Table 12.2). Small variations in these parameters did not significantly affect the comparison of the model predictions with measurements, so long as the values of  $B$ ,  $R_{cont}$  and  $R_{leak}$  remained within the narrow ranges of  $\pm 1.0$   $A.K^{1/2}/Pa.m^2$ ,  $\pm 0.004$   $\Omega.cm^2$  and  $\pm 0.07$   $\Omega$ , respectively. At a hot side temperature of 1123 K, this cell delivered a peak electric power of 3.71  $W_e$  at a terminal voltage of 2.06 V.

At the operating conditions expected on board the Pluto/Express spacecraft ( $T_{hot} \sim 1200$  K,  $T_{cd} \sim 573$  K, Schock et al. 1997b), the best performing PX-3G cell, #1 would have operated at BASE braze and evaporator temperatures of 1170 K and 1070 K, respectively, with a low temperature margin (the temperature difference between the cold end of the BASE tubes and the evaporator) of only +3 K, and would have produced 5  $W_e$  at a voltage output of 3 V (Figures 12.4 and 12.5). These values are still significantly lower than those needed for meeting the Pluto/Express mission power requirements in the OSC 16-cell power system configuration (Schock et al. 1997b) (8.2  $W_e$  at 3.5 V, per cell). Therefore, further improvements in cell design, as well as other power system configurations, are needed in order to meet the EOM power requirement for the Pluto/Express spacecraft.

Figure 12.6 compares the calculated and measured load-following characteristics of the PX-3G cell #1. The cell electric power initially increased rapidly with decreasing load demand (or increasing external load resistance,  $R_L$ ), reaching a peak of 3.71  $W_e$  at about 1.2  $\Omega$  when operated at  $T_{hot} = 1123$  K and  $T_{cd} = 553$  K. Beyond this point, the cell electrical power output decreased slowly with decreasing load demand. In Figure 12.6, the portion of the characteristic, to the right of the peak power, is of practical interest because it is where the cell is *load-following*. As shown

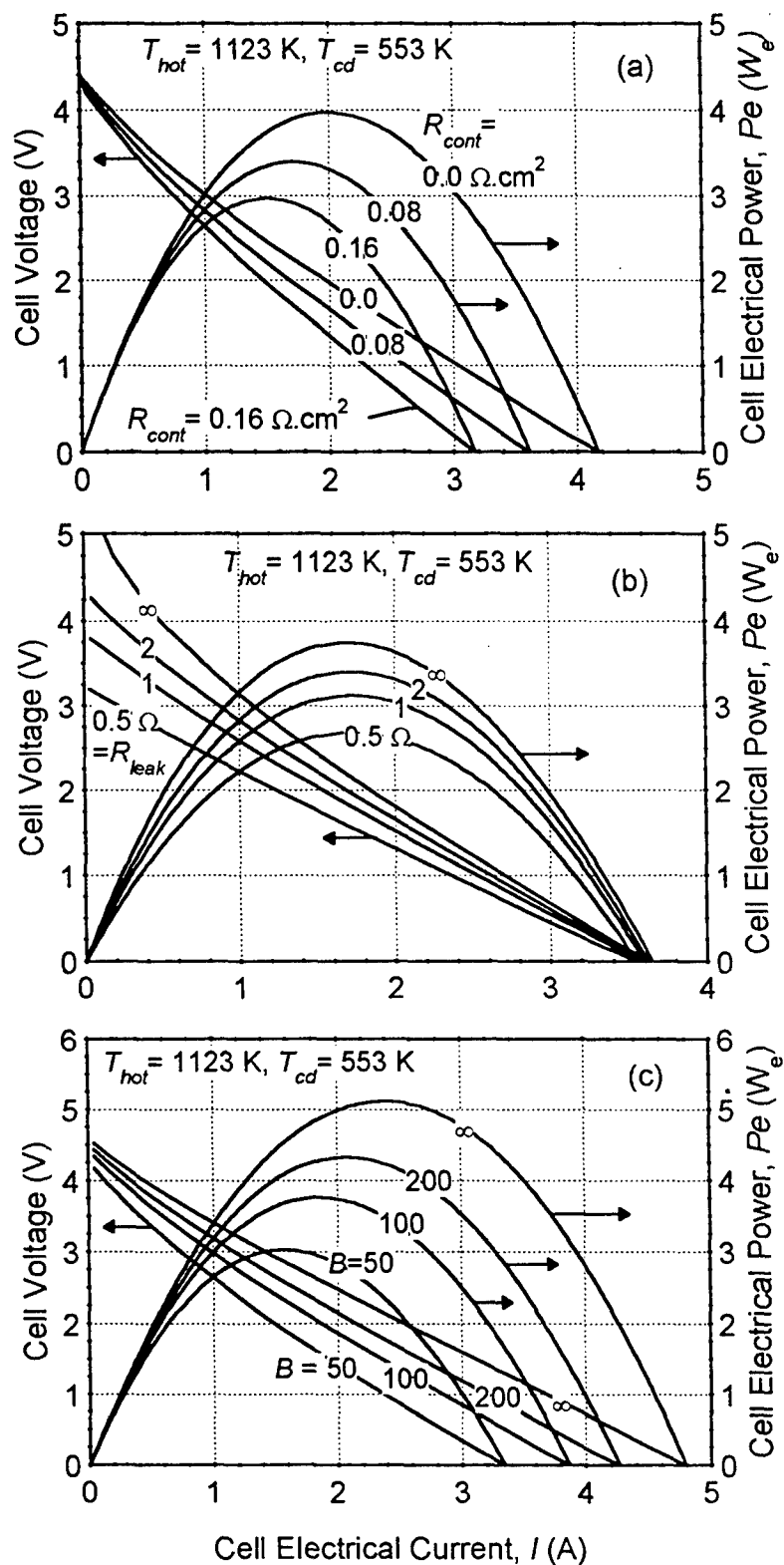


Figure 12.3. Effects of  $R_{cont}$ ,  $R_{leak}$  and  $B$  parameters on I-V Characteristic and Electrical Power Output of PX-3G Cell #1.

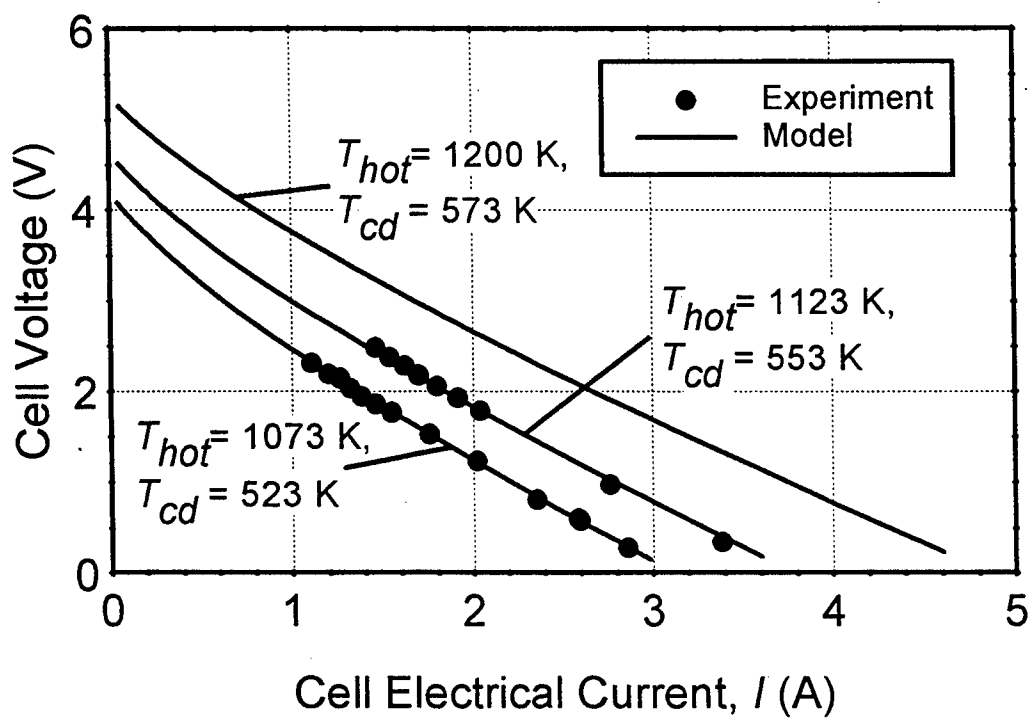


Figure 12.4. I-V Characteristic of PX-3G Cell #1.

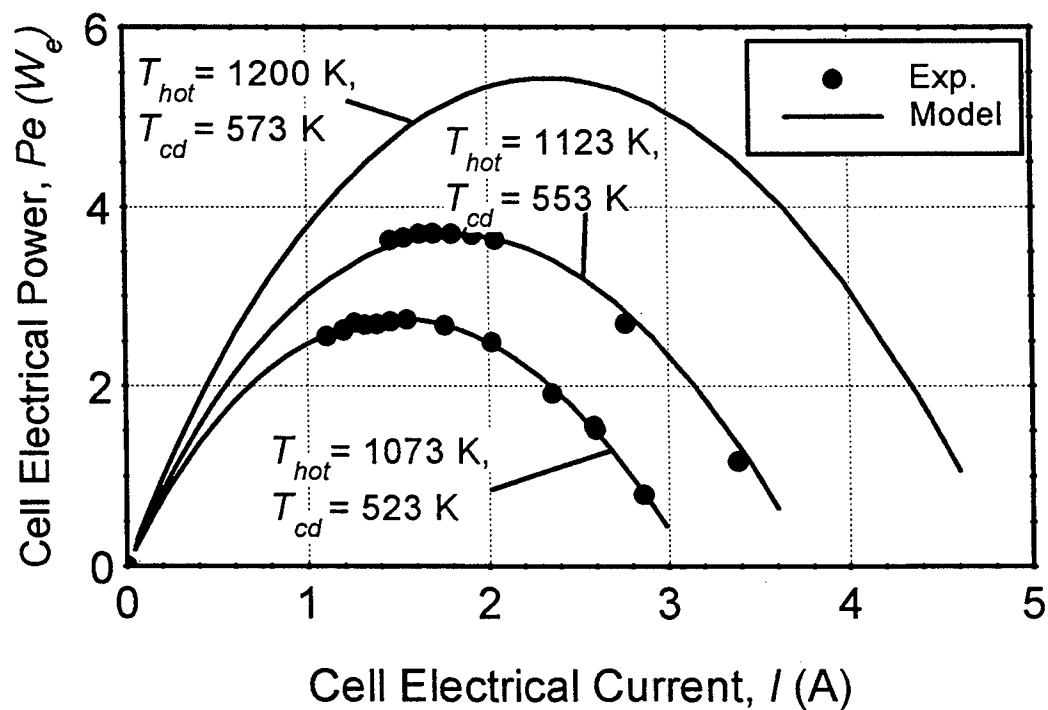


Figure 12.5. Electric Power Output of PX-3G Cell #1.

in Figures 12.4 – 12.6, the cell voltage and output electric power predicted by APEAM matched very well the test data of the PX-3G cells.

At a hot side temperature of 1123 K, the best performing PX-3G cell operated at a higher conversion efficiency (13.1%) than the PX-5A single cell (11.8%), which was of similar design. This is because in the single-cell tests, parasitic heat losses through the cell wall were much larger ( $Q_{loss} \sim 7 W_{th}$  or 20% of the heat input) than in the ground demo tests (averaging only  $\sim 2 W_{th}$  per cell). In the latter, the cells were grouped together and insulated from each other with Min-K, reducing the overall heat losses to the surroundings. The higher conversion efficiency of the PX-3G cells was possible, despite the fact that the condenser temperature was  $\sim 70$  K lower than in the PX-5A single-cell test. Higher cell condenser temperatures could not be achieved in the GD vacuum test because of the very efficient radiative heat transfer between the black, aluminum alloy housing of the GD and the liquid nitrogen-cooled shroud.

The measured and predicted I-V characteristics and electric power outputs of the ground demo are depicted in Figures 12.7 and 12.8. APEAM's predictions compared well with the test data. The total peak electrical power output of the ground demo at  $T_{hot} = 1123$  K and  $T_{cd} = 553$  K was 27 We, at  $I = 1.7$  A (an external load resistance of 9.3  $\Omega$ ) and terminal voltage of 15.9 V. The characteristic parameters of the average PX-3G cell were obtained by fitting the I-V characteristic of the GD, after dividing the output voltage by the number of cells (8). An "average" PX-3G cell would have had  $B = 70 \text{ A.K}^{1/2}/\text{Pa.m}^2$ ,  $R_{cont} = 0.08 \text{ } \Omega.\text{cm}^2$ , and  $R_{leak} = 2.0 \text{ } \Omega$  (Table 12.2).

Analysis results suggested the existence of large electrical leakage currents in some of the PX-3G cells (Table 12.2, Figure 12.3b). Figure 12.9 shows the predicted leakage current  $I_{leak}$  through the metal-ceramic braze in the average PX-3G cell as a function of cell current,  $I$ . At the peak electric power and  $T_{hot} = 1123$  K,  $I = 1.7$  A and  $I_{leak} = 0.17$  A per BASE tube. When the external load resistance,  $R_L$  increased, the cell electric current decreased (Figures 12.4 – 12.6), and the increased voltage drop between the anode and cathode electrodes stimulated larger current leakage through the metal-ceramic braze joint between the BASE tubes and the SS support plate. When  $R_L$  decreased, the cell current increased and the voltage difference between the anode and cathode electrodes decreased, causing  $I_{leak}$  to decrease (Figure 12.9).

The predicted temperatures of the evaporator and cold end of the BASE tube in the average PX-3G cell are shown in Figure 12.10. For a constant hot side temperature, the evaporator temperature decreased linearly with the cell current. This is because the heat needed to vaporize the liquid sodium is proportional to the sodium flow rate (or cell current), and must be conducted up the standoff structure and metal rings to the evaporator (Figure 12.2a). At  $T_{hot} = 1123$  K,  $T_{ev}$  decreased from 1040 K to 960 K as  $I$  increased from 1 A to 2 A (Figure 12.10).

The effect of cell current on the BASE tube's cold end temperature was much less pronounced (Figure 12.10). As a result, the evaporator and BASE tube temperatures became equal when  $I = 1.3$  A. Below 1.3 A, the evaporator temperature was greater than that of the BASE tubes, and the temperature margin  $\Delta T$  (the temperature difference between the cold end of the BASE tubes and the evaporator) became negative. This means that condensation of sodium vapor could occur

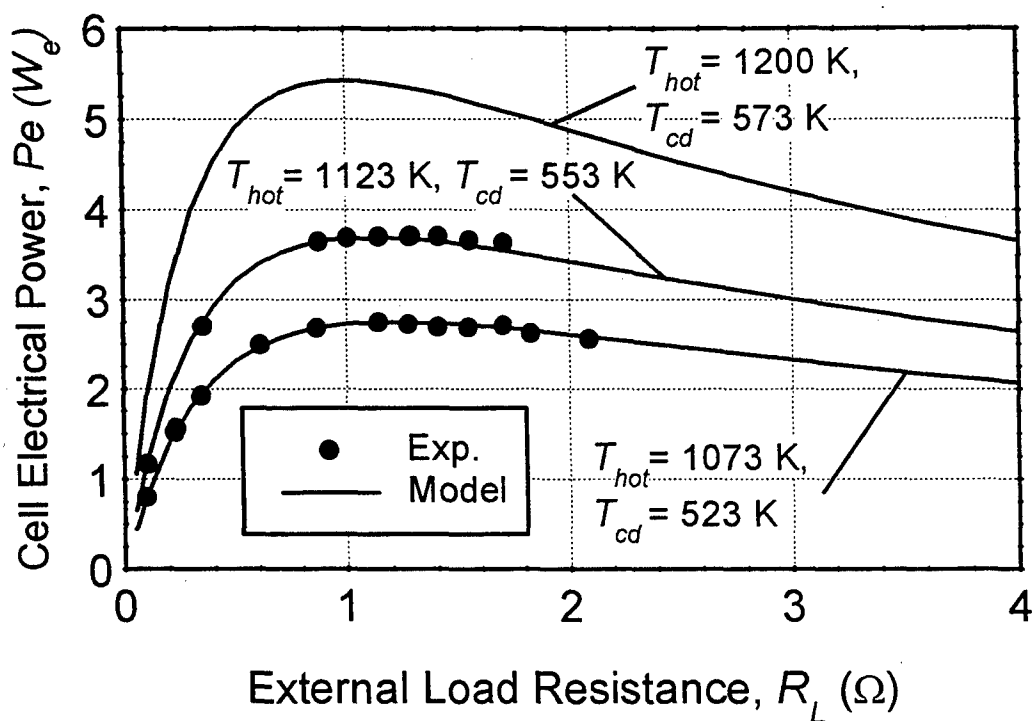


Figure 12.6. Load-Following Characteristic of PX-3G Cell #1.

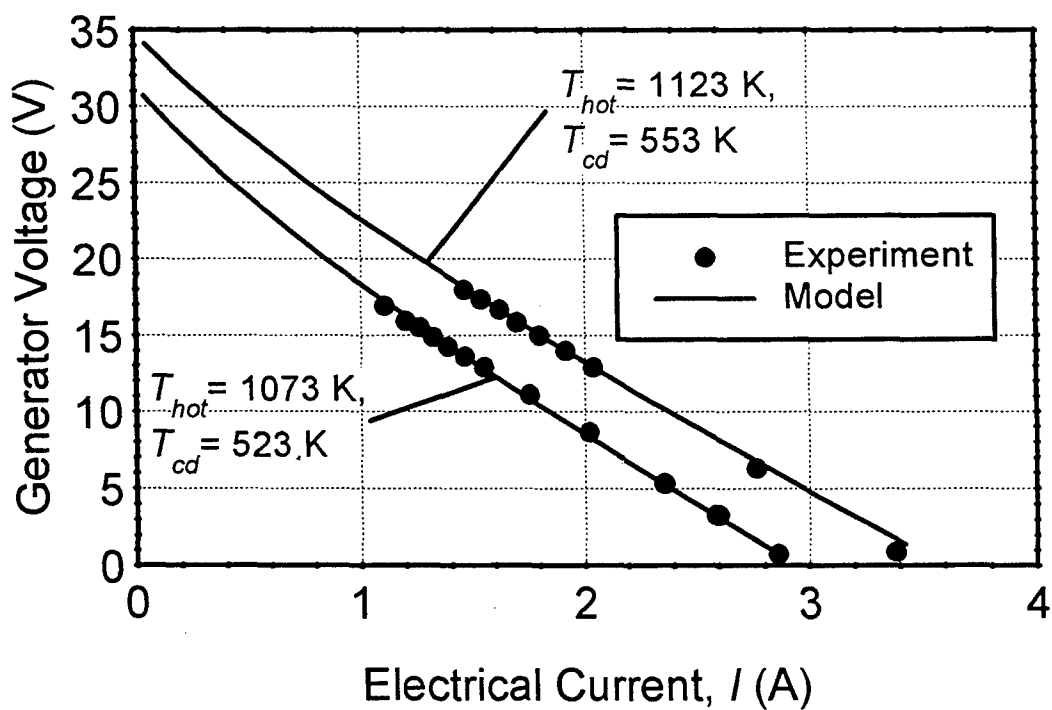


Figure 12.7. I-V Characteristic of Ground Demo.

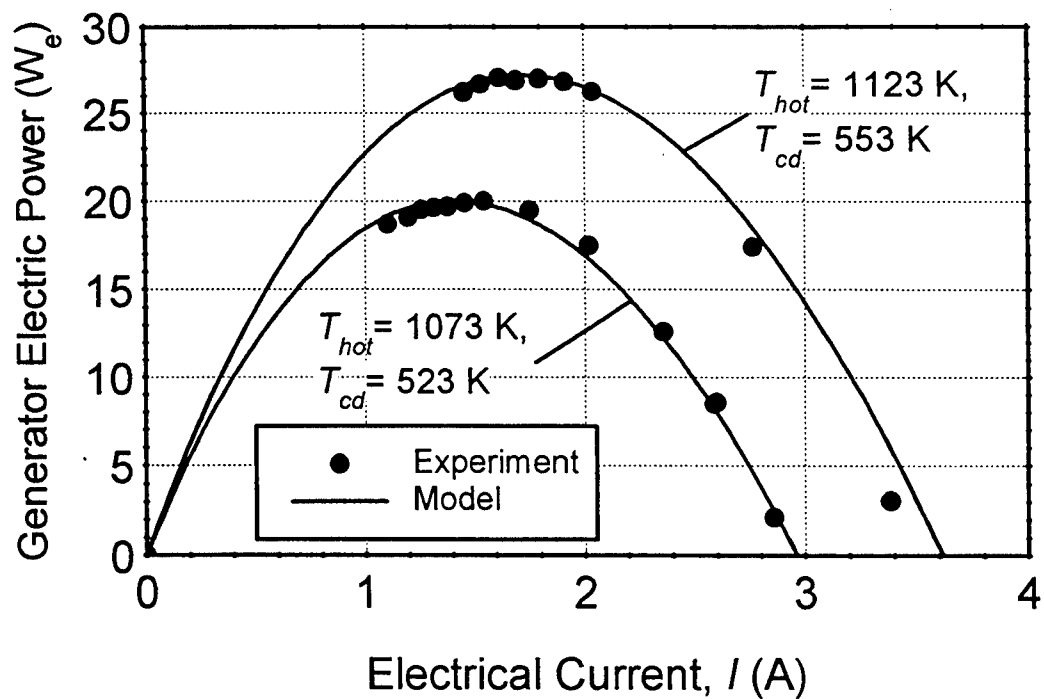


Figure 12.8. Electric Power Output of Ground Demo.

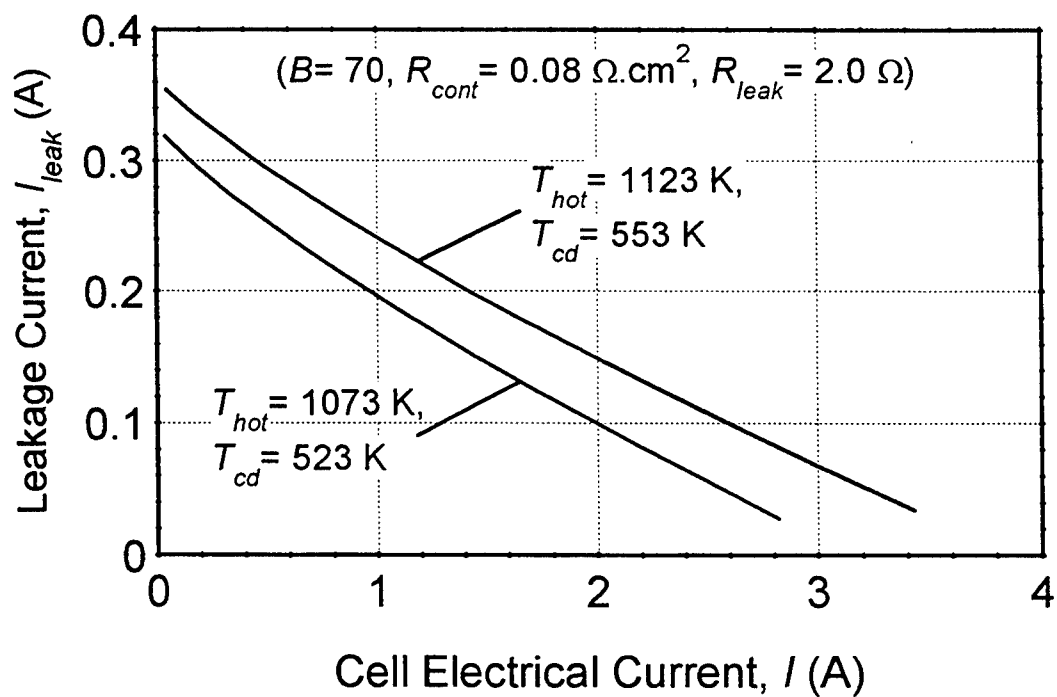


Figure 12.9. Predicted Leakage Current in the Average PX-3G Cell.

inside the BASE tubes. Such condensation would be detrimental to the cell operation, since it could deplete the working fluid circulating in the cell, and may short circuit the BASE tubes in the cell.

Figure 12.11 shows the predicted temperature margin in the average PX-3G cell as functions of cell current and hot side temperature. The cut-off current (0.9 A, 1.3 A and 1.6 A at  $T_{hot} = 1073$  K, 1123 K and 1200 K, respectively) increased with  $T_{hot}$ . In the experiments, care was taken to avoid operating at a negative  $\Delta T$ . As shown in Figures 12.7 and 12.8, the ground demo was operated at  $I > 1.1$  A when  $T_{hot} = 1073$  K, and at  $I > 1.45$  A when  $T_{hot} = 1123$  K. Therefore, according to the present results of the ground demo test, the PX-3G cells operated with a positive temperature margin. It is worth noting that developing accurate methods for measuring the BASE and evaporator temperatures, and also the leakage current through the BASE metal-ceramic braze, would provide needed means to confirm the present results.

## 12.6 SUMMARY AND CONCLUSIONS

Results of recent tests of an 8-cell, AMTEC ground demo, electric power generator were analyzed and the performance parameters of the individual PX-3G cells were analyzed and compared. The ground demo produced a peak electrical power of 27 W<sub>e</sub> at a voltage of 16 V, when tested at hot and cold side temperatures of 1123 K and 553 K, respectively. Test data showed that the electric power outputs and terminal voltages of the individual PX-3G cells differed by as much as 25%, from 2.94 to 3.76 W<sub>e</sub>, and 1.73 to 2.21 V, respectively. These variations in the individual cells' performance parameters were attributed, in an order of decreasing importance, to differences in: (a) the contact resistances between the BASE/metal electrodes and the electrodes/current collectors ( $R_{cont}$ ); (b) the current leakage between anode and cathode electrodes through the metal-ceramic braze joint between BASE tubes and SS support plate ( $R_{leak}$ ); and (c) the charge-exchange polarization losses ( $B$ ). The values of  $B$ ,  $R_{cont}$ , and  $R_{leak}$  for the individual PX-3G cells, deduced from the comparison of measured and calculated I-V characteristics, varied between 64 – 75 A.K<sup>1/2</sup>/Pa.m<sup>2</sup>, 0.06 – 0.12 Ω. cm<sup>2</sup>, and 1.3 – 6.0 Ω, respectively.

Test and modeling results showed that the PX-3G cells of the GD operated at a higher conversion efficiency than the PX-5A single cell, which was of similar design, because of the reduced heat losses from the cell wall in the GD. Model's predictions compared well with measured voltage and electric power output of the individual PX-3G cells. Results suggested the existence of large electrical leakage currents in some of the PX-3G cells, and that the cells operated with a positive temperature margin in the tests. To add further confidence in the present results, there is a need to develop accurate means for measuring the BASE and evaporator temperatures in the tests, for comparison with models' predictions. In addition, detection of the leakage current, if any, through the BASE metal-ceramic brazes, as well as measuring the electrodes charge-exchange polarization losses, would be useful. Without such measurements, it is difficult to benchmark existing cell models and effectively guide future technology effort to design better cells and address potential lifetime issues.



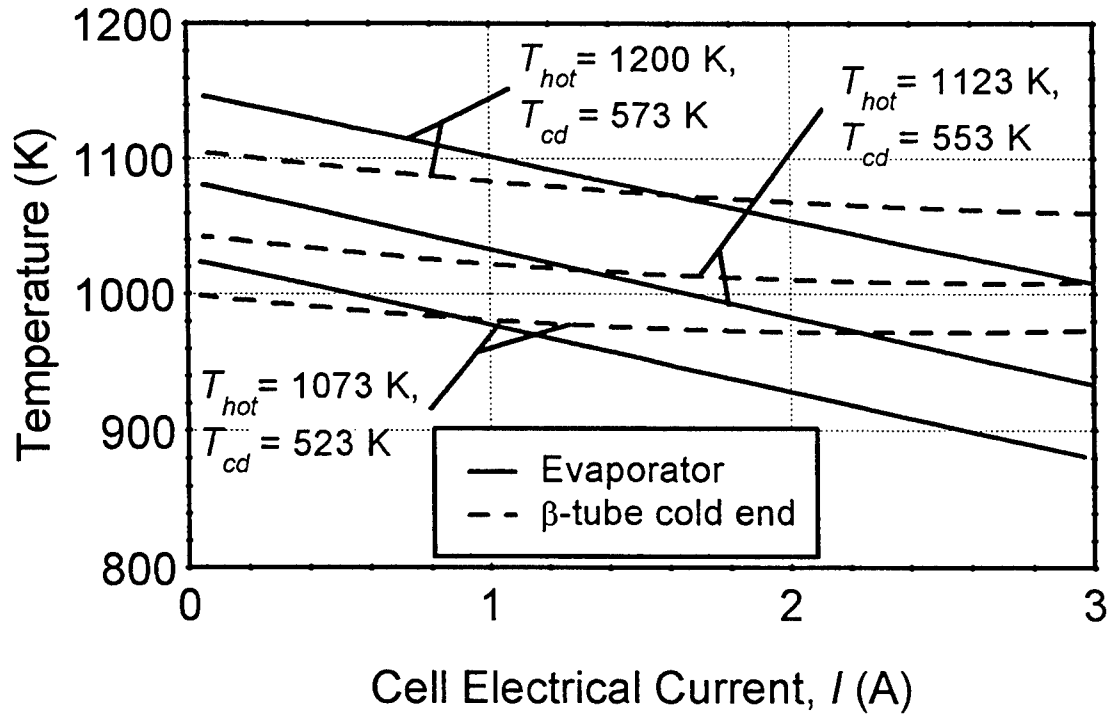


Figure 12.10. Effect of Cell Current on Evaporator and BASE Tube Temperatures in the Average PX-3G Cell.

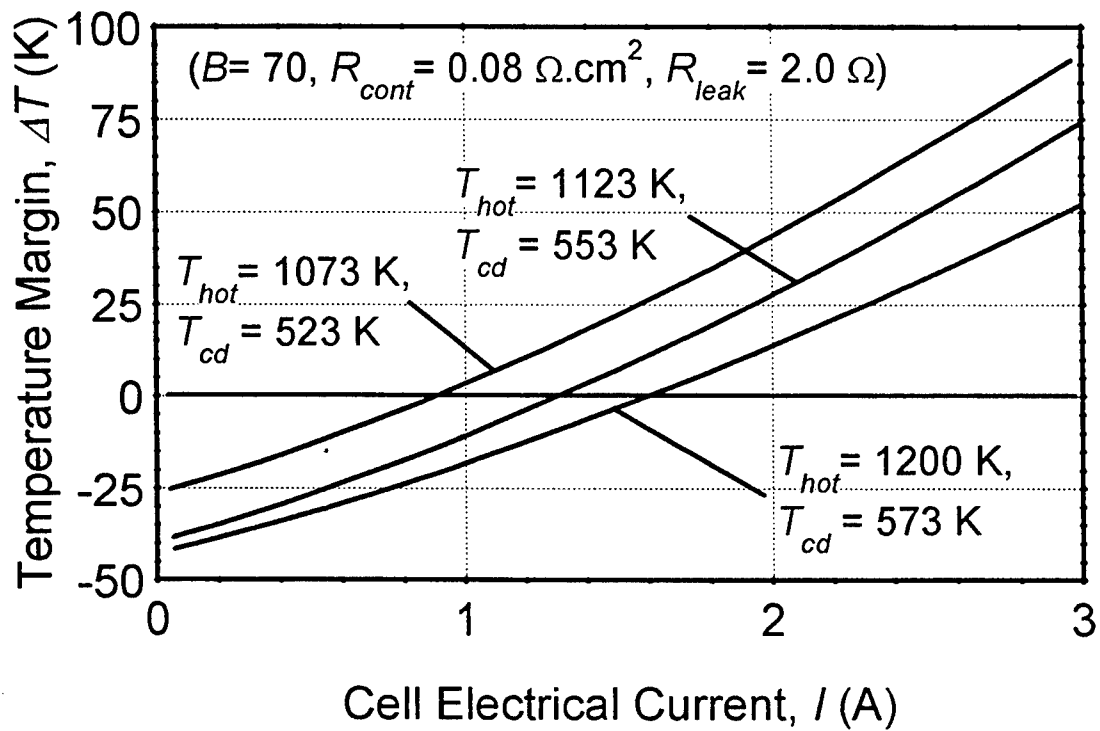


Figure 12.11. Effect of Cell Current on Temperature Margin in the Average PX-3G Cell.

At the operating conditions expected on board the Pluto/Express spacecraft ( $T_{hot} \sim 1200$  K,  $T_{cd} \sim 573$  K), the best performing PX-3G cell #1 would have delivered 5 W<sub>e</sub> at a voltage output of 3 V. These values, however, are still significantly lower than those needed (8.2 W<sub>e</sub> at 3.5 V, per cell) for meeting the Pluto/Express mission power requirements in the OSC 16-cell power system configuration (Figure 12.1) (Schock et al. 1997b). Results suggest that further improvements in cell design, as well as other power system configurations, are needed in order to meet the power requirement for the Pluto/Express spacecraft.

Numerical analyses performed in the next chapter show that increasing the number of BASE tubes from 6 to 7 in the PX-3G cells, and the TiN electrodes length from 25.4 mm to 29.0 mm would increase the electric power output by about 30%. Also, substituting refractory metals such as Ni or Mo for the SS on the hot side of the cell would increase the hot plenum conductance by a factor 2.5 to 5, and the power output by another 20%. An added benefit of using Ni or Mo is their lower emissivity ( $\epsilon = 0.17$  or  $0.08$ ), which reduces the parasitic heat losses. However, brazing the refractory metal structure to a lower thermal conductivity material, such as SS or Haynes-25, could be a technological challenge.

To enhance heat conduction to the cell evaporator, Ni rings could be stacked along the evaporator standoff. However, in order to avoid Na condensation in the BASE tubes, new means for increasing the BASE temperature, such as using corrugated BASE tubes and higher conductance brazes, might be necessary.

The study of the effect of such cell design changes on the cell' performance is described next in Chapter 13.

### 13. PERFORMANCE ANALYSES OF PLUTO/EXPRESS, MULTI-TUBE CELLS

In this chapter, the AMTEC Performance and Evaluation Analysis Model (APEAM) is used to investigate the effects of various design changes on the performance of the PX-series cells. These changes were: (a) using a Creare condenser; (b) changing the number of BASE tubes and the electrode length; (c) using other electrode materials; (d) using molybdenum (Mo) structure on the hot side of the cell; and (e) using reflective rhodium coatings in the low vapor pressure cavity of the cell. Results showed that a stainless steel (SS) structure cell with improved electrodes (50% lower contact resistance than TiN, and an exchange current coefficient =  $200 \text{ A.K}^{1/2}/\text{Pa.m}^2$ ) could deliver 7.1 We at 3.5 V and an efficiency of 19.5%. When Mo was substituted for the SS on the hot side of the cell, the electrical power output increased to 8.8 We and the cell efficiency increased to 20.2%. Using rhodium coatings in the Mo/SS cell increased the electrical power output to 9.7 We and the conversion efficiency to 22.5%.

#### 13.1 NOMENCLATURE

##### English

$B$	Temperature-independent, charge-exchange current coefficient ( $\text{A.K}^{1/2}/\text{Pa.m}^2$ )
$I$	Cell electrical current (A)
$L_E$	Electrode length (m)
$Mo$	Molybdenum
$N_B$	Number of BASE tubes in cell (electrically connected in series)
$Ni$	Nickel
$P_e$	Cell electrical power output (We)
$Q$	Heat flow (W)
$Q_{in}$	Cell heat input (W)
$R_{cont}$	Contact resistance between BASE/electrode/current collector ( $\Omega.\text{cm}^2$ )
$Rh$	Rhodium (reflective coating)
$R_L$	External load resistance per cell ( $\Omega$ )
$SS$	Stainless steel
$T$	Temperature (K)

##### Greek

$\Delta T$	Temperature margin, $\Delta T = T_\beta - T_{ev}$ (K)
$\varepsilon$	Surface radiative emissivity
$\eta$	Cell overall conversion efficiency (%)

## Subscript / Superscript

air	Air calorimeter at condenser end
braze	BASE tube metal-to-ceramic braze
cond	Cell condenser
ev	Wick evaporator
hot	Cell's hot end
in	Input at hot end of cell
loss	Side wall losses
max	Maximum value
plen	Plenum side wall
stud	Conduction stud
wall	Cell's side wall
$\beta$	Cold end of BASE tube

## 13.2 PARAMETRIC ANALYSIS AND DESIGN RECOMMENDATIONS

APEAM was used also to investigate the effects of various design changes, on the electrical power output and conversion efficiency of PX-type, AMTEC cells. The present analyses evaluated the effects on the cell performance of: (a) reducing the heat losses from the cell wall; (b) using a Creare condenser; (c) changing the number of BASE tubes and the length of their electrodes; (d) changing the electrode material; (e) using Mo structure on the hot side of the cell; and (f) using reflective rhodium coatings in the low vapor pressure cavity of the cell. The geometry of the reference cell used in these parametric analyses was identical to that of PX-5A, except that the evaporator wick surface was flat, and located 16 mm above the BASE tubes' support plate. The thickness of the evaporator standoff was adjusted to ensure that a constant temperature margin,  $\Delta T = 50$  K (the temperature difference between the cold end of the BASE tubes and the evaporator) is maintained in the cell. Such a positive (and albeit conservative) temperature margin prevents condensation of sodium vapor inside the BASE tubes, hence avoiding an electrical shortage of the BASE tubes in the cell. The analyses were performed at a constant hot side temperature of 1200 K, to avoid overheating the BASE tubes brazes in the cell, and a constant condenser temperature of 623 K. This condenser temperature is near optimum for AMTEC operation, and is also compatible with the heat rejection of the proposed PX-power system (Schock et al. 1997b). Results of the various design changes investigated in the present analyses are listed in Table 13.1. This table also shows the predicted performance parameters of the cells at the three conditions of interest: (a) peak electrical power output; (b) peak conversion efficiency; and (c) a load voltage of 3.5 V.

### 13.2.1 Effect of Heat Losses through the Cell Wall

Figure 13.1a shows that in the experimental setup at AFRL, about  $8 W_{th}$  were lost through the cell wall, to the Min-K insulation. These heat losses were almost independent of the load

Table 13.1. Predicted Performance of a PX-5A Type Cell due to Various Design Changes  
( $T_{hot} = 1200\text{ K}$ ,  $T_{cond} = 623\text{ K}$ ,  $\Delta T = 50\text{ K}$ ).

Case Number	#1	#2	#3	#4	#5	#6	#7	#8	#9	#10	#11	#12	#13	#14	#15
<b>Cell design:</b>	Mink	foils	adiab	foils	foils	foils	foils	foils	foils	foils	foils	adia.	adia.	adia.	adia.
Side wall insulation	yes	yes	yes	no	yes	yes	yes	yes	yes	yes	yes	yes	yes	yes	yes
CREARE Condenser	6	6	6	6	5	7	7	7	7	7	7	7	7	7	7
Number of $\beta$ -tubes	25.4	25.4	25.4	25.4	25.4	25.4	29.0	29.0	29.0	29.0	29.0	29.0	29.0	29.0	29.0
Electrode length (mm)	0.08	0.08	0.08	0.08	0.08	0.08	0.08	0.04	0.04	0.08	0.08	0.08	0.04	0.04	0.04
$R_{cont}$ ( $\Omega \cdot \text{cm}^2$ )	120	120	120	120	120	120	120	120	200	120	120	120	200	200	200
$B$ ( $\text{A} \cdot \text{K}^{1/2} / \text{Pa} \cdot \text{m}^2$ )	SS	SS	SS	SS	SS	SS	SS	SS	SS	Mo	Mo	SS	SS	Mo	Mo
Hot end material	-	-	-	-	-	-	-	-	-	-	Rh	-	-	-	Rh
Cold cavity coating	-	-	-	-	-	-	-	-	-	-	-	-	-	-	-
<b>(a) Peak power:</b>															
Efficiency, $\eta$ (%)	12.41	14.36	15.28	12.60	13.32	15.11	15.81	16.38	17.06	16.14	17.81	16.61	17.85	17.72	19.30
Power, $Pe^{max}$ (We)	4.96	5.35	5.48	4.93	4.64	5.99	6.80	7.49	8.27	8.23	8.88	6.95	8.45	10.41	11.23
Load, $R_L$ ( $\Omega$ )	0.80	0.80	0.80	0.80	0.65	0.95	0.82	0.73	0.66	0.71	0.70	0.82	0.66	0.51	0.51
Load Voltage (V)	1.99	2.07	2.09	1.99	1.74	2.39	2.36	2.34	2.34	2.42	2.49	2.39	2.36	2.30	2.39
<b>(b) Peak efficiency:</b>															
Efficiency, $\eta^{max}$ (%)	12.88	15.07	16.12	13.09	13.84	15.97	16.92	17.71	18.56	17.46	19.61	17.98	19.62	20.21	22.52
Power, $Pe$ (We)	4.76	5.04	5.13	4.70	4.43	5.58	6.30	6.84	7.45	7.44	7.77	6.35	7.44	9.0	9.24
Load, $R_L$ ( $\Omega$ )	1.26	1.34	1.40	1.28	1.05	1.69	1.55	1.46	1.37	1.42	1.56	1.63	1.48	1.27	1.45
Load Voltage (V)	2.45	2.60	1.91	2.45	2.16	3.07	3.12	3.16	3.19	3.25	3.48	3.22	3.32	3.38	3.66
<b>(c) Load Voltage = 3.5 V:</b>															
Efficiency, $\eta$ (%)	10.0	12.73	14.03	9.93	5.55	15.54	16.58	17.43	18.33	17.32	19.60	17.78	19.49	20.18	22.46
Power, $Pe$ (We)	2.97	3.46	3.65	2.86	1.23	4.98	5.67	6.22	6.84	6.92	7.75	5.89	7.08	8.75	9.72
Load, $R_L$ ( $\Omega$ )	4.12	3.54	3.36	4.28	10.0	2.46	2.16	1.97	1.79	1.77	1.58	2.08	1.73	1.40	1.26

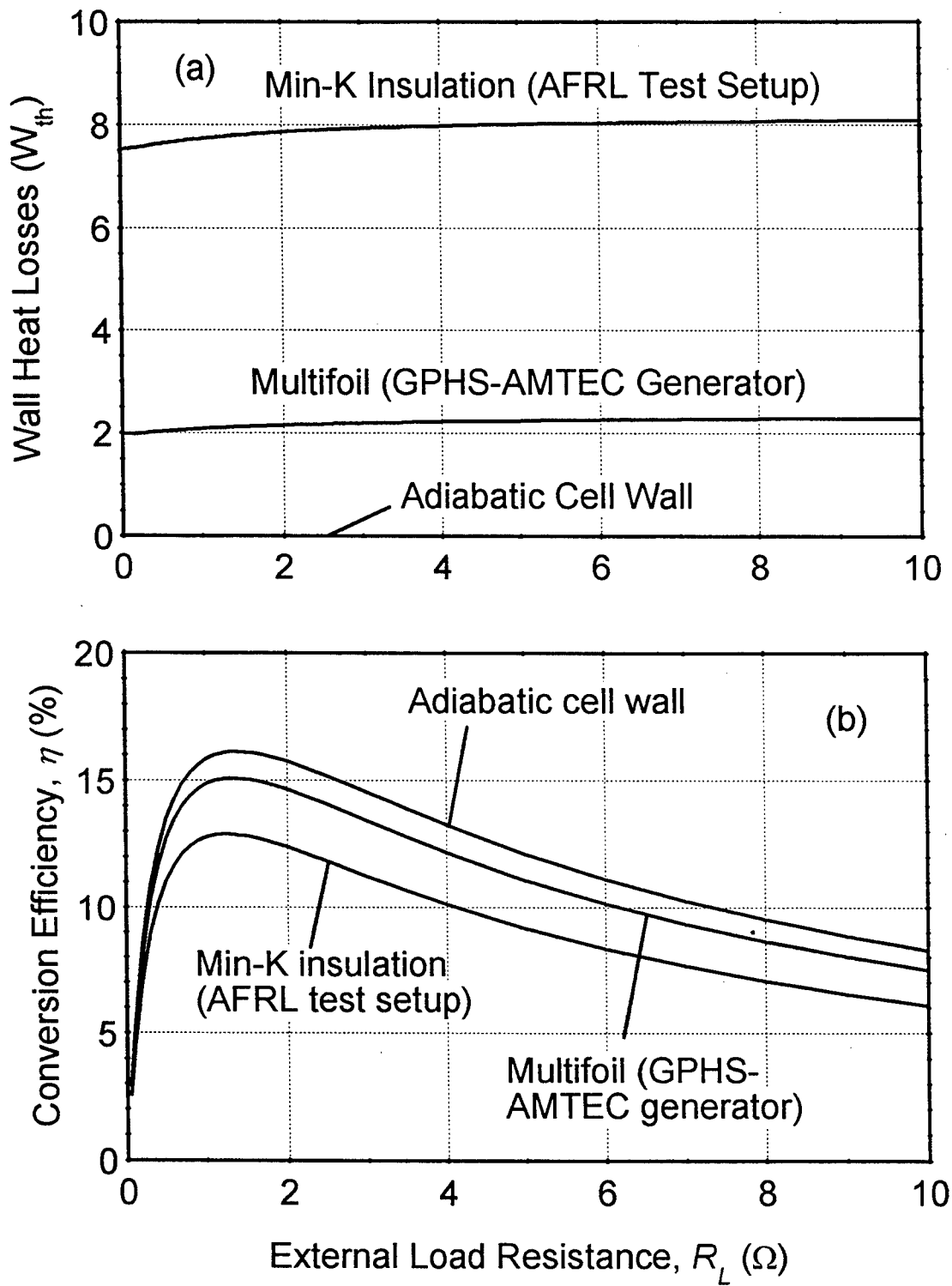


Figure 13.1. Cell Wall Heat Losses and Conversion Efficiency (Cases #1, 2 and 3).

resistance (or the cell electrical current), and amounted to about 20% of the heat input to the cell, when  $R_L = 0.8 \Omega$ . The present cell analyses predicted a peak electrical power of 5.0 We, at a conversion efficiency of 12.4% (Figure 13.1b).

When the cell was assumed to have an adiabatic side wall, the efficiency of the cell increased by 2.9 points, to 15.3% (Table 13.1, cases #1 and 3). The wall heat losses in the GPHS-AMTEC generator for the Pluto/Express mission (Schock et al. 1997b) were predicted to be slightly higher than  $2 W_{th}$ . This case was labelled "multifoil insulation" in Figures 7a and 7b. The reduction in wall heat losses from  $8 W_{th}$  to about  $2 W_{th}$  caused a 2.2 points increase in the peak cell efficiency, from 12.9% to 15.1% (Table 13.1, cases #1 and 2). The following analyses use the "multifoil insulation" operation conditions for the base case.

### 13.2.2 Effect of Condenser Design

The effect of changing the condenser type on the base-case cell performance is shown in Figure 13.2. The stainless steel mesh pad covering the condenser surface was replaced by a Creare type condenser. The latter ensures the formation of a continuous film of liquid sodium on its surface, for high reflectivity. In this design, the smooth stainless steel surface is covered with parallel rounded grooves or drainage holes. Because of the large surface tension of liquid sodium at the low condenser temperatures of interest (less than 650 K), the condenser surface provides a capillary force an order of magnitude larger than the hydrostatic force at earth gravity. This means that the capillary forces are large enough to wet the condenser surface even if gravity resists the fluid motion. The drainage channels connect the condenser surface to the drainage artery below. The size of the drainage grooves vary between 200 and 300  $\mu m$ , requiring a suction pressure of 23 cm of sodium to draw the liquid sodium film into the structure. Experiments performed at Creare Inc. have shown that this new condenser design performed well, as intended (Crowley and Izenson 1993).

The effective emissivity of the Creare condenser surface was taken equal to 0.05 in the model, while that of the SS mesh pad condenser was assumed equal to 0.15. As shown in Figure 13.2, the Creare condenser reduced the parasitic radiation losses to the condenser, thus increasing the BASE tubes and evaporator temperatures. The cell peak electrical power increased by 0.5 We, from 4.9 We to 5.4 We, and the peak cell efficiency increased by 2 points, from 13.1% to 15.1% (Table 13.1, cases #2 and 4). The use of a Creare condenser was retained, in all the subsequent analyses.

### 13.2.3 Effect of Number of BASE Tubes and Length of Electrodes

As shown in Figure 13.3a, the cell internal resistance increased linearly with increasing number of BASE tubes; the BASE tubes in the cell were connected electrically in series. The internal electrical resistance of the cell also decreased with increasing electrode length (Figure 13.3a).

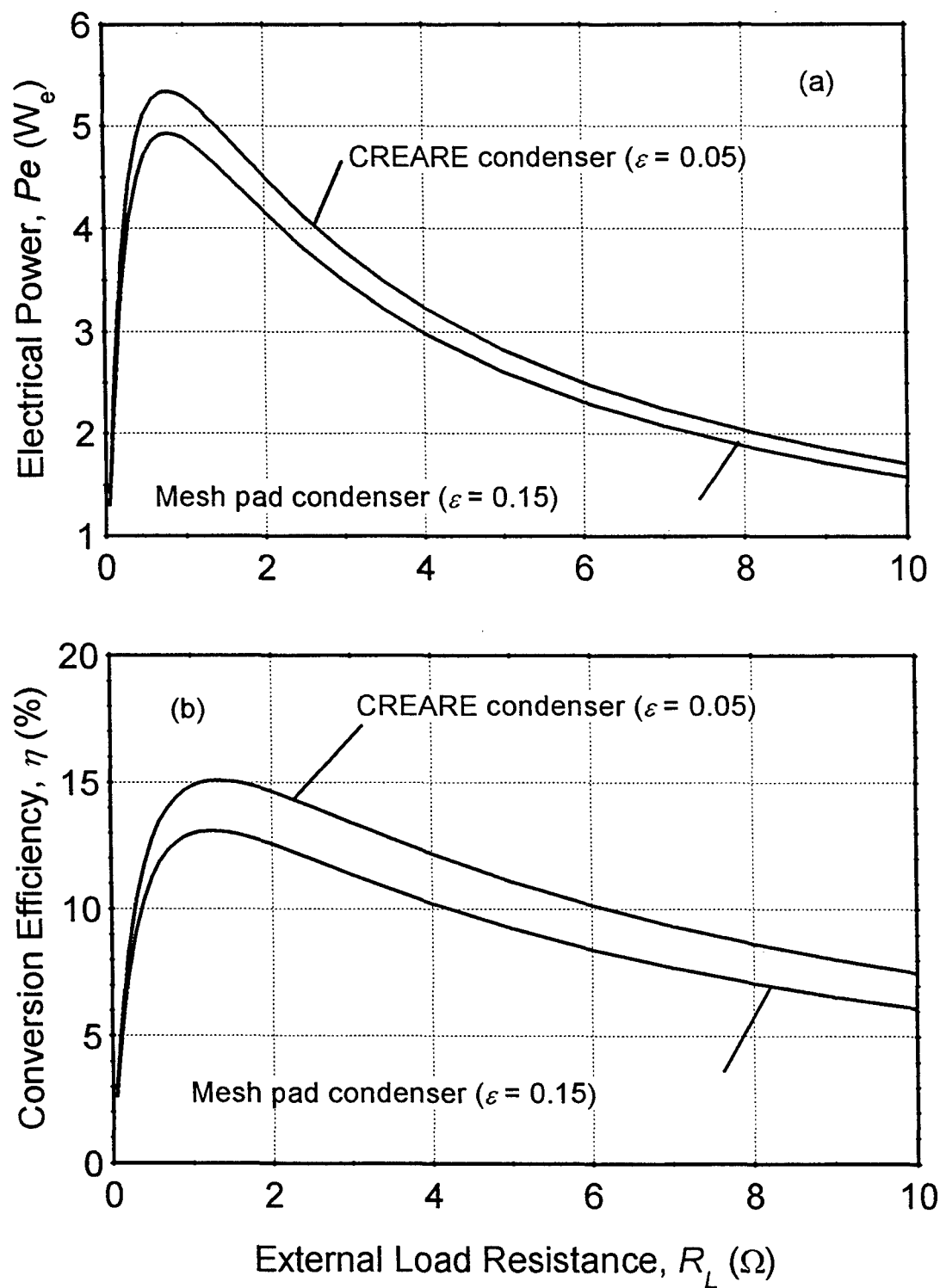


Figure 13.2. Effect of Condenser Type on Cell Electrical Power and Conversion Efficiency (Cases #2 and 4).



The major components of the cell internal resistance are: (a) the ionic resistance of the BASE, which is proportional to the  $\beta''$ -alumina solid electrolyte thickness; and (b) the contact resistances between the BASE and the metallic electrodes, and between the electrodes and the current collectors. The ohmic losses in the 40-mesh, molybdenum electric current collectors on the anode and cathode sides of the BASE tubes were negligible.

Figure 13.3c shows that the cell electrical power output increased with increasing number of BASE tubes. Near the peak electrical power, every BASE tube in the cell provided about 0.9 We (Table 13.1, cases #5, 2, 6 and 7). However, the electrical power output per BASE tube decreased slowly, with increasing number of BASE tubes in the cell. The increase in cell voltage, and the associated increase in the cell electrical current, caused the charge-exchange polarization losses and the concentration losses in the cell to also increase. This is because the sodium vapor pressure at the BASE/cathode interface increased with increasing sodium mass flow rate, or cell current (Figure 13.3b). Also, increasing the number of BASE tubes in the cell increased the radiant heat exchange to the colder surfaces in the cell cavity above the BASE tubes. As a result, increasing the number of BASE tubes increased the internal parasitic losses in the cell, and reduced somewhat the temperatures of the BASE tubes and the evaporator.

Nonetheless, Figure 13.3d shows that the conversion efficiency of the cell still increased with increasing the number of BASE tubes, because the temperature margin in the cell was kept constant, at  $\Delta T = 50$  K. As more BASE tubes were added to the cell, the evaporator standoff thickness was adjusted to keep the temperature margin at 50 K. Model results have also shown that if the evaporator standoff geometry was kept unchanged, the cell conversion efficiency would have been highest with 6 BASE tubes. However, an identical cell with 7 BASE tubes, covered with longer electrodes, could deliver 1 We more, at the same peak efficiency. When the number of BASE tubes was increased, while keeping  $\Delta T$  constant at 50 K, the gain in the cell electrical power output more than compensated for the increase in the cell internal parasitic losses, resulting in a higher cell efficiency.

To improve the electrical power output of an AMTEC cell with 7 BASE tubes, the length of their electrodes was extended from 25.4 mm to 29.0 mm. Such increase in the electrode length is possible with the present 40 mm-long BASE tubes, by reducing the length of the braze section. The braze section can be reduced in height to less than 7 mm, which was done by AMPS in the PX-3A cell. Figure 13.3a shows that extending the electrode length reduced the cell internal resistance from  $0.38 \Omega$  to  $0.34 \Omega$ , and increased the cell current (which varied proportionally with the surface areas of electrodes in the cell), increasing the electrical power output by 0.8 We, from 6 We to 6.8 We. As a result, the peak efficiency of the cell also increased to 16.9% (Figure 13.3d).

Note that the peak electrical power output and the peak cell conversion efficiency shifted to a higher load resistance (lower cell current) as the cell internal electrical losses increased (Figures 13.3c and 13.3d). In summary, a PX-5A-type cell having 7 BASE tubes with 29.0 mm-long TiN electrodes, can provide a peak electrical power output of 6.8 We, at a conversion efficiency of 15.8%, when operated at a hot end temperature of 1200 K. These values represent 1.5 We more

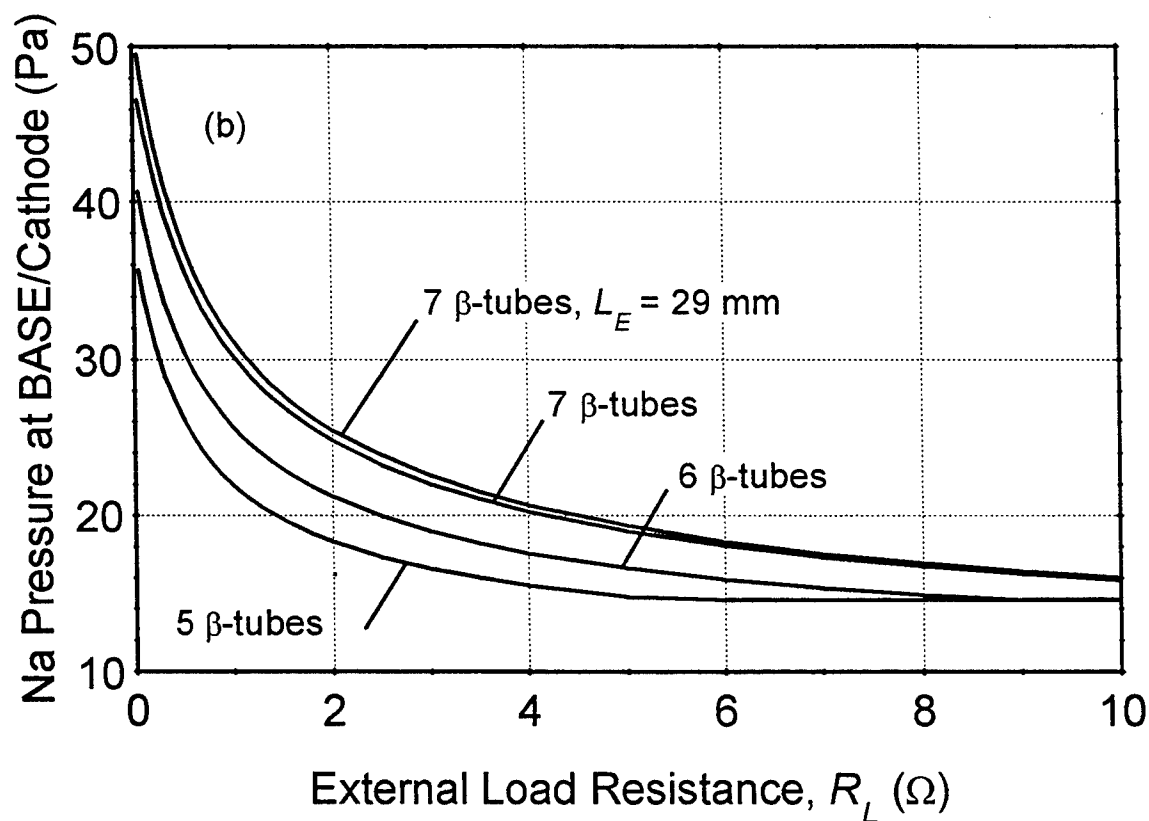
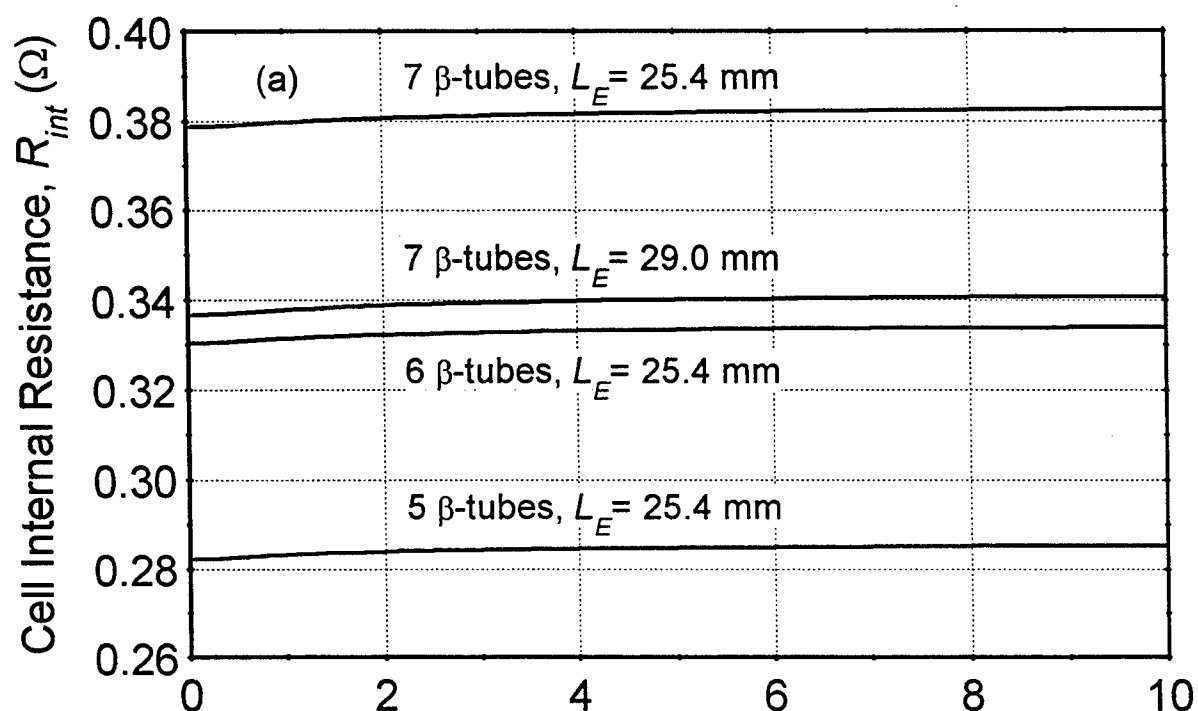


Figure 13.3. Effects of Changing the Number of BASE Tubes and the Electrode Length,  $L_E$ , on Cell Performance (Cases #5, 2, 6 and 7).

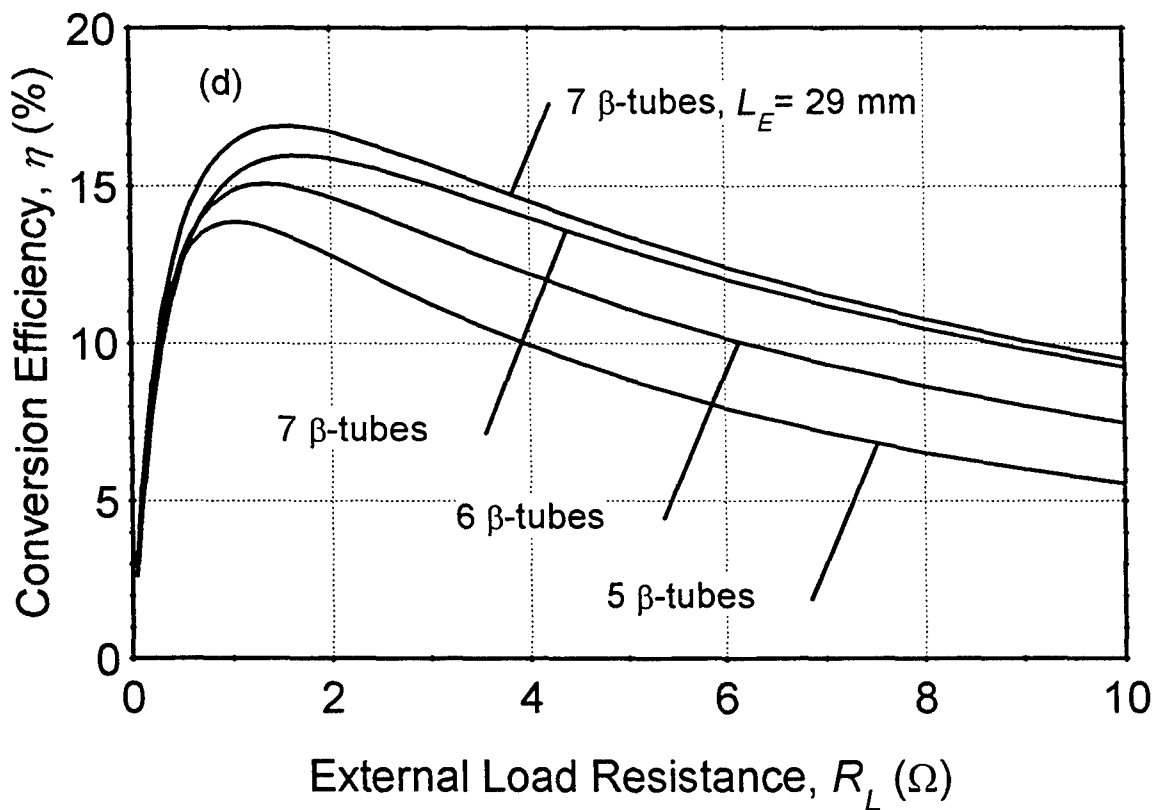
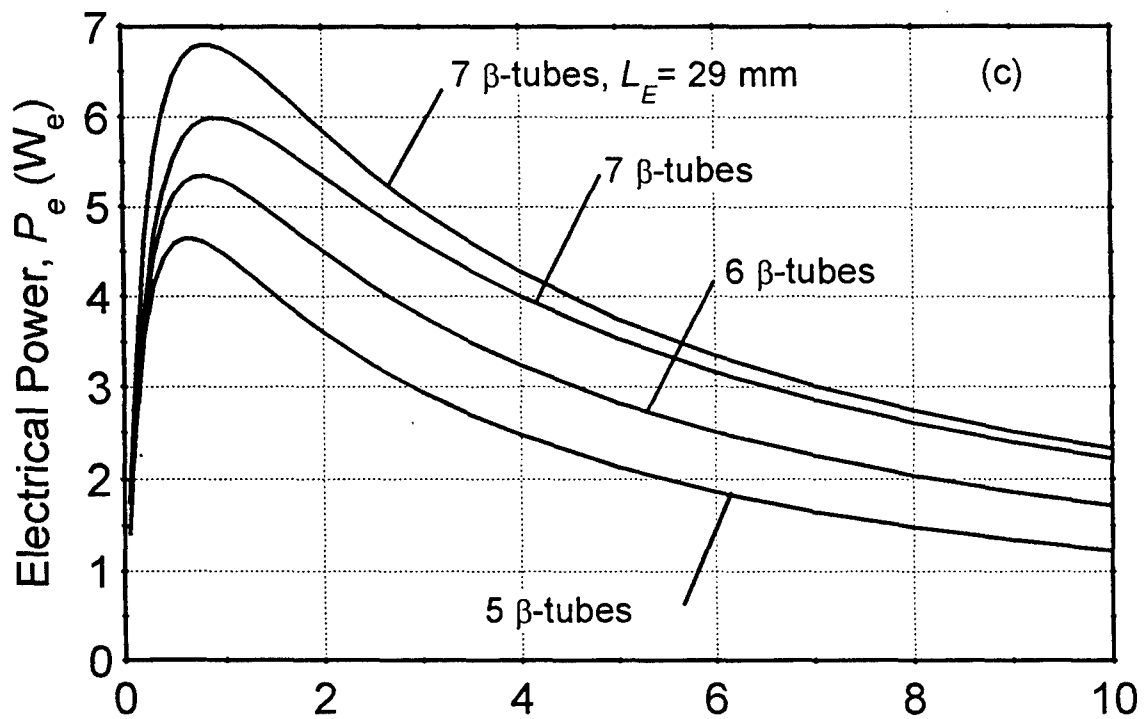


Figure 13.3. Effects of Changing the Number of BASE Tubes and the Electrode Length,  $L_E$ , on Cell Performance (Cases #5, 2, 6 and 7) (*Cont.*).

electrical power and an 1.5 points increase in the conversion efficiency, compared to the actual PX-5A cell, which had 6 BASE tubes with 25.4 mm-long TiN electrodes (Table 13.1, cases #2 and 7).

### 13.2.4 Effect of Electrode Material

AMTEC cells which use TiN electrodes have relatively large internal electrical losses. These electrodes are about 90% porous, their temperature-independent exchange current is relatively low ( $B = 120 \text{ A.K}^{1/2}/\text{Pa.m}^2$ ), and their contact resistance with the BASE and the current collector is relatively large ( $R_{cont} = 0.08 \text{ } \Omega.\text{cm}^2$ ). As a result, the concentration losses in the cell (the effect of sodium vapor pressure at the BASE/cathode interface) are small, when compared to the charge-exchange polarization and internal ohmic losses. A cell with seven, 0.5 mm-thick BASE tubes, and 29.0 mm-long TiN electrodes, would have an internal resistance of  $0.34 \text{ } \Omega$  (Figure 13.3a). It is the sum of the ionic resistance of the BASE,  $0.16 \text{ } \Omega$  (or  $0.14 \text{ } \Omega.\text{cm}^2$ ), and the contact resistances with the electrodes,  $0.18 \text{ } \Omega$  ( $2 \times 0.08 = 0.16 \text{ } \Omega.\text{cm}^2$ ). The latter is about 53% of the total internal resistance in the cell.

Figure 13.4 shows the effect of decreasing the contact resistance on the performance of the cell. A 50% reduction in  $R_{cont}$  (from  $0.08 \text{ } \Omega.\text{cm}^2$  to  $0.04 \text{ } \Omega.\text{cm}^2$ ) reduced the cell internal resistance,  $R_{int}$  by 26% (from  $0.34 \text{ } \Omega$  to  $0.25 \text{ } \Omega$ ), resulting in a 0.7 We increase in the cell peak electrical power (to 7.5 We), and increasing the cell peak efficiency by 0.8 point, to 17.7%. Furthermore, increasing the exchange current, from  $B = 120$  to  $B = 200 \text{ A.K}^{1/2}/\text{Pa.m}^2$ , reduced the polarization losses in the cell, increasing the peak electrical power of the cell by another 0.8 We (to 8.3 We), and the cell peak efficiency by another 0.9 point, to about 18.6% (Table 13.1, cases #8 and 9).

In summary, developing advanced electrode materials, with a lower interfacial contact resistance and a higher exchange current, would markedly improve the AMTEC cell performance. A 50% reduction in  $R_{cont}$ , to  $0.04 \text{ } \Omega.\text{cm}^2$ , or increasing the exchange current from 120 to 200  $\text{A.K}^{1/2}/\text{Pa.m}^2$ , are only moderate changes, that are achievable in the near term (2 to 3 years). For example, oxide-free Mo electrodes have contact resistances  $< 0.015 \text{ } \Omega.\text{cm}^2$ , and  $B > 400 \text{ A.K}^{1/2}/\text{Pa.m}^2$  (Sievers and Bankston 1988). Unfortunately, Mo electrodes degrade quickly when operated at high temperatures. Exchange currents as high as  $200 \text{ A.K}^{1/2}/\text{Pa.m}^2$  have been measured for uncontaminated  $\text{Rh}_2\text{W}$  electrodes at the Jet Propulsion Laboratory (Ryan et al. 1992). In addition to enhancing the cell performance, the electrodes must also be stable at high temperatures, for the expected mission lifetime (10 to 15 years).

### 13.2.5 Effect of Hot-Side Structural Material and High-Reflectivity Coatings

In the vapor anode, multi-tube AMTEC cell, heat is transported from the cell hot end to the BASE tubes and to the evaporator standoff mostly by conduction. Therefore, using a highly conductive Mo structure, instead of SS, on the hot side of the cell (plenum, conduction stud, support plate, the portion of the wall facing the BASE tubes, and the evaporator standoff) would

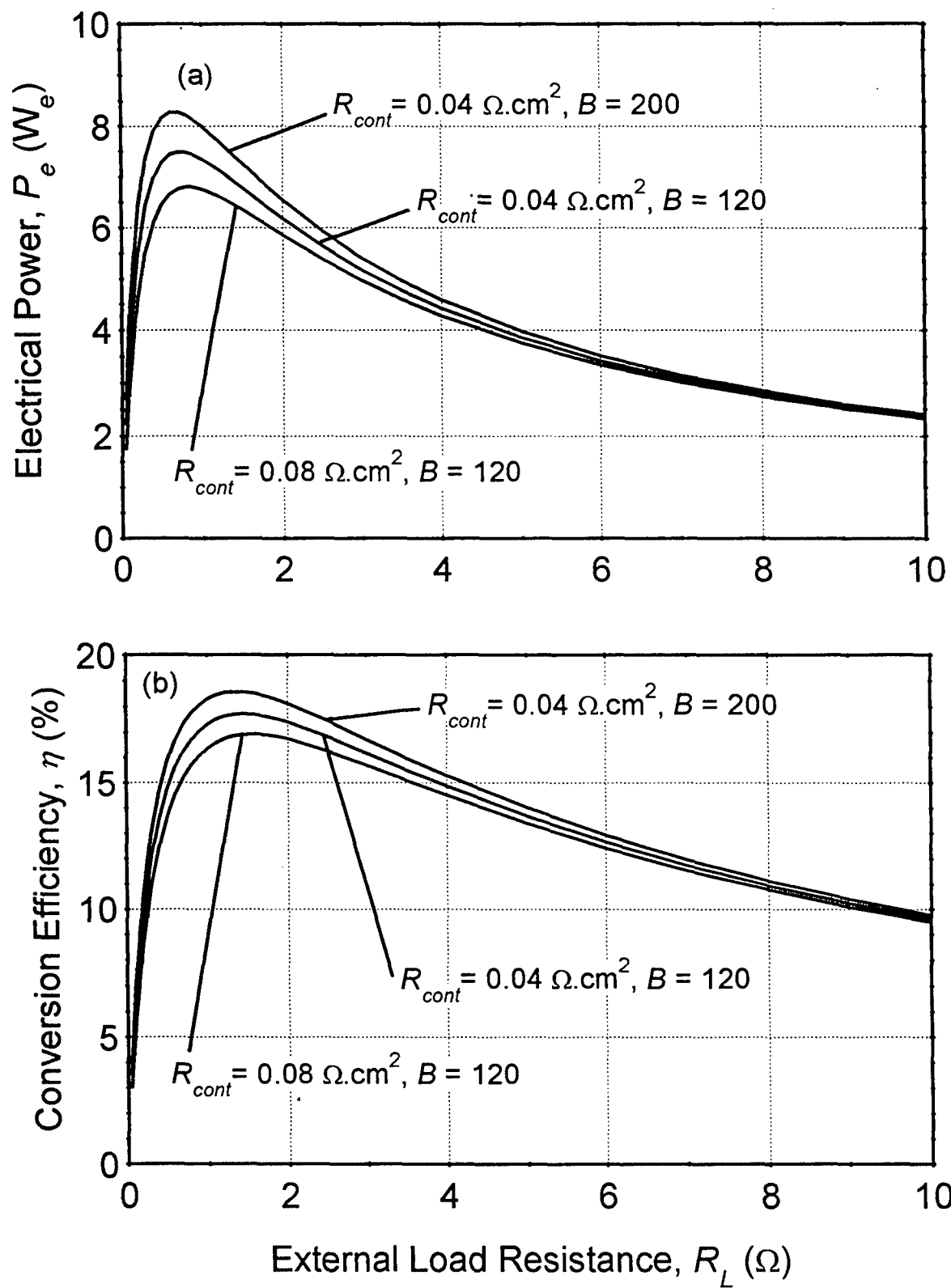


Figure 13.4. Effect of Electrode Material on Cell Performance (Cases #7, 8 and 9).

increase the structure's conductance on the hot side by a factor 3. An added benefit of using Mo is its very low emissivity ( $\varepsilon = 0.07 - 0.12$ , versus  $\varepsilon = 0.25 - 0.30$  for SS), which reduces the parasitic radiation heat losses from the hot support plate, evaporator standoff, and hot cell wall, to the cooler surfaces in the cell cavity, above the BASE tubes.

Figure 13.5 shows the results of substituting Mo for SS as the structure material on the hot side of the cell. The cell peak electrical power increased by 1.4 We (to 8.2 We), while the peak efficiency increased by 0.5 points (to 17.5%). The BASE tubes and evaporator temperatures, as well as the parasitic heat losses in the cell, also increased. The BASE tubes brazes temperature increased by about 10 K, while the BASE tubes cold end temperature increased by about 20 K. Note that it was necessary to reduce the thickness of the evaporator standoff rings in order to keep a 50 K temperature margin in the cell. Results showed that if the evaporator standoff geometry was kept unchanged, the use of Mo on the hot side would result in a larger gain in cell electrical power output; however, the temperature margin would become negative,  $\Delta T = -20$  K. Therefore, the thickness (or cross section area) of the evaporator standoff rings would have to be reduced, in order to maintain an adequate temperature margin in the Mo/SS cell. In summary, the use of Mo on the hot side of the AMTEC cell resulted in significant improvements in the cell performance. The use of Mo on the hot side of the AMTEC cell, however, requires that the Mo hot wall and the Mo evaporator standoff be brazed to a lower thermal conductivity material, such as SS, which is a technological challenge.

When the artery, the internal circumferential heat shield, and the cell wall above the BASE tubes were coated with a high-reflectivity material, such as rhodium ( $\varepsilon = 0.05 - 0.07$ ), the parasitic heat losses in the cell were reduced and the BASE tubes and evaporator temperatures increased, increasing both  $Pe$  and  $\eta$ . Figure 13.5a shows that the use of Rh coatings increased the cell peak electrical power by 0.7 We (from 8.2 We to 8.9 We), and increased the cell peak conversion efficiency (Figure 13.5b) by 2.1 points (Table 13.1, cases #10 and 11). The Mo/SS cell with Rh coatings could deliver 7.8 We at the peak efficiency of 19.6%, at a load voltage of 3.5 V. Note that the performance of this cell narrowly missed the goals of 8 We electric power output with a conversion efficiency above 20%. In conclusion, high-reflectivity coatings could improve the performance of the AMTEC cell, given that these coatings can survive at high temperature in a sodium vapor environment for the entire time of the mission.

### 13.2.6 Improved Performance Parameters of an Adiabatic, PX-Series Cell

In order to evaluate the maximum performance potential of PX-series AMTEC cells, the calculations were performed assuming an adiabatic cell wall, and incorporating all the design changes investigated earlier. Figure 12 shows that a stainless steel structure cell with 7 BASE tubes and 29.0 mm-long electrodes (assuming 50% lower contact resistance than TiN, and a higher exchange current,  $B = 200 \text{ A.K}^{1/2}/\text{Pa.m}^2$ ) would have a peak electrical power of 8.5 We and a peak conversion efficiency of 19.6%, when operated at a hot end temperature of 1200 K. This cell could deliver 7.1 We at an efficiency of 19.5% (close to the peak value), for a load

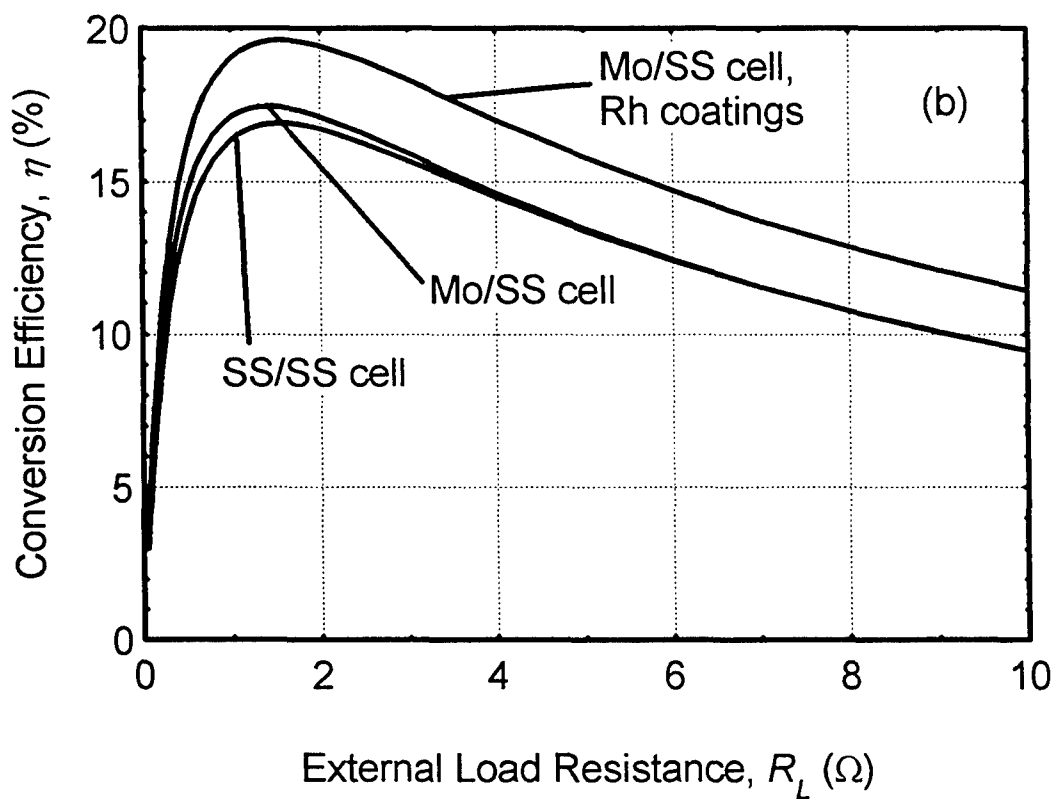
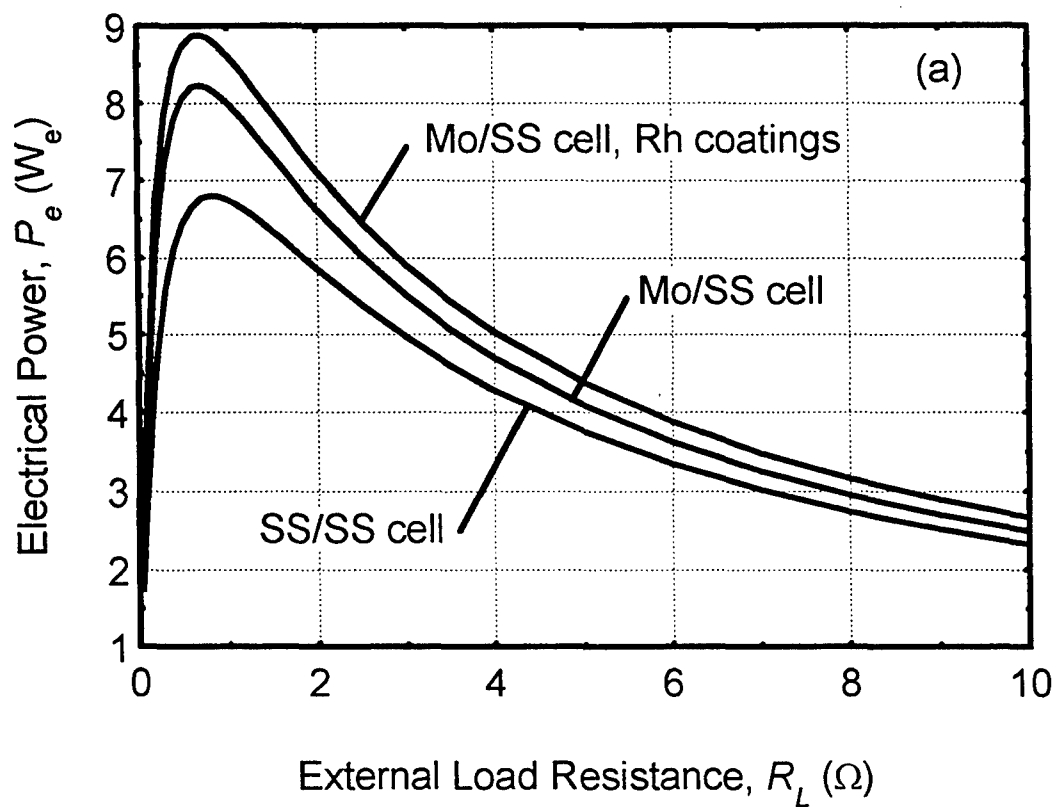


Figure 13.5. Effect of Changing Structure Material and Using High-Reflectivity Coatings on Cell Performance (Cases #7, 10 and 11).

voltage of 3.5 V. When Mo replaces SS on the hot side of the cell, the peak electrical power and peak conversion efficiency increased by 2 We and 0.6 point, to 10.4 We and 20.21%, respectively (Table 13.1, cases #13 and 14). This Mo/SS cell could deliver 8.8 We with an efficiency of 20.18% (very close to the peak value), at the same load voltage of 3.5 V. These results represent a 24% increase in the cell electric power output, and a 3.6 points increase in the cell conversion efficiency.

Figure 13.6 shows that using rhodium coatings in the Mo/SS cell increased the peak electrical power by 0.8 We (from 10.4 We to 11.2 We), and increased the peak conversion efficiency of the cell by 2.3 points, to 22.5% (Table 13.1, cases #14 and 15). The Mo/SS cell with Rh coatings could deliver 9.7 We with an efficiency of 22.5% (close to the peak value), when the load voltage = 3.5 V. Substituting Mo for SS on the hot side increased the BASE tube brazes temperature by 12 K, near the peak conversion efficiency, to about 1170 K, while using rhodium coatings only resulted in an additional 3 K increase in the temperature of the brazes (Figure 13.6d).

### 13.3 SUMMARY AND CONCLUSIONS

In this work, the AMTEC Performance and Evaluation Analysis Model (APEAM) was used to conduct performance and design optimization analyses of Pluto/Express AMTEC cells. The parametric analyses performed in this work evaluated the effects of the following design changes: (a) reducing the heat losses through the cell wall; (b) using a Creare type condenser; (c) changing the number of BASE tubes and the electrode length; (d) changing the electrode material; (e) using Mo structure on the hot side of the cell; and (f) using reflective rhodium coatings in the low vapor pressure cavity of the cell. The analyses were performed at fixed hot and cold end temperatures of 1200 K and 623 K, respectively, and employed a PX-5A type cell design, with a Creare condenser, a Mo circumferential radiation shield, and 7 BASE tubes connected in series, and 29 mm-long TiN electrodes. This cell design could deliver a 3.5-V voltage to the load at a conversion efficiency close to the peak value. The peak efficiency always occurred at a load resistance greater than that corresponding to the peak electrical power output, a suitable operating point in the load-following curve of the cell. A SS structure cell, with negligible heat losses through its wall, and TiN electrodes, would deliver 5.9 We at an efficiency of 17.8%, and a load voltage of 3.5 V.

Results showed that a SS structure cell with improved electrodes (50% lower contact resistance,  $R_{cont}$ , than TiN, and a higher exchange current,  $B = 200 \text{ A.K}^{1/2}/\text{Pa.m}^2$ ) could deliver 7.1 We with an efficiency of 19.5%, at a load resistance and voltage of  $1.73 \Omega$  and 3.5 V, respectively. Current TiN electrodes have  $R_{cont} = 0.08 \Omega.\text{cm}^2$ , and  $B = 120 \text{ A.K}^{1/2}/\text{Pa.m}^2$ . When Mo was substituted for SS on the hot side of this cell, the new cell delivered 8.8 We with an efficiency of 20.2%, at a load resistance of  $1.40 \Omega$  and a load voltage of 3.5 V. The Mo hot wall and evaporator standoff, however, would need to be brazed to the low thermal conductivity material (such as SS) in the colder portion of the cell, which is a technology challenge. Using rhodium coatings in the Mo/SS cell increased the electrical power output of the cell by 1 We, to 9.7 We,



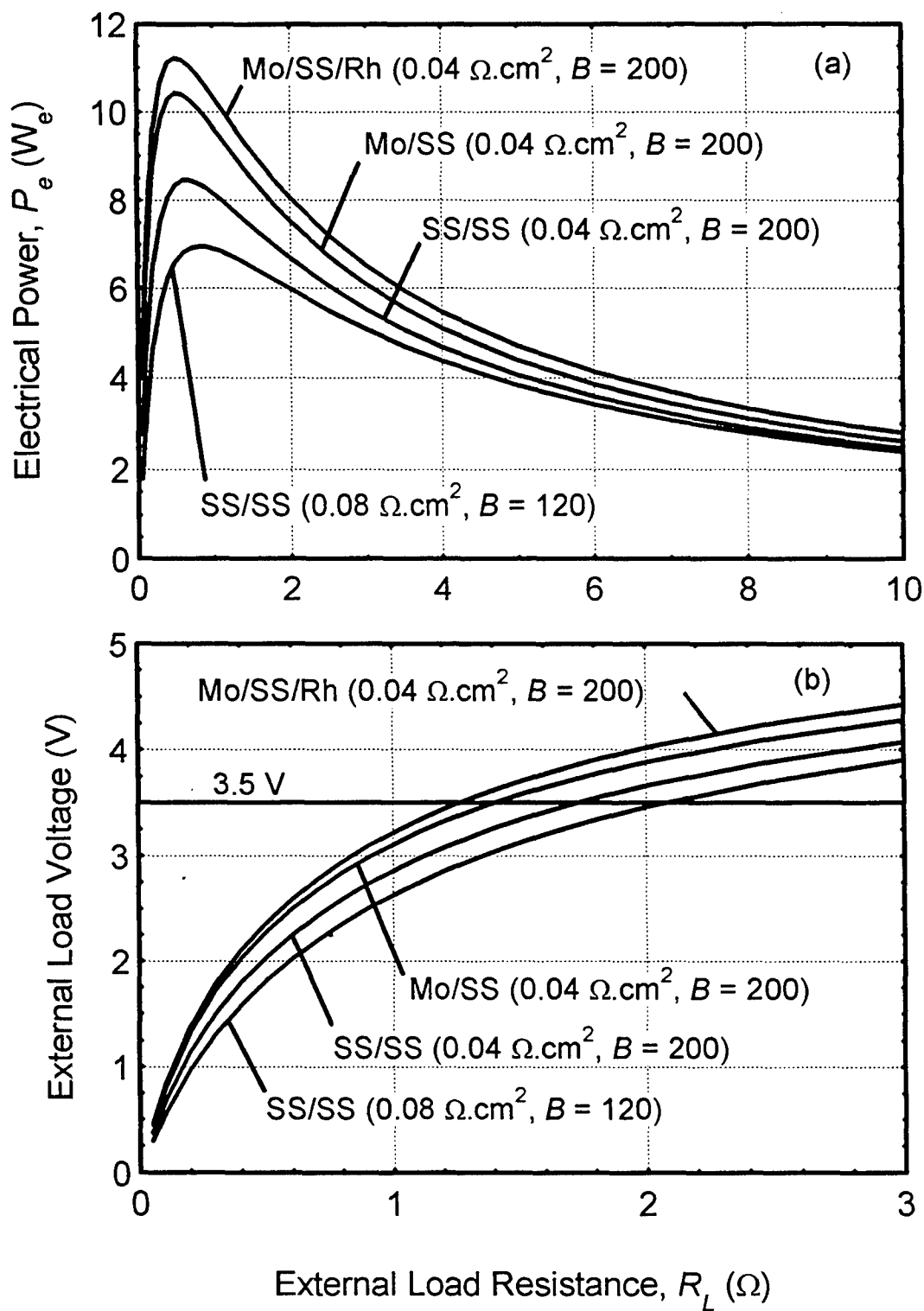


Figure 13.6. Performance of Adiabatic PX-Series AMTEC Cells (Cases #12, 13, 14 and 15).

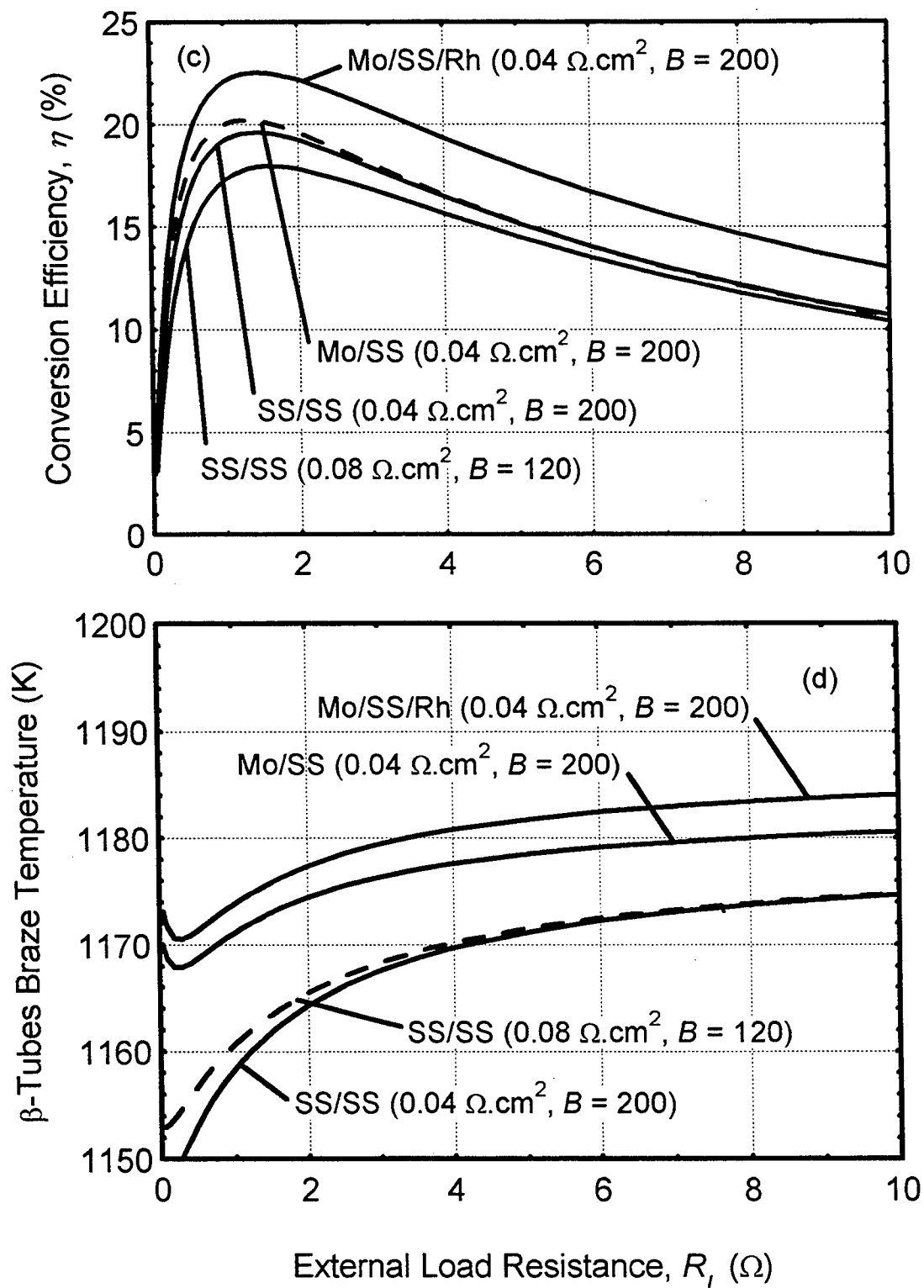


Figure 13.6. Performance of Adiabatic PX-Series AMTEC Cells (Cases #12, 13, 14 and 15) (Cont).

and increased the conversion efficiency by 2.3 points, to 22.5%, at a load resistance of 1.26  $\Omega$  and load voltage of 3.5 V.

The present analyses showed that Pluto/Express-type AMTEC cells could achieve performance that exceeds the mission goals of 8 W<sub>e</sub> at a load voltage of 3.5 V, and a conversion efficiency > 20%, when the different changes investigated herein were incorporated into the cell design. Some of the design changes proposed, however, would require resolving key technology issues, such as brazing of Mo and stainless steel, applying rhodium coating that could last the mission lifetime in a corrosive sodium vapor atmosphere, and developing new electrode materials with lower contact resistance and higher exchange current.

The next chapter explores several design changes using the basic configuration of the PX-3G cell, to improve the cell performance. Also, several integration options of the improved PX-3G cells with General-Purpose Heat Source (GPHS) modules in the configuration proposed by OSC are investigated for an electric power level of 130 W<sub>e</sub> and a 15-year mission. The options explored include varying the number of GPHS modules and AMTEC cells, and using fresh or aged fuel. The effects of changing the generators' output voltage (24 V or 28 V) on the evaporator and BASE metal-ceramic brazes temperatures and temperature margin in the cell are also examined.

## 14. ANALYSIS OF RADIOISOTOPE POWER SYSTEMS USING IMPROVED CELLS

Recently, a ground demo of eight AMTEC (PX-3G) cells has been tested successfully in vacuum at the Air Force Research laboratory (AFRL). Results showed that the electric power output and voltage of the best performing PX-3G cell are short of meeting the requirements of the Pluto/Express (PX) mission (see Chapter 12). Using the basic configuration of the PX-3G cell, several design changes are explored, to improve the cell performance. Also, several integration options of the improved PX-3G cells with General-Purpose Heat Source (GPHS) modules in the configuration proposed by OSC, are investigated for an electric power level of 130 W<sub>e</sub> and a 15-year mission. The options explored include varying the number of GPHS modules and AMTEC cells, and using fresh or aged fuel. The effects of changing the generators' output voltage (24 V or 28 V) on the evaporator and BASE metal-ceramic brazes temperatures and temperature margin in the cell are also examined.

### 14.1 NOMENCLATURE

#### English

$B$	Temperature-independent, charge-exchange current coefficient ( $A.K^{1/2}/Pa.m^2$ )
$I$	Cell electrical current (A)
$L_E$	Electrode length (m)
$N_B$	Number of BASE tubes in cell (electrically connected in series)
$P_e$	Cell electrical power output (W <sub>e</sub> )
$Q_{in}$	Cell heat input (W)
$R_{cont}$	Contact resistance between BASE/electrode/current collector ( $\Omega.cm^2$ )
$R_L$	External load resistance per cell ( $\Omega$ )
$R_{leak}$	Leakage resistance of BASE braze joint ( $\Omega$ )
$T$	Temperature (K)

#### Greek

$\Delta T$	Temperature margin, $\Delta T = T_\beta - T_{ev}$ (K)
$\eta$	Cell conversion efficiency (%)

#### Subscript / Superscript

braze	BASE tube metal-to-ceramic braze
cd	Cell condenser
ev	Wick evaporator
hot	Cell's hot end
max	Maximum value
$\beta$	Cold end of BASE tube

## 14.2 INTRODUCTION

During the past three years, several vapor anode, multi-tube Alkali Metal Thermal-to-Electric Converter (AMTEC) cells of different designs have been fabricated by Advanced Modular Power Systems (AMPS) and tested in vacuum at AFRL (Merrill et al. 1998). These cells are being considered for providing electric power to the Pluto Express (PX) flyby spacecraft, scheduled for launch early next century. The power requirement for this mission is 130 W<sub>e</sub> at 28 V D.C., for 15 years (Mondt et al. 1997).

Several generator configurations have been proposed for meeting the power requirements of the PX-mission (Hendricks et al. 1997, Schock et al. 1997b and 1998a). The PX power system proposed by Schock et al. (1997b and 1998a) consists of 2, <sup>238</sup>PuO<sub>2</sub> radioisotope GPHS modules (each provides 220 W<sub>th</sub> at end of mission) and 16 AMTEC cells in two parallel strings. Each string consists of 8 cells connected in series. Therefore, each cell must provide about 8.2 W<sub>e</sub> at 3.5 V. These cells would operate at hot and cold temperatures of ~1200 K and ~600 K, respectively. While the system analyses performed by Schock et al. (1997b and 1998a) have been very comprehensive, the predicted cell performance is yet to be matched with experimental data.

To demonstrate the performance of a typical PX-multi-cell generator, an 8-cell ground-demo has been manufactured by AMPS (Carlson et al. 1998) and recently tested in vacuum at AFRL. The ground-demo consisted of 8, PX-3G type cells connected electrically in series and operated at almost the same hot and cold side temperatures. The PX-3G cells were electrically heated in vacuum inside a shroud cooled with liquid nitrogen.

## 14.3 DESCRIPTION OF PX-3G CELLS

The PX-3G cells used in the ground-demo each have 6 BASE tubes connected electrically in series, and each tube has a 6-cm<sup>2</sup> cathode electrode. The TiN anode and cathode porous electrodes of the BASE are covered with molybdenum mesh current collectors, to minimize internal electrical losses. The PX-3G cells have a 100-mm<sup>2</sup> metal stud to enhance heat conduction from the hot plate to the cell evaporator and the BASE tubes. In addition, several nickel rings are placed around the evaporator standoff, to further enhance the heat conduction to the cell evaporator. More details on PX-3G cell design and test conditions can be found in Chapter 12.

Analysis of ground demo test results indicated a difference of about 25% in the electric power output and voltage of individual cells. This difference was attributed to the different values of the charge-exchange current, contact resistance between BASE/electrode/current collector, and current leakage. This conclusion was based on extensive analyses performed using the AMTEC Performance and Evaluation Analysis Model (APEAM). These analyses included extensive single-effect calculations to match the measured voltage-current characteristics of the individual PX-3G cells (see Chapter 12).

The best performing PX-3G cell delivered a peak electric power of 3.71 W<sub>e</sub> at 2.2 V, when tested at hot and cold side temperatures of 1123 K and 553 K, respectively. The outer diameter of PX-

3G cells is 38.1 mm (1.5 in). At the operating conditions expected on board the PX spacecraft ( $T_{hot} \sim 1200$  K,  $T_{cd} \sim 600$  K), this cell would have delivered 5  $W_e$  at 3 V. These values, however, are significantly lower than those needed for the PX mission (8.2  $W_e$ , 3.5 V).

The objectives of this chapter are to: (a) investigate different design changes for improving the performance (peak electric power and voltage) of PX-3G type cells; (b) propose an improved design of 1.25-in diameter cell, that is suitable for integrating up to 8 cells on one side of the GPHS module, in the configuration proposed by Schock et al. (1997b and 1998a); and (c) explore various options of integrating the improved 1.25-in diameter cells with GPHS modules. It is important to note that the AMTEC cells that will eventually be used to meet the power needs of the PX-mission could be different in design than the cells proposed in this work. Nonetheless, the present analysis provides useful information regarding the integration issues of AMTEC cells with GPHS modules. The options explored include changing the number of GPHS modules and the number of cells per generator, and using either fresh or aged  $^{238}\text{PuO}_2$  fuel. The effects of the output voltage (24 V or 28 V) on the generator electric power output as well as on the evaporator and BASE metal-ceramic brazes temperatures and temperature margin in the cells are also examined.

#### 14.4 IMPROVED PX-3G CELL DESIGN

The present analyses are performed at a constant heat input,  $Q_{in}=31.25$   $W_{th}$  per cell, which corresponds to that in a PX-power system consisting of 16 PX-3G type cells and two GPHS modules of fresh-fuel. Each GPHS module provides 250  $W_{th}$  at Beginning Of Mission (BOM), decreasing to 220  $W_{th}$  at the End-Of-Mission (EOM). Heat rejection from the cell condenser and wall is radiated to space from the generator housing (Schock et al. 1997b). The load resistance is selected to provide an output voltage of 3.5 V per cell. Results are summarized in Table 14.1. It is worth noting that because the cells' output voltage was kept at 3.5 V, the electric power values listed in Table 14.1 are lower than their peak values. At the above operating conditions, the best performing PX-3G cell (design #1) would have generated an electric power of 4.56  $W_e$  at an efficiency of 14.6%. However, the metal-ceramic brazes of the BASE tubes would have operated at 1177 K, which is above the 1123 K limit for TiNi brazes (Merrill et al. 1998, Sievers et al. 1998). Also, the very high evaporator temperature (1095 K) would probably cause the flow of liquid sodium in the return wick to be capillary limited (see Chapter 6). The PX-3A cell tested earlier at AFRL, however, has operated successfully at an evaporator temperature of  $\sim 1050$  K and electric current of  $\sim 2$  A (Merrill et al. 1998). Thus, it is reasonable to use 1050 K as the limit for  $T_{ev}$  in cells that use felt-metal evaporator wicks (Sievers et al. 1998).

Results in Table 14.1 also show that the best performing PX-3G cell would have operated at a negative temperature margin,  $\Delta T = -10$  K ( $\Delta T$  is the temperature difference between the cold end of the BASE tubes and the evaporator), raising the possibility of sodium vapor condensation inside the BASE tubes, potentially shorting them.

Design changes investigated herein aimed at improving the cell performance, increasing the temperature margin, and lowering the metal-to-ceramic brazes temperature. Design changes

Table 14.1. Predicted Performance of PX-3G type Cells ( $Q_{in} = 31.25 \text{ W}_{th}$  and 3.5 V).

<b>Cell design:</b>	#1 (*)	#2	#3	#4	#5	#6	#7
Number of BASE tubes	6	7	7	7	7	7	7
Electrode length (mm)	25.4	25.4	29.0	29.0	29.0	29.0	29.0
Collector wire diam. ( $\mu\text{m}$ )	163	163	163	163	163	163	326
Radiation shield	SS	SS	SS	Mo	Mo	Mo	Mo
Hot-side structure	SS	SS	SS	SS	Ni	Ni	Ni
Evaporator standoff (mm)	0.71 (SS)	0.71 (SS)	0.71 (SS)	0.71 (SS)	0.71 (Ni)	0.71 (Ni)	0.71 (Ni)
Standoff rings (mm)	1.25 (Ni)	1.25 (Ni)	1.25 (Ni)	1.25 (Ni)	1.25 (Ni)	None	none
<b>Cell Performance:</b>							
Electric power ( $W_e$ )	4.56	4.69	4.81	5.02	5.19	5.06	5.0
Predicted efficiency (%)	14.6	15.0	15.4	16.0	16.6	16.2	15.9
<b>Temperatures:</b>							
Hot side, $T_{hot}$ (K)	1209	1176	1167	1171	1132	1154	1145
BASE braze (K)	1177	1144	1136	1140	1111	1129	1120
Evaporator, $T_{ev}$ (K)	1095	1050	1039	1040	1064	1048	1043
Temperature margin (K)	-10	+6	+10	+14	-26	+1	+16
Condenser, $T_{cd}$ (K)	583	584	584	583	582	583	583

(\*) Best Performing PX-3G cell in the 8-cell ground-demo system.

pursued included increasing the number of BASE tubes and the surface area of their electrodes, and increasing the thermal conductance of the cell's hot side and the BASE tubes. Also investigated is the effect of replacing the stainless steel (SS) thermal shield with a molybdenum (Mo) shield.

Increasing the number of BASE tubes from 6 to 7 increases the electric power output by 130 mW<sub>e</sub> and the conversion efficiency by 0.4% points, while decreasing the temperatures of the BASE tube brazes and evaporator by 33 K and 45 K, respectively (cell design #2, Table 14.1). As a result, this cell would operate at a positive temperature margin,  $\Delta T = +6 \text{ K}$ .

Increasing the length of the TiN electrodes from 25.4 mm to 29.0 mm (i.e., increasing electrode area per tube from 6 to 6.85 cm<sup>2</sup>) also increases the electric power output of the cell by an additional 120 mW<sub>e</sub> (to 4.81 W<sub>e</sub>) and the conversion efficiency by 0.4% points (to 15.4%), and decreases the brazes and evaporator temperatures by 8 K and 11 K, to 1136 K and 1039 K, respectively (cell design #3, Table 14.1). Also, the cell temperature margin increases by another +4 K, to  $\Delta T = +10 \text{ K}$ .

The effect of replacing the SS radiation shield with a Mo shield is indicated in Table 14.1 by comparing designs #3 and #4. The higher reflectivity of Mo ( $\epsilon = 0.08$ , versus  $\epsilon = 0.25\text{--}0.30$  for SS) reduces the parasitic heat losses, increasing the cell efficiency to 16.0%, and the hot side, BASE tubes braze temperature, and temperature margin by 4 K each. The electric power output of the cell also increases by an additional 210 mW<sub>e</sub>, to 5.02 W<sub>e</sub>.

Substituting nickel for the SS as the structure material on the hot side of the cell increases the conductance of the hot side structure by a factor 2.5. The hot side structure includes the cell's hot plate, conduction stud, BASE tubes support plate, the sidewall facing the BASE tubes, and the evaporator standoff. An added benefit of Ni is its lower emissivity ( $\epsilon \sim 0.17$ ), which reduces the parasitic heat losses. When nickel was substituted for SS as the structural material on the hot side of the cell, the hot side temperature decreased by 39 K, and the BASE tubes braze temperature decreased by 29 K (cell design #5, Table 14.1). The improved conductance of the nickel evaporator standoff in the cell, however, raised the evaporator temperature, resulting in a negative temperature margin,  $\Delta T = -26$  K.

To eliminate this negative temperature margin, while retaining some of the performance improvement of the cell (design #5 in Table 14.1), the Ni rings around the evaporator standoff are removed. The cell electric power output decreased by 130 mW<sub>e</sub> to 5.06 W<sub>e</sub>, and the cell efficiency decreased by 0.4% points to 16.2% (design #6, Table 14.1), but the lower evaporator temperature increased the temperature margin by 27 K, to  $\Delta T = +1$  K. The BASE tubes braze temperature, however, increased to 1129 K, slightly above the recommended operation limit (1123 K) for TiNi brazes.

Figure 14.1 shows the calculated temperatures along the BASE tubes of the cell design #6. Because of the low conductance of the  $\alpha$ -alumina and BASE materials, there is a 34 K temperature difference between the hot braze and the electrode. The temperature drop along the current collector section is 45 K. To avoid Na condensation inside the BASE tubes, it is therefore necessary to decrease the temperature drop along the BASE tubes, for example using higher conductance brazes and current collectors. When the wire of the one-layer, 60-mesh (Mo) current collectors in the cell design #6 was doubled in diameter, the temperature drop along the current collector decreased by 22 K, lowering the brazes temperature by 9 K and increasing  $\Delta T$  by 15 K, to +16 K (Figure 14.2, and Table 14.1, design #7).

The cell design #7 delivers an electric power of 5 W<sub>e</sub> at a conversion efficiency of 15.9%, without exceeding the current temperature limits of the TiNi metal-to-ceramic brazes (1123 K) and the evaporator (1050 K). This is a significant improvement over the PX-3G cell (design #1 in Table 14.1). The cell design #7 delivers 440 mW<sub>e</sub> more electric power (5.0 W<sub>e</sub>), and 1.3 points higher efficiency (15.9%). At the same time, the BASE tubes braze and evaporator temperatures are lower by 57 K and 52 K, respectively, increasing the temperature margin by 26 K, to +16 K.

In addition to improving the operation parameters of the cell, some considerations must also be given to the structure materials compatibility. Lifetime acceleration tests and corrosion studies have shown that SS might not be suitable for use in long-term space missions (Alger 1997, Svedberg et al. 1997). A concern is that iron in the condenser mesh pad would be dissolved rapidly by liquid sodium, saturating liquid sodium in the return wick. As Fe precipitates at the intake of the return wick, the wick permeability will gradually decrease, increasing the pressure drop in the return wick. The dissolved Mn, Cr and Fe could also contaminate the TiN electrodes



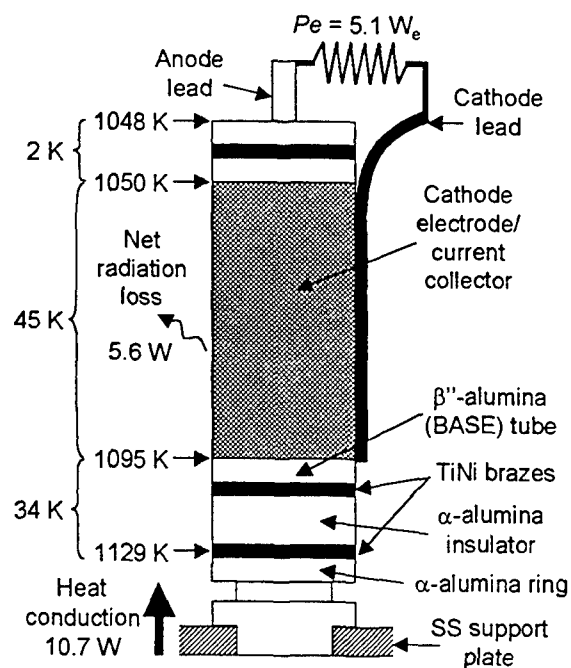


Figure 14.1. Predicted Temperatures and Heat Flow in BASE Tubes of Cell Design #6 (3.5 V,  $Q_{in}=31.3 W_{th}$ ).

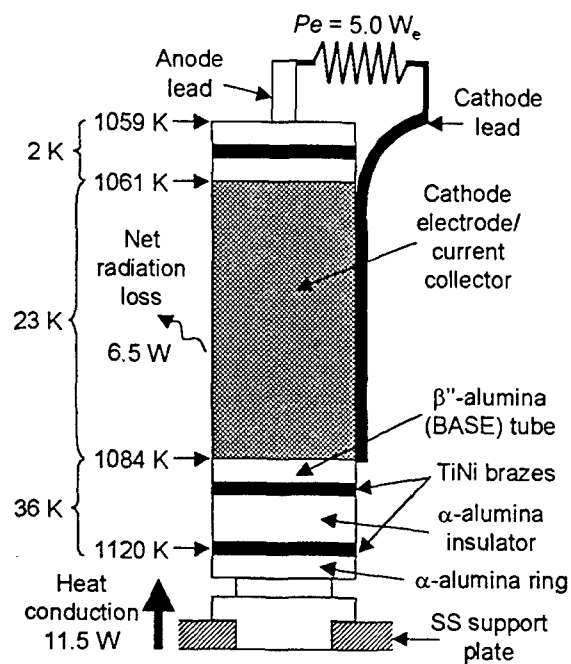


Figure 14.2. Predicted Temperatures and Heat Flow in BASE Tubes of Cell Design #7 (3.5 V,  $Q_{in}=31.3 W_{th}$ ).

surfaces, degrading their performance, and could increase the electrons leakage between anode and cathode electrodes, through the brazes.

## 14.5 MULTI-CELL POWER SYSTEMS INTEGRATION ANALYSIS

This section presents the results of an analysis performed to design multi-cell radioisotope power systems in the configuration proposed by OSC that could provide  $> 130 W_e$  for up to 15-year space missions. The multi-cell generators of the power system are electrically connected in parallel to insure system's redundancy at the highest level. Also, the two strings of cells, one at each end of the generator, are connected in parallel (Schock et al. 1997b and 1998a). Analyses are performed at constant heat input to the cells, depending upon the number of GPHS modules and cells used in the generators. The heat rejection from the AMTEC cells is radiated to space by the outer surface of the power system housing (each end face is  $\sim 146 \text{ cm}^2$ ).

Because the surface area available on one side of the GPHS module is a square of  $\sim 100 \text{ mm} \times 100 \text{ mm}$ , a maximum of 5 improved PX-3G cells (design #7 in Table 14.1) could be fitted on one side. As a result, every cell had to operate at a high voltage and low current, causing  $\Delta T < 0$ . To overcome this integration problem, the cell diameter of the improved PX-3G type cell (design #7 in Table 14.1) was reduced from 38.1 mm (1.5 in) to 31.75 mm (1.25 in), which allows up to 8 cells to be fitted on each end of the GPHS modules. This decrease in cell diameter reduced the number of BASE tubes from 7 to 5 per cell and decreased the evaporator standoff outside diameter from 11.58 to 7 mm. All other design parameters were identical to those of design #7 in Table 14.1.

Figure 14.3a shows the calculated voltage and electric power output of the 1.25-in diameter cell, as functions of heat input and electric current. Since the electric power curves are somewhat flat near their peaks, the cell can be operated at various combinations of current and voltage, without deviating much from the peak electric power. For example, at  $Q_{in} = 35.7 W_{th}$ , the peak electric power output is  $6.54 W_e$ , at 2.17 A and 3.01 V. The same cell could produce  $6.37 W_e$  at 1.77 A and 2.54 V, which correspond to output voltages of 3.6 V and 2.51 V, respectively.

Figure 14.3b shows that both the evaporator ( $T_{ev}$ ) and BASE tubes braze ( $T_{braz}$ ) temperatures increase with increasing heat input, but decrease with increasing cell current. For  $Q_{in} = 35.7 W_{th}$ ,  $T_{braz} = 1273 \text{ K}$  and  $T_{ev} = 1148 \text{ K}$  at the peak electric power ( $I = 2.17 \text{ A}$ ). At  $I = 1.77 \text{ A}$ , the metal-to-ceramic brazes and evaporator temperatures increase to 1311 K and 1208 K, respectively. As shown in Figure 14.3b, an electric power of  $6.37 W_e$  can also be obtained at  $I = 2.54 \text{ A}$ , at much lower  $T_{braz}$  (1243 K) and  $T_{ev}$  (1100 K). These temperatures are 30 K, and 48 K lower, respectively, than when the cell is operated at the peak power ( $6.54 W_e$ ), which is only  $\sim 2\%$  higher.

As shown in Fig. 14.3c,  $\Delta T$  decreases as the heat input increases, but increases with increasing cell current. At  $Q_{in} = 35.7 W_{th}$ ,  $\Delta T$  at the peak electric power ( $I = 2.17 \text{ A}$ ) is +34 K. This temperature margin decreases to  $\Delta T = -8 \text{ K}$  at lower current,  $I = 1.77 \text{ A}$ , but it is as much as +57 K when the cell current increases to 2.54 A.

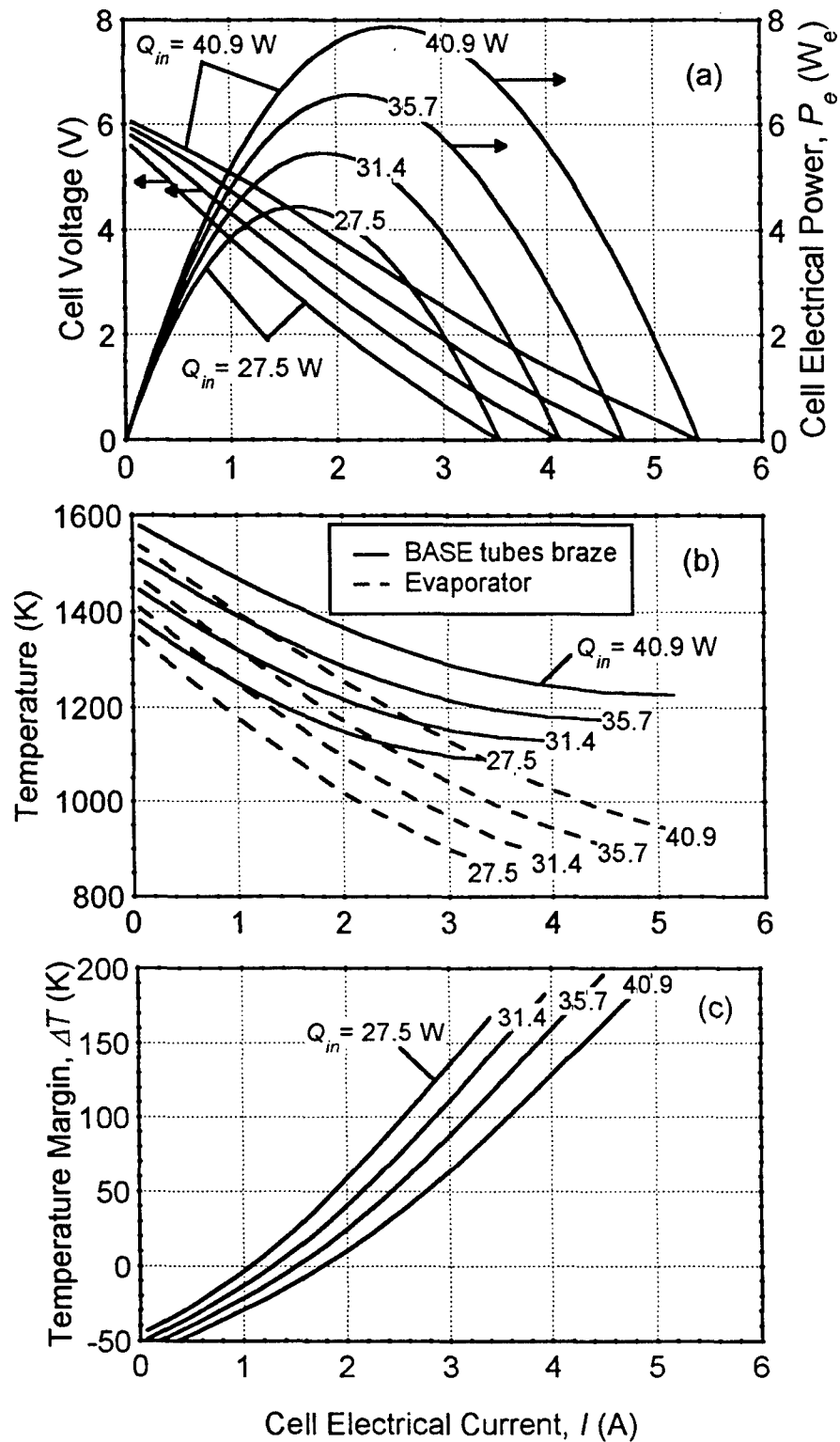


Figure 14.3. Calculated Performance of an Improved 1.25-in Diameter, PX-3G Type Cell Design.

In order to determine the appropriate number of cells and GPHS modules needed for meeting the PX-mission power requirements, the present power system model computed the maximum electric power output of the 1.25-in PX-type cell as a function of its heat input. As shown in Figure 14.4, the cell's peak electric power output increases linearly with  $Q_{in}$ . This figure also shows the predicted conversion efficiency at the peak electric power. For  $Q_{in} = 35.7 \text{ W}_{th}$  per cell, the cell peak power output is  $6.54 \text{ W}_e$ , at which the conversion efficiency is 18.3%.

When the number of cells in the PX-generator is reduced, the heat input per cell increases, increasing the total electric power output of the generator. However, this also increases the evaporator and metal-to-ceramic brazes temperatures, decreasing the temperature margin in the cells (Figures 14.3b and 14.3c).

In the following analysis, the PX-power systems are designed to provide at least  $156 \text{ W}_e$  at EOM (or  $130 \text{ W}_e$  with a provision for a 20% degradation in cell performance after 15-year operation lifetime). Since the exact performance degradation of the cells is not known at the present time, an allowance for 20% degradation in the cell electric power at EOM is used, until more reliable figures can be justified. Assuming that the improved 1.25-in diameter, PX-3G type cells would operate near their peak electric power point, the number of cells needed is obtained by dividing  $156 \text{ W}_e$  by the cell's peak power at EOM. The corresponding heat input required from the GPHS modules is obtained by multiplying the above number of cells by the cell's heat input. Since the number of cells in the generator is limited by the number of GPHS modules used and their integration, results presented in Figure 14.5 are provided only for illustration purpose. Actual cell/GPHS generator integration studies are conducted next, and summarized in Table 14.2. The mass of each generator was obtained assuming a cell mass of 0.15 kg, 1.8 kg per GPHS module, and a total insulation mass of 2.3 kg around the cells. The mass figures in Table 14.2 are comparable to those reported by Schock et al. (1998a).

As indicated in Table 14.2, the generator's heat input is limited by the number of GPHS modules used. A fresh-fuel GPHS module provides  $250 \text{ W}_{th}$  at BOM, and  $220 \text{ W}_{th}$  at EOM. An aged-fuel GPHS (1982) module, originally produced as spares for the Galileo mission, provides  $218 \text{ W}_{th}$  at BOM and  $194 \text{ W}_{th}$  at EOM (Schock et al. 1997b). Note that the present analysis accounts for radioactive decay of  $^{238}\text{PuO}_2$  and for thermal heat losses in the generator, assuming a mission lifetime of 15 years.

Figure 14.5 shows that 3 different combinations of GPHSs could provide the heat input needed. A heat source that consists of 6 fresh-fuel GPHS modules provides  $1320 \text{ W}_{th}$  at EOM. If these GPHS modules could be integrated to 75 cells, they would provide exactly the needed electric power output of  $156 \text{ W}_e$  at EOM. Since each single-GPHS generator only accepts a maximum of 16 cells (eight at each end), this system will consist of 6 identical generators, each with one GPHS module and 12 cells. Such a power system would provide  $\sim 160 \text{ W}_e$  at EOM, but would be quite heavy and have a very low specific power of  $\sim 5 \text{ W}_e/\text{kg}$ , comparable to that of GPHS-RTGs.

The first generator design considered in the present analysis consists of 3 separate generators, each has 16 cells and a heat source consisting of 2 aged-fuel GPHS modules (Figure 14.6 and Table 14.2, power system #1). This design provides a total heat input of  $1164 \text{ W}_{th}$  at EOM

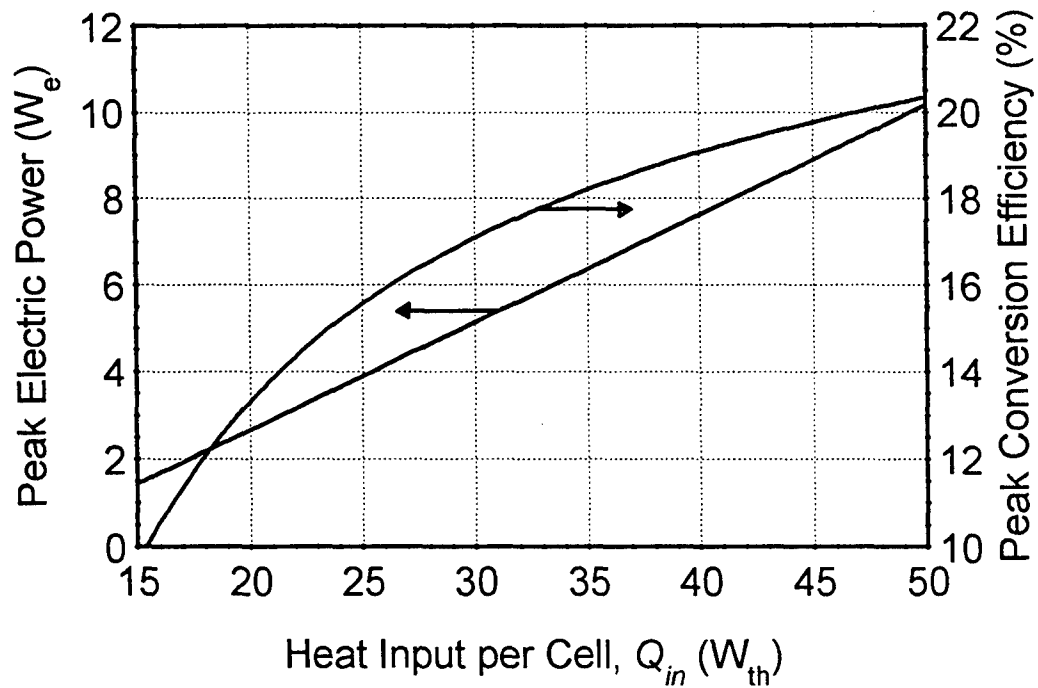


Figure 14.4. Peak Electric power of Improved 1.25-in Diameter, PX-3G Type Cell.

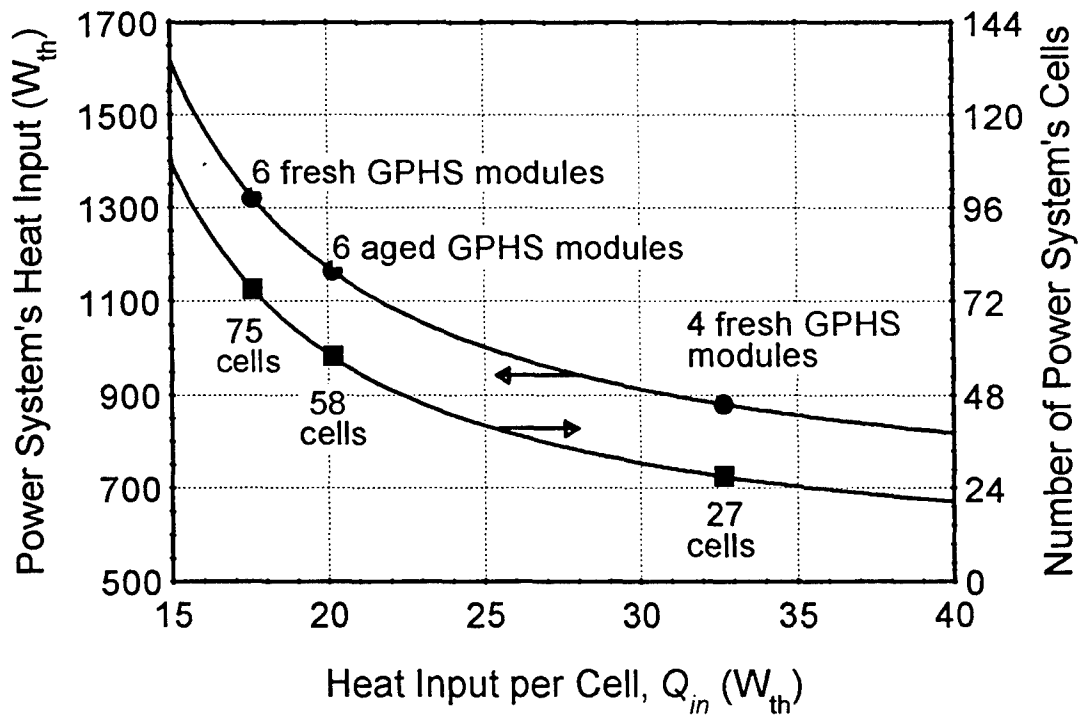


Figure 14.5. Number of Improved 1.25-in Diameter Cells and Total Heat Input for a Multi-cell Generator with 156  $W_e$  Output at EOM.

Table 14.2. Predicted Performance of Radioisotope Power Systems with Improved 1.25-in Diameter, PX-3G Cells.

Power System design	#1				#2				#3				#4			
Number of generators	3				2				2				2			
GPHSs / generator	2 aged-fuel				2 fresh-fuel				2 fresh-fuel				3 aged-fuel			
# of cells / generator	16				16				14				16			
Output voltage (V)	28		24		28		24		28		24		28		24	
<b>System Performance:</b>	BOM	EOM	BOM	EOM	BOM	EOM	BOM	EOM	BOM	EOM	BOM	EOM	BOM	EOM	BOM	EOM
Heat input ( $W_{th}$ )	1308	1164	1308	1164	1000	880	1000	880	1000	880	1000	880	1308	1164	1308	1164
Output power ( $W_e$ )	200	156	211	169	168	133	175	140	168	135	181	148	252	211	251	215
Overall efficiency (%)	15.3	13.4	16.1	14.5	16.8	15.1	17.5	16.0	16.8	15.3	18.1	16.8	19.3	18.1	19.2	18.5
Generators mass (kg)	3 x 8.3 = 24.9				2 x 8.3 = 16.6				2 x 8.0 = 16.0				2 x 10.1 = 20.2			
Specific power ( $W_e/kg$ )	8.0	6.3	8.5	6.8	10.1	8.0	10.6	8.4	10.5	8.4	11.3	9.3	12.5	10.4	12.4	10.6
<b>Temperatures:</b>	BOM	EOM	BOM	EOM	BOM	EOM	BOM	EOM	BOM	EOM	BOM	EOM	BOM	EOM	BOM	EOM
Cell top, $T_{hot}$ (K)	1262	1227	1230	1196	1302	1262	1269	1230	1378	1335	1339	1297	1392	1350	1362	1318
BASE tubes brazes (K)	1229	1198	1198	1168	1265	1229	1234	1198	1336	1298	1298	1261	1346	1308	1316	1277
Evaporator, $T_{ev}$ (K)	1146	1126	1123	1082	1170	1146	1121	1100	1244	1217	1188	1163	1224	1199	1175	1149
Margin, $\Delta T$ (K)	+6	+3	+23	+17	+12	+7	+29	+23	-1	-4	+19	+14	+22	+17	+42	+37
Cell condenser, $T_{cd}$ (K)	613	597	613	596	631	613	631	613	649	632	648	631	668	651	670	652

(Figure 14.5), to 48 cells. The 3 generators are electrically connected in parallel. The cells in each generator are divided equally between two parallel strings, and the cells in each string are connected in series. This power system will more than meet the power requirement of the PX-mission at either 28 V or 24 V output voltage. At these voltages, the cells will operate at positive temperature margins,  $\Delta T > +3$  K and  $> +17$  K, respectively.

The next power system considered consists of 2 generators, each uses 2 fresh-fuel GPHS modules. Each generator will employ either 16 or 14 cells (power systems #2 and #3 in Figure 14.6 and Table 14.2, respectively). Since system #2 has 2 more cells per generator than system #3, the heat input per cell will be less, and the electric power output will be lower than system #3. Thus the electric power output of system #2 would be short of the 156  $W_e$  needed at EOM (see Figure 14.5 and Table 14.2).

Another power system considered in this analysis consists of 2 generators, each has a stack of 3 aged-fuel GPHS modules and 16 cells (power system #4 in Table 14.2). The power system #4 has only 32 cells, and will deliver an electric power output that exceeds the PX mission requirement, at high specific power ( $> 10.6$   $W_e/kg$ ), but at very high evaporator and brazes temperatures of 1175 K and 1316 K, respectively.

Figure 14.5 and Table 14.2 indicate that the cells in the power system with the higher specific power generally operate at higher metal-to-ceramic brazes temperature and higher evaporator temperature margin. Even in the most conservative power system #1, at an output voltage of 24 V, the cells' brazes and evaporator temperatures would be about 75 K higher than current limits. Operating the PX-generators at lower output voltage lowers the brazes and evaporator

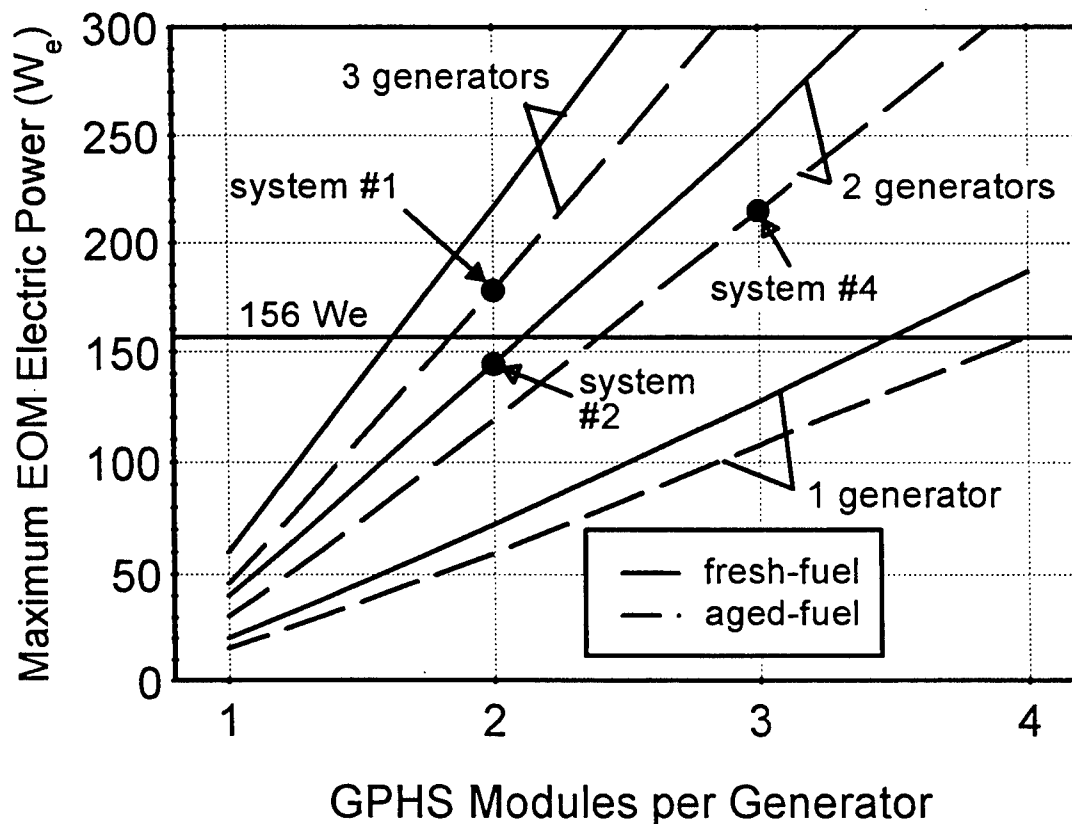


Figure 14.6. Maximum Electric Power Output of 16-Cell Generator Power Systems at EOM.

temperatures, and increases the temperature margin in the cells (Table 14.2). Note that, at an output voltage of 24 V, the cells operate very near their peak electric power point.

#### 14.6 SUMMARY AND CONCLUSIONS

A number of design changes were examined for improving the performance of PX-3G cells. Results indicated that a PX-3G type cell, with 7 BASE tubes, 14% longer electrodes, a Mo heat shield and a Ni structure on the hot side, could deliver an electric power of 5  $W_e$  at a conversion efficiency of 15.9%, and a 3.5 V output voltage, when operated at a constant heat input,  $Q_{in} = 31.25 W_{th}$ . This cell would not exceed the temperature limits of the BASE tubes, metal-to-ceramic TiNi braze (1123 K) and current-technology evaporator (1050 K). These performance parameters are a significant improvement over the ground-demo PX-3G cell (440 m $W_e$  more electric power at 1.3 points higher efficiency, 57 K lower BASE tube brazes temperature, 52 K lower evaporator temperature, and 26 K higher temperature margin).

Radioisotope power systems in the configuration proposed by OSC, using improved-design PX-3G type cells, of smaller diameter (1.25 in) and only 5 BASE tubes each, are investigated for meeting the power requirement of the Pluto/Express mission ( $> 130 W_e$  at voltage  $> 28 V$  at

EOM). The present analysis identified 2 power systems, that could meet the specified electric power requirement, but at a slightly lower output voltage of 24 V.

The first power system (design #1 in Table 14.2) consists of 3 generators connected in parallel, each comprised of 2 aged-fuel GPHS modules and 16 cells. Each generator produces 56.3 W<sub>e</sub> at EOM, for a total electric power output of 169 W<sub>e</sub>, at an overall conversion efficiency of 14.5% and specific power of 6.8 W<sub>e</sub>/kg. This generator would deliver 130 W<sub>e</sub> at EOM, even if the cells' performance degrades by as much as 30% in the 15-year duration of the mission. In this power system, the BASE tubes brazes would operate at 1198 K at BOM, which is above the 1123 K limit of the current TiNi brazes. Also, the high evaporator temperature (1123 K) could cause the flow of liquid sodium in the return wick to be capillary limited. However, the temperature margin in the cells would be positive (> +17 K).

The second power system (design #2 in Table 14.2) consists of 2 generators, each comprised of 16 cells and 2 fresh-fuel GPHS modules. This power system would provide 140 W<sub>e</sub> at EOM (which allows for ~8% degradation in the cells' performance in the 15-year duration of the mission), a higher conversion efficiency of 16.0%, and higher specific power (8.4 W<sub>e</sub>/kg) than power system #1. The BASE tubes brazes in the cells of power system #2, however, would operate at 1234 K (36 K higher than in power system #1). Metal-to-ceramic braze materials, that can operate at temperatures up to 1250 K, need to be developed. Also, evaporator structures with pores < 4 μm in diameter, that can operate at temperatures up to 1123 K, are needed.

In the next chapter, a number of design changes are investigated for improving the performance of super-alloy, PX-series AMTEC cells, and various options of integrating these cells with General Purpose Heat Source (GPHS) modules in the generator configuration proposed by Advanced Modular Power Systems are explored, for satisfying the electric power requirements for the Pluto/Express mission, 130 W<sub>e</sub> and 28 V d.c. at End of Mission (EOM).



## 15. SUPER-ALLOY, AMTEC CELLS FOR THE PLUTO/EXPRESS MISSION

In this chapter, a number of design changes are investigated for improving the performance of super-alloy, Alkali-Metal Thermal-to-Electric Conversion cells, and various options of integrating these cells with General Purpose Heat Source (GPHS) modules in the generator configuration proposed by Advanced Modular Power Systems are explored, for satisfying the electric power requirements for the Pluto/Express mission, 130 W<sub>e</sub> and 28 V d.c. at End of Mission (EOM). Options explored included changing the number of GPHS modules and cells per generator, using either fresh or aged <sup>238</sup>PuO<sub>2</sub> fuel, and varying the number of BASE tubes in the cell by changing the cell diameter. A power system consisting of 6 fresh-fuel GPHSs and 48 7-tube cells connected electrically in 4 parallel strings would weight 28.75 kg and provide 174 W<sub>e</sub> at EOM at an overall efficiency of 13.2%. The cells would operate at low BASE brazes and evaporator temperatures of 1059 K and 971 K at Beginning Of Mission (BOM), respectively. A power system consisting of 5 fresh-fuel GPHS modules and 4 parallel strings of 8, 9-tube cells each would deliver 156 W<sub>e</sub> at EOM (assuming no cell performance degradation) at 28 V d.c.. The cells in this system would operate at BASE brazes and evaporator temperatures of 1071 K and 995 K at BOM, respectively. This generator would weight 24.53 kg only and have a specific power of 6.4 W/kg at EOM.

### 15.1 NOMENCLATURE

#### English

<i>B</i>	Temperature-independent, charge-exchange current coefficient (A.K <sup>1/2</sup> /Pa.m <sup>2</sup> )
<i>G</i>	Dimensionless factor for pressure losses
<i>I</i>	Cell electrical current (A)
<i>L<sub>E</sub></i>	Electrode length (m)
<i>Mo</i>	Molybdenum
<i>Ni</i>	Nickel
<i>Pe</i>	Cell electrical power output (W <sub>e</sub> )
<i>P<sub>sat</sub></i>	Saturation pressure of sodium (Pa)
<i>Q<sub>in</sub></i>	Cell heat input (W)
<i>R<sub>cont</sub></i>	Contact resistance between BASE/electrode/current collector (Ω.cm <sup>2</sup> )
<i>R<sub>L</sub></i>	External load resistance per cell (Ω)
<i>R<sub>leak</sub></i>	Leakage resistance of BASE braze joint (Ω)
<i>SS</i>	Stainless steel
<i>T</i>	Temperature (K)
<i>V<sub>L</sub></i>	External load voltage (V)

#### Greek

$\Delta T$	Temperature margin (temperature difference between BASE tubes cold end and evaporator), $\Delta T = T_{\beta} - T_{\varepsilon\omega}$ (K)
------------	--

$\varepsilon$	Surface radiative emissivity
$\eta$	Cell conversion efficiency
$\eta_G$	Generator overall efficiency, $\eta_G = \eta \times \eta_{th}$
$\eta_{th}$	Generator thermal efficiency

#### Subscript / Superscript

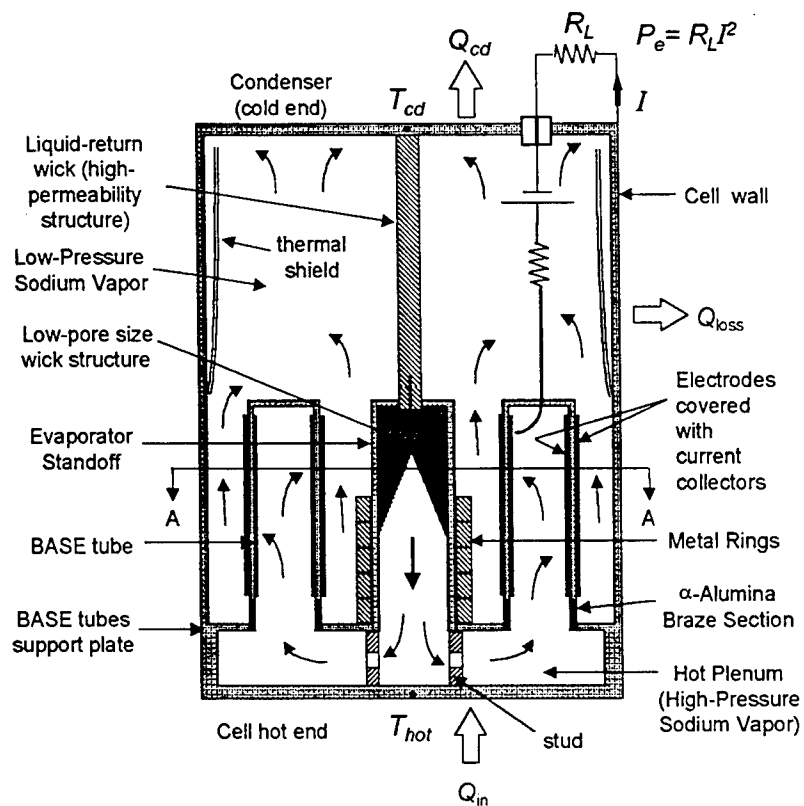
braz	BASE tube metal-to-ceramic braze
cond	Cell condenser
E	Cathode metal electrode
ev	Wick evaporator end
hot	Cell hot end
$\beta$	Cold end of BASE tube

## 15.2 INTRODUCTION

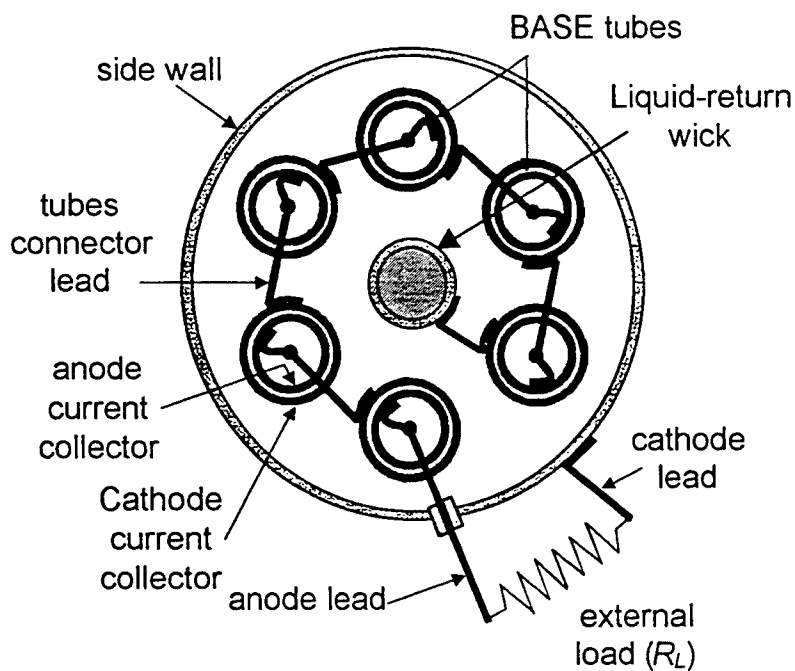
Vapor anode, multi-tube Alkali Metal Thermal-to-Electric Converter (AMTEC) cells are being considered for providing electric power to the Pluto Express (PX) flyby spacecraft, scheduled for launch early next century. The End-Of-Mission (EOM) electric power requirement is 130 W<sub>e</sub> at a 28 V d.c. load voltage. For this 15-year mission (Mondt et al. 1997), the PX-radioisotope electric power system design should account not only for the decrease in the thermal power of the <sup>238</sup>PuO<sub>2</sub> General-Purpose Heat Source (GPHS) due to natural radioactive decay of <sup>238</sup>Pu (half-life = 86 yr), but also for potential performance degradation of the AMTEC cells. In order to reduce the amount of <sup>238</sup>PuO<sub>2</sub>, achieve higher overall system's specific power than the state-of-art General Purpose Heat Source (GPHS)-Radioisotope Thermoelectric Generators (RTGs) (5.4 W/kg), and satisfy the EOM electric power requirements for the PX-mission, there is a need to develop high performance and high efficiency AMTEC cell designs.

During the past three years, several vapor anode, multi-tube AMTEC cell designs (Figure 15.1) have been fabricated by Advanced Modular Power Systems (AMPS) and tested in vacuum at the Air Force Research Laboratory/Phillips Site (AFRL/PS) (Merrill et al. 1998). Two electric power generator configurations have also been proposed for meeting the power requirements of the PX-mission. The power generator consists basically of a stack of GPHS units (or bricks) that are thermally coupled to a number of AMTEC cells. These cells are typically connected electrically in series, in two parallel strings for enhanced system redundancy. The PX-power system may consist of one or more generators.

The PX-generator proposed by Orbital Science Corporation (OSC) consists of a stack of two or three GPHS units (each provides 220 W at EOM) and 8-16 AMTEC cells (depending on the cell diameter). The cells are mounted on the top and bottom end faces of the GPHS stack (Figure 15.2) (Schock et al. 1997b, 1998b and 1998c). The cells are thermally insulated on the side using fibrous Min-K type insulation, a lightweight material recommended for use up to 1350 K, even in load-bearing application. The GPHS stack and the cells' Min-K insulation are surrounded by multifoil insulation with zirconia-particle spacers. The length of the foils is graded near the top



(a) Elevation



(b) Plan View (Section A-A)

Figure 15.1. Cross-sectional Views of PX-3G Type Cell (Not to Scale).

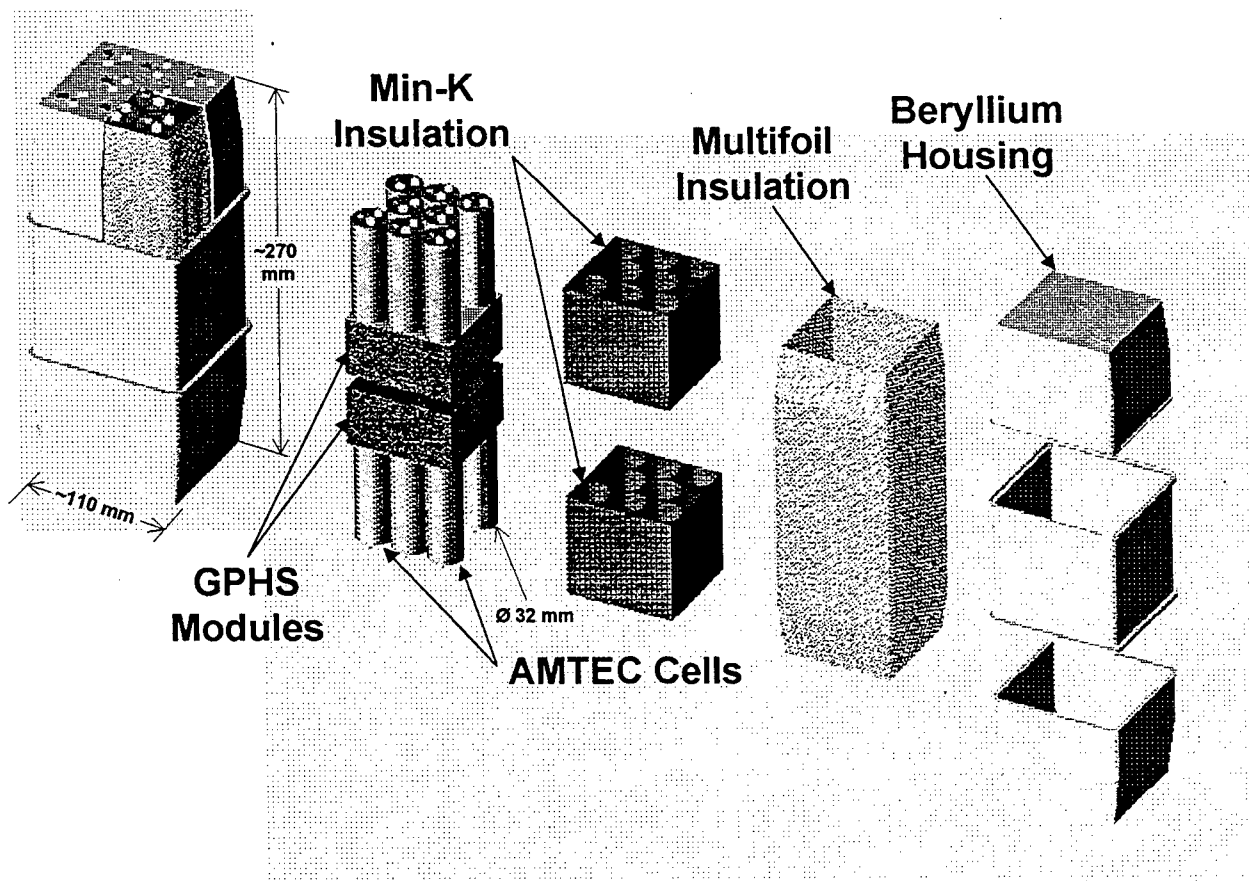


Figure 15.2. OSC's PX-Generator Design, with 2 GPHS Modules and Sixteen 31.75 mm (1.25") Dia. Cells (Schock et al. 1998c).

and bottom surfaces to reduce axial conduction losses in the metallic foils near the condenser end of the cells (Schock et al. 1997b). Excess heat from the cells' condensers is radiated to space from the top, bottom and side surfaces of the metallic housing of the generator. Analyses performed of the OSC generator (Schock et al. 1998b and 1998c) have been very comprehensive, however, the predicted cell performance is yet to be matched with experimental data.

AMPS has proposed a different PX-generator configuration (Hendricks et al. 1997 and 1998), which has a predicted thermal efficiency (~93%) slightly higher than OCS's (~91%). Instead of mounting the cells on the top and bottom faces of the GPHS stack, in AMPS design the cells are mounted onto the 4 sides of the GPHS stack (Figure 15.3). AMPS's generator also uses a combination of Min-K and multifoil insulation for the cells and the GPHS stack. Excess heat from the cells' condensers is radiated to space through the outer surface of the generator's aluminum or beryllium housing.

In OSC's PX-generator design, the number of cells per generator – a maximum of sixteen 31.75 mm (1.25") dia., ten 38.1 mm (1.5") dia., or four 44.45 mm (1.75") dia. cells – is limited by the surface area available for mounting the cells, the top and bottom faces of the GPHS stack.

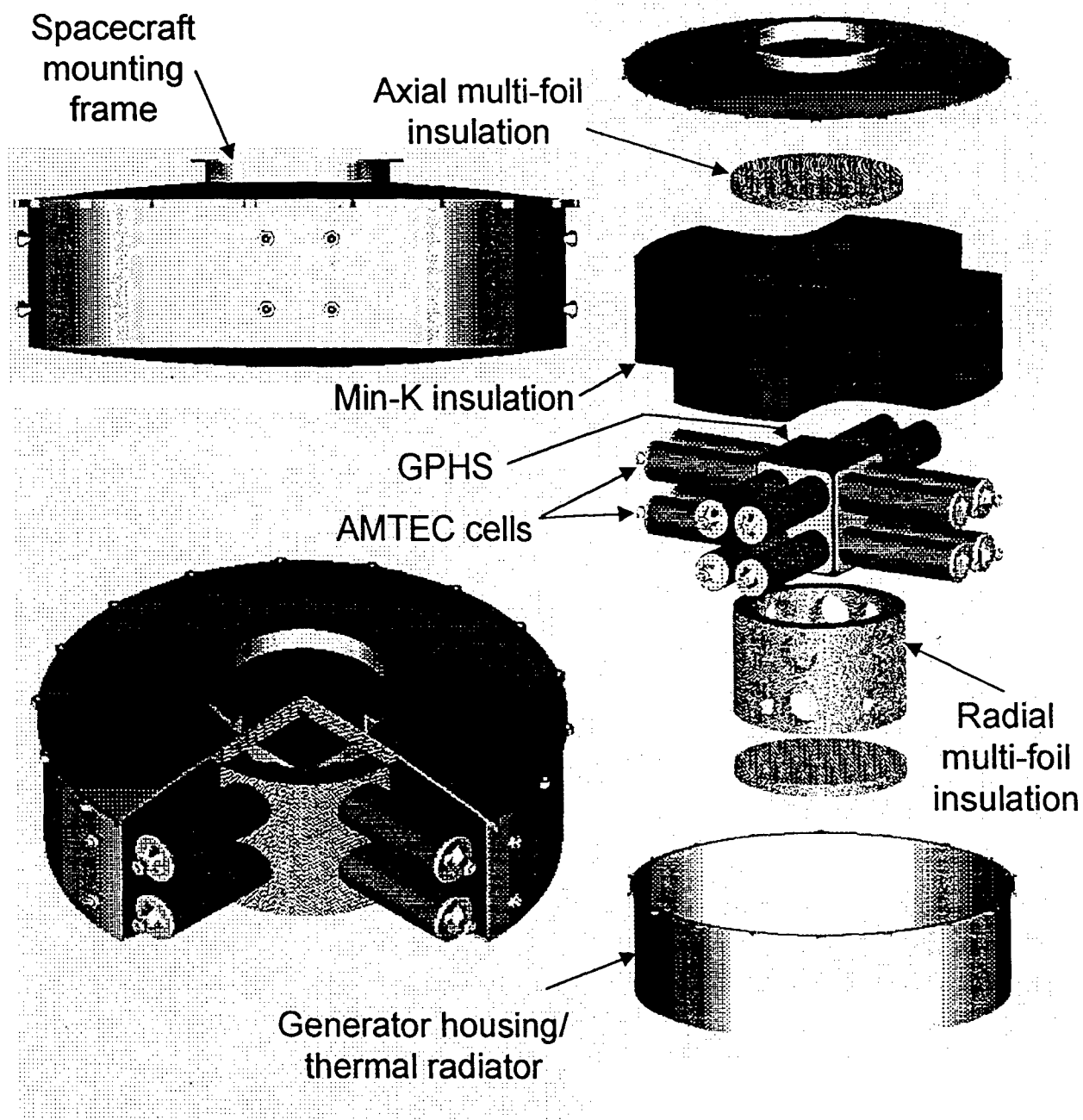


Figure 15.3. AMPS's PX-Generator Design, with 4 GPHS Modules and Sixteen 44.45 mm (1.75") Dia. AMTEC Cells (Hendricks et al. 1998).

Therefore, in OSC's generator design, there is a drive to increase the length of the Beta"-Alumina Solid Electrolyte (BASE) tubes and of the electrodes to increase the cell's electric current, and to operate at higher heat input to increase the overall electric power output and efficiency of the cells. In so doing, the design calls for using high-temperature refractory metals or metal-alloys (such as Nb or Nb-1%Zr) for the cell structure. However, since the temperatures of the BASE tubes and the evaporator in the cells will also increase, a major concern in this case is potential

acceleration of the performance degradation of the cells. As a result, the generator design should allow for a larger design margin to account of such effect, which would result in a heavier generator.

The AMPS's generator configuration, however, does not suffer from the cells' number limitation of the OSC design, due to the larger surface area of the four sides of the GPHS stack, hence offering greater flexibility in cells' integration and operation conditions. In the AMPS's design, however, mounting more cells does not necessarily means higher system performance, since the same amount of thermal energy is shared by a larger number of cells, reducing the heat input and operation temperatures of the cells. These effects would result in lower electric power output and overall efficiency of the generator. Therefore, the generator design should optimize for the appropriate number of cells and overall system performance. In AMPS's system design, there has also been a drive to develop high-temperature refractory cells, to reduce the number of GPHS modules needed, hence increasing the electric power density of the generator.

Until the inherent concerns associated with the use of high-temperature refractory cells are resolved, the authors views are to explore using super-metal or super-alloy (such as nickel or nickel alloys) cells instead of refractory-metal cells. These views are worthy of consideration, in light of the fact that there are only few data available at present on performance degradation of the cells as functions of operation time and temperature. However, it is expected that degradation in cell performance (e.g. of the BASE, metal-ceramic braze between the BASE tubes and the metal support plate, BASE electrodes, electric feedthroughs, etc.) could be rapidly accelerated as the operation temperature of the cell increases.

In the previous chapter (14), the authors proposed an improved design of 31.75 mm (1.25") dia., nickel cell with five BASE tubes supporting 29 mm-long TiN electrodes, and investigated various options of integrating these cells with GPHS bricks in OSC's configuration. The analysis assumed that the AMTEC cells in the generator were electrically connected in series, in two parallel strings, to enhance redundancy. Results showed that a generator comprised of a 2 aged-fuel GPHS stack and sixteen cells could deliver 52 W<sub>e</sub> at 28 V, at EOM. Thus, a total of 3 such generators connected in parallel would provide 156 W<sub>e</sub> at EOM, or 130 W<sub>e</sub> with a provision for a 20% degradation in generator performance after 15-year operation lifetime. In this generator, however, the BASE tubes' brazes and the evaporator would operate at very high temperatures at BOM (1229 K and 1146 K, respectively), partly due to the fact that each cell had to provide a load voltage of 3.5 V (Chapter 14). Using higher-diameter cells with more and/or longer BASE tubes would reduce the cell temperatures, but at the expense of decreasing the generator's electrical power. In view of these considerations, the objectives of the present analysis were to: (a) investigate different design changes for improving the performance (peak electric power and efficiency) of nickel super-alloy cells for satisfying the EOM electric power requirements for the PX-mission; and (b) explore various options of integrating the improved super-alloy cells with GPHS modules in the generator configuration proposed by AMPS (Figure 15.3). Options explored included changing the number of GPHS modules and the number of cells per generator, using either fresh or aged <sup>238</sup>PuO<sub>2</sub> fuel, increasing the BASE and electrode lengths, and varying the number of BASE tubes in the cell by changing the cell diameter. In some cases, the number of parallel strings of cells in the power system were reduced to only two. The associated decrease in

the overall system redundancy, however, could be alleviated by connecting a diode in parallel with each cell, so that the loss of one cell in a string of cells would not lead to the loss of the whole string, as recently proposed by Schock et al. (1998c). The effects of these design changes on the generator electric power output as well as on the temperatures of the cells' evaporator ( $T_{ev}$ ), BASE metal-ceramic brazes ( $T_{braz}$ ), and temperature margin,  $\Delta T$  in the cells, were also examined. The analyses were performed using the AMTEC Performance and Evaluation Analysis Model (APEAM).

### 15.3 VALIDATION OF APEAM WITH PX-3G GROUND DEMO DATA

The Pluto/Express generator ground-demo, manufactured by AMPS (Carlson et al. 1998), and recently tested in vacuum at AFRL/PS, consisted of 8 cells, designated PX-3G. In the test, the cells were connected electrically in series and operated at almost the same hot and cold side temperatures. Each cell had 6, series-connected BASE tubes with 6-cm<sup>2</sup> (25.4 mm-long) TiN electrodes (Fig. 1). The TiN anode and cathode electrodes were covered with molybdenum mesh current collectors to minimize internal electrical losses in the cell. The PX-3G cells were 101.6 mm (4.0") long, 38.1 mm (1.5") in diameter, and had a 100-mm<sup>2</sup> metal stud to enhance heat conduction from the hot plate to the shallow-cone evaporator and BASE tubes. The stainless steel (SS) evaporator standoff was 0.71 mm-thick, had an outer diameter of 11.6 mm, and a height of 12.4 mm. Several nickel rings were placed around the standoff to enhance heat conduction to the evaporator. The PX-3G cells used circumferential, SS internal heat shields, and a Creare-type condenser wick, to ascertain the formation of a continuous thin film of liquid sodium on the wick surface, thus reducing parasitic heat losses in the cell. More details on PX-3G cell design and test conditions can be found in Chapter 12).

Test results indicated unequal terminal voltage of the individual PX-3G cells and a difference of about 25% in the electric power output. This difference was attributed to the differences among the individual cells in the values of the charge-exchange current coefficient,  $B$ , contact resistance between BASE/electrode/current collector,  $R_{cont}$ , and the current leakage resistance through the BASE brazes,  $R_{leak}$ .

Internal electric losses in an AMTEC are comprised of ohmic losses (BASE tubes ionic resistances, contact losses between BASE/electrode/current collector, and resistances of current collectors and connecting leads), leakage current between anode and cathode electrodes through the BASE braze joint, and concentration and charge-exchange polarization losses in the cathode electrode. The latter are characterized by the charge-exchange current coefficient  $B$ , which affects the Nernst voltage developed across the BASE due to the isothermal, electrochemical expansion of Na ions through the BASE. Polarization losses increase logarithmically with the cell current, reducing the voltage differential across the BASE. The concentration losses, or effect of increased sodium vapor pressure at the BASE/cathode electrode interface, increase with cell current (or sodium flow rate) and temperature of the cell's condenser. The pressure drop across the cathode electrode is characterized by a dimensionless "geometric" factor  $G_E$ . Both  $B$  and  $G_E$  are characteristics of the type of electrodes used in the cell and are determined experimentally. Typical TiN electrodes have  $B \sim 80$  and  $G_E \sim 50$  (Ryan et al. 1998). The analysis of the test

results of the PX-3G cells indicated that for the individual cells  $B$  could have varied from 64 to 75  $\text{A.K}^{1/2}/\text{Pa.m}^2$ ,  $R_{\text{cont}}$  from 0.06 to 0.12  $\Omega.\text{cm}^2$ , and  $R_{\text{leak}}$  from 1.3 to 6.0  $\Omega$ .

The measured and predicted I-V characteristics and electric power outputs of the best performing PX-3G cell (cell #1) are shown in Figures 15.4 and 15.5. The cell delivered a peak electric power of 3.71  $\text{W}_e$  at a load voltage,  $V_L = 2.2$  V, when tested at hot and cold side temperatures of 1123 K and 553 K, respectively. The agreement of APEAM's predictions with measurements in these figures was for  $B = 75 \text{ A.K}^{1/2}/\text{Pa.m}^2$ ,  $R_{\text{cont}} = 0.06 \Omega.\text{cm}^2$ , and  $R_{\text{leak}} = 3.0 \Omega$ , with  $G_E = 50$ . These values are used in all subsequent analyses for all cells with TiN electrodes. The focus of these analyses is to investigate the effect of different design changes on the performance parameters of PX-3G type cell. The subsequent section will investigate the effects of changing the cell diameter and the numbers and length of the BASE tubes on the cell performance.

#### 15.4 IMPROVED DESIGN OF PX-3G TYPE CELL

The analyses in this section were performed at an input thermal power  $Q_{\text{in}} = 40$  W per cell. This power equals that at EOM in a OSC-type PX-generator consisting of 10 PX-3G type cells and a stack of two GPHSs of fresh-fuel, assuming a thermal efficiency of 91%. Each GPHS module provides 250 W at BOM, decreasing to 220 W at EOM. The cold end temperature was kept constant at 640 K and the terminal voltage per cell was kept constant at 2.8 V. At such output voltage the electric power figures listed in table 15.1 were below their peak values. At these operating conditions, cell #1 in Table 15.1 produced 6.09  $\text{W}_e$  at an efficiency of 15.2%. However, the temperature of the BASE tubes' brazes was 1203 K, above the recommended 1123 K limit for the TiNi brazes (Merrill et al. 1998, Sievers et al. 1998). Also, the relatively high evaporator temperature ( $T_{\text{ev}} = 1088$  K) would probably cause the flow of liquid sodium in the return wick to be capillary limited (Table 15.1). The PX-3A cell tested earlier at AFRL/PS, however, had operated successfully at an evaporator temperature of  $\sim 1050$  K and electric current of  $\sim 2$  A (Merrill et al. 1998). Thus, it is reasonable to use  $T_{\text{ev}} = 1050$  K as an operation limit for similar cells that use current felt-metal evaporator wicks (Sievers et al. 1998). Table 15.1 also shows that the cell #1 had a relatively small temperature margin,  $\Delta T = +8$  K. A negative  $\Delta T$  should be avoided since it raises the possibility of sodium vapor condensation inside the BASE tubes, potentially shorting them.

Design changes investigated, which aimed at improving the cell performance, increasing the temperature margin, and lowering the metal-to-ceramic brazes and evaporator temperatures, included increasing the number of BASE tubes, surface area of BASE electrodes, and thermal conductance of the hot plenum of the cell and of the BASE tubes. Also investigated was the effect of replacing the SS thermal shield with a nickel shield. Results indicated that increasing the number of BASE tubes from 6 to 7 slightly reduced the performance of the cell, but decreased the temperatures of the brazes and the evaporator by 30 K and 45 K, respectively (cell #2 in Table 15.1). As a result, this cell had a much higher temperature margin,  $\Delta T = +28$  K, than cell #1. Increasing the length of the BASE tubes to 50.8 mm (2") and of the TiN electrodes from 25.4 mm to 38.1 mm (i.e., increasing the electrodes surface area per tube by 50%, from 6 to 9  $\text{cm}^2$ ) increased the cell electric power output by 6% (or 370  $\text{mW}_e$ ) to 6.37  $\text{W}_e$ , the cell efficiency by



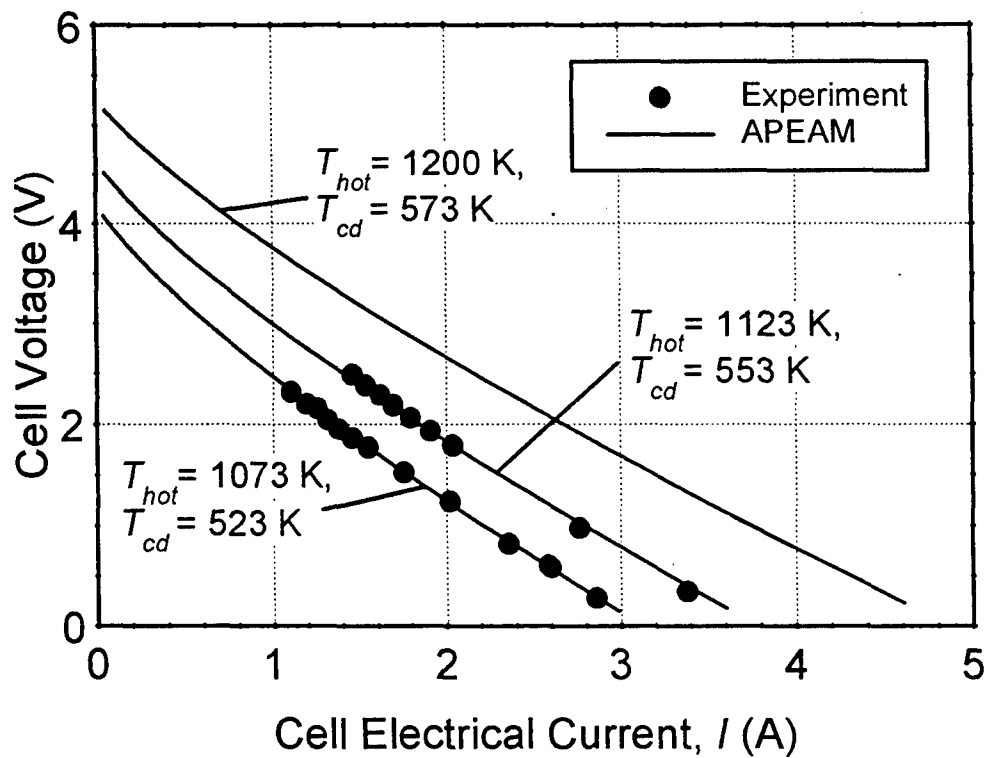


Figure 15.4. I-V Characteristic of Cell Design #1.

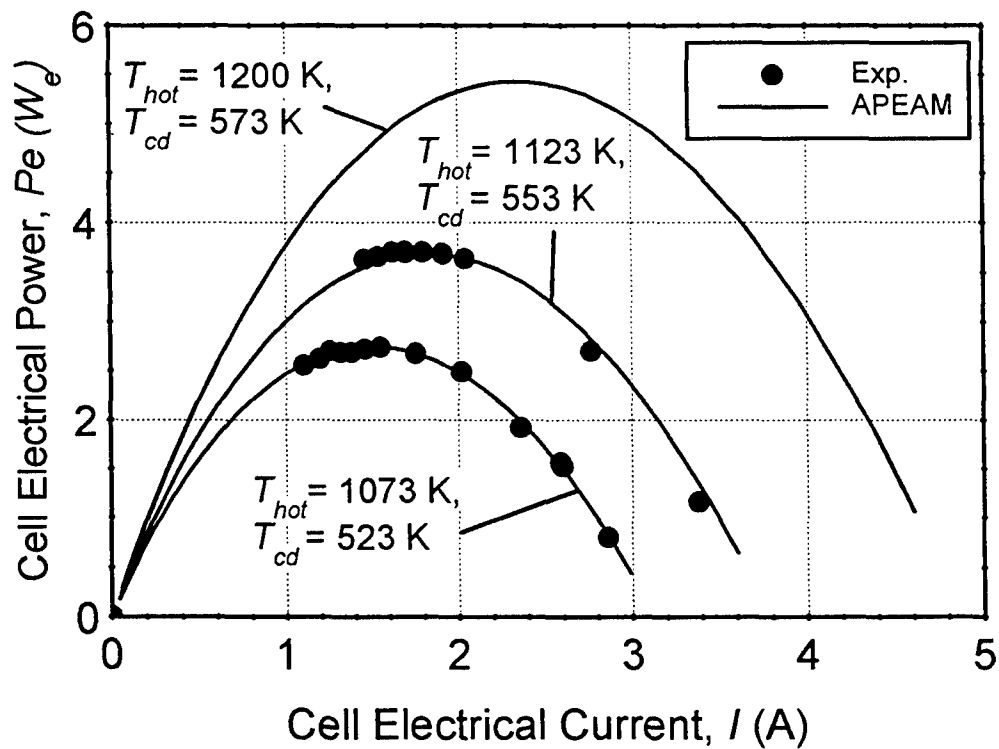


Figure 15.5. Electrical Power of Cell Design #1.

Table 15.1. Predicted Performance of Improved PX-3G Type Cell Design ( $Q_{in} = 40$  W,  $T_{cond} = 640$  K, and  $V_L = 2.8$  V).

<b>Cell Design:</b>	<b>#1 (*)</b>	<b>#2</b>	<b>#3</b>	<b>#4</b>	<b>#5</b>	<b>#6</b>	<b>#7</b>	<b>#8</b>	<b>#9</b>
Cell length (mm)	101.6	101.6	101.6	101.6	101.6	101.6	101.6	101.6	<b>127</b>
Number of BASE tubes	6	7	7	7	7	7	7	7	7
BASE tube length (mm)	40.0	40.0	<b>50.8</b>	50.8	50.8	50.8	50.8	50.8	50.8
Electrode length (mm)	25.4	25.4	<b>38.1</b>	38.1	38.1	38.1	38.1	38.1	38.1
Collector wire diam. ( $\mu$ m)	163	163	163	163	163	163	163	<b>326</b>	326
<b>Radiation shield</b>	SS	SS	SS	Ni	Ni	Ni	Ni	Ni	Ni
<b>Hot-side structure</b>	SS	SS	SS	SS	Ni	Ni	Ni	Ni	Ni
<b>Evaporator wick</b>	SS	SS	SS	SS	Ni	Ni	Ni	Ni	Ni
<b>Cold-side wall</b>	SS	SS	SS	SS	Ni	Ni	Haynes	Haynes	Haynes
<b>Liquid-return wick</b>	SS	SS	SS	SS	Ni	Ni	Haynes	Haynes	Haynes
Evaporator standoff	SS	SS	SS	SS	Ni	Ni	Ni	Ni	Ni
Nickel standoff rings (mm)	1.25	1.25	1.25	1.25	1.25	<b>none</b>	none	none	none
<b>Cell Performance:</b>									
Electric power ( $W_e$ )	6.09	6.0	6.37	6.56	5.88	5.63	6.80	6.67	6.98
Cell efficiency (%)	15.2	15.0	15.9	16.4	14.7	14.1	17.0	16.7	17.5
<b>Temperatures:</b>									
Hot side, $T_{hot}$ (K)	1240	1209	1190	1194	1115	1148	1168	1161	1166
BASE tubes' brazes (K)	<b>1203</b>	<b>1173</b>	<b>1155</b>	<b>1159</b>	1093	1122	1142	1133	1137
Electrode hot end (K)	1150	1121	1112	1117	1059	1084	1105	1096	1099
Electrode cold end (K)	1098	1073	1042	1049	1009	1027	1049	1062	1065
Evaporator, $T_{ev}$ (K)	<b>1088</b>	1043	1014	1016	1031	1009	1025	1016	1022
Margin, $\Delta T$ (K)	<b>+8</b>	<b>+28</b>	<b>+26</b>	<b>+31</b>	<b>-24</b>	<b>+16</b>	<b>+22</b>	<b>+44</b>	<b>+41</b>

(\*) PX-3G cell #1 in the vacuum tests of the ground-demo system.

0.9% points to 15.9%, and at the same time decreased the brazes and evaporator temperatures by an additional 18 K and 29 K, to 1155 K and 1014 K, respectively (cell #3 in Table 15.1).

The effect of replacing the SS radiation shield with a Ni shield is indicated in Table 15.1 by comparing the performance parameters of cells #3 and #4. The higher reflectivity of Ni ( $\epsilon = 0.09 - 0.13$ , versus  $0.24 - 0.31$  for SS) reduced parasitic heat losses, increasing the cell efficiency to 16.4%, and the hot side temperature, BASE tubes' braze temperature and temperature margin by 4 K each. The cell electric power output also increased by an additional 3% (or 190 mW<sub>e</sub>) to 6.56 W<sub>e</sub>. Another advantage of using nickel instead of SS as the structure material is the reduction of the performance degradation of the cell during the mission lifetime. Recent lifetime acceleration tests and corrosion studies have shown that SS is not suitable for use in long-term space missions (Alger 1997, Svedberg et al. 1997). The iron dissolved from SS by liquid sodium in the condenser mesh pad can rapidly saturate liquid sodium in the return wick, and hence precipitate at the intake of the return wick, gradually decreasing its permeability. Also, volatile Mn, Cr and Fe from the SS at the hot end of the cell would contaminate the TiN electrodes,

degrading their performance, and could increase the leakage current between anode and cathode electrodes, through the brazes.

To alleviate these concerns, in cell # 5 nickel was substituted for SS as the structure material. Nickel increased the thermal conductance of the hotter portion of the cell's structure (which includes the cell's hot plate, conduction stud, BASE tubes support plate, the side wall facing the BASE tubes, and the evaporator standoff, see Figure 15.1) by a factor of 2.5. As a result,  $T_{hot}$  decreased by 79 K, and the BASE tubes' braze temperature decreased by 66 K, and the temperature drop across the BASE braze joints was only 22 K. The much higher thermal conductance of the nickel evaporator standoff, however, raised the evaporator temperature by 15 K, and decreased the BASE temperature by  $\sim 40$  K, resulting in a negative temperature margin,  $\Delta T = -24$  K. Substituting Ni for SS also increased the internal heat losses in the cell. Even though the parasitic radiation heat losses in the cell decreased (Ni has lower emissivity than SS), the conduction losses through the 0.101 mm-thick (4 mil) colder portion of the sidewall increased by a factor of  $\sim 2.5$ , decreasing the cell electrical power output by  $\sim 10\%$ , from 6.56  $W_e$  to 5.88  $W_e$ , and the cell efficiency by 1.7 points. Removing the Ni rings around the evaporator standoff decreased the cell electric power output by an additional 250 m $W_e$ , to 5.63  $W_e$ , and the cell efficiency by 0.6% points, to 14.1% (cell #6 in Table 15.1), but increased the temperature margin by 40 K, to  $\Delta T = +16$  K.

When Haynes-25, which has 25% lower thermal conductivity than SS-316, was used for the colder portion of the sidewall and in the liquid-return wick, the conduction heat losses in the wall were reduced by a factor of  $\sim 2.5$ , increasing the cell electrical power output by 1.2  $W_e$ , to 6.8  $W_e$ , and the cell efficiency by 3 points, to 17% (cell #7 in Table 15.1). The hot side temperature, however, increased by about 20 K, causing the BASE tubes' braze temperature to increase to 1142 K, slightly above the recommended operation limit of 1123 K for TiNi brazes. Haynes-25 is a cobalt-based alloy (50% Co, 20% Cr and 1.5% Mn). Because of the volatility of Cr and Mn at evaporator wall temperature  $> 1023$  K, Haynes-25 is not suitable for long-term operation, unless the cell design insures that the evaporator temperature remains below 1023 K (cell #7 in Table 15.1).

Figure 15.6a shows the calculated temperatures along the BASE tubes in cell #7. Because of the low conductance of the alpha-alumina in the brazes and of the BASE material (beta"-alumina), there was a 37 K temperature drop between the hot braze and the electrode. The temperature drop along the current collector/electrode was 55 K. To increase the temperature margin in the cell, the temperature drop along the BASE tubes was decreased by doubling the wire diameter of the 60-mesh (Mo) current collectors in the cell (design #8). The temperature drop along the current collector decreased by 21 K, lowering the BASE brazes' temperature by 9 K and increasing  $\Delta T$  by 22 K, to +44 K (Fig. 15.6b, and cell #8 in Table 15.1). The slightly lower evaporator temperature decreased the cell electric power output by  $\sim 1.9\%$ .

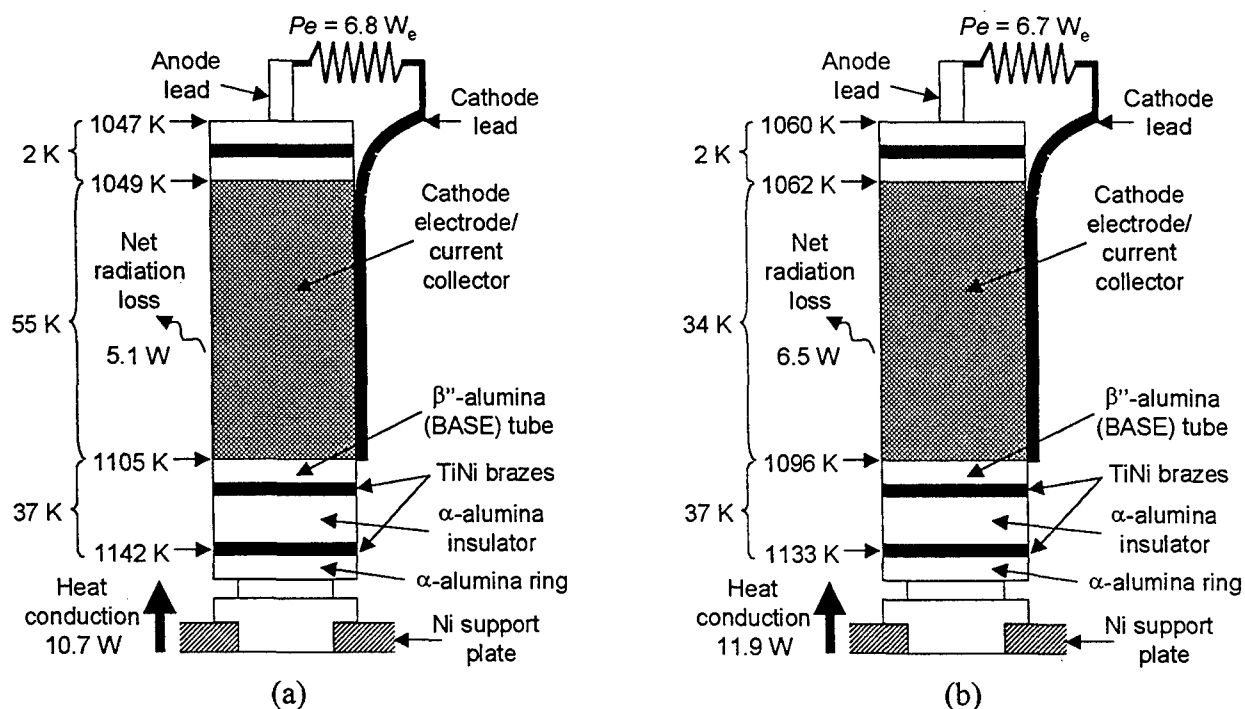


Figure 15.6. Predicted Temperatures and Heat Flow in the Cell's BASE Tubes. (a) Cell Design #7; (b) Cell Design #8.

Finally, the effect of increasing the cell length was investigated. Results showed that for given number and length of BASE tubes and a given cell diameter, increasing the cell length decreased the radiation and conduction parasitic losses, increasing the cell efficiency and electrical power output. This result is clearly illustrated in Table 15.1 by comparing the performance parameters of cells #8 and #9. In the latter, the cell length was increased by 25%, from 101.6 mm (4.0") to 127 mm (5.0"). The reduction in parasitic heat losses increased the evaporator and electrodes temperatures by only  $\sim 4$  K, but the cell electric power output increased by  $\sim 5\%$ , to  $6.98 W_e$  at an efficiency of 17.5%, without exceeding the current temperature limit of the evaporator (1023 K). However, the temperature of the BASE brazes (1137 K) was slightly above the limit for the TiNi braze filler material (1123 K). Nonetheless, cell design #9 is a significant improvement over design #1; it delivers 14.6% (or 890 mW<sub>e</sub>) more electric power ( $6.98 W_e$ ), and 2.3 points higher efficiency (17.5%). At the same time, the BASE tubes' brazes and evaporator temperatures were 66 K lower, while the temperature margin was 33 K higher, to  $\Delta T = +41$  K. The next section investigates the effect of changing the cell diameter, and hence the number of BASE tubes per cell, on the cell performance.

Table 15.2. Design parameters of the Super-Alloy, Multi-Tube AMTEC Cells Investigated in the Present Study.

Design Parameter	Cell A	Cell B	Cell C	Cell D	Cell E
Number of BASE tubes	5	6	7	8	9
Cell diameter (mm) (in.)	31.75 (1.25")	34.93 (1.375")	38.1 (1.5")	41.27 (1.625")	44.45 (1.75")
Diameter of BASE circle (mm)	19.3	21.9	24.5	28.2	32.0
Evaporator standoff O.D. (mm)	7.0	9.3	11.6	13.3	15.0
Estimated cell mass (gm)	123	145	168	192	217

## 15.5 ANALYSIS AND DISCUSSION

The reference cell used in the analyses performed in this section was cell design # 9 in Table 15.1. This cell was 127 mm (5.0") high, used TiN electrodes, had 38.1 mm (1.5") long BASE electrodes, used a 100-mm<sup>2</sup> Ni stud between the hot plate and the BASE tubes' Ni support plate, and a Ni circumferential heat shield. The Ni evaporator standoff was 0.71 mm thick and 12.4 mm long.

As the diameter and number of BASE tubes in the cell were changed, a minimum spacing of ~3.5 mm was maintained between the outer surfaces of any two adjacent BASE tubes, and a spacing of ~2.5 mm was maintained between the BASE outer surface and the sidewall of the cell. Keeping the cell diameter to a minimum for a given number of BASE tubes insured minimum conduction and radiation parasitic heat losses in the cells. Also, the outer diameter of the evaporator standoff was adjusted concomitant with the number of BASE tubes in the cell, in order to insure enough temperature margin ( $\Delta T > 25$  K) in the cells when operated at the same heat input  $Q_{in}$ . Relevant design parameters of the cells investigated in this section are listed in Table 15.2.

### 15.5.1 Effect of Condenser Temperature

Figures 15.7 and 15.8 show the effect of changing the condenser temperature on the performance of cell B in Table 15.2. The heat input to the cell,  $Q_{in} = 25.6$  W, corresponded to EOM cell power input in an AMPS-type PX-generator comprised of 24, type B cells and a stack of three, fresh-fuel GPHSs, with a thermal efficiency of 93%. As Figure 15.7 indicates, increasing the cell's load resistance (or load voltage) from  $R_L = 1.0 \Omega$  to  $1.5 \Omega$  significantly increased its efficiency, but negligibly affected the sodium vapor pressure at the BASE/cathode interface (Figure 15.8). At  $R_L = 1.5 \Omega$ , the cell efficiency peaked at  $T_{cond} = 650$  K (Figure 15.7). Below 650 K, increasing the condenser temperature decreased both the parasitic radiation losses and the conduction heat losses (through the cell sidewall and the liquid-return wick) to the condenser, resulting in a net increase in the cell efficiency and electrical power output. This trend held true so long as the sodium vapor pressure at the condenser temperature was low enough, as not to significantly increase the Na vapor at the BASE/cathode interface, which was the case when  $T_{cond}$

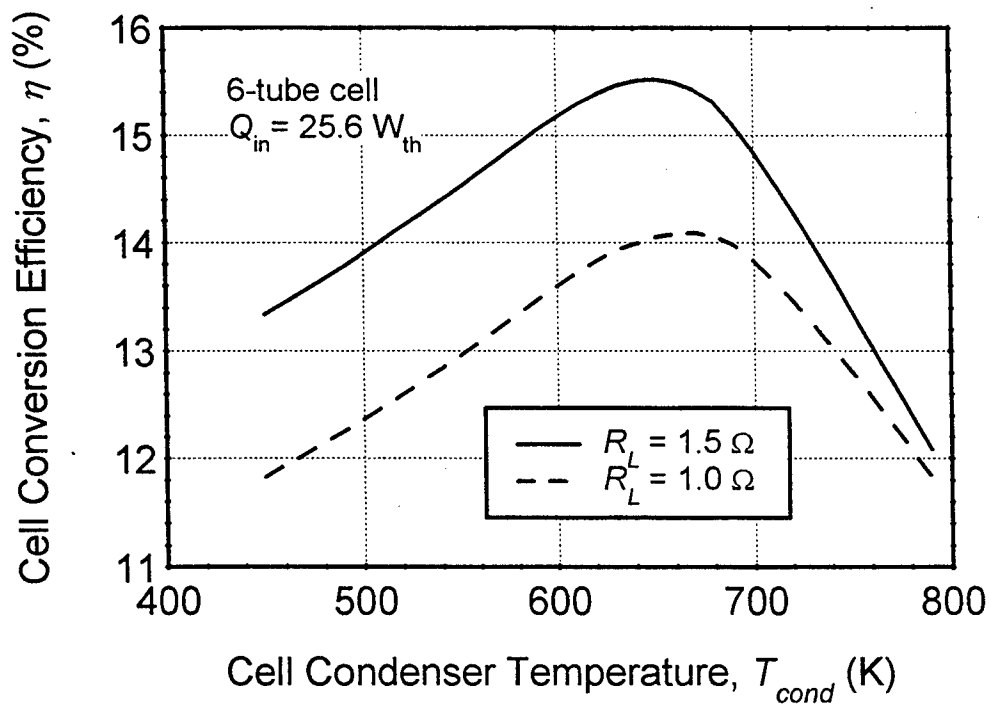


Figure 15.7. Effect of Condenser Temperature on Conversion Efficiency of Cell B.

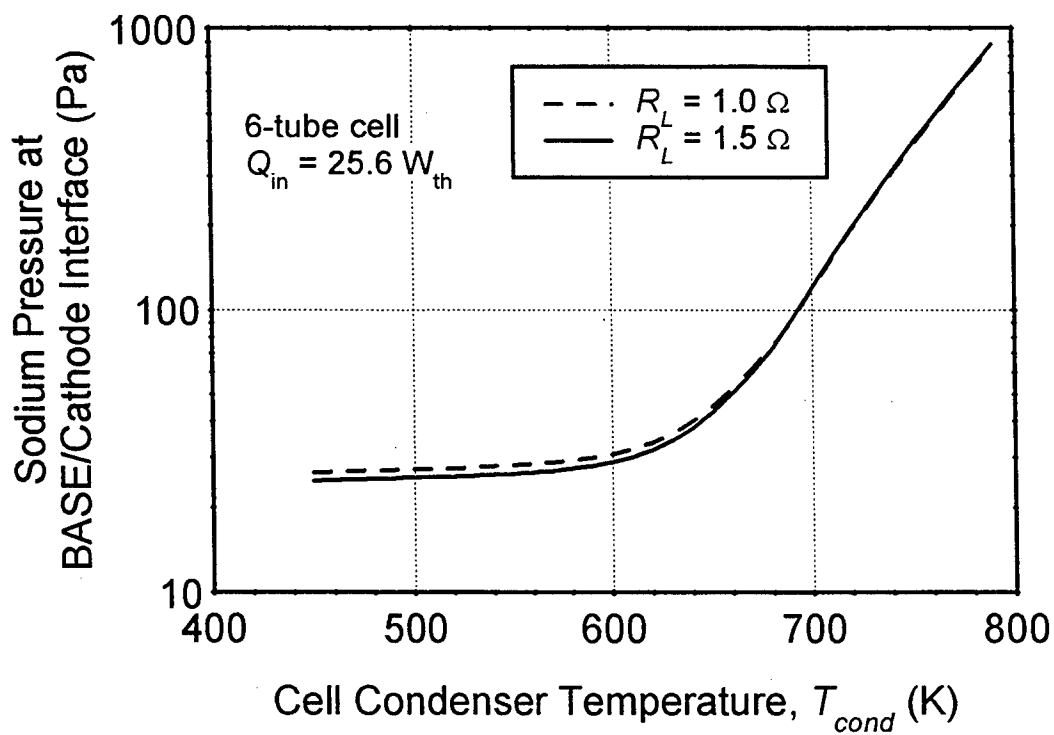


Figure 15.8. Effect of Condenser Temperature on Sodium Vapor Pressure on Cathode Side of the BASE in Cell B.

< 600 K (Figure 15.8). Above 600 K, however, the Na vapor pressure increases exponentially with temperature; it is 5 Pa, 10 Pa, 25 Pa, and 41 Pa at 600 K, 620 K, 650 K and 667 K, respectively. The Na vapor pressure at the BASE/cathode interface equals that corresponding to the condenser temperature plus the pressure losses due to Na vapor flow in the low-pressure cavity of the cell, between the BASE/cathode interface and the condenser (see Chapter 3).

Therefore increasing the condenser temperature beyond 600 K increased the Na vapor pressure at the BASE/cathode interface (Figure 15.8), reducing the Nernst potential due to the isothermal expansion of Na ions through the BASE. The cell performance peaked at  $T_{cond} = 650$  K, as the decrease in the cell efficiency and electric power output due to the decrease in the Nernst voltage equals the increase due to the reduced parasitic radiation and conduction losses in the cell. At  $T_{cond} = 650$  K and  $R_L = 1.5 \Omega$ , the cell efficiency peaked at 15.5% (Figure 15.7), where  $Pe = 3.97 W_e$ ,  $I = 1.63$  A, and the load voltage  $V_L = 2.44$  V. Also, the Na vapor pressure at the condenser was 25 Pa, and the vapor pressure losses in the low-pressure cavity of the cell totaled 18 Pa, causing the vapor pressure at the BASE/cathode interface to reach 43 Pa. The pressure drop in the low-pressure cavity of the cell corresponded to an effective dimensionless factor  $G = 210$  (Figure 15.8). Increasing the condenser temperature beyond 650 K resulted in a net decrease in cell efficiency, due to the rapid decrease in the cell's Nernst voltage.

Figure 15.7 also shows that lowering the external load resistance (or load voltage) to  $1.0 \Omega$  decreased the cell efficiency, due to the increase in the internal electric losses caused by the higher cell current. The cells' peak efficiency also shifted to a slightly higher condenser temperature,  $T_{cond} = 667$  K, where  $Pe = 3.6 W_e$ ,  $I = 1.9$  A, and  $V_L = 1.9$  V. The cell's higher electric current corresponded to a higher sodium mass flow rate, which slightly increased the pressure losses in the low-pressure cavity, and the sodium vapor pressure at the BASE/cathode interface (Figure 15.8). The combined effects of lower Nernst voltage and higher internal electric losses at low load resistance caused the cell efficiency and electric power output to decrease (Figure 15.7).

Results of similar analyses of the C-, D- and E-type cells, at various values of  $Q_{in}$  and typical load voltage in a PX-generator design, have shown that the optimum condenser temperature, corresponding to the cell's peak efficiency, varied between 640 K and 670 K. Based on these results, the lower condenser temperature,  $T_{cond} = 640$  K was selected and kept constant in the following system analyses, in order to maintain the hot side temperature of the cells as low as possible.

### 15.5.2 PX-Power Systems Integration Options

In the following analyses, the multi-cell PX-electric power generators were designed to provide a constant output voltage of 28 V d.c. and generate at least 156  $W_e$  at EOM, or 130  $W_e$  at EOM assuming a 20% decrease in the electric performance of the cells after a 15-year operation lifetime. The later figure is not necessarily accurate, but might be considered as a design goal, until a more reliable figure can be justified.

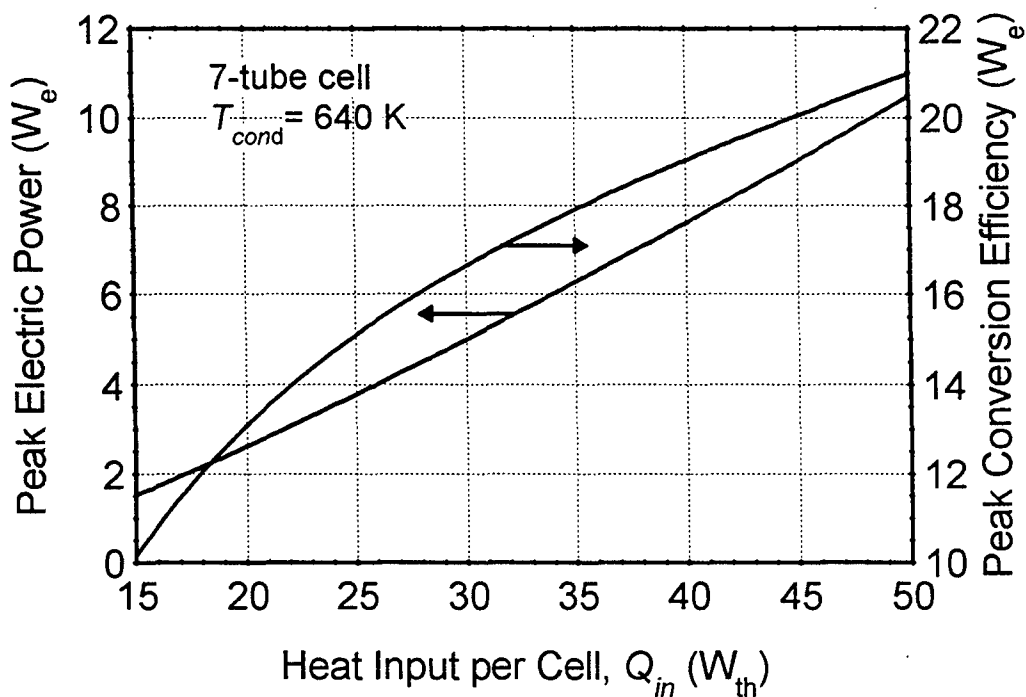


Figure 15.9. Peak Electric Power and Peak efficiency of Cell C.

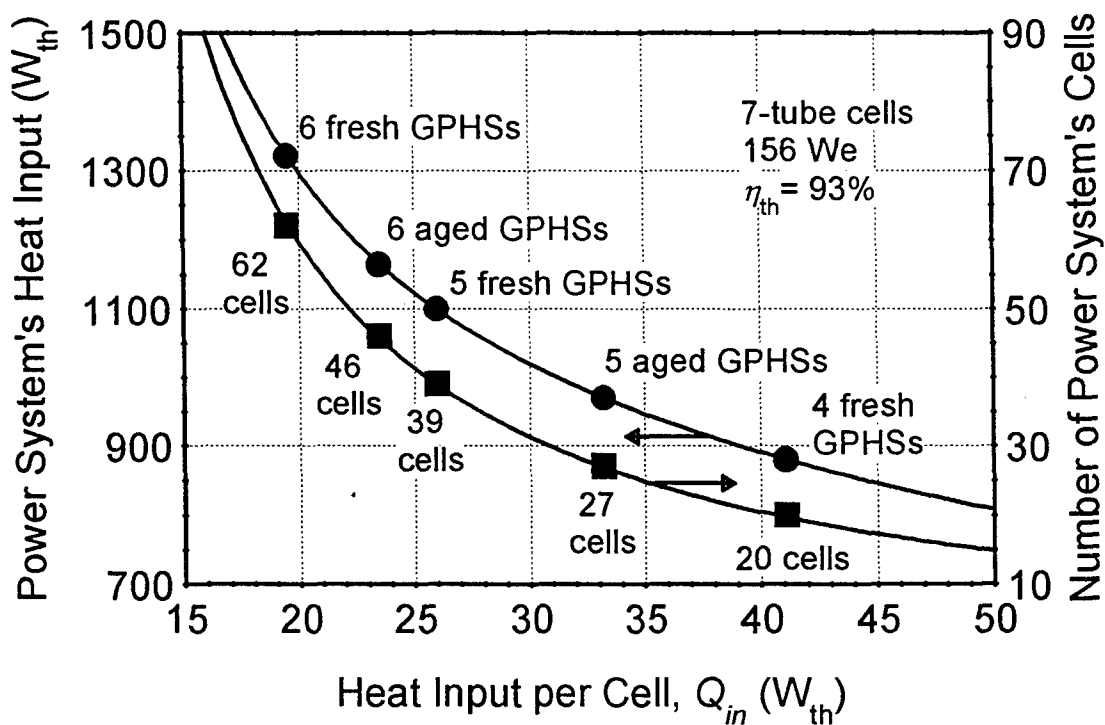


Figure 15.10. Number of C-Type Cells and Total Thermal Energy Requirements for a Power System Generating  $156 W_e$  @ EOM.



The system configuration selected in the present analysis is that of AMPS (Figure 15.3). In this configuration, highly conductive, 1 mm-thick TZM plates are mounted on the 4 sides of the GPHS stack to ensure a uniform hot side temperature for the cells. Analyses are performed at a constant heat input per cell, whose value depends upon the number of GPHS modules and cells used in the generator. The generator is assumed to have a thermal efficiency of 93% (Hendricks et al. 1997 and 1998). The cell sidewall is separated from the surrounding Min-K insulation by a small gap to reduce parasitic heat losses from the wall. A typical C-type cell subjected to a heat input  $Q_{in} = 25.6$  W would lose  $\sim 2$  W to the surrounding Min-K insulation. These wall radiation losses increase with increasing  $Q_{in}$  and, to a lesser extent, with increasing cell diameter. The excess heat from the cells' condenser is radiated to space from the outer surface of the generator housing. Assuming a low and conservative surface emissivity of 0.25, the housing surface area was found large enough, in all cases, to radiate the excess heat at a surface temperature below 600 K. To insure a near-optimum cell condenser temperature,  $T_{cond} = 640$  K at EOM, an alumina or zirconia washer of appropriate thickness is inserted between the cell's cold end and the generator housing. For example, a generator consisting of a stack of 6 fresh-fuel, GPHS modules and 48, B-type cells would have a beryllium housing surface area of  $0.689$  m<sup>2</sup> that could radiate 1132 W of excess heat to space at a temperature of 583 K, a temperature that is 57 K lower than  $T_{cond}$ .

Results delineated in Figure 15.9 show that the C-type cell's peak electric power output increased almost linearly with  $Q_{in}$ . In the range of  $Q_{in}$  of interest, the cell's peak efficiency also increased, but at a rate decreasing with increasing  $Q_{in}$ . When  $Q_{in} = 29.1$  W, the cell's electric power output peaked at  $4.7$  W<sub>e</sub>, and the cell efficiency peaked at 16.3%. As indicated earlier, the PX-power systems are being designed herein to provide at least 156 W<sub>e</sub> at EOM. Assuming that the improved AMTEC cells would operate near their peak electric power point, the number of cells needed in the generator was obtained by dividing 156 W<sub>e</sub> by the cell's peak power at EOM. The corresponding thermal energy requirement (or number of GPHS modules needed for the generator) was obtained by multiplying the number of cells by the cell's heat input, divided by the thermal efficiency of the generator,  $\eta_{th} = 93\%$  (Figure 15.10). The number of GPHS modules used and the way they are thermally integrated to the cells determines the number of cells needed in a PX-generator. Therefore, the results presented in Figure 15.10 for the C-type cells are provided only for illustration purpose.

The results of integrating the different cell designs in Table 15.2 to the GPHS modules in the PX-electric power system are summarized in Tables 15.3 and 15.4. As indicated in Table 15.3, the PX-generator heat input depends on the number of GPHS modules used. A fresh-fuel GPHS module provides 250 W at BOM, and 220 W at EOM. An aged-fuel GPHS module, originally assembled in 1982 as spares for the Galileo mission, provides 218 W at BOM and 194 W at EOM (Schock et al. 1997b).

Figure 15.10 shows that several combinations of GPHS modules and C-cells could provide the heat input and satisfy the electrical power requirements for the PX-mission. If a heat source that consists of 6 fresh-fuel GPHS modules (providing 1320 W at EOM) is integrated to  $4 \times 15 = 60$  cells, the power system would provide  $\sim 156$  W<sub>e</sub> at EOM, but would be quite heavy. It will have

Table 15.3. Predicted Performance of PX-Power Systems with 6 Fresh-Fuel GPHS Modules and 48 Cells ( $V_L = 28$  V).

Power System Design	#1		#2		#3		#4		#5	
Type of AMTEC cells	<b>A</b>		<b>B</b>		<b>C</b>		<b>D</b>		<b>E</b>	
Power system mass (kg)	1 x <b>26.69</b>		1 x <b>27.71</b>		1 x <b>28.75</b>		1 x <b>29.80</b>		1 x <b>30.86</b>	
(3-GPHS generator units)	(2 x 14.48)		(2 x 14.99)		(2 x 15.51)		(2 x 16.04)		(2 x 16.57)	
<b>System Performance:</b>	BOM	EOM	BOM	EOM	BOM	EOM	BOM	EOM	BOM	EOM
Total heat input (W)	1500	1320	1500	1320	1500	1320	1500	1320	1500	1320
Thermal efficiency (%)	93.0%	93.0%	93.0%	93.0%	93.0%	93.0%	93.0%	93.0%	93.0%	93.0%
Heat input per cell (W)	29.1	25.6	29.1	25.6	29.1	25.6	29.1	25.6	29.1	25.6
Total power output ( $W_e$ )	241	<b>202</b>	224	<b>188</b>	207	<b>174</b>	189	<b>159</b>	172	<b>145</b>
Overall efficiency (%)	16.1%	15.3%	14.9%	14.3%	13.8%	13.2%	12.6%	12.0%	11.5%	11.0%
Specific power ( $W_e/kg$ )	9.0	<b>7.6</b>	8.1	<b>6.8</b>	7.2	<b>6.1</b>	6.3	<b>5.3</b>	5.6	<b>4.7</b>
(3-GPHS generator units)	(8.3)	(7.0)	(7.5)	(6.3)	(6.7)	(5.6)	(5.9)	(5.0)	(5.2)	(4.4)
<b>Temperatures:</b>	BOM	EOM	BOM	EOM	BOM	EOM	BOM	EOM	BOM	EOM
Cell top, $T_{hot}$ (K)	1199	1163	1131	1099	1079	1049	1043	1014	1011	985
BASE tubes' brazes (K)	<b>1171</b>	1138	<b>1107</b>	1078	<b>1059</b>	1032	<b>1025</b>	999	<b>995</b>	973
Evaporator, $T_{ev}$ (K)	<b>1052</b>	1032	<b>1006</b>	987	<b>971</b>	953	<b>942</b>	925	<b>918</b>	904
Margin, $\Delta T$ (K)	+42	<b>+36</b>	+34	<b>+30</b>	+34	<b>+30</b>	+34	<b>+30</b>	+35	<b>+30</b>
Condenser, $T_{cond}$ (K)	664	640	665	640	665	640	665	640	664	640

a specific power of 5.1  $W_e/kg$ , that is lower than that of current GPHS-RTGs (5.4  $W_e/kg$ ). A generator with a smaller number of cells, say  $4 \times 12 = 48$  cells (or 2 per side face of each GPHS brick) would provide as much as 174  $W_e$  at EOM (power system #3 in Table 15.3), and would have a higher specific power of 6.1  $W_e/kg$ . When the number of cells in the PX-generator was reduced, the heat input per cell increased, increasing the total electric power output of the generator. However, this also increased the evaporator and the BASE metal-ceramic brazes temperature (Table 15.3).

Table 15.3 shows the performance results of PX-power systems, each employing 6 fresh-fuel GPHS modules and 48 cells connected electrically in 4 parallel strings of 12 cells each. In order to provide the required load voltage of 28 V, each cell must provide a voltage of 2.33 V. If C-type cells were used, the power system would provide 174  $W_e$  at EOM at an overall efficiency of 13.2% and +30 K temperature margin (power system #3 in Table 15.3). The cells would operate at quite low BASE braze and evaporator temperatures of 1059 K and 971 K at BOM, respectively, which is a plus for minimizing the cell performance degradation over the long mission lifetime of 15 years. Furthermore, the generator performance could degrade by as much as 34% over the mission duration, and the power system would still provide 130  $W_e$  at EOM.

A 6-GPHS power system would weight 28.75 kg and have a specific power of 6.1  $W_e/kg$  at EOM. This power system could also be designed as two 3-GPHS units connected in parallel, each unit comprised of 2 parallel strings of 12 cells each and providing 87  $W_e$  at 28 V d.c. at EOM. However, the resulting power system would be slightly heavier ( $2 \times 15.51 = 31.02$  kg) and

Table 15.4. Predicted Performance of the Top Performing PX-Power Systems in this Study ( $V_L = 28$  V).

Power System Design	#3		#6		#2		#7		#8	
# of GPHS modules	6 fresh-fuel		5 fresh-fuel		6 fresh-fuel		5 fresh-fuel		4 fresh-fuel	
Type of AMTEC cells	C		E		B		B		D	
Number of cells	48		32		48		28		16	
Number of parallel strings	4		4		4		2		2	
Voltage per cell (V)	2.33		3.5		2.33		2.0		3.5	
Power system mass (kg)	1 x <b>28.75</b>		1 x <b>24.53</b>		1 x <b>27.71</b>		1 x <b>21.66</b>		1 x <b>16.49</b>	
(3-GPHS generator units)	(2 x 15.51)				(2 x 14.99)					
<b>System Performance:</b>	BOM	EOM	BOM	EOM	BOM	EOM	BOM	EOM	BOM	EOM
Total heat input (W)	1500	1320	1250	1100	1500	1320	1250	1100	1000	880
Thermal efficiency (%)	93.0%	93.0%	93.0%	93.0%	93.0%	93.0%	93.0%	93.0%	93.0%	93.0%
Heat input per cell (W)	29.1	25.6	36.3	32.0	29.1	25.6	41.5	36.5	58.1	51.2
Total power output ( $W_e$ )	207	<b>174</b>	184	<b>156</b>	224	<b>188</b>	189	<b>161</b>	181	<b>156</b>
Overall efficiency (%)	13.8%	13.2%	14.7%	14.2	14.9%	14.3%	15.1%	14.6	18.1%	17.7
Specific power ( $W_e/kg$ )	7.2	<b>6.1</b>	7.5	<b>6.4</b>	8.1	<b>6.8</b>	8.7	<b>7.4</b>	11.0	<b>9.5</b>
(3-GPHS generator units)	(6.7)	(5.6)			(7.5)	(6.3)				
<b>Temperatures:</b>	BOM	EOM	BOM	EOM	BOM	EOM	BOM	EOM	BOM	EOM
Cell top, $T_{hot}$ (K)	1079	1049	1092	1064	1131	1099	1202	1162	1242	1204
BASE tubes' brazes (K)	<b>1059</b>	1032	<b>1071</b>	1045	<b>1107</b>	1078	<b>1169</b>	1134	<b>1205</b>	1171
Evaporator, $T_{ev}$ (K)	<b>971</b>	953	<b>995</b>	978	<b>1005</b>	987	<b>1015</b>	994	<b>1080</b>	1058
Margin, $\Delta T$ (K)	+34	<b>+30</b>	+21	<b>+17</b>	+35	<b>+30</b>	+67	<b>+61</b>	+33	<b>+29</b>
Condenser, $T_{cond}$ (K)	665	640	665	640	665	640	664	640	668	640

have a lower specific power (5.6  $W_e/kg$  at EOM, see Table 15.3) than a 6-GPHS power unit. A mass breakdown of the PX- power system #3 can be found in Table 15.5, for both the 6-GPHS unit and the 3-GPHS unit. The system masses in Tables 15.3, 15.4 and 15.5 include: the GPHS modules (1.44 kg each), the 1 mm-thick TZM hot plates, the AMTEC cells, the cells' mounting structure (50 gm per cell), the multifoil and Min-K insulations, and the beryllium generator housing (assumed 1.66 mm-thick). The multifoil insulations are made of 7.6  $\mu m$ -thick (0.3 mil-thick) molybdenum foils spaced with zirconia particles. Seventy foils are used in the radial insulation around the cells, while 100 foils are used in the axial (top and bottom) insulation (Figure 15.3). Finally, a provision of 0.3 kg was made to account for the masses of the spacecraft mounting bracket, pressure relief valve, and support structure (such as  $ZrO_2$  studs, bolts, and electrical connectors).

Table 15.3 and Figures 15.11 and 15.12 also show the effect of changing the cell design on the performance of power system #3. A cell with a smaller number of BASE tubes, subjected to the same heat input, would provide a higher peak power, and operate at higher evaporator ( $T_{ev}$ ) and BASE tubes' braze ( $T_{braz}$ ) temperatures, since the heat input per BASE tube would increase, but each BASE tube would also have to provide a higher voltage. A power system consisting of 6 fresh-fuel GPHS modules and 48 B-type cells (power system #2, Table 15.3) would provide 14  $W_e$  more at a 1.1 points higher efficiency at EOM than power system #3 which uses C-type cells.

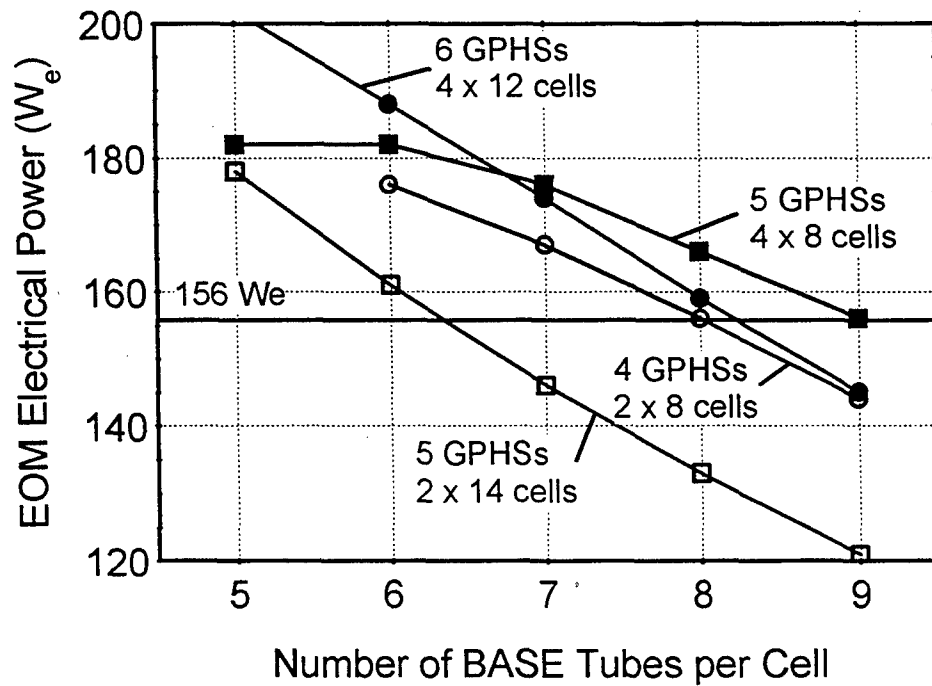


Figure 15.11. Electrical Power of Generators at EOM for Different Cell Designs.

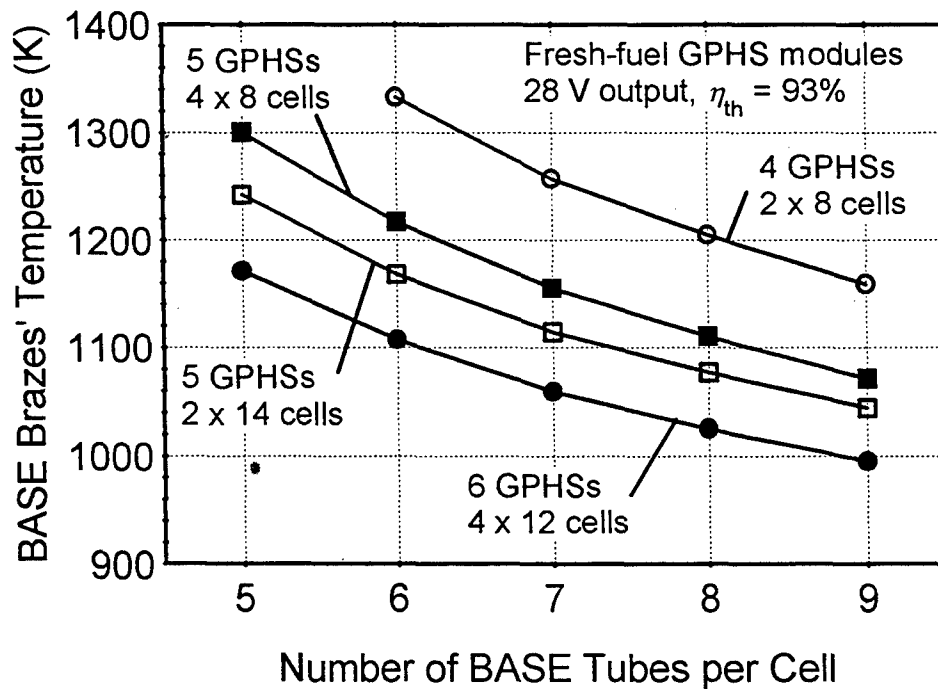


Figure 15.12. BASE Tubes' Braze Temperature at BOM for Different Cell Designs.

Table 15.5. Mass Breakdown of Pluto/Express Power Systems #3 (with C-Type Cells).

# of GPHS modules	3	6
# of C-type cells	24	48
<b>Component masses (kg)</b>		
GPHS modules	4.320	8.640
TZM hot plates	0.618	1.235
AMTEC cells	4.032	8.064
Cells' mounting	1.200	2.400
Top/bottom multifoils	1.003	1.003
Radial multifoils	0.299	0.584
Min-K insulation	2.252	4.402
Beryllium housing	1.485	2.122
Miscellaneous	0.300	0.300
<b>TOTAL MASS (kg)</b>	<b>15.509</b>	<b>28.750</b>

This power system #2 would also be about 1 kg lighter than system #3, resulting in a net 11% increase in specific power (from 6.1 to 6.8 W/kg at EOM). However, the BASE brazes and evaporator in the B-type cells of power system #2 would operate at higher temperatures (48 K and 35 K higher, respectively) than in the C-type cells of system #3.

In summary, a generator using smaller AMTEC cells would provide higher electrical power output (Fig. 15.11) and have a higher specific power than a generator using larger AMTEC cells with more BASE tubes, but at the expense of much higher cell components temperatures (Figure 15.12). In the present analysis, a number of power system integration designs were considered based on the results of Figure 15.10, and generators were selected based on electrical power output, specific power and cell components temperatures. For example, power systems #5 and #4 in Table 15.3 were eliminated because system #5 could not provide 156 W<sub>e</sub> at EOM, while the specific power of system #4 was too low, below that of GPHS-RTGs. Also, power system #1 was eliminated because the cells' evaporator temperature was 37 K higher than that in power system #7 (Table 15.4), which had similar specific power. The fact that system #1 provided 41 W<sub>e</sub> more power than system #7 was not a factor of importance, since this power was very much in excess of the requirements for the Pluto/Express mission. Power system #1 was also 5 kg heavier than generator #7.

The multi-cell power systems selected in this study to power the Pluto/Express mission are collected in Table 15.4, by order of increasing specific power. Power systems #2 and #3 of Table 15.3 appear again in Table 15.4, since they are attractive in terms of electrical power and temperature levels. Their specific power, however, is somewhat low. As shown in Table 15.4, the trend observed earlier still applies. The cells of a generator of higher specific power will generally operate at higher temperatures. Power system #6 in Table 15.4 seems to be a good compromise between higher cell components temperature and lower mass. This generator consists of 5 fresh-fuel GPHS modules and 4 parallel strings of 8, E-type cells each. The 8 cells are uniformly distributed over the TZM plate covering each side of the heat source. This power

system will meet the power requirement of the PX-mission at 28 V output voltage, with provision for a 20% degradation in performance over the duration of the mission. The overall efficiency of power system #6 is comparable to that of system #2, and the E-type cells in system #6 operate at cooler BASE brazes and evaporator temperatures than the B-type cells of generator #2. Even though the specific power of generator #6 is lower (6.4 versus 6.8 W<sub>e</sub>/kg at EOM, Table 15.4), this generator is 3.2 kg lighter than power system #2.

These multi-cell radioisotope power systems are being designed for providing electric power to the Pluto Express (PX) and Europa flyby spacecraft, scheduled for launch early next century. Earlier planetary exploration missions, such as Pioneer, Voyager, Galileo and Cassini, have used Radioisotope Thermoelectric Generators (RTGs). A GPHS-RTG consists of 18 GPHS modules and 572 SiGe-GaP thermoelectric uncouples operating at hot and cold shoe temperatures of 1273 K and 573 K, respectively. The GPHS-RTG weighs 55.9 kg, and provides 305 W<sub>e</sub> at EOM, at an overall efficiency of only 6.8%. For comparison purposes, 2 multi-cell power systems #6 (Table 15.4) would weight about 49 kg, and provide 260 W<sub>e</sub> at EOM (assuming 20% performance degradation) at an overall efficiency of 11.8%. This multi-cell power system would use 10 GPHS modules only, and the 64 E-type cells would operate at hot and cold side temperatures of 1092 K and 665 K, respectively. These characteristics are a very significant improvement over that of the old GPHS-RTGs, considering that we are still years away from benefiting from the full capabilities of AMTEC technology.

Power systems #7 and #8, of much higher power density (7.4 and 9.5 W<sub>e</sub>/kg at EOM, respectively), are also listed in Table 15.4 to illustrate the potential growth of this technology for space power. These generators are much lighter (21.7 and 16.5 kg, respectively) and can provide the required 130 W<sub>e</sub> at 28 V d.c. for the Pluto/Express mission, with provision for a 20% degradation in cell performance over the duration of the mission (15 years). The BASE brazes of the B-type and D-type cells of these generators, however, would operate at the prohibitively high temperatures of 1169 K and 1205 K at BOM, respectively, for the current technology of super-alloy materials.

It is worth mentioning that the selection of a PX-power system operating at much cooler temperatures is recommended, since it would somewhat alleviate the concerns associated with cells performance degradation over the duration of the long-term mission. Also, it would be a safer choice for the upcoming Pluto/Express mission, considering that this would be the first time in the history of space power that such multi-cell power systems will be flown in space. Therefore, the present study recommends the PX-power system design #3 or #6 (Table 15.4). Although these generators have a low specific power (6.1 and 6.4 W<sub>e</sub>/kg at EOM, respectively), they can provide the power requirements for the Pluto/Express mission, with provision for a > 20% degradation in cell performance over the duration of the mission. The BASE brazes and evaporator of the C-type cells in generator #3 (Table 15.4) would operate at the relatively low temperatures of 1059 K (786 °C) and 971 K (698 °C) respectively, compatible with the use of super-alloy materials for long-term missions, while the temperatures in the E-type cells of power system #6 would be about 20 K higher than that in the cells of generator #3.

### 15.5.3 Effect of Cell Length on Generator Specific Power

Results of a previous section have shown that increasing the length of the multi-tube cells reduces the internal radiation and conduction parasitic losses, and increases the cells' conversion efficiency and electrical power output. However, increasing the cells' length also results in increased generator mass (Tables 15.2 and 15.3). Therefore, there exists an optimum cell length which maximizes the generator specific power. All generator analyses described above assumed a 127 mm (5 inch) cell length. A parametric analysis was performed to illustrate the effects of cell length on the electrical power output and specific power of the PX-power system #2 (Table 15.4). Results are shown in Figures 15.13 and 15.14. Even so the generator's power output keeps increasing with increasing cell length (at a rate of about 10  $W_e$  per inch for a 6-GPHS unit), the specific power of the 6-GPHS unit peaks at a value of 6.80  $W_e/kg$ , for a cell length of about 114 mm (4.5 inch). Similar results apply for the 3-GPHS unit generator (Figure 15.14). Note that the peak specific power is very shallow, over the range 4 to 5 inch in cell length. Similar results apply to PX-power systems #3 and #6. A cell length of 4.5 inch is recommended for power system #3, while a cell length of 5 inch should be used for generator #6, since this system provides exactly the design power level of 156  $W_e$  (130  $W_e$  with provision for 20% degradation in cell performance over 15 years). Using a smaller cell length in this power system would reduce its EOM output below 156  $W_e$ .

## 15.6 SUMMARY AND CONCLUSIONS

Vapor anode, multi-tube AMTEC cells are being developed for providing electric power to the Pluto/Express flyby spacecraft, scheduled for launch early next century. The electric power requirement is 130  $W_e$  at 28 V d.c. at EOM. In this work, different design changes were investigated for improving the performance of nickel super-alloy cells for satisfying the EOM electric power requirements for the PX-mission, and various options of integrating the improved super-alloy cells with GPHS modules in the generator configuration proposed by AMPS were explored. The analyses were performed using the AMTEC Performance and Evaluation Analysis Model (APEAM) developed at UNM-ISNPS. Model results had been successfully benchmarked using data of a Pluto/Express generator ground demo of 8 PX-3G cells manufactured by AMPS and tested in vacuum at AFRL (see Chapters 11 and 12).

A number of design changes were examined for improving the performance of PX-3G cells. Analyses performed at an input thermal power  $Q_{in} = 40$  W, cold end temperature,  $T_{cond} = 640$  K and fixed terminal voltage per cell of 2.8 V indicated that a 25% longer (5.0"-long) PX-3G type cell with 7 BASE tubes, 50% longer electrodes (1.5"-long), Mo current collectors of improved thermal conductance, a Ni heat shield, a Ni structure on the hot side, and a Haynes-25 cold side wall, could deliver an electric power of 6.98  $W_e$  at a conversion efficiency of 17.5%. This cell would operate at BASE tubes' brazes and evaporator temperatures of 1137 K and 1022 K, respectively, and a temperature margin  $\Delta T = +41$  K. These performance parameters are a significant improvement over the ground-demo, stainless steel PX-3G cell (890 m $W_e$  more electric power at 2.3 points higher efficiency, 66 K lower BASE tubes' brazes and evaporator temperatures, and 33 K higher temperature margin). Because Haynes-25 contains Cr and Mn

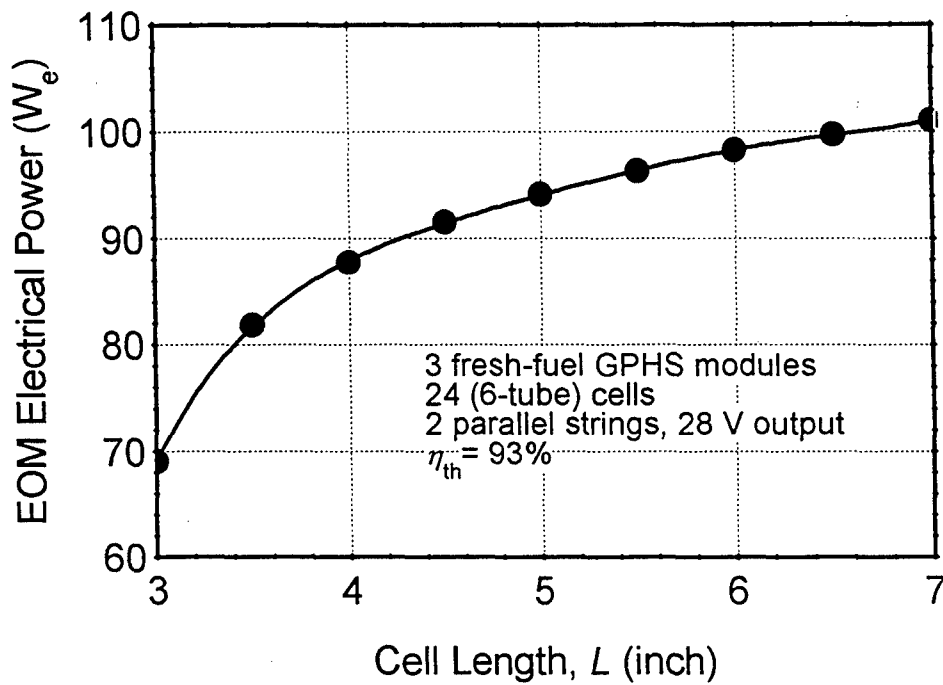


Figure 15.13. Electrical Power of Generator #2 at EOM as a Function of Cell Length.

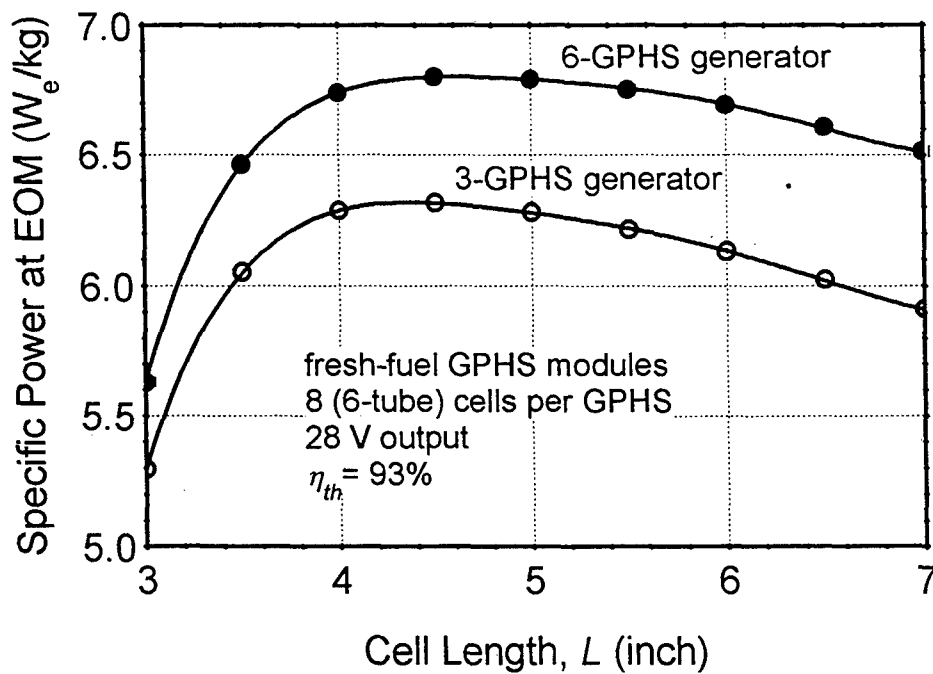


Figure 15.14. Specific Power of Generator #2 at EOM as a Function of Cell Length.



elements, which are volatile at temperature  $> 1023$  K and would contaminate the TiN metal electrodes, and since it is expected that degradation in cell performance would be rapidly accelerated as the operation temperature of the cell increases, the cell and integration designs must insure that the evaporator temperature remains low, below 1023 K.

Next, various options of integrating the improved super-alloy cells with GPHS modules in the generator configuration proposed by AMPS were explored. In this configuration, the cells are mounted onto the 4 sides of the GPHS stack. The AMPS's generator configuration, therefore, does not suffer from the cells' number limitation of the OSC design, and offers greater flexibility in cells' integration and operation conditions. Options explored included changing the number of GPHS modules and the number of cells per generator, using either fresh or aged  $^{238}\text{PuO}_2$  fuel, and varying the number of BASE tubes in the cell by changing the cell diameter. The effects of these design changes on the generator mass and electric power output, as well as on the temperatures of the cells' evaporator and BASE metal-ceramic brazes were also examined.

The PX-radioisotope power systems were designed to provide an output voltage of 28 V d.c. and at least 156  $W_e$  at EOM, or 130  $W_e$  at EOM assuming a 20% decrease in the electric performance of the cells after a 15-year mission lifetime. Super-alloy cells of improved design, with 5 to 9 BASE tubes, were designed for these generators. For a given number of BASE tubes, the cell diameter was kept to a minimum to insure minimum conduction and radiation parasitic heat losses in the cells. Also, the outer diameter of the evaporator standoff was adjusted concomitant with the number of BASE tubes in the cell, in order to insure enough temperature margin in the cells. Assuming a conservative surface emissivity of 0.25, the housing surface area was large enough, in all cases, to radiate the excess heat at a surface temperature below 600 K. Therefore, inserting an alumina or zirconia washer of appropriate thickness between the cell's cold end and the generator housing would insure a near-optimum cell condenser temperature,  $T_{cond} = 640$  K at EOM.

Results showed that when the number of cells in the PX-generator was reduced, or when cells with a smaller number of BASE tubes were used, the mass of the generator decreased, and the total electric power output of the generator increased. However, these changes also caused the evaporator and the BASE tubes' brazes temperatures in the cells to increase. The analysis identified a number of power systems of increasing specific power, that used super-alloy AMTEC cells and could meet the specified electric power requirement (28 V d.c. output, and  $Pe > 156$   $W_e$  at EOM). The first power system (#3 in Table 15.4) consisted of 6 fresh-fuel GPHS modules and 48 C-type cells connected electrically in 4 parallel strings of 12 cells each. This power system would provide 174  $W_e$  at EOM at an overall efficiency of 13.2%. The C-type cells would operate at low BASE brazes and evaporator temperatures of 1059 K and 971 K at BOM, respectively, which is a plus for minimizing the cell performance degradation over the long mission lifetime. Furthermore, the cells' performance could degrade by as much as 30% over the mission duration, and the power system would still provide 130  $W_e$  at EOM. A 6-GPHS power system #3 would weight 28.75 kg and have a specific power of 6.1  $W_e/\text{kg}$  at EOM. This power system could also be designed as two 3-GPHS units connected in parallel, each unit comprised of 2 parallel strings of 12 cells each and providing 87  $W_e$  at 28 V d.c. at EOM. However, the resulting power system would be slightly heavier ( $2 \times 15.51 = 31.02$  kg) and have a lower specific power (5.6  $W_e/\text{kg}$  at EOM) than a 6-GPHS power unit.

A power system consisting of 6 fresh-fuel GPHS modules and 48 B-type cells (power system #2, Table 15.3) would provide 14 W<sub>e</sub> more at a 1.1 points higher efficiency at EOM than power system #3. This power system would also be about 1 kg lighter than system #3, resulting in a net 11% increase in specific power (from 6.1 to 6.8 W<sub>e</sub>/kg at EOM). However, the BASE brazes and evaporator in the B-type cells of power system #2 would operate at higher temperatures (48 K and 35 K higher, respectively) than in the C-type cells of system #3.

Another attractive power system consisted of 5 fresh-fuel GPHS modules and 4 parallel strings of 8, E-type cells each (power system #6 in Table 15.4). The 8 cells were uniformly distributed over the TZM plate covering each side of the GPHS stack. This power system would provide 156 W<sub>e</sub> at EOM (assuming no cell performance degradation) at 28 V d.c. output voltage. The E-type cells in system #6 would operate at cooler BASE brazes ( $T_{braz} = 1071$  K) and evaporator ( $T_{ev} = 995$  K) temperatures than the B-type cells of generator #2. Even though the specific power of generator #6 would be lower (6.4 versus 6.8 W<sub>e</sub>/kg at EOM), this generator would be 3.2 kg lighter than power system #2, and would weight 24.53 kg only.

## 16. SUMMARY AND CONCLUSIONS

Alkali-Metal Thermal-to-Electric Converters (AMTEC) are being considered for a number of potential space missions, requiring low mass, low cost, long life, and high-efficiency power systems. These devices are very attractive for these applications, because they are static and can provide high efficiencies at relatively low operating temperatures. An optimized, state-of-the-art AMTEC cell can potentially provide a theoretical conversion efficiency between 20 and 30%, when operated at hot-side temperatures between 1100 K and 1200 K and a cold-side temperature in the range 500 K-700 K. AMTEC devices are modular and are inherently radiation hard.

Since the mid-1980s, a number of programs to develop the technology of liquid- and vapor-anode AMTECs have been initiated at several organizations: the Ford Motor Company; the Jet Propulsion Laboratory; the Electrotechnical Laboratory and Kyushu University in Japan; Advanced Modular Power Systems (AMPS) and the Environmental Research Institute of Michigan; the U.S. Air Force Research Laboratory/Phillips Site. While these programs have successfully resolved a number of key technology issues associated with the fabrication and design of AMTECs, the performance levels achieved then in laboratory tests were still below the theoretical potential of these devices.

A comprehensive AMTEC modeling and testing program is underway at the Air Force Research Laboratory/Phillips Site (AFRL/PS). A joint program with AMPS and the University of New Mexico's Institute for Space and Nuclear Power Studies (UNM-ISONPS) has been carried out during the past 3 years, to demonstrate the readiness of AMTEC technology for flight on the NASA's Pluto/Express spacecraft and Europa Orbiter, and future U.S. Air Force space missions. The goal of this program was to improve the design and performance of AMTECs and demonstrate high system efficiencies. An important component of this collaborative effort was to develop a comprehensive performance model of liquid-anode single-tube and vapor-anode multi-tube cells, to support the ongoing cell testing, perform parametric analyses and evaluate cell design changes to improve the converter performance.

A number of calibration experiments were designed and performed to evaluate the heat losses in the heater block of the cell and the surrounding insulation, and identify critical loss paths. The results were used to improve the experimental setup at AFRL. A two-dimensional, transient heat conduction model was developed, and benchmarked, and used in conjunction with the temperature measurements to predict the heat losses in the alumina powder insulation of the PX-1 series of cells. A specially-designed thermocouple arrangement was used to provide temperature distributions along the boundaries of the insulation package. These measurements provided the necessary boundary conditions to the 2-D conduction model, to predict the heat losses through the insulation. Calculations were consistent with experimental measurements. Knowledge of the heat losses and heat flux profiles at the different insulation boundaries, and examination of the test and model results led to some improvements in the insulation of single-cell setups, and helped in the development of the cell model developed in this work.

Results of the electrochemical and thermal-lumped model developed during the first phase of this effort showed that Mo and NbN electrodes initially exhibit high  $B$  values between 400 and 600  $\text{A.K}^{1/2}/\text{Pa.m}^2$ , and have the potential for peak power densities slightly above  $1 \text{ W/cm}^2$ , with efficiencies as high as 28%. In contrast, TiN electrodes have lower temperature-independent exchange currents, between 120 and 135  $\text{A.K}^{1/2}/\text{Pa.m}^2$ , before maturation, corresponding to lower peak power densities between 0.5 and  $0.75 \text{ W/cm}^2$ , and efficiencies below 24% at a BASE temperature of 1200 K. These values of  $B$  compared well with that reported by other investigators for new electrodes/BASE systems.

While TiN electrodes have lower performance than Mo and NbN electrodes, lifetime studies at high temperature have shown that they are more stable for long-term operation. At temperatures above 1100 K, molybdenum electrodes sinter and experience significant grain growth, particularly in sodium vapor environment. As voids open in the electrode, the electronic sheet resistance increases and the exchange current density decreases with time, degrading the performance of the AMTEC cell. Because the performance of AMTEC cells is strongly dependent on the values of the dimensionless parameters  $G$  and  $Z$ , which characterize the vapor pressure losses and radiation parasitic heat losses between the BASE tubes and the condenser, further modeling and experimental studies are needed to obtain accurate values of these parameters. The designs of interest are state-of-the-art, vapor anode, multi-tube cells using remote condensing and internal radiation shields. Also, design studies are needed to insure that the evaporator temperature remains close to the BASE temperature but below it, to avoid condensation of sodium onto the solid electrolyte. Such condensation could cause electrical shorting of the BASE tubes in the cell and/or thermal shocking of the BASE tubes.

A comprehensive AMTEC Performance and Evaluation Analysis Model (APEAM) was developed at UNM-ISONPS to support ongoing tests at AFRL and evaluate the performance of PX-series AMTEC cells. The model was developed in Standard Fortran 77, and runs on a PC Compatible DOS machine. It also runs on a UNIX or VMS operating system machine, without any modification. It uses a modular input file, and automatically generates output files, and graphs which are readable by the Easy-Plot plotting package.

APEAM consists of three major building blocks, which are interactively coupled: (a) a *sodium vapor pressure loss model*, which models free-molecular, transition and continuum vapor flow regimes and calculates the sodium vapor pressure at the interface between the cathode electrode and the BASE (Chapter 3); (b) a *cell electrochemical and electric model*, which calculates the effective potential developed across the BASE due to the isothermal expansion of sodium ions, determines the resistances of the BASE, electrodes, current collectors and conductor leads to the external load, and calculates the cell's electrical potentials, electrode current density, and the cell's total electric current (Chapter 4); and (c) a *radiation/conduction heat transfer model*, which accounts for all heat exchanges between the different components of the cell and calculates the temperatures throughout the cell (Chapter 5). An efficient iterative solution procedure was developed, that ensured good couplings between the different submodels (Chapter 5, Section 5.4).

APEAM's results showed that the vapor flow on the low-pressure side of the PX-1A multi-tube AMTEC cell was in the transition regime, with Knudsen numbers ranging between 0.04 and 0.4. At a cell electrical current of about 1.5 A (or sodium mass flow rate of about 9 gm/hr), the vapor axial Reynolds number was less than 10. The vapor axial Mach number peaked at 0.25 at the condenser, a value low enough to justify neglecting the vapor compressible effects in the conical chevron's shield model.

The major contributions to the vapor pressure losses between condenser and BASE tubes surface were, in order of decreasing magnitude: flow through the chevron's shield, condensation of sodium vapor on the condenser surface, and sudden expansion of flow area at the top of BASE tubes. For a radiation shield clearance of 48 mm, the AMTEC cell analyzed had an effective dimensionless factor for vapor pressure losses  $G = 143$  with chevron's shield, and  $G = 71$  without shield. The pressure loss through the chevron's radiation shield dominated, by far, all other pressure losses, contributing more than half the total pressure losses between the condenser and cathode/solid electrolyte surface. The total vapor pressure drop in the cell varied linearly with the cell electric current, which is a characteristic of the free-molecule and transition flow regimes. For these flow regimes, the flow diffusion coefficients were weak functions of the vapor mass flow rate.

The increase in vapor pressure losses on the cathode side of the vapor anode, multi-tube AMTEC cell, due to the presence of the chevron's shield, however, only resulted in a 5% decrease in cell electrical power output. This was because the concentration losses in the TiN electrodes were small compared to the charge-exchange polarization and internal ohmic losses of the cell.

The vapor pressure loss model was also used to optimize the chevrons' geometry for minimizing the vapor pressure loss through the shield. For the shield geometry which ensured minimum blockage of all direct radiation between BASE tubes and condenser ( $\alpha=0$ ), the lowest pressure loss occurred when the chevrons angle was about  $60^\circ$ , and using 4 or 5 chevrons. The vapor pressure loss was not particularly sensitive to the chevrons angle near the optimum value, allowing some tolerance for manufacturing the shield. The pressure loss through the chevrons shield increased quickly as the packing factor,  $\alpha$ , was increased. The larger the value of  $\alpha$ , the larger the optimum number of chevrons  $N$ . In the case of separated conical chevrons, the optimum geometry had 3 or 4 chevrons, with an angle of  $62^\circ$ , for which the pressure loss was about 25% higher than that in non-separated chevrons.

Modeling results of several PX-series cells which have been tested at AFRL showed that the electrical losses in the current collector networks and the connecting leads were negligible. However, the polarization/concentration losses in the TiN electrodes were the largest, amounting to 25–50% of the theoretical Nernst electric power. Contact losses, combined with BASE ionic losses, amounted to less than 16% of the theoretical Nernst power. The cell model's results matched the experimental data of the PX-3G cell when  $B = 75 \text{ A.K}^{1/2}/\text{Pa.m}^2$ ,  $R'_{cont} = 0.06 \text{ } \Omega.\text{cm}^2$  and  $R_{leak} = 3 \text{ } \Omega$ . The PX-3G cell delivered a peak power of 3.7 W<sub>e</sub> at  $I = 1.8 \text{ A}$  and overpotential of 2.4 V, when operated at  $T_{hot} = 1123 \text{ K}$  and  $T_{cd} = 553 \text{ K}$ . This cell had six 0.508 mm-thick BASE tubes, and 25.4 mm-long TiN electrodes, and a predicted internal resistance,  $R_{int} = 0.274 \text{ } \Omega$ . The ionic resistance of the BASE contributed 39.3% of  $R_{int}$ , while the contact resistances

between the BASE and the metallic electrodes, and between the electrodes and the current collectors contributed 42.9% of  $R_{int}$ . The ohmic losses in the current collectors and leads constituted the remaining of  $R_{int}$ .

Results also showed that a PX-3G cell with  $Rh_2W$  or other advanced electrodes, exhibiting  $B$  values in the range 120–200  $A \cdot K^{1/2} / Pa \cdot m^2$ , could have delivered a peak load electrical power in the range 4.2–4.6  $W_e$  (which is 14% to 25% more than the PX-3G cell with TiN electrodes). However, even if a perfect electrode were used (i.e.  $B = +\infty$ ), the overpotential would not reduce to zero, because of the concentration losses or the effect of sodium vapor pressure on the cathode side of the BASE tube. The PX-3G cell had a predicted total geometric factor  $G = 192$  for vapor pressure losses. The pressure drop through the TiN electrode contributed only 26% of the total vapor pressure losses in the low-pressure cavity.

A thermal-hydraulic model was developed to calculate the pressure losses and determine the capillary limit of the liquid-sodium return wick in the PX-2C, vapor anode, multi-tube AMTEC cell. The model was used to examine the effects of the wick parameters and evaporator temperature on the liquid sodium circulation. Results showed that, for a wick porosity of 0.2 and a sodium mass flow rate of 7.2 gm/hr, the calculated pressure losses in the wick were 3.5 kPa, 6.1 kPa, and 14.4 kPa, at effective pore radii of 20  $\mu m$ , 15  $\mu m$ , and 10  $\mu m$ , respectively. To operate a PX-type AMTEC cell at evaporator temperatures of 950 K, 1025 K and 1100 K, maximum wick pore radii of 27  $\mu m$ , 10  $\mu m$ , and 4  $\mu m$ , respectively, are needed, to overcome the evaporator saturation pressure (10 kPa, 27 kPa and 61 kPa, respectively). At evaporator temperatures  $> 1050$  K, the liquid pressure losses in a single pore size, homogeneous wick would be prohibitively high. Therefore, a wick that is comprised of two sections, a long section with a large permeability, to reduce the liquid pressure losses, and a short evaporator section, with a much smaller pore size, to provide a high capillary pressure head, is recommended.

Two homogenous, high temperature insulation materials were investigated at AFRL. These materials were alumina powders having average particle sizes of 1.0  $\mu m$  and 0.01  $\mu m$  and porosities of 91.4% and 96.2%, respectively, and molded Min-K (TE1800). The Min-K is the commercial name of a thermal insulation material, which is a mixture of titanium oxide and silica, fabricated in the form of solid disks. The thermal conductivities of two particle-size alumina powders and molded Min-K insulation materials were determined experimentally in vacuum, as functions of temperature in the range from 340 to 900 K (Chapter 7). The developed thermal conductivity correlations for the alumina powders were in agreement with the experimental data to within  $\pm 10\%$ , while that for the Min-K was within  $\pm 5\%$  of the data. The thermal conductivities of all three materials are strong functions of temperature, increasing with increased temperature above 400 K. Below 400 K, all three materials have similar thermal conductivities. The thermal conductivity of the alumina powder having a particle size of 0.01  $\mu m$  increased faster with increasing temperature, followed by the 1  $\mu m$  alumina powder, then the molded Min-K. The Min-K has the lowest thermal conductivity of all three materials above 400 K.

The determined experimental measurement uncertainty in the AFRL vacuum tests of both single-cell and multi-cell systems was the greater of  $\pm 1.1\%$  or 1.7 K in temperature;  $\pm 1.2\%$  in the cell

electric power output,  $\pm 0.7\%$  in the heat input,  $\pm 6.2\%$  in air flow rate, and as much as  $\pm 6.5\%$  in heat rejection. Another uncertainty associated with the measurements of the BASE tube and evaporator temperatures in these tests was caused by the placement of the thermocouples (TCs) in the respective cavities and the fin effect of the TC guide tubes.

In order to calculate the uncertainty associated with the placement of the TCs in the BASE and evaporator cavities, a heat transfer model was developed. This model coupled heat conduction in the TC guide tube, to forced convection, and thermal radiation to the walls of the evaporator and the BASE tube cavities. The model predictions were in good agreement with the readings of the BASE and evaporator TCs in PX-5A cell. However, the TC readings of the BASE and evaporator temperatures in PX-4C cells were about 15–18 K and 4–47 K, higher, respectively, than what they might have been, depending upon the TC placement, cell electric current, and the hot and cold temperatures in the tests. Results of a parametric analysis indicated that increasing the length of the TC guide tubes for the BASE and evaporator cavities would reduce the readings of the TCs, to be more representative of the actual BASE tube and evaporator temperatures.

APEAM's predictions of the performance parameters of PX-2C, PX-4C, PX-5A and PX-3A cells tested in vacuum at AFRL, at different hot side temperatures, were in good agreement with experimental data. These parameters were the load electrical power and voltage outputs, the hot and cold end temperatures, the BASE tubes' cold end temperature, and the condenser heat rejection. Such good agreement confirmed the soundness of the modeling approach and the solution procedure used. Results showed that the conical evaporators of the cells provided an anode sodium vapor pressure that was almost independent of current, when the cells were operated at fixed hot and cold end temperatures. The anode sodium vapor pressure increased with cell hot end temperature. Also, cell designs with reduced internal parasitic heat losses provided a higher anode sodium vapor pressure.

Results showed that the use of a Creare condenser in PX-5A, in lieu of the mesh pad condenser of PX-4C, combined with an increased condenser temperature (from 565 K to 623 K), reduced the parasitic heat losses in the cell, and increased the cell electrical power output and predicted conversion efficiency (from 10.5% to 11.8%). Predicted peak efficiency of PX-3A was 13.0%, at a hot side temperature of 1123 K. This cell efficiency was 1.2 points higher than that predicted for PX-5A at identical hot and cold side temperatures. In fact, PX-3A only provided 3.9  $W_e$  (PX-5A reached a peak power of 4.2  $W_e$ ), because it had only 5 BASE tubes, while PX-5A had 6. However, the reduced diameter of PX-3A, and the shorter BASE tubes in PX-3A, significantly decreased the radiation and conduction parasitic heat losses in the cell, as well as the heat losses through the side wall, increasing the cell conversion efficiency (from 11.8% to 13.0%). Best performance was obtained for PX-3A at a hot side temperature of 1173 K. It reached a peak power of 4.6  $W_e$  and predicted peak efficiency of 14.2 %. About 6.1 W were lost at the cell wall through the Min-K insulation.

APEAM was also used to analyze recent vacuum test results of a Pluto/Express electric power generator ground demo. The 8 ground demo cells, designated PX-3G, produced a peak electrical power of 27  $W_e$  at a voltage of 16 V, when tested at hot and cold side temperatures of 1123 K and 553 K, respectively. Analysis of test data showed that the electric power outputs and

terminal voltages of the individual PX-3G cells differed by as much as 25%, from 2.94 to 3.76  $W_e$ , and 1.73 to 2.21 V, respectively. These variations in the individual cells' performance parameters were attributed, in an order of decreasing importance, to differences in: (a) the contact resistances between the BASE/metal electrodes and the electrodes/current collectors ( $R_{cont}$ ); (b) the current leakage between anode and cathode electrodes through the metal-ceramic braze joint between BASE tubes and SS support plate ( $R_{leak}$ ); and (c) the charge-exchange polarization losses ( $B$ ). The values of  $B$ ,  $R_{cont}$ , and  $R_{leak}$  for the individual PX-3G cells, deduced from the comparison of measured and calculated I-V characteristics, varied between 64 – 75  $A \cdot K^{1/2} / Pa \cdot m^2$ , 0.06 – 0.12  $\Omega \cdot cm^2$ , and 1.3 – 6.0  $\Omega$ , respectively.

Test and modeling results showed that the PX-3G cells of the ground demo operated at a higher conversion efficiency than the PX-5A single cell, which was of similar design, because of the reduced heat losses from the cell wall in the ground demo. Model's predictions compared well with measured voltage and electric power output of the individual PX-3G cells. Results suggested the existence of large electrical leakage currents in some of the PX-3G cells, and that the cells operated with a positive temperature margin in the tests. To add further confidence in the present results, there is a need to develop accurate means for measuring the BASE and evaporator temperatures in the tests, for comparison with models' predictions. In addition, detection of the leakage current, if any, through the BASE metal-ceramic brazes, as well as measuring the electrodes charge-exchange polarization losses, would be useful. Without such measurements, it is difficult to benchmark existing cell models and effectively guide future technology effort to design better cells and address potential lifetime issues.

At the operating conditions expected on board the Pluto/Express spacecraft ( $T_{hot} \sim 1200$  K,  $T_{cd} \sim 573$  K), the best performing PX-3G cell #1 would have delivered 5  $W_e$  at a voltage output of 3 V. These values, however, are still significantly lower than those needed (8.2  $W_e$  at 3.5 V, per cell) for meeting the Pluto/Express mission power requirements in the Orbital Sciences Corporation's (OSC) 16-cell power system configuration. Results suggested that further improvements in cell design, as well as other power system configurations, are needed in order to meet the power requirement for the Pluto/Express spacecraft.

The AMTEC Performance and Evaluation Analysis Model (APEAM) was used to conduct performance and design optimization analyses of Pluto/Express AMTEC cells (Chapter 13). The parametric analyses performed in this work evaluated the effects of the following design changes: (a) reducing the heat losses through the cell wall; (b) using a Creare type condenser; (c) changing the number of BASE tubes and the electrode length; (d) changing the electrode material; (e) using Mo structure on the hot side of the cell; and (f) using reflective rhodium coatings in the low vapor pressure cavity of the cell. The analyses were performed at fixed hot and cold end temperatures of 1200 K and 623 K, respectively, and employed a PX-5A type cell design, with a Creare condenser, a Mo circumferential radiation shield, and 7 BASE tubes connected in series, and 29 mm-long TiN electrodes. This cell design could deliver a 3.5-V voltage to the load at a conversion efficiency close to the peak value. The peak efficiency always occurred at a load resistance greater than that corresponding to the peak electrical power output, a suitable operating point in the load-following curve of the cell. A SS structure cell, with negligible heat



losses through its wall, and TiN electrodes, would deliver 5.9 We at an efficiency of 17.8%, and a load voltage of 3.5 V.

Results showed that a SS structure cell with improved electrodes (50% lower contact resistance,  $R_{cont}$ , than TiN, and a higher exchange current,  $B = 200 \text{ A.K}^{1/2}/\text{Pa.m}^2$ ) could deliver 7.1 We with an efficiency of 19.5%, at a load resistance and voltage of  $1.73 \text{ } \Omega$  and 3.5 V, respectively. Current TiN electrodes have  $R_{cont} = 0.08 \text{ } \Omega.\text{cm}^2$ , and  $B = 80 \text{ A.K}^{1/2}/\text{Pa.m}^2$ . When Mo was substituted for SS on the hot side of this cell, the new cell delivered 8.8 We with an efficiency of 20.2%, at a load resistance of  $1.40 \text{ } \Omega$  and a load voltage of 3.5 V. The Mo hot wall and evaporator standoff, however, would need to be brazed to the low thermal conductivity material (such as SS) in the colder portion of the cell, which is a technology challenge. Using rhodium coatings in the Mo/SS cell increased the electrical power output of the cell by 1 We, to 9.7 We, and increased the conversion efficiency by 2.3 points, to 22.5%, at a load resistance of  $1.26 \text{ } \Omega$  and load voltage of 3.5 V.

The present analyses showed that Pluto/Express-type AMTEC cells could achieve performance that exceeds the mission goals of 8 We at a load voltage of 3.5 V, and a conversion efficiency > 20%, when the different changes investigated herein were incorporated into the cell design. Some of the design changes proposed, however, would require resolving key technology issues, such as brazing of Mo and stainless steel, applying rhodium coating that could last the mission lifetime in a corrosive sodium vapor atmosphere, and developing advanced electrode materials with lower contact resistance and higher exchange current.

A number of design changes were also examined for improving the performance of PX-3G cells (Chapter 14). Results indicated that a PX-3G type cell, with 7 BASE tubes, 14% longer electrodes, a Mo heat shield and a Ni structure on the hot side, could deliver an electric power of 5 We at a conversion efficiency of 15.9%, and a 3.5 V output voltage, when operated at a constant heat input,  $Q_{in} = 31.25 \text{ W}_{th}$ . This cell would not exceed the temperature limits of the BASE tubes, metal-to-ceramic TiNi braze (1123 K) and current-technology evaporator (1050 K). These performance parameters are a significant improvement over the ground-demo PX-3G cell (440 mWe more electric power at 1.3 points higher efficiency, 57 K lower BASE tube brazes temperature, 52 K lower evaporator temperature, and 26 K higher temperature margin).

Radioisotope power systems in the configuration proposed by Orbital Sciences Corporation (OSC), using improved-design PX-3G type cells, of smaller diameter (1.25 in) and only 5 BASE tubes each, were investigated for meeting the power requirement of the Pluto/Express mission (> 130 We at voltage > 28 V at EOM). The analysis identified 2 power systems, that could meet the specified electric power requirement, but at a slightly lower output voltage of 24 V. The first power system (design #1 in Table 14.2) consisted of 3 generators connected in parallel, each comprised of 2 aged-fuel GPHS modules and 16 cells. Each generator produced 56.3 We at EOM, for a total electric power output of 169 We, at an overall conversion efficiency of 14.5% and specific power of  $6.8 \text{ W/kg}$ . This generator would deliver 130 We at EOM, even if the cells' performance degrades by as much as 30% in the 15-year duration of the mission. In this power system, the BASE tubes brazes would operate at 1198 K at BOM, which is above the 1123 K limit of the current TiNi brazes. Also, the high evaporator temperature (1123 K) could cause the

flow of liquid sodium in the return wick to be capillary limited. However, the temperature margin in the cells would be positive ( $> +17$  K).

The second power system (design #2 in Table 14.2) consisted of 2 generators, each comprised of 16 cells and 2 fresh-fuel GPHS modules. This power system would provide 140 W<sub>e</sub> at EOM (which allows for ~8% degradation in the cells' performance in the 15-year duration of the mission), a higher conversion efficiency of 16.0%, and higher specific power (8.4 W/kg) than power system #1. The BASE tubes brazes in the cells of power system #2, however, would operate at 1234 K (36 K higher than in power system #1). Metal-to-ceramic braze materials, that can operate at temperatures up to 1250 K, need to be developed. Also, evaporator structures with pores  $< 4$   $\mu$ m in diameter, that can operate at temperatures up to 1123 K, are needed.

Advanced Modular Power Systems (AMPS) has proposed a different PX-generator configuration, which has a predicted thermal efficiency (~93%) slightly higher than OCS's (~91%). Instead of mounting the cells on the top and bottom faces of the GPHS stack, in AMPS design the cells are mounted onto the 4 sides of the GPHS stack. In OSC's PX-generator design, the number of cells per generator – a maximum of sixteen 31.75 mm (1.25") dia., ten 38.1 mm (1.5") dia., or four 44.45 mm (1.75") dia. cells – is limited by the surface area available for mounting the cells, the top and bottom faces of the GPHS stack.

In Chapter 15, different design changes for improving the performance (peak electric power and efficiency) of nickel super-alloy cells were investigated, and various options of integrating the improved super-alloy cells with GPHS modules in the generator configuration proposed by AMPS were explored, such as changing the number of GPHS modules and the number of cells per generator, using either fresh or aged  $^{238}\text{PuO}_2$  fuel, increasing the BASE and electrode lengths, and varying the number of BASE tubes in the cell by changing the cell diameter. In some cases, the number of parallel strings of cells in the power system were reduced to only two. The associated decrease in the overall system redundancy, however, could be alleviated by connecting a diode in parallel with each cell, so that the loss of one cell in a string of cells would not lead to the loss of the whole string, as recently proposed by Schock et al. (1998c). The effects of these design changes on the generator electric power output as well as on the temperatures of the cells' evaporator ( $T_{ev}$ ), BASE metal-ceramic brazes ( $T_{braz}$ ), and temperature margin,  $\Delta T$  in the cells, were also examined.

Analyses performed at an input thermal power  $Q_{in} = 40$  W, cold end temperature,  $T_{cond} = 640$  K and fixed terminal voltage per cell of 2.8 V indicated that a 25% longer (5.0"-long) PX-3G type cell with 7 BASE tubes, 50% longer electrodes (1.5"-long), Mo current collectors of improved thermal conductance, a Ni heat shield, a Ni structure on the hot side, and a Haynes-25 cold side wall, could deliver an electric power of 6.98 W<sub>e</sub> at a conversion efficiency of 17.5%. This cell would operate at BASE tubes' brazes and evaporator temperatures of 1137 K and 1022 K, respectively, and a temperature margin  $\Delta T = +41$  K. These performance parameters are a significant improvement over the ground-demo, stainless steel PX-3G cell (890 mW<sub>e</sub>, more electric power at 2.3 points higher efficiency, 66 K lower BASE tubes' brazes and evaporator temperatures, and 33 K higher temperature margin). Because Haynes-25 contains Cr and Mn elements, which are volatile at temperature  $> 1023$  K and would contaminate the TiN metal

electrodes, and since it is expected that degradation in cell performance would be rapidly accelerated as the operation temperature of the cell increases, the cell and integration designs must insure that the evaporator temperature remains low, below 1023 K.

PX-radioisotope power systems were designed in the configuration proposed by AMPS to provide an output voltage of 28 V d.c. and at least 156 W<sub>e</sub> at EOM, or 130 W<sub>e</sub> at EOM assuming a 20% decrease in the electric performance of the cells after a 15-year mission lifetime. Super-alloy cells of improved design, with 5 to 9 BASE tubes, were designed for these generators. For a given number of BASE tubes, the cell diameter was kept to a minimum to insure minimum conduction and radiation parasitic heat losses in the cells. Also, the outer diameter of the evaporator standoff was adjusted concomitant with the number of BASE tubes in the cell, in order to insure enough temperature margin in the cells. Assuming a conservative surface emissivity of 0.25, the housing surface area was large enough, in all cases, to radiate the excess heat at a surface temperature below 600 K. Therefore, inserting an alumina or zirconia washer of appropriate thickness between the cell's cold end and the generator housing would insure a near-optimum cell condenser temperature,  $T_{cond} = 640$  K at EOM.

Results showed that when the number of cells in the PX-generator was reduced, or when cells with a smaller number of BASE tubes were used, the mass of the generator decreased, and the total electric power output of the generator increased. However, these changes also caused the evaporator and the BASE tubes' brazes temperatures in the cells to increase. The analysis identified a number of power systems of increasing specific power, that used super-alloy AMTEC cells and could meet the specified electric power requirement (28 V d.c. output, and  $P_e > 156$  W<sub>e</sub> at EOM). The first power system (#3 in Table 15.4) consisted of 6 fresh-fuel GPHS modules and 48 C-type cells connected electrically in 4 parallel strings of 12 cells each. This power system would provide 174 W<sub>e</sub> at EOM at an overall efficiency of 13.2%. The C-type cells would operate at low BASE brazes and evaporator temperatures of 1059 K and 971 K at BOM, respectively, which is a plus for minimizing the cell performance degradation over the long mission lifetime. Furthermore, the cells' performance could degrade by as much as 30% over the mission duration, and the power system would still provide 130 W<sub>e</sub> at EOM. A 6-GPHS power system #3 would weight 28.75 kg and have a specific power of 6.1 W<sub>e</sub>/kg at EOM. This power system could also be designed as two 3-GPHS units connected in parallel, each unit comprised of 2 parallel strings of 12 cells each and providing 87 W<sub>e</sub> at 28 V d.c. at EOM. However, the resulting power system would be slightly heavier ( $2 \times 15.51 = 31.02$  kg) and have a lower specific power (5.6 W<sub>e</sub>/kg at EOM) than a 6-GPHS power unit.

A power system consisting of 6 fresh-fuel GPHS modules and 48 B-type cells (power system #2, Table 15.3) would provide 14 W<sub>e</sub> more at a 1.1 points higher efficiency at EOM than power system #3. This power system would also be about 1 kg lighter than system #3, resulting in a net 11% increase in specific power (from 6.1 to 6.8 W<sub>e</sub>/kg at EOM). However, the BASE brazes and evaporator in the B-type cells of power system #2 would operate at higher temperatures (48 K and 35 K higher, respectively) than in the C-type cells of system #3.

Another attractive power system consisted of 5 fresh-fuel GPHS modules and 4 parallel strings of 8, E-type cells each (power system #6 in Table 15.4). The 8 cells were uniformly distributed over

the TZM plate covering each side of the GPHS stack. This power system would provide 156 W<sub>e</sub> at EOM (assuming no cell performance degradation) at 28 V d.c. output voltage. The E-type cells in system #6 would operate at cooler BASE brazes ( $T_{braz e} = 1071$  K) and evaporator ( $T_{ev} = 995$  K) temperatures than the B-type cells of generator #2. Even though the specific power of generator #6 would be lower (6.4 versus 6.8 W<sub>e</sub>/kg at EOM), this generator would be 3.2 kg lighter than power system #2, and would weight 24.53 kg only.

The results of this research, supported with the extensive database generated in more than a dozen single-cell vacuum tests and one multi-cell test performed at AFRL, have given the vapor anode, multi-tube AMTEC cell technology a quantum push, making it quite attractive for many future Air Force missions. Specific Air Force missions that can benefit from the AMTEC technology are those requiring high electric power output in excess of 30 kW<sub>e</sub>, and which take advantage of the high output voltage (2.5 to 3.5 V per cell) and the inherent radiation hardness of AMTEC cells. Future research, however, should focus on investigating lifetime issues related to potential performance degradation of AMTEC cells in long duration space missions of up to 15 years.

## REFERENCES

- Alger, D. L. (1997) "Some Corrosion Failure Mechanisms of AMTEC Cells," in *Proceedings of the 32nd Intersociety Energy Conversion Engineering Conference*, held in Honolulu, HI, July 27 - August 1, 1997, American Chemical Society, Paper No. 97014, 2:1224-1229.
- Anderson, W. G. (1992) "Sodium Wick Pumping Experiments for a Vapor-Fed AMTEC System," in *Proceedings of the 27th Intersociety Energy Conversion Engineering Conference*, held in San Diego, CA, August 3-7, 1992, Paper No. 929146, Society of Automotive Engineers, Inc., 3:111-116.
- Anderson, W. G., J. J. Bland, J. F. Ivanenok, III, and R. K. Sievers (1993) "Design of a Wick-Pumped, Vapor-Fed AMTEC System," in *Proceedings of the 28th Intersociety Energy Conversion Engineering Conference*, held in Atlanta, GA, August 8-13 1993, Paper No. 93038, American Chemical Society, 1:835-841.
- Angelo, J. A., Jr., and D. Buden (1985) *Space Nuclear Power*, Orbit Book Company, Inc., Malabar, Florida.
- Angrist, S. W. (1965) *Direct Energy Conversion*, Allyn and Bacon Series in Mechanical Engineering and Applied Mechanics, F. Kreith, Ed., Allyn and Bacon, Inc., Boston, 89.
- Beckwith, T. G., and R. D. Marangoni (1990) *Mechanical Measurements*, 4th Edition, Addison-Wesley Publishing Company, pp. 43-48.
- Bird, R. B., W. E. Stewart, and E. N. Lightfoot (1960) *Transport Phenomena*, Section 1.4, pp. 19-26, John Wiley & Sons, Inc., New York.
- Blackwell, B. F. et al. (1996) "Estimation of Thermal Conductivity of  $\text{Al}_2\text{O}_3$  Powder, with and without Binder Present," in *Proceedings of the 32nd National Heat Transfer Conference*, held August 3-5, in Houston, TX, AIAA Paper No. 96-3969.
- Bomelburg, H. J., and C. R. F. Smith (1972) "Chapter I - Physical Properties," in *Sodium-NaK Engineering Handbook*, Volume I - Sodium Chemistry and Physical Properties, O. J. Foust, Ed., Gordon and Breach, Science Publishers, Inc., 52-59.
- Carlson, M. E., J. C. Giglio, and R. K. Sievers (1998) "Design and Fabrication of Multi-Cell, AMTEC Power Systems for Space Applications," in *Proceedings of the 3<sup>rd</sup> Space Technology and Applications International Forum (STAIF-98)*, CONF-980103, M. S. El-Genk, ed., American Institute of Physics, New York, NY, AIP Conference Proceedings No. 420, 3:1486-1490.

Chi, S. W. (1976) *Heat Pipe Theory and Practice*, Hemisphere Publishing Corporation, Washington, D.C., Chapter 2, pp. 47-51.

Cole, T. (1983) "Thermoelectric Energy Conversion with Solid Electrolytes," *Science*, 221(4614):915-920.

Crowley, C. J., and M. G. Izenson (1993) "Condensation of Sodium on a Micromachined Surface for AMTEC," in *Proceedings of the 10th Symposium on Space Nuclear Power and Propulsion*, CONF-930103, M. S. El-Genk, Ed., American Institute of Physics, New York, NY, AIP Conference Proceedings No. 271, 2:897-904.

Cunningham, R. E., and R. J. J. Williams (1980) *Diffusion in Gases and Porous Media*, Chapters 1, 2 and 3, Plenum Press, New York.

El-Genk, M. S., and J.-M. Tournier (1995) "A Critical Review of Free-Molecular and Transition Flow Regimes in Heat Pipes," in *Proceedings of the 9th International Heat Pipe Conference*, held in Albuquerque, NM, May 1-5, 1995, M. A. Merrigan, Ed., Los Alamos National Laboratory, Los Alamos, NM.

Ergun, S. (1952) "Fluid Flow Through Packed Columns," *Chemical Engineering Process*, 48 (2): 89-94 (February 1952).

Evans, J. V. (1998) "New Satellites for Personal Communications," *Scientific American*, April 1998, 70-77.

Fang, Q., and R. Knödler (1992) "Porous TiB<sub>2</sub> Electrodes for the Alkali-Metal Thermoelectric Converter," *Journal of Material Sciences*, 27:6725-6729.

Golub, G. H., and C. F. van Loan (1984) *Matrix Computation*, 2<sup>nd</sup> Edition, The Johns Hopkins University Press, Baltimore and London.

Hendricks, T. J., C. Huang, and R. K. Sievers (1997) "AMTEC Radioisotope Power System Design and Analysis for Pluto/Express Flyby," in *Proceedings of the 32nd Intersociety Energy Conversion Engineering Conference*, Paper No. 97382, American Chemical Society, 1:501-508.

Hendricks, T. J., C. A. Borkowski, and C. Huang (1998) "Development and Experimental Validation of a SINDA / FLUINT Thermal / Fluid / Electrical Model of a Multi-Tube AMTEC Cell," in *Proceedings of the 3rd Space Technology and Applications International Forum (STAIF-98)*, CONF-980103, M. S. El-Genk, ed., American Institute of Physics, New York, NY, AIP Conference Proceedings No. 420, 3:1491-1501.

Hendricks, T. J., and C. Huang (1998) "System Design Impact on Optimization of the Advanced Radioisotope Power System (ARPS) AMTEC Cell," in *Proceedings of the 33rd Intersociety Energy Conversion Engineering Conference*, held August 2-6, 1998, in Colorado Springs, CO, Paper No. 98407, American Nuclear Society, Chicago, IL.

Hirschfelder, J. O., C. F. Curtiss, and R. B. Bird (1954) *Molecular Theory of Gases and Liquids*, Chapters 7 and 8, John Wiley & Sons, Inc., New York.

Holman, J. P. (1984) *Experimental Methods for Engineers*, McGraw-Hill Book Company, WY.

Howell, J. R. (1982) *A Catalog of Radiation Configuration Factors*, McGraw-Hill Book Company, Inc., New York and London.

Huang, L., M. S. El-Genk, and M. J. Schuller (1997) "Measurements of Thermal Conductivities of Alumina Powders and Min-K in Vacuum," in *Proceedings of the 32th Intersociety Energy Conversion Engineering Conference*, held in Honolulu, HI, July 27–August 1, 1997.

Huang, L. and M. S. El-Genk (1998), in *Proceedings of the Space Technology and Applications International Forum (STAIF-98)*, CONF-980103, M. S. El-Genk, ed., American Institute of Physics, New York, NY, AIP Conference Proceeding No. 420, 3:1471-1478.

Hunt, T. K., N. Weber, and E. N. Sickafus (1982) *Research and Development Program of a Sodium Heat Engine*, Final Report No. DOE/ER/10347—T1, Ford Motor Company, Dearborn, MI 48121, October 1982.

Hunt, T. K., R. K. Sievers, J. F. Ivanenok, III, J. E. Pantolin, and D. A. Butkiewicz (1993) "Capillary Pumped AMTEC Module Performance," in *Proceedings of the 28th Intersociety Energy Conversion Engineering Conference*, held in Atlanta, GA, August 8–13 1993, Paper No. 93307, American Chemical Society, 1:849–854.

Idelchik, I. E. (1986) *Handbook of Hydraulic Resistance*, 2nd Edition, Erwin Fried, English-Edition Ed., Hemisphere Publishing Corporation, Washington, D. C., Chapter 4, pp. 145-155.

Incropera, F. P., and D. P. Dewitt (1990) *Fundamentals of Heat and Mass Transfer*, 3rd Edition, John Wiley & Sons, pp. A15.

Ivanenok, J. F., III, R. K. Sievers, and W. W. Schultz (1994) "Modeling of Remote Condensing AMTEC Cells," in *Proceedings of the 11th Symposium on Space Nuclear Power Systems*, CONF-940101, M. S. El-Genk, ed., American Institute of Physics, New York, NY, AIP Conference Proceedings No. 301, III:1501-1506.

Ivanenok, J. F., III, and R. K. Sievers (1995) "AMTEC Radioisotope Power System for the Pluto Express Mission," in *Proceedings of the 30th Intersociety Energy Conversion Engineering Conference*, American Society of Mechanical Engineers, Paper No. AP-395, I: 661–666.

Ivanenok, J. F., III, and R. K. Sievers (1996) "AMTEC Powered Residential Furnace and Auxiliary Power," in *Proceedings of the 31st Intersociety Energy Conversion Engineering Conference*, held in Washington, D.C., August 11–16, 1996, Institute of Electrical and Electronics Engineers, Paper No. 96185, II: 894–898.

Izenson, M. G., and C. J. Crowley (1993) "Micromachined Evaporator for AMTEC Cells," in *Proceedings of the 28th Intersociety Energy Conversion Engineering Conference*, held in Atlanta, GA, August 8-13 1993, Paper No. 93221, American Chemical Society, 1:829-834.

Izenson, M. G., and C. J. Crowley (1996) "Micromachined Evaporators for AMTEC Cells," in *Proceedings of the 31st Intersociety Energy Conversion Engineering Conference*, held in Washington, D.C., August 11-16, 1996, Paper No. 96262, Institute of Electrical and Electronics Engineers, 4:2226-2231.

Johnson, G. A. (1992) "The Alkali Metal Thermoelectric Converter (AMTEC) Radioisotope Thermoelectric Generator (RTG)," in *Proceedings of the 27th Intersociety Energy Conversion Engineering Conference*, held in San Diego, CA, August 3-7, 1992, Paper No. 929063, Society of Automotive Engineers, Inc., 3:203-207.

Johnson, G. A. (1994) "Study of the Rarefied Sodium Vapor Flow in the Pluto Fast Flyby AMTEC Cell," in *Proceedings of the 11th Symposium on Space Nuclear Power and Propulsion*, CONF-940101, M. S. El-Genk, ed., American Institute of Physics, New York, NY, AIP Conference Proceedings No. 301, 2: 581-585.

Juul, N. H. (1982) "View Factors in Radiation Between Two Parallel Oriented Cylinders of Finite Lengths," *ASME Journal of Heat Transfer*, 104: 384-388.

Kato, A., K. Tsuchida, T. Hashimoto, H. Nakata, and T. Nagata (1992) "Characteristics of Ceramic Electrode for AMTEC," in *Proceedings of the 27th Intersociety Energy Conversion Engineering Conference*, held in San Diego, CA, August 3-7, 1992, Society of Automotive Engineers, Inc., Paper No. 929006, III:3.1-3.18.

Kato, A., H. Nakata, and K. Tsuchida (1993) "Characteristics of Ceramics Electrode for AMTEC - II. Structure of Electrode and Power Density," in *Proceedings of the 28th Intersociety Energy Conversion Engineering Conference*, held in Atlanta, GA, August 8-13, 1993, American Chemical Society, Paper No. 93027, I:1.809-1.814.

Kennard, E. H. (1938) *Kinetic Theory of Gases*, First Edition, McGraw-Hill Book Company, Inc., New York and London, 60-67.

Kummer, J. T., and N. Weber (1968), U. S. Patent No. 3,458,356 assigned to the Ford Motor Company.

Lee, S. L. (1989) "A Strongly Implicit Solver for Two-Dimensional Elliptic Differential Equations," *Numerical Heat Transfer*, Part B, 16: 161-178.

Levenson, L. L., N. Milleron, and D. H. Davis (1961) *1960 Vacuum Symposium Transactions*, Pergamon Press, London.



Merrill, J., M. J. Schuller, R. K. Sievers, C. A. Borkowski, L. Huang, and M. S. El-Genk (1997) "Vacuum Testing of High-Efficiency Multi-Tube AMTEC Cells," in *Proceedings of the 32nd Intersociety Energy Conversion Engineering Conference*, held in Honolulu, HI, July 27 – August 1, 1997, American Chemical Society, Paper No. 97379, 2:1184-1189.

Merrill, J., M. J. Schuller, and L. Huang (1998) "Vacuum Testing of High-Efficiency Multi-Tube AMTEC Cells: February 1997-October 1997," in *Proceedings of the 3<sup>rd</sup> Space Technology and Applications International Forum (STAIF-98)*, CONF-980103, M. S. El-Genk, Ed., American Institute of Physics, New York, NY, AIP Conference Proceedings No. 420, 3:1613-1620.

Mondt, J. F., M. L. Underwood, and B. J. Nesmith (1997) "Future Radioisotope Power Needs for Missions to the Solar System," in *Proceedings of the 32nd Intersociety Energy Conversion Engineering Conference*, Paper No. 97244, American Chemical Society, 1:460-464.

Ohse, R. W., Editor (1985) *Handbook of Thermodynamic and Transport Properties of Alkali Metals*, International Union of Pure and Applied Chemistry, Blackwell Scientific Publications, Oxford.

Patankar, S. V. (1980) *Numerical Heat Transfer and Fluid Flow*, Hemisphere Publishing Co., Washington, D.C..

Ryan, M. A., B. Jeffries-Nakamura, R. M. Williams, M. L. Underwood, D. O'Connor, and S. Kikkert (1992) "Advances in Materials and Current Collecting Networks for AMTEC Electrodes," in *Proceedings of the 27th Intersociety Energy Conversion Engineering Conference*, Paper No. 929007, Society of Automotive Engineers, 3:7-12.

Ryan, M. A., A. Kisor, R. M. Williams, B. Jeffries-Nakamura, M. L. Underwood, and D. O'Connor (1993) "Emissivities and Thermal Characterization of Components for AMTEC Cells," in *Proceedings of the 28th Intersociety Energy Conversion Engineering Conference*, held in Atlanta, GA, August 8-13, 1993, American Chemical Society, Paper No. 93322, 1:1.815-1.818.

Ryan, M. A., R. M. Williams, C. Saipetch, A. Kisor, D. O'Connor, M. L. Underwood, and B. Jeffries-Nakamura (1994) "Developments in AMTEC Devices, Components and Performance," in *Proceedings of the 11th Symposium on Space Nuclear Power Systems*, held in Albuquerque, NM, January 1994, Conference No. 940101, American Institute of Physics, 3:1495-1500,

Ryan, M. A., R. M. Williams, M. L. Homer, W. M. Phillips, L. Lara, and J. Miller (1998a) "Lifetime Modeling of TiN Electrodes for AMTEC Cells," in *Proceedings of the 3<sup>rd</sup> Space Technology and Applications International Forum (STAIF-98)*, CONF-980103, M. S. El-Genk, Ed., American Institute of Physics, New York, NY, AIP Conference Proceedings No. 420, 3: 1607-1612.

Ryan, M. A., R. M. Williams, L. Lara, R. H. Cortez, M. L. Homer, V. B. Shields, J. Miller, and K. S. Manatt (1998b) "The Sodium Exposure Test Cell to Determine Operating Parameters for AMTEC Electrochemical Cells," in *Proceedings of the 33rd Intersociety Energy Conversion*

*Engineering Conference*, held August 2-6, 1998, in Colorado Springs, CO, Paper No. 98335, American Nuclear Society, Chicago, IL.

Saad, M. A. (1966) *Thermodynamics for Engineers*, Prentice-Hall, Inc., Englewood Cliffs, New Jersey, Chapters 3 and 4; 243-245.

Schock, A. (1974) *Compressible Flow Through a Tube Connecting a Continuum and a Vacuum*, Report FSEC-NSG-217-74/38A, Fairchild Space Company, Germantown, MD.

Schock, A., and C. Or (1997) "Coupled Thermal, Electrical, and Fluid Flow Analyses of AMTEC Multi-Tube Cell with Adiabatic Cell Wall," in *Proceedings of the 2nd Space Technology and Applications International Forum (STAIF-97)*, CONF-970115, M. S. El-Genk, ed., American Institute of Physics, New York, NY, Conference Proceedings No. 387, 3:1381-1394.

Schock, A., H. Noravian, C. Or, and V. Kumar (1997a) "Parametric Analyses of AMTEC Multi-Tube Cells and Recommendation for Revised Cell Design," in *Proceedings of the 2nd Space Technology and Applications International Forum (STAIF-97)*, CONF-970115, M. S. El-Genk, ed., American Institute of Physics, New York, NY, Conference Proceedings No. 387, 3:1395-1404.

Schock, A., H. Noravian, C. Or, and V. Kumar (1997b) "Design and Analysis of Radioisotope Power System Based on Revised Multi-Tube AMTEC Cell Design," in *Proceedings of the 2nd Space Technology and Applications International Forum (STAIF-97)*, CONF-970115, M. S. El-Genk, ed., American Institute of Physics, New York, NY, Conference Proceedings No. 387, 3:1411-1423.

Schock, A., V. Kumar, H. Noravian, and C. Or (1998a) "Recommended Design and Fabrication Sequence of AMTEC Test Assembly," in *Proceedings of the 3rd Space Technology and Applications International Forum (STAIF-98)*, CONF-980103, M. S. El-Genk, ed., American Institute of Physics, New York, NY, AIP Conference Proceedings No. 420, 3:1107-1118.

Schock, A., H. Noravian, C. Or, and V. Kumar (1998b) "Illustrative Application of AMTEC Cell Analysis with Overpotential Correction, and Predicted Cell Performance for a Wide Range of Design and Operating Parameters," in *Proceedings of the 33rd Intersociety Energy Conversion Engineering Conference*, held August 2-6, 1998, in Colorado Springs, CO, Paper No. 98243, American Nuclear Society, Chicago, IL.

Schock, A., H. Noravian, C. Or, and V. Kumar (1998c) "Improved OSC AMTEC Generator Design to Meet Goals of JPL's Candidate Europa Orbiter Mission," in *Proceedings of the 33rd Intersociety Energy Conversion Engineering Conference*, held August 2-6, 1998, in Colorado Springs, CO, Paper No. 98245, American Nuclear Society, Chicago, IL.

Schornhorst, J. R., and R. Viskanta (1968) "An Experimental Examination of the Validity of the Commonly Used Methods of Radiant Heat Transfer Analysis," *Journal of Heat Transfer*, 90 (4): 429-436.

Schuller, M. J., and R. A. LeMire (1994) "Long Life Testing and Efficiency Measurement of High Efficiency Alkali-Metal Thermal-to-Electric Converter Cells," in *Proceedings of the 45th Congress of the International Astronautical Federation*, held in Jerusalem, Israel, October 9-14, 1994, IAF, Paper No. IAF-94-R.4.390.

Schuller, M., P. Hausgen, E. Reiners, J. Merrill, R. Sievers, R. Svedberg, J. Ivanenok, III, C. Crowley, and M. Izenson (1996) "Vacuum Testing of High Efficiency AMTEC Cells," in *Proceedings of the 31st Intersociety Energy Conversion Engineering Conference*, held in Washington, D.C., August 11-16, 1996, Paper No. 96184, Institute of Electrical and Electronics Engineers, 2:877-884.

Shah, R. K., and A. L. London (1978) "Laminar Flow, Forced Convection in Ducts," *Advances in Heat Transfer, Supplement*, No. 1.

Siegel, R., and J. R. Howell (1981) *Thermal Radiation Heat Transfer*, Second Edition, Hemisphere Publishing Corporation, New York and London, Section 9.3, 283-292.

Sievers, R. K., and C. P. Bankston (1988) "Radioisotope Powered Alkali Metal Thermoelectric Converter Design for Space Systems," in *Proceedings of the 23rd Intersociety Energy Conversion Engineering Conference*, held in Denver, Colorado, July 31 - August 5, 1988, Paper No. 889082, Goswami, D. Y., Ed., American Society of Mechanical Engineers, 3:159-167.

Sievers, R. K., R. A. Markley, J. E. Schmidt, N. Weber, J. R. Rasmussen, S. L. Olsen, and T. K. Hunt (1989) "Alkali Metal Thermoelectric Converter Design for Space Power Systems Applications," in *Space Nuclear Power Systems 1988*, El-Genk, M. S., and M. D. Hoover, Eds., Orbit Book Company, Malabar, FL, 1989, Chapter 63, 9:531-540.

Sievers, R. K., T. K. Hunt, R. M. Williams, and M. L. Underwood (1992) "Assessment of the U.S. Industrial Program for AMTEC Development," in *Proceedings of the 27th Intersociety Energy Conversion Engineering Conference*, held in San Diego, CA, August 3-7, 1992, Paper No. 929065, Society of Automotive Engineers, Inc., 3:215-220.

Sievers, R. K., T. K. Hunt, J. F. Ivanenok III, Jr., J. E. Pantolin, and D. A. Butkiewicz (1993) "Modular Radioisotope AMTEC Power System," in *Proceedings of the 10th Symposium on Space Nuclear Power and Propulsion*, CONF-930103, M. S. El-Genk, Ed., American Institute of Physics, New York, AIP Conference Proceedings No. 271, 1:319-324.

Sievers, R. K., J. R. Rasmussen, C. A. Borkowski, T. J. Hendricks, and J. E. Pantolin (1998) "PX-5 AMTEC Cell Development," in *Proceedings of the 3rd Space Technology and Applications International Forum (STAIF-98)*, CONF-980103, M. S. El-Genk, ed., American Institute of Physics, New York, NY, AIP Conference Proceedings No. 420, 3:1479-1485.

Steinbruck, M., V. Heinzl, F. Huber, W. Peppeler, H. Will, and M. Voss (1993) "Investigations of Beta-Alumina Solid Electrolytes for Application in AMTEC Cells," in *Proceedings of the 28th*

*Intersociety Energy Conversion Engineering Conference*, held in Atlanta, GA, August 8-13, 1993, Paper No. 93108, American Chemical Society, I:1.799-1.807.

Stone, H. L. (1968) "Iterative Solution of Implicit Approximations of Multidimensional Partial Differential Equations," *SIAM Journal of Numerical Analysis*, 5: 530-558.

Svedberg, R. C., D. A. Schaupner, and A. J. Appleby (1997) "Accelerated Testing for Extended-Service AMTEC Cells," in *Proceedings of the 32nd Intersociety Energy Conversion Engineering Conference*, held in Honolulu, HI, July 27 - August 1, 1997, American Chemical Society, Paper No. 97458, 2:1230-1235.

Tanaka, K., A. Negishi, and T. Masuda (1992) "Structure of Current Collector and Flow Characteristics of Sodium Vapor for the Alkali Metal Thermoelectric Converter," in *Proceedings of the 27th Intersociety Energy Conversion Engineering Conference*, held in San Diego, CA, August 3-7, 1992, Paper No. 929008, Society of Automotive Engineers, Inc., 3:13-18.

Tanaka, K., R. M. Williams, M. L. Underwood, and M. A. Ryan (1993) "Designing a Wick for Sodium Recirculation of AMTEC Cells," in *Proceedings of the 28th Intersociety Energy Conversion Engineering Conference*, held in Atlanta, GA, August 8-13 1993, Paper No. 93043, American Chemical Society, 1:823-828.

Tournier, J.-M. (1996) "HPTAM, A Two-Dimensional Heat Pipe Transient Analysis Model, Including the Startup from a Frozen State," A Dissertation in partial fulfillment of the requirements for the Degree of Doctor of Philosophy in Engineering, the University of New Mexico, Albuquerque, NM, May 1996.

Tournier, J.-M., and M. S. El-Genk (1996) "A Vapor Flow Model for Analysis of Liquid-Metal Heat Pipe Startup from the Frozen State," *International Journal of Heat and Mass Transfer*, 39 (18): 3767-3780.

Underwood, M. L., R. M. Williams, B. Jeffries-Nakamura, C. P. Bankston, and T. Cole (1988) "Progress in AMTEC Electrode Experiments and Modeling," in *Proceedings of the 23rd Intersociety Energy Conversion Engineering Conference*, held in Denver, Colorado, July 31 - August 5, 1988, Paper No. 889110, Goswami, D. Y., Ed., The American Society of Mechanical Engineers, I:227-233.

Underwood, M. L., D. O'Connor, R. M. Williams, B. Jeffries-Nakamura, M. A. Ryan, and C. P. Bankston (1990) "Thermal Characterization of an AMTEC Recirculating Test Cell," in *Proceedings of the 25th Intersociety Energy Conversion Engineering Conference*, held in Reno, Nevada, August 12-17, 1990, Nelson, P. A., W. W. Schertz, and R. H. Till, Eds., American Institute of Chemical Engineers, II:407-411.

Underwood, M. L., R. M. Williams, M. A. Ryan, B. Jefferies-Nakamura, and D. O'Connor (1992) "An AMTEC Vapor-Vapor Series Connected Cell," in *Proceedings of the 9th Symposium on Space Nuclear Power Systems*, CONF-920104, held in Albuquerque, NM, January 12-15,

1992, American Institute of Physics, New York, AIP Conference Proceedings No. 246, 3:1331-1337.

van Atta, C. M. (1965) *Vacuum Science and Engineering*, McGraw-Hill Book Company, New York, Chapter 2, pp. 23-61.

Vargaftik, N. B. (1975) *Tables on the Thermophysical Properties of Liquids and Gases, in Normal and Dissociated States*, 2nd Edition, Hemisphere Publishing Corporation, Washington, D.C.

Weber, N. (1974) "A Thermoelectric Device Based on Beta-Alumina Solid Electrolyte," *Energy Conversion*, 14(1), 1-7.

White, F. M. (1991) *Fluid Mechanics*, 2nd Edition, McGraw-Hill Publishing Company, New York, Section 6.6, pp. 321-332.

Williams, R. M., M. E. Loveland, B. Jeffries-Nakamura, M. L. Underwood, C. P. Bankston, H. Leduc, and J. T. Kummer (1990a) "Kinetics and Transport at AMTEC Electrodes - I. The Interfacial Impedance Model," *Journal of the Electrochemical Society*, 137 (6): 1709-1716.

Williams, R. M., B. Jeffries-Nakamura, M. L. Underwood, C. P. Bankston, and J. T. Kummer (1990b) "Kinetics and Transport at AMTEC Electrodes - II. Temperature Dependence of the Interfacial Impedance of Na(g)/Porous Mo/Na-Beta" Alumina," *Journal of the Electrochemical Society*, 137 (6): 1716-1723.

Williams, R. M., B. Jeffries-Nakamura, M. L. Underwood, D. O'Connor, M. A. Ryan, S. Kikkert, and C. P. Bankston (1990c) "Lifetime Studies of High Power Rhodium/Tungsten and Molybdenum Electrodes for Application to AMTEC," in *Proceedings of the 25th Intersociety Energy Conversion Engineering Conference*, held in Reno, Nevada, August 12-17, 1990, AIChE Publisher, II:413-419.

Williams, R. M., B. Jeffries-Nakamura, M. A. Ryan, M. L. Underwood, A. Kisor, D. O'Connor, and S. Kikkert (1993) "Advances in Studies of Electrode Kinetics and Mass Transport in AMTEC Cells," in *Proceedings of the 28th Intersociety Energy Conversion Engineering Conference*, held in Atlanta, GA, August 8-13 1993, Paper No. 93373, I:1.819-1.822, American Chemical Society.

## APPENDIX A: SODIUM VAPOR FLOW PROPERTIES AND CHARACTERISTICS

In this appendix, properties of the sodium vapor, such as dynamic viscosity and mean free path, are evaluated. Also, the sodium vapor flow is characterized by several dimensionless numbers, such as Knudsen number, Reynolds number, and Mach number. These characteristics are calculated herein. A nomenclature of the variables used in this appendix can be found in Chapter 3 (Section 3.1).

### A.1 DYNAMIC VISCOSITY OF SODIUM VAPOR

For a pure monoatomic gas, the Lennard-Jones spherical energy potential is adequate, and the dynamic viscosity is given by the kinetic theory of gases as (Bird et al. 1960):

$$\mu = \frac{5}{16\sigma^2} \sqrt{\frac{mkT}{\pi}} \times \frac{1}{\Omega^*} , \quad (A1)$$

where  $\sigma = 3.58 \times 10^{-10}$  m is the molecular diameter of sodium,  $m = M / N_a$  is the molecular mass of sodium,  $N_a = 6.022 \times 10^{23}$  atoms / mole is the Avogadro number, and  $k = 1.3806 \times 10^{-23}$  J / K is the Boltzmann constant ( $R_g = k \times N_a$ ). The function  $\Omega^*$  is a dimensionless collision integral which indicates the deviation of the Lennard-Jones molecular energy potential (of parameters  $\sigma$  and  $\epsilon$ , maximum energy of attraction between a pair of molecules) from the idealized rigid-sphere model. It is a tabulated function of the dimensionless temperature (Hirschfelder et al. 1954):

$$T^* = \frac{kT}{\epsilon} \approx 1.3 \frac{T}{T_{cr}} , \quad (A2)$$

where  $T_{cr} = 2,510$  K is the critical temperature of sodium. The approximation in Equation (A2) arises from the principle of corresponding states. To a good approximation, the function  $\Omega^*$  can be expressed as:

$$\Omega^*(T^*) = 3.7721 - 3.8365 \times T^* + 1.6637 \times (T^*)^2 , \quad (A3)$$
$$0 < T^* < 1 .$$

As an illustration, at  $T = 1,000$  K, we obtain  $T^* = 0.518$ ,  $\Omega^* = 2.231$ , and  $\mu = 1.416 \times 10^{-5}$  kg / m.s.

### A.2 MEAN FREE PATH AND KNUDSEN NUMBER OF SODIUM VAPOR

The dimensionless Knudsen number is the ratio of the molecules mean free path,  $\lambda$ , to the channel equivalent diameter  $D_e$  :

$$Kn = \frac{\lambda}{D_e} . \quad (A4)$$

The gas flow through a channel can be classified into three types, depending on the value of  $Kn$ . At small values ( $Kn < 0.01$ ), the mean free path is very small compared to the diameter of the channel, and the flow is in the *viscous or continuum regime*, which can be described by the continuum or Navier-Stokes model. In this regime, the mass and momentum transfers are dominated by the molecule-molecule collisions. The second type of flow, the *free-molecular flow regime*, occurs when the mean free path of the gas is large compared to the channel diameter ( $Kn > 1.0$ ). This flow regime, which is limited by the molecular collisions with the walls, is best modeled using the kinetics theory. Between these two extreme flow regimes, an intermediate or *transition flow regime* exists, in which both molecule-molecule and molecule-wall collisions are important.

The mean free path of the gas molecules is given by the kinetic theory of gases as (Cunningham and Williams 1980):

$$\lambda = \frac{M}{\sqrt{2}\pi\sigma^2 N_a \rho} \quad (A5)$$

### A.3 REYNOLDS NUMBER OF SODIUM VAPOR FLOW

The axial Reynolds number of the vapor flow has the expression :

$$Re(z) = \frac{D_e \dot{m}_z''(z)}{\mu} \quad (A6)$$

For the case of a uniform current density across the BASE tubes,  $N_B = 7$  and  $L_B = 2 \times 10^{-2}$  m, we obtain using Equation (3.13):

$$\begin{aligned} \dot{m}_z^{\max} &= L_B \frac{d\dot{m}_z(z)}{dz} = L_B (N_B \pi D_B) \times \frac{M}{F} J_r(z) \\ &= J_r [A / cm^2] \times 0.6672 \times 10^{-5} \quad [kg / s] \end{aligned} \quad (A7)$$

Using Equations (3.11) and (3.12) one obtains  $D_e = 9.28 \times 10^{-3}$  m and  $A = 612. \times 10^{-6}$  m<sup>2</sup>, so that the Reynolds number at the top of the BASE tubes has the value:

$$Re_3 = \frac{D_e \dot{m}_z^{\max}}{\mu A} = J_r [A / cm^2] \times 7.1 \quad (A8)$$

Clearly,  $Re < 2300$  (actually  $Re < 15$ ) for all practical operating conditions in the AMTEC cell, and the vapor flow is always laminar.

#### A.4 MACH NUMBER OF SODIUM VAPOR FLOW

The axial Mach number of the vapor flow has the expression :

$$\begin{aligned} Ma(z) &= \frac{\bar{U}_z(z)}{\text{sonic velocity}} = \frac{\dot{m}_z''(z) / \rho}{\sqrt{\gamma R_g T / M}} = \frac{\dot{m}_z''(z)}{\sqrt{\gamma \rho P}} \\ &= \frac{\dot{m}_z''(z)}{P(z)} \sqrt{\frac{R_g T}{\gamma M}} \end{aligned} \quad (A9)$$

where  $\gamma$  is the specific heat ratio. For monoatomic gas,  $\gamma = 5/3$ . At a temperature  $T = 1,000$  K, the Mach number at the top of the BASE tubes can be calculated as:

$$Ma_3 = \frac{\dot{m}_z^{\max}}{AP} \sqrt{\frac{R_g T}{\gamma M}} = 5.1 \times \frac{J_r [A / cm^2]}{P [Pa]} \quad (A10)$$

If the pressure at the top of the BASE tubes is less than 20 Pa, the Mach number is greater than 0.2, which means that the vapor flow is compressible. Therefore, the incompressible laminar viscous friction coefficient must be corrected for compressible effects.



## APPENDIX B: FLOW CONDUCTANCES IN THE FREE-MOLECULAR VAPOR FLOW REGIME

Approximate formulas for molecular flow rates through channels and apertures of any shapes were developed principally by Knudsen using the kinetic theory of gases. When the mean free path of the gas molecules is large as compared to the cross-sectional dimension of the channel, the flow conductance is independent of the pressure. For most purposes, the conductance formulas derived by Knudsen are sufficiently accurate. A nomenclature of the variables used in this appendix can be found in Chapter 3 (Section 3.1).

In the free-molecular flow regime, the pressure drop across a channel of uniform cross section  $A$  and length  $L$  is given by (Van Atta 1965):

$$\Delta P = \frac{L}{D^K} \left( \frac{R_g T}{M} \right) \dot{m}_z'' = \frac{A}{C} \left( \frac{R_g T}{M} \right) \dot{m}_z'', \quad (\text{B1})$$

where  $C$  is the flow conductance [ $\text{m}^3/\text{s}$ ].

### B.1 CONDUCTANCE OF A LONG CHANNEL AT LOW PRESSURE

The conductance of a long channel of length  $L$  is given by:

$$C_L = \frac{16}{3L} \left( \frac{R_g T}{2\pi M} \right)^{1/2} \frac{A^2}{\text{Perimeter}}, \quad (\text{B2})$$

which proves to agree well with experimental results (van Atta 1965).

### B.2 CONDUCTANCE OF AN APERTURE AT LOW PRESSURE

When the channel is short, the end effects become non-negligible. In the limit when the length is decreased to zero, the result is an aperture of cross-sectional area  $A$ . The formula for the conductance of the channel must therefore become equal to that of the aperture as the length shrinks to zero. The conductance of an aperture of area  $A$  of any shape has the expression:

$$C_o = \left( \frac{R_g T}{2\pi M} \right)^{1/2} A. \quad (\text{B3})$$

### B.3 CONDUCTANCE OF A CHANNEL AT LOW PRESSURE, CORRECTED FOR END EFFECTS

A channel of finite length may be modeled as an aperture, the two sides of which are separated and connected in series by a channel of length  $L$ . The result, called the Dushman formula (Van Atta 1965), is a combination of two conductances in parallel (since the pressure drop is inversely proportional to the conductance):

$$C = \frac{C_o C_L}{C_o + C_L} = \frac{C_o}{1 + \frac{3L}{16} \frac{\text{Perimeter}}{A}} = \frac{C_o}{1 + \frac{3L}{4D_e}} \quad (\text{B4})$$

$$= \frac{A}{1 + \frac{3L}{4D_e}} \left( \frac{R_g T}{2\pi M} \right)^{1/2}$$

Combining Equations (B1) and (B4) one finds that the diffusion coefficient for free-molecular flow through a channel of arbitrary cross section has the expression:

$$D^K = \frac{L}{A} C = \frac{L}{1 + \frac{3L}{4D_e}} \left( \frac{R_g T}{2\pi M} \right)^{1/2} \quad (\text{B5})$$

The method of Knudsen, by which Equation (B5) for diffusion coefficient at low gas pressure was derived, is only approximate. However, it was found to perform surprisingly well for channels of various cross sections and shape, when compared with experimental data and numerical results obtained using the Monte-Carlo calculation method (van Atta 1965). For tubes of circular cross section, Clausing has carried out a much more exact calculation (Equation 3.7b). The use of the Dushman formula (Equation B5) for circular tubes results in a maximum error of 11.4% at a length to diameter ratio  $L/D_e = 2$  (Figure B1). The Clausing formula was also used to calculate the conductance of a 90° bent elbow (the length was taken equal to the centerline length of the bent tube) and was found to be very accurate (Figure B2). The importance of this result is that in the free-molecular flow regime very little additional resistance to flow is introduced by the presence of bends in the channels. For the conductance of a cylindrical annulus, the Dushman formula is surprisingly good, with maximum deviations of about 10% only when compared with numerical results obtained using the Monte-Carlo calculation method (Figure B3). Also the use of the Dushman formula for rectangular louver and chevron baffles results in a maximum error of 10% when compared with experimental data (Figures B4 and B5).

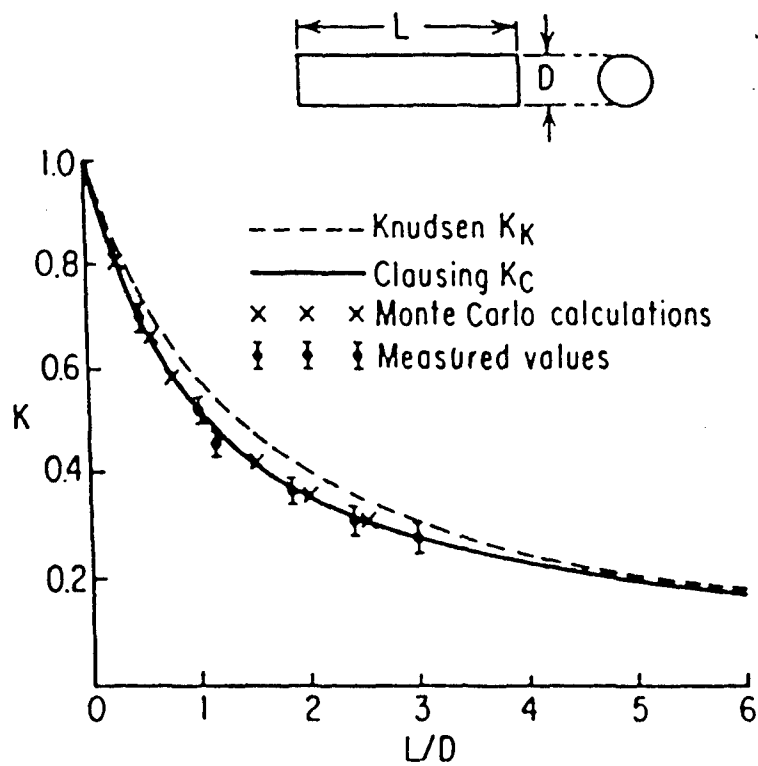


Figure B1. Free-Molecular Flow Conductance Ratio,  $C/C_0$ , for a Circular Tube (Levenson et al. 1961).

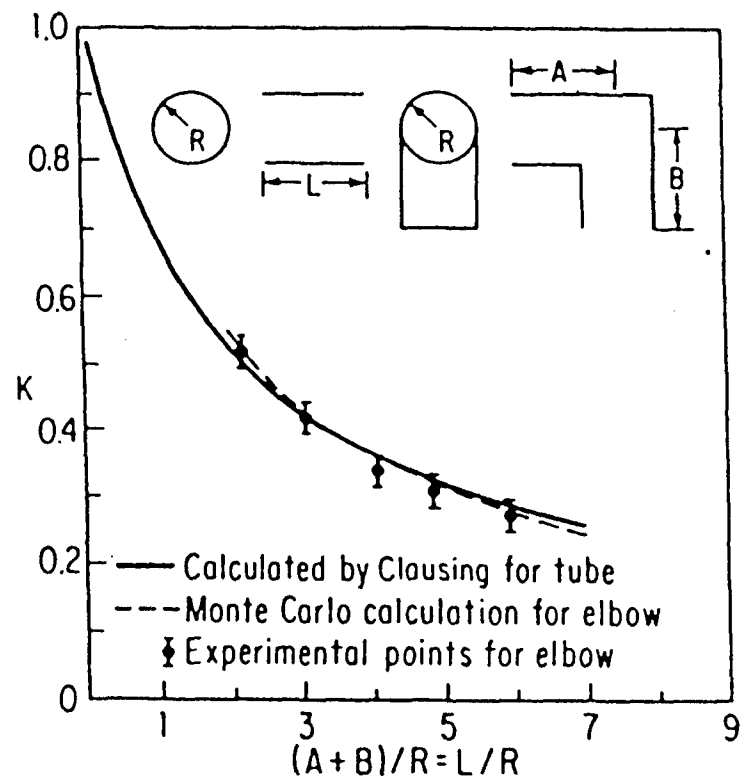


Figure B2. Free-Molecular Flow Conductance Ratio,  $C/C_0$ , for a 90° Bent Elbow (Levenson et al. 1961).

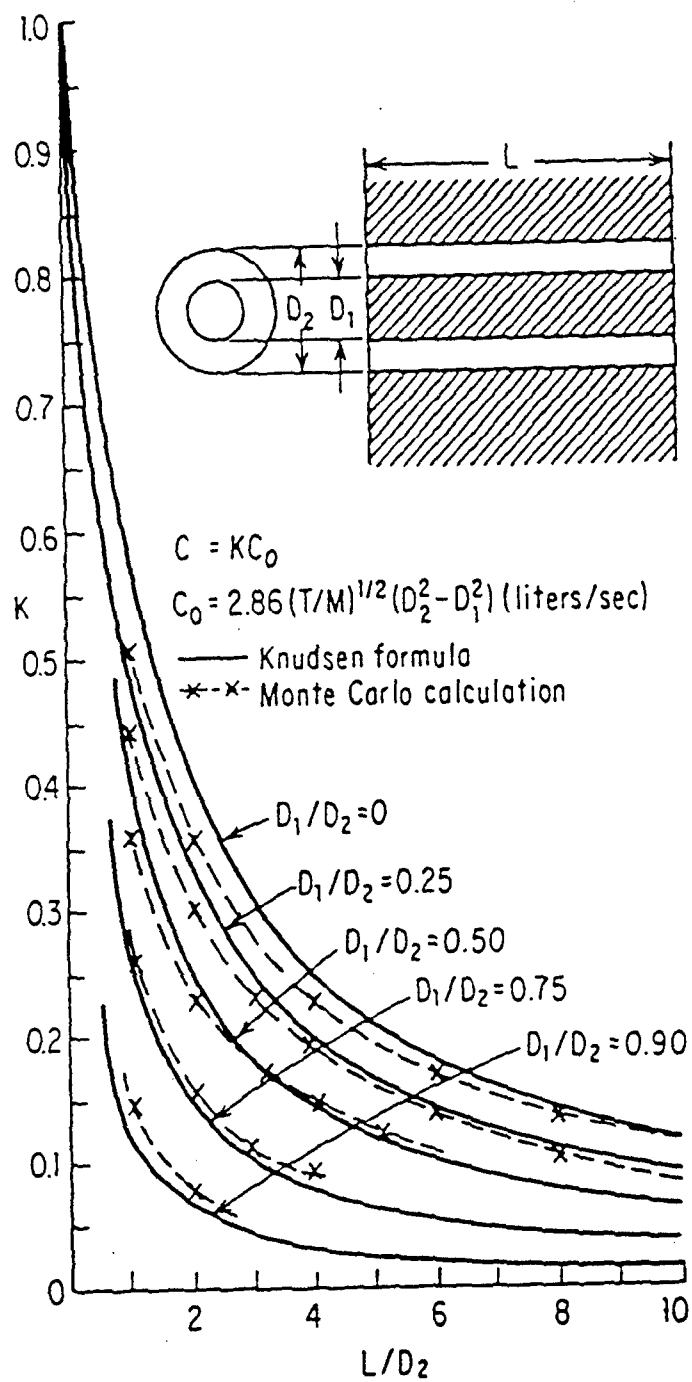


Figure B3. Free-Molecular Flow Conductance Ratio,  $C/C_0$ , for a Cylindrical Annulus (Levenson et al. 1961).

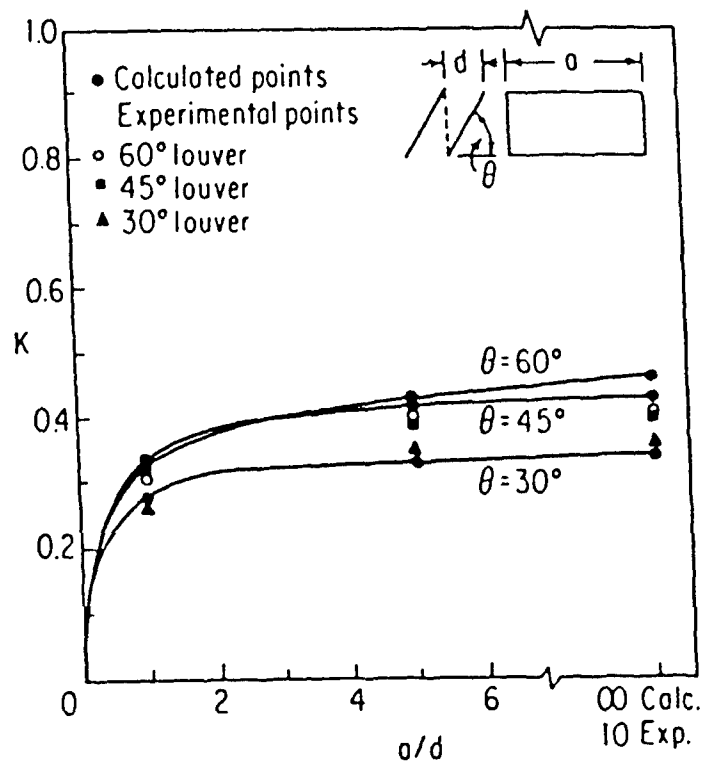


Figure B4. Free-Molecular Flow Conductance Ratio,  $C/C_0$ , for Rectangular Louvers (Levenson et al. 1961).

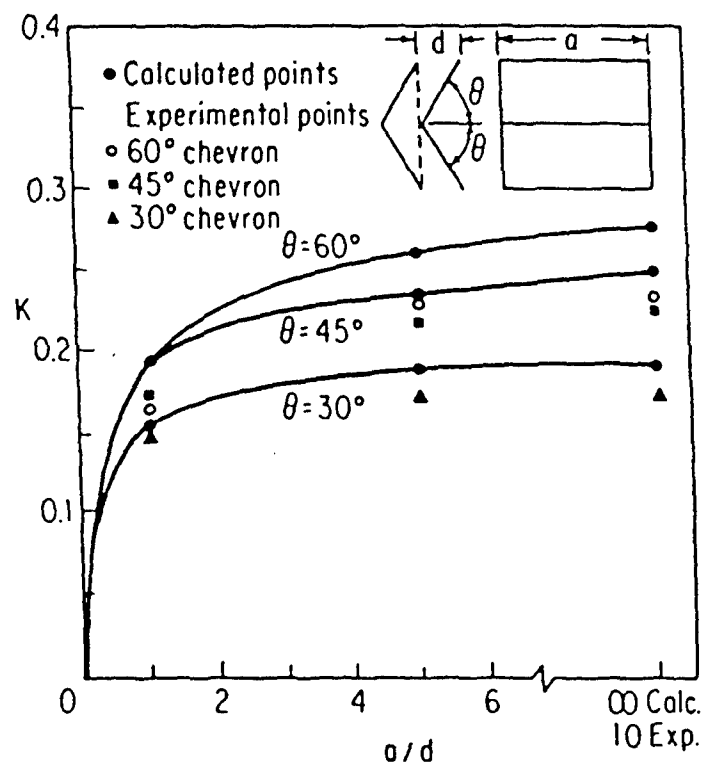


Figure B5. Free-Molecular Flow Conductance Ratio,  $C/C_0$ , for Chevrons Baffles (Levenson et al. 1961).

## APPENDIX C: RADIATION VIEW FACTORS IN PX MULTI-TUBE AMTEC CELL

All radiation view factors are calculated from a set of basic geometric factors for cylindrical cavity, coaxial cylindrical enclosure, and between parallel cylinders of finite length. The basic set of factors is described in the next subsection. The definition of the variables used in this appendix can be found in Chapter 5, Section 5.1.

### C.1 ELEMENTARY RADIATION VIEW FACTORS

The first set of elementary view factors allows us to calculate all factors between surface elements in a circular cylindrical enclosure. Such elements are finite sections of right cylinder and rings of the top and bottom ends of the cylinder.

#### C.1.1. View Factor between Inside Surface of Right Cylinder and itself (C-37, Howell 1982)

$$F_{11} = 1 + X - (1 + X^2)^{1/2}, \quad (C1)$$

where  $X = \frac{h}{2R_c}$ .

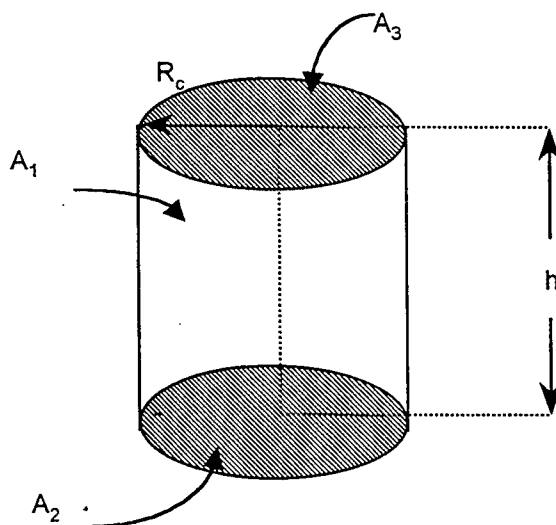


Figure C1.

#### C.1.2. View Factor between Inside Surface of Right Cylinder and Base Disk

The enclosure relation for surface  $A_1$  can be written (Figure C1):

$$F_{11} + F_{12} + F_{13} = 1.$$

Since  $F_{12} = F_{13}$  by symmetry, we find that:

$$F_{12} = \frac{1}{2}(1 - F_{11}), \quad (C2)$$

where  $F_{11}$  is given by Equation (C1).

**C.1.3 View Factor between Finite Section of Right Cylinder and another Separated Section (C-82, Howell 1982)**

$$X = \frac{h_2}{R_c}, \quad Y = \frac{a + h_2}{R_c}, \quad Z = \frac{h_1 + a + h_2}{R_c}$$

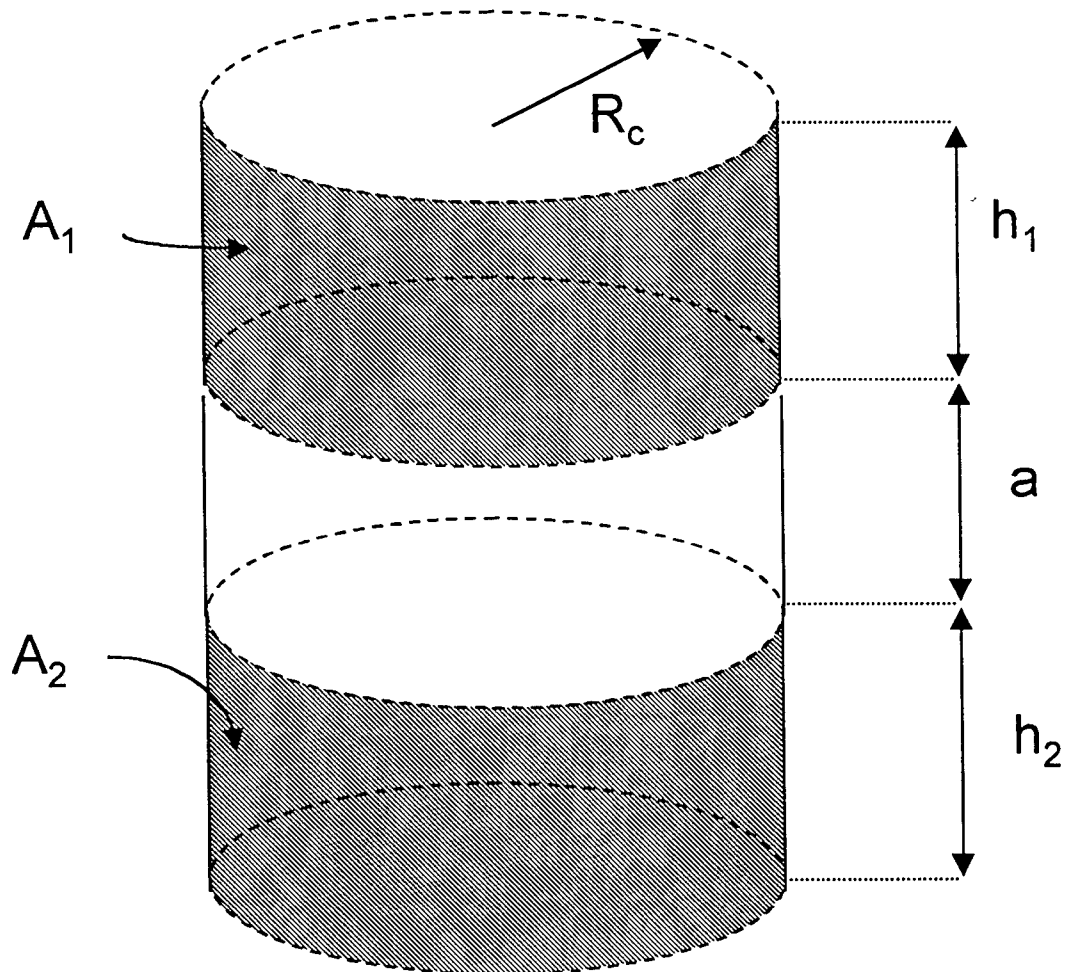


Figure C2.

$$F_{12} = \frac{1}{4(Z-Y)} \left\{ (Z-X)\sqrt{4+(Z-X)^2} - (Y-X)\sqrt{4+(Y-X)^2} + Y\sqrt{4+Y^2} - Z\sqrt{4+Z^2} \right\} + \frac{X}{2} \quad (C3)$$

**C.1.4. View Factor between Finite Section of Right Cylinder and Separated Base Ring (C-80, Howell 1982)**

$$X = \frac{a}{R_c}, \quad Y = \frac{a+h}{R_c}, \quad V = \frac{R_i}{R_c}, \quad W = \frac{R_o}{R_c}$$

$$F_{12} = \frac{-1}{4(Y-X)} \left[ \frac{\sqrt{Y^4 + 2Y^2(1+V^2) + (1-V^2)^2} - \sqrt{Y^4 + 2Y^2(1+W^2) + (1-W^2)^2}}{\sqrt{X^4 + 2X^2(1+W^2) + (1-W^2)^2} - \sqrt{X^4 + 2X^2(1+V^2) + (1-V^2)^2}} \right] \quad (C4)$$

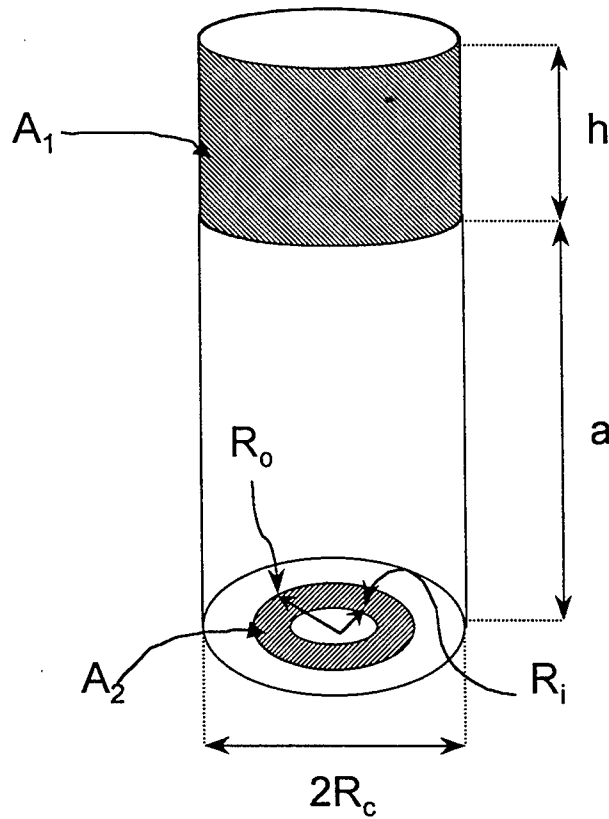


Figure C3.



### C.1.5. View Factor between Disk and Coaxial Parallel Ring (C-44, Howell 1982)

$$X = \frac{a}{R_c}, \quad V = \frac{R_i}{R_c}, \quad W = \frac{R_o}{R_c}$$

$$F_{12} = \frac{1}{2} \left\{ W^2 - V^2 - \sqrt{(1 + W^2 + X^2)^2 - 4W^2} + \sqrt{(1 + V^2 + X^2)^2 - 4V^2} \right\}. \quad (C5)$$

The next set of basic view factors allows to calculate all factors between surface elements in a coaxial cylindrical enclosure. The elements of interest are finite sections of inner and outer cylinders and rings of the top and bottom annular ends of the enclosure.

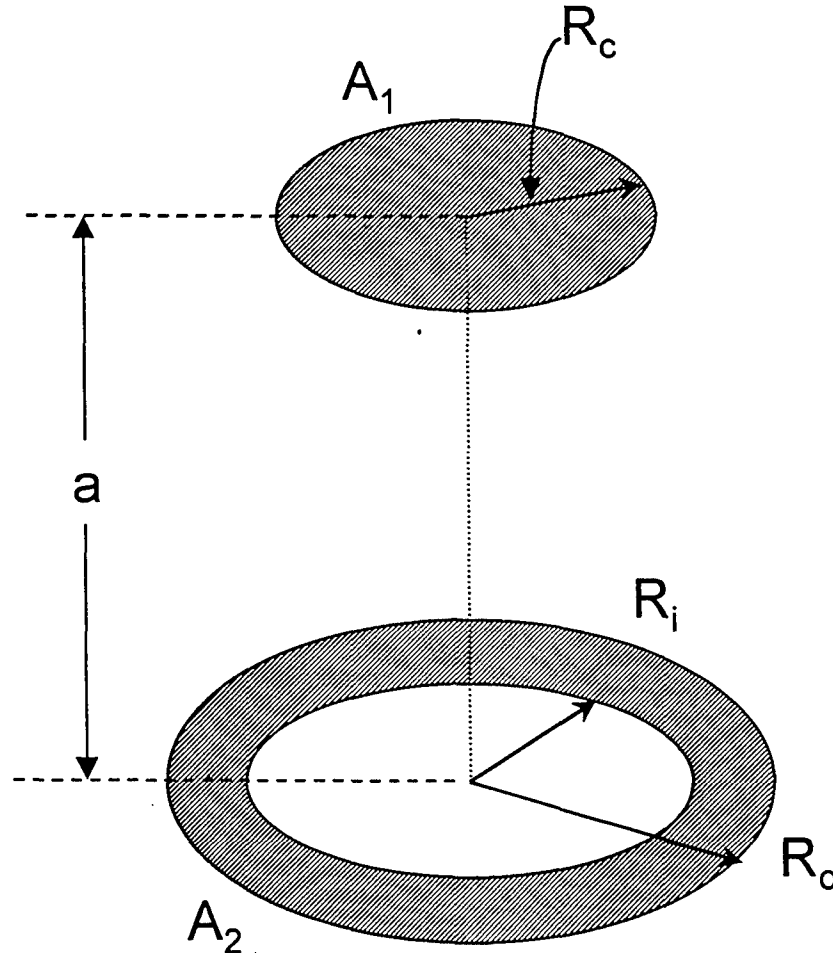


Figure C4.

**C.1.6. View Factor between Interior Surface of Outer Coaxial Cylinder and itself (Sparrow and Cess 1970, Appendix A)**

$$R = \frac{R_o}{R_i}, \quad Z = \frac{h}{R_i}$$

$$F_{11} = 1 - \frac{1}{R} + \frac{2}{\pi R} \tan^{-1} \frac{2\sqrt{R^2 - 1}}{Z} - \frac{Z}{2\pi R} \left\{ \frac{\sqrt{4R^2 + Z^2}}{Z} \sin^{-1} \left[ \frac{4(R^2 - 1) + \frac{Z^2}{R^2}(R^2 - 2)}{Z^2 + 4(R^2 - 1)} \right] - \sin^{-1} \left( \frac{R^2 - 2}{R^2} \right) + \frac{\pi}{2} \left( \frac{\sqrt{4R^2 + Z^2}}{Z} - 1 \right) \right\}$$

(C6)

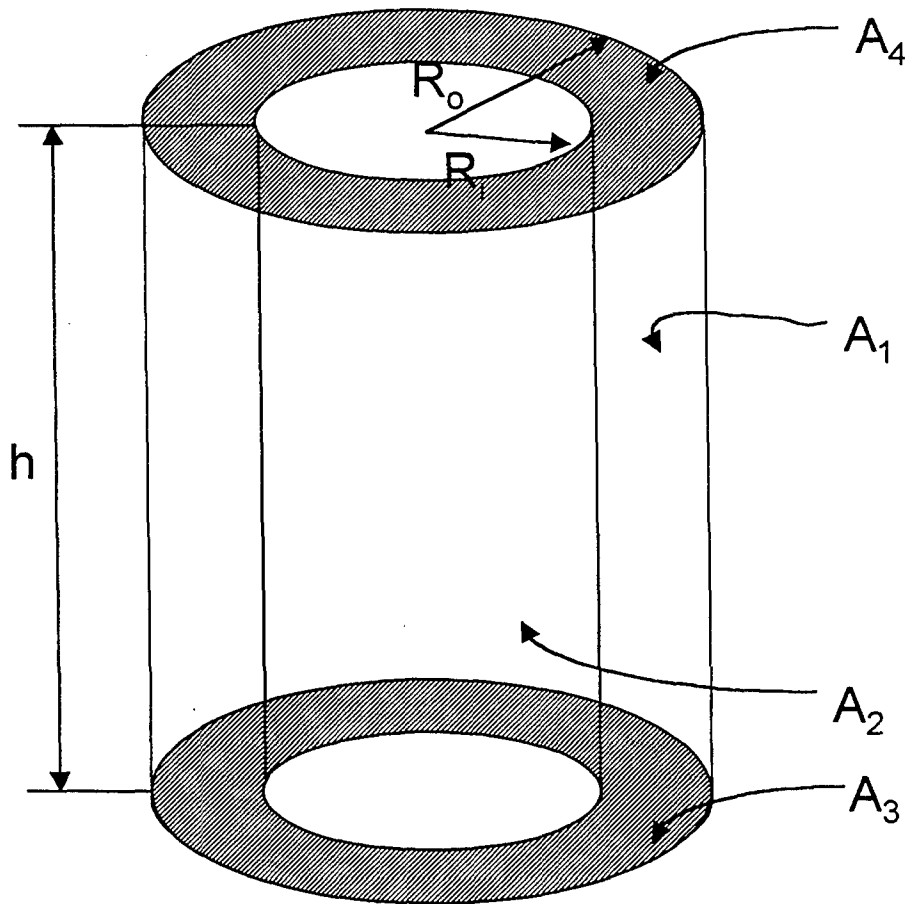


Figure C5.

**C.1.7. View Factor between Interior Surface of Outer Coaxial Cylinder and Exterior Surface of Inner Coaxial Cylinder (Sparrow and Cess 1970, Appendix A)**

$$R = \frac{R_o}{R_i}, \quad Z = \frac{h}{R_i}, \quad V = Z^2 + R^2 - 1, \quad W = Z^2 - R^2 + 1$$

$$F_{12} = \frac{1}{R} - \frac{1}{\pi R} \left\{ \cos^{-1} \frac{W}{V} - \frac{1}{2Z} \left[ \sqrt{(V+2)^2 - (2R)^2} \cos^{-1} \frac{W}{RV} + W \sin^{-1} \frac{1}{R} - \frac{\pi V}{2} \right] \right\}$$

(C7)

Note that for any argument  $\xi$ , the inverse circular functions are defined such that  $-\frac{\pi}{2} \leq \sin^{-1} \xi \leq \frac{\pi}{2}$  and  $0 \leq \cos^{-1} \xi \leq \pi$ .

**C.1.8. View Factor between Interior Surface of Outer Coaxial Cylinder and Annular Base of Coaxial Enclosure**

the enclosure relation for surface  $A_1$  reads (see Figure C5):

$$F_{11} + F_{12} + 2F_{13} = 1, \text{ so that}$$

$$F_{13} = \frac{1}{2}(1 - F_{11} - F_{12}),$$

(C8)

where  $F_{11}$  and  $F_{12}$  are given by Equations (C6) and (C7), respectively.

**C.1.9. View Factor between Exterior Surface of Inner Coaxial Cylinder and Annular End between Coaxial Cylinders**

The enclosure relation for surface  $A_2$  can be written (Figure C5):

$$F_{21} + 2F_{23} = 1.$$

By reciprocity, we have  $F_{21} = \frac{A_1}{A_2} F_{12} = R F_{12}$ , so that finally,

$$F_{23} = \frac{1}{2}(1 - R F_{12}),$$

(C9)

where  $F_{12}$  is given by Equation (C7).

### C.1.10. View Factor between Annular Base of Coaxial Cylindrical Enclosure and Opposit Annular End

The enclosure relation for surface  $A_3$  can be written (Figure C5):  $F_{31} + F_{32} + F_{34} = 1$ .

By reciprocity,

$$F_{31} = \frac{A_1}{A_3} F_{13} = \frac{2R}{R^2 - 1} Z F_{13}, \text{ and } F_{32} = \frac{A_2}{A_3} F_{23} = \frac{2Z}{R^2 - 1} F_{23}. \text{ Finally:}$$

$$F_{34} = 1 - \frac{2Z}{R^2 - 1} (F_{23} + R F_{13}), \text{ or}$$

$$F_{34} = 1 - \frac{Z}{R^2 - 1} \{1 + R(1 - F_{11} - 2F_{12})\}, \quad (C10)$$

where  $F_{11}$  and  $F_{12}$  are given by Equations (C8) and (C7), respectively.

### C.1.11. View Factor between Ring on Base of Coaxial Cylindrical Enclosure and Inner Surface of Outer Cylinder

There is no closed-form expression available in the literature for the case where the radii of the ring are different from the radii of the concentric cylinders. Instead the contour integral method is used to derive a closed-form expression for the view factor  $F_{dA_1-A_2}$ , between a differential ring on the annular end plane and the outer cylindrical wall of the enclosure (Figure C6). This expression can then be integrated numerically using Simpson's integration rule to obtain the desired view factor. If we define the following reduced variables with respect to  $R_o$ :

$$Z = \frac{h}{R_o}, \quad R = \frac{R_i}{R_o}, \quad P_1 = \frac{R_1}{R_o}, \quad P_2 = \frac{R_2}{R_o}, \text{ and } x = \frac{r}{R_o}, \text{ then } \frac{A_1}{A_2} = \frac{\pi(R_2^2 - R_1^2)}{2\pi R_o h} = \frac{P_2^2 - P_1^2}{2Z}.$$

The differential view factor between the differential ring  $[r, r + dr]$  and the outer cylinder wall  $A_2$  can be written (Minning 1979):

$$F_{dr \rightarrow A_2} = \frac{1}{\pi} \tan^{-1} \left[ \frac{1+x}{1-x} \tan\left(\frac{\omega}{2}\right) \right] - \frac{1}{\pi} \frac{1-x^2-Z^2}{\sqrt{(1+x^2+Z^2)^2 - (2x)^2}} \times \tan^{-1} \left[ \frac{\sqrt{(1+x^2+Z^2)^2 - (2x)^2}}{1+x^2+Z^2-2x} \tan\left(\frac{\omega}{2}\right) \right], \quad (C11)$$

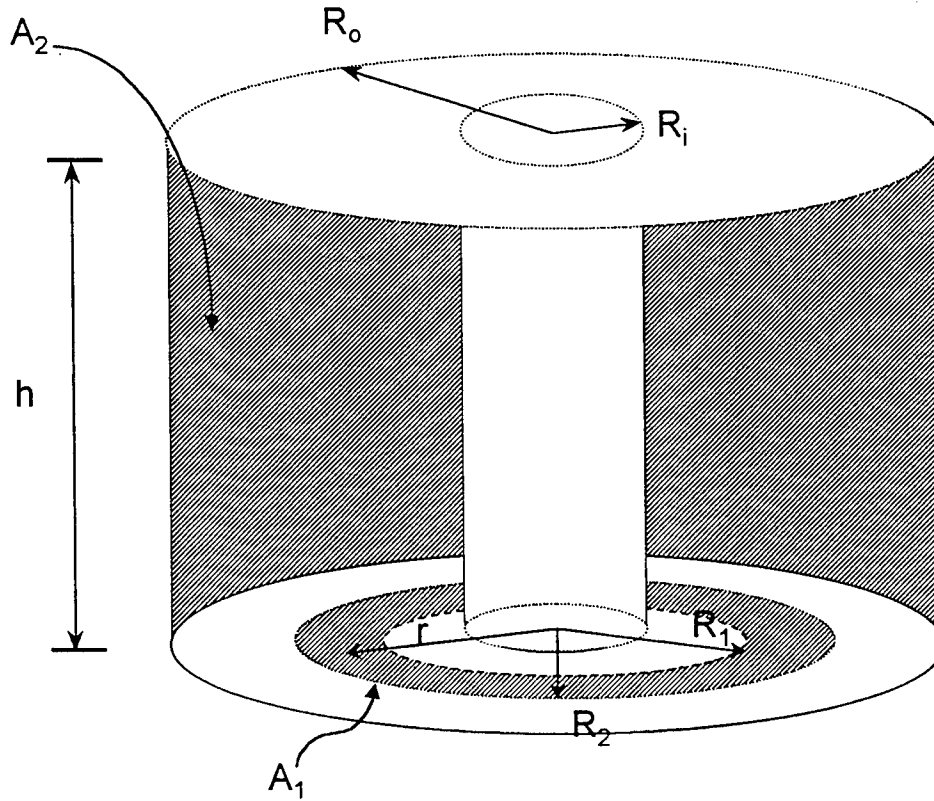


Figure C6.

where  $\omega = \cos^{-1}\left(\frac{R}{x}\right) + \cos^{-1}(R)$ . Finally, the integrated view factor has the form:

$$F_{A_1 \rightarrow A_2} = \frac{1}{A_1} \int_{R_1}^{R_2} (2\pi r) F_{dr \rightarrow A_2} dr = \frac{2}{P_2^2 - P_1^2} \int_{P_1}^{P_2} x F_{dr \rightarrow A_2}(x) dx \quad (C12)$$

in reduced variables. The integral is performed numerically using Simpson's rule.

#### C.1.12. View Factor between Ring on Base of Coaxial Cylindrical Enclosure and Separated Inner Shell of Outer Cylinder

This factor is easily obtained by using simple flux algebra:

$$F_{A_1 \rightarrow A_2[a, a+h]} = F_{A_1 \rightarrow A_2[0, a+h]} - F_{A_1 \rightarrow A_2[0, a]}, \quad (C13)$$

where the factors on the right-hand side are calculated from Equation (C12).

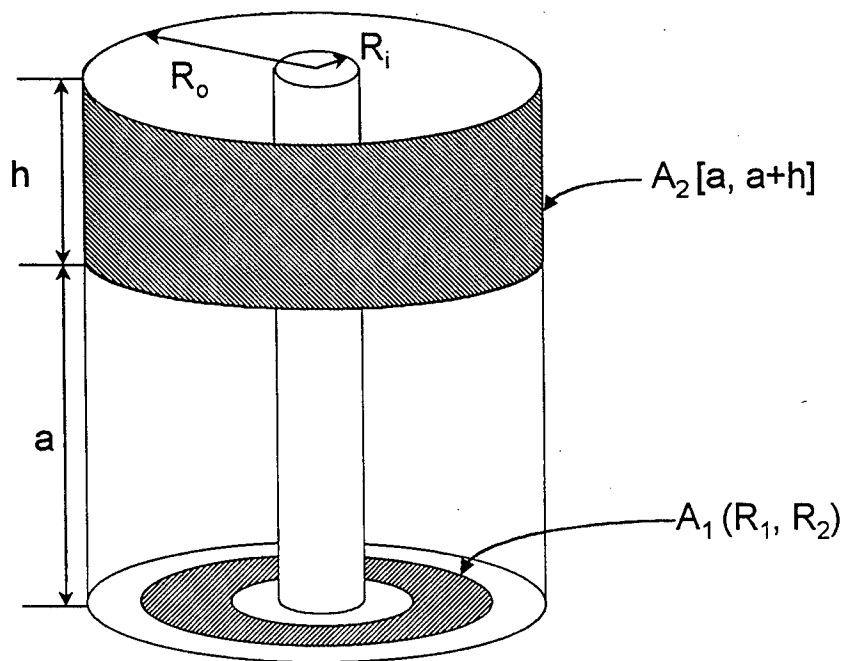


Figure C7.

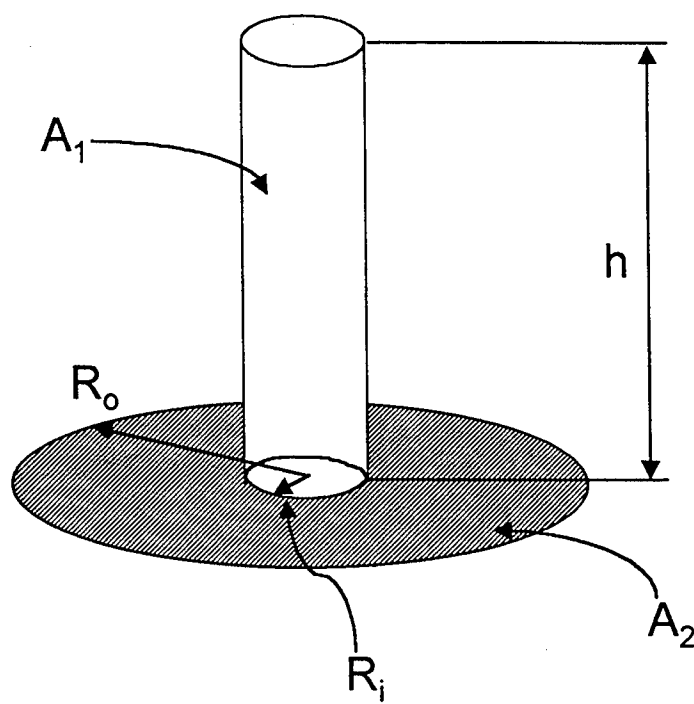


Figure C8.

**C.1.13. View Factor between Outer Surface of Cylinder and Annular Disk at End of Cylinder (Rea 1975)**

$$R = \frac{R_i}{R_o}, Z = \frac{h}{R_o}, \quad V = Z^2 + R^2 - 1, \quad W = Z^2 - R^2 + 1, \quad (C14)$$

$$F_{12} = \frac{W}{8RZ} + \frac{1}{2\pi} \left\{ \cos^{-1} \frac{V}{W} - \frac{V}{2RZ} \sin^{-1} R - \frac{1}{2Z} \cos^{-1} \left( \frac{VR}{W} \right) \times \sqrt{\left( \frac{V+2}{R} \right)^2 - 4} \right\}$$

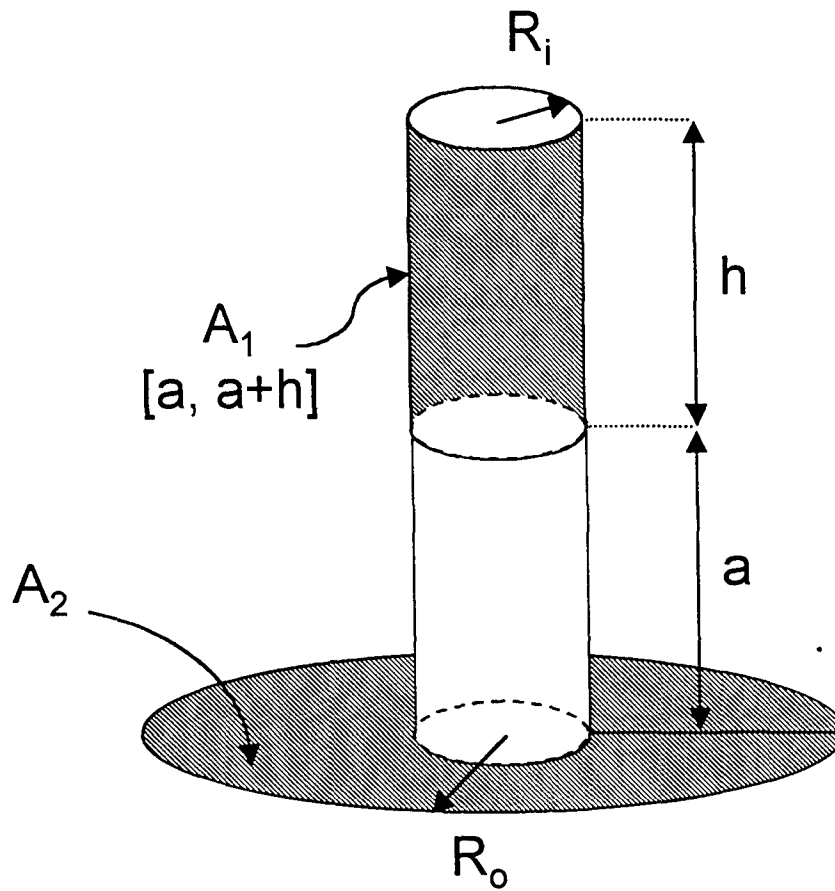


Figure C9.

**C.1.14. View Factor between Outer Surface of Cylinder and Coaxial Annular Disk Separated from Cylinder**

From simple flux algebra, we obtain:

$$F_{A_2 \rightarrow A_1[a, a+h]} = F_{A_2 \rightarrow A_1[0, a+h]} - F_{A_2 \rightarrow A_1[0, a]} .$$

Making use of reciprocity:

$$\begin{aligned} F_{A_1[a, a+h] \rightarrow A_2} &= \frac{A_1[0, a+h]}{A_1[a, a+h]} F_{A_1[0, a+h] \rightarrow A_2} - \frac{A_1[0, a]}{A_1[a, a+h]} F_{A_1[0, a] \rightarrow A_2} \\ &= \left(1 + \frac{a}{h}\right) F_{A_1[0, a+h] \rightarrow A_2} - \frac{a}{h} F_{A_1[0, a] \rightarrow A_2} , \end{aligned} \quad (C15)$$

where the factors on the right-hand side are given by Equation (C14).

#### C.1.15. View Factor between Ring on Base of Coaxial Cylindrical Enclosure and Outer Surface of Inner Cylinder

From simple flux algebra, we have:

$$\begin{aligned} F_{A_2 \rightarrow A_1[R_1, R_2]} &= F_{A_2 \rightarrow A_1[0, R_2]} - F_{A_2 \rightarrow A_1[0, R_1]} . \text{ Making use of reciprocity, we obtain:} \\ F_{A_1[R_1, R_2] \rightarrow A_2} &= \frac{A_2}{A_1[R_1, R_2]} \left( F_{A_2 \rightarrow A_1[0, R_2]} - F_{A_2 \rightarrow A_1[0, R_1]} \right) \\ &= \frac{2R_1 h}{R_2^2 - R_1^2} \left( F_{A_2 \rightarrow A_1[0, R_2]} - F_{A_2 \rightarrow A_1[0, R_1]} \right) , \end{aligned} \quad (C16)$$

where the factors on the right-hand side are given by Equation (C14).

#### C.1.16. View Factor between Ring on Base of Coaxial Cylindrical Enclosure and Opposit Annular End between Cylinders

The enclosure relation for surface  $A_1$  (see Figure C10) can be written:

$$F_{12} = F_{13} + F_{14} = 1, \quad \text{or} \quad F_{14} = 1 - F_{13} - F_{12}, \quad (C17)$$

where  $F_{13}$  is given by Equation (C12), and the factor  $F_{12}$  is given by Equation (C16).



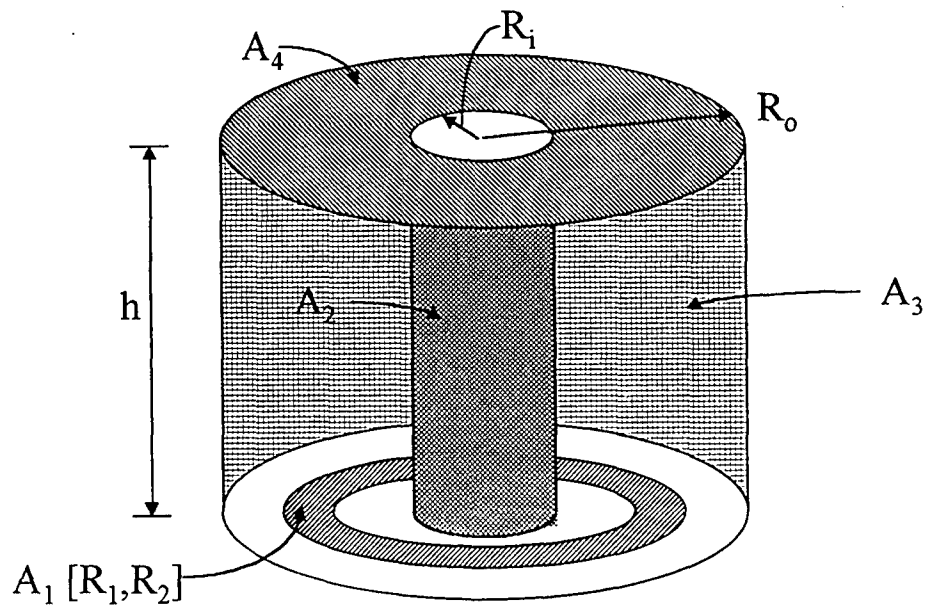


Figure C10.

**C.1.17. View Factor between Outer Surface of Inner Cylinder and Separated Inner Section of Outer Cylinder (Rea 1975)**

We are concerned with the case for which the smaller inner section is completely outside of the larger coaxial section.

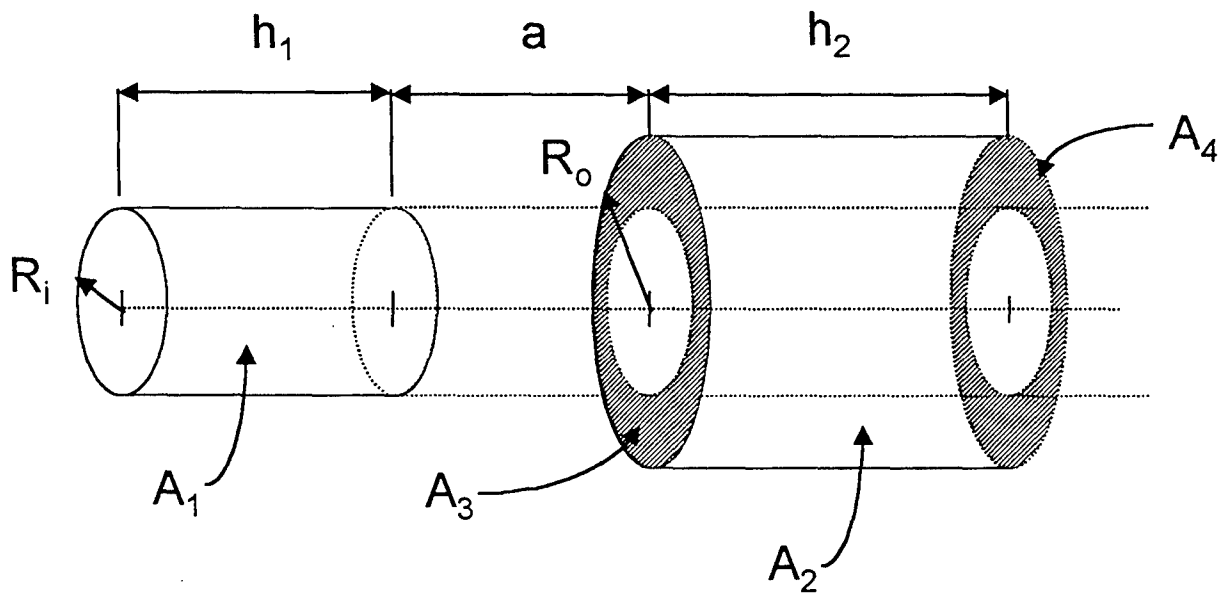


Figure C11.

In Figure C.11, surfaces  $A_3$  and  $A_4$  are imaginary annular disks covering the ends of the outer cylinder section. Simple flux algebra shows that all radiation from  $A_1$  streaming through  $A_3$  will either fall on the cylindrical shell  $A_2$  or escape through the annular end  $A_4$ :

$$F_{12} = F_{13} - F_{14} \quad , \quad (C18)$$

where the factors on the right-hand side are given by Equation (C15).

#### C.1.18. View Factor between Interior Shell of Outer Coaxial Cylinder and Another Interior Shell of Different Length (Reid and Tennant 1973)

The view factor between 2 separated outer shells  $A_1$  and  $A_3$  (Figure C12) can be expressed in terms of other known factors using a flux algebra technique (Reid and Tennant 1973).

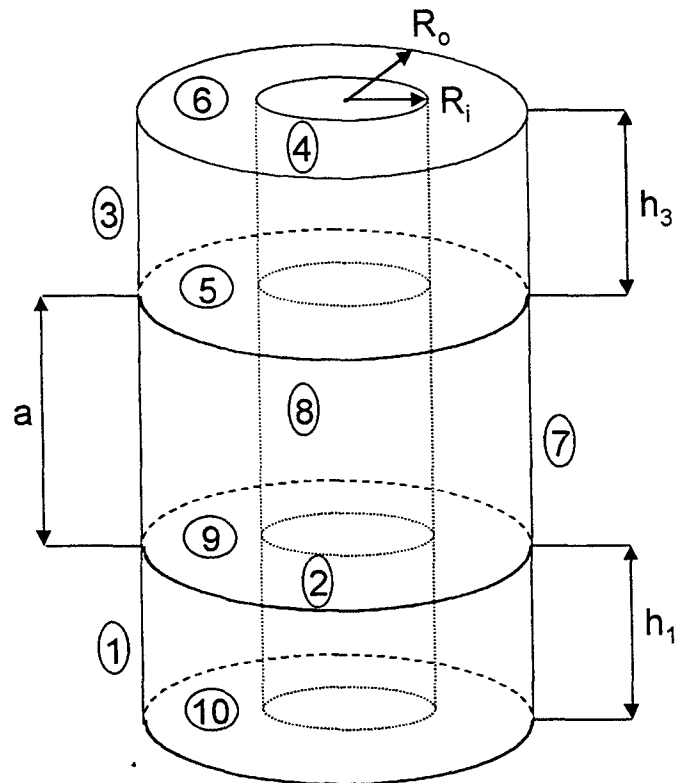


Figure C12.

First, consider the factor between the outer shell  $A_1$  and the annular disk  $A_5$  (Figure C12). We can write:

$$F_{15} = F_{13} + F_{14} + F_{16}, \text{ so that}$$

$$F_{13} = F_{15} - F_{16} - F_{14} = \frac{A_6}{A_1} [F_{51} - F_{61}] - \frac{A_4}{A_1} F_{41}$$

after making use of reciprocity. Again, using flux algebra, we have:

$$\begin{cases} F_{59} = F_{51} + F_{5-10} + F_{52} \\ F_{69} = F_{61} + F_{6-10} + F_{62} \end{cases} ,$$

so that

$$F_{51} - F_{61} = (F_{59} - F_{69}) - (F_{5-10} - F_{6-10}) + (F_{62} - F_{52}).$$

Using reciprocity, the last term can be simplified as:

$$\frac{A_6}{A_1} (F_{62} - F_{52}) = \frac{A_2}{A_1} (F_{26} - F_{25}) = -\frac{A_2}{A_1} F_{23}.$$

Finally, we find that:

$$F_{13} = \frac{A_6}{A_1} \{ (F_{59} - F_{69}) - (F_{5-10} - F_{6-10}) \} - \frac{A_2}{A_1} F_{23} - \frac{A_4}{A_1} F_{41} , \quad (C19)$$

where the view factors between identical annular rings ( $F_{59}$ ,  $F_{69}$ ,  $F_{5-10}$ , and  $F_{6-10}$ ) are given by Equation (C10), and view factors between inner cylindrical shells and outer cylindrical shells ( $F_{23}$  and  $F_{41}$ ) are given by Equation (C18). Note that when the 2 outer shells have identical length ( $h_1 = h_3$ ), then  $A_2 = A_4$  and  $F_{23} = F_{41}$ , and Equation (C19) reduces to that given by Reid and Tennant (1973).

The last set of basic view factors concerns the geometry of parallel and opposed circular cylinders and are used to calculate the radiative energy exchanges between evaporator casing and BASE tubes in the cell. In some cases, the view between 2 opposed cylinders is partially obstructed by another cylinder.

#### C.1.19. View Factors between Two Infinitely-Long Parallel and Opposed Cylinders of Unequal Radii

An analytical expression for  $F_{12}^\infty$  can be obtained by applying the crossed-string method of Hottel (Siegel and Howell 1981, pp. 203-206).

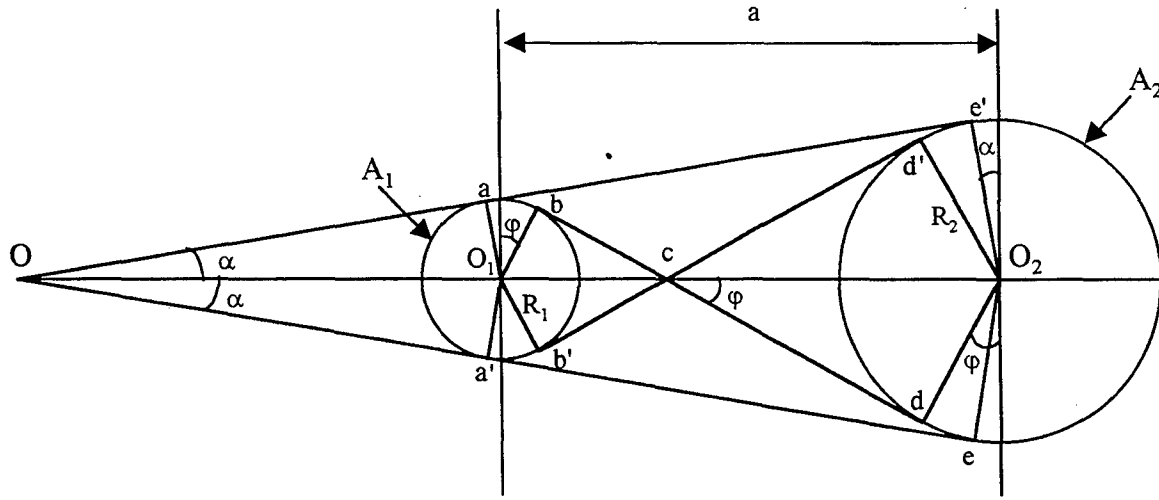


Figure C13.

If we define the surface area of cylinder  $A_1$  which views cylinder  $A_2$  as  $A'_1 = A_{abb'a'}$ , we have by simple flux algebra (Figure C13):

$$F_{A'_1 \rightarrow A_2}^\infty = 1 - F_{A'_1 \rightarrow a'e}^\infty - F_{A'_1 \rightarrow ae'}^\infty = 1 - 2F_{A'_1 \rightarrow a'e}^\infty \quad (C20)$$

However, the arc (ab) of  $A'_1$  does not see the line  $[a',e]$ . If we use reciprocity, it is easy to show that:

$$F_{A'_1 \rightarrow a'e}^\infty = \frac{A_{a'e}}{A'_1} [F_{a'e \rightarrow bb'a'}^\infty + F_{a'e \rightarrow ab}^\infty] = \frac{A_{bb'a'}}{A'_1} F_{bb'a' \rightarrow a'e}^\infty \quad (C21)$$

Now Hottel's crossed-string method allows us to write:

$$A_{bb'a'} \times F_{bb'a' \rightarrow a'e}^\infty = \frac{1}{2} [A_{bb'a'} + A_{a'e} - A_{bcde}] \quad (C22)$$

Substituting Equations (C21) and (C22) into Equation (C20) we obtain:

$$F_{A'_1 \rightarrow A_2}^\infty = 1 - \frac{A_{bb'a'} + A_{a'e} - A_{bcde}}{A'_1} \quad (C23)$$

Since  $A'_1 F_{A'_1 \rightarrow A_2}^\infty = A_2 F_{A_2 \rightarrow A'_1}^\infty = A_2 F_{A_2 \rightarrow A_1}^\infty = A_1 F_{A_1 \rightarrow A_2}^\infty$ , we have :

$$F_{A_1 \rightarrow A_2}^\infty = \frac{A'_1}{A_1} F_{A'_1 \rightarrow A_2}^\infty = \frac{A_{abb'a'} - A_{bb'a'} - A_{a'e} + A_{bcde}}{A_1} \quad (C24)$$

$$\text{or } A_1 F_{A_1 \rightarrow A_2}^{\infty} = \widehat{ab} + \widehat{bc} + \widehat{cd} + \widehat{de} - \widehat{a'e} . \quad (\text{C25})$$

Applying basic trigonometric analysis to the rectangular triangles  $[OO_1a]$  and  $[OO_2e]$ , we obtain:

$$\alpha = \sin^{-1} \left( \frac{R_2 - R_1}{a} \right) = \sin^{-1} \left( \frac{1 - R}{X} \right), \text{ where } R = \frac{R_1}{R_2} \text{ and } X = \frac{a}{R_2} .$$

$$\text{Now } \tan \alpha = \frac{R_1}{Oa'} = \frac{R_2}{Oa' + a'e} , \text{ so that}$$

$$\frac{a'e}{\tan \alpha} = \frac{R_2 - R_1}{\tan \alpha} = a \cos \alpha = a \sqrt{1 - \sin^2 \alpha} = R_2 \sqrt{X^2 - (1 - R)^2} .$$

Applying basic trigonometric analysis to the rectangular triangles  $[cdO_2]$  and  $[cbO_1]$ , we obtain:

$$\varphi = \sin^{-1} \left( \frac{R_1 + R_2}{a} \right) = \sin^{-1} \left( \frac{1 + R}{X} \right) .$$

$$\text{Now: } \widehat{bc} + \widehat{cd} = \frac{R_1 + R_2}{\tan \varphi} = a \cos \varphi = a \sqrt{1 - \sin^2 \varphi} = R_2 \sqrt{X^2 - (1 + R)^2} .$$

Finally, the circular arcs can be calculated as:

$$\widehat{ab} = R_1(\varphi + \alpha), \quad \widehat{de} = R_2(\varphi - \alpha) .$$

The view factor between infinite cylinders 1 and 2 has the form:

$$F_{12}^{\infty} = \frac{1}{2\pi R} \left\{ (1 + R) \sin^{-1} \frac{1 + R}{X} - (1 - R) \sin^{-1} \frac{1 - R}{X} + \sqrt{X^2 - (1 + R)^2} - \sqrt{X^2 - (1 - R)^2} \right\}, \quad (\text{C26})$$

$$\text{where } R = \frac{R_1}{R_2} \text{ and } X = \frac{a}{R_2} .$$

When the cylinders have identical radii,  $R=1$ , and Equation (C26) reduces to:

$$F_{12}^{\infty} = F_{21}^{\infty} = \frac{1}{\pi} \left\{ \sin^{-1} \frac{1}{H} + \sqrt{H^2 - 1} - H \right\}, \quad (\text{C27})$$

where  $H = \frac{X}{2} = \frac{a}{2R_1}$ , which is identical to that given by Siegel and Howell (1981) for this geometry (p. 828).

**C.1.20. View Factor between Two Infinitely-Long Parallel and Opposed Cylinders of Identical Radii Partially Obstructed by Another Parallel Cylinder of Different Radius**

The view factor between two infinitely-long parallel and opposed cylinders  $A_1$  and  $A_1'$  of radii  $R_1$ , partially obstructed by another parallel cylinder  $A_2$  of radius  $R_2$ , can be calculated by applying the crossed-string method of Hottel in a manner similar to that used in section C.1.19. For the case of small obstruction,  $\beta < \varphi$  (see Figure C.14), one obtains:

$$A_1 F_{A_1 \rightarrow A_1'} = [\widehat{ab} + \overline{bc} + \overline{cd} + \widehat{de}] - \frac{1}{2} [\overline{e'f'} + \widehat{ff'} + \overline{fe} + \overline{aa'}]. \quad (\text{C28})$$

If we define the dimensionless factors

$$R = \frac{R_2}{R_1}, \quad X = \frac{a}{2R_1}, \quad \text{and} \quad H = \frac{d - R_2}{R_1} \quad \left( \frac{d}{R_1} = H + R \right), \quad \text{we have from section C.1.19:}$$

$$\varphi = \sin^{-1} \frac{1}{x}, \quad \widehat{ab} = R_1 \varphi, \quad \text{and} \quad \overline{bc} + \overline{cd} = 2\overline{bc} = 2R_1 \sqrt{X^2 - 1}.$$

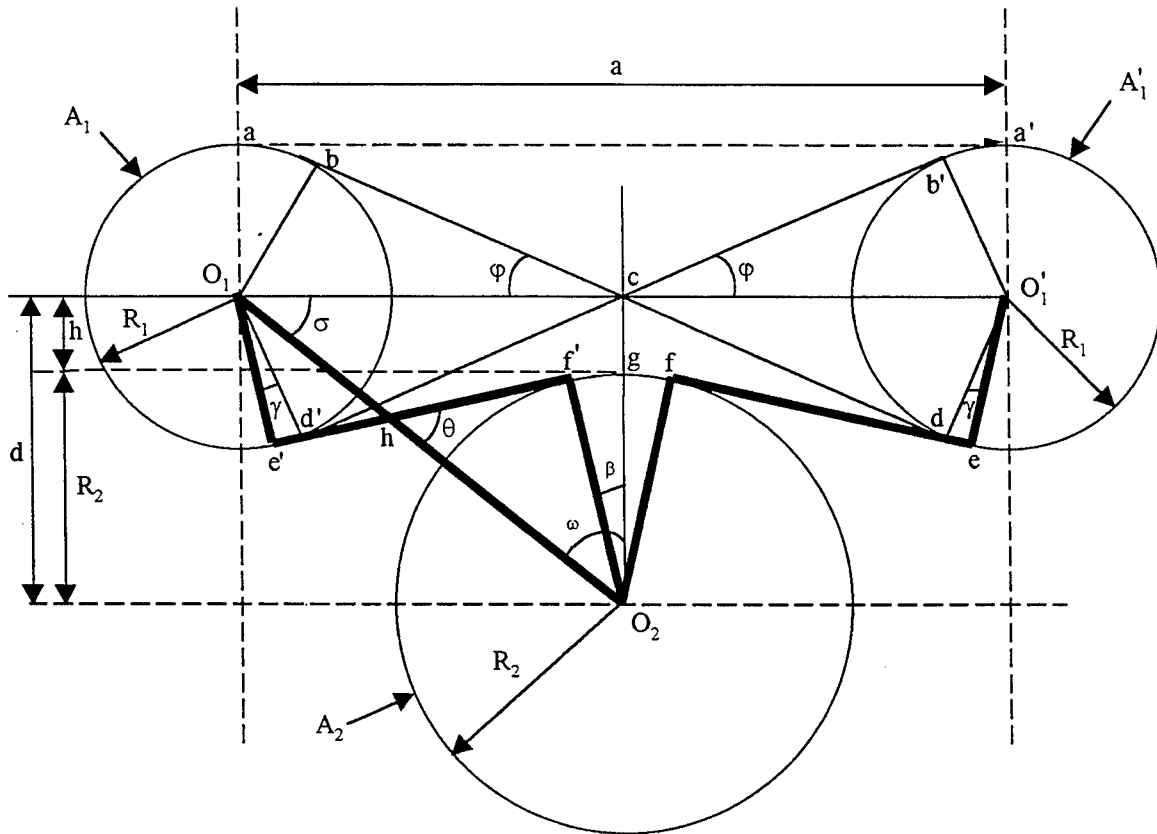


Figure C14 ( $\beta \leq \varphi$ ,  $H \leq 1$ ).

Applying basic trigonometric analysis to the rectangular triangle  $[O_1cO_2]$  we find:

$$\overline{O_1O_2} = \sqrt{d^2 + \frac{a^2}{4}} = R_1 \sqrt{(H+R)^2 + X^2}, \quad \sigma = \tan^{-1} \frac{2d}{a} = \tan^{-1} \frac{(H+R)}{X}, \quad \text{and}$$

$$\omega = \tan^{-1} \frac{a}{2d} = \tan^{-1} \frac{X}{(H+R)}.$$

Using the results of section C.1.19 for the angle  $\varphi$  and segment  $\widehat{bd}$ , we have:

$$\theta = \sin^{-1} \frac{R_1 + R_2}{\overline{O_1O_2}} = \sin^{-1} \frac{1+R}{\sqrt{(H+R)^2 + X^2}}, \quad \text{and}$$

$$\overline{e'f'} = \overline{O_1O_2} \sqrt{1 - \sin^2 \theta} = \sqrt{\overline{O_1O_2}^2 - (R_1 + R_2)^2} = R_1 \sqrt{X^2 + (H+R)^2 - (1+R)^2}.$$

The arc  $\widehat{de} = R_1\gamma$ , where the angle  $\gamma$  has the value  $\gamma = \varphi + \sigma - \theta$ . Finally, the arc  $\widehat{f'g} = R_2\beta$ , where:

$$\beta = \omega - \left( \frac{\pi}{2} - \theta \right).$$

By substitution into Equation (C28), we find:

$$F_{A_1 \rightarrow A'_1} = \frac{1}{\pi} \left\{ \sin^{-1} \frac{1}{X} + \sqrt{X^2 - 1} - X \right\} + \frac{1}{2\pi} \left\{ (\sigma - \theta) - R\beta + X - \sqrt{X^2 + (H+R)^2 - (1+R)^2} \right\},$$

where  $\sigma = \tan^{-1} \frac{H+R}{X}$ ,  $\theta = \sin^{-1} \frac{1+R}{\sqrt{X^2 + (H+R)^2}}$ ,  $\omega = \tan^{-1} \frac{X}{H+R}$ ,

$$R = \frac{R_2}{R_1}, X = \frac{a}{2R_1}, H = \frac{d-R_2}{R_1} = \frac{h}{R_1}, \text{ and } \beta = \omega + \theta - \frac{\pi}{2} (\beta < \varphi, 0 < H < 1). \quad (C29)$$

When  $h=R_1$ ,  $H=1$ , and we have  $\beta=0$ ,  $\gamma=\varphi$  and  $\sigma=\theta$ . In that case, the second bracket in Equation (C29) equals zero and the view factor reduces to that between two unobstructed parallel cylinders of identical radius, Equation (C27). For the case of large obstruction, ( $\beta > \varphi$ ), the view factor between  $A_1$  and  $A'_1$  has the expression (see Figure C15):

$$\begin{aligned} A_1 F_{A_1 \rightarrow A'_1} &= [\widehat{ab} + \widehat{bc} + \widehat{cd} + \widehat{de}] - \frac{1}{2} [\widehat{e'd'} + \widehat{dd'} + \widehat{de} + \widehat{aa'}] \\ &= \widehat{ab} + \widehat{bc} - \widehat{gc} - \frac{1}{2} \widehat{aa'} \\ &= \delta R_1 + \overline{O_1O_2} \sqrt{1 - \sin^2 \alpha} - \delta R_2 - \frac{a}{2}, \quad \text{where} \\ \sin \alpha &= \frac{R_2 - R_1}{\overline{O_1O_2}}, \quad \text{and } \delta = \sigma - \alpha. \end{aligned}$$

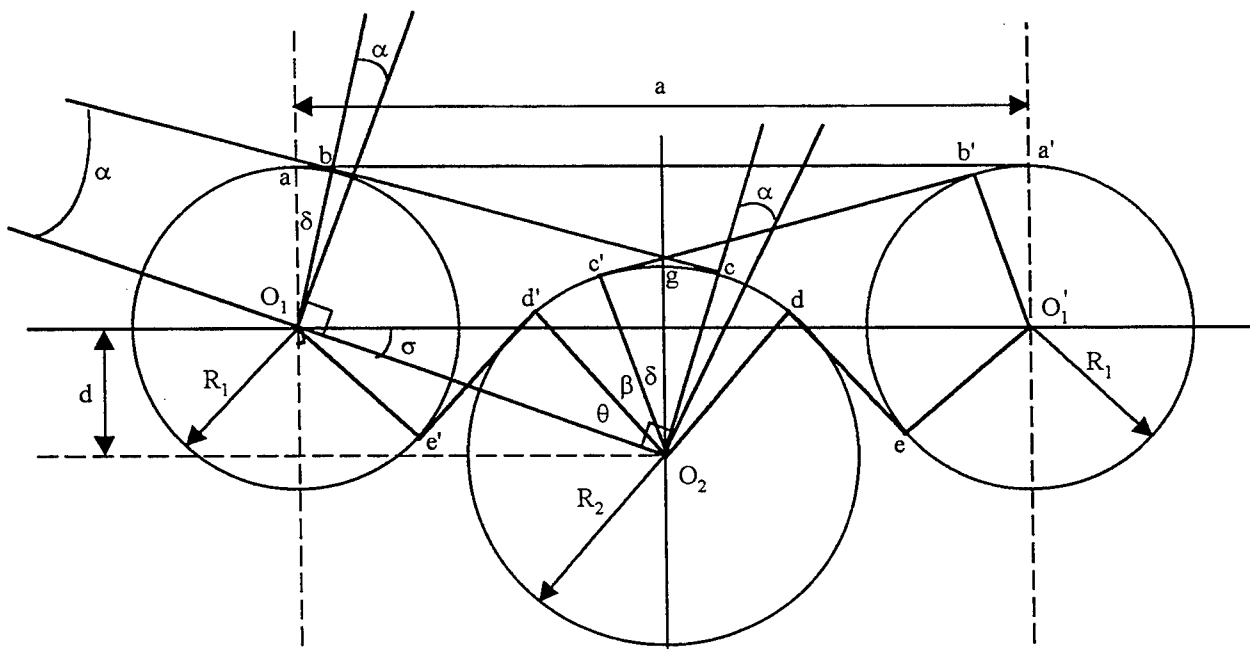


Figure C15 ( $\beta \geq \phi$ ,  $H \geq -1$ ,  $X > R + 1$ ).

Finally, we obtain:

$$F_{A_1 \rightarrow A_1'} = \frac{1}{2\pi} \left\{ (1-R)(\sigma - \alpha) + \sqrt{X^2(H+R)^2 - (1-R)^2} - X \right\}, \text{ where} \quad (C30)$$

$$\sigma = \tan^{-1} \frac{H+R}{X} \quad \text{and} \quad \alpha = \sin^{-1} \frac{R-1}{\sqrt{X^2 + (H+R)^2}} \quad (H < 0)$$

When  $d = R_2 - R_1$ ,  $H = -1$ , and consideration of the rectangular triangle of sides  $X$  and  $|R - 1|$  shows that  $F_{A_1 \rightarrow A_1'}$  reduces to zero: the view between the 2 cylinders  $A_1$  and  $A_1'$  is completely obstructed by cylinder  $A_2$ . Although it is not directly apparent, both Equations (C29) and (C30) give identical results when  $\beta = \phi$ , that is when the cylinder  $A_2$  is in contact with the cross-strings  $\overline{bd}$  and  $\overline{d'b'}$  between the 2 identical cylinders ( $\gamma = 0$ , and  $\delta = \phi$ , see Figures C14 and C15). This is because the view factors are derived from the crossed-string method, and the length of the strings used in the 2 equations are identical when  $\beta = \phi$ .

#### C.1.21. View Factor between Two Parallel and Opposed Cylinders of Unequal Radii and Equal Length (Juul 1982)

There does not exist a closed-form solution for the view factor between 2 parallel cylinders (Figure C16), except for the limiting case of infinitely long cylinders, for which an analytical expression was derived in the previous section by applying the crossed-string method. However, Juul (1982) has developed an approximate analytical expression for the case of opposed cylinders



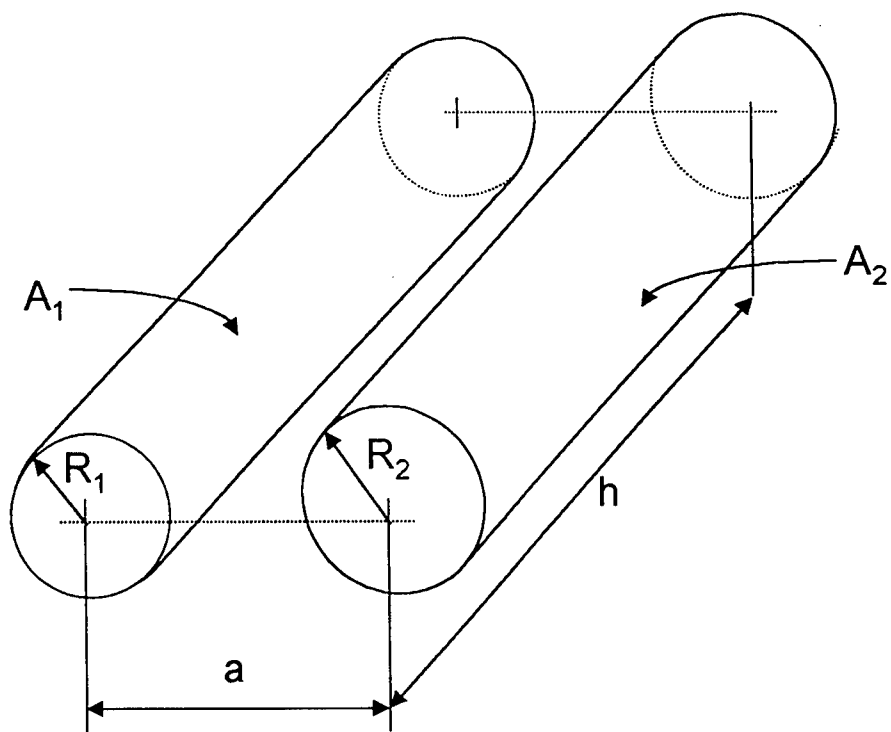


Figure C16.

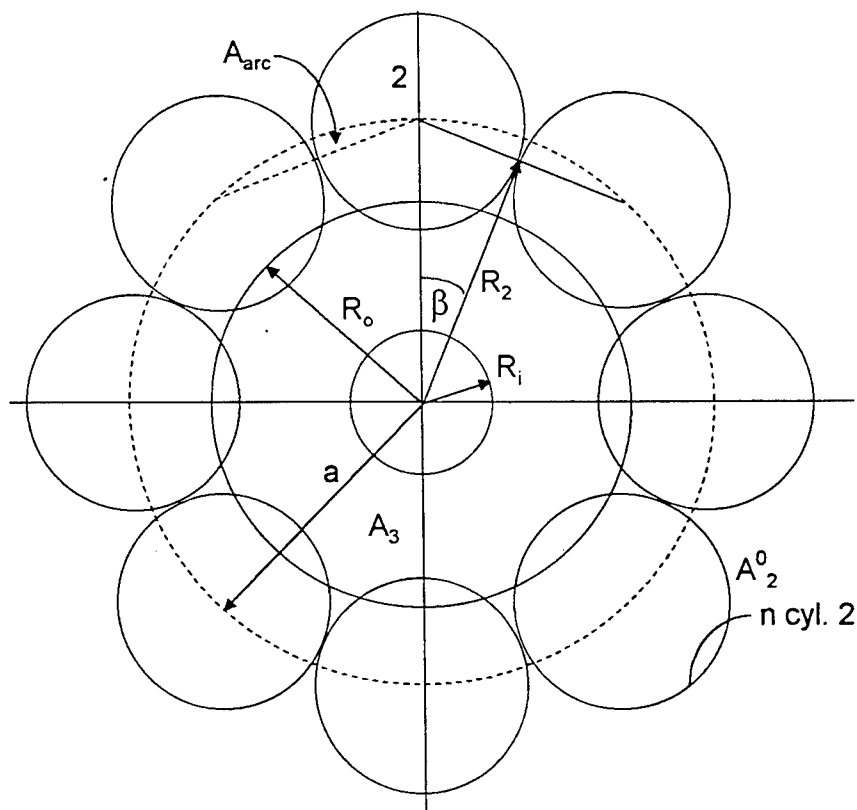


Figure C17.

of finite and equal length and has evaluated its accuracy by comparing its results with that obtained by numerical integration.

The arrangement which was first proposed by Glicksman is shown in Figure C17 where cylinder 1 is completely surrounded by  $n$  identical cylinders of radius  $R_2$ , whose axes lie on a cylinder concentric to cylinder 1 and of radius equal to the spacing  $a$ .

The view factor between cylinder 1 and cylinder 2 is approximately equal to  $F_{12} = F_{1 \rightarrow 2n} / n$ , where  $F_{1 \rightarrow 2n}$  is the view factor between cylinder 1 and the  $n$  cylinders of radius  $R_2$ . The approximation is good if the blockage of the rays between cylinders 1 and 2 by the cylinders adjacent to 2 is small. The factor  $F_{1 \rightarrow 2n}$  is evaluated by applying view factor algebra to the enclosure formed by the curved surface of cylinder 1, the curved surfaces of the  $n$  cylinders 2, and the 2 identical end surfaces 3 and 4 (Figure C17). Thus, we obtain:

$$F_{1 \rightarrow 2n} = 1 - F_{13} - F_{14} = 1 - 2F_{13}.$$

$F_{13}$  is difficult to evaluate since  $A_3$  has a complicated geometry as shown in Figure C17. Therefore, surface  $A_3$  is substituted with a ring surface  $A'_3$  of outer radius  $R_o$ , of equal area.  $A'_3$  can be calculated as:

$$A_3 = n \left[ \frac{\pi a^2}{n} - A_2^o \right] - \pi R^2, \text{ where } A_2^o = \left( \frac{\pi}{2} - \beta \right) R_2^2 + A_{arc}.$$

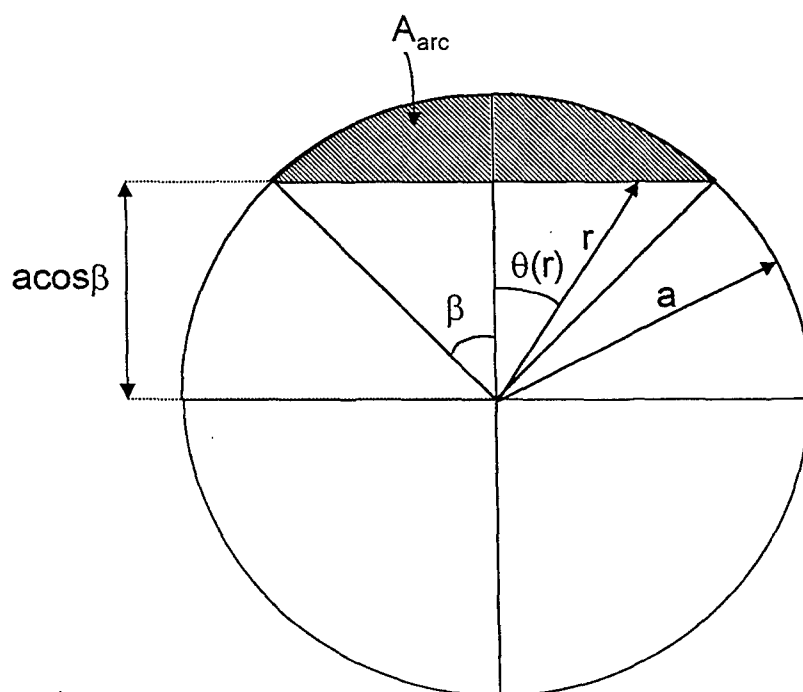


Figure C18.

The surface area of the arc is calculated analytically by integration (Figure C18), as:

$$A_{arc} = \int_{arc} r dr d\theta = 2 \int_0^\beta d\theta \int_{\frac{a \cos \beta}{\cos \theta}}^a r dr = 2 \int_0^\beta \frac{a^2}{2} \left( 1 - \frac{\cos^2 \beta}{\cos^2 \theta} \right) d\theta$$

$$= a^2 \left[ \beta - \cos^2 \beta \tan \beta \right] = a^2 \left[ \beta - \cos \beta \sin \beta \right]$$

Equating  $A_3$  with  $A'_3 = \pi(R_o^2 - R_1^2)$ , we find that the equivalent outer radius  $R_o$  of  $A'_3$  has the expression:

$$\left( \frac{R_o}{a} \right)^2 = \frac{n}{\pi} \left[ \cos \beta \sin \beta - \left( \frac{\pi}{2} - \beta \right) \left( \frac{R_2}{a} \right)^2 \right], \quad (C31)$$

where we used the fact that  $\beta = \pi/n$ . Since  $\sin \beta = R_2/a$ , (see Figure C17), Equation (C31) can be written:

$$\left( \frac{R_o}{R_2} \right)^2 = \frac{n}{\pi} \left[ \frac{\cos \beta}{\sin \beta} - \frac{\pi}{2} + \beta \right] = 1 - \frac{n}{2} + \frac{n}{\pi} \frac{\sqrt{1 - \sin^2 \beta}}{\sin \beta}$$

$$= 1 - \frac{n}{2} + \frac{n}{\pi} \sqrt{\left( \frac{a}{R_2} \right)^2 - 1}, \quad \text{or} \quad (C32)$$

$$\left( \frac{R_o}{R_2} \right)^2 = 1 + \frac{\sqrt{\left( \frac{a}{R_2} \right)^2 - 1} - \frac{\pi}{2}}{\sin^{-1} \frac{R_2}{a}}$$

The approximation assumes that the radiation from cylinder 1 through surface 3 and surface  $A'_3$  is identical, which is approximately satisfied when  $n$  and  $R_o$  are large. Furthermore,  $F_{12}^\infty \approx 1/n$  when the blockage of the rays between cylinders  $A_1$  and  $A_2$  by the cylinders adjacent to  $A_2$  is small. In summary, the view factor between parallel and opposite cylinders 1 and 2 can be approximated by:

$$F_{12} \cong F_{12}^\infty (1 - 2F_{13'}) = F_{12}^\infty \times G_{10}, \quad (C33)$$

where  $F_{12}^\infty$  is the view factor between infinitely-long cylinders 1 and 2, given by Equation (C26), and  $G_{10}$  is the view factor between cylinder 1 and the inner surface of a concentric cylinder of radius  $R_o$ , which is given by Equation (C7). Juul (1982) has compared the results of this approximate method with that obtained by numerical integration and shown that Equation (C33)

was very accurate. Indeed the error was less than 1% when  $R_1 \leq R_2$  and  $3 < h/R_2 < 10$ . For all cases of practical interest, the error on the view factor is less than 3% when using Equation (C33).

#### C.1.22. View Factor between Two Parallel Cylindrical Sections at Different Levels and of Different Length

The approximate method described in the previous section for the case of opposed cylinders of equal length is applied to the present case where the cylinders 1 and 2 are separated by a height  $c$  (see Figure C19):

$$F_{12} = F_{12}^{\infty} \times G_{10}, \quad (C34)$$

where  $A_o$  is the inner surface of a cylinder of radius  $R_o$  which is concentric with cylinder 1 and at the level of cylinder 2 with a height  $h_2$ .  $R_o$  is given by Equation (C32) and  $G_{10}$  is given by Equation (C18). This approximate method is adequate for all cases of practical interest, particularly since the magnitude of the view factor drops sharply as the separation height,  $c$ , increases.

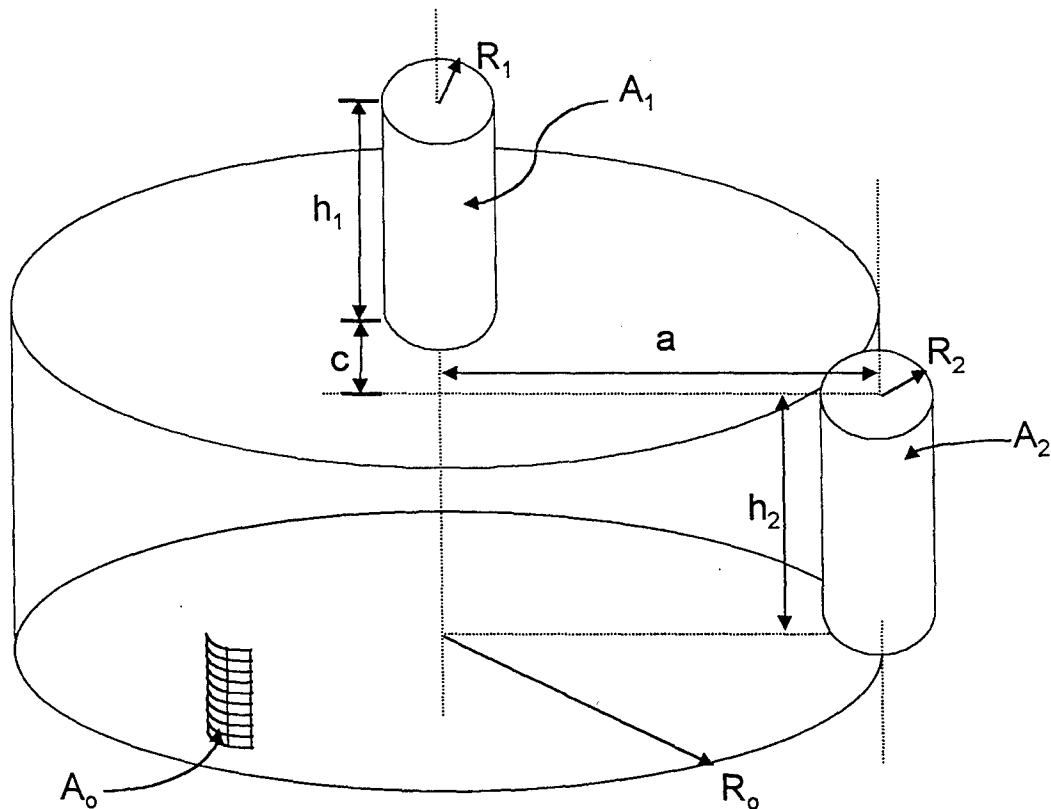


Figure C19.

This ends the section describing the basic view factors used in the heat flow model for PX-series, vapor anode, multi-tube AMTEC cells. Because of the very complex geometry of the inside of such cells, it is necessary to develop other approximate methods in order to calculate all the radiation view factors in the cells. These approximations are described in the next section.

## C.2 CALCULATION OF RADIATION VIEW FACTORS IN PX-SERIES, MULTI-TUBE AMTEC CELLS

Figure C20 shows a schematic of a PX-series multi-tube AMTEC cell assembly and its major components. This figure also shows a typical numerical mesh used by the radiation/conduction heat flow model. The cell is constituted of a pressure-tight container of cylindrical shape, which is made up of a hot circular plate, a cold condenser plate and a thin annular side wall. Inside the cell, a circular plate supports the BASE ( $\beta$ ) tubes and the annular casing of the evaporator standoff. The latter is connected to the wick of the condenser plate through a circular liquid-return artery. The support plate,  $\beta$ -tubes, and evaporator standoff provide a physical boundary between the high-pressure hot plenum and the low vapor pressure zone.

Design changes which have been considered to improve the performance of the cell include the addition of a conduction stud between hot and support plates, and side-wall circumferential radiation heat shields in the annular space above the  $\beta$ -tubes. These components will be considered in a later section.

The mesh generator of the heat flow model discretizes the  $\beta$ -tubes bundle into  $N$  axial sections of identical height, and the coaxial cylindrical cavity above the  $\beta$ -tubes into  $N_w$  identical axial sections. The evaporator standoff shaft is discretized into  $N_c$  identical axial sections while the wick of the evaporator is discretized into  $N_{ev} = N - N_c$  axial sections of equal height (Figure C20). Only one axial section is necessary for the hot plenum wall since the inside height of the plenum is very small, usually less than 2 mm.

As shown in Figure (C20), there are 2 separate enclosures for radiation heat transfer in the cell: the hot plenum, and the low vapor pressure zone. The next section describes the calculation of view factors in the hot plenum enclosure.

### C.2.1. Calculation of Radiation View Factors in the Hot Plenum Enclosure

The high-pressure enclosure is constituted of 3 elementary cavities: a cylindrical hot baffle with hot plate at the bottom end (surface  $\overline{Hot}$ ) and circular side wall (surface  $\overline{Whot}$ ); a cylindrical evaporator standoff shaft of end surfaces  $\overline{C_o}$  and  $\overline{evap}$ , and circular inside wall sections  $\overline{C_1}$  to  $\overline{C_{Nc}}$ ; and a cylindrical  $\beta$ -tube of end surfaces  $\overline{\beta_o}$  and  $\overline{\beta_{N+1}}$ , and circular inside wall sections  $\overline{\beta_1}$  to  $\overline{\beta_N}$ .

The surfaces  $\overline{\beta_o}$  and  $\overline{C_o}$  are fictitious boundaries through which radiative coupling between the 3 elementary cavities occurs. From a radiation point of view, the bundle of  $N_\beta$  tubes is modeled as an equivalent thick-circular ring of inner and outer radii  $\overline{R_o}$  and  $\overline{R_1}$ , where  $\overline{R_o}$  is calculated from Equation (C32) using the inner radius of  $\beta$ -tubes, and  $\overline{R_1}$  is calculated to conserve the total



All the radiation view factors in the elementary cylindrical cavities  $\{\overline{Hot}, \overline{Whot}, \overline{plen}, \overline{\beta_{ring}}, \overline{bot}, \overline{C_o}\}$ ,  $\{\overline{C_o}, \overline{C_1}, \dots, \overline{C_{Nc}}, \overline{evap}\}$ , and  $\{\overline{\beta_o}, \overline{\beta_1}, \dots, \overline{\beta_N}, \overline{\beta_{N+1}}\}$  can be calculated exactly using the closed-form algebraic factors described in section (C.1) and using the reciprocity relations:

$$A_k F_{kp} = A_p F_{pk} . \quad (C36)$$

Because the values of these factors are exact, we find that all the enclosure relations in these cylindrical cavities are satisfied in the model. For example, we have for the evaporator surface *evap*:

$$\sum_{k=1}^{N_c} F_{\overline{evap} \rightarrow \overline{C_k}} + F_{\overline{evap} \rightarrow \overline{C_o}} = 1 . \quad (C37)$$

Next the view factors must be modified to account for the radiative coupling through the fictitious surfaces  $\overline{\beta_o}$  and  $\overline{C_o}$ , and these surfaces must be eliminated.

First the radiative coupling between the hot baffle and evaporator standoff shaft is considered. Since the inside height of the hot baffle is much smaller than its diameter and than the height of the first standoff axial section  $\overline{C_1}$ , all radiation emitted by surface  $\overline{Whot}$  streaming through surface  $\overline{C_o}$  will end into surface  $\overline{C_1}$ . Therefore:

$$\begin{aligned} F_{\overline{Whot} \rightarrow \overline{C_1}} &= F_{\overline{Whot} \rightarrow \overline{C_o}} , \quad F_{\overline{Whot} \rightarrow \overline{C_k}} = 0 \quad \text{for } k > 1, \text{ and} \\ F_{\overline{Whot} \rightarrow \overline{evap}} &= 0 . \end{aligned} \quad (C38)$$

$F_{\overline{C_1} \rightarrow \overline{Whot}}$  is easily calculated by reciprocity, and since surface  $\overline{C_1}$  sees only  $\overline{Whot}$  and  $\overline{Hot}$  through  $\overline{C_o}$ , we have:

$$F_{\overline{C_1} \rightarrow \overline{Hot}} = F_{\overline{C_1} \rightarrow \overline{C_o}} - F_{\overline{C_1} \rightarrow \overline{Whot}} . \quad (C39)$$

Finally, all other surfaces inside the casing shaft see only the hot plate through  $\overline{C_o}$ , so that:

$$\begin{aligned} F_{\overline{C_k} \rightarrow \overline{Hot}} &= F_{\overline{C_k} \rightarrow \overline{C_o}} \quad \text{for } k > 1, \text{ and} \\ F_{\overline{evap} \rightarrow \overline{Hot}} &= F_{\overline{evap} \rightarrow \overline{C_o}} , \end{aligned} \quad (C40)$$

and all other factors between hot baffle and evaporator standoff shaft can be obtained by reciprocity, or are nul.

A similar treatment is applied for the radiative coupling between the inside surfaces of the  $\beta$ -tubes and the surfaces  $\overline{Whot}$  and  $\overline{Hot}$  of the high-pressure baffle. The only difference with the previous



treatment is that the surface areas inside the  $\beta$ -tube must be multiplied by the number of tubes,  $N_\beta$ , before performing the radiative coupling treatment. In the end, all view factors involving surfaces  $\overline{C_o}$  and  $\overline{\beta_o}$  must be set to zero.

Finally, the model verifies that the enclosure relations in the high vapor pressure zone are satisfied. For example, we find that for the hot plenum wall:

$$F_{\overline{Whot} \rightarrow \overline{Hot}} + F_{\overline{Whot} \rightarrow \overline{Whot}} + F_{\overline{Whot} \rightarrow \overline{plen}} + F_{\overline{Whot} \rightarrow \overline{bot}} + F_{\overline{Whot} \rightarrow \overline{C_1}} + F_{\overline{Whot} \rightarrow \overline{\beta_1}} = 1$$

Next the view factors in the low vapor pressure zone must be calculated. The low-pressure enclosure is constituted of 2 radiatively coupled cavities: the evaporator standoff /  $\beta$ -tubes bundle, and the coaxial cylindrical cavity above the  $\beta$ -tubes (between liquid-return artery and cell side wall).

### C.2.2. Calculation of View Factors in a Coaxial Cylindrical Cavity with a Bottom End Constituted of 3 Concentric Rings

A subroutine (VIEW\_COAXIAL) was developed to calculate the view factors in a coaxial cylindrical cavity made up of  $N$  identical axial sections. The bottom annular end of the cavity is constituted of 3 concentric rings. All necessary elementary view factors for this geometry were developed in section C.1. This routine is used to calculate the view factors in the artery coaxial cylindrical cavity above the  $\beta$ -tubes in the cell, and to evaluate intermediate factors in the tubes bundle cavity.

As shown in Figure (C20), the artery coaxial cylindrical cavity is constituted of  $N_w$  identical axial sections, where surfaces  $a_1, a_2, \dots, a_{N_w}$  are the outer surfaces of the cylindrical liquid-return artery, and  $\omega_1$  to  $\omega_{N_w}$  are the inner surfaces of cylindrical wall shells. The top annular end of the cavity is the condenser surface, *cond*.

For the purpose of radiatively coupling this cavity with the bundle cavity below, the bundle of  $\beta$ -tubes is again modeled as an equivalent circular ring of inner and outer radii  $R_o$  and  $R_i$ , where  $R_o$  is calculated from Equation (C32) using the outer radius of tubes, and  $R_i$  is calculated to conserve the total area of the flat top of the  $\beta$ -tubes:

$$\pi(R_i^2 - R_o^2) = N_\beta \times \pi R_{\beta out}^2 \quad (C41)$$

Therefore, the bottom annular end of the artery annular cavity is constituted of a ring of inner and outer radii  $R_a$  and  $R_o$  (surface *ring*), a ring of  $\beta$ -tubes of equivalent radii  $R_o$  and  $R_i$  (surface  $\beta_{N+1}$ ), and an outer ring of radii  $R_i$  and  $R_w$  (surface *ceil*).

All the radiation view factors in the artery annular cavity {*cond*,  $a_1, a_2, \dots, a_{N_w}$ ,  $\omega_1, \omega_2, \dots, \omega_{N_w}$ , *ring*,  $\beta_{N+1}$ , *ceil*} can be calculated accurately using the base factors described in section (C.1) and

using the reciprocity relations (C36). Most configuration factors could be represented by a closed-form algebraic solution. Even so some factors required numerical integration using Simpson's rule, we find that all the enclosure relations in the artery annular cavity are satisfied with an accuracy of  $10^{-5}$  in the model. For example, we find that for the condenser surface:

$$\sum_{k=1}^{N_w} \left( F_{cond \rightarrow \omega_k} + F_{cond \rightarrow a_k} \right) + F_{cond \rightarrow ring} + F_{cond \rightarrow \beta_{N+1}} + F_{cond \rightarrow ceil} = 1 \pm 10^{-5}.$$

### C.2.3. Calculation of View Factors in the Evaporator Standoff / $\beta$ -Tubes Bundle Cavity

Probably the determination of view factors in the  $\beta$ -tubes bundle cavity is the most challenging problem, with that of the radiative coupling between this cavity and the artery annular cavity above.

The bundle cavity is constituted of  $N$  identical axial sections (Figures C20 and C21):  $N$  cylindrical  $\beta$ -tubes outer surfaces ( $\beta_1$  to  $\beta_N$ );  $N$  cylindrical outer shells of the evaporator standoff ( $C_1$  to  $C_N$ );  $N$  inner surfaces of cylindrical wall shells ( $W_1$  to  $W_N$ ); top (surface *top*) and bottom (surface *bot*) inner rings of equivalent radii  $R_{Cout}$  and  $R_o$ , and top (surface *ceil*) and bottom (surface *plen*) outer rings of equivalent radii  $R_1$  and  $R_w$ .

Note that by construction the sum of the surface areas of inner and outer rings ( $A_{plen} + A_{bot}$ ) is equal to the total surface area of the support plate between  $\beta$ -tubes and evaporator standoff.

In this section, we refer to the actual view factors (in the presence of the BASE tubes) as  $F$ , and to the unobstructed view factors (in the absence of  $\beta$ -tubes) as  $G$ . The unobstructed  $G$  factors in the cell are useful for calculating the  $F$  factors. When the BASE tubes are removed, the bundle cavity reduces too a coaxial cylindrical cavity  $\Omega$  of inner and outer radii  $R_{Cout}$  and  $R_w$ , respectively. Therefore, all the unobstructed  $G$  factors can be calculated using the routine VIEW\_COAXIAL described in the previous section C.2.2.

Other intermediate factors used in the model are the view factors  $G^o$  and  $G^l$  in the fictitious coaxial cylindrical cavities  $\Omega^o$  and  $\Omega^l$  (shown in Figure C21). The annular cavity  $\Omega^o$  has inner and outer radii  $R_{Cout}$  and  $R_o$ , respectively, and includes the surfaces  $\{C_k, \Omega_k^o, k=1 \text{ to } N, \text{top}, \text{bot}\}$ , while the annular cavity  $\Omega^l$  has inner and outer radii  $R_1$  and  $R_w$ , respectively, and includes the surfaces  $\{\Omega_k^l, W_k, k=1 \text{ to } N, \text{plen}, \text{ceil}\}$ . All the view factors  $G^o$  and  $G^l$  in these cavities are easily calculated using the routine VIEW\_COAXIAL.

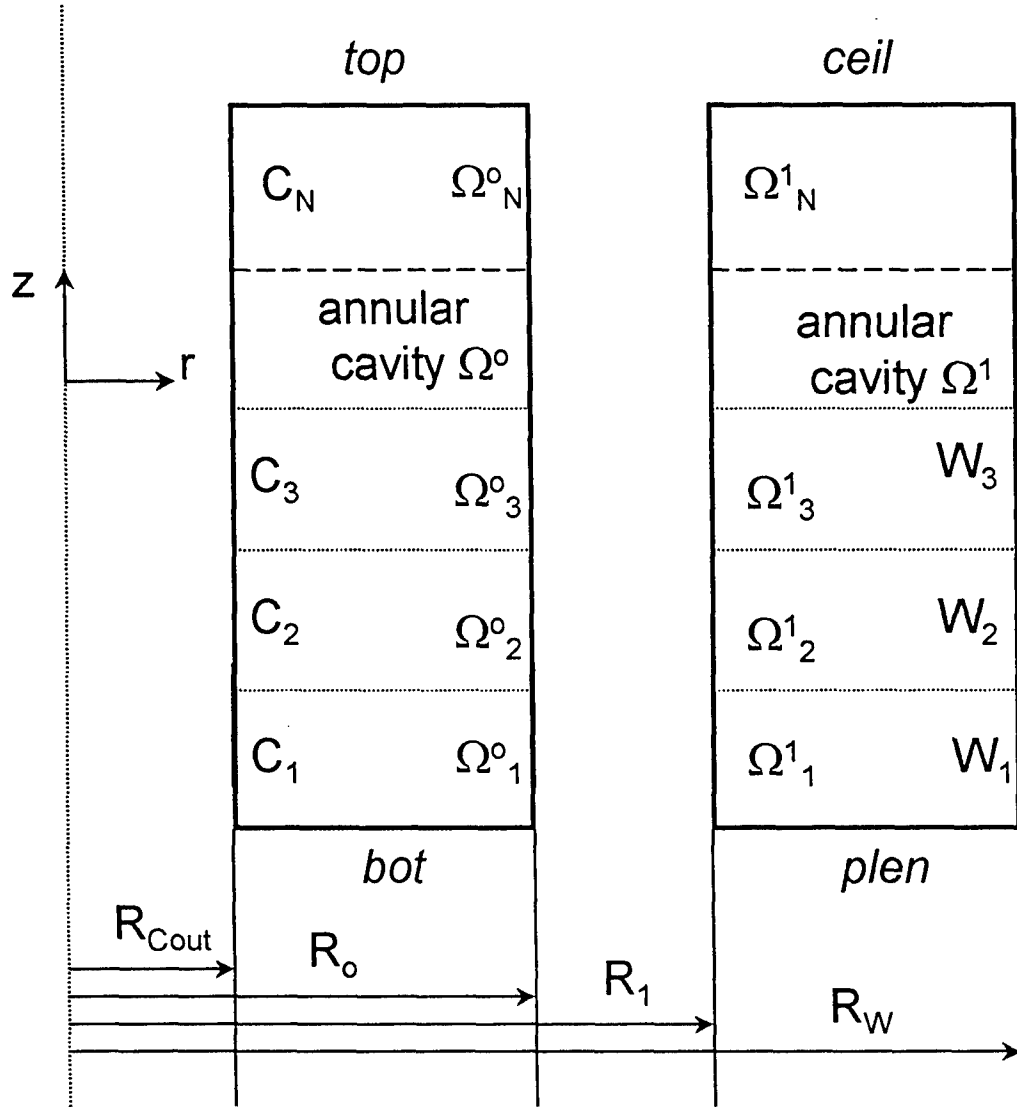


Figure C21.

The view factors  $G$ ,  $G^o$  and  $G^1$  in the coaxial cylindrical cavities  $\Omega = \{N, R_{Cout}, R_w\}$ ,  $\Omega^o = \{N, R_{Cout}, R_o\}$ , and  $\Omega^1 = \{N, R_1, R_w\}$ , respectively, are useful for calculating the view factors  $F$  in the  $\beta$ -tubes bundle cavity. Calculation of these view factors proceeds into several successive steps. Note that the surface areas of the cylindrical  $\beta$ -tubes outer shells  $\{\beta_k\}$  must account for the total number of tubes  $N_\beta$ :

$$A_{\beta_k} = \frac{h_\beta}{N} (2\pi R_{\beta out}) \times N_\beta \quad (C42)$$

a). The view factor between infinitely-long evaporator standoff and  $\beta$ -tubes is calculated as:

$$F_{C \rightarrow \beta}^\infty = N_\beta \times F_{C \rightarrow 1 tube}^\infty \quad (C43)$$

where  $F_{C \rightarrow 1tube}^{\infty}$  is given by Equation (C26).

b). The factors between standoff shells and  $\beta$ -tube sections are calculated using Equation (C34):

$$F_{C_k \rightarrow \beta_p} = F_{C \rightarrow \beta}^{\infty} \times G_{C_k \rightarrow \Omega_p}^o, \quad \text{where } k, p = 1 \text{ to } N. \quad (C44)$$

c). The view factors between the  $N_{\beta}$  infinitely-long  $\beta$ -tubes are calculated. The analysis accounts for obstruction by other tubes and by the evaporator standoff cylinder, and depends on the number of  $\beta$ -tubes.

Figure C22 shows the arrangement for the case of 6  $\beta$ -tubes ( $N_{\beta}=6$ ), uniformly distributed along a ring of radius  $c$ . The view between tubes number 1 and 2 is not obstructed, and  $F_{1 \rightarrow 2}^{\infty}$  can be calculated using Equation (C26). The distance between the centers of tube #1 and tube # $k$  can be calculated as:

$$a_{1k} = 2c \sin \frac{(k-1)\alpha}{2} \quad (C45)$$

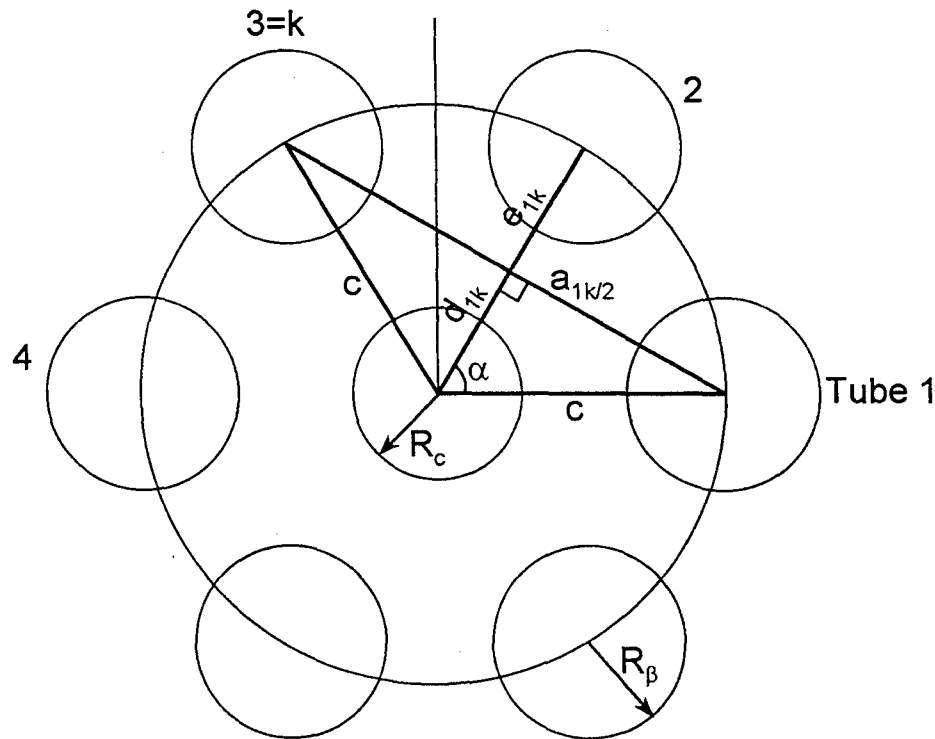


Figure C22.

There is the possibility that the view between 2 non-adjacent tubes is obstructed by the standoff cylinder. The distance  $d_{1k}$  between the center of the standoff and the line joining the tubes #1 and #k is given by:

$$d_{1k} = c \cos \frac{(k-1)\alpha}{2} , \quad (C46)$$

and the view factor between tubes #1 and #k with obstruction by the standoff cylinder,  $F_{1 \rightarrow k}^{\infty(c)}$ , is obtained using Equation (C29) or Equation (C30).

For the practical cases of interest in which the maximum number of  $\beta$ -tubes,  $N_\beta$ , in the cell is equal to 7, the view between tubes #1 and #k can be obstructed by another tube only when  $k=3$ . In that case (see Figure C22), the distance between the center of obstructing tube #2 and the line joining tubes #1 and #3 is given by  $e_{13} = c - d_{13}$ ; the view factor between tubes #1 and #3 with obstruction by tube #2 only,  $F_{1 \rightarrow 3}^{\infty(2)}$ , is calculated using Equation (C29) or Equation (C30). If we define the view factor between infinitely-long tubes #1 and #3 without any obstruction as  $F_{1 \rightarrow 3}^{\infty(no)}$  (given by Equation C26), the view factor between tubes #1 and #3 with obstruction by standoff cylinder and  $\beta$ -tube number 2 is given by:

$$F_{1 \rightarrow 3}^{\infty} = F_{1 \rightarrow 3}^{\infty(c)} + F_{1 \rightarrow 3}^{\infty(2)} - F_{1 \rightarrow 3}^{\infty(no)} . \quad (C47)$$

The other factors between tube #1 and tubes #5 and #6 (see Figure C22) are easily obtained by symmetry:

$$F_{1 \rightarrow 5}^{\infty} = F_{1 \rightarrow 3}^{\infty} \text{ and } F_{1 \rightarrow 6}^{\infty} = F_{1 \rightarrow 2}^{\infty} .$$

Now that the view factors between any pair of infinitely-long  $\beta$ -tubes are known, the factors  $F_{1(\beta_1) \rightarrow k(\beta_p)}$  between section  $\beta_1$  of tube number 1 and section  $\beta_p$  of tube number k can be evaluated using Equation (C34). Since the section  $\beta_p$  of the bundle of tubes is made of the contribution of  $N_\beta$  tubes, the view factor between section  $\beta_1$  of bundle and section  $\beta_p$  of bundle is given by:

$$F_{\beta_1 \rightarrow \beta_p} = \sum_{k=2}^{N_\beta} F_{1(\beta_1) \rightarrow k(\beta_p)} , \quad (C48)$$

since  $F_{1(\beta_1) \rightarrow 1(\beta_1)} = 0$  .

Finally, the view factors between sections  $\beta_k$  and  $\beta_p$  can be deduced from the set of factors  $F_{\beta_1 \rightarrow \beta_p}$  by making use of symmetry:

$$F_{\beta_k \rightarrow \beta_p} = F_{\beta_1 \rightarrow \beta_{|p-k|+1}} \quad (C49)$$

d). The factors  $G^o$  in the coaxial cylindrical cavity  $\Omega^o$  can be used directly to calculate the view factors between evaporator standoff sections and top and bottom rings:

$$\begin{cases} F_{C_k \rightarrow top} = G_{C_k \rightarrow top}^o \\ F_{C_k \rightarrow bot} = G_{C_k \rightarrow bot}^o, \text{ and } F_{top \rightarrow bot} = G_{top \rightarrow bot}^o \end{cases} \quad (C50)$$

The other factors between these surfaces are easily obtained by reciprocity (Equation C36).

e). The view factors between top ring and  $\beta$ -tubes sections are calculated as:

$$F_{top \rightarrow \beta_k} = F_{C \rightarrow \beta}^{\infty} G_{top \rightarrow \Omega_k^o}^o \times \left[ 1 + (\delta - 1) \frac{k-1}{N-1} \right], \quad (C51)$$

where  $\delta > 1$  is defined by the user. The coefficient  $\delta$  accounts for the fact that the fraction of rays from the top ring through  $\Omega_k^o$  which are incident onto  $\beta_k$  increases with  $k$ , or decreases with the distance between top ring and  $\beta$ -tube section. The view factors between bottom ring and  $\beta$ -tube sections are simply obtained by symmetry:

$$F_{bot \rightarrow \beta_k} = F_{top \rightarrow \beta_{N+1-k}} \quad (C52)$$

f). The view factors between the first evaporator standoff section  $C_1$  and the surfaces  $W_k$ , *ceil* and *plen*, are calculated by assuming that the same fraction of rays emitted by  $C_1$  will reach these other surfaces, whether the  $\beta$ -tubes are present or not. These fractions are obtained by using the view factors  $G$  in the annular cavity  $\Omega$  (obtained by removing the  $\beta$ -tubes):

The fraction of rays leaking through the spacing between  $\beta$ -tubes can be calculated as:

$$F_{C_1 \rightarrow leak} = 1 - F_{C_1 \rightarrow top} - F_{C_1 \rightarrow bot} - \sum_{k=1}^N F_{C_1 \rightarrow \beta_k} = \left( 1 - F_{C \rightarrow \beta}^{\infty} \right) \sum_{k=1}^N G_{C_1 \rightarrow \Omega_k^o}^o \quad (C53)$$

If we define:

$$G_{C_1 \rightarrow leak} = G_{C_1 \rightarrow ceil} + G_{C_1 \rightarrow plen} + \sum_{k=1}^N G_{C_1 \rightarrow W_k}, \quad (C54)$$

then

$$\begin{aligned}
F_{C_1 \rightarrow \text{ceil}} &= \frac{G_{C_1 \rightarrow \text{ceil}}}{G_{C_1 \rightarrow \text{leak}}} \times F_{C_1 \rightarrow \text{leak}} , \\
F_{C_1 \rightarrow \text{plen}} &= \frac{G_{C_1 \rightarrow \text{plen}}}{G_{C_1 \rightarrow \text{leak}}} \times F_{C_1 \rightarrow \text{leak}} , \text{ and} \\
F_{C_1 \rightarrow W_k} &= \frac{G_{C_1 \rightarrow W_k}}{G_{C_1 \rightarrow \text{leak}}} \times F_{C_1 \rightarrow \text{leak}} , \quad k = 1 \text{ to } N .
\end{aligned} \tag{C55}$$

Note that the use of fractional view factors insures that the enclosure relation is satisfied for  $C_1$ . The factors  $F_{C_1 \rightarrow W_k}$  can be used to deduce all factors  $F_{C_p \rightarrow W_k}$ . By symmetry:

$$F_{C_p \rightarrow W_k} = F_{C_1 \rightarrow W_{|p-k|+1}} . \tag{C56}$$

Finally the enclosure relation for evaporator standoff section  $C_p$  ( $p > 1$ ) can be used to calculate the fraction of rays which reach the ceiling and plenum rings through the  $\beta$ -tubes:

$$F_{C_p \rightarrow \text{leak}} = \sum_{k=1}^N \left\{ \left( 1 - F_{C \rightarrow \beta}^\infty \right) G_{C_p \rightarrow \Omega_k}^o - F_{C_p \rightarrow W_k} \right\} . \tag{C57}$$

then:

$$\begin{aligned}
F_{C_p \rightarrow \text{ceil}} &= \frac{G_{C_p \rightarrow \text{ceil}}}{G_{C_p \rightarrow \text{ceil}} + G_{C_p \rightarrow \text{plen}}} \times F_{C_p \rightarrow \text{leak}} , \text{ and} \\
F_{C_p \rightarrow \text{plen}} &= \frac{G_{C_p \rightarrow \text{plen}}}{G_{C_p \rightarrow \text{ceil}} + G_{C_p \rightarrow \text{plen}}} \times F_{C_p \rightarrow \text{leak}} , \quad \text{for } p = 2 \text{ to } N .
\end{aligned} \tag{C58}$$

Again, the use of fractions insures that the enclosure relation is satisfied for  $C_p$ ,  $p > 1$ .

At this point all radiation view factors which involve the evaporator standoff shells  $C_p$  are known (after using reciprocity, of course).

g). The fractional analysis described above, which used the annular cavity  $\Omega$ , is used again to obtain the view factors between the top ring and the surfaces *plen* and  $W_k$ . The fraction of rays leaking through the openings between  $\beta$ -tubes can be calculated as:

$$F_{\text{top} \rightarrow \text{leak}} = 1 - F_{\text{top} \rightarrow \text{bot}} - \sum_{k=1}^N \left( F_{\text{top} \rightarrow C_k} + F_{\text{top} \rightarrow \beta_k} \right) . \tag{C59}$$

Introducing:

$$G_{top \rightarrow leak} = G_{top \rightarrow plen} + \sum_{k=1}^N G_{top \rightarrow W_k}, \quad (C60)$$

we obtain:

$$\begin{aligned} F_{top \rightarrow plen} &= \frac{G_{top \rightarrow plen}}{G_{top \rightarrow leak}} \times F_{top \rightarrow leak}, \\ F_{top \rightarrow W_k} &= \frac{G_{top \rightarrow W_k}}{G_{top \rightarrow leak}} \times F_{top \rightarrow leak}, \quad k = 1 \text{ to } N. \end{aligned} \quad (C61)$$

The view factors for the bottom ring are easily obtained by symmetry:

$$\begin{aligned} F_{bot \rightarrow ceil} &= F_{top \rightarrow plen}, \quad \text{and} \\ F_{bot \rightarrow W_k} &= F_{top \rightarrow W_{N+1-k}}. \end{aligned} \quad (C62)$$

At this point, all radiation view factors involving the top and bottom inner rings are known.

h). Fractional analysis is used in the coaxial cylindrical cavity  $\Omega^1$  to calculate the view factors between the first  $\beta$ -tubes section  $\beta_1$  and surfaces  $W_k$ , *ceil* and *plen*. The fraction of rays leaking outwards can be calculated as:

$$F_{\beta_1 \rightarrow leak} = 1 - F_{\beta_1 \rightarrow bot} - F_{\beta_1 \rightarrow top} - \sum_{k=1}^N (F_{\beta_1 \rightarrow \beta_k} + F_{\beta_1 \rightarrow C_k}). \quad (C63)$$

Introducing:

$$G_{\Omega_1^1 \rightarrow leak}^1 = G_{\Omega_1^1 \rightarrow ceil}^1 + \gamma G_{\Omega_1^1 \rightarrow plen}^1 + \sum_{k=1}^N G_{\Omega_1^1 \rightarrow W_k}^1, \quad (C64)$$

we obtain:

$$\begin{aligned} F_{\beta_1 \rightarrow ceil} &= \frac{G_{\Omega_1^1 \rightarrow ceil}^1}{G_{\Omega_1^1 \rightarrow leak}^1} \times F_{\beta_1 \rightarrow leak}, \\ F_{\beta_1 \rightarrow plen} &= \frac{\gamma G_{\Omega_1^1 \rightarrow plen}^1}{G_{\Omega_1^1 \rightarrow leak}^1} \times F_{\beta_1 \rightarrow leak}, \quad \text{and} \\ F_{\beta_1 \rightarrow W_k} &= \frac{G_{\Omega_1^1 \rightarrow W_k}^1}{G_{\Omega_1^1 \rightarrow leak}^1} \times F_{\beta_1 \rightarrow leak}, \quad k = 1 \text{ to } N. \end{aligned} \quad (C65)$$



The factor  $\gamma > 1$  has been introduced to account for increased view factor between first  $\beta$ -tube section and outer ring closest to it.

The factors  $F_{\beta_1 \rightarrow W_k}$  can be used to obtain the view factors between any  $\beta$ -tube section and any outer wall shell. By symmetry:

$$F_{\beta_p \rightarrow W_k} = F_{\beta_1 \rightarrow W_{|p-k|+1}} \quad (C66)$$

Finally the enclosure relation for the  $\beta$ -tube section  $\beta_p$  ( $p > 1$ ) can be used to calculate the fraction of rays which reaches the ceiling and plenum outer rings:

$$F_{\beta_p \rightarrow leak} = 1 - F_{\beta_p \rightarrow bot} - F_{\beta_p \rightarrow top} - \sum_{k=1}^N \left( F_{\beta_p \rightarrow \beta_k} + F_{\beta_p \rightarrow C_k} + F_{\beta_p \rightarrow W_k} \right) \quad (C67)$$

Introducing:

$$G_{\Omega_{p \rightarrow leak}}^1 = \left[ \gamma + (1-\gamma) \frac{k-1}{N-1} \right] G_{\Omega_{p \rightarrow plen}}^1 + \left[ \gamma + (1-\gamma) \frac{N-k}{N-1} \right] G_{\Omega_{p \rightarrow ceil}}^1 \quad (C68)$$

we obtain:

$$F_{\beta_p \rightarrow ceil} = \frac{\left[ \gamma + (1-\gamma) \frac{N-k}{N-1} \right] G_{\Omega_{p \rightarrow ceil}}^1}{G_{\Omega_{p \rightarrow leak}}^1} \times F_{\beta_p \rightarrow leak} \quad \text{and} \quad (C69)$$

$$F_{\beta_p \rightarrow plen} = \frac{\left[ \gamma + (1-\gamma) \frac{k-1}{N-1} \right] G_{\Omega_{p \rightarrow plen}}^1}{G_{\Omega_{p \rightarrow leak}}^1} \times F_{\beta_p \rightarrow leak}$$

At this point, all radiation view factors involving the  $\beta$ -tube sections are known.

i). The view factor between *plen* and *ceil* outer rings is calculated using that in the coaxial cylindrical cavity  $\Omega^1$ :

$$F_{plen \rightarrow ceil} = G_{plen \rightarrow ceil}^1 \quad (C70)$$

The view factors between *plen* ring and cylindrical wall sections are calculated by fractional analysis in the cavity  $\Omega^1$ . The fraction of rays reaching the wall shells can be calculated as:

$$F_{plen \rightarrow leak} = 1 - F_{plen \rightarrow ceil} - F_{plen \rightarrow top} - \sum_{k=1}^N (F_{plen \rightarrow C_k} + F_{plen \rightarrow \beta_k}) . \quad (C71)$$

Finally, the factors are calculated as:

$$F_{plen \rightarrow W_p} = \frac{G_{plen \rightarrow W_p}^1}{\sum_{k=1}^N G_{plen \rightarrow W_k}^1} \times F_{plen \rightarrow leak} , \quad \text{for } p = 1 \text{ to } N. \quad (C72)$$

The view factors between ceiling ring and wall sections are easily obtained by symmetry:

$$F_{ceil \rightarrow W_p} = F_{plen \rightarrow W_{N+1-p}} . \quad (C73)$$

j). At this point, all view factors in the  $\beta$ -tubes bundle cavity are known, except the factors  $F_{W_k \rightarrow W_p}$  between cylindrical wall shells. Because of symmetry, only the  $N$  factors  $F_{W_1 \rightarrow W_p} = \chi_p$  need to be evaluated. In order to obtain a closed system of equations to solve for these  $N$  unknowns, it is necessary to specify  $N$  relations between these factors.

Let us introduce the fraction of rays emitted by wall shell  $W_p$  which falls on the circular wall:

$$F_{W_p \rightarrow wall} = 1 - F_{W_p \rightarrow top} - F_{W_p \rightarrow bot} - F_{W_p \rightarrow ceil} - F_{W_p \rightarrow plen} - \sum_{k=1}^N (F_{W_p \rightarrow C_k} + F_{W_p \rightarrow \beta_k}) . \quad (C74)$$

The enclosure relation for wall section  $p$  can then be written:

$$\sum_{k=1}^N F_{W_p \rightarrow W_k} = F_{W_p \rightarrow wall} . \quad (C75)$$

Because of symmetry, the view factors between wall sections can be written as functions of the  $N$  unknown factors as:

$$F_{W_p \rightarrow W_k} = F_{W_1 \rightarrow W_{|p-k|+1}} = \chi_{|p-k|+1} , \quad (C76)$$

and Equation (C75) takes the form:

$$\sum_{k=1}^N \chi_{|p-k|+1} = F_{W_p \rightarrow wall} . \quad (C77)$$

Because of symmetry, however, the enclosure relations (C77) can provide only  $n$  independent relations, where  $n = N/2$  when  $N$  is even, and  $n = (N+1)/2$  when  $N$  is odd. It is therefore

necessary to provide an additional  $(N-n)$  relations between the  $N$  unknown  $\chi_k$ . The ratio of some view factors is specified, based on the ratio in the coaxial cylindrical cavity  $\Omega^1$ :

$$\frac{\chi_p}{\chi_1} = \frac{G_{W_1 \rightarrow W_p}^1}{G_{W_1 \rightarrow W_1}^1}, \quad \text{for } p=2 \text{ to } N-n+1. \quad (\text{C78})$$

We obtain the following  $N \times N$  linear system for  $\{\chi_p\}$ :

$$\begin{aligned} \sum_{k=1}^N \chi_{|p-k|+1} &= F_{W_p \rightarrow \text{wall}}, \quad p = 1 \text{ to } n \text{ (} n \text{ relations),} \\ G_{W_1 \rightarrow W_p}^1 \chi_1 - G_{W_1 \rightarrow W_1}^1 \chi_p &= 0, \quad p = 2 \text{ to } N-n+1 \text{ (} N-n \text{ relations).} \end{aligned} \quad (\text{C79})$$

The linear system is solved for the unknowns  $\{\chi_p, p=1 \text{ to } N\}$  using Gauss-elimination. Then the view factors between cylindrical wall shells are easily obtained as:

$$F_{W_p \rightarrow W_k} = \chi_{|p-k|+1} \quad (\text{C80})$$

This ends the section describing the calculation of the view factors in the evaporator standoff /  $\beta$ -tubes bundle. By construction, all the reciprocity and enclosure relations are satisfied in the bundle cavity. In the approximate model herein, all view factors entering involving the circular standoff shells are calculated accurately. Also the view factors between any  $\beta$ -tube section and another  $\beta$ -tube section are well approximated. The main sources of errors in the values of the view factors are introduced in sections e) and h), where parameters  $\delta$  and  $\gamma$  are used. The calculations of view factors between top/bottom rings and  $\beta$ -tubes sections are the most uncertain of all. This uncertainty might be corrected by attempting complex numerical integrations to evaluate these factors. However, the use of parameters  $\delta$  and  $\gamma$  allows some flexibility to the present method. When reasonable values of  $\delta$  and  $\gamma$  are used, all view factors are positive and the view factors between the cylindrical wall shells vary as expected.

#### C.2.4. Radiative Coupling between $\beta$ -Tubes Bundle Cavity and Artery Annular Cavity Above

After the view factors in the  $\beta$ -tubes bundle cavity and in the artery coaxial cylindrical cavity above have been calculated (see sections C.2.2 and C.2.3), the view factors in the low vapor pressure zone must be modified to account for the radiative coupling through the fictitious surface rings *ceil*, *top*, and *ring* (see Figure C20). Note that the surface *ring* for the artery coaxial cavity is made of the ring *top* of the  $\beta$ -tubes bundle cavity and of the annular edge (surface *edge*) of the evaporator standoff, which has inner and outer radii  $R_a$  and  $R_{\text{Cout}}$ , respectively.

a). The view factors  $F_{a_k \rightarrow edge}$  between artery axial sections and the edge of the evaporator standoff are calculated using Equation (C15). Next the view factors between artery axial sections and inner bottom ring  $bot$  is obtained as:

$$F_{a_k \rightarrow bot} = \text{Max}\{0, G_{a_k \rightarrow bot} - F_{a_k \rightarrow edge}\}, \quad (C81)$$

where  $G_{a_k \rightarrow bot}$  is the view factor between artery axial section  $a_k$  and a bottom ring on the support plate which has inner and outer radii  $R_a$  and  $R_o$ , respectively, in the absence of obstruction by the edge of the evaporator standoff, which is given by Equation (C15).

b). The view factor between infinitely-long artery and  $\beta$ -tubes bundle is calculated as:

$$F_{a \rightarrow \beta}^{\infty} = N_{\beta} \times F_{a \rightarrow 1tube}^{\infty}, \quad (C82)$$

where  $F_{a \rightarrow 1tube}^{\infty}$  is given by Equation (C26).

When  $F_{a_k \rightarrow bot} > 0$ , the evaporator standoff does not obstruct the view between the artery axial section  $a_k$  and the  $\beta$ -tubes. In that case, the view factors between artery shells  $a_k$  and  $\beta$ -tube sections can be calculated using Equation (C34):

$$F_{a_k \rightarrow \beta_p} = G_{a_k \rightarrow \beta_p} \equiv F_{a \rightarrow \beta}^{\infty} \times G_{a_k \rightarrow \Omega_p^o}, \quad \text{for } p = 1 \text{ to } N. \quad (C83)$$

When  $F_{a_k \rightarrow bot} = 0$ , the evaporator standoff obstructs the view between the artery axial section  $a_k$  and some of the lower axial sections of  $\beta$ -tubes. The total obstruction factor between artery axial section  $a_k$  and  $\beta$ -tubes ring can be calculated as:

$$F_{a_k \rightarrow \beta}^{obs(0)} = F_{a_k \rightarrow edge} - G_{a_k \rightarrow bot}. \quad (C84)$$

First  $F_{a_k \rightarrow \beta}^{obs(0)}$  and  $G_{a_k \rightarrow \Omega_1^o}$  are compared. If  $F_{a_k \rightarrow \beta}^{obs(0)} > G_{a_k \rightarrow \Omega_1^o}$ , then the lowest section of  $\beta$ -tubes ( $p=1$ ) is completely obstructed by the evaporator standoff, and  $F_{a_k \rightarrow \beta_1} = 0$ . The remaining of the obstruction factor is calculated as:

$$F_{a_k \rightarrow \beta}^{obs(1)} = F_{a_k \rightarrow \beta}^{obs(0)} - G_{a_k \rightarrow \Omega_1^o}. \quad (C85)$$

$F_{a_k \rightarrow \beta}^{obs(1)}$  and  $G_{a_k \rightarrow \Omega_2^o}$  are compared. If  $F_{a_k \rightarrow \beta}^{obs(1)} > G_{a_k \rightarrow \Omega_2^o}$ , then section  $p=2$  of  $\beta$ -tubes is also completely obstructed by the evaporator standoff, and  $F_{a_k \rightarrow \beta_2} = 0$ . The remaining of the obstruction factor is calculated as:

$$F_{a_k \rightarrow \beta}^{obs(2)} = F_{a_k \rightarrow \beta}^{obs(1)} - G_{a_k \rightarrow \Omega_2^o} \quad (C86)$$

This procedure is repeated till  $F_{a_k \rightarrow \beta}^{obs(p-1)} < G_{a_k \rightarrow \Omega_p^o}$ . This means that section  $p$  of  $\beta$ -tubes is only partially obstructed by the evaporator standoff. In that case:

$$F_{a_k \rightarrow \beta_p} = F_{a \rightarrow \beta}^\infty \times \left( G_{a_k \rightarrow \Omega_p^o} - F_{a_k \rightarrow \beta}^{obs(p-1)} \right), \quad (C87)$$

and the view factors between the artery axial section  $a_k$  and the axial sections of  $\beta$ -tubes above  $p$  are not obstructed, and are calculated from Equation (C83).

c). Fractional analysis is used again to calculate the view factors between the artery axial sections, and the lower wall sections  $W_p$  and outer ring  $plen$ . The fraction of rays leaking towards these surfaces can be calculated as (Figure C20):

$$F_{a_k \rightarrow leak} = F_{a_k \rightarrow ceil} + F_{a_k \rightarrow ring} - F_{a_k \rightarrow edge} - F_{a_k \rightarrow bot} - \sum_{p=1}^N F_{a_k \rightarrow \beta_p} \quad (C88)$$

Introducing:

$$G_{a_k \rightarrow leak} = G_{a_k \rightarrow plen} + \sum_{p=1}^{N-1} G_{a_k \rightarrow W_p} + \zeta G_{a_k \rightarrow W_N}, \quad (C89)$$

we obtain:

$$\begin{aligned} F_{a_k \rightarrow plen} &= \frac{G_{a_k \rightarrow plen}}{G_{a_k \rightarrow leak}} \times F_{a_k \rightarrow leak}, \\ F_{a_k \rightarrow W_p} &= \frac{G_{a_k \rightarrow W_p}}{G_{a_k \rightarrow leak}} \times F_{a_k \rightarrow leak}, \quad \text{for } p = 1 \text{ to } N-1, \text{ and} \\ F_{a_k \rightarrow W_N} &= \frac{\zeta G_{a_k \rightarrow W_N}}{G_{a_k \rightarrow leak}} \times F_{a_k \rightarrow leak}. \end{aligned} \quad (C90)$$

The factor  $\zeta > 1$  was introduced to account for increased view factors between the artery axial sections and the top wall shell  $W_N$  of the bundle cavity. At this point, all radiation view factors which involve the artery axial sections  $a_k$  are known in the AMTEC cell (after using reciprocity, of course).

d). All view factors for the edge of the evaporator standoff are calculated.  $F_{edge \rightarrow a_k}$  are obtained by reciprocity, and the factors  $F_{edge \rightarrow \omega_k}$  and  $F_{edge \rightarrow cond}$  are calculated using Equations (C13) and (C17), respectively. All other factors are null, since the edge of the evaporator standoff does not see the  $\beta$ -tubes bundle cavity.

e). The view factors between the bottom inner ring *bot* and the upper artery coaxial cavity are calculated. It is assumed that the rays issuing from the ring *bot* which stream through the inner ring *top* fall either on the artery or the condenser, while that which stream through the outer ring *ceil* fall on the upper side wall, only (see Figure C20). In that case:

$$F_{bot \rightarrow cond} = F_{bot \rightarrow top} - \sum_{k=1}^{N_w} F_{bot \rightarrow a_k}, \quad (C91)$$

and fractional analysis gives:

$$F_{bot \rightarrow \omega_k} = \frac{G_{bot \rightarrow \omega_k}}{\sum_{p=1}^{N_w} G_{bot \rightarrow \omega_p}} \times F_{bot \rightarrow ceil}, \quad k = 1 \text{ to } N_w, \quad (C92)$$

where the unobstructed factors  $G$  (in the absence of the  $\beta$ -tubes) are calculated using Equation (C13).

f). The view factors between axial sections of evaporator standoff  $C_p$  and upper wall shells  $\omega_k$  are calculated. The view between  $C_p$  and  $\omega_k$  is obstructed by the ring of  $\beta$ -tubes when:

$$k \leq k_p = \frac{R_w - R_o}{R_o - R_{Cout}} \frac{h_\beta}{h_a} (N - p + 1/2) + 1/2, \quad (C93)$$

where  $R_{Cout}$  is the outer radius of the evaporator standoff,  $R_o$  is the equivalent inner radius of the ring of  $\beta$ -tubes,  $R_w$  is the inner radius of the cell wall, and  $h_\beta$  and  $h_a$  are the heights of the  $\beta$ -tube and artery axial sections, respectively. Therefore:

$$\begin{aligned} F_{C_p \rightarrow \omega_k} &= G_{C_p \rightarrow \omega_k} \times (1 - F_{C \rightarrow \beta}^\infty) \text{ for } k \leq k_p, \text{ and} \\ F_{C_p \rightarrow \omega_k} &= G_{C_p \rightarrow \omega_k} \text{ for } k > k_p. \end{aligned} \quad (C94)$$

The unobstructed view factors  $G_{C_p \rightarrow \omega_k}$  are calculated using Equation (C18).

Finally, the view factors between evaporator standoff axial sections and condenser are easily obtained by flux conservation:

$$F_{C_p \rightarrow cond} = F_{C_p \rightarrow top} + F_{C_p \rightarrow ceil} - \sum_{k=1}^{N_w} F_{C_p \rightarrow \omega_k} \quad (C95)$$

At this point, all view factors between axial sections of evaporator standoff  $C_p$  and the upper artery coaxial cavity are known.

g). The view factor between the bottom outer ring *plen* and the condenser is approximated as:

$$F_{plen \rightarrow cond} = \psi \tilde{G}_{plen \rightarrow cond}[R_1, R_w] \quad (C96)$$

where the factor  $\tilde{G}_{plen \rightarrow cond}[R_1, R_w]$  is calculated using Equation (C10). The coefficient  $\psi > 1$  accounts for the increased view factor through the openings between  $\beta$ -tubes.

Fractional analysis is used again to calculate the view factors between the outer ring *plen* and the upper wall sections  $\omega_k$ . The fraction of rays leaking towards the upper wall can be calculated as (Figure C20):

$$F_{plen \rightarrow leak} = F_{plen \rightarrow ceil} + F_{plen \rightarrow top} - F_{plen \rightarrow cond} - \sum_{k=1}^{N_w} F_{plen \rightarrow \omega_k} \quad (C97)$$

and fractional analysis gives:

$$F_{plen \rightarrow \omega_k} = \frac{\tilde{G}_{plen \rightarrow \omega_k}}{\sum_{p=1}^{N_w} \tilde{G}_{plen \rightarrow \omega_p}} \times F_{plen \rightarrow leak}, \quad k = 1 \text{ to } N_w \quad (C98)$$

where the factors  $\tilde{G}_{plen \rightarrow \omega_k}$  are calculated using Equation (C13) in a coaxial cylindrical cavity of inner and outer radii  $R_1$  and  $R_w$ , respectively. At this point, all view factors between the bottom outer ring *plen* and the upper artery coaxial cavity are known.

h). Next the view factors between lower wall shell sections  $W_p$  and condenser (*cond*) are calculated. The fraction of rays streaming through the openings of the  $\beta$ -tubes towards the condenser is neglected, so that:

$$F_{W_p \rightarrow cond} = \tilde{G}_{W_p \rightarrow cond}[R_p^{in}, R_w] \quad (C99)$$

where  $\tilde{G}_{W_p \rightarrow cond}[R_p^{in}, R_w]$ , the view factor between the wall shell section  $W_p$  and the annular base in a coaxial cylindrical enclosure of inner and outer radii  $R_p^{in}$  and  $R_w$ , respectively, is given by the reciprocal relation of Equation (C13), and

$$R_p^{in} = \text{Max} \left\{ R_a, R_1 - (R_w - R_1) \frac{L_a}{h_\beta (N - p + 1/2)} \right\}, \quad (\text{C100})$$

where  $L_a$  is the length of the liquid-return artery, between the top of the  $\beta$ -tubes and the condenser.

The view factors between the lower wall shells  $W_p$  and the upper wall shells  $\omega_k$  are calculated as follows. The fraction of rays leaking towards the upper wall can be calculated as:

$$F_{W_p \rightarrow \text{leak}} = F_{W_p \rightarrow \text{ceil}} + F_{W_p \rightarrow \text{top}} - F_{W_p \rightarrow \text{cond}} - \sum_{k=1}^{N_w} F_{W_p \rightarrow \omega_k}, \quad (\text{C101})$$

and fractional analysis gives:

$$F_{W_p \rightarrow \omega_k} = \frac{\tilde{G}_{W_p \rightarrow \omega_k}}{\sum_{m=1}^{N_w} \tilde{G}_{W_p \rightarrow \omega_m}} \times F_{W_p \rightarrow \text{leak}}, \quad k = 1 \text{ to } N_w, \quad (\text{C102})$$

where the factors  $\tilde{G}_{W_p \rightarrow \omega_k}$  have the form:

$$\begin{aligned} \tilde{G}_{W_p \rightarrow \omega_k} &= \varphi_{pk} \tilde{G}_{W_p \rightarrow \omega_k [R_a, R_w]} + (1 - \varphi_{pk}) \tilde{G}_{W_p \rightarrow \omega_k [R_1, R_w]}, \quad \text{where} \\ \varphi_{pk} &= \text{Max} \left\{ 0, \frac{(p - N) + k - 1}{N_w - 1} \right\}, \end{aligned} \quad (\text{C103})$$

and  $\tilde{G}_{W_p \rightarrow \omega_k [R_{in}, R_{out}]}$  is the view factor between wall shells  $W_p$  and  $\omega_k$  in a coaxial cylindrical cavity of inner and outer radii  $R_{in}$  and  $R_{out}$ , respectively, and is calculated using Equation (C19). The factor  $\varphi_{pk}$  varies between 0 and 1 and accounts for the obstruction by the evaporator standoff /  $\beta$ -tubes bundle. For example, the view between the deepest lower wall shell  $W_1$  and the upper wall shells  $\omega_k$  is assumed to be completely obstructed by the bundle of tubes, and  $\varphi_{1k} = 0$ . On the other hand, the view between the lower wall shell  $W_N$  near the top of the  $\beta$ -tubes and the upper wall shell  $\omega_{Nw}$  next to the condenser is free of the  $\beta$ -tubes bundle, and  $\varphi_{NN_w} = 1$ . The form of Equation (C103) accounts for the decrease in obstruction as the lower wall shell is situated closer to the top of the  $\beta$ -tubes and as the upper wall shell moves closer to the condenser.

i). Fractional analysis is used to calculate the view factors between the upper wall shells  $\omega_k$  and the  $\beta$ -tubes bundle sections  $\beta_p$ . The fraction of rays leaking towards the  $\beta$ -tubes bundle can be calculated as:



$$F_{\omega_k \rightarrow leak} = F_{\omega_k \rightarrow ceil} + F_{\omega_k \rightarrow ring} - F_{\omega_k \rightarrow edge} - F_{\omega_k \rightarrow plen} - F_{\omega_k \rightarrow bot} - \sum_{p=1}^N \left( F_{\omega_k \rightarrow C_p} + F_{\omega_k \rightarrow W_p} \right), \quad (C104)$$

and fractional analysis gives:

$$F_{\omega_k \rightarrow \beta_p} = \frac{G_{\omega_k \rightarrow \Omega_p^1}}{\sum_{m=1}^N G_{\omega_k \rightarrow \Omega_m^1}} \times F_{\omega_k \rightarrow leak}, \quad p = 1 \text{ to } N, \quad (C105)$$

where the factors  $G_{\omega_k \rightarrow \Omega_p^1}$  are calculated using the reciprocal relation of Equation (C18).

At this point, all view factors between the upper wall and the lower bundle cavity are known.

j). Finally, the enclosure relation for the  $\beta$ -tubes bundle sections is used to calculate the view factors between the sections  $\beta_p$  and the condenser:

$$F_{\beta_p \rightarrow cond} = F_{\beta_p \rightarrow ceil} + F_{\beta_p \rightarrow top} - \sum_{k=1}^{N_w} \left( F_{\beta_p \rightarrow a_k} + F_{\beta_p \rightarrow \omega_k} \right). \quad (C106)$$

This concludes the radiative coupling between the evaporator standoff /  $\beta$ -tubes bundle cavity and the artery coaxial cavity above the tubes. In the end, all view factors involving the fictitious surfaces *ceil*, *top*, and *ring* must be set to zero, and the surfaces which exchange radiant energy in the AMTEC cell are renumbered to eliminate the unnecessary fictitious surfaces.

### C.2.5. Inclusion of Side-Wall Circumferential Radiation Heat Shield in AMTEC Cell

Some multi-tube AMTEC cell designs include a circumferential heat shield above the  $\beta$ -tubes to reduce the internal radiation losses in the cell. Such heat shield configurations are relatively easy to model when it is assumed that the shield is made of a thin cylindrical metallic shell of radius  $R_{sh}$ , that is close to the inner radius of the cell wall. The shield shell, made of  $N_{sh} < N_w$  identical axial sections, starts at some height above the  $\beta$ -tubes (where it is attached to the cell wall), and covers the cell wall all the way to the condenser (but it does not touch it).

If one assumes that the heat shield cylindrical shell is close to the cell wall ( $R_w - R_{sh} \ll R_w$ ), then the view factors calculated in the low-pressure cavity are unchanged, with the difference that the upper wall shells  $k = N_w - N_{sh} + 1$  to  $N_w$  are actually the inner cylindrical shells of the heat shield. The view factors in the annulus between cell wall and circumferential heat shield are calculated using the routine VIEW\_COAXIAL developed in section C.2.2., using the actual shield average radius  $R_{sh}$ . The top and bottom rings of this annular cavity are assumed to be perfect reflectors, so as not to disturb the radiant energy exchange in the rest of the AMTEC cell enclosure. This

assumption is realistic since the bottom ring is actually closed at the weld between shield and cell wall, and because the top ring sees a portion of the condenser surface, which is typically highly reflective (when a Creare condenser design is used, the effective reflectivity of the condenser surface is close to that of a sodium liquid film, 0.95).

#### C.2.6. Inclusion of Conduction Stud in Hot Plenum of AMTEC Cell

Numerical and experimental analyses have shown that the performance of early-design multi-tube AMTEC cells was limited by their ability to supply the required sodium latent heat of vaporization (proportional to the cell electrical current) to the evaporator. New cell designs include a thick metallic stud between the cell hot plate and the evaporator standoff /  $\beta$ -tubes support plate, to enhance the conduction path to the evaporator wick. The addition of this stud would require the modification of the view factors in the hot plenum cavity. However, analyses have shown that, because of the large cross section areas of the stud and the hot plenum side wall, and since the hot plenum of the cell is very thin (the inside height of the plenum is usually less than 2 mm), the heat input to the cell is essentially transported by conduction between the cell hot end and the  $\beta$ -tubes support plate, with a relatively small temperature drop. Therefore, the contribution of radiative transport in the hot plenum cavity is negligible compared to the transport by conduction, and need not be modeled accurately. Note that the transports of heat by radiation between the cell hot end and the insides of the  $\beta$ -tubes and the evaporator standoff are still correctly accounted for by the original view factors model in the plenum cavity without a conduction stud. In conclusion, no special radiation treatment is necessary when a conduction stud is placed in the hot plenum cavity of the cell.

#### C.2.7. Conservation of Radiant Energy in AMTEC Cell

By construction, all enclosure and reciprocity relations are satisfied in the model, that is:

$$\sum_{k=1}^{N_{rad}} F_{pk} = 1, \text{ for } p=1 \text{ to } N_{rad}, \text{ and} \quad (C107)$$

$$A_p F_{pk} - A_k F_{kp} = 0, \text{ for } p, k = 1 \text{ to } N_{rad},$$

where  $N_{rad}$  is the total number of surfaces exchanging radiation in the AMTEC cell. The satisfaction of these relations is necessary to insure conservation of radiant energy exchange in the enclosures of the AMTEC cell.

## APPENDIX D: THERMAL CONDUCTIVITY MEASUREMENT DATA AND PROCESSING

This appendix compiles the original experimental data and data processing of the thermal conductivity measurements of alumina powder (size 1 and 0.01  $\mu\text{m}$ ) and molded Min-K. The calculation procedure for extracting the thermal conductivity values from the measured temperature profiles and heat input is described in details in Chapter 7.

Table D1 shows the experimental data and calculated thermal conductivities for the alumina powder of 1  $\mu\text{m}$  particle size. Figures D1 to D4 show the experimental data and fitting curves of the measured radial temperature distributions (from two symmetric sides of the test setup). The fits were obtained by using Equation (7.1). As shown in these figures, the experimental radial temperature profiles were matched well by this equation.

Table D2 and Figures D5 to D8 show the experimental data and calculated thermal conductivities for the alumina powder of 0.01  $\mu\text{m}$  particle size. As these figures show, the measured radial temperature distribution of 0.01  $\mu\text{m}$  powder was also well represented by the same function, Equation (7.1).

The experimental thermal conductivity of molded Min-K was obtained using the same data processing analysis used for the alumina powders, and results are collected in Table D3 and Figures D9 to D12.

The uniformity of the radial heat flux along the heater in the thermal conductivity experiment can be verified by examining Figure D13, which shows the measured radial temperature distribution at various axial locations. The experimental data showed that the axial temperature distribution along the heater changed only slightly near the mid-section of the heater tube (by  $\sim 1\%$  within 1 inch from the mid-section) but more significantly in the region near the end of the effective heater length (by  $\sim 7\%$ ), see Figure D13. For example, at a heater mid-section temperature of 1084 K, the temperature one inch away was 1074 K; however, the temperature was 1010 K two inches from the mid-section or a half inch from the end of effective heater length. Therefore, the test setup basically provided a uniform radial heat flux within  $\pm 1$  inch from the mid-section of the heater, and the axial heat losses was just seen near the two ends of the heater. In conclusion, heat transfer near the mid-plane of the heater can be reasonably considered as “one-dimensional axial-symmetry radial heat transfer”, as assumed in the data processing of thermal conductivity investigations.

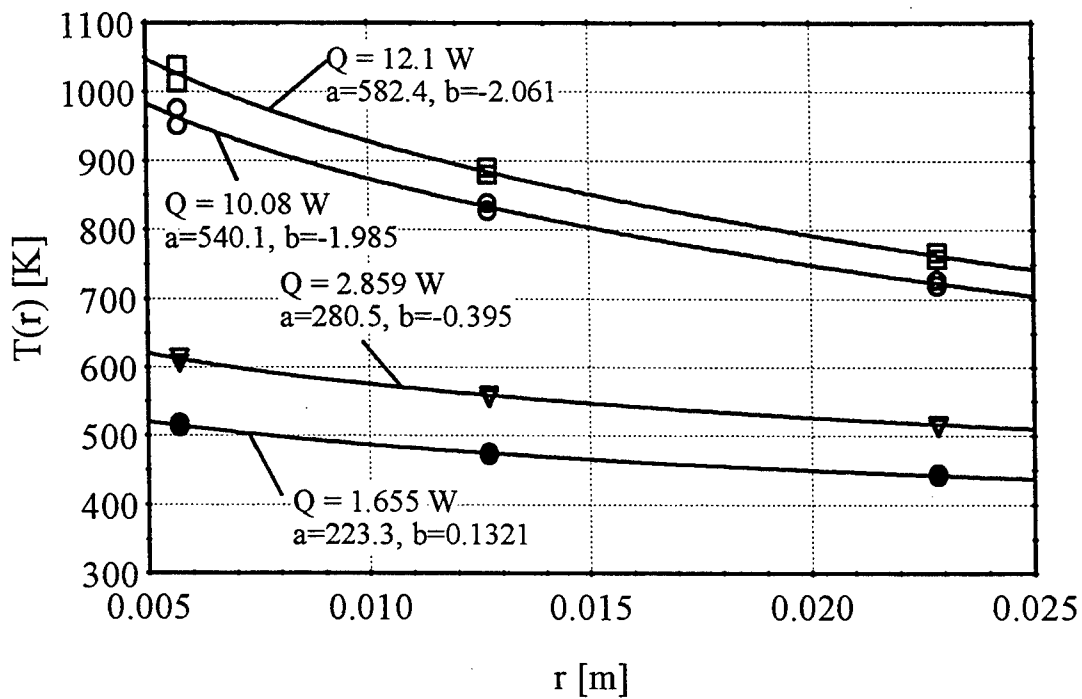


Figure D1. Radial Temperature Profiles in 1-μm Alumina Powder (Group 1).

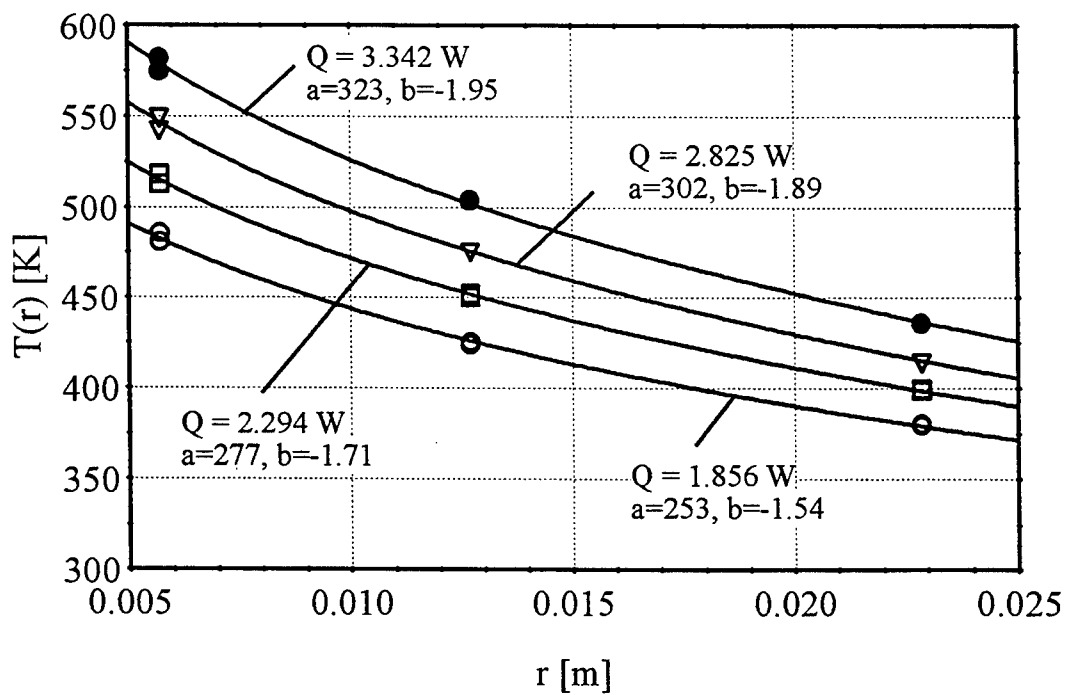


Figure D2. Radial Temperature Profiles in 1-μm Alumina Powder (Group 2).

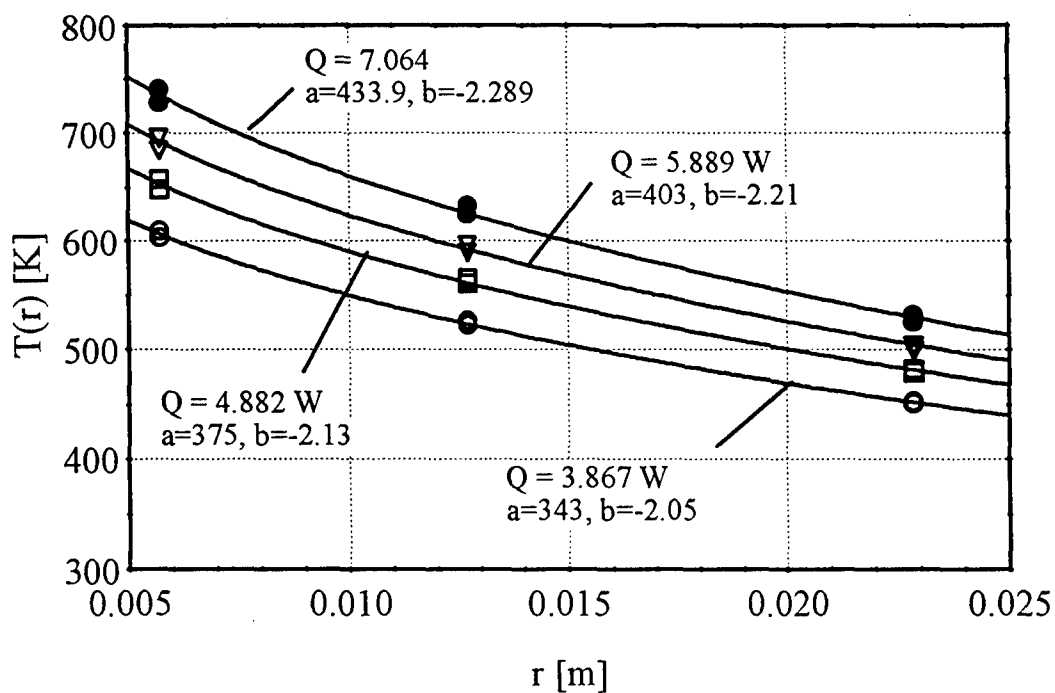


Figure D3. Radial Temperature Profiles in 1- $\mu\text{m}$  Alumina Powder (Group 3).

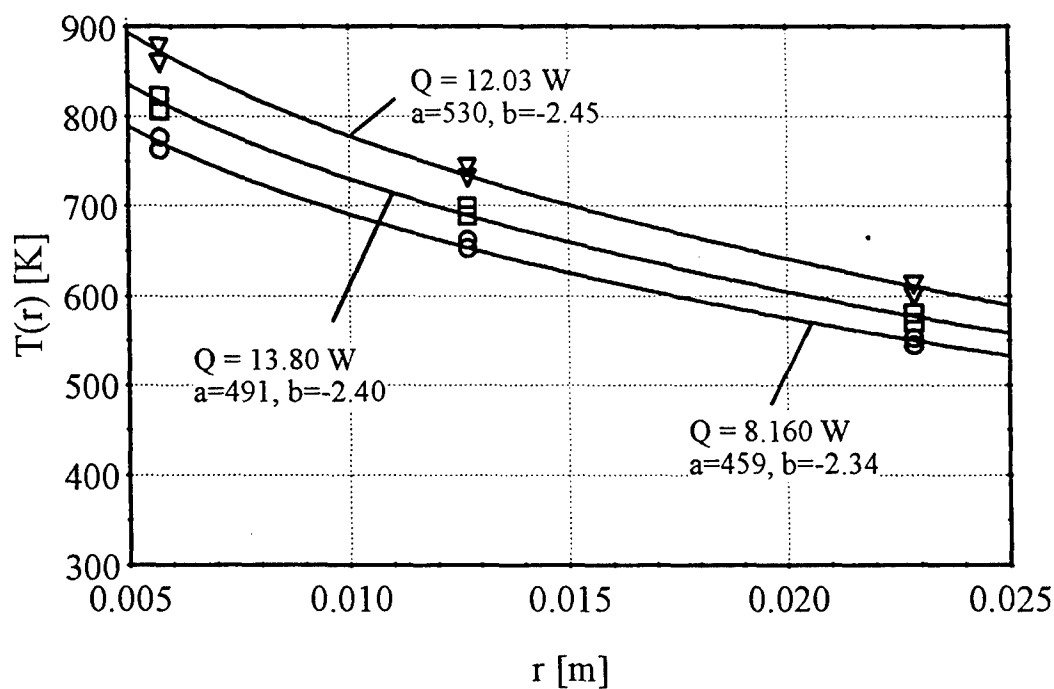


Figure D4. Radial Temperature Profiles in 1- $\mu\text{m}$  Alumina Powder (Group 4).

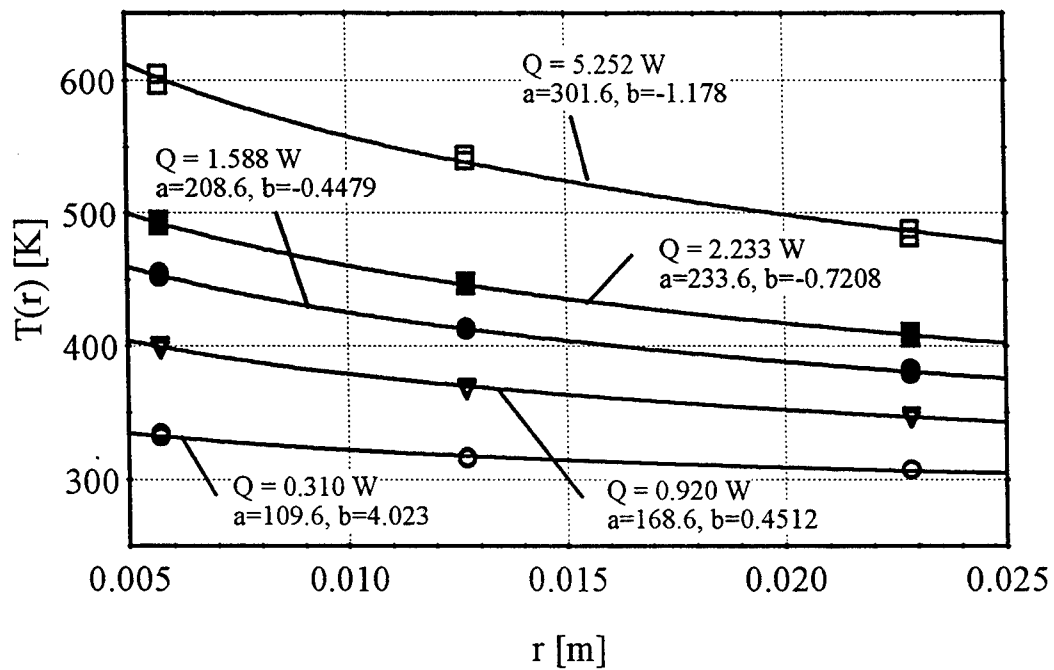


Figure D5. Radial Temperature Profiles in 0.01-μm Alumina Powder (Group 1).

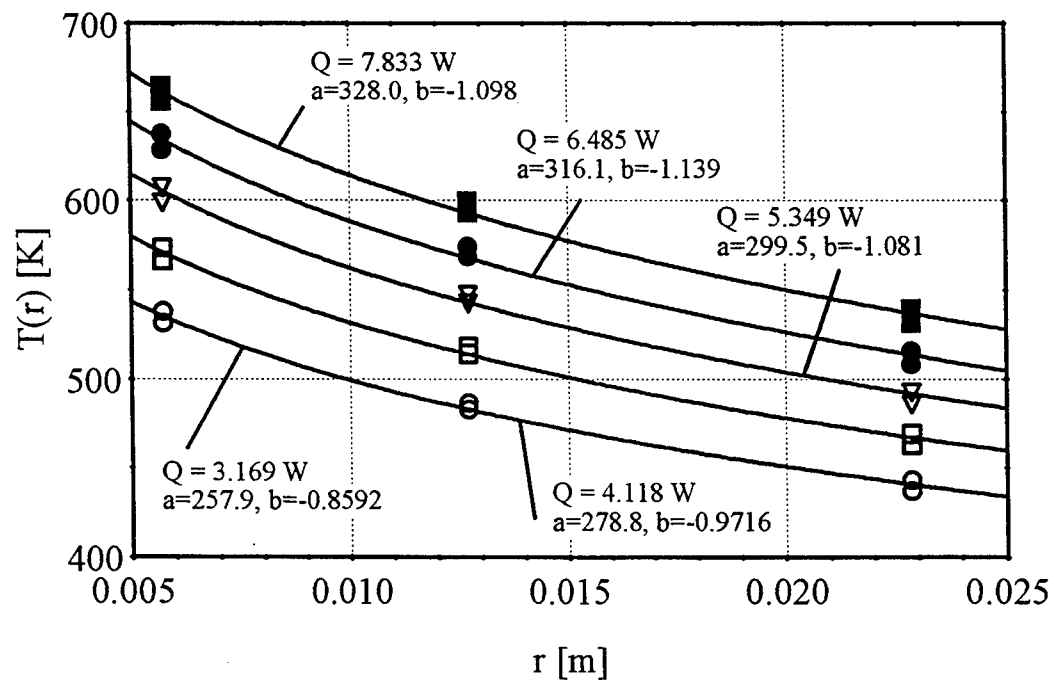


Figure D6. Radial Temperature Profiles in 0.01-μm Alumina Powder (Group 2).

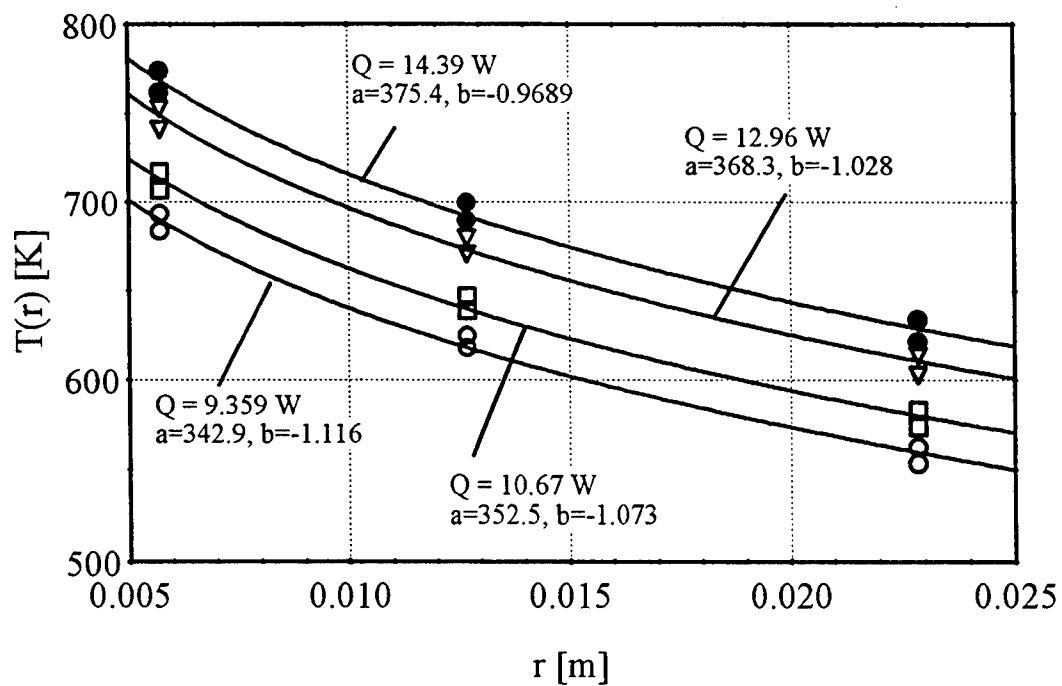


Figure D7. Radial Temperature Profiles in 0.01- $\mu\text{m}$  Alumina Powder (Group 3).

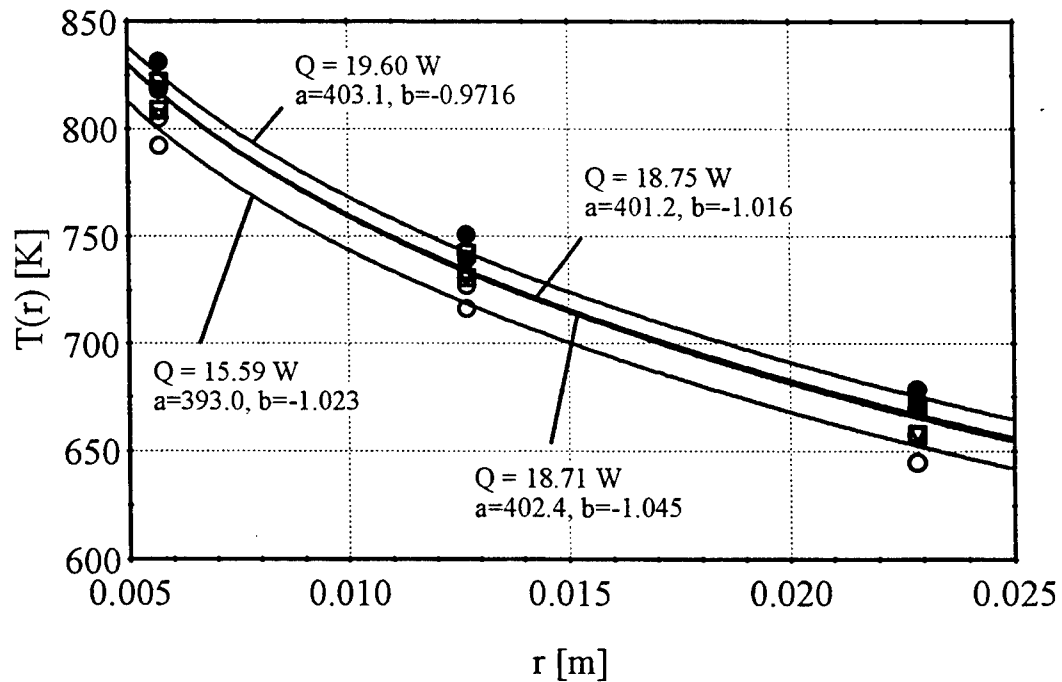


Figure D8. Radial Temperature Profiles in 0.01- $\mu\text{m}$  Alumina Powder (Group 4).

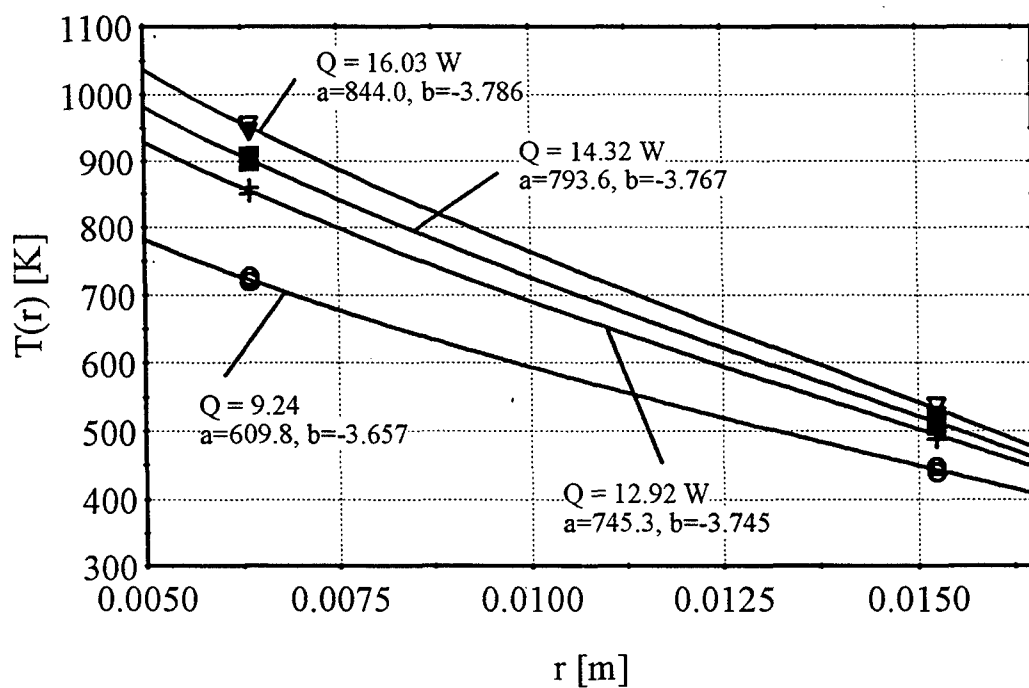


Figure D9. Radial Temperature Profiles in Molded Min-K (Group 1).

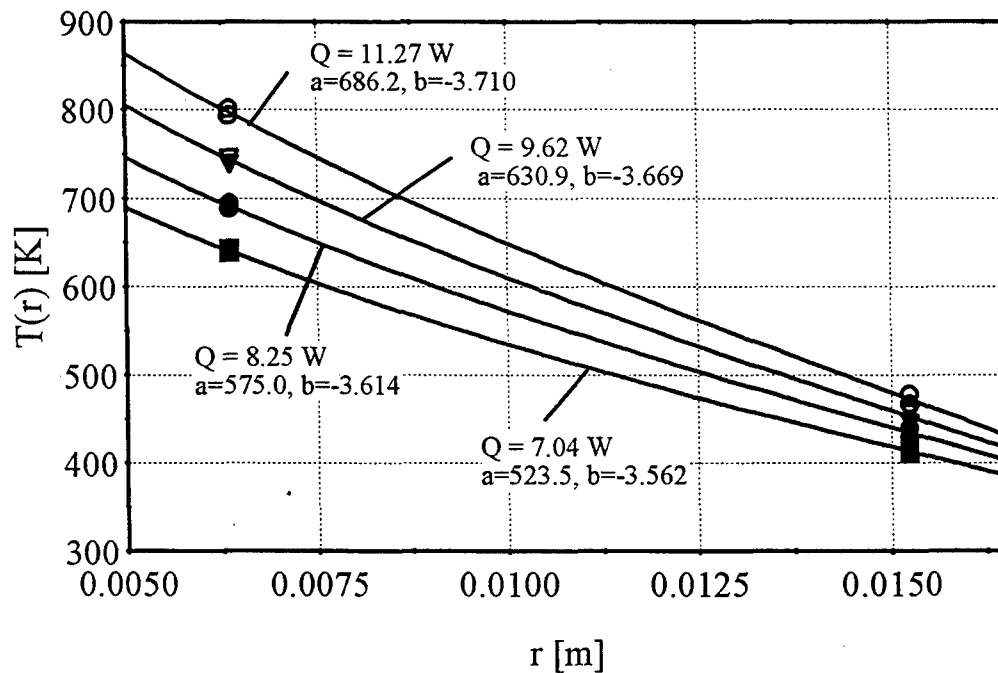


Figure D10. Radial Temperature Profiles in Molded Min-K (Group 2).



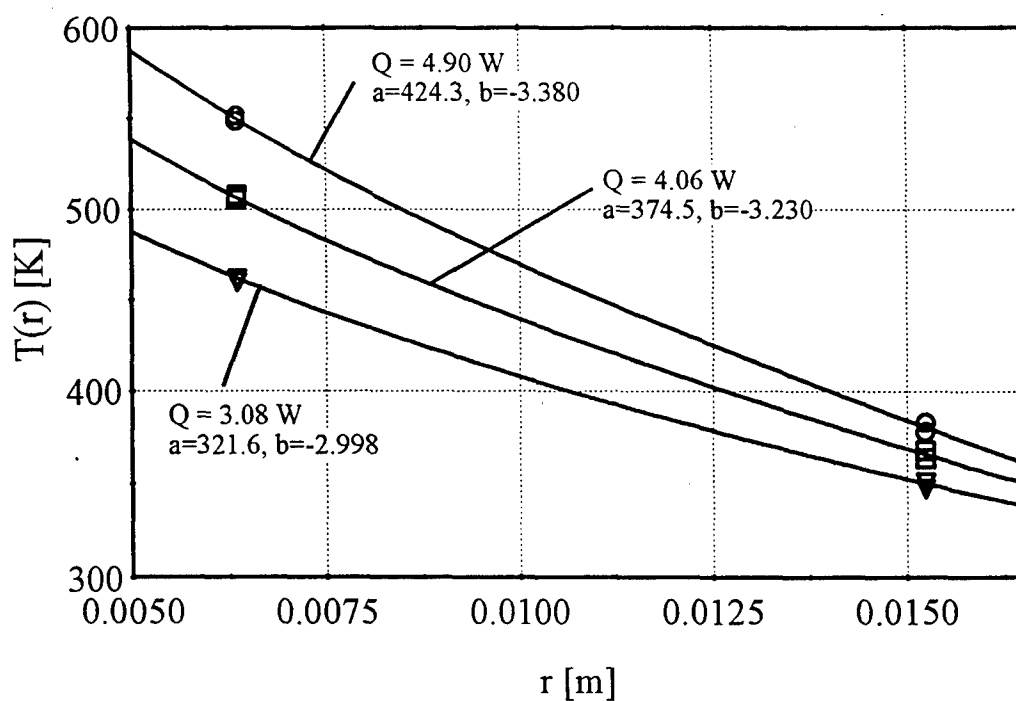


Figure D11. Radial Temperature Profiles in Molded Min-K (Group 3).

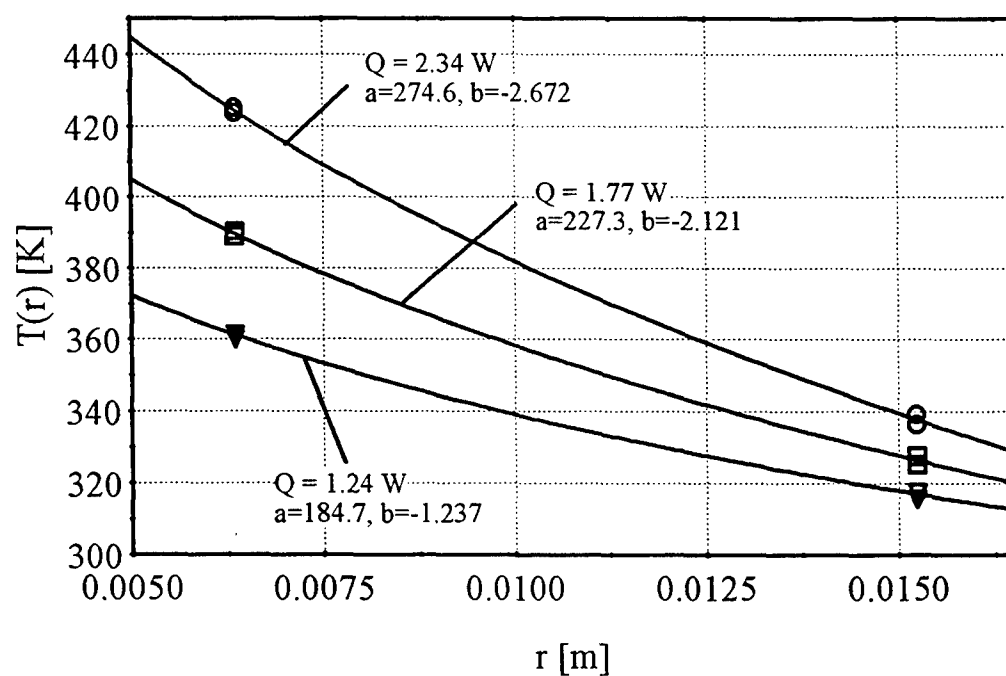


Figure D12. Radial Temperature Profiles in Molded Min-K (Group 4).

Table D1. Experimental Data and Processing of Thermal Conductivity of 1  $\mu\text{m}$  Alumina Powder.

powder size = 1 μm, porosity = 91.4%											
r3 = 5.715 mm											
r1 = 22.86 mm											
r2 = 12.7 mm											
Original Experimental Data, $k_{av} = (P/0.127)^2 \cdot 2.3026 \cdot \log(ro/ri) / (6.2832 / (To-Ti))$ [w/m k]											
TIME	V [v]	I [A]	P [w]	Vac.	T1 [k]	F2 [k]	F3 [k]	HEATER	F4 [k]	F5 [k]	F6 [k]
10/22,8:52	12.76	0.393	5.015	3.00E-06	583.1	653.7	745.7	506.2	729.4	648.0	578.8
10:15	14.02	0.435	6.099	3.00E-06	599.8	681.1	785.6	548.8	767.4	674.8	594.5
11:54	15.01	0.467	7.010	3.80E-06	619.1	708.6	822.1	585.6	802.5	701.6	612.9
13:15	16.54	0.519	8.584	1.40E-05	648.2	750.6	878.2	641.8	856.0	742.7	641.2
14:15	17.9	0.563	10.078	1.30E-05	682.0	795.0	935.3	696.6	911.4	786.6	674.5
16:20	17.9	0.563	10.078	1.10E-05	696.4	807.9	946.9	706.1	922.9	799.3	688.4
16:30	17.9	0.563	10.078	1.60E-05	700.8	811.9	950.5	709.3	926.5	803.3	692.8
10/23,7:00	17.9	0.563	10.078	3.80E-05	727.7	837.8	975.6	735.3	951.6	827.2	719.9
9:30	19.457	0.622	12.102	6.90E-06	755.8	878.7	1029.5	791.9	1003.9	869.0	746.7
12:45	19.457	0.622	12.102	3.50E-06	743.8	868.6	1021.3	784.6	996.3	859.1	734.7
14:00	19.457	0.622	12.102	2.50E-06	755.9	879.5	1030.4	793.0	1005.2	869.7	746.4
14:45	19.457	0.622	12.102	2.00E-06	758.1	881.2	1061.7	794.2	1006.4	871.4	748.6
15:40	19.457	0.622	12.102	1.60E-06	761.5	884.1	1034.0	796.3	1008.8	874.2	751.9
16:25	19.457	0.622	12.102	6.92E-06	763.1	885.5	1035.1	797.4	1009.9	875.6	753.5
10/24,7:00	19.457	0.622	12.102	3.80E-06	767.7	890.0	1038.5	801.3	1013.2	880.0	758.4
9:40	17.175	0.802	13.774	3.50E-06	785.5	889.6	1005.9	888.6	983.0	877.7	775.3
14:15	16.436	0.785	12.902	9.20E-06	769.4	868.6	979.6	859.8	957.6	856.6	759.5
10/25,8:15	8.311	0.344	2.859	1.30E-06	518.1	560.8	616.6	385.9	608.9	556.9	514.1
8:50	8.311	0.344	2.859	1.30E-06	517.8	560.6	616.3	385.7	608.6	556.6	513.8
9:30	6.358	0.257	1.634	1.30E-06	506.2	535.7	571.8	593.8	566.4	532.8	502.9
10:54	6.375	0.257	1.638	1.30E-06	491.5	519.6	556.6	580.0	551.2	516.9	488.6
16:08	6.407	0.257	1.647	1.30E-06	464.5	493.3	533.8	560.2	528.4	490.4	461.8
10/28,8:32	6.44	0.257	1.655	1.30E-08	443.4	473.6	517.2	545.7	511.5	471.1	440.8
10/29,7:00	6.95	0.267	1.856	8.20E-07	379.5	425.1	485.5	535.8	480.6	423.9	380.1
10/30,7:20	7.671	0.299	2.294	4.40E-07	398.7	451.6	518.1	572.8	512.8	450.0	399.3
10/30,14:1	8.459	0.334	2.825	4.40E-07	415.0	476.0	550.0	611.0	543.0	476.0	415.0
10/31,7:30	9.132	0.366	3.342	3.60E-07	435.8	503.3	581.9	648.6	574.6	503.5	435.6
11/1,7:30	9.789	0.395	3.867	2.90E-07	452.0	526.0	609.0	683.0	603.0	522.0	451.0
11/1,16:30	10.921	0.447	4.882	2.90E-07	481.7	564.8	657.2	742.2	647.6	560.0	479.1

Table D1. Experimental Data and Processing of Thermal Conductivity of 1  $\mu\text{m}$  Alumina Powder.

11/2,10:31	11.873	0.496	5.889	2.90E-07	505.2	597.4	697.2	793.3	686.1	591.2	501.3
11/3,9:57	12.891	0.548	7.064	2.90E-07	531.0	632.4	740.5	847.9	728.0	624.5	525.1
11/4,7:50	13.761	0.593	8.160	2.50E-07	552.2	661.3	776.3	893.7	762.3	652.4	544.4
11/4,16:00	14.91	0.654	9.751	2.50E-07	580.2	699.2	823.0	954.7	806.6	688.8	570.0
11/5,7:05	16.338	0.736	12.025	4.50E-07	614.4	745.4	879.8	1032.8	861.3	733.1	602.0
11/6,7:00	17.208	0.802	13.801	3.60E-07	637.5	775.8	915.9	1089.4	894.7	761.4	623.4
11/6,14:35	17.372	0.921	16.000	3.60E-07	654.9	794.7	933.4	1136.3	911.6	779.9	640.3
11/11,8:15	4.766	0.198	0.944	1.36E-07	343.4	366.8	404.9	436.9	400.5	365.2	341.8
11/12,7:30	2.846	0.109	0.310	8.20E-06	307.4	316.3	334.4	356.0	331.6	315.3	307.0
11/13,7:05	10.852	0.484	5.252	2.59E-06	487.8	544.3	604.8	685.4	596.5	539.6	481.0
TIME	V [V]	I [A]	P [w]	Vac.	FT #1 [K]	FT #2 [K]	FT #3 [K]	HEATER	FT #4 [K]	FT #5 [K]	FT #6 [K]
thermal conductivity from the fitting curve of measured temperature, $T = a(b \cdot \ln(x))^{0.5}$											
$T_{av}$ [K]	k [W/mK]	$T_{av}$ [K]	k [W/mK]	$T_{av}$ [K]	k [W/mK]	$T_{av}$ [K]	k [W/mK]	$T_{av}$ [K]	k [W/mK]	$T_{av}$ [K]	k [W/mK]
604.7	0.05506	780.9	0.04133	473.2	0.03439	505.4	0.03787	535.9	0.04160	567.6	0.04557
572.6	0.05214	756.3	0.04003	439.5	0.03194	467.4	0.03503	493.2	0.03829	521.6	0.04187
549.9	0.05007	739.4	0.03913	415.3	0.03018	440.1	0.03298	462.4	0.03590	488.2	0.03919
532.2	0.04846	726.4	0.03844	396.0	0.02878	418.3	0.03134	437.7	0.03398	461.4	0.03704
517.5	0.04712	715.7	0.03788	379.9	0.02761	399.9	0.02997	416.8	0.03235	438.7	0.03522
$T_{av}$ [K]	k [W/mK]	$T_{av}$ [K]	k [W/mK]	$T_{av}$ [K]	k [W/mK]	$T_{av}$ [K]	k [W/mK]	$T_{av}$ [K]	k [W/mK]	$T_{av}$ [K]	k [W/mK]
592.9	0.04885	639.5	0.05565	677.8	0.06160	719.5	0.067631	754.0	0.07319	797.5	0.08085
543.1	0.04474	584.2	0.05084	617.4	0.05611	653.5	0.061427	683.5	0.06635	721.2	0.07311
506.9	0.04176	544.0	0.04733	573.3	0.05211	605.1	0.05688	631.7	0.06132	665.0	0.06741
477.8	0.03936	511.5	0.04450	537.7	0.04887	565.9	0.053194	589.6	0.05724	619.2	0.06277
453.0	0.03732	483.8	0.04210	507.3	0.04610	532.3	0.050037	553.6	0.05374	579.8	0.05878
$T_{av}$ [K]	k [W/mK]	$T_{av}$ [K]	k [W/mK]	$T_{av}$ [K]	k [W/mK]	$T_{av}$ [K]	k [W/mK]	$T_{av}$ [K]	k [W/mK]	$T_{av}$ [K]	k [W/mK]
852.7	0.09149	886.2	0.10024	904.5	0.11608	397.2	0.02901				
769.4	0.08255	798.9	0.09037	817.2	0.10488	377.1	0.02754				
707.9	0.07596	734.5	0.08308	752.9	0.09662	362.9	0.02650				
657.8	0.07058	681.8	0.07712	700.5	0.08990	351.9	0.02570				
614.5	0.06594	636.4	0.07199	655.3	0.08410	342.7	0.02503				



Table D2. Experimental Data and Processing of Thermal Conductivity of 0.01  $\mu\text{m}$  Alumina Powder.

311.0	0.02707	510.5	0.06658	357.0	0.03121	395.3	0.03573	425.4	0.04161	459.9	0.05083
319.2	0.02177	539.0	0.07932	372.4	0.03047	415.1	0.03815	447.6	0.04622	484.1	0.05838
$T_{av}$ [K]	k [W/mK]	$T_{av}$ [K]	k [W/mK]	$T_{av}$ [K]	k [W/mK]	$T_{av}$ [K]	k [W/mK]	$T_{av}$ [K]	k [W/mK]	$T_{av}$ [K]	k [W/mK]
493.6	0.06187	521.0	0.07225	544.7	0.08166	569.3	0.09647	593.5	0.10969	614.9	0.12330
545.8	0.07428	578.1	0.08949	605.5	0.10281	631.8	0.12017	659.0	0.13723	681.8	0.15250
540.1	0.07893	571.6	0.09542	598.5	0.10874	624.3	0.12582	650.7	0.14303	672.7	0.15850
488.4	0.05930	515.3	0.06970	538.4	0.07905	562.2	0.09321	585.6	0.10661	606.2	0.11966
514.5	0.06921	543.3	0.08251	568.3	0.09380	593.3	0.10957	618.3	0.12493	639.9	0.13932
$T_{av}$ [K]	k [W/mK]	$T_{av}$ [K]	k [W/mK]	$T_{av}$ [K]	k [W/mK]	$T_{av}$ [K]	k [W/mK]	$T_{av}$ [K]	k [W/mK]	$T_{av}$ [K]	k [W/mK]
647.6	0.14574	666.6	0.16157	679.2	0.16988	692.1	0.16454	706.1	0.19136	707.5	0.19385
716.9	0.17716	736.5	0.19395	750.9	0.20540	765.9	0.20041	782.0	0.23470	782.8	0.23652
706.7	0.18421	725.6	0.19998	739.7	0.21138	754.2	0.20556	769.8	0.24080	770.4	0.24242
637.6	0.14079	655.7	0.15610	667.9	0.16447	680.3	0.15998	694.0	0.18669	695.2	0.18868
672.8	0.16291	691.7	0.17868	704.8	0.18858	718.3	0.18340	732.9	0.21444	733.9	0.21630
$T_{av}$ [K]	k [W/mK]	$T_{av}$ [K]	k [W/mK]	$T_{av}$ [K]	k [W/mK]	$T_{av}$ [K]	k [W/mK]	$T_{av}$ [K]	k [W/mK]	$T_{av}$ [K]	k [W/mK]
714.5	0.19974										
790.8	0.24458										
778.5	0.24937										
704.5	0.20856										
743.8	0.23027										

Table D3. Experimental Data and Processing of Thermal Conductivity of Molded Min-K.

--	--	--	--	--	--	--	--	--	--	--	--	--	--	--	--	--	--	--	--	--	--	--	--	--	--	--	--	--	--	--	--	--	--	--	--	--	--	--	--	--	--	--	--	--	--	--	--	--	--	--	--	--	--	--	--	--	--	--	--	--	--	--	--	--	--	--	--	--	--	--	--	--	--	--	--	--	--	--	--	--	--	--	--	--	--	--	--	--	--	--	--	--	--	--	--	--	--	--	--	--	--	--	--	--	--	--	--	--	--	--	--	--	--	--	--	--	--	--	--	--	--	--	--	--	--	--	--	--	--	--	--	--	--	--	--	--	--	--	--	--	--	--	--	--	--	--	--	--	--	--	--	--	--	--	--	--	--	--	--	--	--	--	--	--	--	--	--	--	--	--	--	--	--	--	--	--	--	--	--	--	--	--	--	--	--	--	--	--	--	--	--	--	--	--	--	--	--	--	--	--	--	--	--	--	--	--	--	--	--	--	--	--	--	--	--	--	--	--	--	--	--	--	--	--	--	--	--	--	--	--	--	--	--	--	--	--	--	--	--	--	--	--	--	--	--	--	--	--	--	--	--	--	--	--	--	--	--	--	--	--	--	--	--	--	--	--	--	--	--	--	--	--	--	--	--	--	--	--	--	--	--	--	--	--	--	--	--	--	--	--	--	--	--	--	--	--	--	--	--	--	--	--	--	--	--	--	--	--	--	--	--	--	--	--	--	--	--	--	--	--	--	--	--	--	--	--	--	--	--	--	--	--	--	--	--	--	--	--	--	--	--	--	--	--	--	--	--	--	--	--	--	--	--	--	--	--	--	--	--	--	--	--	--	--	--	--	--	--	--	--	--	--	--	--	--	--	--	--	--	--	--	--	--	--	--	--	--	--	--	--	--	--	--	--	--	--	--	--	--	--	--	--	--	--	--	--	--	--	--	--	--	--	--	--	--	--	--	--	--	--	--	--	--	--	--	--	--	--	--	--	--	--	--	--	--	--	--	--	--	--	--	--	--	--	--	--	--	--	--	--	--	--	--	--	--	--	--	--	--	--	--	--	--	--	--	--	--	--	--	--	--	--	--	--	--	--	--	--	--	--	--	--	--	--	--	--	--	--	--	--	--	--	--	--	--	--	--	--	--	--	--	--	--	--	--	--	--	--	--	--	--	--	--	--	--	--	--	--	--	--	--	--	--	--	--	--	--	--	--	--	--	--	--	--	--	--	--	--	--	--	--	--	--	--	--	--	--	--	--	--	--	--	--	--	--	--	--	--	--	--	--	--	--	--	--	--	--	--	--	--	--	--	--	--	--	--	--	--	--	--	--	--	--	--	--	--	--	--	--	--	--	--	--	--	--	--	--	--	--	--	--	--	--	--	--	--	--	--	--	--	--	--	--	--	--	--	--	--	--	--	--	--	--	--	--	--	--	--	--	--	--	--	--	--	--	--	--	--	--	--	--	--	--	--	--	--	--	--	--	--	--	--	--	--	--	--	--	--	--	--	--	--	--	--	--	--	--	--	--	--	--	--	--	--	--	--	--	--	--	--	--	--	--	--	--	--	--	--	--	--	--	--	--	--	--	--	--	--	--	--	--	--	--	--	--	--	--	--	--	--	--	--	--	--	--	--	--	--	--	--	--	--	--	--	--	--	--	--	--	--	--	--	--	--	--	--	--	--	--	--	--	--	--	--	--	--	--	--	--	--	--	--	--	--	--	--	--	--	--	--	--	--	--	--	--	--	--	--	--	--	--	--	--	--	--	--	--	--	--	--	--	--	--	--	--	--	--	--	--	--	--	--	--	--	--	--	--	--	--	--	--	--	--	--	--	--	--	--	--	--	--	--	--	--	--	--	--	--	--	--	--	--	--	--	--	--	--	--	--	--	--	--	--	--	--	--	--	--	--	--	--	--	--	--	--	--	--	--	--	--	--	--	--	--	--	--	--	--	--	--	--	--	--	--	--	--	--	--	--	--	--	--	--	--	--	--	--	--	--	--	--	--	--	--	--	--	--	--	--	--	--	--	--	--	--	--	--	--	--	--	--	--	--	--	--	--	--	--	--	--	--	--	--	--	--	--	--	--	--	--	--	--	--	--	--	--	--	--	--	--	--	--	--	--	--	--	--	--	--	--	--	--	--	--	--	--	--	--	--	--	--	--	--	--	--	--	--	--	--	--	--	--	--	--	--	--	--	--	--	--	--	--	--	--	--	--	--	--	--	--	--	--	--	--	--	--	--	--	--	--	--	--	--	--	--	--	--	--	--	--	--	--	--	--	--	--	--	--	--	--	--	--	--	--	--	--	--	--	--	--	--	--	--	--	--	--	--	--	--	--	--	--	--	--	--	--	--	--	--	--	--	--	--	--	--	--	--	--	--	--	--	--	--	--	--	--	--	--	--	--	--	--	--	--	--	--	--	--	--	--	--	--	--	--	--	--	--	--	--	--	--	--	--	--	--	--	--	--	--	--	--	--	--	--	--	--	--	--	--	--	--	--	--	--	--	--	--	--	--	--	--	--	--	--	--	--	--	--	--	--	--	--	--	--	--	--	--	--	--	--	--	--	--	--	--	--	--	--	--	--	--	--	--	--	--	--	--	--	--	--	--	--	--	--	--	--	--	--	--	--	--	--	--	--	--	--	--	--	--	--	--	--	--	--	--	--	--	--	--	--	--	--	--	--	--	--	--	--	--	--	--	--	--	--	--	--	--	--	--	--	--	--	--	--	--	--	--	--	--	--	--	--	--	--	--	--	--	--	--	--	--	--	--	--	--	--	--	--	--	--	--	--	--	--	--	--	--	--	--	--	--	--	--	--	--	--	--	--	--	--	--	--	--	--	--	--	--	--	--	--	--	--	--	--	--	--	--	--	--	--	--	--	--	--	--	--	--	--	--	--	--	--	--	--	--	--	--	--	--	--	--	--	--	--	--	--	--	--	--	--	--	--	--	--	--	--	--	--	--	--	--	--	--	--	--	--	--	--	--	--	--	--	--	--	--	--	--	--	--	--	--	--	--	--	--	--	--	--	--	--	--	--	--	--	--	--	--	--	--	--	--	--	--	--	--	--	--	--	--	--	--	--	--	--

## APPENDIX E: CALCULATION OF MEASUREMENT UNCERTAINTIES IN VACUUM TESTS OF PX-SERIES CELLS

This appendix regroups detailed calculations of the measurement uncertainties in the vacuum tests of PX-series cells at AFRL. A nomenclature of the variables used in this appendix can be found in Chapter 9 (Section 9.1).

In the test setup, all detected analog signals (voltage) by the sensors are read and converted into digital signals by a HP3852 data acquisition/controller system. The experimental uncertainty in the reading depends on whether a parameter is directly measured, or is calculated based on measured quantities. The former is obtained directly from the calibration of the measuring devices, while the latter is determined in terms of the uncertainties of measured quantities contributing to it. When an experimental quantity,  $y$ , is expressed in terms of measured parameters,  $x_1, x_2, \dots, x_n$ ,

$$y = f(x_1, x_2, \dots, x_n), \quad (E1)$$

its uncertainty,  $\delta y$ , can be calculated as (Beckwith and Marangoni 1990):

$$\delta y = \sqrt{\left(\frac{\partial y}{\partial x_1} \delta x_1\right)^2 + \left(\frac{\partial y}{\partial x_2} \delta x_2\right)^2 + \dots + \left(\frac{\partial y}{\partial x_n} \delta x_n\right)^2}, \quad (E2)$$

where  $\delta x_i$  is the uncertainty in measured quantity,  $x_i$ .

An HP44705A card is used with the HP3852 to scan the voltage signals. The setting for Integration Time in Number of Power Line Cycles (NPLC) is 0.005, and its reading accuracy depends on the voltage range (including one-year-later modification of 0.1%):

$$\text{Read} * 0.03\% + 0.02 \text{ mV} \quad \text{Reading} < 30 \text{ mV} \quad (E3)$$

$$\text{Read} * 0.018\% + 0.04 \text{ mV} \quad 30 \text{ mV} < \text{Reading} < 3000 \text{ mV} \quad (E4)$$

$$\text{Read} * 0.018\% + 0.4 \text{ mV} \quad 0.3 \text{ V} < \text{Reading} < 3 \text{ V} \quad (E5)$$

$$\text{Read} * 0.018\% + 4 \text{ mV} \quad 3 \text{ V} < \text{Reading} < 30 \text{ V} \quad (E6)$$

In the following analysis, an uncertainty is the maximum possible measurement error, which, in most cases, occurs at the lowest reading.

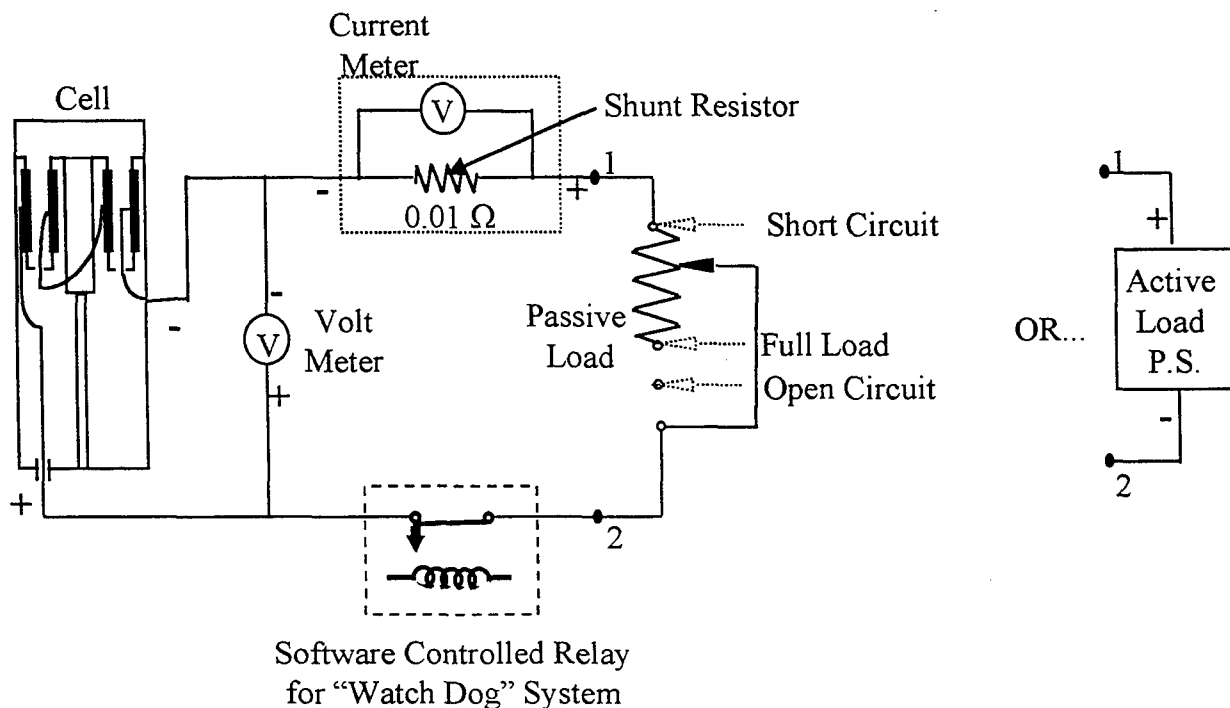


Figure E1. Electric Circuit Measurement for Single-Cell Test.

## E.1 CELL ELECTRIC OUTPUT

The electric load circuit and the electric power output measurement are shown in Figure E1. The output electric power of a cell is measured by measuring the current and voltage of the cell.

The voltage is measured at the electrodes just outside the cell in order to include all external voltage (voltage loss) of the cell. In the tests, the cell output voltage ranges between 0.24 V (nominal short circuit) and 5 V (open circuit). It crosses two accuracy ranges, see Equations (E3) and (E4). The uncertainty is:

$$\frac{\delta V_e}{V_e} = 0.018\% + \frac{0.04}{V_e} \leq 0.0347\%, \text{ for } V_e = 0.24 \sim 0.3 \text{ V, and}$$

$$\frac{\delta V_e}{V_e} = 0.018\% + \frac{0.4}{V_e} \leq 0.151\%, \text{ for } V_e = 0.3 \sim 5 \text{ V.}$$

So, the uncertainty in the measured cell voltage is 0.151% over the cell operation range.



The cell current is measured by reading the voltage,  $V_A$ , across a shunt resistor,  $R_A$ , see Figure E1. The current is a function of  $R_A$  and  $V_A$ :

$$I_e = \frac{V_A}{R_A} \quad (E7)$$

In the test, the cell current varies in the range 0.5 – 5 A, which corresponds to a change in  $V_A$  between 0.005 – 0.05 V from Equation (E7). Using Equation (E2), the uncertainty in the cell current is given by:

$$\frac{\delta I_e}{I_e} = \sqrt{\left(\frac{\delta V_A}{V_A}\right)^2 + \left(\frac{\delta R_A}{R_A}\right)^2} \quad (E8)$$

where,  $\frac{\delta R_A}{R_A} = 0.01$ , and  $\frac{\delta V_A}{V_A}$  is determined by Equations (E3) and (E4):

for  $I_e = 0.5 - 3$  A,

$$\frac{\delta I_e}{I_e} = \left[ \left( 0.03\% + \frac{0.02}{10I_e} \right)^2 + 0.01^2 \right]^{0.5} = 1.09\% ; \quad (E9)$$

for  $I_e = 3 - 5$  A

$$\frac{\delta I_e}{I_e} = \left[ \left( 0.018\% + \frac{0.04}{10I_e} \right)^2 + 0.01^2 \right]^{0.5} = 1.01\% . \quad (E10)$$

Therefore, the uncertainty in the measured cell current is 1.09%.

The cell power output is determined by the measured cell voltage and current:

$$P_e = V_e I_e \quad (E11)$$

From Equation (E2), the uncertainty is:

$$\frac{\delta P_e}{P_e} = \sqrt{\left(\frac{\delta V_e}{V_e}\right)^2 + \left(\frac{\delta I_e}{I_e}\right)^2} = \sqrt{0.00151^2 + 0.01089^2} = 1.1\% \quad (E12)$$

Therefore, the uncertainty in the measured cell power output is 1.1%.

## E.2 HEATING POWER, $Q_{in}$

The cell is heated by a Boro-electric heater controlled by a HP6554A DC power supply, with an output capacity of 0–60 V/ 0–9 A. Both voltage and current (converted to voltage signal for measurement) are read by the HP3852/44705A. The range of the heating power is 30 – 70 W. The accuracy of the power supply @  $25 \pm 5^\circ\text{C}$  is:

$$\text{Voltage:} \quad \text{Read} * 0.07\% + 40 \text{ mV}, \quad (\text{E13})$$

$$\text{Current} \quad \text{Read} * 0.15\% + 4.1 \text{ mA}. \quad (\text{E14})$$

The voltage range of the heating power of the heater is 15 – 30 V, which is directly measured by the HP3852/HP44705A. From Equation (E13):

$$\frac{\delta V_{in}}{V_{in}} = 0.018\% + \frac{0.004}{15} = 0.0447\%, \quad (\text{E15})$$

The uncertainty in the measured voltage of the heater is 0.0447%.

The power supply has a voltage signal output for the current measurement. In the application, this voltage signal is measured and converted back to the current. The conversion factor is 0.5556 V/A. The range of the heater current is 1.5 – 3 A, corresponding to a voltage reading of 0.833 – 1.67 V. Combining Equations (E6) and (E13) gives:

$$\begin{aligned} \left(\frac{\delta I_{in}}{I_{in}}\right)_{\text{supply}} &= 0.15\% + \frac{0.0041}{1.5} = 0.177\% \\ \left(\frac{\delta V_{I_{in}}}{V_{I_{in}}}\right)_{\text{HP3852}} &= 0.018\% + \frac{0.004}{0.833} = 0.498\%, \\ \left(\frac{\delta I_{in}}{I_{in}}\right)_{\text{max}} &= 0.675\% \end{aligned} \quad (\text{E16})$$

and the uncertainty in the measured heater current is 0.675%.

The heating power of the heater is determined by the measured voltage and current from the power supply:

$$Q_e = V_{in} I_{in}. \quad (\text{E17})$$

Using Equation (E2), one obtains:

$$\frac{\delta Q_{in}}{Q_{in}} = \sqrt{\left(\frac{\delta V_{in}}{V_{in}}\right)^2 + \left(\frac{\delta I_{in}}{I_{in}}\right)^2} = 0.676\% . \quad (E18)$$

The uncertainty in the measured heating power is 0.676%.

### E.3 TEMPERATURE, T

K-type thermocouples are used in the test setup, which have an accuracy of 1.1 °C or 0.4% of reading, whichever is greater. The thermocouples are scanned by HP44708A and HP44710A multi-plexers with software thermal compensation (0.1 °C error), and measured by an HP3852. The uncertainty in the measured temperature is caused by error of thermocouple sensor and reading sensor voltage.

The lowest temperature (corresponding to the largest uncertainty) measured in the tests is the room temperature (and inlet temperature in the air loop),  $T_{room} = 21^\circ\text{C}$ , which has a sensor voltage of  $EMF = 0.838\text{ mV}$ . Using Equation (E3), the uncertainty in room temperature is:

$$\left(\frac{\delta V_T}{V_T}\right) = 0.03\% + \frac{0.02}{0.838} = 2.42\%$$

$$\delta V_T = 0.838 * 0.03\% + 0.02 = 0.02025\text{mV},$$

$$\delta T_V = 0.492^\circ\text{C},$$

$$\delta T_{room} = 1.1 + 0.1 + 0.49 = 1.69^\circ\text{C},$$

$$\left(\frac{\delta T_{room}}{T_{room}}\right) = 8.05\% . \quad (E19)$$

Therefore, the uncertainty in measured room temperature is 8.05%.

Besides the measured room temperature and air loop inlet temperature, all other measured temperatures are greater than 450 K (177 °C), which correspond to  $EMF = 7.26\text{ mV}$ .

$$\delta V_T = 7.26 * 0.03\% + 0.2 = 0.02218\text{ mV}$$

$$\delta T_V = 0.5707^\circ\text{C}$$

$$\frac{\delta T}{T} = \frac{1.1 + 0.1 + 0.548}{177} = 0.99\% , \quad (E20)$$

or

$$\frac{\delta T}{T} = 0.4\% + \frac{0.548}{177} = 0.71\% . \quad (E21)$$

Therefore, the uncertainty in other measured temperatures is 0.99%.

#### E.4 HEAT REJECTION AT THE CELL CONDENSER, $Q_{air}$

The heat rejection at the cell condenser is a combination of several measured parameters:

$$Q_{air} = \int_{T_{in}}^{T_{out}} \dot{m} C_p dT, \quad (E22)$$

where  $\dot{m}$  is the mass flow rate of the cooling air, and is independent of air temperature. It can be directly converted from the standard volumetric flow rate,  $V_{air,st}$ , measured using an FMA-772-V-AIR air flow meter/controller from OMEGA:

$$\dot{m} = \rho_{st} V_{air,st}, \quad (E23)$$

where  $\rho_{st}$  and  $V_{air,st}$  are the air density and flow rate at the standard conditions ( $P = 1$  atm and  $T = 21.1$  °C).  $C_p$  is the air thermal capacity at temperature  $T$ . It is insensitive to the air temperature in the range observed in the tests. Experimental data of  $C_p$  can be fitted very well by a linear function of the temperature. With a linear  $C_p$  function of temperature, Equation (E22) can be analytically integrated as:

$$Q_{air} = \dot{m} C_{p,av} \Delta T, \quad (E24)$$

where  $C_{p,av}$  is the thermal capacity at the average temperature,  $T_{av}$ , of air inlet,  $T_{in}$ , and outlet,  $T_{out}$ :

$$T_{av} = (T_{in} + T_{out})/2.$$

$\Delta T$  is the temperature difference:

$$\Delta T = T_{out} - T_{in}.$$

Using Equation (E2), the uncertainty in the heat rejection is given by:

$$\frac{\delta Q_{air}}{Q_{air}} = \sqrt{\left(\frac{\delta \rho_{st}}{\rho_{st}}\right)^2 + \left(\frac{\delta C_p}{C_p}\right)^2 + \left(\frac{\delta \Delta T}{\Delta T}\right)^2 + \left(\frac{\delta V_{air,st}}{V_{air,st}}\right)^2}. \quad (E25)$$

At the test temperature, air is an ideal gas and has the density:

$$\rho_{st} = \frac{353.18}{T} \quad (E26)$$

The uncertainty in the air density is negligible.

The smallest temperature difference is:

$$\Delta T = 177 - 21 = 156 \text{ } ^\circ\text{C}$$

From Section E.3:

$$\begin{aligned} \delta T &= \sqrt{\delta T_{21}^2 + \delta T_{177}^2} \\ &= \sqrt{1.69^2 + 1.75^2} = 2.433 \end{aligned}$$

and

$$\frac{\delta \Delta T}{\Delta T} = \frac{2.433}{156} = 1.56\%$$

Therefore, the uncertainty in the measured temperature difference is 1.56%.

Experimental data of air specific heat capacity was taken from Incropera and Dewitt (1990). The fitting curve of the data is a linear function of temperature:

$$C_p = 0.9562 + 1.588 \times 10^{-4} T_{av}.$$

Discrepancy in the fitting is less than 0.5%.

A FMA-772-V-AIR air flow/meter/controller is used to measure and control the cooling air flow. The measurement range (full scale) is 20 SLPM (Standard Litter Per Minute). Its accuracy is  $\pm 1.5\%$  of full scale, or 0.3 SLPM. The sensor converts the flow rate into electric voltage, with a conversion factor of 4 SLPM/V, which is read by the HP3852/HP44705. In the tests, the minimum flow rate for carrying out the heat rejection is 4.8 L/min, which has a reading of 1.2 V. Combining the two uncertainties from the flow meter itself and voltage reading:

$$\frac{\delta V_{air}}{V_{air}} = \frac{0.3}{4.8} + \left( 0.018\% + \frac{0.4}{1.2 * 1000} \right) = 6.29\%,$$

the uncertainty in the measured air flow rate is 6.29%.

Using Equation (E25) and the results from Sections E.1 to E.4, the uncertainty in the measured heat rejection is:

$$\frac{\delta Q_{\text{air}}}{Q_{\text{air}}} = \sqrt{0.0149^2 + 0.005^2 + 0.06285^2} = 6.48\% .$$

Results of the uncertainty analysis of the experimental setup are summarized in Table E1.

Table E1. Measurement Uncertainty Analysis of PX-Series Cell Tests at AFRL.

Measured Parameters	Measurement Equipment	Test Measurement Range	Equipment Accuracy	Uncertainty $\pm$	Note
Cell Voltage, $V_e$	HP3852/44705A	0.24 ~ 5 V	Read 0.018%+0.04mV, 0.03~0.3 V Read 0.018%+0.4mV, 0.3~3 V Read 0.018%+4mV, 3~30 V	0.2%	
Cell Current, $I_e$	HP3852/44705A	0.5 ~ 5 A ( $V_A=5\sim60\text{mV}$ )	$V_A 0.02\%+0.02\text{mV}$ , $V_A < 30\text{ mV}$ $V_A 0.018\%+0.04\text{mV}$ , $V_A = 30\sim300\text{ mV}$	1.1%	$V_A = I_e R_A$ $R_A = 0.01 \pm 1\% \Omega$
Cell Power, $P_e$	$P_e = V_e I_e$			1.2%	
Heater Voltage, $V_{in}$	HP6554A Supply HP3852/44705A	DC 1.5 ~ 3 A	Read 0.07%+40 mV	0.05%	
Heater Current, $I_{in}$	HP6554A Supply HP3852/44705A	DC 15 ~ 30 V	Read 0.15%+4.1 *mV	0.68%	
Heater Power, $Q_{in}$	$Q_{in} = V_{in} I_{in}$			0.7%	
Temperature, T	K-Type HP3852/44705A /44708	< 177 °C 450 ~ 1300 K	max{1.1 °C, read0.4%} + 0.1 + $\delta T_v$ Note: $\delta T_v$ is the error from the reading of voltage from a thermocouples, using HP3852/44705A	1.7% 1.0%	
Temperature, $(T_{out}-T_{in})_{air}$	K-Type HP3852/44705A /44708	156 ~ 300 °C		1.56	
Air Flow Rate, $V_{air}$	FMA-772-V-AIR Controller/Meter HP3852/44705A	4.8 ~ 20 SLM	1.5% of full scale (20 SLM) (0.3 + $\delta V_{air}$ )/reading Note: $\delta V_{air}$ is the error from the reading of voltage from a thermocouples, using HP3852/44705A	6.29	standard condition of meter: 1 atm and 21.1 °C
Rejected Heat, $Q_{air}$	$Q_{air} = p V_{air} C_p (T_{out}-T_{in})$			6.48	

## DISTRIBUTION LIST

AUL/LSE

Bldg 1405 - 600 Chennault Circle

Maxwell AFB, AL 36112-6424 1 cy

DTIC/OCP

8725 John J. Kingman Rd, Suite 0944

Ft Belvoir, VA 22060-6218 2 cys

AFSAA/SAI

1580 Air Force Pentagon

Washington, DC 20330-1580 1 cy

AFRL/PSTL

Kirtland AFB, NM 87117-5776 2 cys

AFRL/PSTP

Kirtland AFB, NM 87117-5776 1 cy

Institute for Space and Nuclear Power Studies

Department of chemical and Nuclear Engineering

University of New Mexico

Farris Engineering Center, Room 239

Albuquerque, NM 87131 1 cy

AFRL/VS/Dr Fender

Kirtland AFB, NM 87117-5776 1 cy

Official Record Copy

AFRL/VSDV/CLAY MAYBERRY 4 cys